OPG's DEEP GEOLOGIC

REPOSITORY

FOR LOW & INTERMEDIATE LEVEL WASTE

Hydrogeologic Modelling

March 2011

Prepared by: J.F. Sykes, S.D. Normani, and Y. Yin

NWMO DGR-TR-2011-16

OPG's DEEP GEOLOGIC

REPOSITORY

FOR LOW & INTERMEDIATE LEVEL WASTE

Hydrogeologic Modelling

March 2011

Prepared by: J.F. Sykes, S.D. Normani, and Y. Yin

NWMO DGR-TR-2011-16

THIS PAGE HAS BEEN LEFT BLANK INTENTIONALLY

Document History

Title:	Hydrogeologic Modelling		
Report Number:	NWMO DGR-TR-2011-16		
Revision:	R000	**Date:**	March 2011
AECOM Canada Ltd.			
Prepared by:	J.F. Sykes (University of Waterloo), S.D. Normani (University of Waterloo), Y. Yin (University of Waterloo)		
Reviewed by:	R.E.J. Leech		
Approved by:	R.E.J. Leech		
Nuclear Waste Management Organization			
Reviewed by:	M. Jensen		
Accepted by:	M. Jensen		

THIS PAGE HAS BEEN LEFT BLANK INTENTIONALLY

EXECUTIVE SUMMARY

A Deep Geologic Repository (DGR) for Low and Intermediate Level Waste (L&ILW) has been proposed by Ontario Power Generation (OPG) for the Bruce nuclear site in the Municipality of Kincardine, Ontario, Canada. This report presents hydrogeologic modelling and analyses that were completed as part of the Geosynthesis DGR work program. As envisioned, the proposed DGR would be constructed at a depth of about 680 m below ground surface within the argillaceous Ordovician limestone of the Cobourg Formation. The objectives of this report are to develop the regional-scale hydrogeological conceptual model for the DGR site, to undertake numerical modelling using the computational models FRAC3DVS-OPG and TOUGH2-MP and to support the safety case for the DGR. A primary focus of the numerical modelling study is the investigation of a DGR program hypothesis that solute transport in the Ordovician sediments is diffusion dominant.

Within the geologic setting of southern Ontario, the Bruce nuclear site is positioned along the eastern flank of the Michigan Basin. Regional well logs from the Oil, Gas and Salt Resources (OGSR) Library in London, Ontario and data from deep boreholes of the DGR field study at the Bruce nuclear site were used to define the structural contours at the regional and site scale of the up to 31 bedrock units/formation/groups present above the Precambrian crystalline basement. The regional-scale domain encompasses an area of approximately 18,000 km^2 and extends to the deepest points in Lake Huron and Georgian Bay. From a hydrogeologic perspective, the domain can be subdivided into three ground water systems at the Bruce nuclear site: a shallow zone characterized by the units of the Devonian and extending to the base of the Bass Islands Formation; an intermediate zone that extends from the base of the Bass Islands Formation to the Manitoulin Formation and includes the low permeability units of the Salina and the more permeable Niagaran Group; and a deep groundwater domain or zone that extends from the base of the Manitoulin to the Precambrian. A significant aquifer in the intermediate zone is the Niagaran Group which includes the Guelph, Goat Island, Gasport and Lions Head units. While these units can be differentiated in the DGR boreholes at the Bruce nuclear site, the OGSR well logs do not allow their identification. The Cambrian sandstone is the most significant aquifer in the deep zone at the DGR site. This formation is absent over the Algonquin Arch and outcrops west of Lake Michigan and north of Sault Sainte Marie, Ontario in a small band more than 300 km northwest of the DGR site.

The conceptual model for the ground water system was developed using data from the DGR site characterization program. Hydraulic parameters for the model hydrostratigraphic units were defined using data from the DGR site boreholes and from lab analyses of cores. Borehole data included hydraulic conductivities from straddle-packer hydraulic tests and pressure measurements from the Westbay MP38 and MP55 multi-level groundwater monitoring system. Data from this system indicate that units of the Salina and the Ordovician sediments are under-pressured relative to hydrostatic levels associated with ground surface at the DGR site. The Niagaran is slightly over-pressured while the Cambrian is significantly over-pressured. Core analyses yielded estimates of porosity, Young's modulus, Poisson's ratio, water saturations and gas saturations. Rock cores and opportunistic water samples were used to define the spatial distribution of the total dissolved solids concentration and water density. Layer dependent specific storage coefficients and one-dimensional loading efficiencies were calculated using field and laboratory data. The conceptual model of the Bruce DGR site required the development of constitutive models that relate the fluid density and viscosity to the fluid total dissolved solids concentration and water pressure.

The hydrogeological modelling strategy adopted for the proposed DGR at the Bruce nuclear site was to explore the processes and mechanisms relevant to groundwater system stability and the long-term performance of the multiple geologic barriers hosting and isolating the DGR. This study used four different numerical models and two different computational models to evaluate groundwater flow and solute transport. The modelling examined: regional-scale saturated density-dependent flow for a domain centred on the DGR; site-scale saturated density-dependent flow for a domain centred on the DGR; density-dependent flow for an approximately east-west cross section of the Michigan Basin; and, one-dimensional two-phase gas and water flow analyses of a stratigraphic column at the DGR. The regional-scale, site-scale, and basin cross-section modelling were accomplished using the computational model FRAC3DVS-OPG. To investigate the hypothesis that the under-pressures in the Ordovician sediments may indicate the presence of a gas phase, the two-phase air and water model TOUGH2-MP was used. The parameter perturbation and scenarios analyses of the hydrogeological modelling study involved a large number of simulations using the four numerical models.

Important in the analyses of the hydrogeologic modelling study is the selection of the performance measure used to evaluate the system. The traditional metric of average water particle travel time is based solely on advective velocities. It is an inappropriate measure for geologic units where solute transport is controlled by diffusion. The use of lifetime expectancy and the related groundwater age is a more appropriate metric for such a system. Lifetime expectancy, a stochastic variable, can be estimated by determining the probability density function of the time required for water particles at a spatial position in a groundwater system to reach potential outflow points. The particles can migrate to the outflow points by both advection and hydrodynamic dispersion. The hydrodynamic dispersion includes both mechanical dispersion and diffusion. In this study only the first moment of the life expectancy is estimated, with the measure being expressed as the Mean Life Expectancy (MLE). Conservative tracers also are used to evaluate issues such as the diffusive dominance of solute transport in the low permeability units at the DGR site. Péclet numbers are used to assess whether solute transport is dominated by diffusion or advection. The Péclet number is a ratio of the product of the pore water velocity and a characteristic length to the effective diffusion coefficient. While literature indicates that the characteristic length used to estimate Péclet numbers should be to the order of the size of grains, conservative estimates are determined in this study by using a characteristic length of 1 metre.

Energy gradients and groundwater velocities in the Michigan Basin are density-dependent and hence a fully-coupled transient flow and brine transport analysis is required for their estimation. The coupling of the flow equation and the brine transport equation results because both the water density and viscosity are dependent on the Total Dissolved Solids (TDS) concentration. A solution with a TDS concentration of zero will correspond to a water density of 1,000 kg/m^3 at standard pressure and temperature. In comparison, water with a TDS concentration of 300 g/L will have a density of approximately 1,200 kg/m^3. The study methodology determined a pseudo-equilibrium solution for density-dependent flow at one million years after the imposition of an initial total dissolved solids distribution in the regional domain.

The environmental head profile from the assumed TDS concentrations and measured pressures at the DGR boreholes indicates that the Cambrian is over-pressured relative to the elevation of the surface while the Ordovician shale and limestone units are significantly under-pressured. An essential requirement of the abnormal pressures of the Cambrian is overlying extensive low hydraulic conductivity strata. The low pressures in the Ordovician may be the result of stress relief as a result of significant removal of mass through erosion, that was at a rate greater than that of water influx to these units from the over- and under-lying units with higher pressure; the pressure distribution is still evolving. The low pore fluid pressures also may indicate the presence

of a trapped non-wetting gas phase that would result in an effective hydraulic conductivity that is significantly less than the corresponding saturated hydraulic conductivities for the units. Other possible explanations of the under-pressures include osmosis, crustal flexure and glaciation. Consistent with the various theories for the under-pressures is the requirement of vertical hydraulic conductivities that are on the order of 1×10^{-14} m/s or lower for the Ordovician units. The DGR straddle-packer hydraulic tests yielded data that support this finding.

The under-pressures in the Ordovician can be explained by the presence of a gas phase in the rock. The two-phase air water computational model TOUGH2-MP was used in the analyses. The analyses indicate that the gas phase will be reduced by partitioning of methane to the water phase and then solute transport of the dissolved methane to the higher porosity Cambrian that underlies the Black River Group. The results also indicate that solute diffusion is most likely being overestimated in the analyses of this study.

Using a site-scale numerical model developed from the base-case regional-scale model using the embedment approach and a conservative tracer, this study concludes that solute transport in the Ordovician limestone and shale is diffusion dominant. Péclet numbers for the Cobourg limestone were estimated to be less than 0.001 for all of the analyses undertaken in the numerical modelling study. The Mean Life Expectancy or average time for particles at the location of proposed DGR to reach the boundary of the base-case regional-scale groundwater system was estimated to be 164 Ma. All scenarios that honoured the parameters of the field and laboratory study yielded estimated MLEs that are greater than 150 Ma.

A hypothetical undetected 2 km long discrete fracture zone between the Cambrian and the Niagaran located at various distances from the location of the proposed DGR was investigated using the site-scale numerical model. It is concluded that the presence of such a transmissive fracture zone located 1 km or closer to the location of the proposed DGR is inconsistent with the vertical gradient observed in the DGR boreholes. If a transmissive fracture were present, it would lower the heads in the Cambrian and raise the heads in the Niagaran relative to the heads expected for the non-fractured rock. The chemical characteristics of the water in the Niagaran (Guelph) as compared to that of the Cambrian sandstone are also inconsistent with that expected if a transmissive fracture were present proximal to the location of the proposed DGR. Regardless, breakthrough of a conservative tracer to the Niagaran and the Cambrian is insensitive to a hypothetical discrete fracture zone 1 km west of the location of the proposed DGR.

The impact of glaciation and deglaciation on the groundwater system was investigated in paleohydrogeologic scenarios. The model results indicated that basal meltwater does not penetrate below the units of the Salina at the DGR site. The most significant consequence of glacial loading is the generation, when ice is present, of higher pressures throughout the rock column, with the level dependent on the one-dimensional loading efficiency of the rock mass. The estimation of the pressures during glaciation was undertaken assuming saturated flow conditions; the presence of a possible gas phase in the Ordovician would result in the rock carrying a greater load and exert less influence on the water pressure distribution. The simulations of the paleohydrogeologic scenarios support the finding that it is unlikely that either the under-pressures or over-pressures measured in the DGR boreholes are related to stress loading during glaciation and stress relief during deglaciation. Significant factors contributing to this conclusion are the pressure boundary condition at the base of the glacier, the time of ice-sheet loading relative to the duration of load relief, and the relatively low storage coefficients for the Ordovician rock.

An investigation of density-dependent saturated flow in a cross-section of the Michigan Basin suggests that the over-pressures in the Cambrian are a result of the topography,

hydrostratigraphic layer geometry and the spatial distribution of the total dissolved solids concentration in the Michigan Basin. Other findings of the analysis are that the pore waters in the Ordovician are stagnant.

The suite of analyses undertaken in this hydrogeological modelling study support the hypothesis that solute transport in the Ordovician sediments is diffusion dominant even when the rock is perturbed by factors such as glaciation and deglaciation. The permeability of the Ordovician rock measured in the straddle-packer hydraulic testing is significantly lower than that required for advection to contribute to solute migration. Regardless of the cause of the under-pressures in the Ordovician limestone and shale, it will take considerably more than 1 Ma for the pressures to equilibrate to the levels in the Cambrian and Niagaran group. During this period, gradients will continue to be inward until the water deficit in the Ordovician is met. The analyses of this study indicate that there are multiple barriers between the location of the proposed DGR and the biosphere. In addition to the long travel times that result when diffusion is the major, if not sole, transport mechanism, other barriers include the long travel paths in the Niagaran and Cambrian should solute reach those units, and the attenuation capacity of the Salina and units of the lower Silurian where solute transport, if it can occur, is diffusion dominant.

TABLE OF CONTENTS

LIST OF TABLES

LIST OF FIGURES

Page

THIS PAGE HAS BEEN LEFT BLANK INTENTIONALLY

1. INTRODUCTION

A Deep Geologic Repository (DGR) for Low and Intermediate Level Waste (L&ILW) has been proposed by Ontario Power Generation (OPG) for the Bruce nuclear site situated in the municipality of Kincardine (Figure 1.1). The DGR is to be excavated at a depth of approximately 680 m within the argillaceous limestone of the Ordovician Cobourg Formation (Figure 1.2). In order to reasonably assure safety of the radioactive waste at the site and to better understand the geochemistry and hydrogeology of the formations surrounding the proposed DGR, a multi-scale numerical modelling study has been completed, as reported herein. This numerical modelling study provides a framework to investigate the groundwater flow system as it relates to and potentially affects the safety and long-term performance of the DGR. The integrity and long-term stability of the sedimentary sequence that isolates the DGR from the biosphere is assessed for time frames of one million years (1 Ma) and beyond.

This report presents the hydrogeologic modelling results developed for the geosynthesis program of the DGR investigation. The hydrogeologic modelling study is one of twelve studies that comprise the Geosynthesis Program of the DGR (NWMO 2011). The other studies that are pertinent to the work of this report include:

- *Descriptive Geosphere Site Model* (INTERA 2011)[1];
- *Regional Geology – Southern Ontario* (AECOM and ITASCA CANADA 2011);
- *Regional Three-Dimensional Geological Framework* (ITASCA CANADA and AECOM 2011);
- *Regional Hydrogeochemistry – Southern Ontario* (Hobbs et al. 2011);
- *Long-Term Climate Change* (Peltier 2011); and
- Site specific *Long-Term Geomechanical Stability Analysis* (ITASCA 2011).

The analyses of the modelling study were designed to gain insight on regional-scale and site-scale groundwater system hydrodynamics and evolution relevant to an understanding of groundwater pathways and solute migration from the location of the proposed DGR in the Cobourg Formation (refer to Figure 1.2). The regional-scale modelling integrated aspects of the cited Geosynthesis studies in one framework through the development and analysis of a regional and site-scale geosphere conceptual model; the conceptual model for the DGR site was defined by the Geosynthesis reports. The hydrogeologic modelling report does not develop, summarize, or reproduce the findings of the other reports. The work product of the Regional Geology Study defines the geologic framework of the conceptual model. The pore water chemistry was defined by the Hydrogeochemistry Study, as well as data from the site characterization. The long-term climate change study defined the glacial loading and the evolution of the formation properties for paleohydrogeologic analyses.

The modelling strategy followed in this study is an issues based approach based on reasoning and modelling lines of evidence for hypothesis testing. The spatial scale, temporal scale, processes governing groundwater flow, and data requirements are such that approximations and simplifications are required in order to make the numerical models tractable. The issues based approach is described in Section 1.1 of this introduction.

From a hydrogeologic perspective, the domain at the Bruce nuclear site can be subdivided into three horizons:

---

[1] Currently known as Geofirma Engineering Ltd.

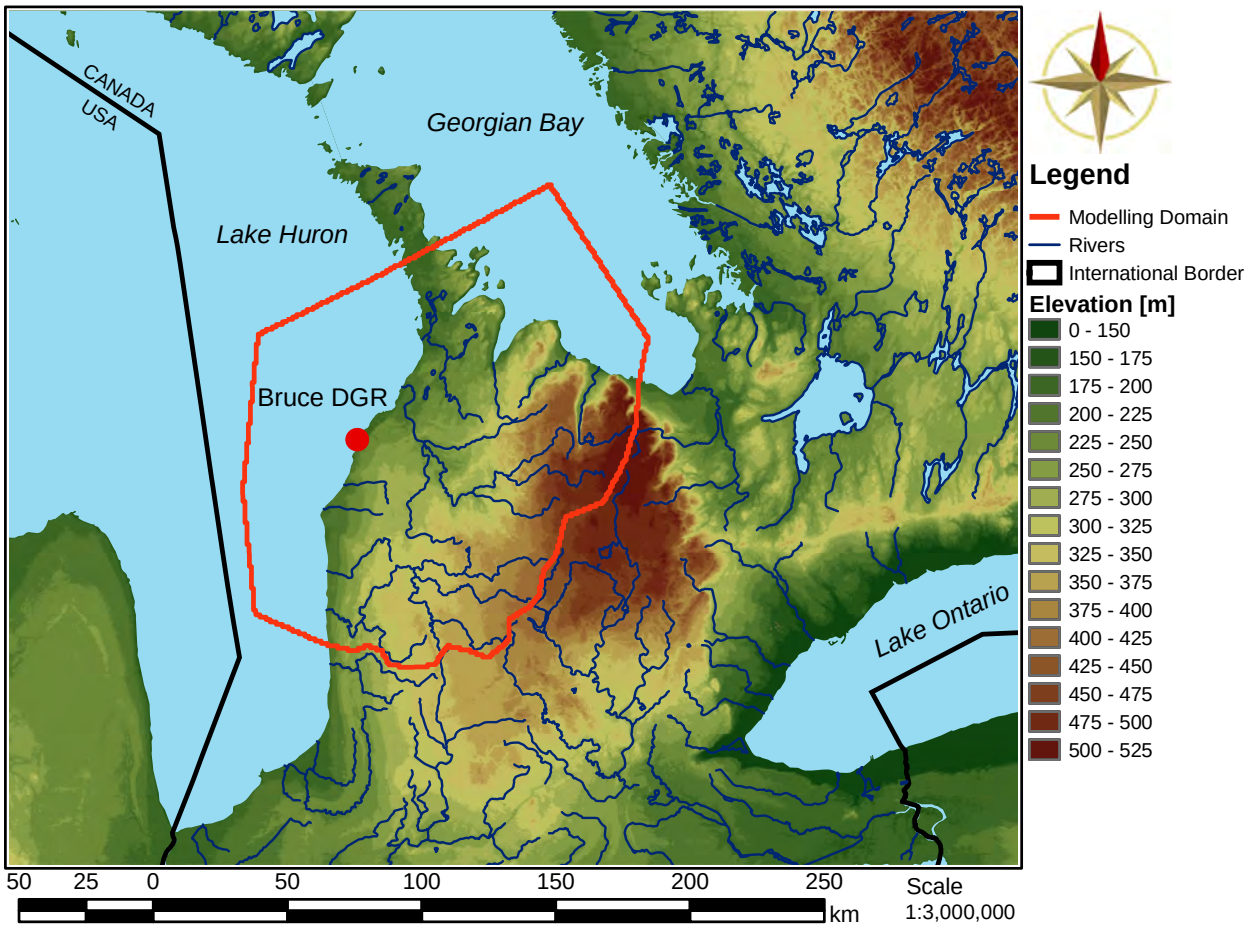

Figure 1.1: Location of Proposed DGR Site, Regional-Scale Elevations and River Courses

- A shallow zone characterized by the dolomite and limestone units of the Devonian and upper Silurian that have higher permeability and groundwater composition with a relatively low total dissolved solids content; the direction of groundwater flow in the shallow zone is expected to be strongly influenced by topography;
- An intermediate zone comprised of the low permeability carbonates, shale, salt and evaporite units of the Upper Silurian, the more permeable Niagaran Group (including the Guelph, Goat Island, Gasport and Lions Head in Figure 1.2) and the Lower Silurian carbonates and shales; and
- A deep groundwater zone extending to the Precambrian and characterized by the Ordovician shales and carbonate formations and the Cambrian sandstones and dolomites. Pore water in the deeper zone is thought to be stagnant and has high Total Dissolved Solids (TDS) concentrations that can exceed 300 g/L with a corresponding specific gravity of 1.2 for the fluids. The more permeable formations in the deep zone include the Cambrian (Figure 1.2).

The low-permeability intermediate zone isolates the deep groundwater domain from the influence of local-scale topographic changes. Flow in the deep domain, as it may occur, most likely will be controlled by basin wide topography and potential formational facies changes. With the deep fluids having a specific gravity that is greater than the shallow groundwater, fluid density gradients may also influence regional flow, if it occurs, in the deep units. A hypothesis of this study is that

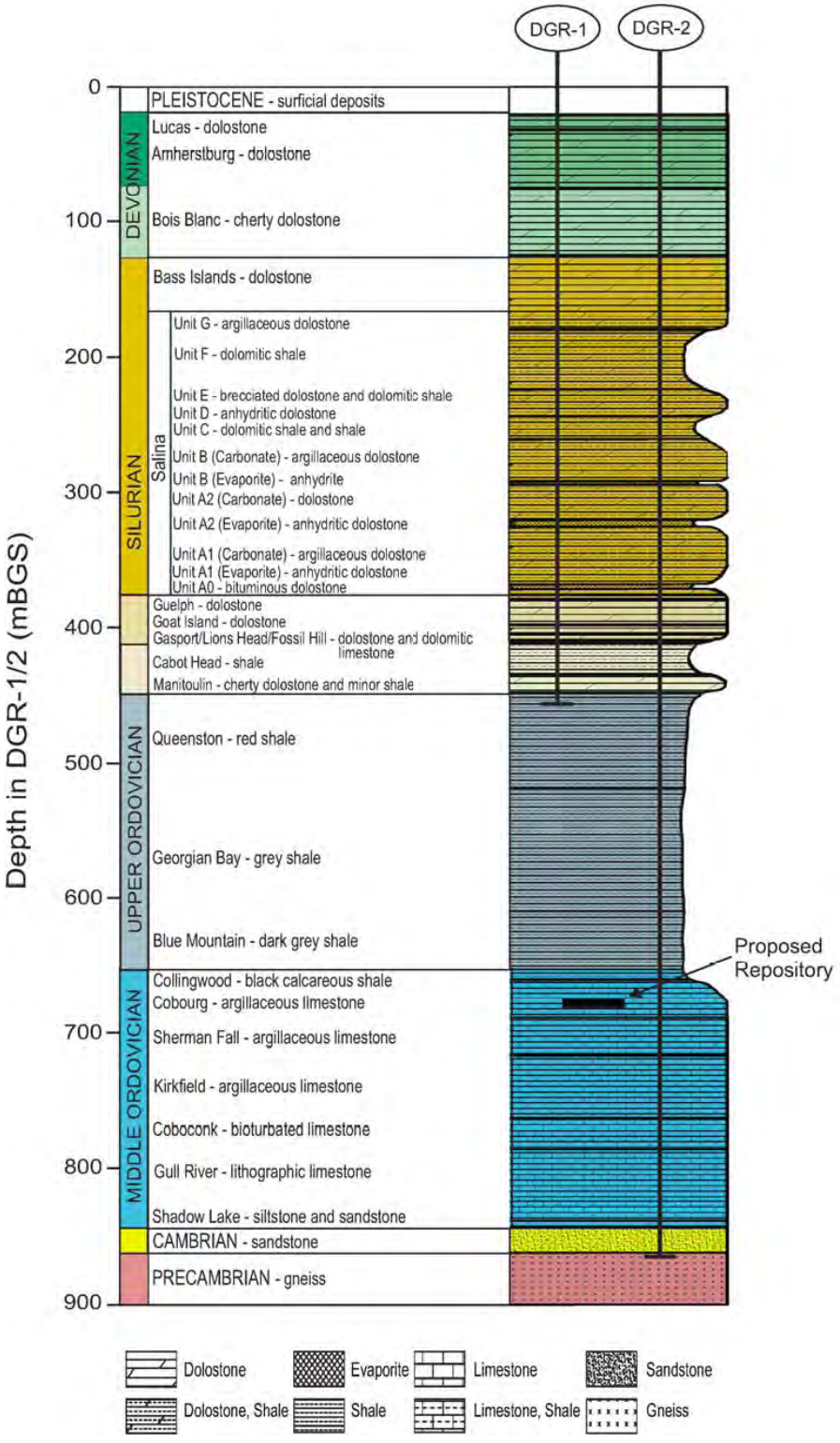

Note: From (INTERA 2011).

Figure 1.2: Reference Stratigraphic Column at the Bruce Nuclear Site Based on DGR-1 and DGR-2 Borehole Data

horizontal gradients that govern flow in the deep domain are expected to be low resulting in diffusion dominated solute transport.

In this study, the term stagnant is used to define groundwater in which solute transport is dominated by molecular diffusion. This definition results from the fact that advective velocities calculated using Darcy's law will be zero only if either or both of the energy gradient or the permeability are zero. The measurement of a zero permeability for a porous medium is beyond current field instrumentation methods. A zero gradient is also difficult to either measure or estimate. Thus, stagnant must imply that the advective velocity is low in some sense - in this case relative to transport by molecular diffusion.

A *computational model* is typically described as the numerical or software implementation of physical, chemical, and biological processes which have been defined using mathematical relationships between the relevant parameters. The attributes of a numerical model are defined by the site *conceptual model*. The term *numerical model* is used to describe the computer data files which contain the site specific geometry, parameters, properties, characteristics, loads, and boundary conditions for use in a computational model. The regional-scale and site-scale numerical modelling was accomplished using FRAC3DVS-OPG version 1.2.1. Developed from FRAC3DVS (Therrien et al. 2004), this computational model provides a solution of three-dimensional density-dependent groundwater flow and solute transport in porous and discretely-fractured media. Details of the FRAC3DVS-OPG model that are pertinent to this study are described in Chapter 3. This report investigates the hypothesis that the under-pressures in the Ordovician sediments may indicate the presence of a gas phase. To investigate this hypothesis from a modelling perspective, this report uses the two-phase air and water computational model TOUGH2-MP version 2.0 (Pruess et al. 1999). Developed at Lawrence Berkeley Laboratories, the TOUGH2-MP model is a numerical simulator for non-isothermal flow of multi-component, multi-phase fluids in one, two, and three-dimensional porous and fractured media. The chief applications for which TOUGH2-MP is designed are geothermal reservoir engineering, nuclear waste disposal, environmental assessment and remediation, and unsaturated and saturated zone hydrology. The modelling process requires a large computational effort for this horizontally layered geological sequence. Pre- and post-processors are essential for data interpretation, synthesis, manipulation, management and visualization.

1.1 An Issues Approach to Hydrogeological Modelling

An important attribute of the Ordovician sediments as a host for a deep geologic repository is their very low permeability. From a groundwater flow perspective, the very slow rate of fluid migration resulting from the low permeability will yield travel times that are millions of years for an average water particle to transit from the horizon of the DGR to a point of interest such as the biosphere. It is a hypothesis of the DGR study that solute transport in the Ordovician sediments is dominated by diffusion. To analyse transport over millions of years, both the evolution of the basin and the investigation of perturbing factors such as continental glaciation must be considered. The groundwater flow may also be influenced by basin wide factors such as topography and spatial differences in fluid density. In summary, groundwater flow in the Michigan Basin is dynamic, it is influenced by processes at a large spatial scale, and it is governed by physics that include mechanical, geochemical and possibly multi-phase flow processes.

The objective of the hydrogeological modelling study, as part of the geosynthesis program and site characterization, is to assist in developing the safety case for the proposed Bruce Deep Geologic Repository. This assistance is provided by characterizing and analysing the groundwater system in the deep geologic formations by creating a robust numerical groundwater

model. In order to properly characterize the flow in the deep geological units, it is especially pertinent to ensure that the basis for the numerical model is developed from sound geologic interpretations and models. This will contribute to a more accurate distribution of unit properties such as permeability for a given numerical model and an appropriate realization of the domain geometry. The distribution of permeability is of importance due to the requirement of sufficient thickness and lateral contiguity, and predictability of the geologic units that may be potentially impacted by the proposed repository.

Argillaceous media are being considered by many countries as potential host rocks for radioactive waste. Numerical modelling, whether as part of site-characterization, geosynthesis, performance assessment or safety assessment, provides an important tool in the evaluation of the features, events and processes that may be relevant to the long-term safety of a repository. The modelling requires a sound understanding of the basic physical and chemical processes that govern water and solute transport through the host media. A framework that facilitates the evaluation of the suitability of a proposed repository involves the development and the use of Features, Events and Processes CATalogues (FEPCATs), with this being an acronym for “features, events and processes catalogue” (Mazurek et al. 2003). For a repository system hosted in argillaceous media, there are three separate FEPCATs that are most relevant to this study with these being transport mechanisms, retardation mechanisms and paleohydrogeology.

Transport of a radionuclide within and from a deep geologic repository occurs by a number of possible transport mechanisms, and it is counteracted by a number of retardation mechanisms (Mazurek et al. 2003). Numerical models, laboratory experiments and field experiments are components that are considered in the assessment and resolution of transport and retardation mechanisms. The transport mechanisms and factors or processes that influence it include:

- Stratigraphy/hydrostratigraphy - predictability/homogeneity/bedrock layering (3-D Geometry);
- Hydraulic gradients - gravity, density, anomalous;
- Saturated hydraulic conductivities or permeabilities - extremely low; anisotropic, inter-formational/intra-formational;
- Presence of a gas phase - rock dependent capillary saturation relationships, relative permeability, residual water saturation and residual gas saturation, hysteresis, interphase transfer, diffusion in a phase;
- Hydrogeochemistry - brine viscosity, formation distinct pore fluid compositions (elemental/isotopic), scale dependency as in laboratory (cm) versus field scale (10s of m);
- Diffusivities - Cobourg/Ordovician shales (i.e. pore geometry/connectivity, porosity, pore space, anisotropy);
- Structural geology - geometry of regional/local scale discontinuities; and
- Colloid transport - principles, process and likelihood.

The parameters and features that are relevant in the determination of the retardation mechanisms that modify the rate at which solutes migrate through the groundwater system include:

- Grain size distribution/mineralogy;
- Pore water composition (inorganic/organic);
- Dissolution/precipitation of secondary mineral phases; and
- Matrix diffusion where fracture flow occurs.

Numerical modelling at both the regional-scale and the site-scale plays an important role in demonstrating and illustrating the transport and retardation mechanisms. In an issues based approach, this report will contribute to the assessment of these mechanisms through the use of the models FRAC3DVS-OPG and TOUGH2-MP to demonstrate and illustrate:

- Flow, transport or time domain probability estimates of particle residence time in the regional flow system based on estimates of the transport mechanisms of advection, dispersion and diffusion;
- Flow system anisotropy at inter-/intra-formational scale;
- Influence of variable density flow (i.e. horizontal stratification);
- Influence of basin hydrostratigraphy and geometry on absence of exfiltration zones;
- Migration of unretarded/non-decaying environmental isotopes within the Ordovician sediments;
- Sensitivity of transport in the Ordovician sediments to the domain boundary conditions (lateral and surface);
- Influence of a gas phase in the Ordovician sediments on the spatial distribution and temporal evolution of water pressure and the influence of a gas phase on solute migration; and
- Role/implications of sub-vertical transmissive features in a variably dense groundwater flow domain.

The evaluation of a feature or process using numerical models can be accomplished using, in part, a sensitivity analysis that estimates the change in a system performance measure to changes in a system parameter. These estimated sensitivity coefficients are local derivatives evaluated in terms of the base-case parameters that describe the system. The robustness of the sensitivity coefficients for large changes or perturbations of parameters also can be assessed. The performance measures that can be used to characterize the system can include, but are not restricted to:

- Darcy fluxes and average linear velocities for both steady-state and transient, density-dependent flow;
- Salinity and environmental isotope concentrations;
- Fluid pressures and energy gradients for both steady-state and transient, density-dependent flow;
- Average water particle paths;
- Time domain probabilities of fluid particle residence times (Mean Life Expectancy); and
- Flow system discharge.

Regional-scale modelling can provide the framework for the assessment of paleohydrogeology. Based on the work of Peltier (2002, 2003), it is clear that to address the long-term safety of a deep geologic repository, long-term climate change and, in particular, a glaciation scenario, needs to be incorporated into geosynthesis modelling activities. In addition, by simulating flow system responses to the last Laurentide (North American) glacial episode, insight is gained into the role of significant past stresses (mechanical, thermal and hydrological) on determining the nature of present flow system conditions, and by extension, the likely impact of similar, future boundary condition changes on long-term flow system stability. The Wisconsinian glacial episode, that occurred over a 120,000 year time period, included at least three cycles of glacial advance and retreat, with maximum ice thickness over the southern Ontario DGR site reaching more than 2.5 km. Between glacial episodes were extensive periods of transient, peri-glacial conditions during which permafrost could impact the subsurface, depending on location, to several hundreds of metres. Near the end of a glacial episode, significant basal meltwater production occurred. This study will restrict itself to the development of a model domain and parameters that will provide a framework for the assessment of paleohydrogeology. This assessment includes:

- Evaluating the expected flow system perturbation by glacial events (boreal, peri-glacial or ice sheet);
- Assessing the depth of penetration by glacial meltwater into Paleozoic formations;

- Illustrating numerically the transient influence of glacial event(s) on the DGR site flow system;
- Estimating pore fluid residence times during Quaternary glacial events;
- Determining the impact of glaciation on the spatial distribution and temporal evolution of water pressure in the Ordovician sediments; and
- Determining the influence on water pressure evolution of a residual gas phase in the Ordovician sediments.

Abnormal pressures have been measured in the DGR boreholes with the pressure in the Cambrian sandstone being elevated relative to hydrostatic levels and the Ordovician sediments being under-pressured. A requirement of the abnormal pressures is low hydraulic conductivities in the over and underlying rocks (Neuzil 1995). This report investigates the abnormal pressures using an issues based approach with the two objectives being:

- The assessment of the impact of the spatial distribution and temporal evolution of the abnormal pressures on solute transport in the Ordovician sediments and the determination of the robustness of a conclusion that transport in the sediments is diffusive; and
- The development of possible explanations of the over-pressure in the Cambrian and the under-pressure in the Ordovician sediments.

The analyses undertaken to resolve the first objective include numerical modelling at the site-scale with the boundary conditions being determined using the embedment approach. One-dimensional TOUGH2-MP two phase gas and water flow is also developed to address the objective. The second objective involves the assessment of possible mechanisms that can cause abnormal pressures. The processes commonly invoked to explain over-pressures are compaction, hydrocarbon migration, diagenesis, tectonic stress or more simply topographic effects (Gonçalvès et al. 2004). Osmotic influences across shale membranes (Bader and Kooi 2005), the presence of a non-wetting gas phase in pores, and geomechanical effects including crustal flexure (Johnston et al. 1998) are explanations of abnormal under-pressures. Hydrogeological modelling for the analysis is limited to regional-scale saturated flow in paleohydrogeologic scenarios using FRAC3DVS-OPG (refer to Section 5.1), saturated flow in a cross-section of the Michigan Basin (refer to Section 6.2), and one-dimensional vertical two-phase gas and water flow using TOUGH2-MP (refer to Section 6.3).

The multi-scale two- and three-dimensional modelling of the DGR site using FRAC3DVS-OPG is restricted to saturated isothermal flow. The computational model does not include the capability for the modelling of a separate gas phase. The extent of the regional domain is defined in Figure 1.1. Analyses include both steady-state, density-independent flow and transient flow that couples the density-dependent flow equation with the equation that describes the transport of the total dissolved solids within the system domain. The assessment of the impact of parameter perturbations on system performance measures that can include fluid pressure, fluid velocity, groundwater life expectancy and groundwater age will be accomplished using direct parameter sampling and, to a limited extent, a sensitivity derivative framework. The base-case parameters that describe the regional domain are dependent on the geological and geochemical framework and the field investigations at the Bruce nuclear site with these being described in Chapter 2.

Methods to calibrate or estimate model parameters, such as permeabilities, are well developed in literature. The most common method involves the assumption of an estimator or objective function with the sum of the square of the difference between observed heads and model estimated head values being most common. The goal of calibration is to minimize the objective function subject to parameter constraints such as permeability bounds. Regardless of the optimization algorithm selected, numerous function calls or model evaluations are required in

order to determine a minimum of the objective function; it is common for the minimum to be a local rather than a global optimum.

The establishment of defendable parameter constraints is an important part of parameter estimation methods as the constraints define the solution space. Gradient based search algorithms are often used to facilitate calibration, although ad-hoc or trial-and-error procedures are also commonly used. At the regional scale of this study, formal model calibration cannot be achieved due to both the computational burden of repeated model calls and spatial data representing the full solution domain are not sufficient. However, the predictability of lithology will permit reasonable and defendable extrapolation and upscaling of point estimates and the development of parameter bounds or constraints. The investigation of the impact of parameter constraints is an important aspect of this study. The investigation is achieved through sensitivity analyses in which parameters are perturbed within reasonable and acceptable limits. The impact of the parameter perturbation on the groundwater system and solute transport is then determined. A performance measure such as the mean travel time for water particles or Mean Life Expectancy (MLE) (refer to Section 3.6.2) is used to facilitate the interpretation of the results.

1.2 The FRAC3DVS-OPG Computational Model

The multi-scale saturated (i.e., no mobile gas phase) modelling was accomplished using FRAC3DVS-OPG version 1.2.1. Developed from FRAC3DVS (Therrien et al. 2004), the model provides a solution of three-dimensional density-dependent groundwater flow and solute transport in porous and discretely-fractured media. Details of the FRAC3DVS-OPG model that are pertinent to this study are described in Therrien et al. (2004) and in Normani et al. (2007). FRAC3DVS-OPG is developed and maintained as nuclear grade software in a Quality Assurance framework in accordance with Nuclear Waste Management Organization (NWMO) Technical Computing Software Procedure document number NWMO-PROC-EN-0002 (NWMO 2009).

1.3 Scope and Objectives of Hydrogeological Modelling

The overall objective of the groundwater modelling study, as part of the geosynthesis program, is to assist in developing the safety case for the proposed Deep Geologic Repository at the Bruce nuclear site. The specific objectives of the hydrogeologic modelling study are to:

- Develop a base-case regional-scale and site-scale numerical model that honours both regional-scale data and data from the Bruce DGR site characterization study (INTERA 2011);
- Investigate the hypothesis that solute transport in the Ordovician shale and limestone at the DGR is diffusion dominant;
- Investigate the sensitivity of groundwater flow and solute transport to salinity and hence fluid density variation in the regional-scale domain;
- Investigate using different numerical models, flow in the more transmissive units such as the Niagaran Group and Cambrian and the hypothesis (refer to Section 2.6) that at a point in units/formations beneath Lake Huron either a divide for groundwater flow occurs or horizontal flow is negligible;
- Investigate the impact on solute transport in the Ordovician shale and limestone of paleoclimate perturbations;
- Explore, in an issues based approach with simulations using different computational models and numerical models, the abnormal pressures observed in the DGR boreholes; and
- Investigate the impact on the flow domain of a hypothetical discrete transmissive fracture zone between the Cambrian and the Niagaran Group proximal to the DGR.

The modelling requires a sound understanding of the basic physical and chemical processes that govern water and solute transport through the host media. An important aspect of the work of this report is that while computational models that include all of the thermal, hydrological, mechanical and chemical processes have been described in literature, the models are intractable for the extent of the spatial and temporal scale necessary for the description of the deep groundwater system at the DGR. Data for a computational model that includes the integration of all of the processes at the spatial and temporal scale used in this study certainly are limited. Approximations and simplifications are a necessary part of the work. Examples of simplifications that are invoked include the reduction of dimensionality or the assumption of saturated flow. Approximations include, for example, the use of an air and water equation of state module EOS3 in TOUGH2-MP. An objective of the work then, is to determine the robustness of the study assessments and conclusions relative to the assumptions and simplifications invoked. This study uses four different numerical models to achieve this goal. These models are:

- Regional-scale saturated density-dependent flow using FRAC3DVS-OPG for an approximately 18,000 km^2 domain centred on the DGR;
- Site-scale saturated density-dependent flow using the embedment option in FRAC3DVS-OPG for an approximately 400 km^2 domain centred on the DGR;
- Saturated density-dependent flow using FRAC3DVS-OPG in a 677 km west to east cross-section of the Michigan Basin; and
- One-dimensional two-phase gas and water flow analyses of a stratigraphic column at the DGR using TOUGH2-MP.

The use of the four numerical models strengthens the conclusions of this report through the use of multiple lines of evidence. A summary of the various scenarios undertaken in this study for each numerical model is shown in Figure 1.3. The scenarios or simulations are listed by their identifier.

The supporting data for the conceptual model for the regional-scale and site-scale hydrogeologic modelling are contained in the DGR Descriptive Geosphere Site Model (INTERA 2011) plus all of the Geosynthesis reports. The conceptual model's base case parameters that describe the regional domain are dependent on the geological and geochemical framework and the field investigations at the Bruce nuclear site with these being described in Chapter 2. The chapter also addresses issues of scale and the rationale for the selection of the extent of the spatial domain investigated in this study. The computational model and the relevant equations are described in Chapter 3. The parameters for the base-case analysis at both the regional-scale and site-scales are presented in Section 4.1. The regional-scale analyses are presented in Chapter 4, while the paleohydrogeologic analyses are presented in Chapter 5. Site-scale analyses that investigate solute transport in the Ordovician shale and limestone are presented in Section 4.5. The investigation of the abnormal pressures observed in the DGR boreholes is the subject of Chapter 6. The analyses include paleohydrogeologic simulations using the regional-scale model and the simulation of saturated flow in a west to east cross-section of the Michigan Basin to investigate both over-pressures measured in the Cambrian at the DGR site and horizontal gradients in the deep layers beneath Lake Huron. FRAC3DVS-OPG with an orthogonal grid is used for the Michigan Basin cross-section analyses. The study of two-phase gas and water flow at the DGR using the model TOUGH2-MP (Pruess et al. 1999) is designed to investigate the impact on water pressures of a gas phase in the Ordovician sediments. The study conclusions are presented in Chapter 7.

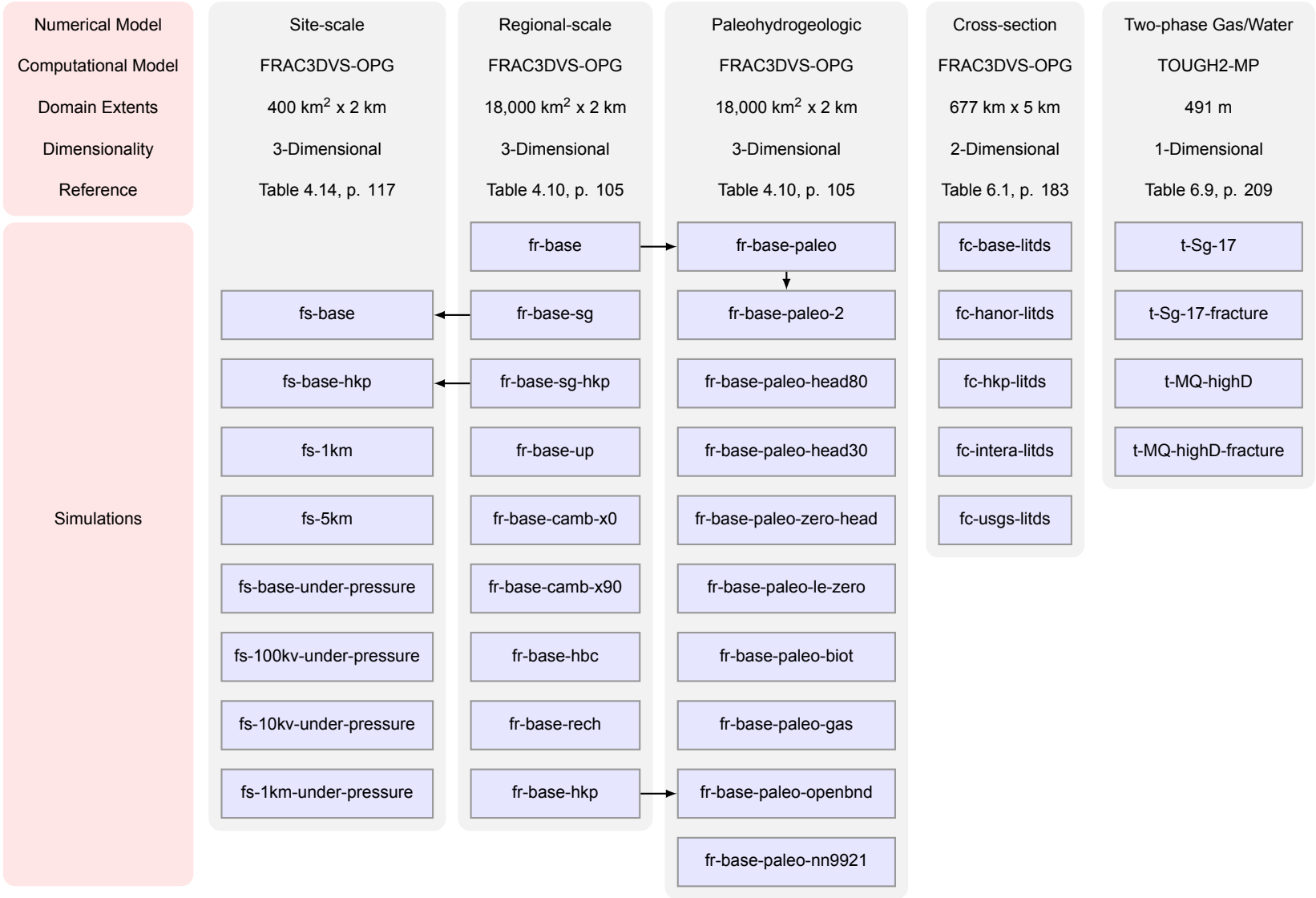

Note: Parameter and scenario analyses (simulations) are shown in the blue rectangles. Arrows indicate that the initial conditions of a scenario depend on the outputs of another scenario.

Figure 1.3: Suite of Simulations Performed and Discussed as Part of This Hydrogeologic Modelling Study

2. CONCEPTUAL MODEL

The Michigan Basin, shown in Figure 2.1, is a nearly circular deep intracratonic basin approximately 400 km in diameter and 5 km deep (Howell and van der Pluijm 1999, Chernicoff et al. 2002). Subsidence within the Michigan Basin resulted in approximately 5 km of sedimentation over a period of more than 200 Ma during the Paleozoic. According to Howell and van der Pluijm (1999), a definitive origin for the subsidence has not yet been found, although various mechanisms have been proposed. The northern edge of the basin rim represents the interface between the depositionally continuous Paleozoic sediments and the underlying Precambrian rocks (Stonehouse 1969). The eastern limit of the Michigan Basin is defined by the Algonquin Arch (refer to Figure 2.2) which separates the Michigan Basin from the Appalachian Basin to the southeast. The Algonquin Arch is a feature in the crystalline basement rock of the Precambrian and ranges in elevation from approximately 200–300 m where it outcrops, towards the northeast, to −1,000 m at the Chatham Sag (refer to Figure 2.1); the Findlay Arch represents the southwest continuation of the Algonquin Arch, also separating the Michigan Basin from the Appalachian Basin (Carter et al. 1996, Mazurek 2004, Ellis 1969).

The Algonquin Arch essentially divides southwestern Ontario into two megablocks: the Bruce Megablock to the northwest, and the Niagara Megablock to the southeast (Sanford et al. 1985). The Niagara Megablock is characterized by intersection fracture lineaments that act as oil and gas traps (Carter et al. 1996); the Bruce Megablock has a less dense fracture pattern, as conceptualized by Sanford et al. (1985) (refer to Figure 2.3). However, the validity of the fracture model has not been tested or resolved in the literature. AECOM and ITASCA CANADA (2011) review the Sanford et al. (1985) model. According to Sanford et al. (1985) and Carter et al. (1996), vertical offsets at faults are required to explain reserves of trapped oil and gas. These offsets prevent lateral flow and interrupt the continuity of the various formations that comprise the Michigan Basin. Such discontinuities are important in limiting the connectivity of high permeability units that can connect near surface groundwater flow systems to much deeper groundwater flow systems. One such highly permeable unit is the Cambrian, found immediately above the Precambrian basement rock.

This section summarizes the key elements of the conceptual model developed in the hydrogeologic modelling study. The data for the conceptual model are derived from the Geosynthesis work and data acquired from the ongoing descriptive geosphere site model work (INTERA 2011). The elements presented include: the geological framework that defines the geometry, stratigraphy and lithology of the regional and site-scale spatial domain; the geochemical framework that defines the chemical characteristics of the system relative to the assessment of density-dependent flow; the hydrogeological framework that defines the boundary conditions, issues, and solution methodology for saturated density-dependent flow; and, the model parameters as obtained from the descriptive geosphere site model work.

2.1 Geological Units

The Paleozoic stratigraphic units at the Bruce nuclear site (listed in Table 2.7 and in Figure 1.2) were deposited on crystalline Precambrian basement rock. The Precambrian rocks underlying southern Ontario are metamorphic rock types ranging from felsic gneisses to mafic metavolcanics to marble (Armstrong and Carter 2006). The following summary from Armstrong and Carter (2006) describes the Paleozoic rocks encountered within the regional study area.

The Cambrian units of Ontario, deposited over the irregular and weathered Precambrian surface, are composed primarily of quartzose sandstones with dolomitic quartz sandstones and sandy

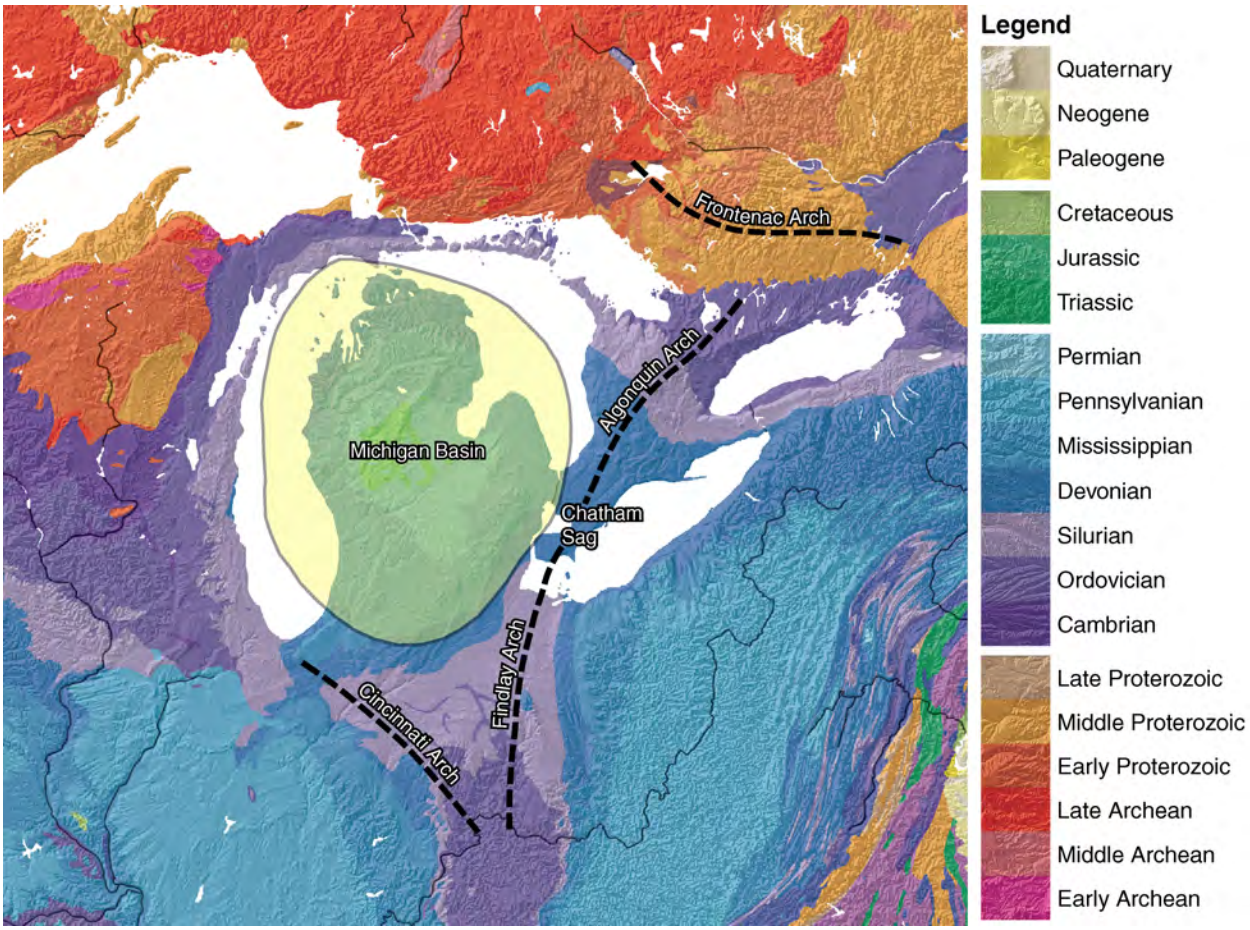

Note: Geologic map is coloured by geologic age from Quaternary to Archean. Adapted from geologic map courtesy of the United States Geological Survey (Barton et al. 2003).

Figure 2.1: Spatial Extent of the Michigan Basin and Locations of the Frontenac Arch, Algonquin Arch, Chatham Sag, Findlay Arch, and Cincinnati Arch

dolostones (Armstrong and Carter 2006). Cambrian deposits extend from the Appalachian Basin to the Michigan Basin but have largely been eroded over the Algonquin Arch (Bailey Geological Services Ltd. and Cochrane 1984). Well log records obtained from the Oil, Gas and Salt Resources (OGSR) Library in London, Ontario indicate that Cambrian deposits are present at isolated locations over the arch. It is possible that these deposits are remnants of the eroded Cambrian or they represent isolated patches of sandstones of unknown origin/age as described by Bailey Geological Services Ltd. and Cochrane (1984). As a result, the Cambrian sediments are not continuous throughout the regional model domain. Its permeability is significantly higher than both of its bounding units.

The Cambrian sandstones and dolostones are overlain by the low permeability rocks of Ordovician age. When the Cambrian rocks are not present, as is the case at the Algonquin Arch, the Ordovician rocks directly overlay the Precambrian basement rock. The first unit of Ordovician age is the Black River Group. This Group consists of the Shadow Lake, Gull River and Coboconk Formations. The Shadow Lake Formation in southern Ontario is composed of red and green shales, argillaceous sandstones and argillaceous dolostones (Armstrong and Carter 2006). The

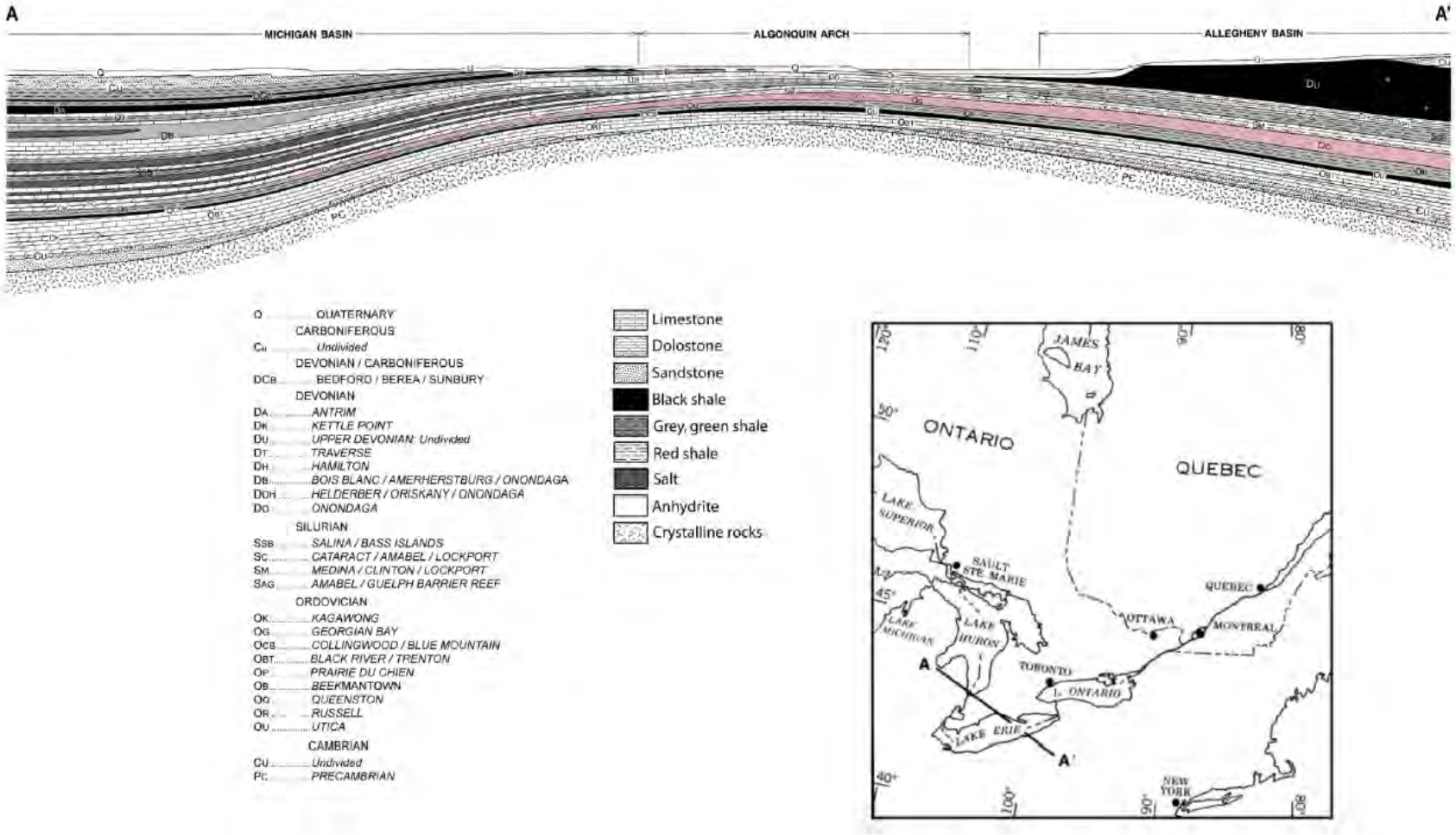

Note: Cross-section location is shown as A-A' in inset map. From Sanford (1993).

Figure 2.2: Geological Cross-section from Allegheny (Appalachian) to Michigan Basin Across the Algonquin Arch

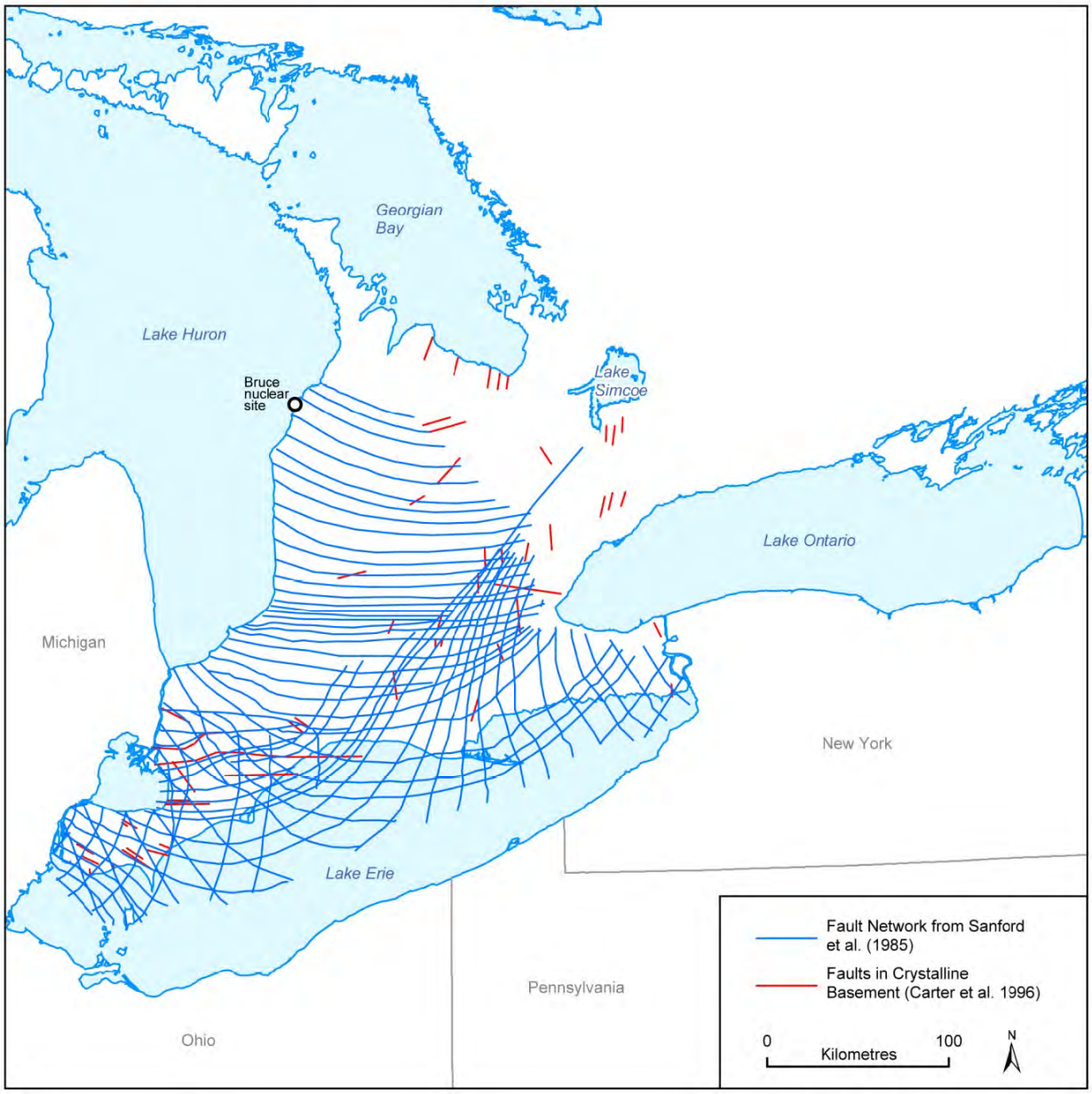

Note: Compilation includes faults interpreted the displace the Paleozoic-Precambrian unconformity surface. Figure is modified from Mazurek (2004), after Sanford et al. (1985) and Carter et al. (1996).

Figure 2.3: Proposed Fracture Framework and Mapped Faults of Southern Ontario

second geological formation that comprises the Black River Group is the Gull River Formation. The Gull River Formation consists primarily of very fine grained limestone with minor dolostone and shale interbeds. The Coboconk Formation is the youngest Black River Group unit and consists of fine-medium grained bioclastic limestones (Armstrong and Carter 2006). Oil stains have been observed in the DGR cores from the Coboconk.

The overlying Trenton Group includes the Kirkfield, Sherman Fall, and the Cobourg Formations. The Kirkfield Formation is composed of fossiliferous limestones, while the overlying Sherman Fall Formation ranges in lithology from argillaceous limestones, found lower in the formation, to bioclastic limestone that characterize the upper portions of the formation (Armstrong and Carter 2006). The upper (youngest) formation of the Trenton Group is the Cobourg Formation. The Cobourg Formation is the proposed horizon for the DGR (INTERA 2006). The Cobourg Formation consists of very fine-coarse grained, fossiliferous limestones and argillaceous limestones. The upper member of the Cobourg Formation is known as the Collingwood Member, which is described by Armstrong and Carter (2006) as dark grey to black, organic-rich, calcareous shales.

Overlying the Cobourg Formation are the Upper Ordovician Georgian Bay and Blue Mountain Formations. These units consist of thick non-calcareous shales with minor limestone, siltstone and sandstone interbeds. The youngest Upper Ordovician unit is the Queenston Formation, which consists of red to maroon, noncalcareous to calcareous shale with minor siltstone, sandstone and limestone interbeds (Armstrong and Carter 2006).

The Silurian rocks comprise the intermediate groundwater zone or domain. The oldest units forming the intermediate groundwater domain are comprised of the Lower Silurian Manitoulin dolostones and shales of the Cabot Head Formation. The lower hydrostratigraphic regime is isolated from the upper groundwater regime, in part, by the low hydraulic conductivities of units in the intermediate groundwater domain, specifically the horizontally bedded Upper Silurian Salina Formation.

The Middle Silurian at the DGR site consists of dolostones of the Fossil Hill Formations, Lions Head Formation, Gasport Formation, Goat Island Formation and the more permeable dolostones of the Guelph Formation. The Guelph Formation ranges from reef to inter-reef lithologies throughout southern Ontario. At the DGR site, the Guelph Formation is characterized by thin inter-reef dolostones (Sterling 2010).

The Upper Silurian Formations are comprised of the Salina Group and the Bass Islands Formations. These units consist of sequences of dolostones/limestones, argillaceous dolostones/limestones, shale, and evaporite (i.e., gypsum, anhydrite, salt). The Salina Group is subdivided into 11 members which are in order of succession A-0, A-1 Evaporite, A-1 Carbonate, A-2 Evaporite, A-2 Carbonate, B Unit, C Unit, D Unit, E Unit, F Unit, and G Unit. The Bass Islands Formation dolostones overlay the Salina Group. The evaporite, shale and argillaceous dolostone units in the Salina Formation will form a major barrier impeding the vertical hydraulic connection of deeper geologic formations with shallower formations.

Above the Bass Islands Formation is the Lower Devonian aged Bois Blanc Formation. The Bois Blanc Formation is described as a fossiliferous and cherty dolostone (Armstrong and Carter 2006). The Bois Blanc Formation is overlain by the Middle Devonian Amherstburg and Lucas formations of the Detroit River Group. These units are characterized by fossiliferous dolostones/limestones to poorly fossiliferous limestones with minor evaporite (Armstrong and Carter 2006). The Detroit River Group comprises the upper or shallow groundwater zone. In the southern portion of the regional study area (model domain) the limestones and dolostones of the Middle Devonian Dundee Formation overlies the Detroit River Group.

2.2 The Geologic Framework Model

AECOM and ITASCA CANADA (2011) and ITASCA CANADA and AECOM (2011) developed a geological framework model that was used as the basis of the analyses and simulations presented in this hydrogeologic modelling study. The framework extends from the top of the

Precambrian basement to surface topography, including watershed features (lakes, rivers), and bathymetry and covers an area of 32,000 km^2, measuring 160 km east-to-west, and 200 km north-to-south. A plan view of the Regional Study Area (RSA) is shown in Figure 2.4 (ITASCA CANADA and AECOM 2011).

Itasca Consulting Canada Inc. was retained by OPG to work closely with the study team of AECOM and ITASCA CANADA (2011) in developing the 3D Geologic Framework (3DGF) model used in this report (ITASCA CANADA and AECOM 2011). With Itasca, the framework was designed using the advanced 3D earth modelling and scientific visualization technology Gocad™ software. Interpolation was accomplished by the iterative Discrete Surface Interpolation (DSI) method. Unlike Kriging, DSI does not provide a point estimation of the precision of the interpolation. Details on the use of DSI are provided in ITASCA CANADA and AECOM (2011).

The Precambrian basement rock represents the base of the geologic framework, extending upward to surface topography (AECOM and ITASCA CANADA 2011). The primary data source for the 3DGF was the Oil, Gas and Salt Resources Petroleum Wells Subsurface Database. This database included fields such as geological formation tops, logging records, and oil/gas/water intervals for tens of thousands of petroleum wells throughout Ontario. As shown in Figure 2.5, the vast majority of these wells are located in southwestern Ontario along the shore of Lake Erie extending towards Sarnia/Lambton County. The RSA contained 341 wells, reduced to 299 wells after a data validation process. Fewer wells were located in the RSA, reflecting the lack of oil and gas resources in that area. These wells were drilled to investigate salt resources near the southern portion of the RSA, and to investigate oil and gas resources in the Silurian and Ordovician strata.

Additional well information was obtained for 76 petroleum wells from the Michigan State Geological Survey Digital Well Database, and 57 petroleum reference wells from Armstrong and Carter (2006); these reference wells were used by Armstrong and Carter (2006) to generate a series of representative geologic cross-sections across southern Ontario. This was also used to verify and to provide consistency for the development of the 3DGF, and to ensure the geological nomenclature matched that of the Ontario Geological Survey (OGS). Other data sources included downhole geophysics, which was used to verify geologic contacts and picks, a 1:50,000 OGS Digital Bedrock Geology of Ontario, Michigan State Geological Survey mapping and Petroleum Well Database, OGS Digital Bedrock topography and overburden thickness mapping, and National Oceanic and Atmospheric Administration (NOAA) digital bathymetric mapping of Lake Huron and Georgian Bay (AECOM and ITASCA CANADA 2011). For the 3DGF, the bathymetry mapping was used as a tool to correlate scarp faces within Lake Huron with the stratigraphic data extrapolated from the subsurface well data and bedrock maps. Note that no well data exists within Lake Huron, as a result, the State of Michigan geological mapping and selected petroleum well data were used to provide some guidance for extrapolating data beneath Lake Huron.

The remaining data sources were published literature, government reports (i.e., Ministry of Natural Resources (MNR) and OGS), and consulting reports. These data sources were useful for confirming the extent and predictability of geological units across the RSA and as guidance for understanding detailed stratigraphic relationships in the subsurface.

The data base from which the geological framework model was developed is continually being updated; data from additional boreholes can be added to the database and used to develop a new spatial model. The marginal benefit of the new data will depend on factors such as the location of a new well and the reliability of the data as compared to that from nearby wells.

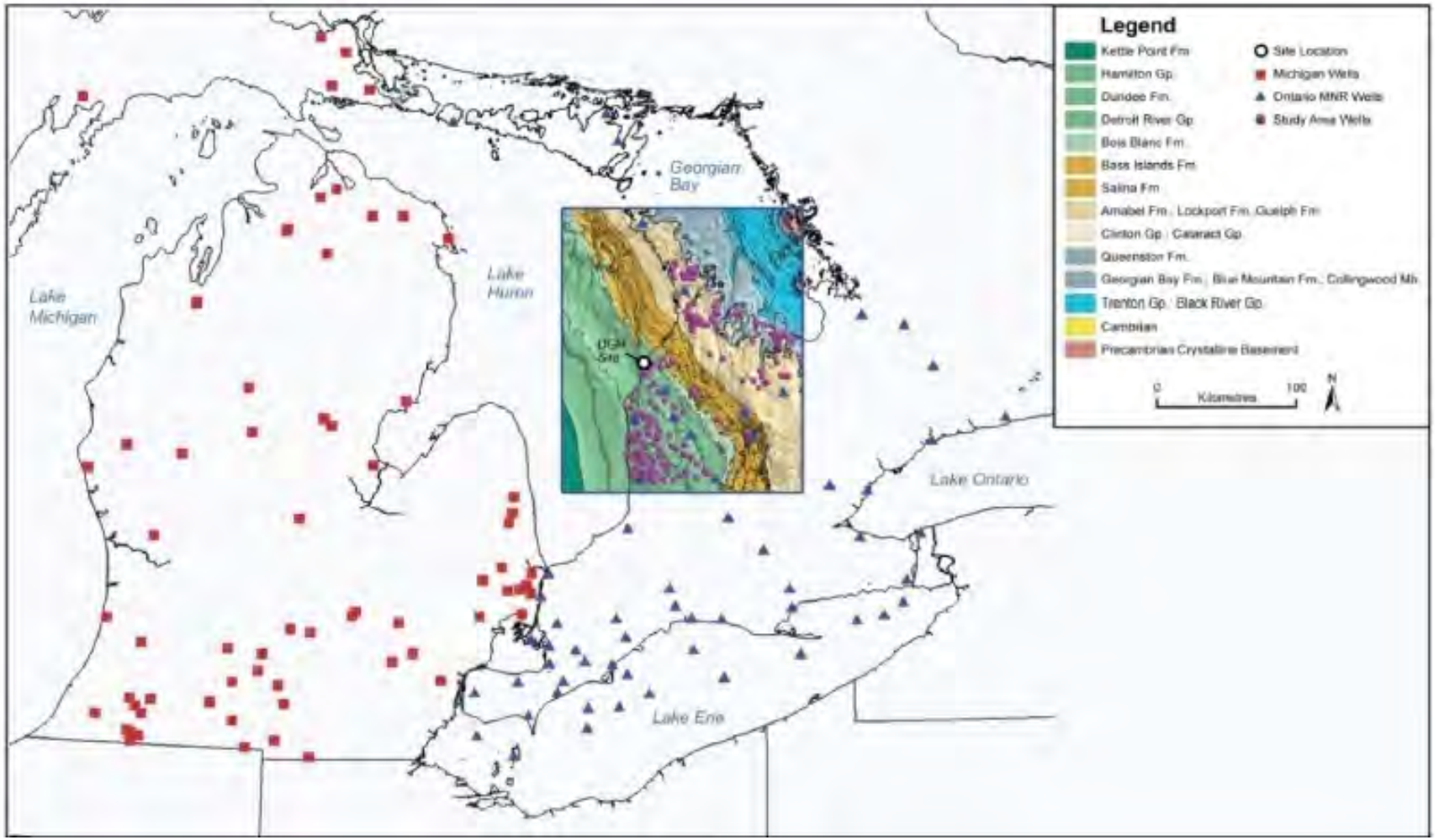

Note: From ITASCA CANADA and AECOM (2011).

Figure 2.4: 3D Geological Framework Study Boundary with Paleozoic Geology and Well Locations

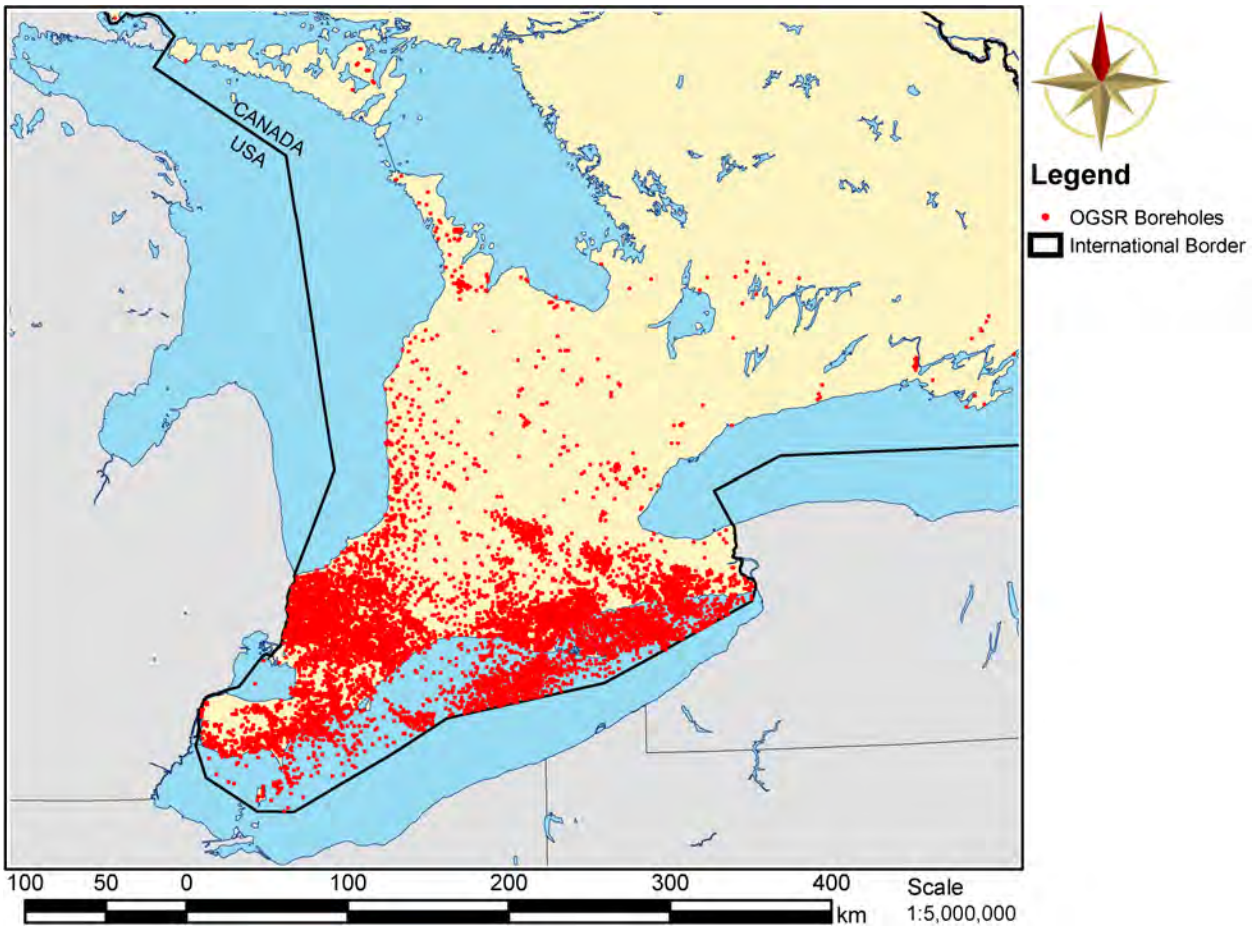

Figure 2.5: Locations of Oil, Gas and Salt Resources (OGSR) Boreholes in Southwestern Ontario

Data validation required both geological software modelling techniques as well as expert judgement. Well logs are usually of varying quality, and the OGSR database was no exception. A number of issues identified by AECOM and ITASCA CANADA (2011) include: various formations grouped together, missing formations, interface contacts inconsistent with current OGS nomenclature, and incorrect well locations and elevations. Various approaches including manual inspection and correction of logs, as well as semi-automated or automated means, guided by the visualization capabilities and tools of Gocad™ were utilized. The 31 layers identified by AECOM and ITASCA CANADA (2011) represent the maximum number of units/formations/groups that could reliably be interpreted within the study area. Table 4.1 in AECOM and ITASCA CANADA (2011) lists the unit groupings, while Table 4.1 in this report lists the relationship between the formations at the DGR site and the groupings from the 3DGF which were used for both the regional-scale and site-scale numerical models. AECOM and ITASCA CANADA (2011) state that several units were not consistently logged within the OGSR data base but rather were grouped within other larger units/formations. Referring to Figure 1.2 and the units logged in the DGR-1 and DGR-2 boreholes (Table 2.1), the grouping is as follows: the Lucas and Amherstburg were combined; the B Unit and the C Unit were combined; the A0 Unit was not identified in the regional domain; the Guelph, Goat Island, Gasport and Lions Head were combined as the Niagaran as the contacts for the individual units were not consistently picked; and, the Georgian Bay, Blue

Mountain and Collingwood were combined as the Collingwood was commonly not individually logged and more likely to have been logged as part of the Blue Mountain Formation shales. The primary method of analysis for the geologic framework model was to interpolate the location of the interface based on neighbouring wells, while a secondary method of using the mean unit thickness at neighbouring wells was also applied, with preference given to the reference wells of Armstrong and Carter (2006).

Table 2.1 summarizes the statistics for the OGSR data, which was also used in part, to develop the ITASCA CANADA and AECOM (2011) geologic framework model. Also listed, for comparison, are the thicknesses of the units observed in the DGR-1 and DGR-2 boreholes. In spite of the variability of the data, it should be noted that the presence of the Ordovician shale and limestone units is easily predictable given the data. When the average thicknesses and their corresponding standard deviations are taken into account, it can be concluded that despite the variability in the thicknesses, the data support the conclusion that the Ordovician shale and limestone units are continuous across the regional domain with large observed thicknesses occurring in the vicinity of the proposed Bruce DGR. A three-dimensional view of the resulting geologic framework is shown in Figure 2.6.

The Release 1.1 3DGF update of the geological framework model developed by ITASCA CANADA and AECOM (2011) was used to define the interfaces between layers of the regional-scale spatial domain that was used as the basis of the analyses presented in this study; details of the framework model are given in their report.

2.3 Regional-Scale Geochemical Framework

The simulation of density-dependent flow requires the spatial distribution of fluid density. The relationship between TDS concentration and density requires the measurement of the concentration of the various ions contributing to the dissolved solids. An analysis and discussion of the regional hydrogeochemical data is presented in Hobbs et al. (2011). A summary of their work, relative to the assessment of the TDS distribution in the Michigan Basin and the determination of fluid density, is presented in the following paragraphs.

The geochemical framework for the DGR study area is defined by both the data obtained from the DGR boreholes and a geochemical database (refer to Hobbs et al. (2011)) that included chemical and isotopic compositions for 202 waters sampled from the eastern margin of the Michigan Basin (southwestern Ontario), the central Michigan Basin (Michigan), and the western margin of the Appalachian Basin (Lake Erie) at depths ranging from 40 m to 3,500 m, although most samples were collected to study fluids in deep sedimentary settings (Hobbs et al. 2011). The sampling locations for the geochemical database are shown in Figure 2.7. It is observed in the figure that data are sparse both north and east of the DGR study area; from a modelling perspective, there is little data topographically upgradient of the site to define the transition zone between infiltrating fresh water at recharge areas, and the higher TDS waters at depth. The Michigan Basin is characterized in Hobbs et al. (2011), into two geochemical systems:

- Shallow – depths < 200 m below ground surface comprised of fresh to brackish waters classified as either Na−Cl, Na−Mg−Ca−Cl, or Ca−SO_4, based on their concentration of major ions. These shallow waters have stable $\delta^{18}O$ and $\delta^{2}H$ isotopic compositions, indicating the mixing of more saline waters with glacial meltwater or recharge from precipitation; and
- Intermediate to Deep – high TDS brines (200–400 g/L) > 200 m depth classified as Na−Ca−Cl, or Ca−Na−Cl. These waters are enriched relative to the Global Meteoric Water Line (GMWL) with $-6‰ < \delta^{18}O < 3‰$ and $-55‰ < \delta^{2}H < 20‰$.

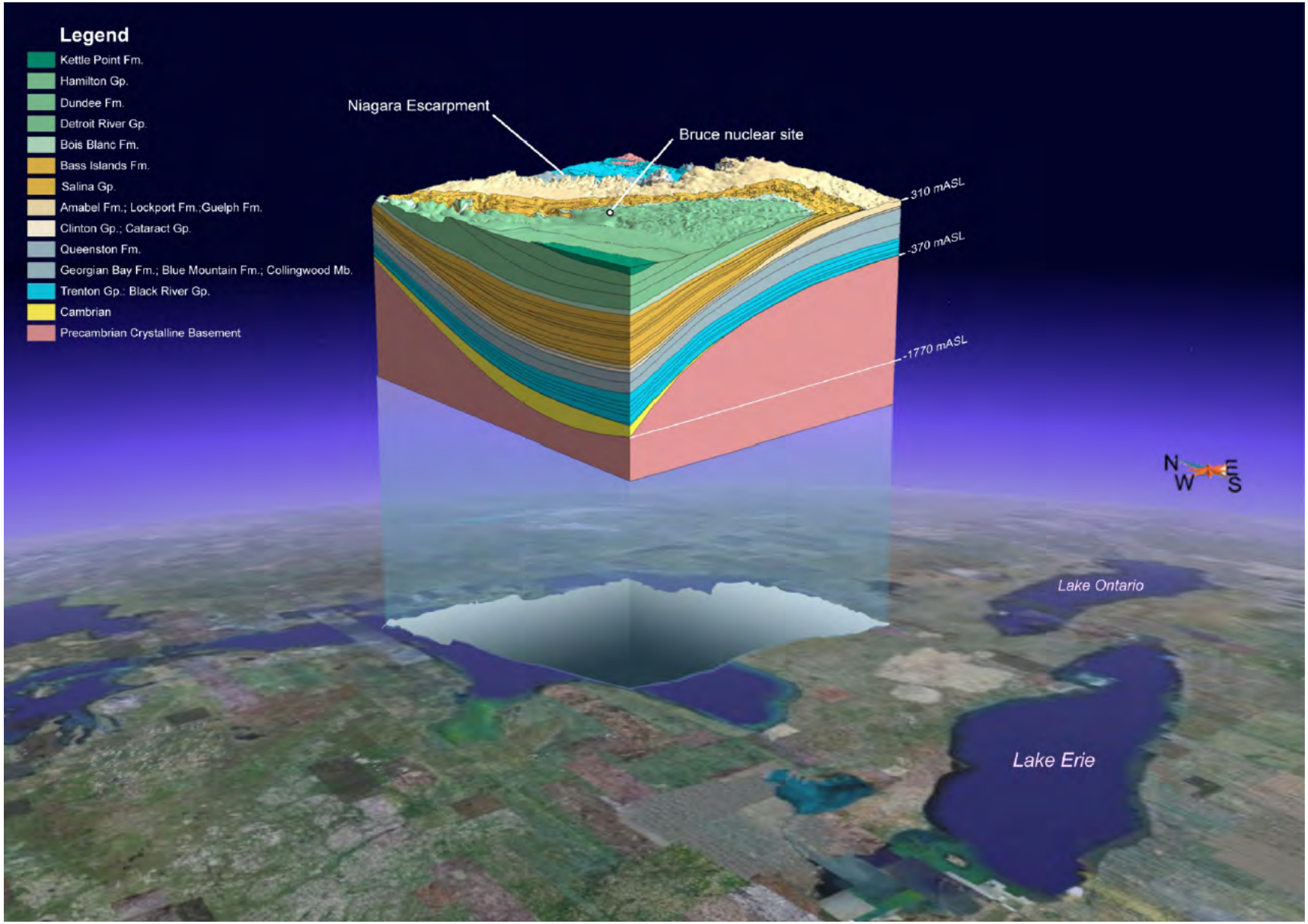

Note: From AECOM and ITASCA CANADA (2011).

Figure 2.6: 3D Geological Framework Box Diagram of the Regional Study Area

Table 2.1: Statistics for OGSR Data Which Was Also Used in Part to Develop the 3DGF Model and Compared with DGR Site Data Unit Thicknesses

Geological Unit	Samples	Mean Thickness [m]	Standard Deviation of Thickness [m]	Thickness at DGR [m] †
Dundee	67	15	8	*
Detroit River	94	103	31	**
Bois Blanc	93	52	19	49
Bass Islands	121	50	17	45.3
G Unit	90	9	6	9.3
F Unit	9	46	4	44.4
F Salt	10	15	6	*
E Unit	43	27	7	20.0
D Unit	44	9	3	1.6
B and C Units	88	28	7	46.6
B-Anhydrite/Salt	84	49	31	1.9
A-2 Carbonate	87	33	10	26.6
A-2 Anhydrite/Salt	85	13	11	5.8
A-1 Carbonate	82	36	8	41.5
A-1 Evaporite	82	5	4	3.5
Niagaran	109	55	39	34.1
Reynales/Fossil Hill	105	7	4	2.3
Cabot Head	71	21	12	23.8
Manitoulin	71	11	4	12.8
Queenston	72	85	25	70.3
Georgian Bay/Blue Mtn.	84	135	50	133.6
Cobourg	76	48	17	28.6
Sherman Fall	73	44	13	28.0
Kirkfield	70	39	11	45.9
Coboconk	73	13	8	23.0
Gull River	77	45	16	53.6
Shadow Lake	26	9	8	5.2
Cambrian	20	7	5	16.9

Note: † thickness of units at DGR-1 and DGR-2; * not present at site; ** full thickness not present at site.

Water samples were collected at various depths ranging from near surface to almost 4 km. A large variation in TDS is observed for the waters, with TDS values ranging from less than 1,000 mg/L to more than 400,000 mg/L. Applying the classification scheme developed by (Carpenter 1978, Section 5.1), 67% of the waters are brines, 20% are saline and 10% are brackish. Only 3% of the waters in the database are classified as fresh waters. The TDS values of waters are plotted as a function of sampling depth in Figure 2.8 for those waters where the depth of sampling was known. Most formation waters have high TDS values of between 140,000 and 400,000 mg/L. The highest salinity formation water reported from the Michigan Basin is a Ca−Na−Cl type brine sampled from the Salina Formation of the Michigan Basin with TDS values of 643,000 mg/L (Case 1945). In the current database, the most saline formation waters (TDS of approximately 400,000 mg/L) are also Ca−Na−Cl type waters, sampled in central Michigan from the Silurian carbonates of the Niagaran Formation at depths between 1,200 and 1,400 m and from Ordovician sandstones of the Prairie du Chien formation at depths of greater than 3,200 m. Three formation waters from Ordovician-aged carbonates sampled at depths of 200 m or less

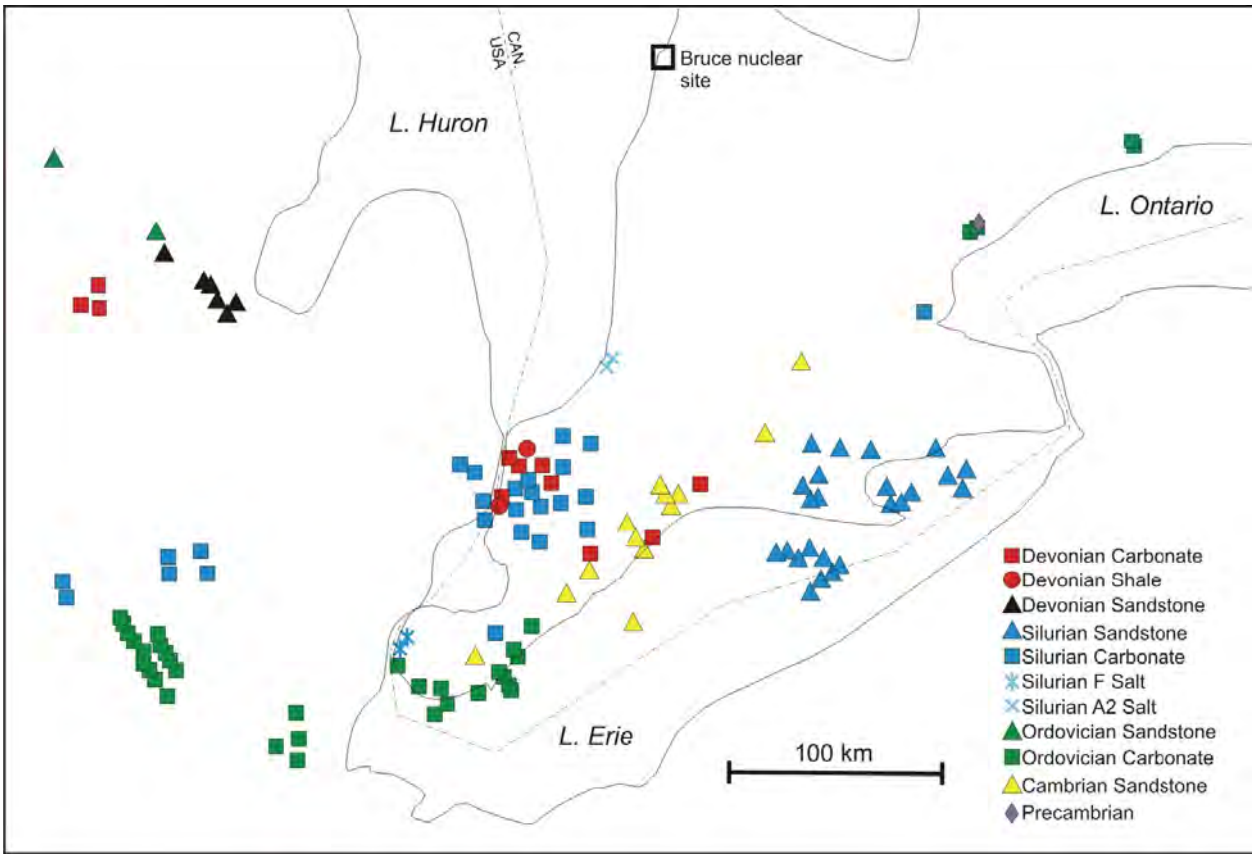

Note: From Hobbs et al. (2011). Samples collected from the sedimentary formations in southwestern Ontario and in central and eastern Michigan, USA. Modified from Frape et al. (1989).

Figure 2.7: Map Showing the Sampling Locations for Fluids in the UW Database

have TDS values ranging from 44,000 to 100,000 mg/L. Waters from Devonian carbonate formations and some Silurian carbonate formations sampled at depths of 300 m or less have TDS values below 20,000 mg/L. It is clear from Figure 2.8 that the TDS concentration for a given depth below surface varies significantly over the study area. The variation of TDS concentration is related to factors that include dissolution from halite and evaporite, rock water interactions, the state of marine waters at the time of sediment deposition, and flushing of TDS concentrations by infiltrating meteoric and basal meltwater.

Regarding the hydrogeochemistry of the Michigan Basin, the groundwater can be typified as being Na−Ca−Cl or Ca−Na−Cl brines. A summary of the water type data is presented in Table 2.2. The estimation over the regional-scale domain of the spatial distribution of TDS concentration and hence fluid density will have considerable uncertainty given the sparsity of data east and north of the DGR site, the large range in TDS concentrations for a given depth, the fact that the water type is not constant over the study area, and the lack of data to define the chemical evolution of pore fluids. In this hydrogeologic modelling study, the approach that was taken to define the regional-scale distribution of TDS concentration was to assign an initial spatially constant concentration for each rock layer and to allow that concentration to evolve and redistribute in the absence of source terms as meteoric or basal meltwater infiltrates the system.

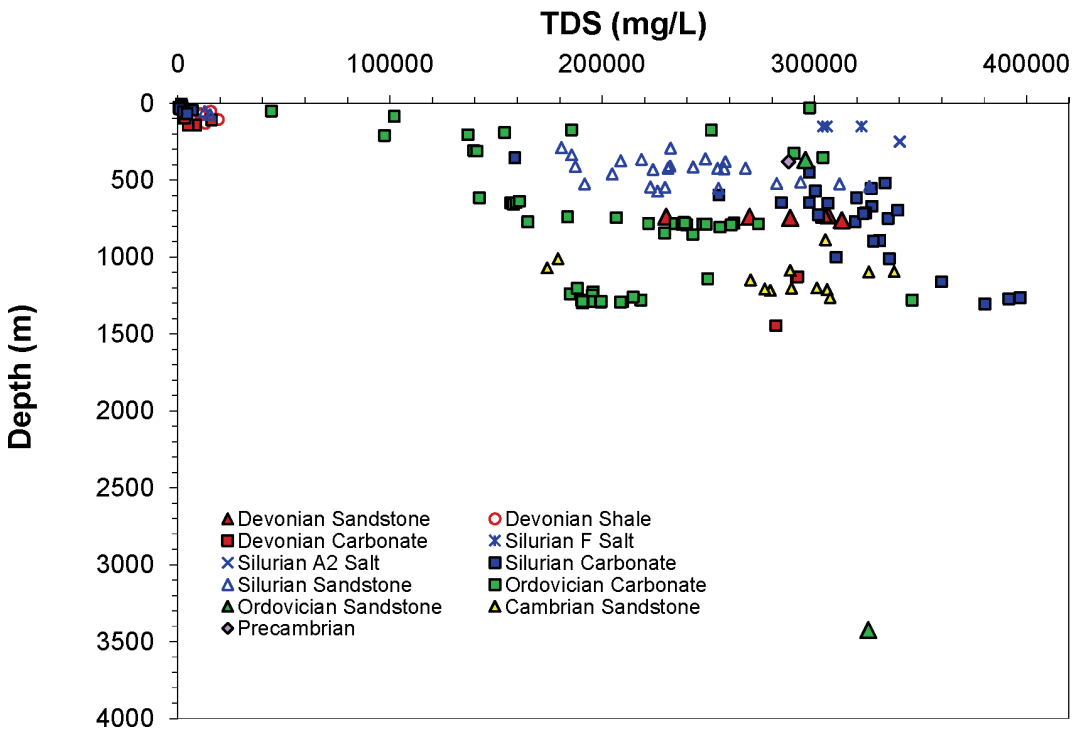

Note: From Hobbs et al. (2011). Only samples with depth information are included. The majority of waters are brines with TDS values between 150,000 and 400,000 mg/L.

Figure 2.8: Total Dissolved Solids Measured in Formation Waters from Southwestern Ontario Plotted as a Function of Sampling Depth

This conceptual model results in lower concentrations in recharge areas and higher concentrations at depth.

Isotopic signatures of glacial meltwaters have been found in central Ontario municipal wells screened at depths of 129 m in shallow bedrock, and at depths of 125 m in overburden, both comprising the Alliston aquifer system (Aravena et al. 1995). McIntosh and Walter (2006) state that paleowaters, originating in the Late Pleistocene and recharging from the Laurentide Ice-sheet into the subsurface along the northern margin of the Michigan Basin, have migrated to depths of nearly 900 ft (274 m) into Silurian-Devonian carbonate aquifers, significantly depressing the freshwater-saline interface.

In paleohydrology studies, the isotopic composition of groundwater can be used to determine its origin, and the temperature conditions that must have existed at that time. Precipitation at higher latitudes is associated with a depletion of the heavier isotopes, and can be correlated with lower temperatures. Deuterium (^{2}H) and oxygen-18 (^{18}O) compositions of water are commonly measured with respect to the Standard Mean Ocean Water (SMOW) standard (Domenico and Schwartz 1990). Since both ^{2}H and ^{18}O are heavier isotopes of hydrogen and oxygen, respectively, the evaporation and condensation processes of the hydrologic cycle will affect the

Table 2.2: Types of Waters Sampled from Different Formations Within the Database, Based on Dominant Ion Concentrations Expressed in meq/L

Age	Formation	Rock Type	Depth/ Range (m)	Water Type	Exceptions	TDS (mg/L)
Devonian	Berea	Sandstone	720-760 m**	Na-Ca-Cl	Campbell #7 and 9 (Ca-Na-Cl)	176,000 to 380,000
	Kettle Point	Shale	40-50	Na-Cl-HCO_3	LD-90-3-5 (Na-Cl)	640 to 15,500
	Hamilton	Shale	65-130	Na-Cl	-	7500 to 19,100
	Antrim	Shale	Not Known	Na-Cl	-	123,000 to 241,000
	Dundee	Carbonate	100-140	Na-Mg-Ca-Cl	LD-90-3-1 (Na-SO_4-Cl); DD-2 (Ca-Na-Cl) DD-1, DOW-90-3-1 (Na-Cl) PD-COCH (Na-Ca-Mg-Cl) RA-NE, RA-SE, RA-SW (Na-Ca-Cl)	3300 to 25,200
		Carbonate	1130	Na-Ca-Cl		292,000
	Detroit River	Carbonate	100-120	Na-Ca-Mg-Cl	CFN-C, CFS-D, LBO-2 (Na-Mg-Ca-Cl)	13,150 to 48,700
	Richfield	Carbonate	1445	Ca-Na-Cl	-	282,000
Silurian	Salina F	Salt	150	Na-Cl	-	305,000 to 322,000
	Salina A2	Salt	250	Ca-Na-Mg-Cl	-	340,000
	Salina A1	Carbonate	650	Ca-Na-Cl	-	284,000 to 306,000
	Guelph	Carbonate	355-770	Ca-Na-Cl	SG-1, -2, -3, -5 and -12 (Na-Ca-Cl)	159,000 to 335,000
	Guelph/Lockport/ Goat Island	Carbonate	5-65	Ca-Mg-SO_4	87-2-2 (Na-Ca-Cl); 87-1-2, 87-2-3 (Ca-Na-Mg-SO_4-Cl); 88-1-5	480 to 15,100

Age	Formation	Rock Type	Depth/ Range (m)	Water Type	Exceptions	TDS (mg/L)
					(Ca-Mg-HCO_3)	
	Niagaran	Carbonate	715-1305	Ca-Na-Cl	Cold Springs WH1-29; SN-6 (Ca-Cl); SN-3, SN-4 (Ca-Mg-Cl)	310,000 to 397,000
	Grimsby/Thorhold	Sandstone	290-570	Na-Ca-Cl	SGr-18,-19, -20 and -21 (Ca-Na-Cl)	181,000 to 326,000
	Thorhold	Sandstone	55-75	Na-Ca-Cl	-	12,600 to 15,200
	Whirlpool	Sandstone	360-460	Ca-Na-Cl	-	205,000 to 268,000
Ordovician	Blue Mountain	Carbonate	173	Ca-Na-Cl	-	186,000
	Trenton: Lindsay	Carbonate	50 200	Na-Ca-Cl Ca-Na-Cl	-	44,100 to 137,000
	Trenton: Verulum	Carbonate	85	Na-Ca-Cl	-	102,000
	Trenton: Bobcaygeon	Carbonate	30-325	Ca-Na-Cl	UN-2 #5 (Ca-Na-Mg-Cl)	251,000 to 298,000
	Black River: Gull River	Carbonate	190-350	Ca-Na-Cl	-	97,000 to 304,000
	Black-River: Shadow Lake	Sandstone	370	Ca-Na-Cl	-	154,000
	Trenton-Black River (undifferentiated)	Carbonate	310 to 1300	Na-Ca-Cl	OT-30 (Ca-Na-Cl)	141,000 to 346,000
	Prairie du Chien	Sandstone	3234 or 3425	Ca-Cl	Depth unknown for 3 samples Foster 1-21, OP-1 (Ca-Na-Cl)	325,000 to 392,000
Cambrian	(undifferentiated)	Sandstone	890-1265	Ca-Na-Cl	C-6 (Na-Ca-Cl)	174,000 to 338,000

Note: **Depth unknown for 7 samples. From Hobbs et al. (2011).

isotopic ratios of $^{2}H/^{1}H$ and $^{18}O/^{16}O$. The depletion or enrichment of a particular isotope is stated as a deviation from a standard as follows:

$$\delta = \frac{R_{\text{sample}} - R_{\text{standard}}}{R_{\text{standard}}} \times 1000 \qquad (2.1)$$

where δ is reported in permil (‰), and R is the isotope ratio for either the sample or standard. A $\delta^{18}O$ value of -20‰ means that the sample is depleted in ^{18}O relative to the standard by -20‰ or -2% (Domenico and Schwartz 1990).

2.4 Regional-Scale Hydrogeologic Parameters

An important aspect in characterizing the regional-scale groundwater system will be the assignment of reasonable permeabilities to the hydrostratigraphic units. Careful estimation of permeability values will help increase the accuracy of the hydrogeologic model. The estimated horizontal hydraulic conductivities developed from the field investigation at the Bruce nuclear site are presented in Section 2.5.5.1. Other data from previous insitu measurements at other sites in Ontario are listed in Table 2.3, Table 2.4, Table 2.5 and Table 2.6. The minimum and maximum values of hydraulic conductivity that are reported in the tables represent the range of values for a given unit. It should be noted that in many instances, the minimum hydraulic conductivities reported are at the measurement limit of the hydrogeologic testing equipment used in these previous studies; the values do not reflect the hydraulic conductivities or permeabilities that would be measured with testing equipment and protocols commensurate with those used in the DGR site investigation. The values reported in the tables generally represent point estimates at boreholes with the hydraulic conductivities reflecting a small volume around the borehole wall; that is, they are not up-scaled values that may be more representative of a regional-scale flow domain beyond the skin of the borehole. Finally, the tables include values for the various units of the Niagaran Group rather than an integrated value for that group.

In each of the tables, the formations with the lowest measured hydraulic conductivities are the Ordovician shales and limestones, with hydraulic conductivities typically in the range of approximately 1×10^{-11} m/s; the values measured in the DGR boreholes using improved techniques are significantly lower (refer to Table 2.8 in the following section). The low permeability Ordovician and Lower Silurian units are bounded above by the Niagaran Group, which is more permeable with reported horizontal hydraulic conductivities typically estimated at 1×10^{-8} m/s, and bounded below by the Cambrian Formation which, based on field measurements performed on the DGR boreholes at the Bruce nuclear site, has a horizontal hydraulic conductivity value of 3×10^{-6} m/s. Further, based on data from the field program (refer to Figure 2.15 in Section 2.5.3), the Cambrian is significantly over-pressured with respect to the overlying Ordovician units. Present day hydraulic gradients at the Bruce nuclear site are upward from the Cambrian to the Ordovician units. Similar to the Cambrian, the Niagaran Group has a much higher permeability than the underlying Lower Silurian and Ordovician formations, and is also bounded immediately above by the Salina Formation and bounded below by low permeability formations such as the Cabot Head shale; the Niagaran Group is also highly continuous.

2.5 DGR Site Data

This section presents an overview of the DGR site data (INTERA 2011) relevant to the development of the regional-scale and site-scale conceptual model. It also presents the geochemical profiles for selected species in the DGR boreholes as the data are relevant to the assessment of the hypothesis that pore water in the Ordovician sediments is stagnant. A full

Table 2.3: Paleozoic Hydraulic Conductivities from Raven et al. (1992)

Formation	Borehole	K_{min} [m/s]	K_{max} [m/s]
Dundee	MDMW-1 Sarnia	4.0×10^{-13}	1.3×10^{-7}
Lucas	MDMW-1 Sarnia	2.5×10^{-9}	3.2×10^{-7}
Amherstburg	MDMW-1 Sarnia	3.2×10^{-11}	7.9×10^{-9}
Guelph	USNI-1 Niagara Falls	1.6×10^{-7}	1.0×10^{-5}
Guelph	NI-1 Niagara Falls	7.9×10^{-9}	6.3×10^{-5}
Goat Island	USNI-1 Niagara Falls	3.2×10^{-8}	1.0×10^{-5}
Goat Island	NI-1 Niagara Falls	3.2×10^{-9}	2.0×10^{-5}
Gasport	USNI-1 Niagara Falls	1.0×10^{-13}	1.0×10^{-13}
Gasport	NI-1 Niagara Falls	2.0×10^{-8}	2.0×10^{-8}
Rochester	USNI-1 Niagara Falls	1.0×10^{-13}	2.5×10^{-7}
Rochester	NI-1 Niagara Falls	1.3×10^{-9}	1.3×10^{-7}
Reynales/Fossil Hill	USNI-1 Niagara Falls	1.0×10^{-12}	2.5×10^{-11}
Reynales/Fossil Hill	USNI-1 Niagara Falls	3.2×10^{-11}	3.2×10^{-11}
Cabot Head	NI-1 Niagara Falls	6.3×10^{-11}	6.3×10^{-11}
Queenston	USNI-1 Niagara Falls	2.5×10^{-13}	2.0×10^{-11}
Queenston	USNI-1 Niagara Falls	4.0×10^{-11}	1.0×10^{-9}
Georgian Bay	OHD-1 Lakeview	1.0×10^{-13}	4.0×10^{-12}
Collingwood	OHD-1 Lakeview	1.0×10^{-12}	1.0×10^{-12}
Cobourg	OHD-1 Lakeview	1.0×10^{-13}	6.3×10^{-12}
Cobourg	UN-2 Darlington	6.3×10^{-14}	1.6×10^{-11}
Sherman Fall	OHD-1 Lakeview	2.0×10^{-14}	1.3×10^{-12}
Sherman Fall	UN-2 Darlington	1.0×10^{-13}	7.0×10^{-9}
Kirkfield	OHD-1 Lakeview	1.0×10^{-13}	4.0×10^{-12}
Kirkfield	UN-2 Darlington	1.0×10^{-13}	4.0×10^{-12}
Gull River	OHD-1 Lakeview	2.5×10^{-14}	2.5×10^{-11}
Gull River	UN-2 Darlington	1.0×10^{-13}	1.0×10^{-12}
Shadow Lake	OHD-1 Lakeview	1.0×10^{-13}	1.0×10^{-9}
Shadow Lake	UND-1 Darlington	1.0×10^{-13}	1.0×10^{-12}

Table 2.4: Paleozoic Hydraulic Conductivities from GOLDER (2003)

Formation	Borehole	K_{min} [m/s]	K_{max} [m/s]
Bois Blanc	Bruce	5.0×10^{-11}	9.0×10^{-5}
Cobourg	DDH01/02 Bowmanville	1.3×10^{-12}	4.0×10^{-11}
Sherman Fall	DDH01/02 Bowmanville	5.0×10^{-13}	2.0×10^{-9}
Kirkfield	DDH01/02 Bowmanville	1.0×10^{-11}	6.3×10^{-9}
Gull River	DDH01/02 Bowmanville	2.0×10^{-11}	6.3×10^{-9}
Shadow Lake	DDH01/02 Bowmanville	5.0×10^{-9}	1.0×10^{-8}

Table 2.5: Paleozoic Hydraulic Conductivities from Novakowsi and Lapcevic (1988)

Formation	Borehole	K_{min} [m/s]	K_{max} [m/s]
Guelph	Niagara	1.4×10^{-8}	2.8×10^{-4}
Goat Island	Niagara	7.8×10^{-11}	5.5×10^{-4}
Gasport	Niagara	1.0×10^{-11}	1.7×10^{-6}
Rochester	Niagara	1.0×10^{-11}	1.7×10^{-6}
Reynales/Fossil Hill	Niagara	1.0×10^{-11}	1.7×10^{-6}
Cabot Head	Niagara	1.0×10^{-11}	2.0×10^{-7}
Queenston	Niagara	1.0×10^{-11}	2.4×10^{-10}

Table 2.6: Paleozoic Hydraulic Conductivities from INTERA (1988)

Formation	Borehole	K_{min} [m/s]	K_{max} [m/s]
Dundee	Sarnia	5.0×10^{-12}	1.0×10^{-9}
Dundee	Ojibway Mine	1.0×10^{-7}	1.0×10^{-6}
Lucas	Sarnia	1.0×10^{-8}	1.0×10^{-7}
Lucas	Goderich Mine	1.0×10^{-7}	1.0×10^{-6}
Lucas	Ojibway Mine	1.0×10^{-7}	1.0×10^{-6}
Amherstburg	Sarnia	1.0×10^{-11}	1.0×10^{-9}
Amherstburg	Goderich Mine	1.0×10^{-7}	1.0×10^{-6}
Amherstburg	Ojibway Mine	1.0×10^{-7}	1.0×10^{-6}
Bois Blanc	Nanticoke Tunnel	1.0×10^{-9}	1.0×10^{-8}
Bass Islands	Goderich Mine	1.0×10^{-7}	1.0×10^{-6}
Bass Islands	Ojibway Mine	1.0×10^{-7}	1.0×10^{-6}
Cobourg	Darlington Tunnels	1.0×10^{-12}	1.0×10^{-12}
Cobourg	Wesleyville	1.0×10^{-11}	1.0×10^{-8}
Cobourg	Wesleyville	2.0×10^{-10}	4.0×10^{-6}
Sherman Fall	Wesleyville	1.0×10^{-11}	1.0×10^{-8}

description of the DGR site data and the Descriptive Geosphere Site Model is provided in INTERA (2011).

2.5.1 Stratigraphic Units

The thickness and depth below ground surface for the stratigraphic units at DGR-1 and DGR-2 are listed in Table 2.7 (INTERA 2011). In the table, the member units of the Niagaran Group (Guelph, Goat Island, Gasport and Lions Head units – refer to Figure 1.2) that are observed in the boreholes are listed. The F-Unit defines the top of the intermediate regime or zone. Between the Guelph dolomites and the Cambrian sandstones and carbonates there is approximately 460 m of low permeability shale and limestone that includes the Cobourg, the target horizon for the proposed DGR.

2.5.2 Major Ions and Environmental Isotopes

Inorganic data for the DGR boreholes (INTERA 2011) are given in Figure 2.9, Figure 2.10, Figure 2.11 and Figure 2.12. Variation of geochemistry is evident; the difference in the total dissolved solids concentration measured in core samples from the four DGR boreholes (Figure 2.10) is more than 200 g/L for the Cobourg; the range in TDS for the other units in the Ordovician shales and limestones is approximately 100 g/L or more. The core samples from the

Table 2.7: Unit Thickness and Depth to Top of Formation Data for DGR-1 and DGR-2

Unit	Thickness [m]	Depth to Top [m]
Lucas	10.4	20.0
Amherstburg	44.6	30.4
Bois Blanc	49.0	75.0
Bass Islands	45.3	124.0
Salina G Unit	9.3	169.3
Salina F Unit	44.4	178.6
Salina E Unit	20.0	223.0
Salina D Unit	1.6	243.0
Salina C Unit	15.7	244.6
Salina B Unit-Carb	30.9	260.3
Salina B Unit-Evap	1.9	291.2
Salina A2 Unit - Carb	26.6	293.1
Salina A2 Unit-Evap	5.8	319.7
Salina A1 Unit - Carb	41.5	325.5
Salina A1 Unit -Evap	3.5	367.0
Salina A0 Unit	4.0	370.5
Guelph‡	4.1	374.5
Goat Island‡	18.8	378.6
Gasport‡	6.8	397.4
Lions Head‡	4.4	404.2
Fossil Hill	2.3	408.7
Cabot Head	23.8	411.0
Manitoulin	12.8	434.8
Queenston	70.3	447.6
Georgian Bay	90.9	518.0
Blue Mountain	42.7	608.9
Collingwood Member	7.9	651.6
Cobourg	28.6	659.5
Sherman Fall	28.0	688.1
Kirkfield	45.9	716.1
Coboconk	23.0	762.0
Gull River	53.6	785.0
Shadow Lake	5.2	838.6
Cambrian	16.9	843.8
Precambrian	–	860.7

Note: ‡ The Guelph, Goat Island, Gasport and Lions Head comprise the Niagaran Group. From INTERA (2011).

DGR boreholes also indicates that there are significant differences in the concentrations of the major cations of Na, Ca, and Mg. The data of Figure 2.9 for the Ordovician shales and limestones indicates that, generally, Na concentrations are highest in DGR-2 and lowest in DGR-4. The calcium data of Figure 2.11 shows a similar trend with the concentrations being highest in DGR-2 and lowest in DGR-4; the same figure shows that the magnesium concentrations are highest in DGR-3 and lower in DGR-2. The range in Na concentrations in a given horizon is more than 1,500 mmol/kgw. The range in the Ca concentrations can be 900 mmol/kgw while the concentration range for Mg can be up to 1,000 mmol/kgw.

The result of the variation in inorganic concentrations between the DGR boreholes is further exemplified in the plot of the Cl/Na ratio in Figure 2.12. The data of the figure indicates a greater range at the bottom of the Ordovician limestone than at the top with the ratios generally being lower for core samples from DGR-2 than for core samples from DGR-4. It also is noted that the difference in concentrations in the Cambrian at the DGR boreholes is less than the variation in concentrations in the Ordovician. To explain the range in the inorganic concentrations in the core samples from the same horizon in the Ordovician shale and limestone, it is hypothesized that in the absence of concentration differences that could be explained by laboratory and measurement techniques, the range in the data indicates a diminished impact of diffusion as a solute transport mechanism and that the chemistry has weak spatial dependence.

The $\delta^{18}O$ and δD profiles in the DGR boreholes are presented in Figure 2.13 and Figure 2.14 respectively. It can be observed in the figures that there is a considerable range in the concentrations at a given horizon in the Ordovician limestone with the variation in the data being greatest at the bottom. The range in the $\delta^{18}O$ can be 5‰ or more with the general trend in the levels at a given depth in the Ordovician limestone being the DGR-2 values (red symbols) are the lowest, the DGR-3 values (green symbols) are intermediate and the DGR-4 values (blue symbols) are highest. Referring to Figure 2.14, it is observed that the δD varies by more than 50‰ with a spatial pattern being evident. The levels for both $\delta^{18}O$ and δD are approximately the same in the Cambrian water samples. Both the $\delta^{18}O$ and δD profiles support the hypothesis postulated in the preceding paragraph on the major ions that for the Ordovician limestone, that assuming similar laboratory and measurement procedures, there is a degree of spatial independence in the geochemical data measured in the DGR boreholes. This implies that either the solute transport processes are different at the locations of the boreholes or that the concentrations are relatively insensitive to transport and that there is a greater dependence on local-scale rock water interactions.

An important implication of the spatial difference in the major ion concentrations is that fluid densities will also vary both between units and within a given unit. The estimation of the horizontal water gradient in a unit or formation is dependent on estimates of fluid density and punctual measurements of pressure (refer to Section 3.5). The uncertainty in estimates of horizontal water gradients within a unit from borehole pressure data will be dependent on the uncertainty of the fluid density estimates. The DGR site data do not permit the estimation of a unique horizontal water gradient within a given unit.

2.5.3 Measured Pressures in the DGR Boreholes

Pressure data obtained on June 6, 2009 and later dates from the Westbay MP multi-level casing in the DGR-4 borehole have been used to estimate the vertical profile of equivalent freshwater head and the environmental head from the ground surface to the Precambrian at the Bruce nuclear site (refer to Figure 2.15). The estimation of environmental heads from the measured pressures is based on either the measured or estimated water density at the point of pressure

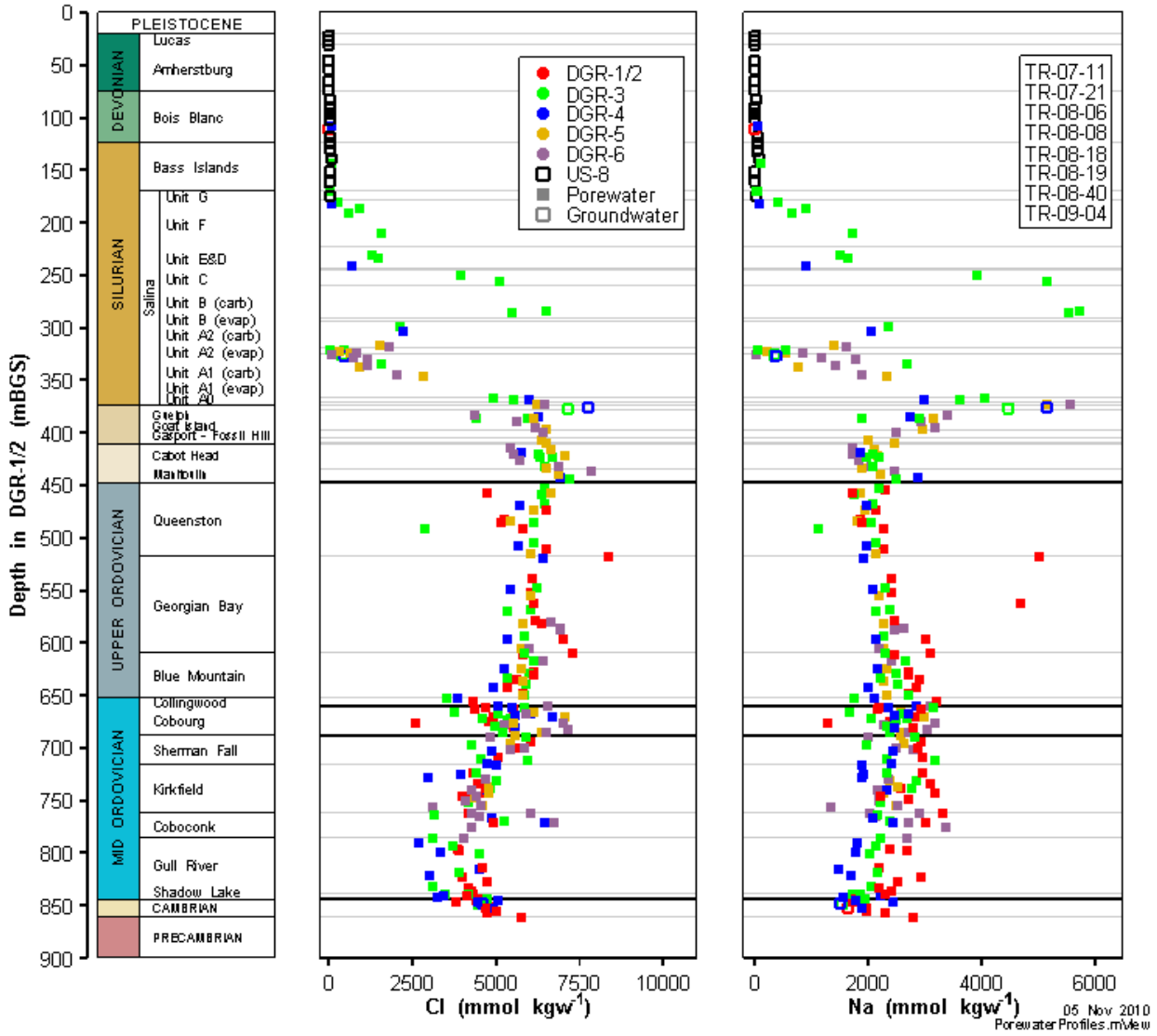

Note: From (INTERA 2011).

Figure 2.9: Profiles of Chloride and Sodium Concentrations in Porewater and Groundwater from US-8 and DGR Boreholes

measurement. Water density estimates are derived using total dissolved solids concentrations. The environmental heads, which can be used to estimate vertical groundwater gradients, were approximated from the measured pressure (density) profile within the open borehole prior to inflation of Westbay casing packers of the hole. Data from subsequent measurement events indicate that the pressures are slowly shifting, particularly for the low permeability units, toward equilibrium values. As such, the pressures used to develop the data shown in Figure 2.15 are not at their final values. Based on a surface elevation of 181.6 mASL, the environmental head profile in DGR-4 clearly shows that the Cambrian is significantly over-pressured with respect to the ground surface; the Ordovician and Lower Silurian are significantly under-pressured while units in the Niagaran are moderately over-pressured. Groundwater gradients are thus upward from the

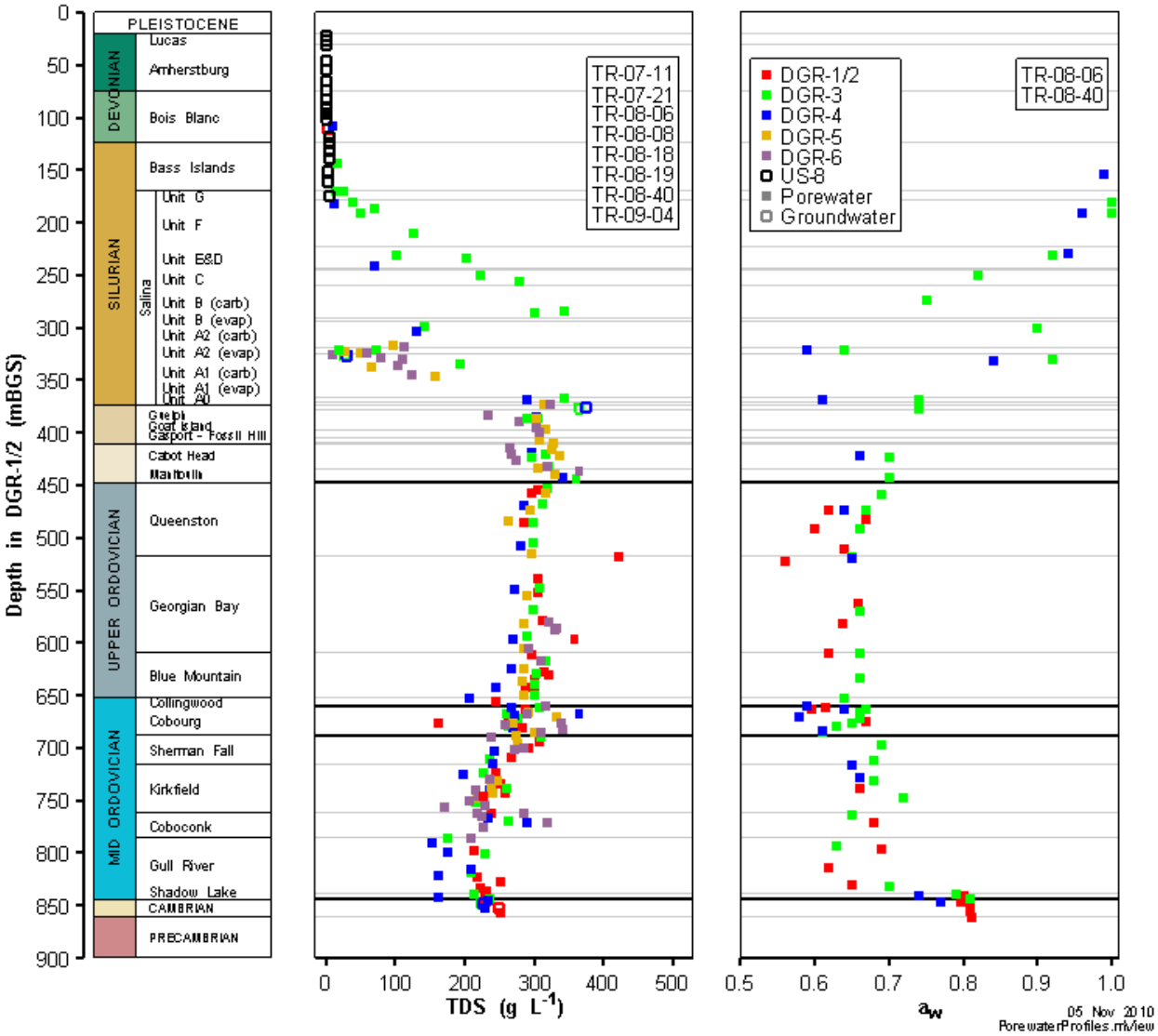

Note: From (INTERA 2011).

Figure 2.10: Profiles of TDS Concentrations and Water Activity in Porewater and Groundwater from US-8 and DGR Boreholes

Cambrian to the Ordovician, and downward from the Niagaran to the Ordovician. The low permeability of the Salina isolates the Niagaran from the more permeable units of the Devonian.

2.5.4 Fluid Saturations

Petrophysical testing of DGR borehole core samples indicates the possible presence of a separate gas phase in the Ordovician and Silurian sediments (INTERA 2011). While the laboratory analysis of the core samples did not reveal the presence of an immiscible oil phase, during the drilling of the DGR boreholes, there were observations of hydrocarbons in cores recovered from the Devonian, Silurian and Ordovician formations (INTERA 2011). The

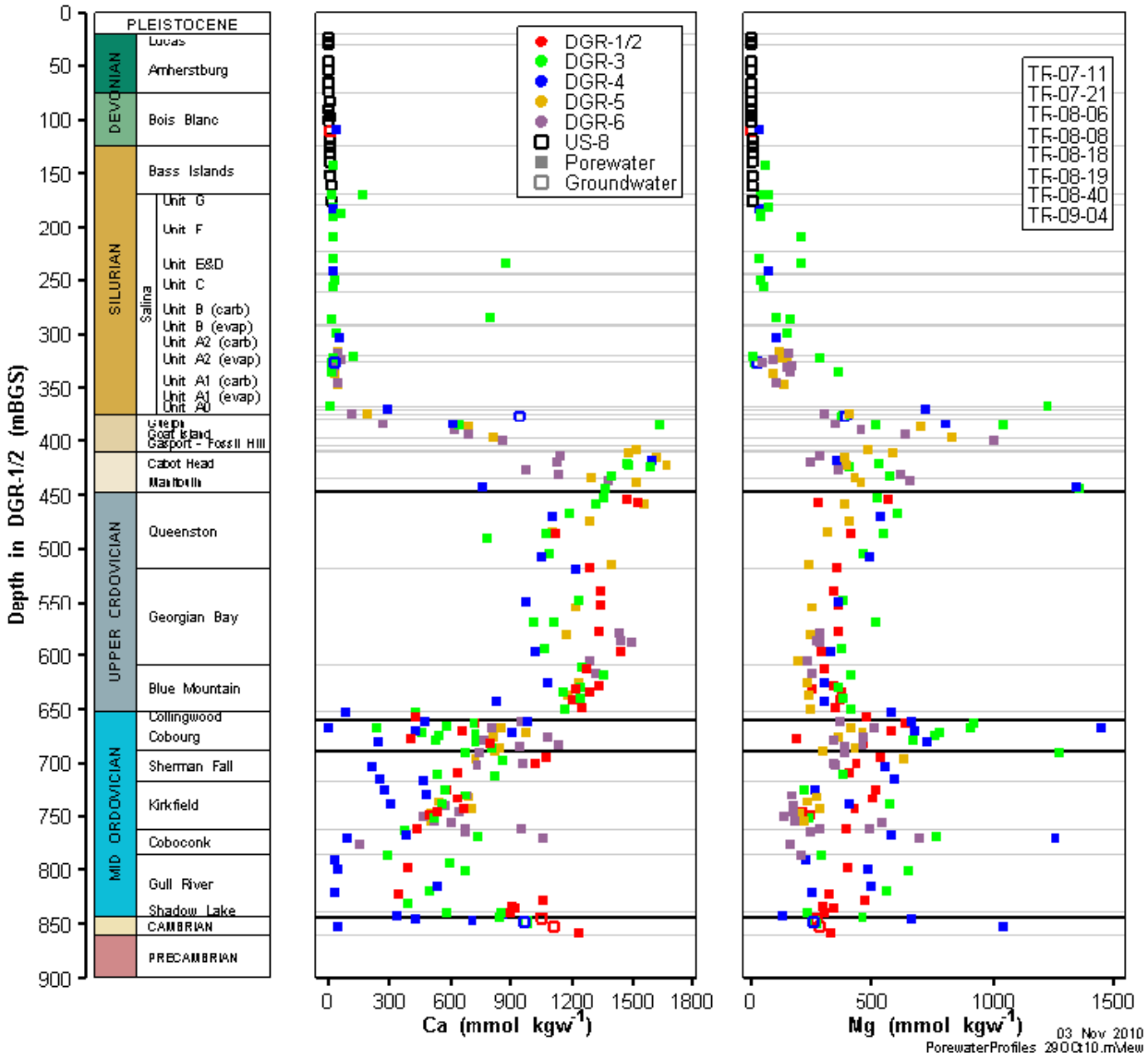

Note: From (INTERA 2011).

Figure 2.11: Profiles of Calcium and Magnesium Concentrations in Porewater and Groundwater from US-8 and DGR Boreholes

hydrocarbon occurrence in zones of the Ordovician Georgian Bay, Collingwood and Blue Mountain member was recorded as petroliferous shale with hydrocarbon odour. The hydrocarbon occurrence in zones of the Cobourg limestone was recorded as bituminous laminations throughout. Observations of zones of the Coboconk, Gull River and Shadow Lake indicate oil weeping (seeping or bubbling) from the core. Taken together, it can be concluded from both the core observations and the analysis of the core samples that an oil phase exists in the Ordovician shales and limestone but the oil phase is not continuous. The saturation of the oil phase is uncertain. Given the presence of a discontinuous oil phase in the Ordovician, it is also possible that a separate but related gas phase occurs. In addition to the evidence for a gas phase

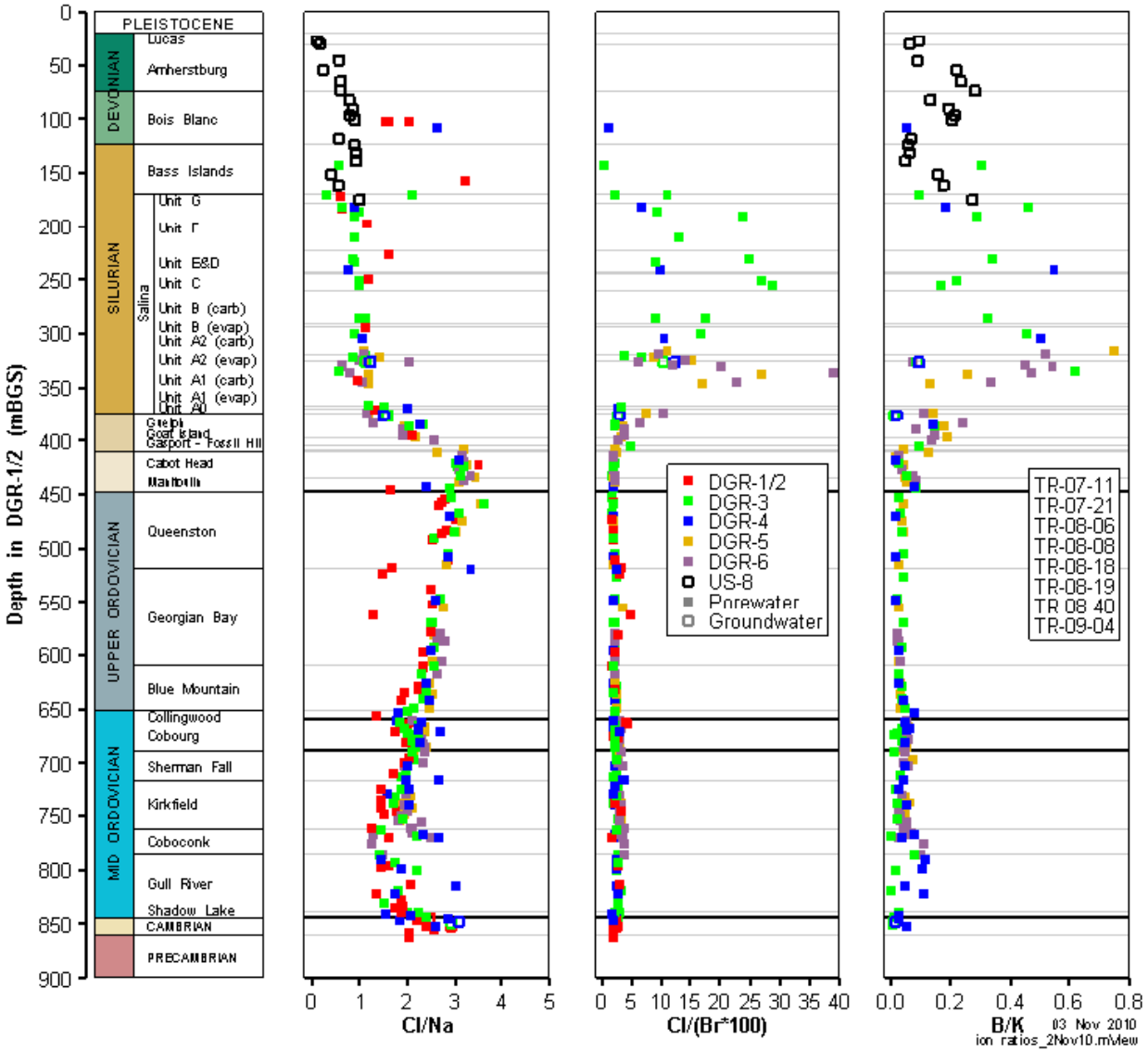

Note: From (INTERA 2011).

Figure 2.12: Profiles of Ion Molal Ratios of Porewater and Groundwater from US-8 and DGR Boreholes

provided by the analysis of the DGR borehole core samples, the interpretation of apparent CH_4 concentrations in pore fluids provides support for the occurrence of a gas phase.

The results for petrophysical testing of saturations are presented graphically in Figure 2.16 (INTERA 2011). The testing of the DGR borehole core samples indicates that the median gas saturation estimated for the Silurian rocks is 14%, for the Ordovician shale it is 11%, and it is 9% for the Ordovician limestone and the Cambrian dolostone/sandstone (Clark et al. 2010). The presence of both a gas content and an oil phase in the Ordovician pore space is expected to contribute to a lowering of the in-situ effective diffusion coefficients D_e such that the laboratory measurements based on water saturation may overestimate the in-situ diffusion values by one or

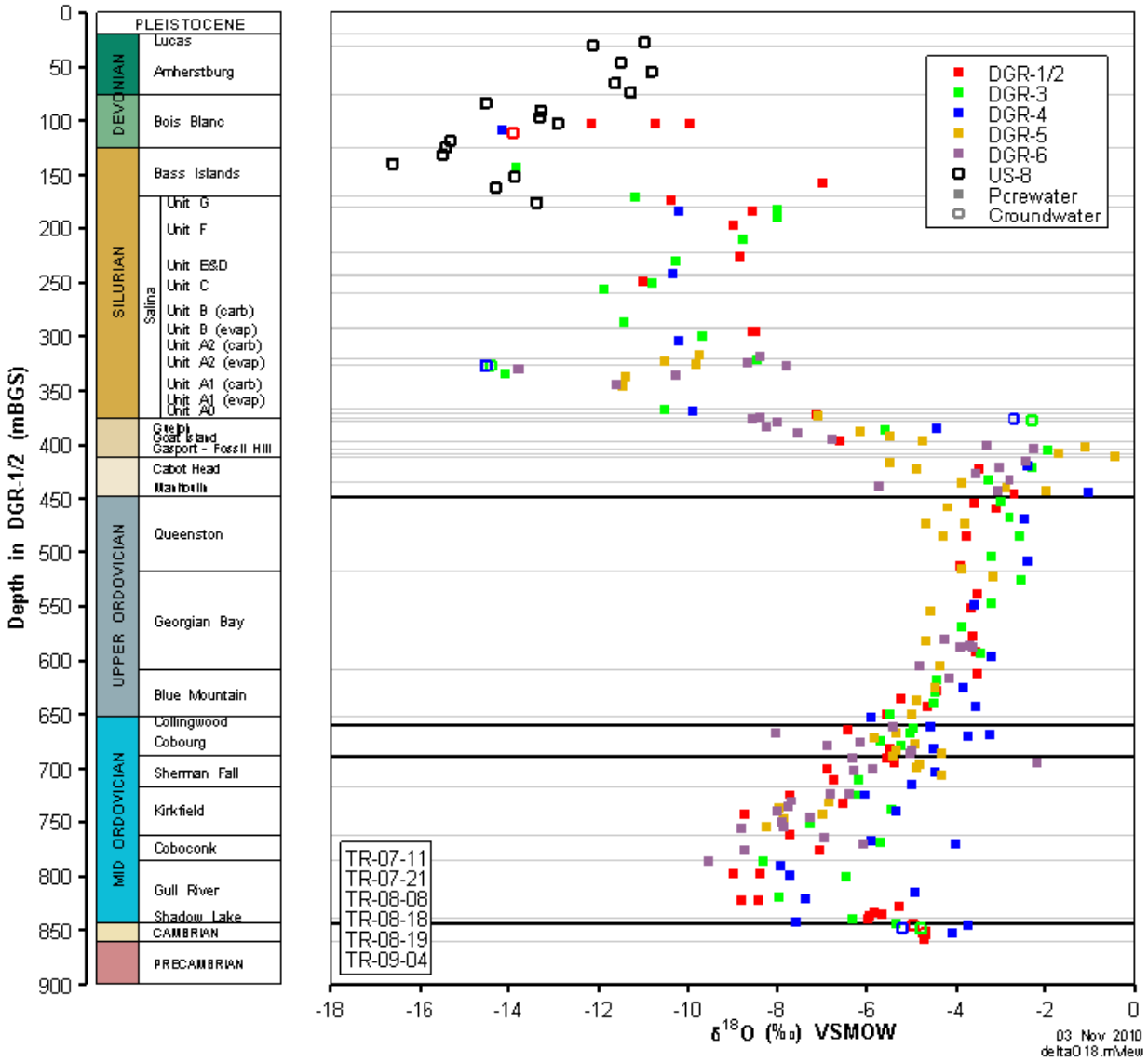

Note: From (INTERA 2011).

Figure 2.13: Profile of $\delta^{18}O$ of Porewater and Groundwater from US-8 and DGR Boreholes

two orders of magnitude in stratigraphic intervals where partial water saturated conditions exist (Saripalli et al. 2002). The presence of a gas phase also impacts geomechanical processes.

The methane concentrations from DGR borehole rock core samples are plotted in Figure 2.17 (INTERA 2011). The methane measured in the porewater were calculated by dividing the mass of methane released from a core sample by the amount of water released from the same sample. The apparent concentration data for CH_4 are thus presented in terms of the mass of gas per mass of water. These apparent concentrations do not provide an accurate measure of dissolved gas content in cases where the pore space may contain a discrete gas phase. However, the

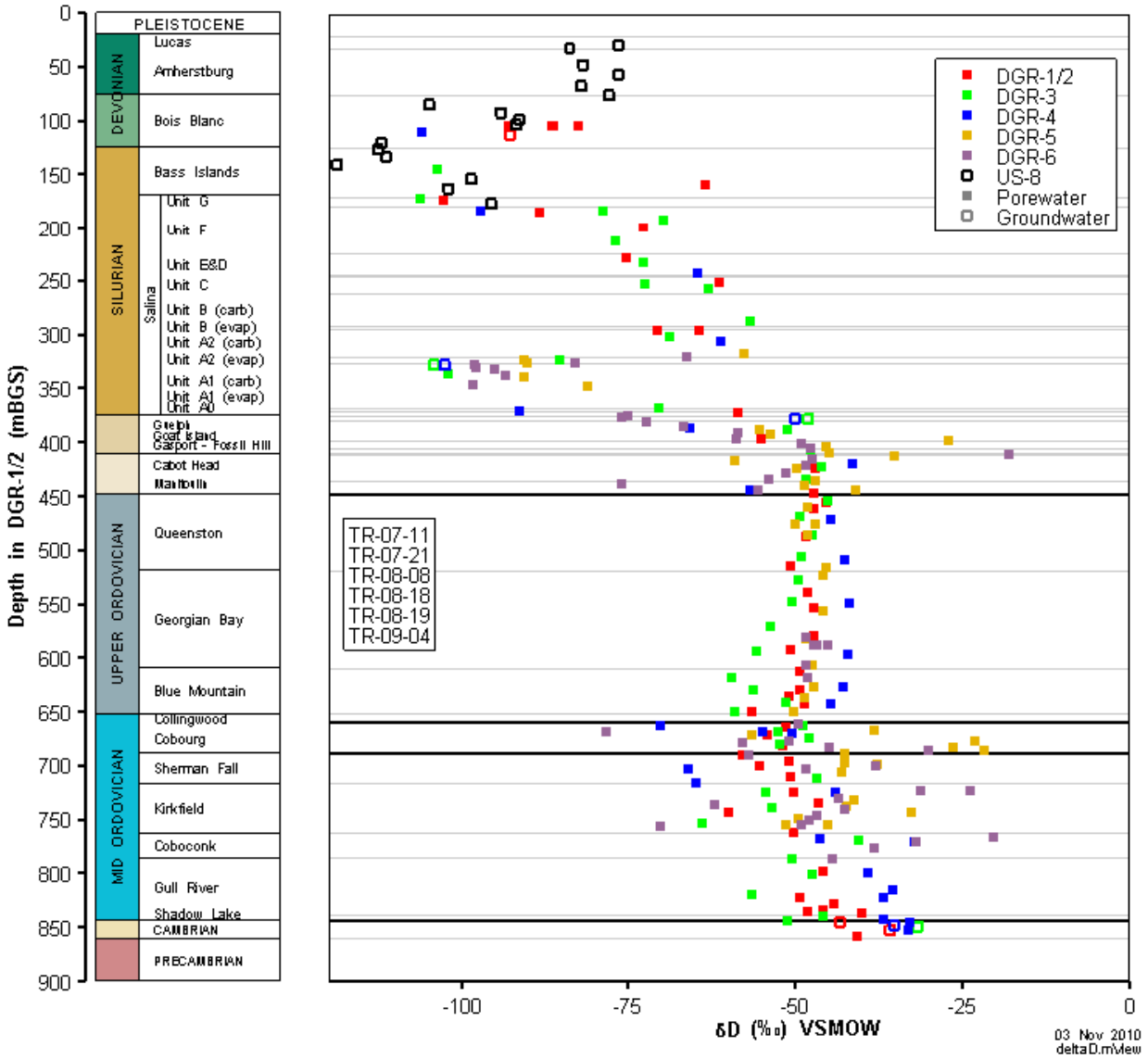

Note: From (INTERA 2011).

Figure 2.14: Profile of δD of Porewater and Groundwater from US-8 and DGR Boreholes

reported “aqueous” gas concentrations can be compared to expected solubility limits, and values in excess of solubility limits provide additional evidence for the presence of a separate gas phase.

Referring to Figure 2.17, the results for DGR-2 cores show increased apparent methane concentrations from the Queenston Formation to the bottom of the Collingwood Member with a maximum methane concentration being measured in the Cobourg Formation. Apparent methane concentrations in DGR-3 and DGR-4 cores increased from near the Cabot Head Formation to the maximum in the Cobourg Formation. Relatively high apparent concentrations were also observed in the Coboconk and Gull River Formations. The apparent differences in the levels of the concentrations between the DGR-2 cores and those of DGR-3 and DGR-4 are related to measurement technique; however, the patterns in the data are similar.

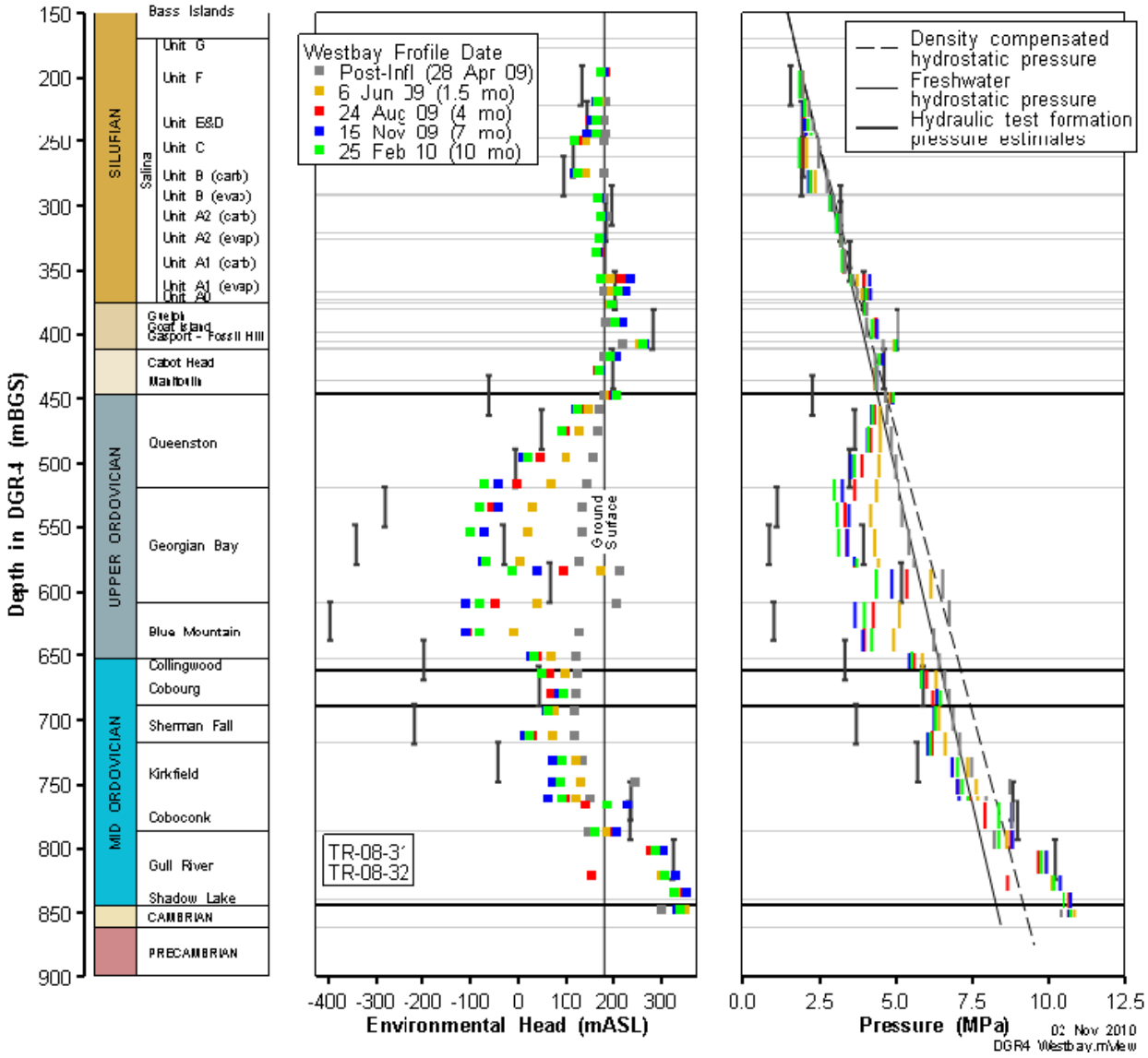

Note: From (INTERA 2011).

Figure 2.15: DGR-4 Formation Pressure and Environmental Head Profiles, April 2009 (Post Inflation), June 2009, August 2009, November 2009 and February 2010

The solubility limit for CH_4 in brine as a function of pressure and temperature has been investigated by (Duan and Mao 2006). The calculations of INTERA (2011) based on the work of (Duan and Mao 2006) indicate a maximum solubility of approximately 0.02 mol/kgw at the pressure and temperature conditions of the Ordovician sedimentary rocks. In the absence of a third liquid petroleum phase, the occurrence in the core samples of CH_4 in excess of this value provides additional evidence that a separate gas phase exists in most samples from the Upper Ordovician shale and the Cobourg Formation. Specifically, the analysis of INTERA (2011) suggests that based on the apparent CH_4 concentrations, methane in a gas phase could be present in the Salina A1 Unit, the Manitoulin, the Georgian Bay, Blue Mountain, Collingwood,

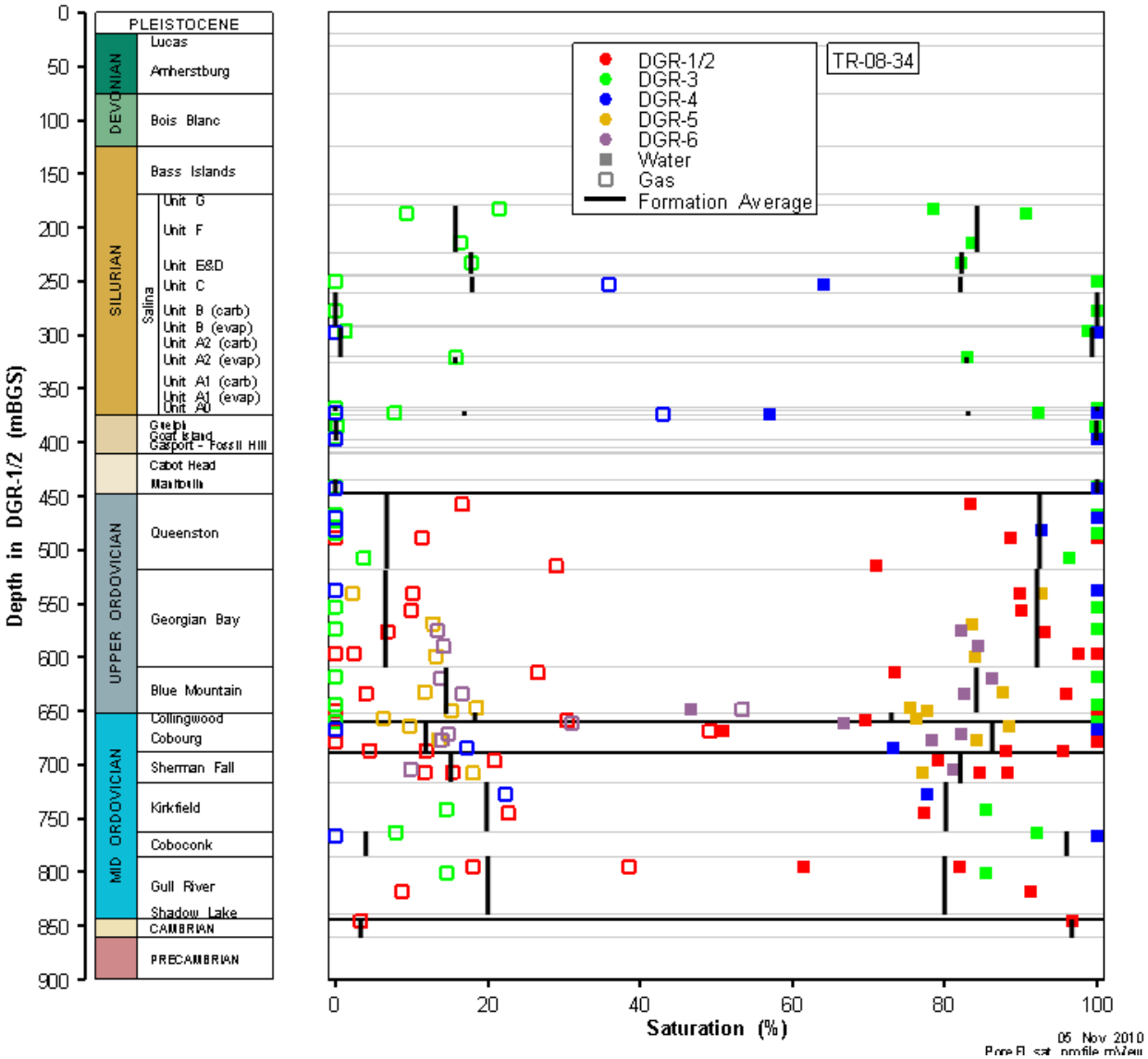

Note: From (INTERA 2011).

Figure 2.16: Pore Water (Brine) and Gas Saturation Profiles in Confined (DGR-2, DGR-3 and DGR-4) and Unconfined (DGR-5 and DGR-6) Cores Showing Point Data and Arithmetic Formation Averages

Cobourg, Coboconk, Sherman Fall and Kirkfield units/formations. Their analysis does not account for methane adsorbed to organic carbon in the formations; methane adsorption to organic carbon may be significant where high Total Organic Carbon (TOC) is present. It is concluded that methane is still likely present as a gas phase in the Collingwood member and possibly the Cobourg and Blue Mountain Formations. INTERA (2011) state that a decrease in pore pressure may cause dissolved methane to exolve from the porewater.

Stable isotope data provide important insight into the origin of the CH_4 (INTERA 2011). The $\delta^{13}C$ and δD data for CH_4 define two fields, one for CH_4 of biogenic origin in the Upper Ordovician

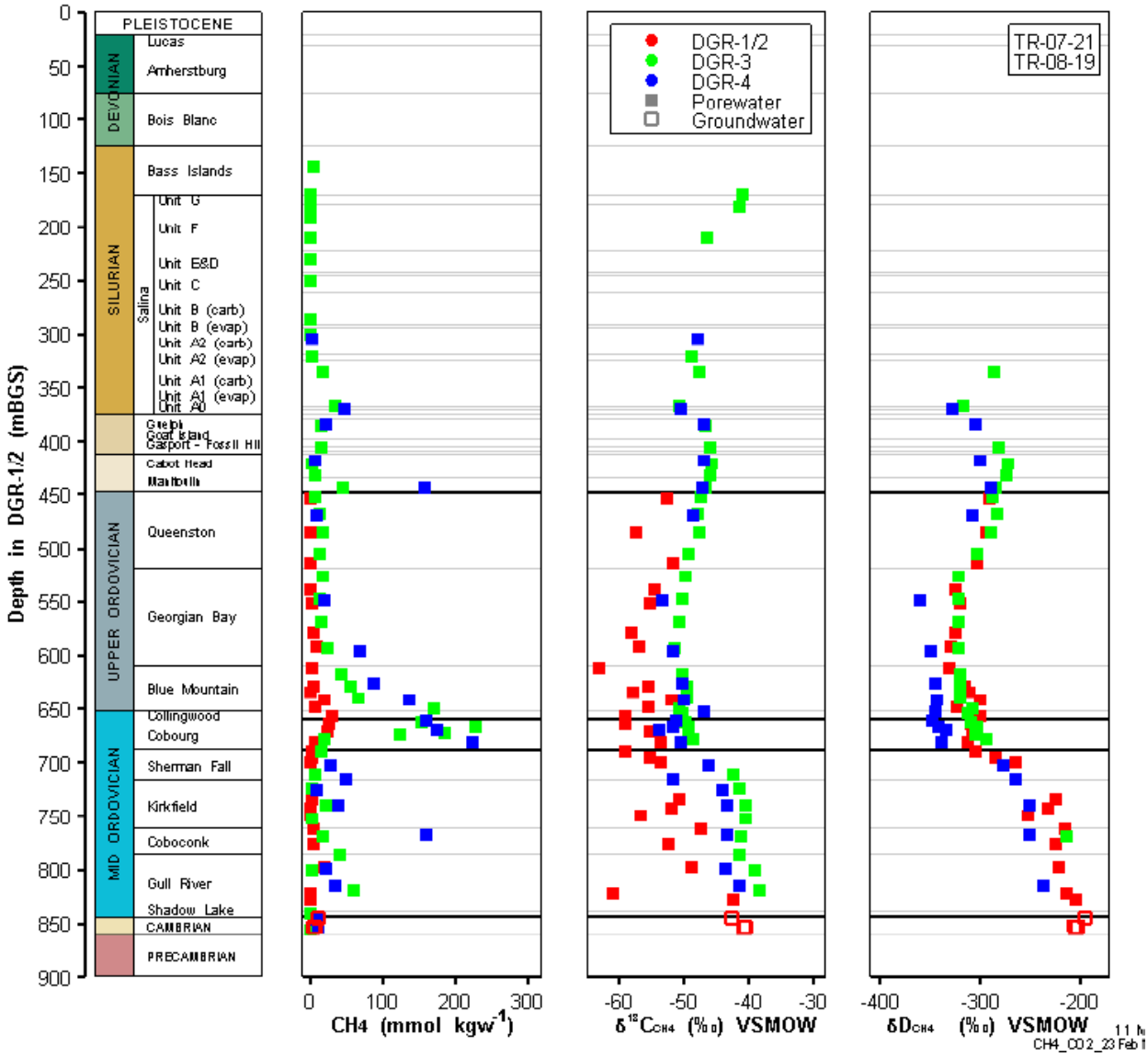

Note: From (INTERA 2011).

Figure 2.17: Profiles of CH_4 Apparent Porewater and Groundwater Concentrations and $\delta^{13}C$ and δD in CH_4 in DGR Boreholes

shale, and a second for CH_4 of thermogenic origin in the Middle Ordovician limestone. Since solute transport is dominated by diffusion for both zones, the clear separation of the biogenic CH_4 and the thermogenic CH_4 suggests that there is no significant cross-formational mixing. This may be explained, in part, by a decrease in effective diffusion coefficients due to the existence of a gas phase and hence partial water saturation (Saripalli et al. 2002), and by the fact that a discontinuous gas phase maintains saturation with respect to CH_4 in the brine. The presence of a gas phase may decrease in-situ effective diffusion coefficients by as much as one or two orders of magnitude from the range measured in the laboratory on saturated samples (10^{-12} m/s^2 or less) (Clark et al. 2010).

2.5.5 DGR Site Data for Groundwater Flow Parameters

Calculations related to groundwater flow require various parameters such as hydraulic conductivity, horizontal to vertical anisotropy ratios for hydraulic conductivity, and porosity. Geomechanical properties of formations are used to calculate specific storage and the one-dimensional loading efficiency (refer to Section 3.2) . The following sections present the site data from both the borehole work and laboratory petrophysics analyses of core samples. The data are used in the development of the hydrological parameters of the numerical models investigated in this study. Details of the site data are described in detail in the Descriptive Geosphere Site Model (INTERA 2011). Section 4.1 develops the hydrological parameters from the site data using the equations presented in Chapter 3.

2.5.5.1 Hydraulic Conductivity

The estimated hydraulic conductivities for the DGR boreholes are plotted versus depth in Figure 2.18 (INTERA 2011). The values for each formation at the DGR site and elsewhere, which are used as the basis for the numerical models in this study, are given in Table 2.8. The horizontal to vertical hydraulic conductivity anisotropy values are listed in Table 2.9.

In the case of grouped lithology, for example, the Niagaran Group, the averaged horizontal hydraulic conductivity K_H and vertical hydraulic conductivity K_V are calculated as:

$$K_H = \frac{\sum_{i=1}^{n} K_{H_i} t_i}{\sum_{i=1}^{n} t_i} \quad \text{and} \quad K_V = \frac{\sum_{i=1}^{n} t_i}{\sum_{i=1}^{n} \frac{t_i}{K_{V_i}}} \tag{2.2}$$

where t_i is the thickness of each unit, K_{H_i} is the horizontal hydraulic conductivity of each unit, and K_{V_i} is the vertical hydraulic conductivity of each unit.

2.5.5.2 Porosity

The estimated liquid porosity for the various stratigraphic layers at the Bruce DGR site are presented graphically in Figure 2.19 (INTERA 2011). The porosity values that are used as the basis for the numerical models are given in Table 2.10.

2.5.5.3 Pore Fluid TDS

The total dissolved solids concentration distribution is shown in Table 2.11 (INTERA 2011). Above the F-Unit, measured TDS concentrations are low. In and below the intermediate zone, TDS concentrations trend to 300 g/L or higher. The total dissolved solids concentration in the Precambrian was not measured.

2.5.5.4 Geomechanical Parameters

As developed in Section 3.2, the specific storage S_s and one-dimensional loading efficiency are calculated based on the Young's Modulus E, Poisson's Ratio ν, the mineral grain modulus K_s for the rock formations, the coefficient of vertical compressibility β' for the drift, and the fluid density ρ. Estimates of the Young's Modulus E (Table 2.12) and Poisson's Ratio ν (Table 2.13) were developed in Table 4.1 of ITASCA (2011). The mineral grain modulus K_s was chosen as being incompressible ($K_s = \infty$) for all layers except for the drift due to a lack of available site specific

Table 2.8: Horizontal Hydraulic Conductivity K_H of Formations at the DGR Site and Elsewhere

Period	Formation	K_H [m/s]	Reference	Note
Quaternary	Drift	1.0×10^{-8}	Freeze and Cherry (1979), Table 2.2	
Devonian	Kettle Point	3.0×10^{-9}	Weaver (1994), Table 3.Ia, Table 3.Ib	Logarithmic mean
	Hamilton Group	2.2×10^{-11}	Weaver (1994), Table 3.Ia, Table 3.Ib	Arithmetic mean
	Dundee	8.4×10^{-8}	Weaver (1994), Table 3.Ib	
	Lucas	1.0×10^{-6}	INTERA (2011), Table A1	
	Amherstburg (top 20 m)	1.0×10^{-6}	INTERA (2011), Table A1	
	Amherstburg (lower 25 m)	1.0×10^{-7}	INTERA (2011), Table A1	
	Bois Blanc	1.0×10^{-7}	INTERA (2011), Table A1	
Silurian	Bass Islands (upper 20m)	1.0×10^{-4}	INTERA (2011), Table A1	
	Bass Islands (lower 25 m)	1.0×10^{-5}	INTERA (2011), Table A1	
	Salina G	1.0×10^{-11}	INTERA (2011), Table A1	
	Salina F	5.0×10^{-14}	INTERA (2011), Table A1	
	Salina E	2.0×10^{-13}	INTERA (2011), Table A1	
	Salina D	2.0×10^{-13}	INTERA (2011), Table A1	
	Salina C	4.0×10^{-13}	INTERA (2011), Table A1	
	Salina B	4.0×10^{-13}	INTERA (2011), Table A1	
	Salina B evaporite	3.0×10^{-13}	INTERA (2011), Table A1	
	Salina A2 carbonate	3.0×10^{-10}	INTERA (2011), Table A1	
	Salina A2 evaporite	3.0×10^{-13}	INTERA (2011), Table A1	
	Salina A1 upper carbonate	2.0×10^{-7}	INTERA (2011), Table A1	
	Salina A1 carbonate	9.0×10^{-12}	INTERA (2011), Table A1	
	Salina A1 evaporite	3.0×10^{-13}	INTERA (2011), Table A1	
	Salina A0	3.0×10^{-13}	INTERA (2011), Table A1	
	Guelph	3.0×10^{-8}	INTERA (2011), Table A1	
	Goat Island	2.0×10^{-12}	INTERA (2011), Table A1	
	Gasport	2.0×10^{-12}	INTERA (2011), Table A1	
	Lions Head	5.0×10^{-12}	INTERA (2011), Table A1	
	Fossil Hill	5.0×10^{-12}	INTERA (2011), Table A1	
	Cabot Head	9.0×10^{-14}	INTERA (2011), Table A1	
	Manitoulin	9.0×10^{-14}	INTERA (2011), Table A1	
Ordovician	Queenston	2.0×10^{-14}	INTERA (2011), Table A1	
	Georgian Bay	3.0×10^{-14}	INTERA (2011), Table A1	
	Blue Mountain	5.0×10^{-14}	INTERA (2011), Table A1	
	Collingwood	2.0×10^{-14}	INTERA (2011), Table A1	
	Cobourg	2.0×10^{-14}	INTERA (2011), Table A1	
	Sherman Fall	1.0×10^{-14}	INTERA (2011), Table A1	
	Kirkfield	8.0×10^{-15}	INTERA (2011), Table A1	
	Coboconk	4.0×10^{-12}	INTERA (2011), Table A1	
	Gull River	7.0×10^{-13}	INTERA (2011), Table A1	
	Shadow Lake	1.0×10^{-9}	INTERA (2011), Table A1	
Cambrian	Cambrian	3.0×10^{-6}	INTERA (2011), Table A1	
Precambrian	Upper Precambrian	1.0×10^{-10}	INTERA (2011), Table A1	
	Precambrian	1.0×10^{-12}	INTERA (2011), Table 4.17	

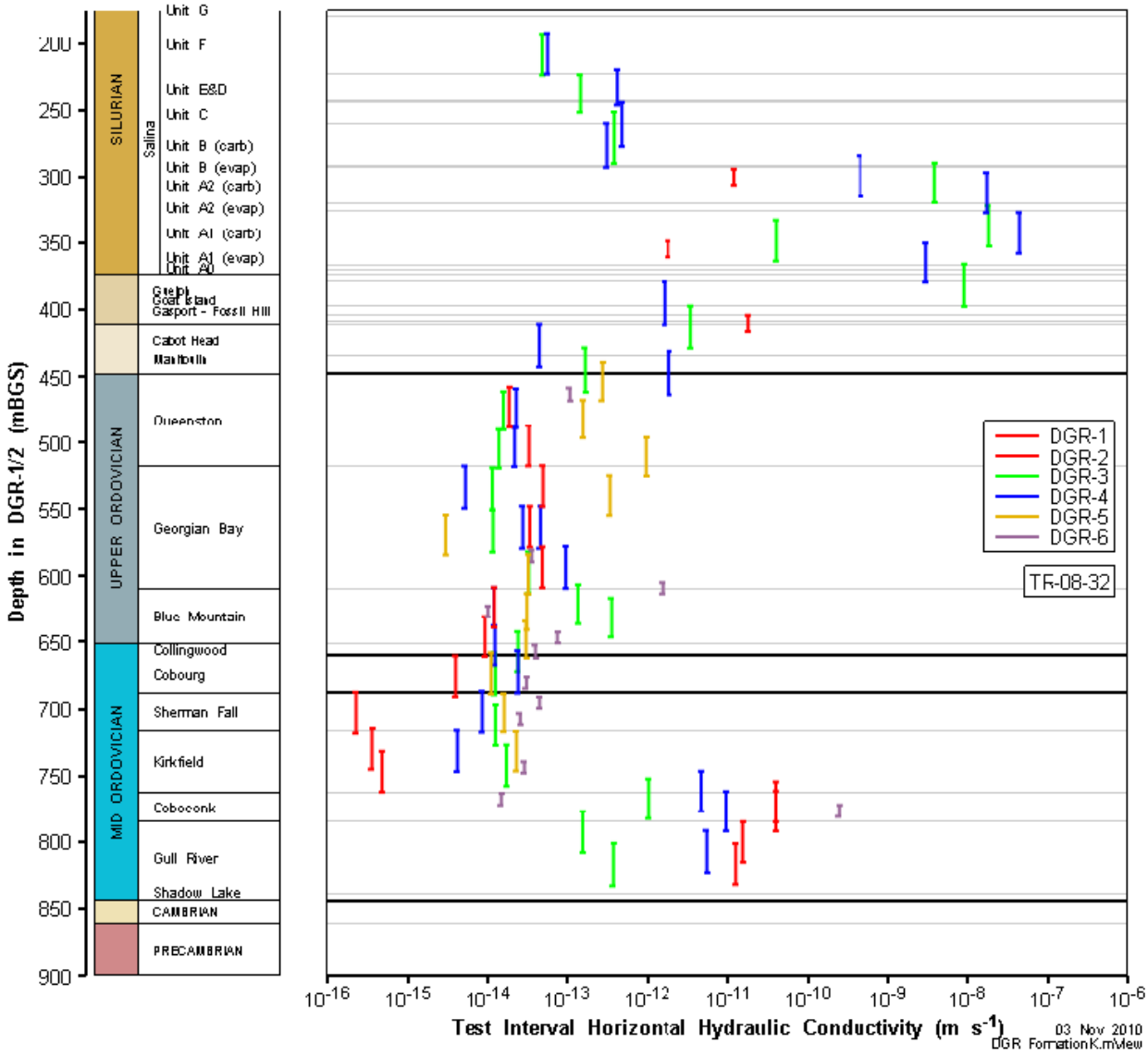

Note: From (INTERA 2011).

Figure 2.18: Profile of Test Interval Hydraulic Conductivity Estimates Determined from Field Straddle-Packer Testing in DGR Boreholes

data, although a Biot coefficient of 0.5 was applied for one paleohydrogeologic simulation. The coefficient of vertical compressibility β' for the drift was set to 1.0×10^{-8} Pa^{-1}.

2.5.5.5 Layer Thicknesses

Layer thicknesses at the DGR site are provided in Table 2.14 and are calculated from depths to formation tops as listed in Table 2.2 in Walsh (2010).

2.5.5.6 Effective Diffusion and Gas Saturation Parameters

The estimated iodide effective diffusion coefficient D_e is provided in Table 2.15. The estimated formation gas saturations are provided in Table 2.16 (INTERA 2011).

2.6 Regional-Scale and Site-Scale Conceptual Model

The low permeability of the Ordovician shale and limestone units (refer to Section 2.5.5.1) contribute significantly to the safety case for the DGR; a hypothesis of this hydrogeologic modelling study is that solute transport in the Ordovician is diffusion dominant. The low permeability Ordovician and Lower Silurian units are bounded above by the Niagaran Group, which is more permeable with reported horizontal hydraulic conductivities typically estimated at 1×10^{-8} m/s, and bounded below by the Cambrian Formation which, based on field measurements performed on the DGR boreholes at the Bruce nuclear site, has a horizontal hydraulic conductivity value of 3×10^{-6} m/s.

Although the hydraulic conductivity for the Cambrian is much higher than the low permeability Ordovician shales and limestones, it is not believed to be a potential pathway for fluid migration. It is bounded above and below by low permeability formations. The Cambrian is absent over the Algonquin Arch to the southeast of the DGR site. The OGSR data and Geologic Framework model (refer to Section 2.2) indicate that it is absent northeast of the DGR site. To the south, referring to Figure 2.3, it is postulated by Sanford et al. (1985), Carter et al. (1996) and Armstrong and Carter (2006) that units such as the Cambrian are discontinuous as a result of compartments and traps with these being more prevalent in the Niagara Megablock. Data supporting compartments or traps includes the drill stem pressures of the OGSR database; the spatial distribution and large variation of the pressures is depicted in Figure 2.20. The pressure data are associated with wells showing gas and oil.

Data only support potential fluid pathways in the Cambrian where it outcrops north of Sault Ste. Marie, Ontario, a distance of more than 300 km to the northwest of the DGR site. A pathway may exist to the west where the unit deepens and thickens towards the centre of the Michigan Basin. Based on data from the field program (refer to Section 2.5.3), the Cambrian is over-pressured with respect to the overlying Ordovician units. Present day hydraulic gradients at the Bruce nuclear site are upward from the Cambrian to the Ordovician units. The United States Geological Survey (USGS) modelled three-dimensional density-dependent groundwater flow in the Michigan Basin (Lampe 2009). For their analyses, the centre of Lake Huron was assumed to be a no-flow boundary for all model layers including those of the Cambrian. Based on the data for the Cambrian observed at the DGR site, on topographic influences on groundwater flow and the USGS study, it is a hypothesis of this study that at a point in all units/formations beneath Lake Huron either a divide for groundwater flow occurs or horizontal flow is negligible. This hypothesis is investigated through the analysis of two-dimensional density-dependent flow in an approximately west to east cross-section of the Michigan Basin. The sensitivity of solute transport in the Ordovician sediments to this hypothesis is investigated using the regional-scale density-dependent numerical model.

Similar to the Cambrian, the Niagaran Group has a much higher permeability than the underlying Lower Silurian and Ordovician formations, and is also bounded immediately above by the Salina Formation and bounded below by low permeability formations such as the Cabot Head shale; the Niagaran Group is also highly continuous. The Niagaran, which includes the Guelph Formation, outcrops and subcrops northeast of the DGR site (Figure 2.4). The unit deepens to the southwest and to the west.

Table 2.9: Horizontal to Vertical Anisotropy for Hydraulic Conductivity K_H:K_V of Formations at the DGR Site and Elsewhere

Period	Formation	K_H:K_V	Reference	Note
Quaternary	Drift	2:1	INTERA (2011), Table A1	
Devonian	Kettle Point	10:1	—	Assumed
	Hamilton Group	10:1	—	Assumed
	Dundee	10:1	—	Assumed
	Lucas	10:1	INTERA (2011), Table A1	
	Amherstburg (top 20 m)	10:1	INTERA (2011), Table A1	
	Amherstburg (lower 25 m)	10:1	INTERA (2011), Table A1	
	Bois Blanc	10:1	INTERA (2011), Table A1	
Silurian	Bass Islands (upper 20m)	10:1	INTERA (2011), Table A1	
	Bass Islands (lower 25 m)	10:1	INTERA (2011), Table A1	
	Salina G	10:1	INTERA (2011), Table A1	
	Salina F	10:1	INTERA (2011), Table A1	
	Salina E	10:1	INTERA (2011), Table A1	
	Salina D	10:1	INTERA (2011), Table A1	
	Salina C	10:1	INTERA (2011), Table A1	
	Salina B	10:1	INTERA (2011), Table A1	
	Salina B evaporite	10:1	INTERA (2011), Table A1	
	Salina A2 carbonate	10:1	INTERA (2011), Table A1	
	Salina A2 evaporite	10:1	INTERA (2011), Table A1	
	Salina A1 Upper carbonate	1:1	INTERA (2011), Table A1	
	Salina A1 carbonate	10:1	INTERA (2011), Table A1	
	Salina A1 evaporite	10:1	INTERA (2011), Table A1	
	Salina A0	10:1	INTERA (2011), Table A1	
	Guelph	1:1	INTERA (2011), Table A1	
	Goat Island	10:1	INTERA (2011), Table A1	
	Gasport	10:1	INTERA (2011), Table A1	
	Lions Head	10:1	INTERA (2011), Table A1	
	Fossil Hill	10:1	INTERA (2011), Table A1	
	Cabot Head	10:1	INTERA (2011), Table A1	
	Manitoulin	10:1	INTERA (2011), Table A1	
Ordovician	Queenston	10:1	INTERA (2011), Table A1	
	Georgian Bay	10:1	INTERA (2011), Table A1	
	Blue Mountain	10:1	INTERA (2011), Table A1	
	Collingwood	10:1	INTERA (2011), Table A1	
	Cobourg	10:1	INTERA (2011), Table A1	
	Sherman Fall	10:1	INTERA (2011), Table A1	
	Kirkfield	10:1	INTERA (2011), Table A1	
	Coboconk	1,000:1	—	Based on modelling
	Gull River	1,000:1	—	Based on modelling
	Shadow Lake	1,000:1	—	Based on modelling
Cambrian	Cambrian	1:1	INTERA (2011), Table A1	
Precambrian	Upper Precambrian	1:1	INTERA (2011), Table A1	
	Precambrian	1:1	INTERA (2011), Table A1	

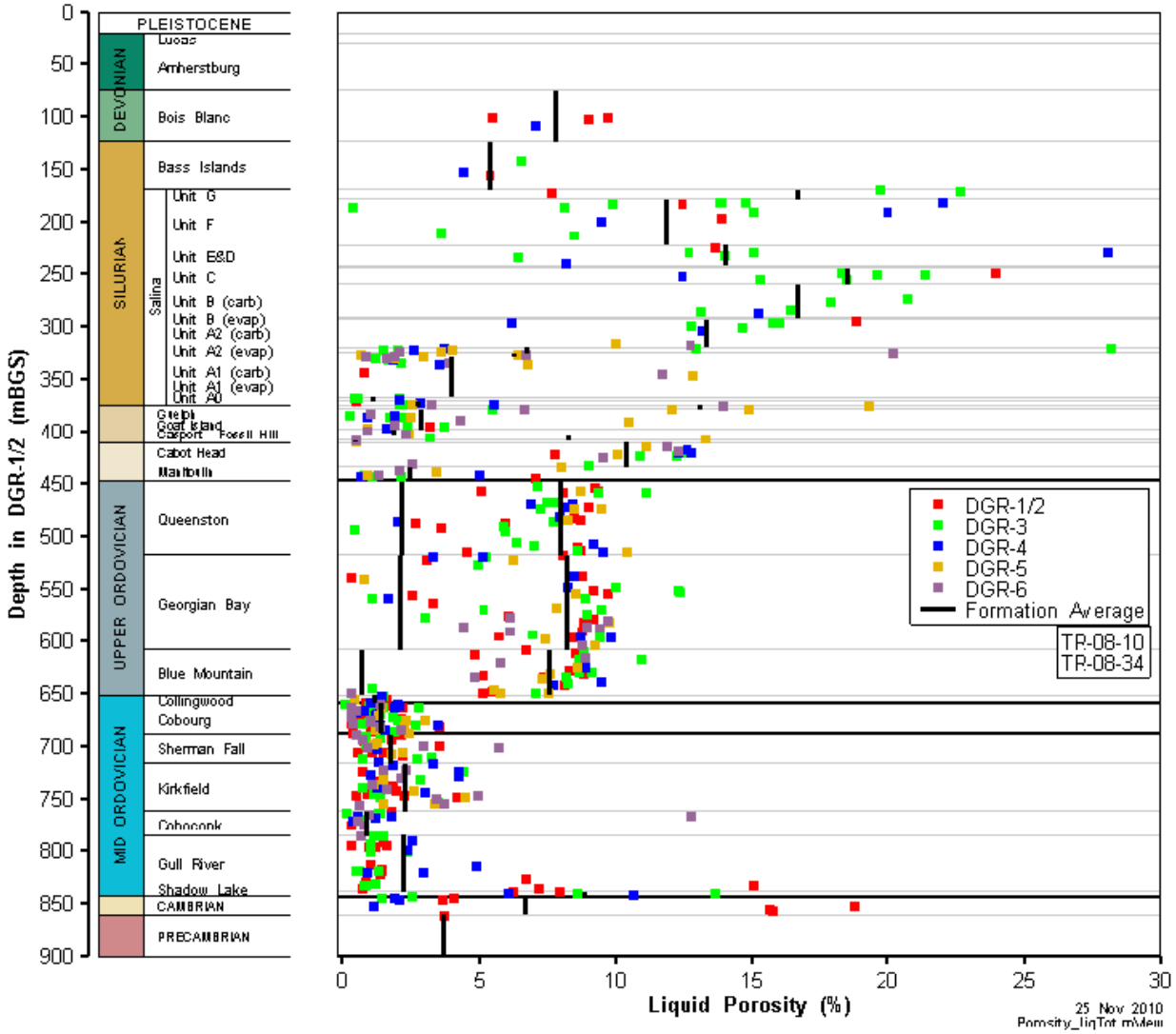

Note: From INTERA (2011).

Figure 2.19: Liquid Porosity Profile for DGR Cores Showing Point Data and Arithmetic Formation Averages

Table 2.10: Porosity θ of Formations at the DGR Site and Elsewhere

Period	Formation	θ	Reference	Note
Quaternary	Drift	0.200	INTERA (2011), Table A2	
Devonian	Kettle Point	0.100	Weaver (1994), Page 206	
	Hamilton Group	0.100	Weaver (1994), Page 206	
	Dundee	0.100	Weaver (1994), Page 206	
	Lucas	0.077	INTERA (2011), Table A2	
	Amherstburg (top 20 m)	0.077	INTERA (2011), Table A2	
	Amherstburg (lower 25 m)	0.077	INTERA (2011), Table A2	
	Bois Blanc	0.077	INTERA (2011), Table A2	
Silurian	Bass Islands (upper 20m)	0.056	INTERA (2011), Table A2	
	Bass Islands (lower 25 m)	0.056	INTERA (2011), Table A2	
	Salina G	0.172	INTERA (2011), Table A2	
	Salina F	0.100	INTERA (2011), Table A2	
	Salina E	0.100	INTERA (2011), Table A2	
	Salina D	0.089	INTERA (2011), Table A2	
	Salina C	0.205	INTERA (2011), Table A2	
	Salina B	0.145	INTERA (2011), Table A2	
	Salina B evaporite	0.089	INTERA (2011), Table A2	
	Salina A2 carbonate	0.120	INTERA (2011), Table A2	
	Salina A2 evaporite	0.089	INTERA (2011), Table A2	
	Salina A1 upper carbonate	0.070	INTERA (2011), Table A2	
	Salina A1 carbonate	0.019	INTERA (2011), Table A2	
	Salina A1 evaporite	0.007	INTERA (2011), Table A2	
	Salina A0	0.032	INTERA (2011), Table A2	
	Guelph	0.057	INTERA (2011), Table A2	
	Goat Island	0.020	INTERA (2011), Table A2	
	Gasport	0.020	INTERA (2011), Table A2	
	Lions Head	0.031	INTERA (2011), Table A2	
	Fossil Hill	0.031	INTERA (2011), Table A2	
	Cabot Head	0.116	INTERA (2011), Table A2	
	Manitoulin	0.028	INTERA (2011), Table A2	
Ordovician	Queenston	0.073	INTERA (2011), Table A2	
	Georgian Bay	0.071	INTERA (2011), Table A2	
	Blue Mountain	0.078	INTERA (2011), Table A2	
	Collingwood	0.012	INTERA (2011), Table A2	
	Cobourg	0.015	INTERA (2011), Table A2	
	Sherman Fall	0.016	INTERA (2011), Table A2	
	Kirkfield	0.021	INTERA (2011), Table A2	
	Coboconk	0.009	INTERA (2011), Table A2	
	Gull River	0.022	INTERA (2011), Table A2	
	Shadow Lake	0.097	INTERA (2011), Table A2	
Cambrian	Cambrian	0.071	INTERA (2011), Table A2	
Precambrian	Upper Precambrian	0.038	INTERA (2011), Table A2	
	Precambrian	0.005	INTERA (2011), Table 4.17	

Table 2.11: Pore Fluid TDS of Formations at the DGR Site and Elsewhere

Period	Formation	*TDS* [g/L]	Reference	Note
Quaternary	Drift	0.0	—	Freshwater
Devonian	Kettle Point	9.0	Weaver (1994), Table 3.Ia, Table 3.Ib	Arithmetic mean
	Hamilton Group	12.0	Weaver (1994), Table 3.Ia, Table 3.Ib	Arithmetic mean
	Dundee	8.0	Weaver (1994), Table 3.Ia, Table 3.Ib	Arithmetic mean
	Lucas	0.5	INTERA (2011), Table A7	
	Amherstburg (top 20 m)	1.0	INTERA (2011), Table A7	
	Amherstburg (lower 25 m)	2.0	INTERA (2011), Table A7	
	Bois Blanc	3.2	INTERA (2011), Table A7	
Silurian	Bass Islands (upper 20m)	6.0	INTERA (2011), Table A7	
	Bass Islands (lower 25 m)	6.0	INTERA (2011), Table A7	
	Salina G	14.8	INTERA (2011), Table A7	
	Salina F	59.6	INTERA (2011), Table A7	
	Salina E	124.0	INTERA (2011), Table A7	
	Salina D	200.0	INTERA (2011), Table A7	
	Salina C	249.0	INTERA (2011), Table A7	
	Salina B	321.0	INTERA (2011), Table A7	
	Salina B evaporite	321.0	INTERA (2011), Table A7	
	Salina A2 carbonate	136.0	INTERA (2011), Table A7	
	Salina A2 evaporite	45.6	INTERA (2011), Table A7	
	Salina A1 Upper carbonate	28.6	INTERA (2011), Table A7	
	Salina A1 carbonate	192.0	INTERA (2011), Table A7	
	Salina A1 evaporite	325.0	INTERA (2011), Table A7	
	Salina A0	360.0	INTERA (2011), Table A7	
	Guelph	370.0	INTERA (2011), Table A7	
	Goat Island	300.0	INTERA (2011), Table A7	
	Gasport	300.0	INTERA (2011), Table A7	
	Lions Head	300.0	INTERA (2011), Table A7	
	Fossil Hill	300.0	INTERA (2011), Table A7	
	Cabot Head	306.0	INTERA (2011), Table A7	
	Manitoulin	350.0	INTERA (2011), Table A7	
Ordovician	Queenston	310.0	INTERA (2011), Table A7	
	Georgian Bay	308.0	INTERA (2011), Table A7	
	Blue Mountain	295.0	INTERA (2011), Table A7	
	Collingwood	225.0	INTERA (2011), Table A7	
	Cobourg	272.0	INTERA (2011), Table A7	
	Sherman Fall	270.0	INTERA (2011), Table A7	
	Kirkfield	234.0	INTERA (2011), Table A7	
	Coboconk	255.0	INTERA (2011), Table A7	
	Gull River	203.0	INTERA (2011), Table A7	
	Shadow Lake	200.0	INTERA (2011), Table A7	
Cambrian	Cambrian	235.0	INTERA (2011), Table A7	
Precambrian	Upper Precambrian	300.0	Frape and Fritz (1987)	
	Precambrian	300.0	Frape and Fritz (1987)	

Table 2.12: Young's Modulus *E* of Formations at the DGR Site and Elsewhere

Period	Formation	*E* [GPa]	Reference	Note
Quaternary	Drift	—	—	
Devonian	Kettle Point	7.7	—	Set to Lucas-Bois Blanc
	Hamilton Group	7.7	—	Set to Lucas-Bois Blanc
	Dundee	7.7	—	Set to Lucas-Bois Blanc
	Lucas	7.7	ITASCA (2011), Table 4.1	
	Amherstburg (top 20 m)	7.7	ITASCA (2011), Table 4.1	
	Amherstburg (lower 25 m)	7.7	ITASCA (2011), Table 4.1	
	Bois Blanc	7.7	ITASCA (2011), Table 4.1	
Silurian	Bass Islands (upper 20m)	4.0	ITASCA (2011), Table 4.1	
	Bass Islands (lower 25 m)	4.0	ITASCA (2011), Table 4.1	
	Salina G	13.9	ITASCA (2011), Table 4.1	
	Salina F	13.9	ITASCA (2011), Table 4.1	
	Salina E	22.6	ITASCA (2011), Table 4.1	
	Salina D	22.6	ITASCA (2011), Table 4.1	
	Salina C	22.6	ITASCA (2011), Table 4.1	
	Salina B	22.6	ITASCA (2011), Table 4.1	
	Salina B evaporite	22.6	ITASCA (2011), Table 4.1	
	Salina A2 carbonate	22.6	ITASCA (2011), Table 4.1	
	Salina A2 evaporite	22.6	ITASCA (2011), Table 4.1	
	Salina A1 Upper carbonate	22.6	ITASCA (2011), Table 4.1	
	Salina A1 carbonate	22.6	ITASCA (2011), Table 4.1	
	Salina A1 evaporite	22.6	ITASCA (2011), Table 4.1	
	Salina A0	22.6	ITASCA (2011), Table 4.1	
	Guelph	37.0	ITASCA (2011), Table 4.1	
	Goat Island	37.0	ITASCA (2011), Table 4.1	
	Gasport	37.0	ITASCA (2011), Table 4.1	
	Lions Head	37.0	ITASCA (2011), Table 4.1	
	Fossil Hill	37.0	ITASCA (2011), Table 4.1	
	Cabot Head	13.8	ITASCA (2011), Table 4.1	
	Manitoulin	13.8	ITASCA (2011), Table 4.1	
Ordovician	Queenston	13.8	ITASCA (2011), Table 4.1	
	Georgian Bay	13.8	ITASCA (2011), Table 4.1	
	Blue Mountain	5.2	ITASCA (2011), Table 4.1	
	Collingwood	31.5	ITASCA (2011), Table 4.1	
	Cobourg	37.1	ITASCA (2011), Table 4.1	
	Sherman Fall	23.9	ITASCA (2011), Table 4.1	
	Kirkfield	23.9	ITASCA (2011), Table 4.1	
	Coboconk	23.9	ITASCA (2011), Table 4.1	
	Gull River	23.9	ITASCA (2011), Table 4.1	
	Shadow Lake	23.9	ITASCA (2011), Table 4.1	
Cambrian	Cambrian	76.6	ITASCA (2011), Table 4.1	
Precambrian	Upper Precambrian	76.6	ITASCA (2011), Table 4.1	
	Precambrian	76.6	ITASCA (2011), Table 4.1	

Table 2.13: Poisson's Ratio ν of Formations at the DGR Site and Elsewhere

Period	Formation	ν	Reference	Note
Quaternary	Drift	—	—	
Devonian	Kettle Point	0.18	—	Set to Lucas-Bois Blanc
	Hamilton Group	0.18	—	Set to Lucas-Bois Blanc
	Dundee	0.18	—	Set to Lucas-Bois Blanc
	Lucas	0.18	ITASCA (2011), Table 4.1	
	Amherstburg (top 20 m)	0.18	ITASCA (2011), Table 4.1	
	Amherstburg (lower 25 m)	0.18	ITASCA (2011), Table 4.1	
	Bois Blanc	0.18	ITASCA (2011), Table 4.1	
Silurian	Bass Islands (upper 20m)	0.30	ITASCA (2011), Table 4.1	
	Bass Islands (lower 25 m)	0.30	ITASCA (2011), Table 4.1	
	Salina G	0.22	ITASCA (2011), Table 4.1	
	Salina F	0.22	ITASCA (2011), Table 4.1	
	Salina E	0.32	ITASCA (2011), Table 4.1	
	Salina D	0.32	ITASCA (2011), Table 4.1	
	Salina C	0.32	ITASCA (2011), Table 4.1	
	Salina B	0.32	ITASCA (2011), Table 4.1	
	Salina B evaporite	0.32	ITASCA (2011), Table 4.1	
	Salina A2 carbonate	0.32	ITASCA (2011), Table 4.1	
	Salina A2 evaporite	0.32	ITASCA (2011), Table 4.1	
	Salina A1 Upper carbonate	0.32	ITASCA (2011), Table 4.1	
	Salina A1 carbonate	0.32	ITASCA (2011), Table 4.1	
	Salina A1 evaporite	0.32	ITASCA (2011), Table 4.1	
	Salina A0	0.32	ITASCA (2011), Table 4.1	
	Guelph	0.37	ITASCA (2011), Table 4.1	
	Goat Island	0.37	ITASCA (2011), Table 4.1	
	Gasport	0.37	ITASCA (2011), Table 4.1	
	Lions Head	0.37	ITASCA (2011), Table 4.1	
	Fossil Hill	0.37	ITASCA (2011), Table 4.1	
	Cabot Head	0.30	ITASCA (2011), Table 4.1	
	Manitoulin	0.30	ITASCA (2011), Table 4.1	
Ordovician	Queenston	0.30	ITASCA (2011), Table 4.1	
	Georgian Bay	0.30	ITASCA (2011), Table 4.1	
	Blue Mountain	0.30	ITASCA (2011), Table 4.1	
	Collingwood	0.25	ITASCA (2011), Table 4.1	
	Cobourg	0.33	ITASCA (2011), Table 4.1	
	Sherman Fall	0.21	ITASCA (2011), Table 4.1	
	Kirkfield	0.21	ITASCA (2011), Table 4.1	
	Coboconk	0.21	ITASCA (2011), Table 4.1	
	Gull River	0.21	ITASCA (2011), Table 4.1	
	Shadow Lake	0.21	ITASCA (2011), Table 4.1	
Cambrian	Cambrian	0.25	ITASCA (2011), Table 4.1	
Precambrian	Upper Precambrian	0.25	ITASCA (2011), Table 4.1	
	Precambrian	0.25	ITASCA (2011), Table 4.1	

Table 2.14: Thicknesses Δz of Formations at the DGR Site Based on DGR-1/2

Period	Formation	Δz [m]	Reference	Note
Quaternary	Drift	—	—	
Devonian	Kettle Point	—	—	
	Hamilton Group	—	—	
	Dundee	—	—	
	Lucas	10.4	Walsh (2010), Table 2.2	
	Amherstburg (top 20 m)	19.6	Walsh (2010), Table 2.2	
	Amherstburg (lower 25 m)	25.0	Walsh (2010), Table 2.2	
	Bois Blanc	49.0	Walsh (2010), Table 2.2	
Silurian	Bass Islands (upper 20m)	20.0	Walsh (2010), Table 2.2	
	Bass Islands (lower 25 m)	25.3	Walsh (2010), Table 2.2	
	Salina G	9.3	Walsh (2010), Table 2.2	
	Salina F	44.4	Walsh (2010), Table 2.2	
	Salina E	20.0	Walsh (2010), Table 2.2	
	Salina D	1.6	Walsh (2010), Table 2.2	
	Salina C	15.7	Walsh (2010), Table 2.2	
	Salina B	30.9	Walsh (2010), Table 2.2	
	Salina B evaporite	1.9	Walsh (2010), Table 2.2	
	Salina A2 carbonate	26.6	Walsh (2010), Table 2.2	
	Salina A2 evaporite	5.8	Walsh (2010), Table 2.2	
	Salina A1 upper carbonate	3.0	Walsh (2010), Table 2.2	
	Salina A1 carbonate	38.5	Walsh (2010), Table 2.2	
	Salina A1 evaporite	3.5	Walsh (2010), Table 2.2	
	Salina A0	4.0	Walsh (2010), Table 2.2	
	Guelph	4.1	Walsh (2010), Table 2.2	
	Goat Island	18.8	Walsh (2010), Table 2.2	
	Gasport	6.85	Walsh (2010), Table 2.2	
	Lions Head	4.45	Walsh (2010), Table 2.2	
	Fossil Hill	2.3	Walsh (2010), Table 2.2	
	Cabot Head	23.8	Walsh (2010), Table 2.2	
	Manitoulin	12.9	Walsh (2010), Table 2.2	
Ordovician	Queenston	70.3	Walsh (2010), Table 2.2	
	Georgian Bay	90.9	Walsh (2010), Table 2.2	
	Blue Mountain	42.7	Walsh (2010), Table 2.2	
	Collingwood	7.9	Walsh (2010), Table 2.2	
	Cobourg	28.6	Walsh (2010), Table 2.2	
	Sherman Fall	28.0	Walsh (2010), Table 2.2	
	Kirkfield	45.9	Walsh (2010), Table 2.2	
	Coboconk	23.0	Walsh (2010), Table 2.2	
	Gull River	53.6	Walsh (2010), Table 2.2	
	Shadow Lake	5.2	Walsh (2010), Table 2.2	
Cambrian	Cambrian	—	—	
Precambrian	Upper Precambrian	—	—	
	Precambrian	—	—	

Table 2.15: Iodide Effective Diffusion Coefficient D_e of Formations at the DGR Site and Elsewhere

Period	Formation	D_e [m^2/s]	Reference	Note
Quaternary	Drift	6.6×10^{-11}	—	Calculated
Devonian	Kettle Point	9.9×10^{-12}	—	Calculated
	Hamilton Group	9.9×10^{-12}	—	Calculated
	Dundee	9.9×10^{-12}	—	Calculated
	Lucas	6.0×10^{-12}	INTERA (2011), Table A6	
	Amherstburg (top 20 m)	6.0×10^{-12}	INTERA (2011), Table A6	
	Amherstburg (lower 25 m)	6.0×10^{-12}	INTERA (2011), Table A6	
	Bois Blanc	6.0×10^{-12}	INTERA (2011), Table A6	
Silurian	Bass Islands (upper 20m)	1.3×10^{-11}	INTERA (2011), Table A6	
	Bass Islands (lower 25 m)	1.3×10^{-11}	INTERA (2011), Table A6	
	Salina G	4.3×10^{-13}	INTERA (2011), Table A6	
	Salina F	4.1×10^{-12}	INTERA (2011), Table A6	
	Salina E	4.7×10^{-12}	INTERA (2011), Table A6	
	Salina D	4.7×10^{-12}	INTERA (2011), Table A6	
	Salina C	1.1×10^{-11}	INTERA (2011), Table A6	
	Salina B	1.2×10^{-11}	INTERA (2011), Table A6	
	Salina B evaporite	7.7×10^{-14}	INTERA (2011), Table A6	
	Salina A2 carbonate	1.2×10^{-12}	INTERA (2011), Table A6	
	Salina A2 evaporite	7.7×10^{-14}	INTERA (2011), Table A6	
	Salina A1 upper carbonate	4.9×10^{-12}	INTERA (2011), Table A6	
	Salina A1 carbonate	1.8×10^{-13}	INTERA (2011), Table A6	
	Salina A1 evaporite	3.0×10^{-14}	INTERA (2011), Table A6	
	Salina A0	3.0×10^{-14}	INTERA (2011), Table A6	
	Guelph	3.2×10^{-12}	INTERA (2011), Table A6	
	Goat Island	1.5×10^{-13}	INTERA (2011), Table A6	
	Gasport	1.5×10^{-13}	INTERA (2011), Table A6	
	Lions Head	6.2×10^{-12}	INTERA (2011), Table A6	
	Fossil Hill	1.6×10^{-11}	INTERA (2011), Table A6	
	Cabot Head	3.1×10^{-12}	INTERA (2011), Table A6	
	Manitoulin	1.5×10^{-13}	INTERA (2011), Table A6	
Ordovician	Queenston	1.0×10^{-12}	INTERA (2011), Table A6	
	Georgian Bay	4.3×10^{-13}	INTERA (2011), Table A6	
	Blue Mountain	8.2×10^{-13}	INTERA (2011), Table A6	
	Collingwood	4.9×10^{-13}	INTERA (2011), Table A6	
	Cobourg	3.7×10^{-13}	INTERA (2011), Table A6	
	Sherman Fall	2.2×10^{-13}	INTERA (2011), Table A6	
	Kirkfield	4.2×10^{-13}	INTERA (2011), Table A6	
	Coboconk	2.7×10^{-13}	INTERA (2011), Table A6	
	Gull River	2.6×10^{-13}	INTERA (2011), Table A6	
	Shadow Lake	6.1×10^{-12}	INTERA (2011), Table A6	
Cambrian	Cambrian	7.7×10^{-12}	INTERA (2011), Table A6	
Precambrian	Upper Precambrian	3.0×10^{-13}	INTERA (2011), Table A6	
	Precambrian	3.0×10^{-13}	INTERA (2011), Table 4.17	

Table 2.16: Gas Saturation S_g of Formations at the DGR Site and Elsewhere

Period	Formation	S_g	Reference	Note
Quaternary	Drift	—	—	
Devonian	Kettle Point	—	—	
	Hamilton Group	—	—	
	Dundee	—	—	
	Lucas	—	—	
	Amherstburg (top 20 m)	—	—	
	Amherstburg (lower 25 m)	—	—	
	Bois Blanc	—	—	
Silurian	Bass Islands (upper 20m)	—	—	
	Bass Islands (lower 25 m)	—	—	
	Salina G	—	—	
	Salina F	0.160	INTERA (2011), Table A7	
	Salina E	0.217	INTERA (2011), Table A7	
	Salina D	—	—	
	Salina C	0.180	INTERA (2011), Table A7	
	Salina B	0.000	INTERA (2011), Table A7	
	Salina B evaporite	—	—	
	Salina A2 carbonate	0.003	INTERA (2011), Table A7	
	Salina A2 evaporite	0.147	INTERA (2011), Table A7	
	Salina A1 upper carbonate	—	—	
	Salina A1 carbonate	—	—	
	Salina A1 evaporite	0.003	INTERA (2011), Table A7	
	Salina A0	0.165	INTERA (2011), Table A7	
	Guelph	—	—	
	Goat Island	0.000	INTERA (2011), Table A7	
	Gasport	—	—	
	Lions Head	—	—	
	Fossil Hill	—	—	
	Cabot Head	—	—	
	Manitoulin	0.000	INTERA (2011), Table A7	
Ordovician	Queenston	0.066	INTERA (2011), Table A7	
	Georgian Bay	0.076	INTERA (2011), Table A7	
	Blue Mountain	0.140	INTERA (2011), Table A7	
	Collingwood	0.241	INTERA (2011), Table A7	
	Cobourg	0.121	INTERA (2011), Table A7	
	Sherman Fall	0.151	INTERA (2011), Table A7	
	Kirkfield	0.203	INTERA (2011), Table A7	
	Coboconk	0.037	INTERA (2011), Table A7	
	Gull River	0.213	INTERA (2011), Table A7	
	Shadow Lake	—	—	
Cambrian	Cambrian	0.035	INTERA (2011), Table A7	
Precambrian	Upper Precambrian	—	—	
	Precambrian	—	—	

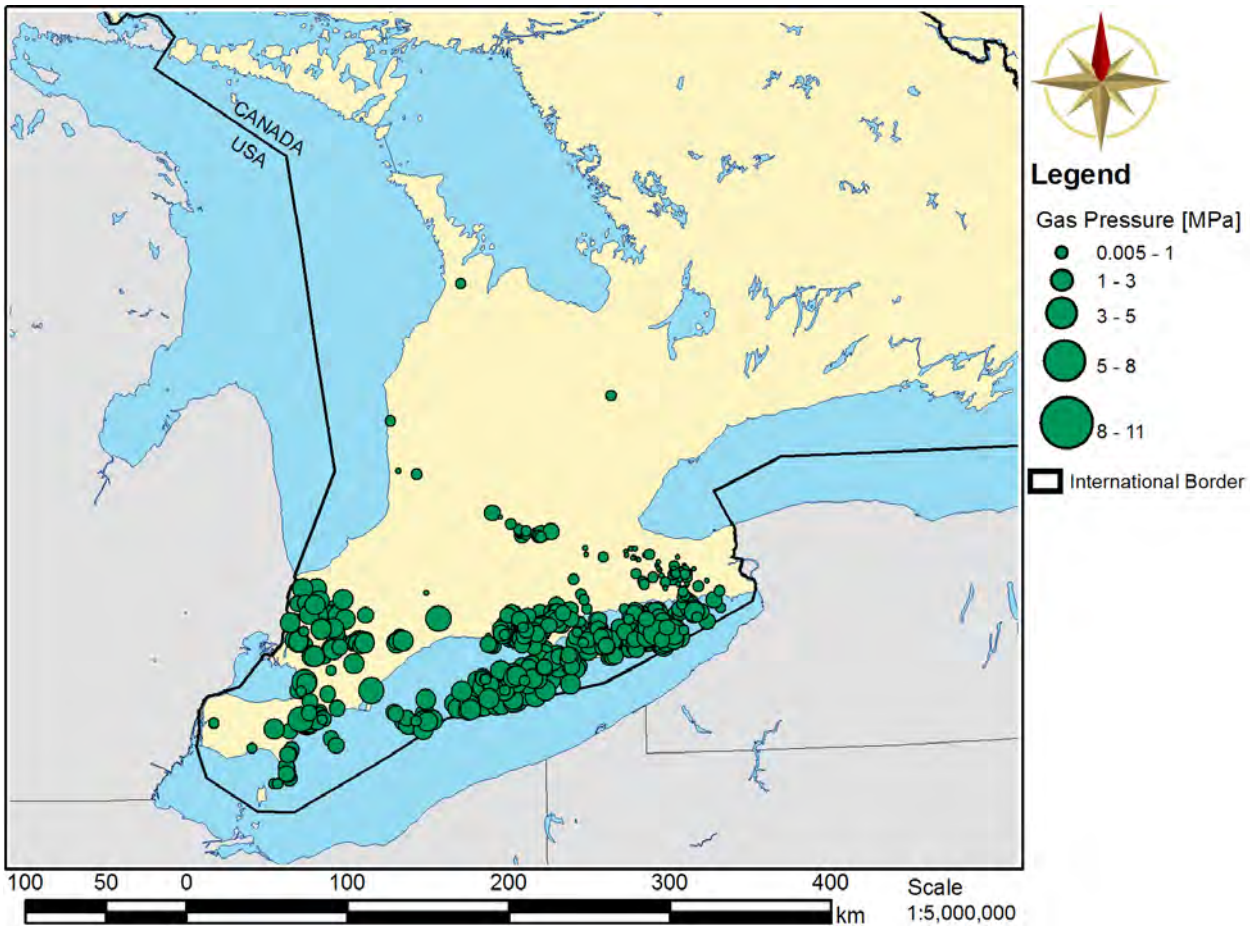

Figure 2.20: Distribution of Gas Pressure Measurements in the OGSR Library Well Database

2.6.1 Model Domain and Spatial Discretization

The spatial scale required to assess solute transport in the Ordovician shale and limestone is on the order of kilometres or less. For paleohydrogeologic analyses and to fully characterize flow in the more permeable units such as the Niagaran including the Guelph dolostones and the Cambrian sandstone, a considerably larger spatial domain is required. Ideally, the spatial domain should include the outcrop and subcrop for the permeable units, such as the Niagaran, that are potential pathways for solute migrating from the Ordovician at the location of the proposed DGR.

The regional-scale spatial domain meets this criteria for all of the units above the Ordovician. While it does not strictly meet this criteria for the Cambrian, potential pathways in the Cambrian can be investigated through scenario analyses as well as through the basin wide cross-sectional analyses of Section 6.2.

The regional-scale modelling domain boundary (Figure 1.1) was chosen by Sykes (2007) according to several criteria. In this report, the modelling domain boundary is used to define the Michigan Basin regional-scale model. The southeastern portion of the boundary follows the regional surface water divides surrounding the DGR site; these divides were determined by using

a Digital Elevation Model (DEM) from the Shuttle Radar Topography Mission (SRTM) and a river network in ArcGIS. Based on the assumption that the water table is a subdued reflection of surface topography, the topographic divides are a reasonable choice for the upper flow regime, and the higher permeability Niagaran Group within the intermediate flow regime. Surface topography can be greatly affected by the advance and retreat of glaciers. Today's topography may not be identical to the topography that existed before the most recent glaciation, although major topographic trends and features would likely remain. Changes in topography would affect the selection of the modelling domain boundary.

The modelling domain includes the local topographic high in southern Ontario, and the domain extends to the deepest portions of both Lake Huron and Georgian Bay. As stated in the preceding section, it is a hypothesis of this study that at a point in all units/formations beneath Lake Huron either a divide for groundwater flow occurs or horizontal flow is negligible. The bathymetric data of both water bodies, provided by NOAA, was combined with the DEM to provide a continuous surface for the top of the Earth's solid surface. DEMs commonly define elevation as the surface elevation of a water body since bathymetric data is usually not available. The eastern boundary of the modelling domain is west of the Algonquin Arch. The model boundary is shown in Figure 1.1, along with a DEM, and major rivers in southwestern Ontario.

The potential energy gradients that occur at depth in the Michigan Basin will be reduced due to the presence of dense saline groundwater found within the formations of the lower regime. Where these formations outcrop at recharge areas, there will be a potential for fresh water to infiltrate the geologic units and displace higher density water until there is a balance between the elevation gradient and the density gradient. At this equilibrium point, the energy gradient will approach zero. With the dense brine, there will be associated higher viscosities which will act to further impede flow. It is hypothesized in this study that the combination of the negligible horizontal energy gradients with the dense brine and low permeabilities in the lower groundwater regime can lead to a system that is dominated by diffusion. Thus, the water in the deep formations of the Michigan Basin is expected to be stagnant.

The base-case data set for the conceptual model consists of 39 model layers, with each of the 31 top layers corresponding to a unit in the stratigraphic section provided by the geologic framework model (refer to Section 2.2). The bottom 8 layers are associated with the Precambrian (7 layers) and the upper Precambrian (1 layer).

A two-dimensional grid was developed to fit within the conceptual modelling boundary as shown in Figure 2.21. Each quadrilateral element measures Δx = 762.794 m by Δy = 900.876 m. The grid has an east-west extent of 151.796 km, a north-south extent of 179.274 km, 27,322 elements, 27,728 nodes, and covers an area of 18,775 km^2. The two-dimensional grid forms a horizontal template to develop the three-dimensional grid by interpolating the vertical position of each node from the 32 interfaces provided by ITASCA CANADA and AECOM (2011). Each interface was provided as a Triangulated Irregular Network (TIN).

A Visual Basic for Applications (VBA) code was written to read the two-dimensional grid and each TIN interface to determine the elevation of each node for the top 31 layers. A grid search algorithm was implemented to significantly reduce the computational time, by a factor greater than 200, of finding the triangle of each TIN that contained the grid node for which an elevation was interpolated. FRAC3DVS-OPG requires a three-dimensional grid whose nodes align vertically for density-dependent calculations; in essence, the two-dimensional grid is stacked vertically for each geologic layer, regardless if the actual geologic layers pinch out.

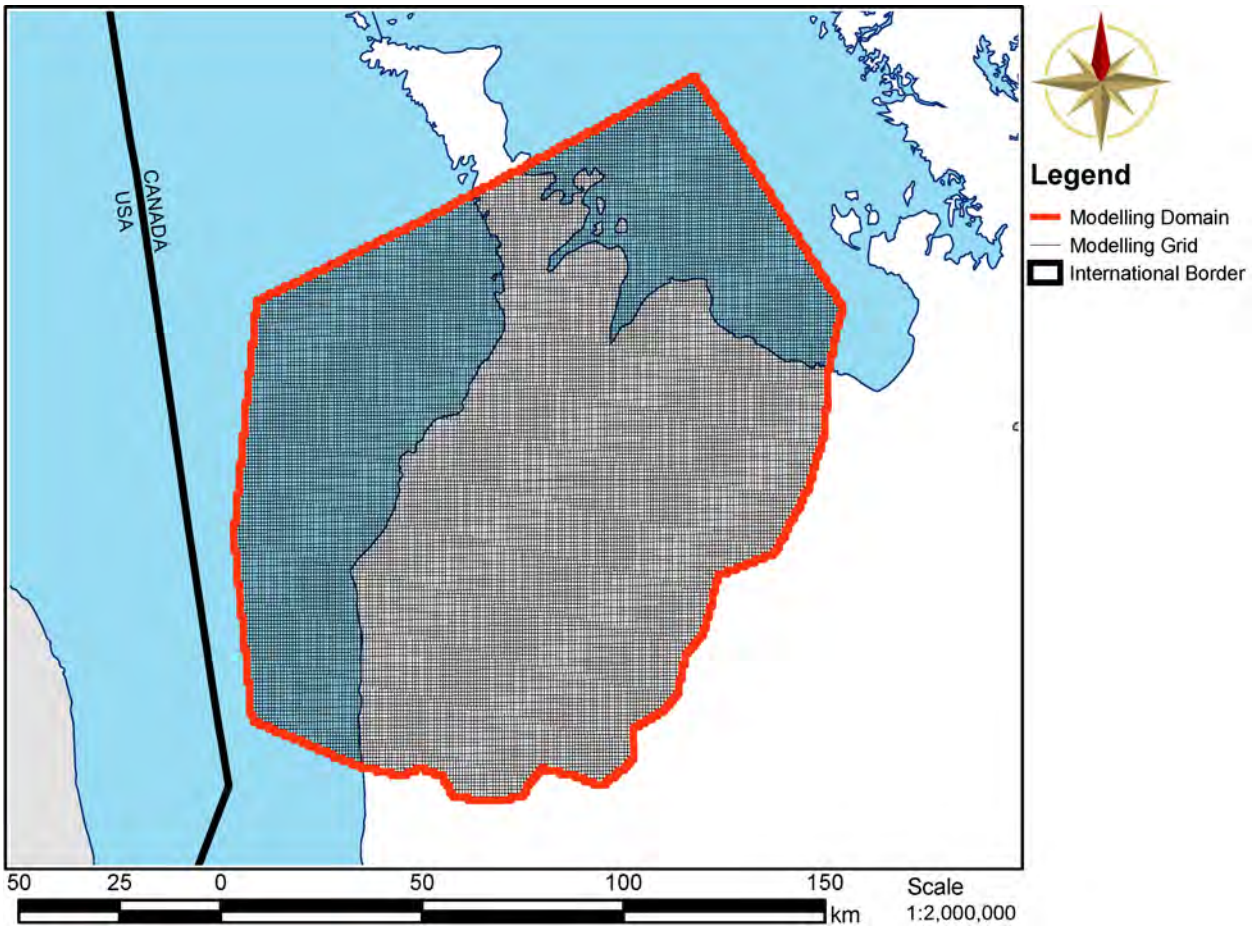

Figure 2.21: FRAC3DVS-OPG Modelling Grid and Modelling Domain Extent in Red

The process used to generate the three-dimensional grid and populate it with geologic properties is as follows:

- Allocate 3D grid array to hold all elevations;
- Set an initial elevation for all 3D nodes of −3,000 m;
- Loop over each interface beginning with the bottom interface, representing the top of the Precambrian;
- Loop over all 27,728 2D nodes and use a grid based search to quickly locate the triangle that contains the grid node and interpolate its elevation;
- If the thickness between the current 3D node and the 3D node immediately below it is negative, set the current 3D node to the same elevation of the node immediately below, resulting in a zero thickness. This is necessary for layers that pinch out;
- Check that all 3D nodes have an elevation greater than the initial elevation of −3,000 m; if not, then signal an error;
- Assign 20 m thickness to the upper Precambrian, divide the remaining Precambrian between the upper Precambrian and an elevation of −1,580 m into 6 layers; set a bottom flat layer of 20 m for the Precambrian;

- Loop over the 3D grid and set minimum thicknesses. If the layer thickness at a node is negative or < 0.5 m, then set thickness to zero. If the layer thickness at a node is ≥ 0.5 m and < 1 m, then set thickness to 1 m;
- Assign a geologic layer identifier to each node, accounting for pinched out geologic layers. If a layer has pinched out, then its thickness is zero, and it assumes the geologic layer identifier of the layer immediately below;
- Evenly distribute geologic layer thicknesses among 3D grid for a set of nodes which represent the same geologic layer. This is to account for layers that pinch out;
- Check once again for negative or zero thickness layers;
- Assign all nodes within 20 m of surface topography to be drift material;
- Up to this point, geologic layer identifiers are assigned to nodes, but they now need to be assigned to elements. Each element could have 4 different geologic layer identifiers since it is comprised of 4 nodes along its top face. The geologic layer identifier associated with the thickest node is assigned to the element; and
- Write Tecplot and Paraview visualization files to disk along with the necessary FRAC3DVS-OPG files.

A block cut view and a fence view of the assigned geologic layer zone identifiers are shown in Figure 2.22 and Figure 2.23, respectively. Each zone identifier is associated with a specific geologic layer or geologic grouping and includes 31 3DGF layers plus the Upper Precambrian and the Precambrian for a total of 33 defined units. Some of the geologic units are listed in Table 2.7. The geologic reconstruction also makes use of the outcrop limits or extent of the various geologic units, coloured by geologic period, as shown in Figure 2.24. Note that the vertical exaggeration is 40:1 in this and other figures describing the regional-scale spatial domain.

The Cambrian Formation, as shown in Figure 2.25, pinches out against the Precambrian flanking the Algonquin Arch (Carter et al. 1996). All wells shown in the figure intersect the Precambrian Formation, but only some of those wells also intersect the Cambrian Formation. A three-dimensional view of the Cambrian Formation as represented in the modelling grid, is shown in Figure 2.26. An important attribute of this more permeable unit is that it is present only over the more westerly part of the domain.

A view of the Middle Silurian geologic units (top of the Niagaran Group) is shown in Figure 2.27; the portion of the surface appearing rougher represents outcrops or subcrops, and has been defined using OGS Digital Bedrock topography and overburden thickness mapping as provided in the ITASCA CANADA and AECOM (2011). The zone with a smooth surface corresponds to the portion of the Niagaran that is overlain by the Upper Silurian.

A view of all geologic units, minus the Quaternary drift deposits is shown in Figure 2.28; pinnacle reef structures are visible in Figure 2.27. Finally, a similar perspective, showing all geologic units and the Quaternary drift deposits, is shown in Figure 2.29 and as a fence view in Figure 2.30.

2.6.2 Flow Boundary Conditions

Various boundary conditions are applied to the regional modelling domain. A Dirichlet (Type 1) hydraulic boundary condition is applied to the top nodes of the domain to set the water table 3 m below ground surface, regardless of streams or other inland water bodies such as lakes or wetlands, but not less than the elevation of Georgian Bay or Lake Huron which were set to a mean water elevation of 176 m (refer to Figure 2.31). The scale of the model and the size of grid blocks preclude the inclusion of any hydrologic features, other than characterizing the water table as a subdued reflection of surface topography. Desbarats et al. (2002) developed a methodology

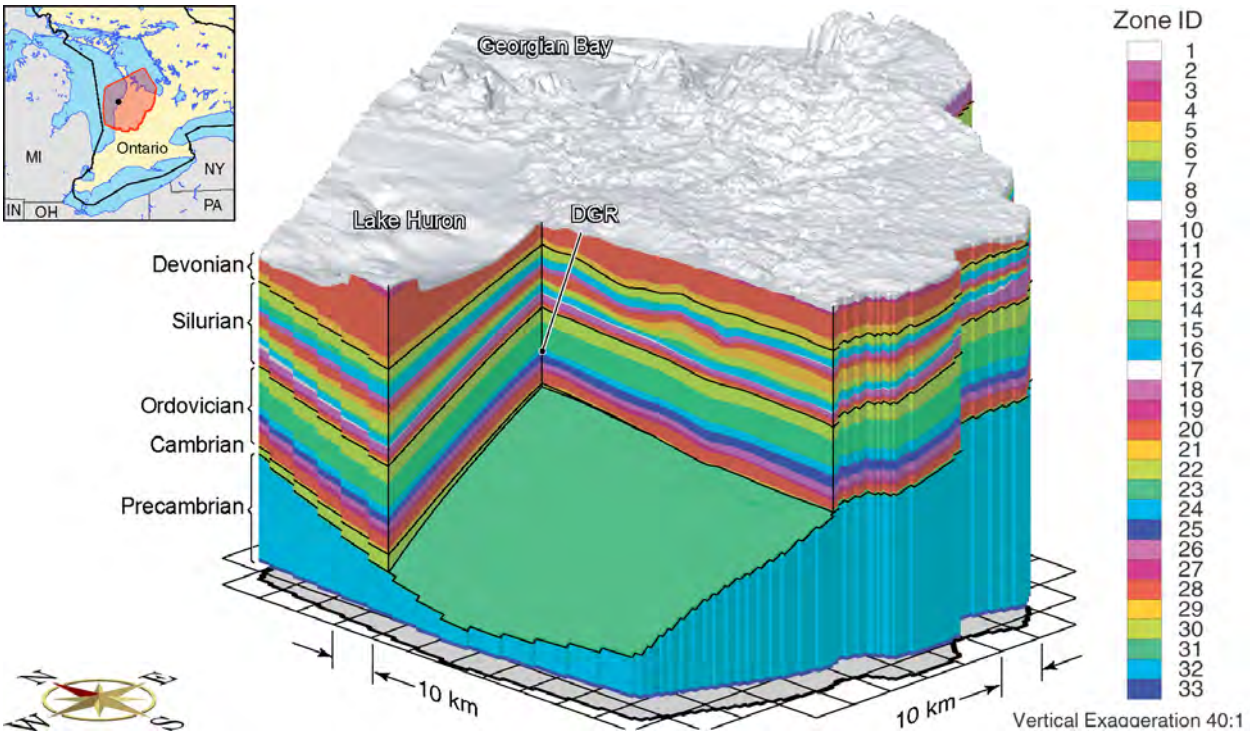

Figure 2.22: Block Cut View of FRAC3DVS-OPG Zone Identifiers for 33 Layers

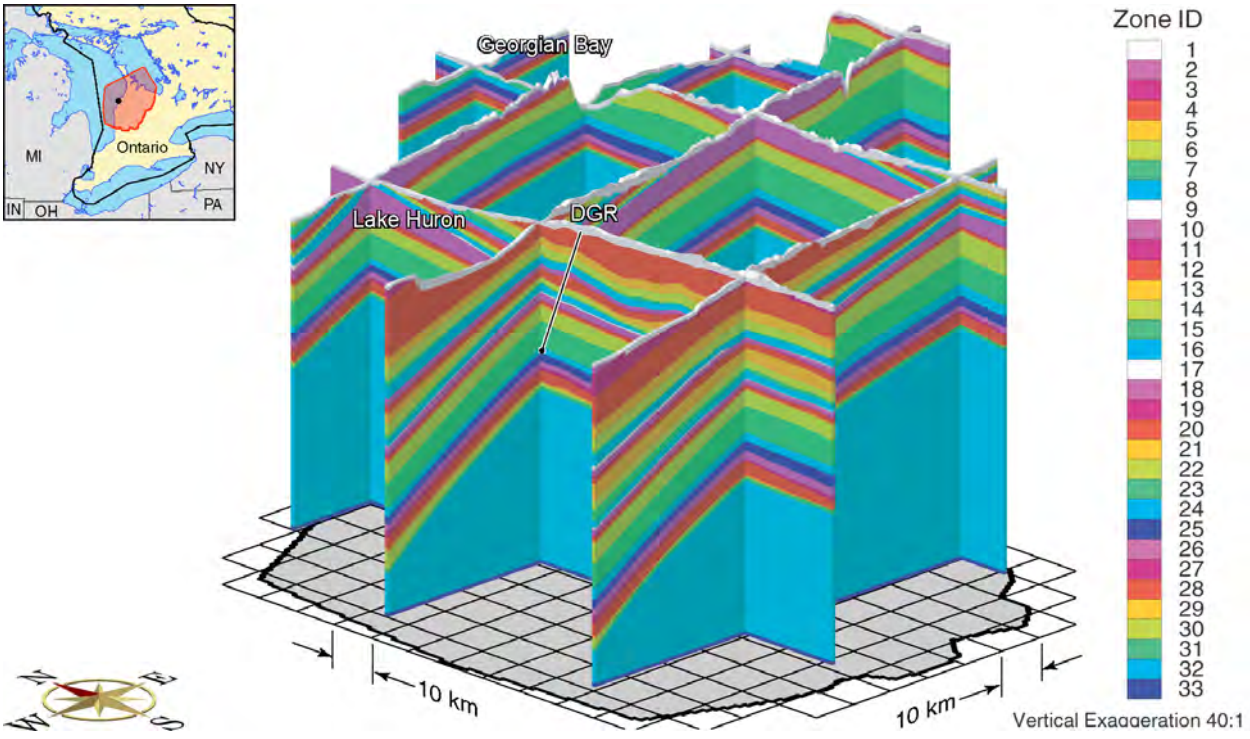

Figure 2.23: Fence View of FRAC3DVS-OPG Zone Identifiers for 33 Layers

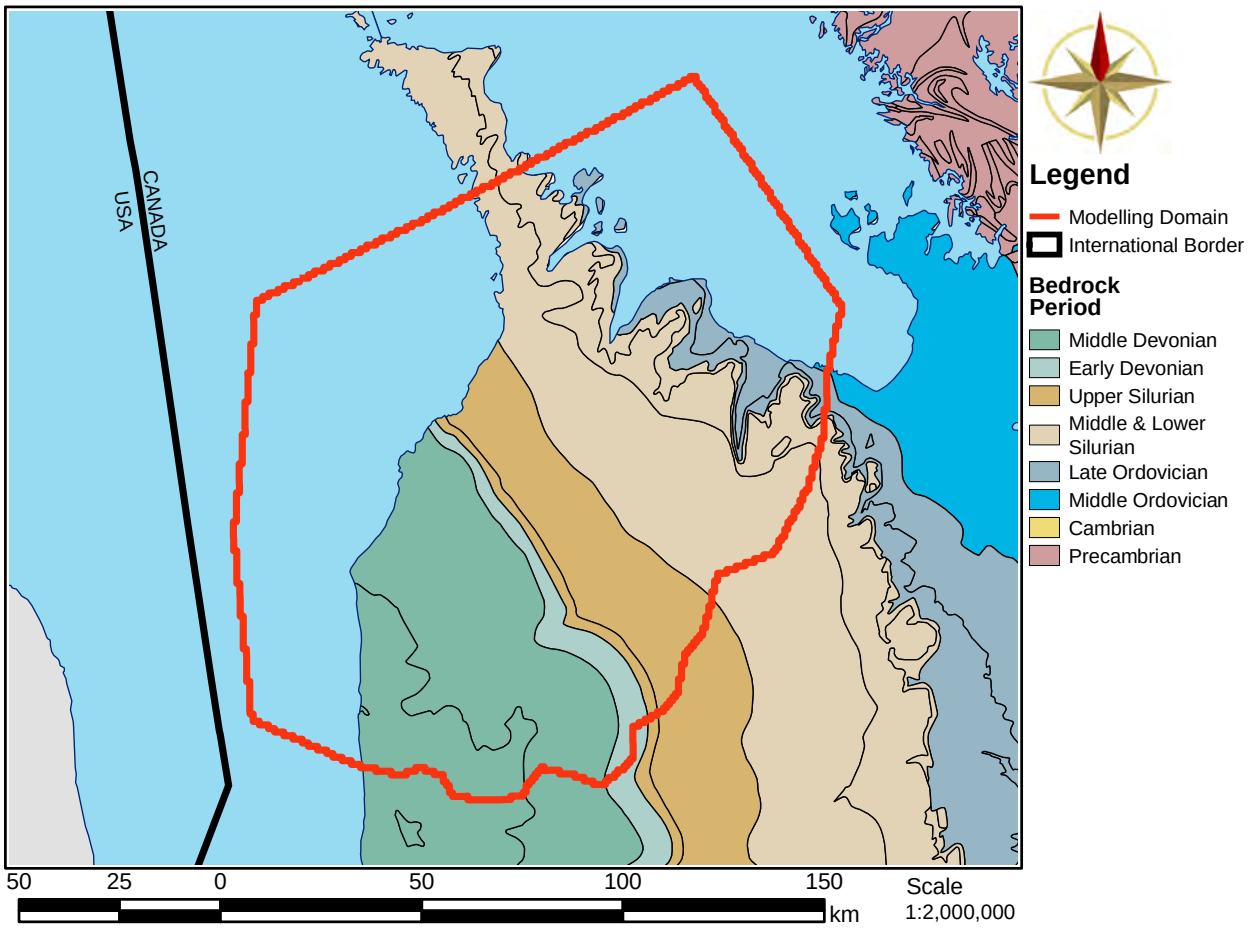

Note: Subcrops coloured by geologic period. Modelling domain is shown in red.

Figure 2.24: Map of Bedrock Subcrops Beneath Quaternary Deposits of Southwestern Ontario

that uses detailed collateral or secondary information from DEMs to supplement sparse observations from water wells in the mapping of the phreatic surface. They proposed estimating the depth to water table using Kriging with an external drift developed with the TOPMODEL (Beven et al. 1984) topographic index, and a residual random error. For the regional-scale grid used in this study, the elevation of the water table is estimated at grid block nodes; the coarseness of the grid (900.9 m by 762.8 m) is not amenable to this procedure given both the error in estimating the surface elevation at a node from a DEM and the nugget expected for the variogram of water table depth at wells.

Both the sides and bottom of the modelling domain are specified as a zero-flux boundary condition. Although this may be appropriate for the upper groundwater flow system, the intermediate and deep flow system contain the high permeability Niagaran Group and Cambrian Formation, respectively; these formations can allow influx and efflux across the model boundary (Sanford et al. 1985). The use of the no-flux boundary condition for the Cambrian beneath Lake Huron is consistent with the hypothesis of this study that at a point in units/formations beneath Lake Huron either a divide for groundwater flow occurs or horizontal flow is negligible. With the assumption that the groundwater system is a subdued reflection of topography, the topographic

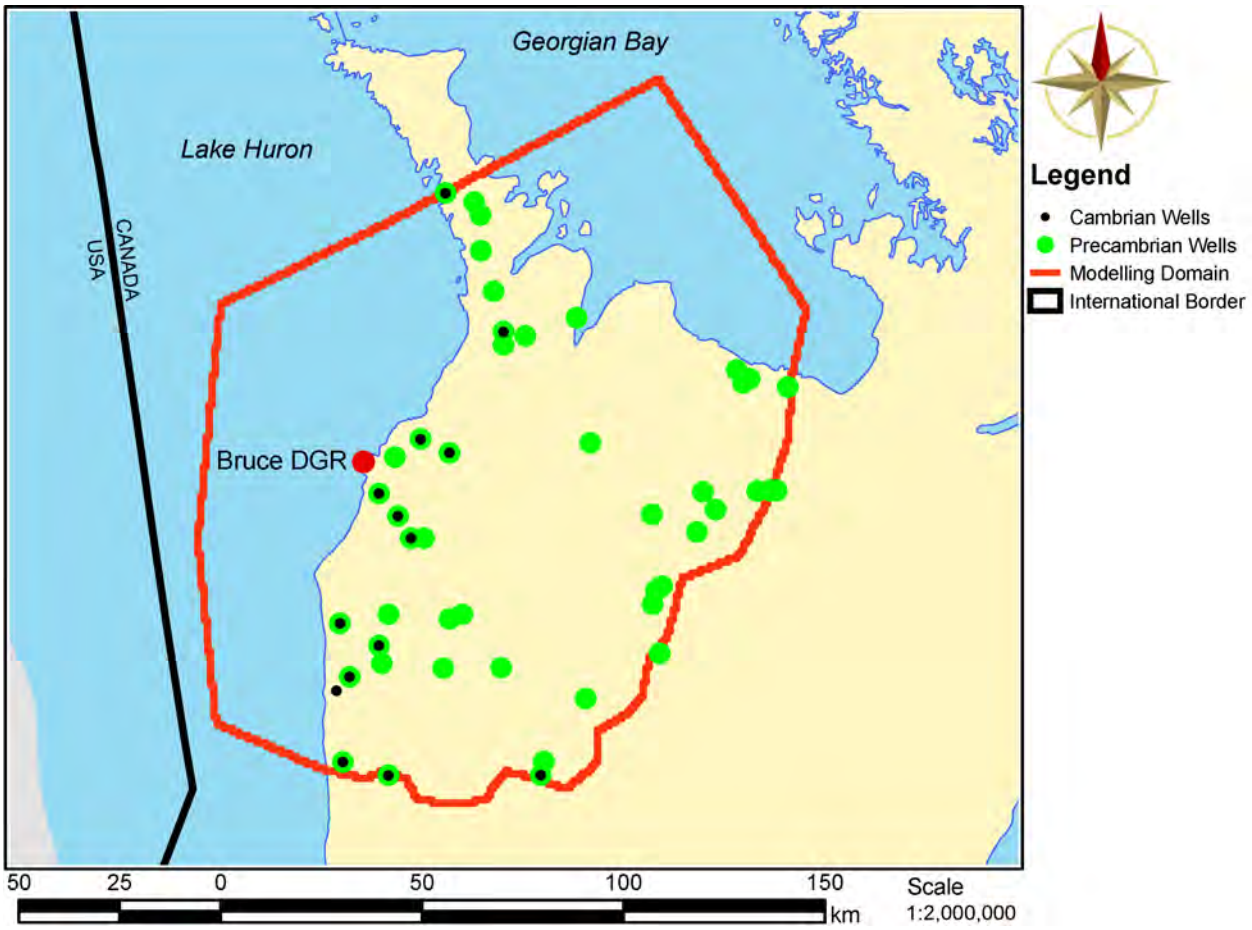

Figure 2.25: Location of Wells Intersecting Cambrian Formation, Precambrian Formation, or Both

divide boundary conditions would only apply to the shallow groundwater zone and the Niagaran Group (included in the Middle to Lower Silurian bedrock) shown in Figure 2.24 of the intermediate groundwater zone. The potential pathways in the Cambrian to the west and northwest (refer to a preceding paragraph) can be investigated through scenario analyses as well as through the basin wide cross-sectional analyses of Section 6.2.

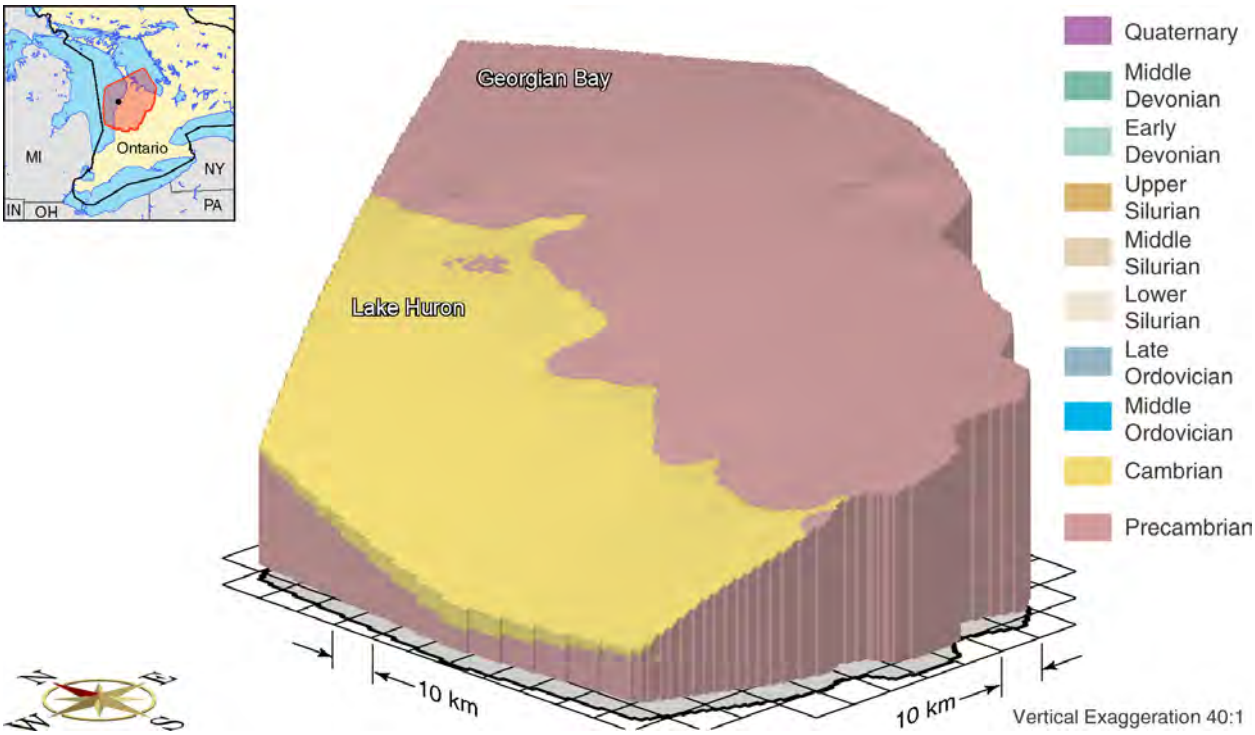

Figure 2.26: Spatial Extent of the Cambrian Formation in Yellow, Underlain by the Precambrian Basement in Pink, for the Regional Modelling Domain

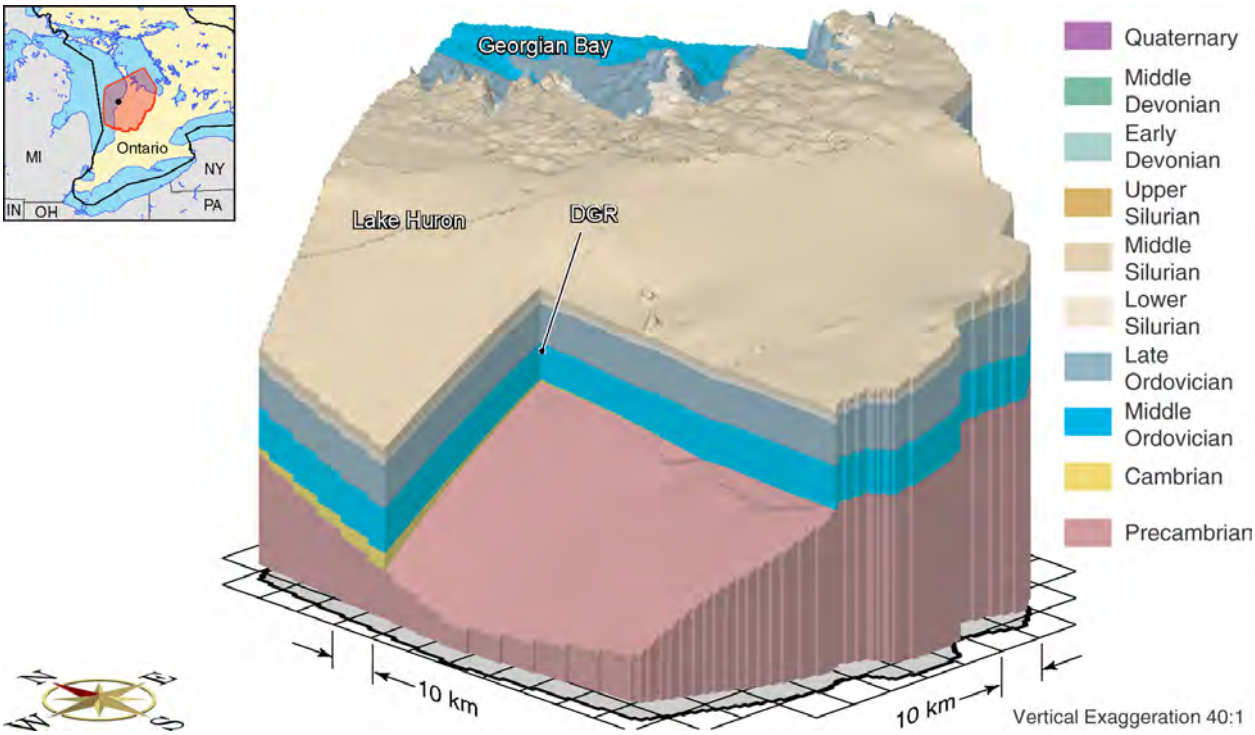

Figure 2.27: Block Cut View Showing Spatial Extent of the Middle Silurian (Top of the Niagaran Group) for the Regional Modelling Domain

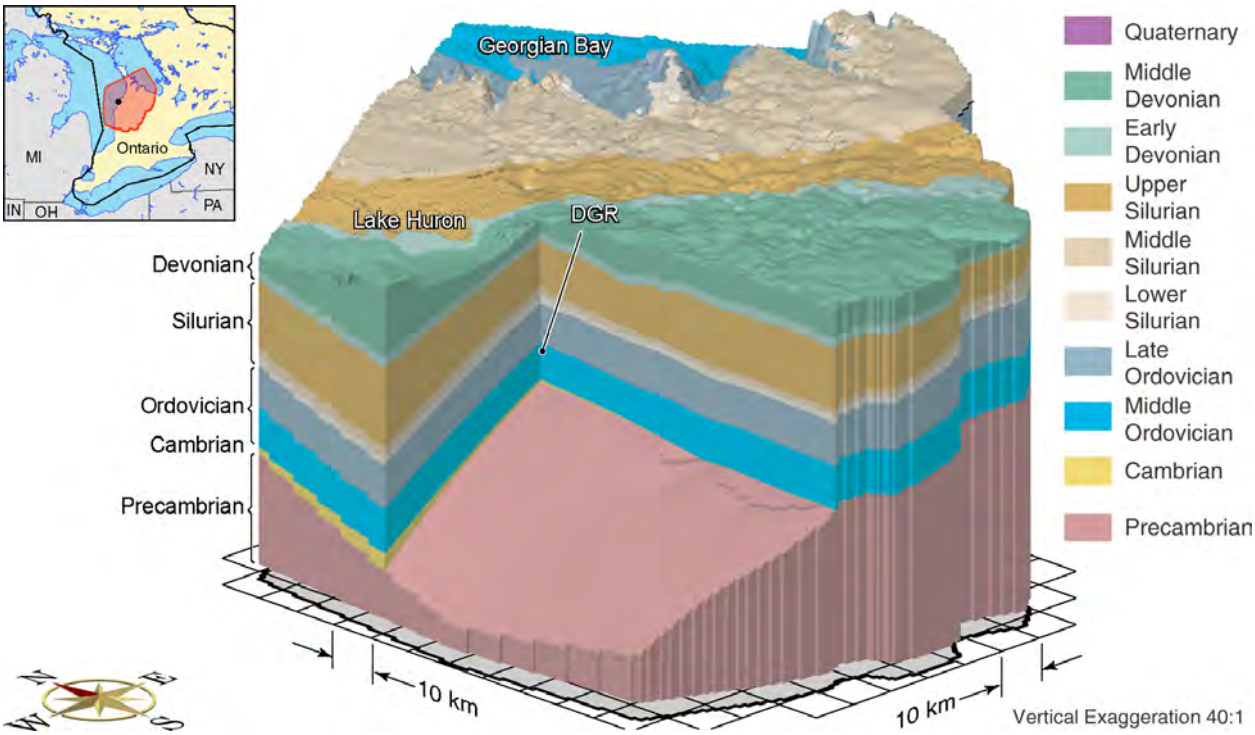

Figure 2.28: Block Cut View Showing Spatial Extent of the Bedrock Units with No Quaternary Drift Deposits for the Regional Modelling Domain

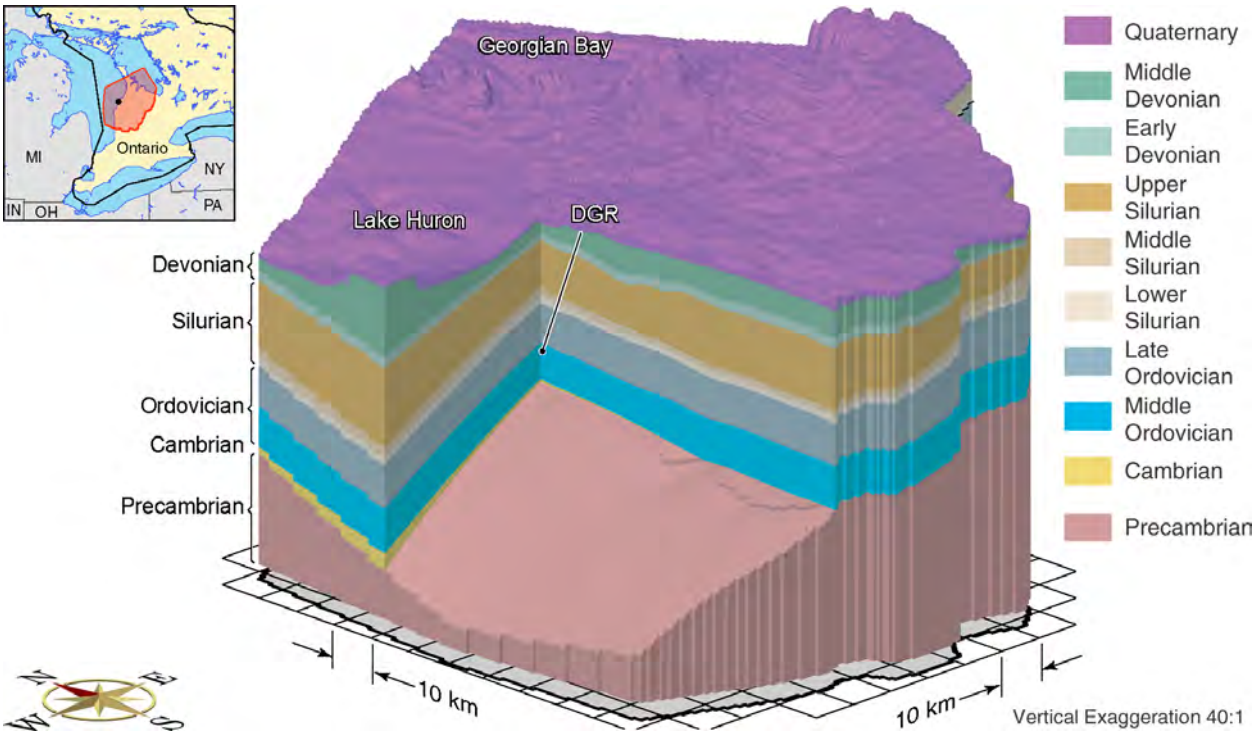

Figure 2.29: Block Cut View Showing Spatial Extent of the Bedrock Units with Quaternary Drift Deposits Assigned to the Top 20 m of the Regional Modelling Domain

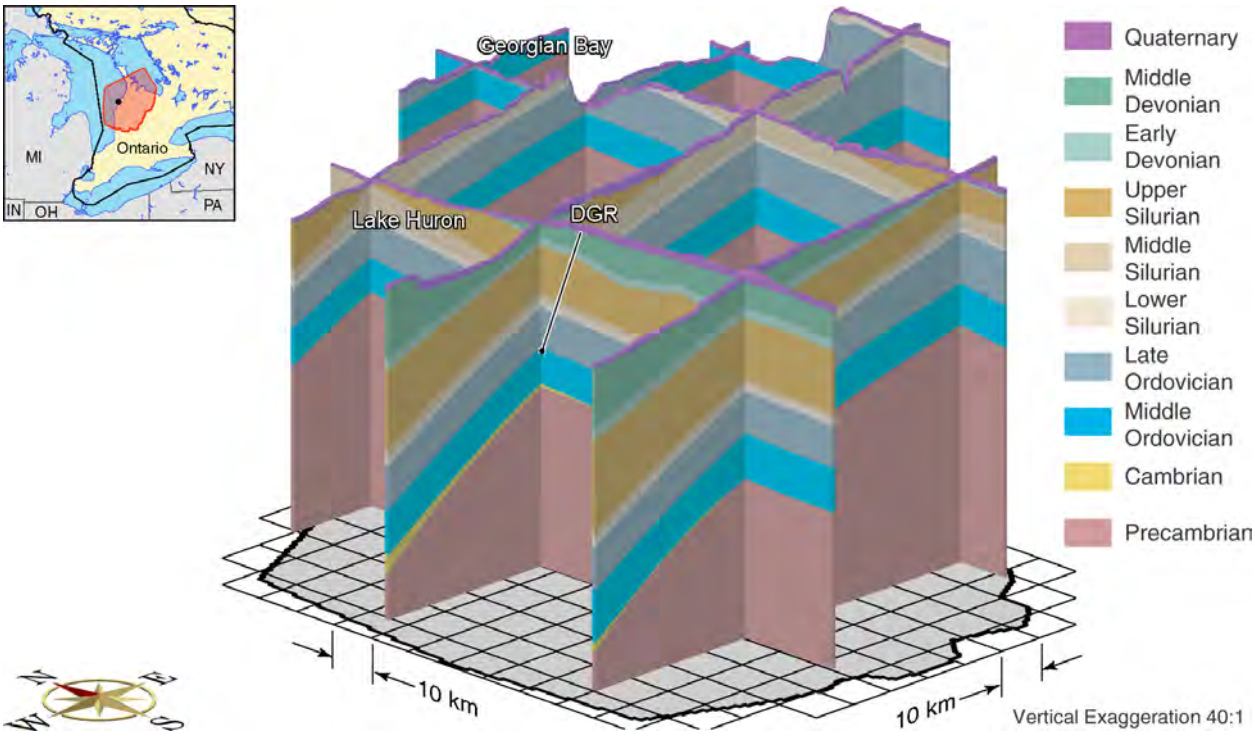

Figure 2.30: Fence View Showing Spatial Extent of the Bedrock Units with Quaternary Deposits Assigned to the Top 20 m of the Regional Modelling Domain

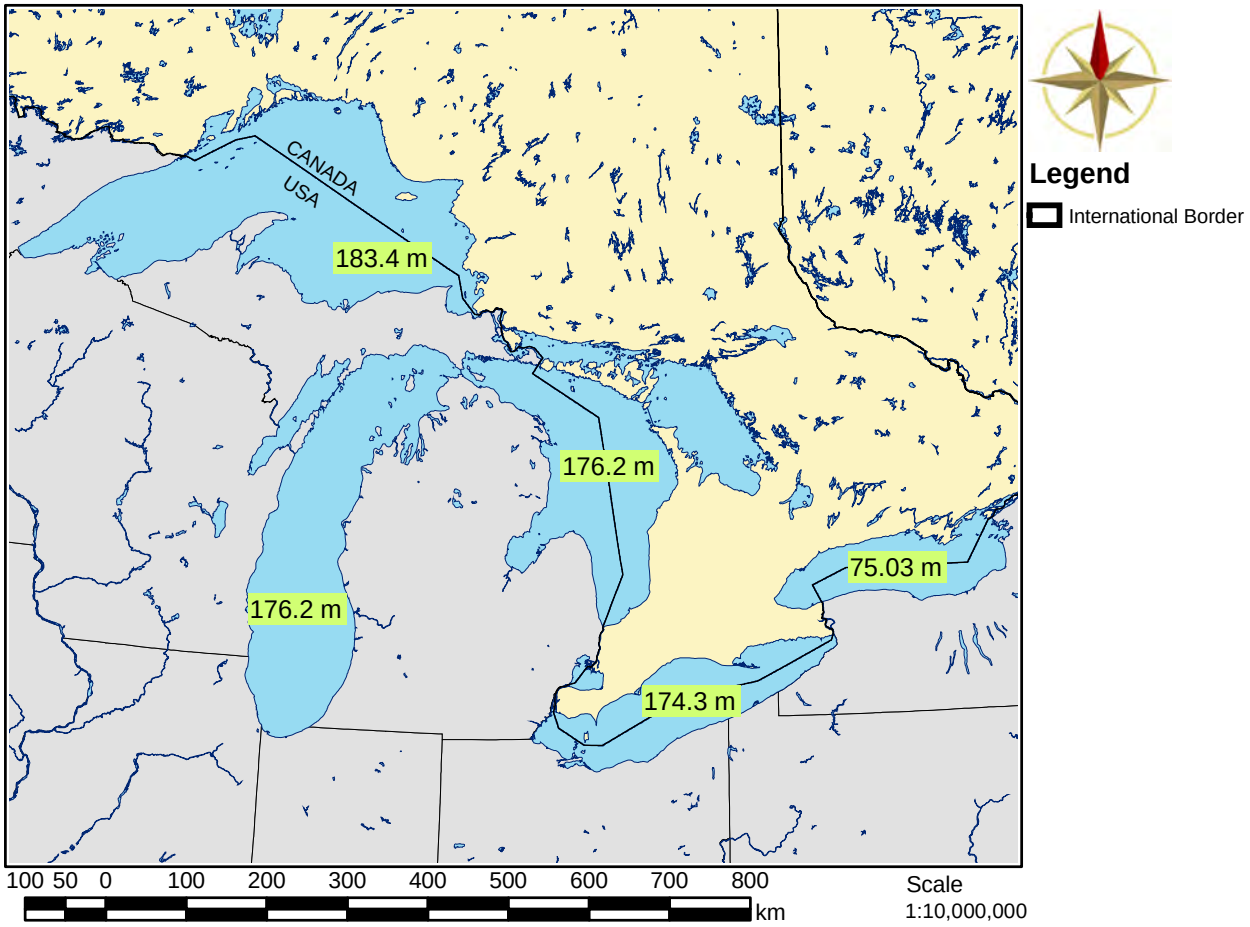

Figure 2.31: Elevation of the Great Lakes

3. GEOSPHERE COMPUTATIONAL MODEL DESCRIPTION AND THEORY

The following sections present the governing equations for groundwater flow, one-dimensional hydromechanical coupling, solute transport, and constitutive relationships for density and concentration. Boundary and initial conditions for the governing equations are not provided herein, but are widely published in the literature, for example, Bear (1988). Parameter definitions follow the equations, with units defined as: L = length, T = time, and M = mass.

3.1 Fluid Flow

According to Bear (1988), the equation of mass conservation for flow in a saturated porous medium is defined as:

$$-\frac{\partial}{\partial x_i}(\rho\, q_i) \pm Q = \frac{\partial}{\partial t}(n\rho) \qquad i = 1,2,3 \tag{3.1}$$

where ρ is the fluid density [M/L^3]; q_i is the Darcy flux vector in direction i [L/T]; Q is the fluid source/sink term [M/L^{3}T]; t is the time [T]; and n is the total porosity [/]. The Darcy equation relating flux to the energy potential of the fluid is defined as (Bear 1988, Frind 1982):

$$q_i = -K_{ij}\left(\frac{\partial h}{\partial x_j} + \rho_r \frac{\partial z}{\partial x_j}\right), \quad h = \frac{p}{\rho_0 g} + z \qquad i,j = 1,2,3 \tag{3.2}$$

where K_{ij} is the porous media hydraulic conductivity tensor [L/T]; h is the freshwater head [L]; ρ_r is the relative fluid density [/]; p is the fluid pressure [M/LT^2]; ρ_0 is the reference fluid density [M/L^3]; g is the gravitational constant [L/T^2]; and z is the fluid elevation [L]. In Equation (3.2), the relative density ρ_r is defined as:

$$\rho_r = \frac{\rho}{\rho_0} - 1 \tag{3.3}$$

The hydraulic conductivity tensor in Equation (3.2) is defined as:

$$K_{ij} = \frac{k_{ij}\,\rho\, g}{\mu} \qquad i,j = 1,2,3 \tag{3.4}$$

where k_{ij} is the porous media permeability tensor [L^2]; and μ is the dynamic viscosity [MT/L]. In combining Equation (3.1) and Equation (3.2), the groundwater flow equation can be simplified to (Freeze and Cherry 1979, Frind 1982):

$$\frac{\partial}{\partial x_i}\left[K_{ij}\left(\frac{\partial h}{\partial x_j} + \rho_r \frac{\partial z}{\partial x_j}\right)\right] \pm Q = S_s \frac{\partial h}{\partial t} \qquad i,j = 1,2,3 \tag{3.5}$$

where S_s is the storage coefficient [L^{-1}]. The storage coefficient is a measure of the compressibility of the porous media and pore fluid, and is defined as the volume of water that a unit volume of aquifer releases from storage under a unit decline of piezometric head (Freeze and Cherry 1979).

3.2 Hydromechanical Coupling

3.2.1 Hydromechanical Computational Modelling

The equations describing hydromechanical computational models are well developed in the literature. However, most published numerical models involve simplifications or assumptions such that an incomplete integration of the components is provided. For models that include the integration of multiple attributes, the computational burden may limit the scale of the problem that can be simulated. Nguyen and Selvadurai (1996) present the equations for thermal-mechanical-hydrogeologic coupling in geological media with saturated fluids of constant concentration; the finite element method was used to develop their FRACON numerical model. To investigate the impact of a gas phase with a low saturation on mechanical coupling, Nguyen and Selvadurai (1996) neglected capillary and surface tension effects and determined the compressibility of the air/water mixture using a volumetric weighting of the compressibilities of the individual fluid phases. With gas compressibility at atmospheric pressure being about four-orders-of-magnitude greater than that of water, their analyses show that the fluid compressibility is dominated by the compressibility of the gas and that as the degree of gas saturation increases from low values (1% to 2.5%), there is a significantly decreased impact of applied stress on pore pressure.

Neuzil (2003) develops the link between the equations of deformation, based on Terzaghi's concept of effective stress, and the fluid mass conservation equation assuming water saturated pores. Simplifications to the equations are then developed including the saturated poroelastic equations for the case when lateral strains are neglected. The resulting equations can be used to describe the compaction and decompaction due to deposition and erosion that involves load changes that are relatively homogeneous areally, especially when viewed on geologic time scales. In this case, for a changing but areally homogeneous load, the lateral strains are assumed to be zero, but changes in vertical stress are not. Lemieux et al. (2008b) used this approach to investigate the impact on saturated density-dependent isothermal groundwater flow at the continental scale of glaciation and deglaciation. Bense and Person (2008) used a similar mechanical hydraulic coupling approach to investigate the impact of glaciation and deglaciation on saturated density-dependent non-isothermal flow in a generic cross-section representing an intracratonic basin. The equations also were the basis of the paleohydrogeologic analyses in the hydrogeologic modelling study of (Normani 2009).

Rutqvist et al. (2001) presents the general governing equations for coupled Thermo-Hydro-Mechanical (THM) processes in saturated and unsaturated geologic formations and reviews four finite element codes for modelling of such systems. In their development, a compositional approach was used with the partially saturated medium being treated as a two-phase system where pores are filled partially with liquid water and partially with gas. Thus each fluid phase has two components: water and dry air. The gas phase was described as an ideal gas mixture composed of dry air and water vapour and the liquid phase consisted of water and dissolved air. The mechanical behaviour of the porous media consisted of the gas, liquid and solid matter responding to local pressure and the overall material response to effective stresses. Coexisting fluid and solid components were assumed to be in local thermal equilibrium. Rutqvist et al. (2002) extends their review paper in the development of a coupling of the TOUGH2 multi-phase, multi-component fluid flow and heat transport numerical model (Pruess et al. 1999) with the FLAC3D code. FLAC3D (ITASCA 1997) is developed for rock and soil mechanics and can also handle coupled thermo-mechanical and hydro-mechanical processes. In the coupled TOUGH2-FLAC3D model, the components in each fluid phase are water, air and CO_2.

A module, designated EOS7C, was developed for TOUGH2 (Oldenburg et al. 2001) so that it can be used to simulate the injection of CO_2 into natural gas reservoirs for carbon sequestration and enhanced CH_4 gas recovery. Nonisothermal conditions were assumed while the components considered were water, brine, non-condensible gas (CO_2, N_2 or air), CH_4 and a tracer. The model did not include a mechanical coupling. The TOUGH2 equation-of-state module EOS7C does not include the formation at appropriate temperatures and pressures of CH_4 hydrates in either a water phase or an ice phase. The numerical model TOUGH+HYDRATE (Moridis et al. 2008) includes such processes and therefore provides the potential for a more complete description of a geologic system that contains methane in both a solution and gaseous form. The computational model includes both an equilibrium and a kinetic model of hydrate formation and dissociation. The model accounts for heat and up to four mass components with these being water, CH_4, hydrate, and water-soluble inhibitors such as salts or alcohols. These components are partitioned among four possible phases (gas phase, liquid phase, ice phase and hydrate phase). Hydrate dissociation or formation, phase changes and the corresponding thermal effects are fully described in the model, as are the effects of inhibitors. The model can describe all possible hydrate dissociation mechanisms such as depressurization, thermal stimulation, salting-out effects and inhibitor-induced effects. By coupling TOUGH+HYDRATE to the geomechanical code FLAC3D (Holditch et al. 2008), the formation and disassociation of CH_4 hydrate during, for example, the pressure and temperature changes of glaciation can be simulated. While the model TOUGH+HYDRATE+FLAC3D allows the simulation of most of the geologic processes that can occur in a paleohydrogeologic scenario, the model is deemed to be inappropriate for the simulation of long-term, three-dimensional regional-scale flow at the Bruce DGR site.

3.2.2 One-Dimensional Loading Efficiency

Simplifying assumptions are required for the simulation of paleohydrogeologic scenarios. The computational time for each of the regional-scale paleohydrogeologic simulations can be up to one week or more. The approach followed in the study was to assume that ice loads were areally homogeneous so that lateral strains could be neglected. With that approach, if a gas phase is present, it can only be included as an immobile phase that impacts fluid compressibility and the effective mobility of the water phase (Nguyen and Selvadurai 1996). Because of computational limitations, the inclusion of lateral strains would require a reduction in the dimensionality of the regional-scale domain.

One-dimensional vertical loading and unloading due to glaciation, erosion, or deposition, is a common simplification that can be applied in hydromechanical coupling (van der Kamp and Gale 1983, Neuzil 2003, Jaeger et al. 2007). Assuming that the porous media, solid grains, and pore fluid are all compressible, the storage coefficient S_s is defined as:

$$S_s = \rho g \left[\left(\frac{1}{K} - \frac{1}{K_s} \right) (1 - \lambda) + n \left(\frac{1}{K_f} - \frac{1}{K_s} \right) \right], \quad \lambda = \frac{2\alpha(1 - 2\nu)}{3(1 - \nu)}, \quad \alpha = 1 - \frac{K}{K_s} \tag{3.6}$$

where K is the drained bulk modulus of the porous media [M/T^{2}L]; K_s is the bulk modulus of the solids in the porous media [M/T^{2}L]; K_f is the bulk modulus of the pore fluid [M/T^{2}L]; α is the Biot coefficient [/]; and ν is the Poisson's ratio [/]. The bulk modulus K is defined as the reciprocal of compressibility, therefore $K = 1/\beta$ (Jaeger et al. 2007).

The effect of mechanically loading the surface of a porous media is to transfer the load to both the porous media, and the pore fluid; the amount of stress transferred depends on the relative compressibility of the porous media to the pore fluid, as well as the porosity. Since the porous media is somewhat elastic, it will compress under load, thereby reducing the size of pores, and

compressing the pore fluid as a result. The pore fluid will compress, and in so doing, will resist the compression of the porous media, which will increase the pore pressure; the effects of mechanical loading and pore pressure affect each other, and are thus coupled. The groundwater flow equation listed as Equation (3.5) can be modified to account for one-dimensional hydromechanical coupling as follows:

$$\frac{\partial}{\partial x_i}\left[K_{ij}\left(\frac{\partial h}{\partial x_j}+\rho_r\frac{\partial z}{\partial x_j}\right)\right] \pm Q = S_s\frac{\partial h}{\partial t} - \frac{S_s\zeta}{\rho g}\frac{\partial \sigma_{zz}}{\partial t} \qquad i,j = 1,2,3 \tag{3.7}$$

where ζ is the one-dimensional loading efficiency [/]; and σ_{zz} is the vertical stress [M/LT^2]. A fundamental assumption of one-dimensional hydromechanical coupling is that strains can only occur in a vertical direction, implying no lateral strains. The loading efficiency is further defined as (van der Kamp and Gale 1983, Neuzil 2003):

$$\zeta = \frac{B(1+\nu)}{3(1-\nu)-2\alpha B(1-2\nu)}, \quad B = \frac{\left(\frac{1}{K}-\frac{1}{K_s}\right)}{\left(\frac{1}{K}-\frac{1}{K_s}\right)+n\left(\frac{1}{K_f}-\frac{1}{K_s}\right)} \tag{3.8}$$

where B is the Skempton coefficient and physically represents the ratio of change in fluid pressure to a change in mean effective stress under undrained conditions (Neuzil 2003). A further simplification is commonly made in considering the solids of the porous media to be incompressible, or rigid, such that $\beta_s \rightarrow 0$ and $K_s \rightarrow \infty$, resulting in:

$$S_s = \rho g(\beta' + n\beta_f), \quad \zeta = \frac{\beta'}{\beta' + n\beta_f} \tag{3.9}$$

where β' is the coefficient of vertical compressibility for the porous media [LT^2/M]; and β_f is the fluid compressibility [LT^2/M]. β' can be calculated from commonly measured rock mechanics properties such as Young's elastic modulus E and Poisson's ratio ν as follows (Neuzil 2003, Jaeger et al. 2007):

$$K = \frac{E}{3(1-2\nu)}, \quad K' = K\frac{3(1-\nu)}{1+\nu}, \quad \beta' = \frac{1}{K'} \tag{3.10}$$

where E is the Young's elastic modulus of the porous media [M/LT^2]; and K' is the drained confined vertical modulus of the porous media [M/LT^2]. Computational models such as TOUGH2-MP, which use pressure as a state variable, require the use of *pore compressibility* instead of specific storage. The pore compressibility β_p is defined as (Gutierrez and Lewis 2002, Birkholzer et al. 2008):

$$\beta_p = \frac{1}{n}\frac{\partial n}{\partial p} = \frac{\beta'}{n} = \frac{S_s}{n\rho g} - \beta_f \tag{3.11}$$

where β_p is the pore compressibility [T^{2}L/M]; and p is the pore pressure [M/T^{2}L]. In TOUGH2-MP, the fluid compressibility is accounted for through the variation of fluid density with pore pressure (Birkholzer et al. 2008).

Since FRAC3DVS-OPG does not account for the geometric deformation of the grid as a mechanical load is applied, the hydromechanical term $\frac{S_s\zeta}{\rho g}\frac{\partial \sigma_{zz}}{\partial t}$ in Equation (3.7) serves as a fluid

source/sink term to effectively increase or decrease the fluid pore pressure, and hence head h, based on the temporal rate of change of vertical stress $\frac{\partial \sigma_{zz}}{\partial t}$, the storage coefficient S_s, and the one-dimensional loading efficiency ζ. A loading efficiency near zero results from a fairly stiff porous media, so little load is transferred to the pore fluid, while a loading efficiency near one represents a porous media that is more compressible than the pore fluid, so the pore fluid will support the majority of the applied load. Both the storage coefficient S_s and the one-dimensional loading efficiency ζ are specified as inputs to FRAC3DVS-OPG.

The one-dimensional loading efficiency ζ is proportional to the Skempton coefficient B which is sensitive to the fluid compressibility (inverse of fluid bulk modulus). The effective fluid compressibility for a gas-water mixture can be estimated as a volumetric weighted average of the gas and water compressibilities (Jaeger et al. 2007, Nguyen and Selvadurai 1996). Figure 3.1a has been estimated using an insitu gas bulk compressibility of 8.0×10^{-8} Pa^{-1}, a brine bulk compressibility of 3.0×10^{-10} Pa^{-1}, and Cobourg Formation parameters which include a drained bulk modulus of the porous media K of 36.4 GPa, a bulk modulus of the solids in the porous media K_s of 72.7 GPa for a Biot coefficient α of 0.5, and a porosity n of 0.015; the results show that a small amount of gas greatly increases the effective fluid compressibility. Based on the effective fluid compressibility, Figure 3.1b shows that the Skempton coefficient B and hence the one-dimensional loading efficiency ζ in Figure 3.1c decrease rapidly even for small gas saturations so that pore pressures induced by mechanical loading become negligible. Figure 3.1b and Figure 3.1c are based on a pressure dependent gas bulk compressibility of 8.0×10^{-8} Pa^{-1} at an insitu gas pressure of 12.5 MPa. The bulk gas compressibility reduces as gas pressure increases yielding increasing mechanical effect for a given gas saturation.

3.3 Solute Transport

The generalized solute transport equation for a saturated porous media is (Bear 1988):

$$\frac{\partial}{\partial x_i}\left(n D_{ij}\frac{\partial C}{\partial x_j}\right) - \frac{\partial}{\partial x_i}(q_i C) \pm \Omega_C = \frac{\partial}{\partial t}(n C) \qquad i,j = 1,2,3 \tag{3.12}$$

where D_{ij} is the hydrodynamic dispersion tensor [L^2/T]; C is the concentration [M/L^3]; and Ω_C is the concentration source/sink term [M/L^{3}T]. D_{ij} is defined by Burnett and Frind (1987) as:

$$n D_{11} = \alpha_L \frac{q_1^2}{|q|} + \alpha_{TH}\frac{q_2^2}{|q|} + \alpha_{TV}\frac{q_3^2}{|q|} + n\tau D_m \tag{3.13a}$$

$$n D_{22} = \alpha_{TH} \frac{q_1^2}{|q|} + \alpha_L\frac{q_2^2}{|q|} + \alpha_{TV}\frac{q_3^2}{|q|} + n\tau D_m \tag{3.13b}$$

$$n D_{33} = \alpha_{TV} \frac{q_1^2}{|q|} + \alpha_{TV}\frac{q_2^2}{|q|} + \alpha_L\frac{q_3^2}{|q|} + n\tau D_m \tag{3.13c}$$

$$n D_{21} = n D_{12} = (\alpha_L - \alpha_{TH})\frac{q_1 q_2}{|q|} \tag{3.13d}$$

$$n D_{31} = n D_{13} = (\alpha_L - \alpha_{TV})\frac{q_1 q_3}{|q|} \tag{3.13e}$$

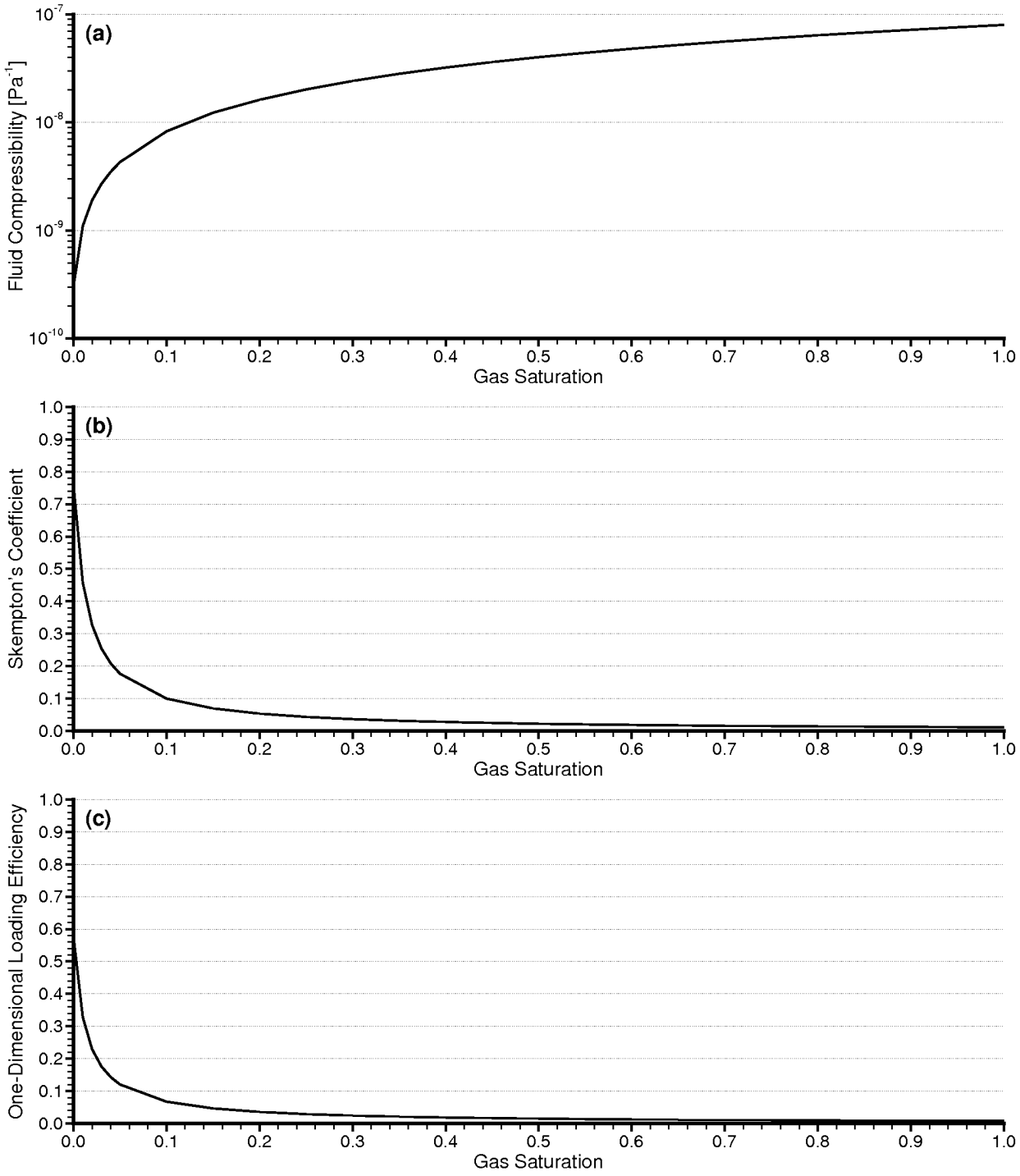

Note: (a) saturation weighted bulk fluid compressibility assuming air and brine (see Section 4.1.1), (b) Skempton's coefficient *B* based on the bulk fluid compressibility, and (c) one-dimensional loading efficiency ζ based on the bulk fluid compressibility, Skempton's coefficient and other parameters for the Cobourg Formation from Table 4.4.

Figure 3.1: Impact of Gas Saturation on the Effective Fluid Compressibility, Skempton's Coefficient, and One-Dimensional Loading Efficiency

$$n D_{32} = n D_{23} = (\alpha_L - \alpha_{TV}) \frac{q_2 q_3}{|q|} \tag{3.13f}$$

where α_L is the longitudinal dispersivity [L]; α_{TH} is the horizontal transverse dispersivity [L]; α_{TV} is the vertical transverse dispersivity [L]; $|q|$ is the magnitude of Darcy flux [L/T]; τ is the tortuosity of the porous medium [/]; and D_m is the molecular diffusion coefficient [L^2/T].

In the literature, the pore water diffusion coefficient is also referred to as the diffusion coefficient of the porous medium (Bear 1988). For the case of variably dense fluids, fluid density in Equation (3.7) depends on pore fluid concentration as follows:

$$\rho_r = \gamma \frac{C}{C_{max}}, \quad \gamma = \frac{\rho_{max}}{\rho_0} - 1 \tag{3.14}$$

where C_{max} is the maximum concentration [M/L^3]; ρ_{max} is the maximum density [M/L^3]; and γ is the maximum relative density [/]. These relationships are commonly used when modelling heavy brines with concentrations of 300 g/L or higher. The following section describes the relationship between concentration, density, and mass fraction for dense pore fluids.

3.4 Constitutive Relationships

Constitutive or functional relationships link fluid or porous media properties to the pressure, temperature or concentration of a system. Bear (1988) and Adams and Bachu (2002) present various state equations with empirically determined coefficients. The theory and implementation manuals of MOTIF (Chan et al. 1999) and SWIFT-III (HSI GeoTrans 2000) also define the state equations for fluid density, $\rho = f(T, P, C)$, and fluid viscosity, $\mu = f(C, T)$. Similar relationships are used in FRAC3DVS-OPG.

The physical properties of groundwaters in deep sedimentary or crystalline rock environments can vary by greater than 25% for density and by one order-of-magnitude for viscosity. Density and viscosity changes may retard or enhance fluid flow or contaminant transport driven by other mechanisms; flow and transport are dependent on fluid density and viscosity as well as media properties such as permeability, porosity, and dispersivity. Thus, variations in fluid density and viscosity may have significant impacts on the flow system with consequences for various relevant processes (Adams and Bachu 2002).

The relationships between concentration expressed as Total Dissolved Solids (TDS), solution density, and mass fraction in characterizing solutes in water are:

$$\rho = \frac{M}{V} \tag{3.15a}$$

$$TDS = \frac{m}{V} \tag{3.15b}$$

$$X = \frac{m}{M} \tag{3.15c}$$

where *TDS* is the total dissolved solids [M/L^3]; *M* is the mass of solution [M]; *V* is the volume of solution [L^3]; *m* is the mass of solute (e.g., NaCl or $CaCl_2$) [M]; and *X* is the mass fraction [/]. By combining these equations, a new relationship for TDS can be determined as:

$$TDS = m \cdot \frac{1}{V} = XM \cdot \frac{\rho}{M} = X\rho \tag{3.16}$$

Adams and Bachu (2002) present a study of brine density and viscosity for the Alberta Basin, consisting primarily of Na−Cl waters. The data and analyses of their paper can be used to illustrate the relationship between brine concentration given as mass fraction and fluid density. Figure 7 in their paper presents a plot of brine density versus mass fraction from 4,854 formation water analyses. A mass fraction of 0.25 matches a density of approximately 1,200 kg/m^3 or 1.2 kg/L. Using Equation (3.16) results in a TDS of 300 kg/m^3, or 300 g/L. For this example, in FRAC3DVS-OPG, ρ_{max} = 1,200 kg/m^3 and C_{max} = 300 g/L.

3.5 Freshwater and Environmental Head

The most common groundwater studies by hydrogeologists involve freshwater systems, implying a constant density for water. The simplification of constant density allows hydrogeologists to use the concept of “head” where gradients and flow velocities can be directly calculated by knowing the difference in head Δh, and the distance between two points ΔL. A gradient *i* is calculated as $i = \Delta h/\Delta L$. Knowing the hydraulic conductivity between the two points and the gradient, Darcy’s Law allows one to calculate the Darcy flux *q* and the direction of flow can be determined where $q = -Ki$. In practical terms, the piezometric head represents the free surface water elevation and is easily determined in the field.

Variable density groundwater flow systems are much less intuitive as the density affects the pore water pressure with depth, resulting in a non-linear pressure profile with depth. Lusczynski (1961) introduces the concepts of point-water head, freshwater head, and environmental-water head. Each approach results in a different elevation for the free surface, depending on the density of the fluid within the well. The head is calculated as the sum of the elevation of the given location and the height of a fluid column, where the fluid pressure at the base of the column equals the pore fluid pressure at that location in the aquifer. Point-water head uses a column of fluid equal in density to the fluid density at the given location, while freshwater head uses a column of freshwater. Due to its lower density, a column of freshwater has a greater height for the same base pressure than a column of point-water. Point-water head and freshwater head are defined as:

$$h_{Pi} = z_i + \frac{p_i}{\rho_i g}, \quad h_{Fi} = z_i + \frac{p_i}{\rho_F g} \tag{3.17}$$

where h_{Pi} is the point-water head at point *i* [L]; z_i is the elevation of point *i* [L]; p_i is the fluid pressure at point *i* [M/LT^2]; ρ_i is the density of fluid at point *i* [M/L^3]; h_{Fi} is the freshwater head at point *i* [L]; and ρ_F is the freshwater density [M/L^3].

Environmental-water head uses a column of water that is identical in fluid density to the water that surrounds the well. One advantage of this definition is that vertical gradients can be determined when comparing the elevation of the free surface in the well casing, to the elevation of the water table immediately adjacent to the well. Unfortunately, a monitoring well in the field is unlikely to contain a fluid whose density precisely matches the fluid immediately outside the casing at any given elevation. Environmental head is more useful when applied to results from modelling

studies, as most groundwater flow models that can simulate variable density flow use freshwater head as the state variable. Environmental head is calculated as follows:

$$h_{Ei} = h_{Fi} - \frac{(\rho_F - \rho_A)(z_i - z_r)}{\rho_F}, \quad \rho_A = \frac{1}{z_r - z_i}\int_{z_i}^{z_r} \rho(z)\,dz \tag{3.18}$$

where h_{Ei} is the environmental-water head at point i [L]; ρ_A is the average density of fluid between z_i and z_r [M/L^3]; z_r is the reference elevation of freshwater above point i [L]; and $\rho(z)$ is the fluid density as a function of z [M/L^3].

In a numerical model using density-dependent flow, such as FRAC3DVS-OPG, the environmental head is calculated from the freshwater head and brine concentration output by the model. Since the finite element nodes are vertically aligned, environmental head is calculated starting at the top of the model, iteratively progressing downwards towards the bottom, where node $j + 1$ is immediately below node j as follows:

$$h_E^{j+1} = h_E^j + \left(h_F^{j+1} - h_F^j\right) - \left(\frac{C^{j+1} + C^j}{2}\right)\left(\frac{\rho_{max} - \rho_F}{\rho_F}\right)\left(z^j - z^{j+1}\right) \tag{3.19}$$

where h_E^{j+1} is the environmental-water head at node $j + 1$ [L]; h_E^j is the environmental-water head at node j [L]; h_F^{j+1} is the freshwater head at node $j + 1$ [L]; h_F^j is the freshwater head at node j [L]; C^{j+1} is the brine concentration at node $j + 1$ [M/L^3]; C^j is the brine concentration at node j [M/L^3]; z^{j+1} is the elevation of node $j + 1$ [L]; and z^j is the elevation of node j [L].

A hydrogeologist must be aware that traditional techniques for determining gradients and groundwater fluxes in constant density freshwater systems *do not* apply to variable density flow systems (Post et al. 2007). Field measurements in variably dense groundwater flow systems should include electrical conductivity and pressure with depth measurements (Post et al. 2007). These measurements can provide insight into how density varies with depth due to known relationships between salinity and electrical conductivity, and between density, salinity and pressure. Lusczynski (1961) states that because "environmental-water heads define hydraulic gradients along a vertical, they are comparable along a vertical. This is evidently not the case for point-water or fresh-water heads. Also, because fresh-water heads define hydraulic gradients along a horizontal in groundwater of variable density, they are comparable along a horizontal. This is not the case for point-water or environmental-water heads."

3.6 System Performance Measures

The DGR safety case relies, in part, on the ability of the far-field to provide a long-term barrier to solute transport. In trying to robustly characterize the groundwater flow and transport regimes in the deeper basinal formations, it is prudent to determine and quantify what impact, if any, the variability of model parameters will have upon the model results. It is by demonstrating and determining the sensitivity of the model to perturbations in model parameters that a more rigourous understanding of the groundwater system at depth can be achieved.

Common measures of the performance of a groundwater system include the flow state variables of equivalent freshwater head or environmental head and the derived pore water velocity, the solute concentration for a conservative tracer, average water particle paths and travel time, the Péclet number of molecular diffusion (Bear 1988, Huysmans and Dassargues 2005) and as developed in Normani et al. (2007), mean lifetime expectancy and groundwater age. Lifetime

expectancy can be estimated by determining the Probability Density Function (PDF) for the time required for water particles at a spatial position in a groundwater system to reach potential outflow points. Particles can migrate to the boundary by both advection and hydrodynamic dispersion; because of hydrodynamic dispersion, particles at a given point in the system will not follow the same path to the boundary. In this study, only the first moment of the PDF for lifetime expectancy is estimated with the value being expressed as the MLE. Groundwater age of water particles at a spatial position can be determined by the PDF for time elapsed since the water particles entered the system from a boundary. Sensitivity analyses using marginal sensitivity coefficients and normalized sensitivity coefficients also provide information on the groundwater system. Each of these performance measures have their advantages and disadvantages. Sensitivity coefficients are local derivatives and for systems with a large number of spatially and possibly temporally varying parameters, there is considerable computational burden in calculating the sensitivity coefficients for each parameter. While average water particle paths can indicate the discharge point for water from a repository, most algorithms are based on steady-state flow and the associated travel time accounts for advection, but neither dispersion nor diffusion. The travel time can thus significantly overestimate the arrival of a contaminant along a path in which diffusion dominates advection. MLE correctly replicates the transport processes, but like all numerical solutions developed for a form of the advection dispersion equation, it is subject to the classical problems of numerical instability. As implemented in FRAC3DVS-OPG, where the dispersion model used for total dissolved solids is the same as that used in the equation used to estimate MLE, to achieve a solution, dispersivity coefficients must be carefully selected as a function of grid block size. For a model with large grid blocks and hence a large dispersivity that meets grid or cell Péclet number criteria, MLE may thus underestimate the average time for particles to reach discharge points. The method does not define either the paths followed by the particles or the discharge points. Details of the Péclet number of molecular diffusion and MLE performance measures are provided in the following section.

3.6.1 Péclet Number of Molecular Diffusion

The Péclet number defining the ratio between the rate of solute transport by advection and the rate of solute transport by molecular diffusion (Bear 1988, Huysmans and Dassargues 2005) is:

$$Pe = \frac{V\ell}{D_e} \tag{3.20}$$

in which ℓ is a characteristic length, V is the pore water velocity and D_e is the effective diffusion coefficient calculated as the product the tortuosity τ [/] of the porous medium and the molecular diffusion coefficient D_m [L^2/T] (refer to Equation (3.13)). Bear (1988) states that a Péclet number of less than 0.4 indicates that solute transport is dominated by molecular diffusion. To simplify the analyses of this study, a characteristic length ℓ = 1 m is used. Bear (1988) indicates that the scale length is that of the mean grain or pore size or any other characteristic medium length. A value of ℓ = 1 m provides conservative estimates of the Péclet number.

3.6.2 Groundwater Age and Life Expectancy

The concept of groundwater age A and groundwater life expectancy E are related to groundwater travel time T as follows: $T = A + E$. Age is associated with forward-in-time equations, while life expectancy is associated with backward-in-time equations of groundwater transport (Cornaton and Perrochet 2006a,b). The relationship between groundwater travel time T, age A, and life expectancy E along a groundwater flow line is shown in Figure 3.2. When the advection-dispersion equation is solved, the age PDF for any position $g_A(x_i, t)$ within a domain

can be calculated. Since MLE accounts for transport both by advection and diffusion, it is an ideal performance measure for characterizing flow systems with both advection and diffusion dominant portions, as shown in Figure 3.3. The age PDF is calculated using the following equation (Cornaton and Perrochet 2006a):

$$\frac{\partial}{\partial x_i}\left(n D_{ij}\frac{\partial g_A}{\partial x_j}\right) - \frac{\partial}{\partial x_i}\left(q_i g_A\right) + q_I \delta(t) - q_O = \frac{\partial}{\partial t}\left(n g_A\right) \qquad i,j = 1,2,3 \tag{3.21}$$

where g_A is the age PDF [T^{-1}]; $\delta(t)$ is the Dirac delta function for time [T^{-1}]; q_I is the fluid source term [T^{-1}]; and q_O is the fluid sink term [T^{-1}]. Similarly, the life expectancy PDF, is calculated as follows (Cornaton and Perrochet 2006a):

$$\frac{\partial}{\partial x_i}\left(n D_{ij}\frac{\partial g_E}{\partial x_j}\right) + \frac{\partial}{\partial x_i}\left(q_i g_E\right) - q_I g_E = \frac{\partial}{\partial t}\left(n g_E\right) \qquad i,j = 1,2,3 \tag{3.22}$$

where g_E is the life expectancy PDF [T^{-1}]. The backwards-in-time nature of the life expectancy equation requires fluxes to be reversed.

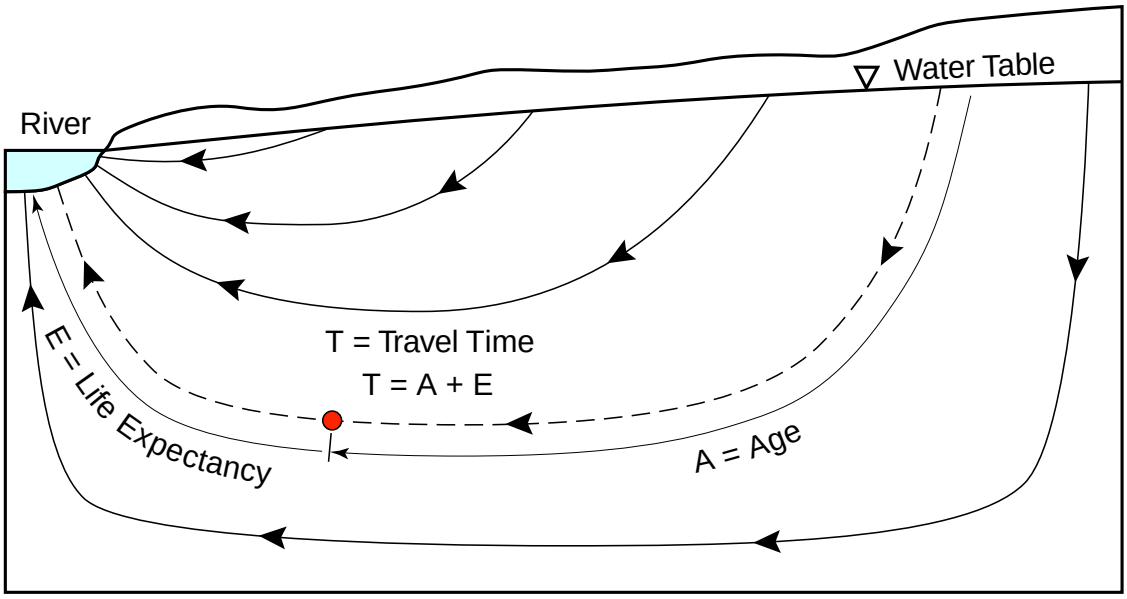

Figure 3.2: Relationship Between Travel Time *T*, Age *A*, and Life Expectancy *E* Along a Groundwater Flow Line for a Representative Cross-Section

For steady-state conditions the first moment of the age and life expectancy PDFs can be calculated to determine the mean of the PDFs resulting in (Cornaton and Perrochet 2006a):

$$\frac{\partial}{\partial x_i}\left(n D_{ij}\frac{\partial \langle A\rangle}{\partial x_j}\right) - \frac{\partial}{\partial x_i}\left(q_i \langle A\rangle\right) - q_O \langle A\rangle + n = 0 \qquad i,j = 1,2,3 \tag{3.23}$$

$$\frac{\partial}{\partial x_i}\left(n D_{ij}\frac{\partial \langle E\rangle}{\partial x_j}\right) + \frac{\partial}{\partial x_i}\left(q_i \langle E\rangle\right) - q_I \langle E\rangle + n = 0 \qquad i,j = 1,2,3 \tag{3.24}$$

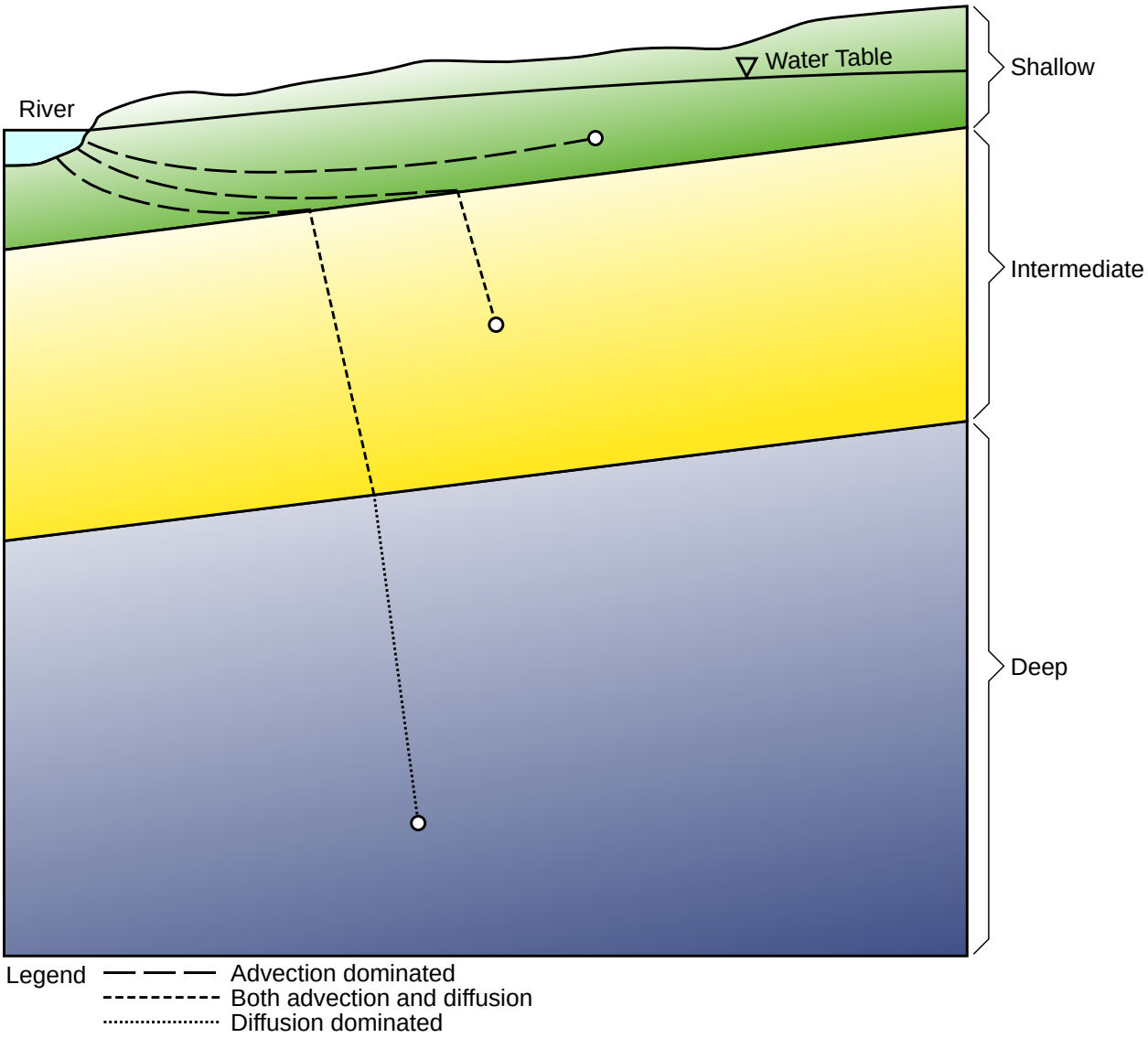

Note: The groundwater system shown is characterized by shallow, intermediate and deep zones. Transport in the shallow zone is advection dominated, transport in the intermediate zone is neither dominated by advection nor diffusion, and transport in the deep zone is diffusion dominated. Flow paths from locations in each zone to an exit boundary are shown.

Figure 3.3: Applicability of MLE to Determine Mean Travel Times from Any Location Within a Domain to an Exit Boundary

where $\langle A \rangle$ is the mean age [T]; and $\langle E \rangle$ is the mean life expectancy [T]. Using these formulations, Mean Ages (MAs) and MLEs will be continuously generated during groundwater flow, because porosity n acts as a source term in Equation (3.23) and Equation (3.24). According to Goode (1996), Equation (3.23) can also be derived using conservation of age mass. Groundwater therefore ages an average of one unit per unit time. Consequently, age and mean life expectancy are sensitive to values of porosity, as well as dispersivity values α_L, α_{TH}, and α_{TV} used in the hydrodynamic dispersion tensor D_{ij}. Both mean age and mean life expectancy are implemented in FRAC3DVS-OPG for steady-state flow only.

4. REGIONAL-SCALE AND SITE-SCALE ANALYSES

The regional-scale and site-scale models provide a framework for the investigation of solute transport in the Ordovician sediments. It is a hypothesis of this study that migration of a solute in the Ordovician limestone and shale from a proposed repository in the Cobourg is dominated by diffusion. The primary objective of the analyses of this section is to investigate this hypothesis through a base-case realization and the assessment of the sensitivity of the conclusion that transport in the Ordovician is diffusive to perturbations of the system parameters including, most importantly, the lateral boundary conditions of the model domain. An additional objective of the regional-scale and site-scale modelling is the explanation of the abnormal pressures observed in the DGR boreholes. Given the constraints of the computational models selected for this study, the assessment of the abnormal pressures follows an indirect approach that uses reasoning and lines of modelling evidence provided by the use of multiple numerical models.

Both the regional-scale and site-scale numerical models are implemented using the FRAC3DVS-OPG computational model; the model, as developed, does not include the capability for modelling a separate immiscible gas phase that does not have infinite mobility. The results using the model, in which only flow of a fully saturated water phase is simulated, will yield conservative estimates of solute transport in the Ordovician. The inclusion of a separate gas phase would reduce water phase flow from that of the saturated case by a reduction of the saturation dependent water mobility. Diffusion would also be reduced as a result of the decrease in the water phase moisture content (product of porosity and water saturation) with the presence of a gas phase.

The regional-scale conceptual model is described in Section 2.6. The hydrologic parameters of the numerical model are developed in Section 4.1 using the computational model equations developed in Chapter 3 and the parameters estimated or measured in the site characterization program (refer to Section 2.5). The description of the solution methodology adopted for the analysis of regional-scale density-dependent flow is provided in Section 4.2.

4.1 Hydrogeologic Parameters

The hydrogeologic parameters defined in this section are applied to the regional-scale and site-scale numerical models. The parameters are based on the DGR borehole investigation rather than the data from previous studies presented in Section 2.4. The rationale for this selection is the improved testing equipment, protocols and quality assurance programs used in the DGR field investigation as compared to the field programs from the 1980s and 1990s. The three-dimensional geologic framework (AECOM and ITASCA CANADA 2011, ITASCA CANADA and AECOM 2011) defines a lithology which aggregates various layers identified at the site-scale. The relationship between the site-scale lithology and the lithology applied to the numerical models is shown in Table 4.1.

In the case of the Niagaran Group (includes the Guelph, Goat Island, Gasport, and Lions Head formations), and other model formations, their parameters are calculated using parameter appropriate averaging of the site formation parameters. The following sections detail the hydrogeological parameters developed from the site specific parameters (refer to Section 2.5.5 and their use in the regional-scale and site-scale numerical models.

Table 4.1: Formations from the 3DGF Define Both the Regional and Site-Scale Model Formations. Model Parameters are Based on Formations at the DGR Site and Elsewhere

Period	Model Formation (3DGF)	Formation
Quaternary	Drift	Drift
Devonian	Kettle Point	Kettle Point
	Hamilton Group	Hamilton Group
	Dundee	Dundee
	Detroit River Group	Lucas Amherstburg (top 20 m) Amherstburg (lower 25 m)
	Bois Blanc	Bois Blanc
Silurian	Bass Islands	Bass Islands (upper 20m) Bass Islands (lower 25 m)
	Unit G	Salina G
	Unit F	Salina F
	Unit F Salt	Salina F
	Unit E	Salina E
	Unit D	Salina D
	Units B and C	Salina C Salina B
	Unit B Anhydrite	Salina B evaporite
	Unit A-2 Carbonate	Salina A2 carbonate
	Unit A-2 Evaporite	Salina A2 evaporite
	Unit A-1 Carbonate	Salina A1 upper carbonate Salina A1 carbonate
	Unit A-1 Evaporite	Salina A1 evaporite Salina A0
	Niagaran Group	Guelph Goat Island Gasport Lions Head
	Reynales / Fossil Hill	Fossil Hill
	Cabot Head	Cabot Head
	Manitoulin	Manitoulin
Ordovician	Queenston	Queenston
	Georgian Bay / Blue Mtn.	Georgian Bay Blue Mountain Collingwood
	Cobourg	Cobourg
	Sherman Fall	Sherman Fall
	Kirkfield	Kirkfield
	Coboconk	Coboconk
	Gull River	Gull River
	Shadow Lake	Shadow Lake
Cambrian	Cambrian	Cambrian
Precambrian	Upper Precambrian	Upper Precambrian
	Precambrian	Precambrian

Note: The 3DGF is described in AECOM and ITASCA CANADA (2011) and ITASCA CANADA and AECOM (2011).

4.1.1 Groundwater Flow Parameters

As developed in Section 3.2, the specific storage S_s and one-dimensional loading efficiency ζ are calculated based on the Young's Modulus E (refer to Table 2.12), Poisson's Ratio ν (refer to Table 2.13), the mineral grain modulus K_s for the rock formations, the coefficient of vertical compressibility β' for the drift, porosity θ (refer to Table 2.10, and the fluid density ρ. The fluid density is determined from the TDS concentration and is further detailed in Section 4.1.4. The pore compressibility β_p, which is used in the TOUGH2-MP simulations, is calculated as per Section 3.2.

All groundwater flow parameters for site formations are summarized in Table 4.2. The porosity, density, and specific storage parameters for grouped layers in Table 4.3 are calculated using a weighted average based on the site formation values in Table 4.2, along with the grouping defined in Table 4.1 and the formation thicknesses in Table 2.14. Also shown in Table 4.2 and Table 4.3 are the one-dimensional loading efficiency ζ values for each formation. A fluid bulk modulus of 3.3 GPa was calculated using a formation thickness and porosity weighted TDS of 234 g/L (~202 g/kg) from the Salina G Unit inclusive to the Cambrian Formation, a temperature of 25 °C, and a pressure of 7 MPa based on the brine equations of state in Batzle and Wang (1992). The one-dimensional loading efficiency ζ needs to be considered in a volumetric context as defined in Equation (3.7). The term $\frac{S_s \zeta}{\rho g} \frac{\partial \sigma_{zz}}{\partial t}$ represents a flux and was used to calculate the average one-dimensional loading efficiency weighted by the formation thickness.

4.1.1.1 Biot Coefficient of 0.5

A Biot coefficient α = 1.0 results from assuming incompressible grains where $K_s \rightarrow \infty$. To investigate the effects of compressible grains, a Biot coefficient of 0.5 is assumed for all layers based on the approach in ITASCA (2011), resulting in $K_s = 2K$, where K is the bulk modulus. The resulting changes to specific storage, loading efficiency, and pore compressibility are shown in Table 4.4 and Table 4.5.

4.1.1.2 Partial Gas Saturation

A partial gas saturation is noted in some layers as per INTERA (2011), and is presented in Table 2.16. The fluid compressibility is the saturation weighted average of the brine compressibility of 3.0×10^{-10} Pa^{-1} and an average air compressibility of 8.0×10^{-8} Pa^{-1} corresponding to an insitu average gas phase pressure of 12.5 MPa, based on TOUGH2-MP modelling. The resulting changes to specific storage, loading efficiency, and pore compressibility are shown in Table 4.6 and Table 4.7.

4.1.1.3 Shallow Weathered Zone

The OGSR borehole data define a thin drift at the surface; in many logs it is less than a metre thick. No shallow weathered zone is identified for the most shallow rock horizons. Where the units of the Silurian and Ordovician outcrop, their low permeability would occur at the surface of the regional-scale domain. To simulate the impact that a weathered zone will have on shallow flow, grid blocks whose tops were within 20 m of the surface of the spatial domain were assigned as drift; the horizontal hydraulic conductivity for the zone was assumed to be 1.0×10^{-8} m/s. The anisotropy ratios of Table 2.9 were assumed to be applicable. The impact of this assumed layer and groundwater recharge were investigated as part of the sensitivity analyses of the hydrogeologic modelling study.

Table 4.2: Summary of Formation Parameters at the DGR Site and Elsewhere

Period	Formation	K_H [m/s]	K_V [m/s]	K_H:K_V	θ	ρ [kg/m^3]	TDS [g/L]	E [GPa]	ν	K_s [GPa]	β' [Pa^{-1}]	S_s [m^{-1}]	ζ	C_{pp} [Pa^{-1}]	τ
Quaternary	Drift	1.0×10^{-8}	5.0×10^{-9}	2:1	0.200	1,000	0.0	—	—	—	1.0×10^{-8}	9.9×10^{-5}	0.99	5.0×10^{-8}	4.0×10^{-1}
Devonian	Kettle Point	3.0×10^{-9}	3.0×10^{-10}	10:1	0.100	1,006	9.0	7.7	0.18	∞	—	1.5×10^{-6}	0.80	1.2×10^{-9}	1.2×10^{-1}
	Hamilton Group	2.2×10^{-11}	2.2×10^{-12}	10:1	0.100	1,008	12.0	7.7	0.18	∞	—	1.5×10^{-6}	0.80	1.2×10^{-9}	1.2×10^{-1}
	Dundee	8.4×10^{-8}	8.4×10^{-9}	10:1	0.100	1,005	8.0	7.7	0.18	∞	—	1.5×10^{-6}	0.80	1.2×10^{-9}	1.2×10^{-1}
	Lucas	1.0×10^{-6}	1.0×10^{-7}	10:1	0.077	1,000	0.5	7.7	0.18	∞	—	1.4×10^{-6}	0.84	1.6×10^{-9}	9.4×10^{-2}
	Amherstburg (top 20 m)	1.0×10^{-6}	1.0×10^{-7}	10:1	0.077	1,001	1.0	7.7	0.18	∞	—	1.4×10^{-6}	0.84	1.6×10^{-9}	9.4×10^{-2}
	Amherstburg (lower 25 m)	1.0×10^{-7}	1.0×10^{-8}	10:1	0.077	1,001	2.0	7.7	0.18	∞	—	1.4×10^{-6}	0.84	1.6×10^{-9}	9.4×10^{-2}
	Bois Blanc	1.0×10^{-7}	1.0×10^{-8}	10:1	0.077	1,002	3.2	7.7	0.18	∞	—	1.4×10^{-6}	0.84	1.6×10^{-9}	9.4×10^{-2}
Silurian	Bass Islands (upper 20m)	1.0×10^{-4}	1.0×10^{-5}	10:1	0.056	1,004	6.0	4.0	0.30	∞	—	2.0×10^{-6}	0.92	3.3×10^{-9}	2.8×10^{-1}
	Bass Islands (lower 25 m)	1.0×10^{-5}	1.0×10^{-6}	10:1	0.056	1,004	6.0	4.0	0.30	∞	—	2.0×10^{-6}	0.92	3.3×10^{-9}	2.8×10^{-1}
	Salina G	1.0×10^{-11}	1.0×10^{-12}	10:1	0.172	1,010	14.8	13.9	0.22	∞	—	1.1×10^{-6}	0.55	3.7×10^{-10}	3.0×10^{-3}
	Salina F	5.0×10^{-14}	5.0×10^{-15}	10:1	0.100	1,040	59.6	13.9	0.22	∞	—	9.5×10^{-7}	0.68	6.3×10^{-10}	4.9×10^{-2}
	Salina E	2.0×10^{-13}	2.0×10^{-14}	10:1	0.100	1,083	124.0	22.6	0.32	∞	—	6.5×10^{-7}	0.51	3.1×10^{-10}	5.7×10^{-2}
	Salina D	2.0×10^{-13}	2.0×10^{-14}	10:1	0.089	1,133	200.0	22.6	0.32	∞	—	6.4×10^{-7}	0.53	3.5×10^{-10}	6.4×10^{-2}
	Salina C	4.0×10^{-13}	4.0×10^{-14}	10:1	0.205	1,166	249.0	22.6	0.32	∞	—	1.1×10^{-6}	0.33	1.5×10^{-10}	6.5×10^{-2}
	Salina B	4.0×10^{-13}	4.0×10^{-14}	10:1	0.145	1,214	321.0	22.6	0.32	∞	—	8.9×10^{-7}	0.41	2.1×10^{-10}	1.0×10^{-1}
	Salina B evaporite	3.0×10^{-13}	3.0×10^{-14}	10:1	0.089	1,214	321.0	22.6	0.32	∞	—	6.9×10^{-7}	0.53	3.5×10^{-10}	1.0×10^{-3}
	Salina A2 carbonate	3.0×10^{-10}	3.0×10^{-11}	10:1	0.120	1,091	136.0	22.6	0.32	∞	—	7.2×10^{-7}	0.46	2.6×10^{-10}	1.2×10^{-2}
	Salina A2 evaporite	3.0×10^{-13}	3.0×10^{-14}	10:1	0.089	1,030	45.6	22.6	0.32	∞	—	5.8×10^{-7}	0.53	3.5×10^{-10}	1.0×10^{-3}
	Salina A1 Upper carbonate	2.0×10^{-7}	2.0×10^{-7}	1:1	0.070	1,019	28.6	22.6	0.32	∞	—	5.2×10^{-7}	0.59	4.4×10^{-10}	8.4×10^{-2}
	Salina A1 carbonate	9.0×10^{-12}	9.0×10^{-13}	10:1	0.019	1,128	192.0	22.6	0.32	∞	—	4.1×10^{-7}	0.84	1.6×10^{-9}	1.1×10^{-2}
	Salina A1 evaporite	3.0×10^{-13}	3.0×10^{-14}	10:1	0.007	1,217	325.0	22.6	0.32	∞	—	3.9×10^{-7}	0.94	4.4×10^{-9}	5.2×10^{-3}
	Salina A0	3.0×10^{-13}	3.0×10^{-14}	10:1	0.032	1,240	360.0	22.6	0.32	∞	—	4.9×10^{-7}	0.76	9.7×10^{-10}	1.1×10^{-3}
	Guelph	3.0×10^{-8}	3.0×10^{-8}	1:1	0.057	1,247	370.0	37.0	0.37	∞	—	4.0×10^{-7}	0.47	2.7×10^{-10}	6.8×10^{-2}
	Goat Island	2.0×10^{-12}	2.0×10^{-13}	10:1	0.020	1,200	300.0	37.0	0.37	∞	—	2.5×10^{-7}	0.72	7.6×10^{-10}	9.0×10^{-3}
	Gasport	2.0×10^{-12}	2.0×10^{-13}	10:1	0.020	1,200	300.0	37.0	0.37	∞	—	2.5×10^{-7}	0.72	7.6×10^{-10}	9.0×10^{-3}
	Lions Head	5.0×10^{-12}	5.0×10^{-13}	10:1	0.031	1,200	300.0	37.0	0.37	∞	—	2.9×10^{-7}	0.62	4.9×10^{-10}	2.4×10^{-1}
	Fossil Hill	5.0×10^{-12}	5.0×10^{-13}	10:1	0.031	1,200	300.0	37.0	0.37	∞	—	2.9×10^{-7}	0.62	4.9×10^{-10}	6.2×10^{-1}
	Cabot Head	9.0×10^{-14}	9.0×10^{-15}	10:1	0.116	1,204	306.0	13.8	0.30	∞	—	1.1×10^{-6}	0.60	4.6×10^{-10}	3.2×10^{-2}
	Manitoulin	9.0×10^{-14}	9.0×10^{-15}	10:1	0.028	1,233	350.0	13.8	0.30	∞	—	7.5×10^{-7}	0.86	1.9×10^{-9}	6.4×10^{-3}
Ordovician	Queenston	2.0×10^{-14}	2.0×10^{-15}	10:1	0.073	1,207	310.0	13.8	0.30	∞	—	9.0×10^{-7}	0.71	7.4×10^{-10}	1.6×10^{-2}
	Georgian Bay	3.0×10^{-14}	3.0×10^{-15}	10:1	0.071	1,205	308.0	13.8	0.30	∞	—	8.9×10^{-7}	0.71	7.6×10^{-10}	7.3×10^{-3}
	Blue Mountain	5.0×10^{-14}	5.0×10^{-15}	10:1	0.078	1,197	295.0	5.2	0.30	∞	—	2.0×10^{-6}	0.86	1.8×10^{-9}	1.3×10^{-2}
	Collingwood	2.0×10^{-14}	2.0×10^{-15}	10:1	0.012	1,150	225.0	31.5	0.25	∞	—	3.4×10^{-7}	0.88	2.2×10^{-9}	4.9×10^{-2}
	Cobourg	2.0×10^{-14}	2.0×10^{-15}	10:1	0.015	1,181	272.0	37.1	0.33	∞	—	2.6×10^{-7}	0.80	1.2×10^{-9}	3.0×10^{-2}
	Sherman Fall	1.0×10^{-14}	1.0×10^{-15}	10:1	0.016	1,180	270.0	23.9	0.21	∞	—	4.9×10^{-7}	0.88	2.3×10^{-9}	1.7×10^{-2}
	Kirkfield	8.0×10^{-15}	8.0×10^{-16}	10:1	0.021	1,156	234.0	23.9	0.21	∞	—	4.9×10^{-7}	0.85	1.8×10^{-9}	2.4×10^{-2}
	Coboconk	4.0×10^{-12}	4.0×10^{-15}	1,000:1	0.009	1,170	255.0	23.9	0.21	∞	—	4.6×10^{-7}	0.93	4.1×10^{-9}	3.6×10^{-2}
	Gull River	7.0×10^{-13}	7.0×10^{-16}	1,000:1	0.022	1,135	203.0	23.9	0.21	∞	—	4.9×10^{-7}	0.85	1.7×10^{-9}	1.4×10^{-2}
	Shadow Lake	1.0×10^{-9}	1.0×10^{-12}	1,000:1	0.097	1,133	200.0	23.9	0.21	∞	—	7.4×10^{-7}	0.56	3.8×10^{-10}	7.6×10^{-2}
Cambrian	Cambrian	3.0×10^{-6}	3.0×10^{-6}	1:1	0.071	1,157	235.0	76.6	0.25	∞	—	3.7×10^{-7}	0.34	1.5×10^{-10}	1.3×10^{-1}
Precambrian	Upper Precambrian	1.0×10^{-10}	1.0×10^{-10}	1:1	0.038	1,200	300.0	76.6	0.25	∞	—	2.6×10^{-7}	0.49	2.9×10^{-10}	9.5×10^{-3}
	Precambrian	1.0×10^{-12}	1.0×10^{-12}	1:1	0.005	1,200	300.0	76.6	0.25	∞	—	1.5×10^{-7}	0.88	2.2×10^{-9}	7.2×10^{-2}

Table 4.3: Summary of Formation Parameters for Regional and Site-Scale Numerical Models

Period	Formation	K_H [m/s]	K_V [m/s]	K_H:K_V	θ	ρ [kg/m^3]	TDS [g/L]	S_s [m^{-1}]	ζ	τ
Quaternary	Drift	1.0×10^{-8}	5.0×10^{-9}	2:1	0.200	1,000	0.0	9.9×10^{-5}	0.99	4.0×10^{-1}
Devonian	Kettle Point	3.0×10^{-9}	3.0×10^{-10}	10:1	0.100	1,006	9.0	1.5×10^{-6}	0.80	1.2×10^{-1}
	Hamilton Group	2.2×10^{-11}	2.2×10^{-12}	10:1	0.100	1,008	12.0	1.5×10^{-6}	0.80	1.2×10^{-1}
	Dundee	8.4×10^{-8}	8.4×10^{-9}	10:1	0.100	1,005	8.0	1.5×10^{-6}	0.80	1.2×10^{-1}
	Detroit River Group	5.9×10^{-7}	2.0×10^{-8}	30:1	0.077	1,001	1.4	1.4×10^{-6}	0.84	9.4×10^{-2}
	Bois Blanc	1.0×10^{-7}	1.0×10^{-8}	10:1	0.077	1,002	3.2	1.4×10^{-6}	0.84	9.4×10^{-2}
Silurian	Bass Islands	5.0×10^{-5}	1.7×10^{-6}	30:1	0.056	1,004	6.0	2.0×10^{-6}	0.92	2.8×10^{-1}
	Unit G	1.0×10^{-11}	1.0×10^{-12}	10:1	0.172	1,010	14.8	1.1×10^{-6}	0.55	3.0×10^{-3}
	Unit F	5.0×10^{-14}	5.0×10^{-15}	10:1	0.100	1,040	59.6	9.5×10^{-7}	0.68	4.9×10^{-2}
	Unit F Salt	5.0×10^{-14}	5.0×10^{-15}	10:1	0.100	1,040	59.6	9.5×10^{-7}	0.68	4.9×10^{-2}
	Unit E	2.0×10^{-13}	2.0×10^{-14}	10:1	0.100	1,083	124.0	6.5×10^{-7}	0.51	5.7×10^{-2}
	Unit D	2.0×10^{-13}	2.0×10^{-14}	10:1	0.089	1,133	200.0	6.4×10^{-7}	0.53	6.4×10^{-2}
	Units B and C	4.0×10^{-13}	4.0×10^{-14}	10:1	0.165	1,198	296.7	9.5×10^{-7}	0.38	8.4×10^{-2}
	Unit B Anhydrite	3.0×10^{-13}	3.0×10^{-14}	10:1	0.089	1,214	321.0	6.9×10^{-7}	0.53	1.0×10^{-3}
	Unit A-2 Carbonate	3.0×10^{-10}	3.0×10^{-11}	10:1	0.120	1,091	136.0	7.2×10^{-7}	0.46	1.2×10^{-2}
	Unit A-2 Evaporite	3.0×10^{-13}	3.0×10^{-14}	10:1	0.089	1,030	45.6	5.8×10^{-7}	0.53	1.0×10^{-3}
	Unit A-1 Carbonate	1.4×10^{-8}	9.7×10^{-13}	14,912:1	0.023	1,120	180.2	4.1×10^{-7}	0.82	1.2×10^{-2}
	Unit A-1 Evaporite	3.0×10^{-13}	3.0×10^{-14}	10:1	0.020	1,229	343.7	4.5×10^{-7}	0.83	1.8×10^{-3}
	Niagaran Group	3.6×10^{-9}	2.5×10^{-13}	14,431:1	0.026	1,206	308.4	2.7×10^{-7}	0.66	1.2×10^{-2}
	Reynales / Fossil Hill	5.0×10^{-12}	5.0×10^{-13}	10:1	0.031	1,200	300.0	2.9×10^{-7}	0.62	6.2×10^{-1}
	Cabot Head	9.0×10^{-14}	9.0×10^{-15}	10:1	0.116	1,204	306.0	1.1×10^{-6}	0.60	3.2×10^{-2}
	Manitoulin	9.0×10^{-14}	9.0×10^{-15}	10:1	0.028	1,233	350.0	7.5×10^{-7}	0.86	6.4×10^{-3}
Ordovician	Queenston	2.0×10^{-14}	2.0×10^{-15}	10:1	0.073	1,207	310.0	9.0×10^{-7}	0.71	1.6×10^{-2}
	Georgian Bay / Blue Mtn.	3.5×10^{-14}	3.3×10^{-15}	11:1	0.070	1,200	299.4	1.2×10^{-6}	0.79	8.8×10^{-3}
	Cobourg	2.0×10^{-14}	2.0×10^{-15}	10:1	0.015	1,181	272.0	2.6×10^{-7}	0.80	3.0×10^{-2}
	Sherman Fall	1.0×10^{-14}	1.0×10^{-15}	10:1	0.016	1,180	270.0	4.9×10^{-7}	0.88	1.7×10^{-2}
	Kirkfield	8.0×10^{-15}	8.0×10^{-16}	10:1	0.021	1,156	234.0	4.9×10^{-7}	0.85	2.4×10^{-2}
	Coboconk	4.0×10^{-12}	4.0×10^{-15}	1,000:1	0.009	1,170	255.0	4.6×10^{-7}	0.93	3.6×10^{-2}
	Gull River	7.0×10^{-13}	7.0×10^{-16}	1,000:1	0.022	1,135	203.0	4.9×10^{-7}	0.85	1.4×10^{-2}
	Shadow Lake	1.0×10^{-9}	1.0×10^{-12}	1,000:1	0.097	1,133	200.0	7.4×10^{-7}	0.56	7.6×10^{-2}
Cambrian	Cambrian	3.0×10^{-6}	3.0×10^{-6}	1:1	0.071	1,157	235.0	3.7×10^{-7}	0.34	1.3×10^{-1}
Precambrian	Upper Precambrian	1.0×10^{-10}	1.0×10^{-10}	1:1	0.038	1,200	300.0	2.6×10^{-7}	0.49	9.5×10^{-3}
	Precambrian	1.0×10^{-12}	1.0×10^{-12}	1:1	0.005	1,200	300.0	1.5×10^{-7}	0.88	7.2×10^{-2}

Table 4.4: Summary of Formation Parameters at the DGR Site and Elsewhere for a Biot Coefficient of 0.5

Period	Formation	K_H [m/s]	K_V [m/s]	K_H:K_V	θ	ρ [kg/m^3]	TDS [g/L]	E [GPa]	ν	K_s [GPa]	β' [Pa^{-1}]	S_s [m^{-1}]	ζ	C_{pp} [Pa^{-1}]	τ
Quaternary	Drift	1.0×10^{-8}	5.0×10^{-9}	2:1	0.200	1,000	0.0	—	—	—	1.0×10^{-8}	9.9×10^{-5}	0.99	5.0×10^{-8}	4.0×10^{-1}
Devonian	Kettle Point	3.0×10^{-9}	3.0×10^{-10}	10:1	0.100	1,006	9.0	7.7	0.18	8.0	—	1.1×10^{-6}	0.54	8.0×10^{-10}	1.2×10^{-1}
	Hamilton Group	2.2×10^{-11}	2.2×10^{-12}	10:1	0.100	1,008	12.0	7.7	0.18	8.0	—	1.1×10^{-6}	0.54	8.0×10^{-10}	1.2×10^{-1}
	Dundee	8.4×10^{-8}	8.4×10^{-9}	10:1	0.100	1,005	8.0	7.7	0.18	8.0	—	1.1×10^{-6}	0.54	8.0×10^{-10}	1.2×10^{-1}
	Lucas	1.0×10^{-6}	1.0×10^{-7}	10:1	0.077	1,000	0.5	7.7	0.18	8.0	—	1.0×10^{-6}	0.56	1.1×10^{-9}	9.4×10^{-2}
	Amherstburg (top 20 m)	1.0×10^{-6}	1.0×10^{-7}	10:1	0.077	1,001	1.0	7.7	0.18	8.0	—	1.0×10^{-6}	0.56	1.1×10^{-9}	9.4×10^{-2}
	Amherstburg (lower 25 m)	1.0×10^{-7}	1.0×10^{-8}	10:1	0.077	1,001	2.0	7.7	0.18	8.0	—	1.0×10^{-6}	0.56	1.1×10^{-9}	9.4×10^{-2}
	Bois Blanc	1.0×10^{-7}	1.0×10^{-8}	10:1	0.077	1,002	3.2	7.7	0.18	8.0	—	1.0×10^{-6}	0.56	1.1×10^{-9}	9.4×10^{-2}
Silurian	Bass Islands (upper 20m)	1.0×10^{-4}	1.0×10^{-5}	10:1	0.056	1,004	6.0	4.0	0.30	6.7	—	1.3×10^{-6}	0.71	2.0×10^{-9}	2.8×10^{-1}
	Bass Islands (lower 25 m)	1.0×10^{-5}	1.0×10^{-6}	10:1	0.056	1,004	6.0	4.0	0.30	6.7	—	1.3×10^{-6}	0.71	2.0×10^{-9}	2.8×10^{-1}
	Salina G	1.0×10^{-11}	1.0×10^{-12}	10:1	0.172	1,010	14.8	13.9	0.22	16.5	—	8.7×10^{-7}	0.36	2.1×10^{-10}	3.0×10^{-3}
	Salina F	5.0×10^{-14}	5.0×10^{-15}	10:1	0.100	1,040	59.6	13.9	0.22	16.5	—	7.2×10^{-7}	0.45	4.0×10^{-10}	4.9×10^{-2}
	Salina E	2.0×10^{-13}	2.0×10^{-14}	10:1	0.100	1,083	124.0	22.6	0.32	41.9	—	5.1×10^{-7}	0.32	1.7×10^{-10}	5.7×10^{-2}
	Salina D	2.0×10^{-13}	2.0×10^{-14}	10:1	0.089	1,133	200.0	22.6	0.32	41.9	—	4.9×10^{-7}	0.35	2.0×10^{-10}	6.4×10^{-2}
	Salina C	4.0×10^{-13}	4.0×10^{-14}	10:1	0.205	1,166	249.0	22.6	0.32	41.9	—	8.8×10^{-7}	0.20	7.2×10^{-11}	6.5×10^{-2}
	Salina B	4.0×10^{-13}	4.0×10^{-14}	10:1	0.145	1,214	321.0	22.6	0.32	41.9	—	7.2×10^{-7}	0.26	1.1×10^{-10}	1.0×10^{-1}
	Salina B evaporite	3.0×10^{-13}	3.0×10^{-14}	10:1	0.089	1,214	321.0	22.6	0.32	41.9	—	5.3×10^{-7}	0.35	2.0×10^{-10}	1.0×10^{-3}
	Salina A2 carbonate	3.0×10^{-10}	3.0×10^{-11}	10:1	0.120	1,091	136.0	22.6	0.32	41.9	—	5.7×10^{-7}	0.29	1.4×10^{-10}	1.2×10^{-2}
	Salina A2 evaporite	3.0×10^{-13}	3.0×10^{-14}	10:1	0.089	1,030	45.6	22.6	0.32	41.9	—	4.5×10^{-7}	0.35	2.0×10^{-10}	1.0×10^{-3}
	Salina A1 Upper carbonate	2.0×10^{-7}	2.0×10^{-7}	1:1	0.070	1,019	28.6	22.6	0.32	41.9	—	3.9×10^{-7}	0.39	2.6×10^{-10}	8.4×10^{-2}
	Salina A1 carbonate	9.0×10^{-12}	9.0×10^{-13}	10:1	0.019	1,128	192.0	22.6	0.32	41.9	—	2.8×10^{-7}	0.62	1.0×10^{-9}	1.1×10^{-2}
	Salina A1 evaporite	3.0×10^{-13}	3.0×10^{-14}	10:1	0.007	1,217	325.0	22.6	0.32	41.9	—	2.6×10^{-7}	0.71	2.8×10^{-9}	5.2×10^{-3}
	Salina A0	3.0×10^{-13}	3.0×10^{-14}	10:1	0.032	1,240	360.0	22.6	0.32	41.9	—	3.5×10^{-7}	0.54	5.9×10^{-10}	1.1×10^{-3}
	Guelph	3.0×10^{-8}	3.0×10^{-8}	1:1	0.057	1,247	370.0	37.0	0.37	94.9	—	3.1×10^{-7}	0.30	1.5×10^{-10}	6.8×10^{-2}
	Goat Island	2.0×10^{-12}	2.0×10^{-13}	10:1	0.020	1,200	300.0	37.0	0.37	94.9	—	1.8×10^{-7}	0.51	4.4×10^{-10}	9.0×10^{-3}
	Gasport	2.0×10^{-12}	2.0×10^{-13}	10:1	0.020	1,200	300.0	37.0	0.37	94.9	—	1.8×10^{-7}	0.51	4.4×10^{-10}	9.0×10^{-3}
	Lions Head	5.0×10^{-12}	5.0×10^{-13}	10:1	0.031	1,200	300.0	37.0	0.37	94.9	—	2.1×10^{-7}	0.42	2.8×10^{-10}	2.4×10^{-1}
	Fossil Hill	5.0×10^{-12}	5.0×10^{-13}	10:1	0.031	1,200	300.0	37.0	0.37	94.9	—	2.1×10^{-7}	0.42	2.8×10^{-10}	6.2×10^{-1}
	Cabot Head	9.0×10^{-14}	9.0×10^{-15}	10:1	0.116	1,204	306.0	13.8	0.30	23.0	—	7.7×10^{-7}	0.41	2.6×10^{-10}	3.2×10^{-2}
	Manitoulin	9.0×10^{-14}	9.0×10^{-15}	10:1	0.028	1,233	350.0	13.8	0.30	23.0	—	5.1×10^{-7}	0.63	1.2×10^{-9}	6.4×10^{-3}
Ordovician	Queenston	2.0×10^{-14}	2.0×10^{-15}	10:1	0.073	1,207	310.0	13.8	0.30	23.0	—	6.4×10^{-7}	0.50	4.4×10^{-10}	1.6×10^{-2}
	Georgian Bay	3.0×10^{-14}	3.0×10^{-15}	10:1	0.071	1,205	308.0	13.8	0.30	23.0	—	6.3×10^{-7}	0.50	4.5×10^{-10}	7.3×10^{-3}
	Blue Mountain	5.0×10^{-14}	5.0×10^{-15}	10:1	0.078	1,197	295.0	5.2	0.30	8.7	—	1.3×10^{-6}	0.66	1.1×10^{-9}	1.3×10^{-2}
	Collingwood	2.0×10^{-14}	2.0×10^{-15}	10:1	0.012	1,150	225.0	31.5	0.25	42.0	—	2.5×10^{-7}	0.60	1.5×10^{-9}	4.9×10^{-2}
	Cobourg	2.0×10^{-14}	2.0×10^{-15}	10:1	0.015	1,181	272.0	37.1	0.33	72.7	—	1.8×10^{-7}	0.58	7.5×10^{-10}	3.0×10^{-2}
	Sherman Fall	1.0×10^{-14}	1.0×10^{-15}	10:1	0.016	1,180	270.0	23.9	0.21	27.5	—	3.7×10^{-7}	0.59	1.7×10^{-9}	1.7×10^{-2}
	Kirkfield	8.0×10^{-15}	8.0×10^{-16}	10:1	0.021	1,156	234.0	23.9	0.21	27.5	—	3.8×10^{-7}	0.56	1.3×10^{-9}	2.4×10^{-2}
	Coboconk	4.0×10^{-12}	4.0×10^{-15}	1,000:1	0.009	1,170	255.0	23.9	0.21	27.5	—	3.4×10^{-7}	0.62	3.0×10^{-9}	3.6×10^{-2}
	Gull River	7.0×10^{-13}	7.0×10^{-16}	1,000:1	0.022	1,135	203.0	23.9	0.21	27.5	—	3.7×10^{-7}	0.56	1.2×10^{-9}	1.4×10^{-2}
	Shadow Lake	1.0×10^{-9}	1.0×10^{-12}	1,000:1	0.097	1,133	200.0	23.9	0.21	27.5	—	5.9×10^{-7}	0.35	2.5×10^{-10}	7.6×10^{-2}
Cambrian	Cambrian	3.0×10^{-6}	3.0×10^{-6}	1:1	0.071	1,157	235.0	76.6	0.25	102.1	—	3.2×10^{-7}	0.19	9.7×10^{-11}	1.3×10^{-1}
Precambrian	Upper Precambrian	1.0×10^{-10}	1.0×10^{-10}	1:1	0.038	1,200	300.0	76.6	0.25	102.1	—	2.2×10^{-7}	0.29	1.9×10^{-10}	9.5×10^{-3}
	Precambrian	1.0×10^{-12}	1.0×10^{-12}	1:1	0.005	1,200	300.0	76.6	0.25	102.1	—	1.1×10^{-7}	0.60	1.5×10^{-9}	7.2×10^{-2}

Table 4.5: Summary of Formation Parameters for Regional and Site-Scale Numerical Models for a Biot Coefficient of 0.5

Period	Formation	K_H [m/s]	K_V [m/s]	K_H:K_V	θ	ρ [kg/m^3]	TDS [g/L]	S_s [m^{-1}]	ζ	τ
Quaternary	Drift	1.0×10^{-8}	5.0×10^{-9}	2:1	0.200	1,000	0.0	9.9×10^{-5}	0.99	4.0×10^{-1}
Devonian	Kettle Point	3.0×10^{-9}	3.0×10^{-10}	10:1	0.100	1,006	9.0	1.1×10^{-6}	0.54	1.2×10^{-1}
	Hamilton Group	2.2×10^{-11}	2.2×10^{-12}	10:1	0.100	1,008	12.0	1.1×10^{-6}	0.54	1.2×10^{-1}
	Dundee	8.4×10^{-8}	8.4×10^{-9}	10:1	0.100	1,005	8.0	1.1×10^{-6}	0.54	1.2×10^{-1}
	Detroit River Group	5.9×10^{-7}	2.0×10^{-8}	30:1	0.077	1,001	1.4	1.0×10^{-6}	0.56	9.4×10^{-2}
	Bois Blanc	1.0×10^{-7}	1.0×10^{-8}	10:1	0.077	1,002	3.2	1.0×10^{-6}	0.56	9.4×10^{-2}
Silurian	Bass Islands	5.0×10^{-5}	1.7×10^{-6}	30:1	0.056	1,004	6.0	1.3×10^{-6}	0.71	2.8×10^{-1}
	Unit G	1.0×10^{-11}	1.0×10^{-12}	10:1	0.172	1,010	14.8	8.7×10^{-7}	0.36	3.0×10^{-3}
	Unit F	5.0×10^{-14}	5.0×10^{-15}	10:1	0.100	1,040	59.6	7.2×10^{-7}	0.45	4.9×10^{-2}
	Unit F Salt	5.0×10^{-14}	5.0×10^{-15}	10:1	0.100	1,040	59.6	7.2×10^{-7}	0.45	4.9×10^{-2}
	Unit E	2.0×10^{-13}	2.0×10^{-14}	10:1	0.100	1,083	124.0	5.1×10^{-7}	0.32	5.7×10^{-2}
	Unit D	2.0×10^{-13}	2.0×10^{-14}	10:1	0.089	1,133	200.0	4.9×10^{-7}	0.35	6.4×10^{-2}
	Units B and C	4.0×10^{-13}	4.0×10^{-14}	10:1	0.165	1,198	296.7	7.7×10^{-7}	0.24	8.4×10^{-2}
	Unit B Anhydrite	3.0×10^{-13}	3.0×10^{-14}	10:1	0.089	1,214	321.0	5.3×10^{-7}	0.35	1.0×10^{-3}
	Unit A-2 Carbonate	3.0×10^{-10}	3.0×10^{-11}	10:1	0.120	1,091	136.0	5.7×10^{-7}	0.29	1.2×10^{-2}
	Unit A-2 Evaporite	3.0×10^{-13}	3.0×10^{-14}	10:1	0.089	1,030	45.6	4.5×10^{-7}	0.35	1.0×10^{-3}
	Unit A-1 Carbonate	1.4×10^{-8}	9.7×10^{-13}	14,912:1	0.023	1,120	180.2	2.8×10^{-7}	0.60	1.2×10^{-2}
	Unit A-1 Evaporite	3.0×10^{-13}	3.0×10^{-14}	10:1	0.020	1,229	343.7	3.1×10^{-7}	0.61	1.8×10^{-3}
	Niagaran Group	3.6×10^{-9}	2.5×10^{-13}	14,431:1	0.026	1,206	308.4	2.0×10^{-7}	0.46	1.2×10^{-2}
	Reynales / Fossil Hill	5.0×10^{-12}	5.0×10^{-13}	10:1	0.031	1,200	300.0	2.1×10^{-7}	0.42	6.2×10^{-1}
	Cabot Head	9.0×10^{-14}	9.0×10^{-15}	10:1	0.116	1,204	306.0	7.7×10^{-7}	0.41	3.2×10^{-2}
	Manitoulin	9.0×10^{-14}	9.0×10^{-15}	10:1	0.028	1,233	350.0	5.1×10^{-7}	0.63	6.4×10^{-3}
Ordovician	Queenston	2.0×10^{-14}	2.0×10^{-15}	10:1	0.073	1,207	310.0	6.4×10^{-7}	0.50	1.6×10^{-2}
	Georgian Bay / Blue Mtn.	3.5×10^{-14}	3.3×10^{-15}	11:1	0.070	1,200	299.4	8.0×10^{-7}	0.58	8.8×10^{-3}
	Cobourg	2.0×10^{-14}	2.0×10^{-15}	10:1	0.015	1,181	272.0	1.8×10^{-7}	0.58	3.0×10^{-2}
	Sherman Fall	1.0×10^{-14}	1.0×10^{-15}	10:1	0.016	1,180	270.0	3.7×10^{-7}	0.59	1.7×10^{-2}
	Kirkfield	8.0×10^{-15}	8.0×10^{-16}	10:1	0.021	1,156	234.0	3.8×10^{-7}	0.56	2.4×10^{-2}
	Coboconk	4.0×10^{-12}	4.0×10^{-15}	1,000:1	0.009	1,170	255.0	3.4×10^{-7}	0.62	3.6×10^{-2}
	Gull River	7.0×10^{-13}	7.0×10^{-16}	1,000:1	0.022	1,135	203.0	3.7×10^{-7}	0.56	1.4×10^{-2}
	Shadow Lake	1.0×10^{-9}	1.0×10^{-12}	1,000:1	0.097	1,133	200.0	5.9×10^{-7}	0.35	7.6×10^{-2}
Cambrian	Cambrian	3.0×10^{-6}	3.0×10^{-6}	1:1	0.071	1,157	235.0	3.2×10^{-7}	0.19	1.3×10^{-1}
Precambrian	Upper Precambrian	1.0×10^{-10}	1.0×10^{-10}	1:1	0.038	1,200	300.0	2.2×10^{-7}	0.29	9.5×10^{-3}
	Precambrian	1.0×10^{-12}	1.0×10^{-12}	1:1	0.005	1,200	300.0	1.1×10^{-7}	0.60	7.2×10^{-2}

Table 4.6: Summary of Formation Parameters at the DGR Site and Elsewhere Which Include the Presence of a Gas Phase

Period	Formation	K_H [m/s]	K_V [m/s]	K_H:K_V	θ	ρ [kg/m^3]	TDS [g/L]	E [GPa]	ν	K_s [GPa]	β' [Pa^{-1}]	S_s [m^{-1}]	ζ	C_{pp} [Pa^{-1}]	τ
Quaternary	Drift	1.0×10^{-8}	5.0×10^{-9}	2:1	0.200	1,000	0.0	—	—	—	1.0×10^{-8}	9.9×10^{-5}	0.99	5.0×10^{-8}	4.0×10^{-1}
Devonian	Kettle Point	3.0×10^{-9}	3.0×10^{-10}	10:1	0.100	1,006	9.0	7.7	0.18	∞	—	1.5×10^{-6}	0.80	1.2×10^{-9}	1.2×10^{-1}
	Hamilton Group	2.2×10^{-11}	2.2×10^{-12}	10:1	0.100	1,008	12.0	7.7	0.18	∞	—	1.5×10^{-6}	0.80	1.2×10^{-9}	1.2×10^{-1}
	Dundee	8.4×10^{-8}	8.4×10^{-9}	10:1	0.100	1,005	8.0	7.7	0.18	∞	—	1.5×10^{-6}	0.80	1.2×10^{-9}	1.2×10^{-1}
	Lucas	1.0×10^{-6}	1.0×10^{-7}	10:1	0.077	1,000	0.5	7.7	0.18	∞	—	1.4×10^{-6}	0.84	1.6×10^{-9}	9.4×10^{-2}
	Amherstburg (top 20 m)	1.0×10^{-6}	1.0×10^{-7}	10:1	0.077	1,001	1.0	7.7	0.18	∞	—	1.4×10^{-6}	0.84	1.6×10^{-9}	9.4×10^{-2}
	Amherstburg (lower 25 m)	1.0×10^{-7}	1.0×10^{-8}	10:1	0.077	1,001	2.0	7.7	0.18	∞	—	1.4×10^{-6}	0.84	1.6×10^{-9}	9.4×10^{-2}
	Bois Blanc	1.0×10^{-7}	1.0×10^{-8}	10:1	0.077	1,002	3.2	7.7	0.18	∞	—	1.4×10^{-6}	0.84	1.6×10^{-9}	9.4×10^{-2}
Silurian	Bass Islands (upper 20m)	1.0×10^{-4}	1.0×10^{-5}	10:1	0.056	1,004	6.0	4.0	0.30	∞	—	2.0×10^{-6}	0.92	3.3×10^{-9}	2.8×10^{-1}
	Bass Islands (lower 25 m)	1.0×10^{-5}	1.0×10^{-6}	10:1	0.056	1,004	6.0	4.0	0.30	∞	—	2.0×10^{-6}	0.92	3.3×10^{-9}	2.8×10^{-1}
	Salina G	1.0×10^{-11}	1.0×10^{-12}	10:1	0.172	1,010	14.8	13.9	0.22	∞	—	1.1×10^{-6}	0.55	3.7×10^{-10}	3.0×10^{-3}
	Salina F	5.0×10^{-14}	5.0×10^{-15}	10:1	0.100	1,040	59.6	13.9	0.22	∞	—	1.4×10^{-5}	0.05	6.3×10^{-10}	4.9×10^{-2}
	Salina E	2.0×10^{-13}	2.0×10^{-14}	10:1	0.100	1,083	124.0	22.6	0.32	∞	—	1.9×10^{-5}	0.02	3.1×10^{-10}	5.7×10^{-2}
	Salina D	2.0×10^{-13}	2.0×10^{-14}	10:1	0.089	1,133	200.0	22.6	0.32	∞	—	6.4×10^{-7}	0.53	3.5×10^{-10}	6.4×10^{-2}
	Salina C	4.0×10^{-13}	4.0×10^{-14}	10:1	0.205	1,166	249.0	22.6	0.32	∞	—	3.5×10^{-5}	0.01	1.5×10^{-10}	6.5×10^{-2}
	Salina B	4.0×10^{-13}	4.0×10^{-14}	10:1	0.145	1,214	321.0	22.6	0.32	∞	—	8.9×10^{-7}	0.41	2.1×10^{-10}	1.0×10^{-1}
	Salina B evaporite	3.0×10^{-13}	3.0×10^{-14}	10:1	0.089	1,214	321.0	22.6	0.32	∞	—	6.9×10^{-7}	0.53	3.5×10^{-10}	1.0×10^{-3}
	Salina A2 carbonate	3.0×10^{-10}	3.0×10^{-11}	10:1	0.120	1,091	136.0	22.6	0.32	∞	—	1.0×10^{-6}	0.32	2.6×10^{-10}	1.2×10^{-2}
	Salina A2 evaporite	3.0×10^{-13}	3.0×10^{-14}	10:1	0.089	1,030	45.6	22.6	0.32	∞	—	1.1×10^{-5}	0.03	3.5×10^{-10}	1.0×10^{-3}
	Salina A1 Upper carbonate	2.0×10^{-7}	2.0×10^{-7}	1:1	0.070	1,019	28.6	22.6	0.32	∞	—	5.2×10^{-7}	0.59	4.4×10^{-10}	8.4×10^{-2}
	Salina A1 carbonate	9.0×10^{-12}	9.0×10^{-13}	10:1	0.019	1,128	192.0	22.6	0.32	∞	—	4.1×10^{-7}	0.84	1.6×10^{-9}	1.1×10^{-2}
	Salina A1 evaporite	3.0×10^{-13}	3.0×10^{-14}	10:1	0.007	1,217	325.0	22.6	0.32	∞	—	4.1×10^{-7}	0.89	4.4×10^{-9}	5.2×10^{-3}
	Salina A0	3.0×10^{-13}	3.0×10^{-14}	10:1	0.032	1,240	360.0	22.6	0.32	∞	—	5.6×10^{-6}	0.07	9.7×10^{-10}	1.1×10^{-3}
	Guelph	3.0×10^{-8}	3.0×10^{-8}	1:1	0.057	1,247	370.0	37.0	0.37	∞	—	4.0×10^{-7}	0.47	2.7×10^{-10}	6.8×10^{-2}
	Goat Island	2.0×10^{-12}	2.0×10^{-13}	10:1	0.020	1,200	300.0	37.0	0.37	∞	—	2.5×10^{-7}	0.72	7.6×10^{-10}	9.0×10^{-3}
	Gasport	2.0×10^{-12}	2.0×10^{-13}	10:1	0.020	1,200	300.0	37.0	0.37	∞	—	2.5×10^{-7}	0.72	7.6×10^{-10}	9.0×10^{-3}
	Lions Head	5.0×10^{-12}	5.0×10^{-13}	10:1	0.031	1,200	300.0	37.0	0.37	∞	—	2.9×10^{-7}	0.62	4.9×10^{-10}	2.4×10^{-1}
	Fossil Hill	5.0×10^{-12}	5.0×10^{-13}	10:1	0.031	1,200	300.0	37.0	0.37	∞	—	2.9×10^{-7}	0.62	4.9×10^{-10}	6.2×10^{-1}
	Cabot Head	9.0×10^{-14}	9.0×10^{-15}	10:1	0.116	1,204	306.0	13.8	0.30	∞	—	1.1×10^{-6}	0.60	4.6×10^{-10}	3.2×10^{-2}
	Manitoulin	9.0×10^{-14}	9.0×10^{-15}	10:1	0.028	1,233	350.0	13.8	0.30	∞	—	7.5×10^{-7}	0.86	1.9×10^{-9}	6.4×10^{-3}
Ordovician	Queenston	2.0×10^{-14}	2.0×10^{-15}	10:1	0.073	1,207	310.0	13.8	0.30	∞	—	5.4×10^{-6}	0.12	7.4×10^{-10}	1.6×10^{-2}
	Georgian Bay	3.0×10^{-14}	3.0×10^{-15}	10:1	0.071	1,205	308.0	13.8	0.30	∞	—	6.0×10^{-6}	0.11	7.6×10^{-10}	7.3×10^{-3}
	Blue Mountain	5.0×10^{-14}	5.0×10^{-15}	10:1	0.078	1,197	295.0	5.2	0.30	∞	—	1.2×10^{-5}	0.14	1.8×10^{-9}	1.3×10^{-2}
	Collingwood	2.0×10^{-14}	2.0×10^{-15}	10:1	0.012	1,150	225.0	31.5	0.25	∞	—	2.9×10^{-6}	0.10	2.2×10^{-9}	4.9×10^{-2}
	Cobourg	2.0×10^{-14}	2.0×10^{-15}	10:1	0.015	1,181	272.0	37.1	0.33	∞	—	1.9×10^{-6}	0.11	1.2×10^{-9}	3.0×10^{-2}
	Sherman Fall	1.0×10^{-14}	1.0×10^{-15}	10:1	0.016	1,180	270.0	23.9	0.21	∞	—	2.7×10^{-6}	0.16	2.3×10^{-9}	1.7×10^{-2}
	Kirkfield	8.0×10^{-15}	8.0×10^{-16}	10:1	0.021	1,156	234.0	23.9	0.21	∞	—	4.3×10^{-6}	0.10	1.8×10^{-9}	2.4×10^{-2}
	Coboconk	4.0×10^{-12}	4.0×10^{-15}	1,000:1	0.009	1,170	255.0	23.9	0.21	∞	—	7.6×10^{-7}	0.56	4.1×10^{-9}	3.6×10^{-2}
	Gull River	7.0×10^{-13}	7.0×10^{-16}	1,000:1	0.022	1,135	203.0	23.9	0.21	∞	—	4.6×10^{-6}	0.09	1.7×10^{-9}	1.4×10^{-2}
	Shadow Lake	1.0×10^{-9}	1.0×10^{-12}	1,000:1	0.097	1,133	200.0	23.9	0.21	∞	—	7.4×10^{-7}	0.56	3.8×10^{-10}	7.6×10^{-2}
Cambrian	Cambrian	3.0×10^{-6}	3.0×10^{-6}	1:1	0.071	1,157	235.0	76.6	0.25	∞	—	2.6×10^{-6}	0.05	1.5×10^{-10}	1.3×10^{-1}
Precambrian	Upper Precambrian	1.0×10^{-10}	1.0×10^{-10}	1:1	0.038	1,200	300.0	76.6	0.25	∞	—	2.6×10^{-7}	0.49	2.9×10^{-10}	9.5×10^{-3}
	Precambrian	1.0×10^{-12}	1.0×10^{-12}	1:1	0.005	1,200	300.0	76.6	0.25	∞	—	1.5×10^{-7}	0.88	2.2×10^{-9}	7.2×10^{-2}

Table 4.7: Summary of Formation Parameters for Regional and Site-Scale Numerical Models Which Include the Presence of a Gas Phase

Period	Formation	K_H [m/s]	K_V [m/s]	K_H:K_V	θ	ρ [kg/m^3]	TDS [g/L]	S_s [m^{-1}]	ζ	τ
Quaternary	Drift	1.0×10^{-8}	5.0×10^{-9}	2:1	0.200	1,000	0.0	9.9×10^{-5}	0.99	4.0×10^{-1}
Devonian	Kettle Point	3.0×10^{-9}	3.0×10^{-10}	10:1	0.100	1,006	9.0	1.5×10^{-6}	0.80	1.2×10^{-1}
	Hamilton Group	2.2×10^{-11}	2.2×10^{-12}	10:1	0.100	1,008	12.0	1.5×10^{-6}	0.80	1.2×10^{-1}
	Dundee	8.4×10^{-8}	8.4×10^{-9}	10:1	0.100	1,005	8.0	1.5×10^{-6}	0.80	1.2×10^{-1}
	Detroit River Group	5.9×10^{-7}	2.0×10^{-8}	30:1	0.077	1,001	1.4	1.4×10^{-6}	0.84	9.4×10^{-2}
	Bois Blanc	1.0×10^{-7}	1.0×10^{-8}	10:1	0.077	1,002	3.2	1.4×10^{-6}	0.84	9.4×10^{-2}
Silurian	Bass Islands	5.0×10^{-5}	1.7×10^{-6}	30:1	0.056	1,004	6.0	2.0×10^{-6}	0.92	2.8×10^{-1}
	Unit G	1.0×10^{-11}	1.0×10^{-12}	10:1	0.172	1,010	14.8	1.1×10^{-6}	0.55	3.0×10^{-3}
	Unit F	5.0×10^{-14}	5.0×10^{-15}	10:1	0.100	1,040	59.6	1.4×10^{-5}	0.05	4.9×10^{-2}
	Unit F Salt	5.0×10^{-14}	5.0×10^{-15}	10:1	0.100	1,040	59.6	1.4×10^{-5}	0.05	4.9×10^{-2}
	Unit E	2.0×10^{-13}	2.0×10^{-14}	10:1	0.100	1,083	124.0	1.9×10^{-5}	0.02	5.7×10^{-2}
	Unit D	2.0×10^{-13}	2.0×10^{-14}	10:1	0.089	1,133	200.0	6.4×10^{-7}	0.53	6.4×10^{-2}
	Units B and C	4.0×10^{-13}	4.0×10^{-14}	10:1	0.165	1,198	296.7	1.2×10^{-5}	0.03	8.4×10^{-2}
	Unit B Anhydrite	3.0×10^{-13}	3.0×10^{-14}	10:1	0.089	1,214	321.0	6.9×10^{-7}	0.53	1.0×10^{-3}
	Unit A-2 Carbonate	3.0×10^{-10}	3.0×10^{-11}	10:1	0.120	1,091	136.0	1.0×10^{-6}	0.32	1.2×10^{-2}
	Unit A-2 Evaporite	3.0×10^{-13}	3.0×10^{-14}	10:1	0.089	1,030	45.6	1.1×10^{-5}	0.03	1.0×10^{-3}
	Unit A-1 Carbonate	1.4×10^{-8}	9.7×10^{-13}	14,912:1	0.023	1,120	180.2	4.1×10^{-7}	0.82	1.2×10^{-2}
	Unit A-1 Evaporite	3.0×10^{-13}	3.0×10^{-14}	10:1	0.020	1,229	343.7	3.2×10^{-6}	0.12	1.8×10^{-3}
	Niagaran Group	3.6×10^{-9}	2.5×10^{-13}	14,431:1	0.026	1,206	308.4	2.7×10^{-7}	0.66	1.2×10^{-2}
	Reynales / Fossil Hill	5.0×10^{-12}	5.0×10^{-13}	10:1	0.031	1,200	300.0	2.9×10^{-7}	0.62	6.2×10^{-1}
	Cabot Head	9.0×10^{-14}	9.0×10^{-15}	10:1	0.116	1,204	306.0	1.1×10^{-6}	0.60	3.2×10^{-2}
	Manitoulin	9.0×10^{-14}	9.0×10^{-15}	10:1	0.028	1,233	350.0	7.5×10^{-7}	0.86	6.4×10^{-3}
Ordovician	Queenston	2.0×10^{-14}	2.0×10^{-15}	10:1	0.073	1,207	310.0	5.4×10^{-6}	0.12	1.6×10^{-2}
	Georgian Bay / Blue Mtn.	3.5×10^{-14}	3.3×10^{-15}	11:1	0.070	1,200	299.4	7.7×10^{-6}	0.12	8.8×10^{-3}
	Cobourg	2.0×10^{-14}	2.0×10^{-15}	10:1	0.015	1,181	272.0	1.9×10^{-6}	0.11	3.0×10^{-2}
	Sherman Fall	1.0×10^{-14}	1.0×10^{-15}	10:1	0.016	1,180	270.0	2.7×10^{-6}	0.16	1.7×10^{-2}
	Kirkfield	8.0×10^{-15}	8.0×10^{-16}	10:1	0.021	1,156	234.0	4.3×10^{-6}	0.10	2.4×10^{-2}
	Coboconk	4.0×10^{-12}	4.0×10^{-15}	1,000:1	0.009	1,170	255.0	7.6×10^{-7}	0.56	3.6×10^{-2}
	Gull River	7.0×10^{-13}	7.0×10^{-16}	1,000:1	0.022	1,135	203.0	4.6×10^{-6}	0.09	1.4×10^{-2}
	Shadow Lake	1.0×10^{-9}	1.0×10^{-12}	1,000:1	0.097	1,133	200.0	7.4×10^{-7}	0.56	7.6×10^{-2}
Cambrian	Cambrian	3.0×10^{-6}	3.0×10^{-6}	1:1	0.071	1,157	235.0	2.6×10^{-6}	0.05	1.3×10^{-1}
Precambrian	Upper Precambrian	1.0×10^{-10}	1.0×10^{-10}	1:1	0.038	1,200	300.0	2.6×10^{-7}	0.49	9.5×10^{-3}
	Precambrian	1.0×10^{-12}	1.0×10^{-12}	1:1	0.005	1,200	300.0	1.5×10^{-7}	0.88	7.2×10^{-2}

4.1.1.4 Hydraulic Conductivity of Permafrost

For paleohydrogeologic simulations, the TIN interpolated permafrost depths were used to select any FRAC3DVS-OPG grid block whose top face was within the permafrost zone for each time step. A permafrost hydraulic conductivity of 5×10^{-11} m/s is applied (McCauley et al. 2002). Since most flow during ice-sheet loading and unloading is vertical, then any permafrost within a grid block would limit vertical flow due to the very low hydraulic conductivity. FRAC3DVS-OPG provides an option to linearly interpolate permafrost values to reduce numerical instabilities.

4.1.2 Groundwater Transport Parameters

Table 4.8 summarizes various transport parameters which are used for brine movement for the variably dense pore fluids, for tracer movement to determine the depth of recharge water penetration, and for mean life expectancy calculations. Smaller dispersivity values were attempted in the preliminary modelling phase of this study, however, severe numerical instabilities resulted due to the large grid spacing in proportion to smaller longitudinal dispersivity values. Dispersivities for MLE calculations are double the values listed in Table 4.8. Transport parameters for the site-scale numerical model are shown in Table 4.9.

The tortuosity parameter varies by layer (see Table 4.2) and is calculated from the sodium iodide effective diffusion coefficient D_e (see Table 2.15), the porosity θ (see Table 2.10), the free solution diffusion coefficient for sodium iodide at 1.0 mol/L of 1.662×10^{-9} m^2/s (Weast 1983, p. F-46), and assuming a diffusion accessible porosity factor of 0.5 for sodium iodide (INTERA 2011).

4.1.3 Precambrian Properties

The Precambrian underlies the sedimentary deposits of the Michigan Basin. Due to a paucity of site specific data for the Precambrian, both the hydraulic conductivity and total dissolved solids

Table 4.8: Groundwater Transport Parameters for Regional-Scale Numerical Model Simulations

Parameter	Value	Reference
Brine Diffusion Coefficient (NaCl at 1 mol/L)	1.484×10^{-9} m^2/s	Weast (1983, p. F-46)
Tracer Diffusion Coefficient ($H_2^{18}O$)	2.66×10^{-9} m^2/s	Singh and Kumar (2005, p. 37)
Longitudinal Dispersivity	500 m	—
Horizontal Transverse Dispersivity	50 m	—
Vertical Transverse Dispersivity	5 m	—

Table 4.9: Groundwater Transport Parameters for Site-Scale Numerical Model Simulations

Parameter	Value	Reference
Brine Diffusion Coefficient (NaCl at 1 mol/L)	1.484×10^{-9} m^2/s	Weast (1983, p. F-46)
Tracer Diffusion Coefficient (NaI at 1 mol/L)	1.662×10^{-9} m^2/s	Weast (1983, p. F-46)
Longitudinal Dispersivity	50 m	—
Horizontal Transverse Dispersivity	5 m	—
Vertical Transverse Dispersivity	0.5 m	—

concentrations below the Cambrian or Shadow Lake formations are based on characteristics derived from studies of the Canadian Shield.

4.1.3.1 Precambrian Hydraulic Conductivity

Based on Normani (2009), both the horizontal and vertical permeabilities as a function of depth are expressed as follows:

$$k_H = 10^{-14.5-4.5(1-e^{-0.002469d})} \tag{4.1}$$

$$k_V = \begin{cases} 10k_H, & \text{for } d \leq 300 \text{ m;} \\ [0.09(400-d)+1]k_H, & \text{for } 300 < d \leq 400 \text{ m;} \\ k_H, & \text{for } d > 400 \text{ m.} \end{cases} \tag{4.2}$$

where k_H is the horizontal permeability [L^2]; k_V is the vertical permeability [L^2]; and d is the depth below ground surface [L]. The matrix permeabilities, defined by Equation (4.1) and Equation (4.2) provide a smoother permeability transition from layer to layer, exponentially decreasing with increasing depth from ground surface. The horizontal and vertical permeabilities as a function of depth are plotted in Figure 4.1.

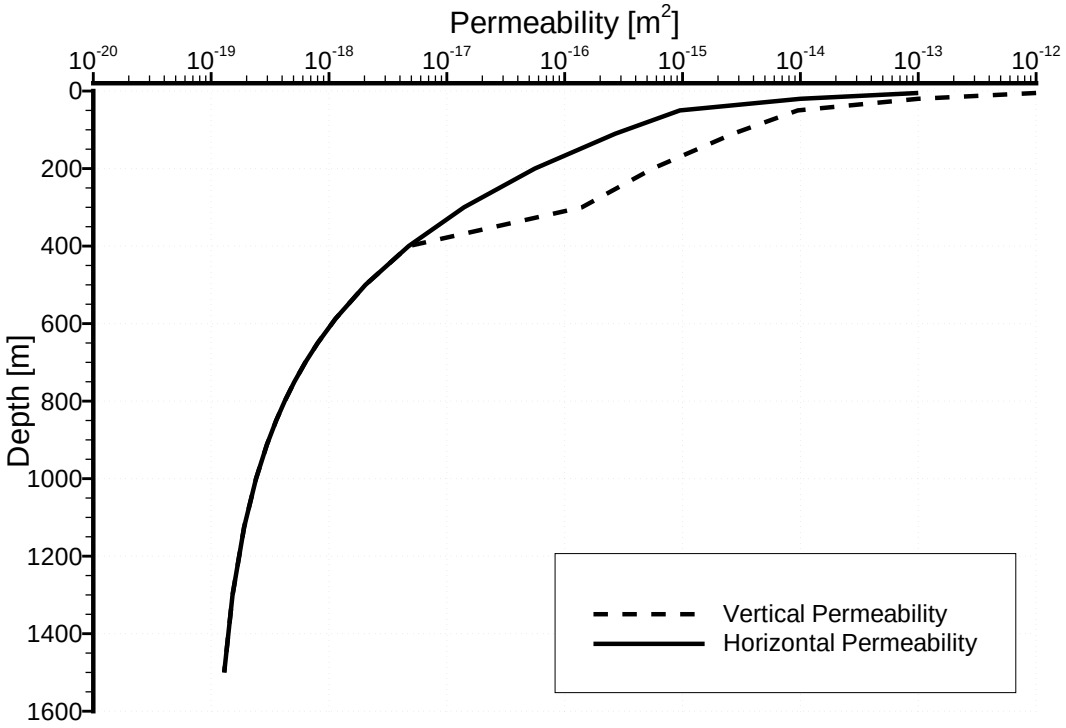

Note: From Normani (2009).

Figure 4.1: Horizontal and Vertical Matrix Permeabilities as a Function of Depth for a Canadian Shield Setting

In both the regional-scale numerical model and the Michigan Basin cross-section numerical model, the hydraulic conductivity of the Precambrian is determined using, in part, Equation (4.1) and Equation (4.2). Since these equations were developed using data from sites where the Canadian Shield is exposed, zero depth is set at an elevation of 176 m. In the case of the Upper Precambrian, if its hydraulic conductivity is greater than that calculated from Equation (4.1) and Equation (4.2), the higher conductivity value is applied.

4.1.3.2 Precambrian Total Dissolved Solids

The salinity of groundwater generally increases with increasing depth in plutonic rock on the Canadian Shield. The highly saline pore fluids can have TDS concentrations up to 300 g/L (Bottomley et al. 2002, Frape and Fritz 1987). Two main theories have been postulated to explain the presence of the high TDS groundwaters in the deeper rock: (1) salinity may have originated from groundwater recharge during episodes of marine intrusion, or (2) the salinity may be a result of rock-water interactions (Bottomley et al. 2002, 2003, Frape and Fritz 1987). The first theory implies that sufficiently permeable fractures or pathways exist in the host rock to allow the migration of saline surface waters to depth, while the second theory implies a relatively impermeable rock mass that provides sufficient time for rock-water interactions to take place at depth (Bottomley et al. 2003, Frape and Fritz 1987). As an example of the former, the Con Mine studies near Yellowknife, of Bottomley et al. (2002, 2003) provide ^{129}I evidence of a marine origin for deep brines. Bottomley et al. (2003) further proposes that the Sudbury/Elliot Lake brines are also of a marine origin, although perhaps by a different mechanism than the Con Mine brines; the Sudbury/Elliot Lake brines could have been formed either by the evaporation or freezing of sea water. Subsequent infiltration of evaporatively concentrated marine brines may have occurred during the episodes of seawater intrusion.

An initial TDS distribution for the Precambrian rock is required for the pseudo steady-state model. A plot of TDS versus depth for groundwaters from the Canadian Shield, based on Figure 2b in Frape and Fritz (1987), is shown in Figure 4.2. The dashed line represents an upper bound for TDS as a function of depth. Equation (4.3) represents the dashed line in Figure 4.2, where *TDS* is in units of g/L.

$$TDS = \begin{cases} 10^{0.001981697d}, & \text{for } d \leq 1{,}250 \text{ m}; \\ 300, & \text{for } d > 1{,}250 \text{ m}. \end{cases} \tag{4.3}$$

When applying Equation (4.3) to both the regional-scale numerical model and the Michigan Basin cross-section numerical model, zero depth is set to an elevation of 176 m, as in the previous section. The TDS values in the Precambrian below the sedimentary rock are set to the higher of either Equation (4.3), or the TDS value of the overlying unit at a given vertical location.

4.1.4 Relationship Between Total Dissolved Solids and Pore Fluid Density

For density-dependent flow, the FRAC3DVS-OPG computational model solves the dependent water conservation of mass equation (see Equation (3.1)) and the solute transport equation (see Equation (3.12)). The state variable for the latter is the total dissolved solids concentration with the coupling between the equations being the fluid density which is defined in terms of the TDS concentration. A relationship between TDS concentration and density was developed for the Michigan Basin by Lampe (2009) using data compiled by Gupta (1993). The relationship is given as

$$\rho = 0.000725 C_{TDS} - 0.999 \tag{4.4}$$

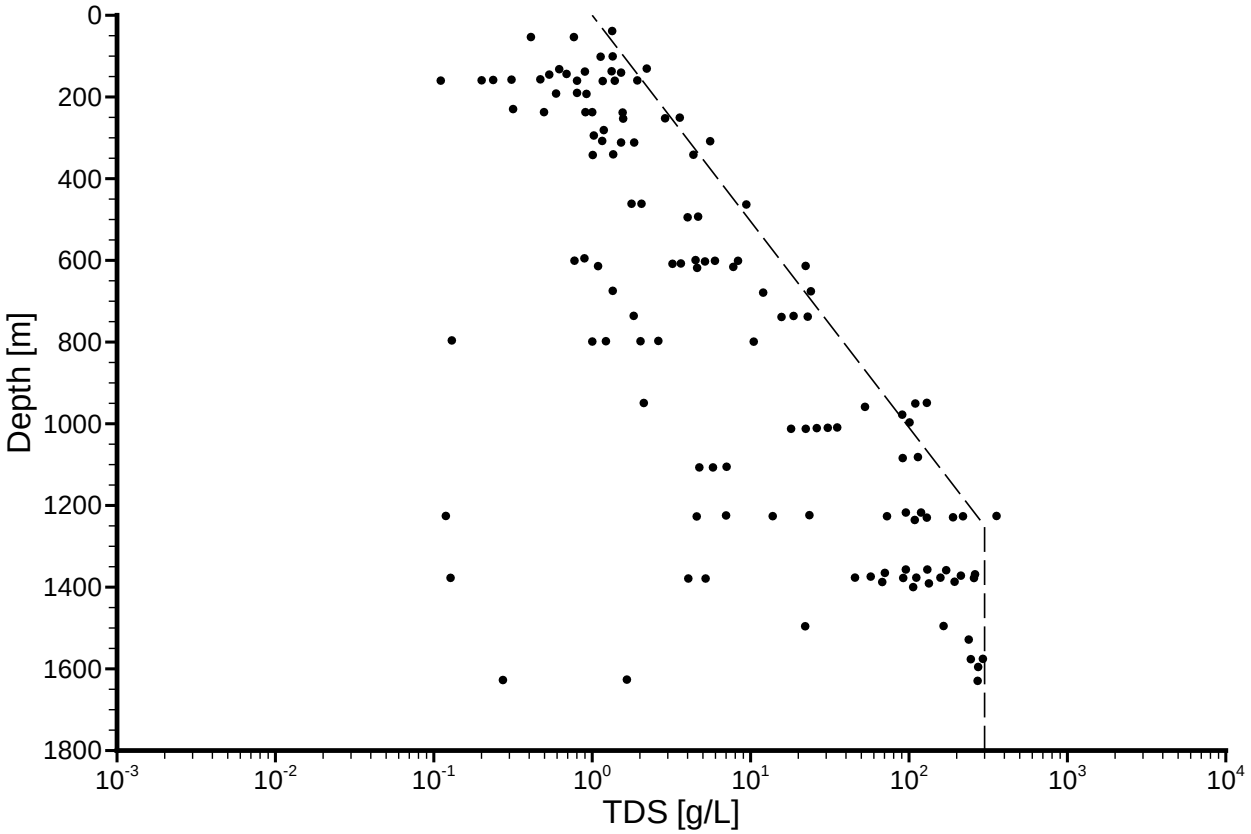

Note: The dashed line represents Equation (4.3). Adapted from Figure 2b in Frape and Fritz (1987).

Figure 4.2: Plot of TDS Versus Depth for Groundwaters from the Canadian Shield

in which C_{TDS} is the TDS concentration in g/L solution and ρ is density expressed as kg/L. The relationship was used by Lampe (2009) to model three-dimensional density-dependent flow in the Michigan Basin. The data and regression equation for the analysis are presented in Figure 4.3.

For the estimation of density from TDS concentrations in porewater samples obtained from the DGR borehole cores and to convert pressures measured in the boreholes to environmental heads, INTERA (2011) used the average groundwater density of the Guelph Formation of 1,234 kg/m^3 and average TDS concentration of 451.8 g/kg of water (equivalent to 384 g/L of solution) for the Guelph Formation to determine the relationship between TDS concentration and density of

$$\rho = 0.000609 C_{TDS} - 1.0 \quad (4.5)$$

For the regional-scale, site-scale and Michigan Basin cross-sectional modelling of this study, a model of TDS concentration versus density must reflect both the DGR site data and the saline waters elsewhere in the Michigan Basin. This study therefore used an average of the models of Gupta (1993) and INTERA (2011), yielding

$$\rho = 0.000667 C_{TDS} - 1.0 \quad (4.6)$$

An important consideration in the use of this relationship is the fact that the TDS concentrations have an uncertainty associated with them. The densities are also uncertain. The three

relationships between TDS concentration and density can be compared in Figure 4.3. In the plot, the lower line is from Lampe (2009) and Gupta (1993), the upper line is used by INTERA (2011) while the middle line is used in this study. The TDS versus density model of Equation (4.6) is used in this study unless otherwise noted.

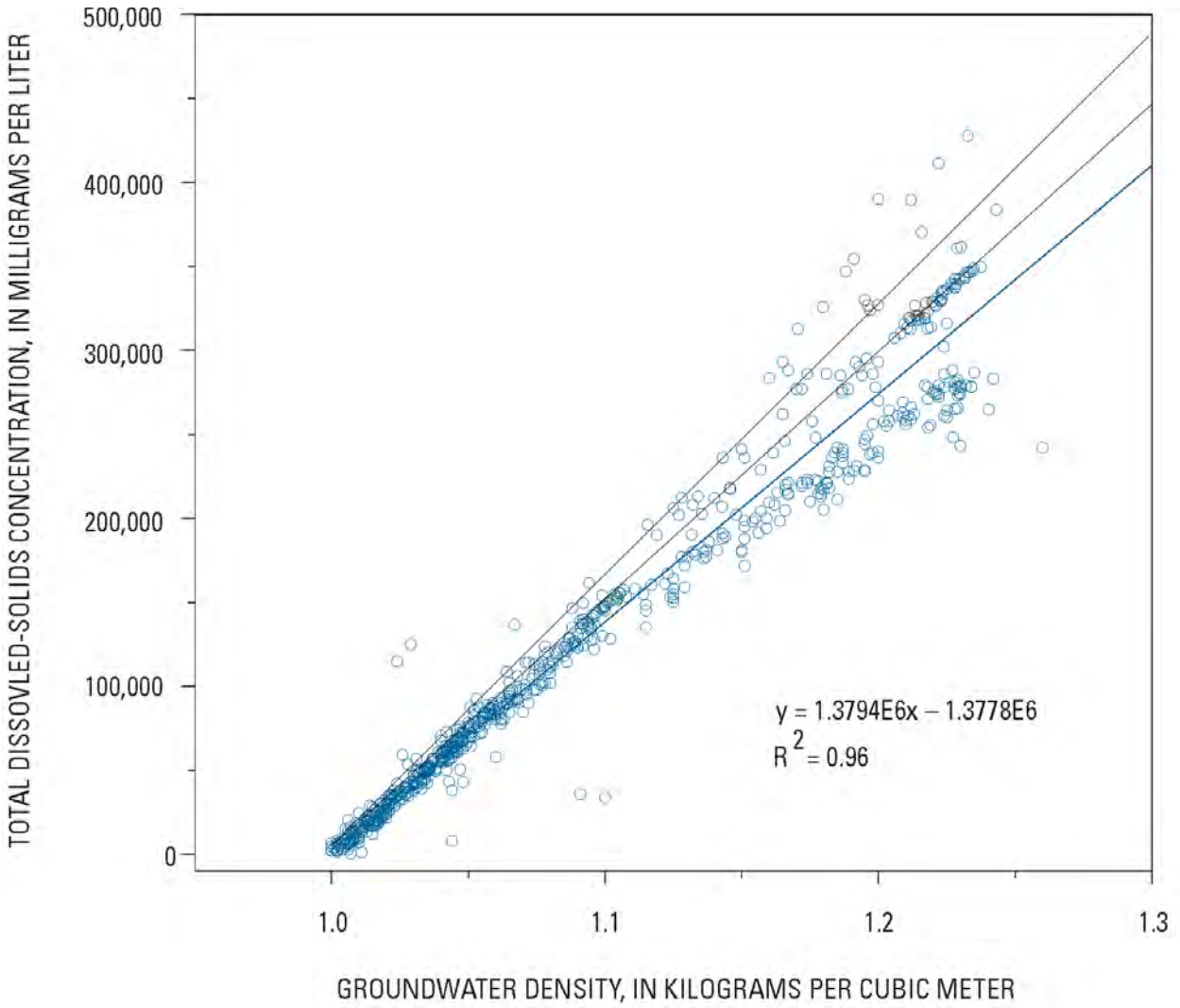

Note: Groundwater density and Total Dissolved Solids concentrations data from Gupta (1993). In the plot, the lower line is from Lampe (2009) using the Gupta (1993) data, the upper line is used by INTERA (2011) while the middle line is used in this study.

Figure 4.3: Plot of Groundwater Density and Total Dissolved Solids Concentrations Data for the Michigan Basin

4.2 Solution of Density-Dependent Flow

Salinity plays an important role with regard to fluid flow at the proposed DGR. As discussed in Section 2.3 and as shown in Figure 4.3, an increase in the concentration of TDS will result in an

increase in the fluid density. The increase in density of the deeper fluids will then act as an inhibiter of active flow at depth (Park et al. 2009). The methodology for developing a solution for regional-scale density-dependent flow is described in the following paragraphs.

In the absence of a source term for salinity, a transient analysis is required to determine an equilibrium solution at a time *t* for density-dependent flow. The analysis requires the specification of an initial distribution throughout the regional-scale spatial domain for both freshwater heads and total dissolved solids concentration. In a transient analysis, the initial prescribed salinity distribution is allowed to equilibrate to a new state that reflects the boundary conditions, hydraulic properties and transport properties of the regional-scale domain. For the coupled density-dependent flow and transport system, fresh water can recharge at the surface, reducing the TDS concentration in the shallow zone. However, the time to flush the dissolved solids from a unit is a function of the permeability of the unit and the energy potential of the displacing fluid as compared to the energy potential of the fluid being displaced. Fluids with lower total dissolved solids, such as recharging water, will have a lower energy potential as compared to higher total dissolved solids water with the same elevation and pressure. Therefore, for low-permeability units with a relatively high total dissolved solids concentration, the time to flush the unit or displace the fluids can be very long (millions of years). Complete flushing may only occur as a result of diffusion because energy gradients and/or low permeabilities may yield low fluid fluxes that may not be sufficient for advective displacement to occur. In using this method to synthesize a spatial salinity distribution, the total mass of dissolved solids and its distribution in the model domain is assumed to be known and will be a maximum initially as there are no sources to generate dissolved solids. With this approach, as time progresses, the dissolved solids will gradually reduce as the groundwater discharges from the system. However, as an alternate model, total dissolved solids can be introduced using a Dirichlet boundary condition at, for example, the bottom of the domain.

The initial condition for total dissolved solids must specify concentrations for all lithologies at all locations in the regional-scale domain. Field data are not available for the spatial distribution of TDS in the shallow low permeability units such as the Queenston shale where it outcrops, or the spatial distribution in the deeper units. The values from Table 4.3 for a given lithology were assigned to all areas of the spatial domain assigned to that zone. For the model zones representing the Precambrian, a depth dependent initial TDS distribution was determined using the data described by the dashed line in Figure 4.2 of Section 4.1.3.2. The depth was relative to a constant reference elevation of 176 m; there is no Precambrian above this elevation in the regional-scale domain. If the concentration from the dashed line in Figure 4.2 at a given depth was lower than that assigned to the lowest sedimentary rock at the location (Shadow Lake or Cambrian sandstone where present), the higher zone TDS concentration was assigned. The rationale for this model is the hypothesis that transport of TDS would have occurred, through long-term diffusion, to the upper crystalline rock from either the overlying higher TDS sediments or the deeper Precambrian rock. The initial TDS distribution developed for this study is shown in block-cut view in Figure 4.4 and in a fence view in Figure 4.5.

For this study, the final freshwater head distribution for the base case analysis was calculated as follows:

i) The distribution of freshwater heads was calculated for regional-scale density-independent steady-state flow. The results for the base-case conceptual model (refer to Chapter 2), parameters (refer to Section 4.1) and boundary conditions (refer to Section 2.6.2) are shown in block-cut view in Figure 4.6 and in fence view in Figure 4.7.

ii) A total dissolved solids concentration distribution was assigned throughout the domain as an initial condition using the procedure described in the preceding paragraph. The density-independent freshwater heads were allowed to equilibrate to the assigned TDS distribution in a transient analysis, while not allowing the TDS distribution to evolve. This step allowed the freshwater heads to reflect the variation of fluid density as specified by the initial TDS distribution. The converged, time invariant results for freshwater heads from this step are shown in block-cut view in Figure 4.8 and in fence view in Figure 4.9.

iii) The TDS distribution was allowed to vary with the freshwater heads in a 1 Ma transient analysis. The results at 1 Ma for freshwater heads are shown in block-cut view in Figure 4.10 and in fence view in Figure 4.11. The final TDS distribution is shown in block-cut view in Figure 4.12 and in fence view in Figure 4.13. The flushing of TDS from the shallow units is revealed with a comparison of these to the figures with the initially assigned distribution shown in Figure 4.4 and Figure 4.5.

The computational burden for the simulation and analysis of density-dependent flow is significant. The computer time is a function of factors including the number of degrees-of-freedom, the length of time steps for the necessary transient analysis, the spatial discretization and the size of grid blocks, and the assigned tolerance level for convergence at a time step. Of these, the length of time steps is most critical. In FRAC3DVS-OPG, the length of a time step is controlled, in part, by the cell Courant number for the grid blocks with higher velocities. Within the regional domain, the shallow Devonian units have significantly higher velocities than the deeper Ordovician units. To control numerical dispersion and potential instability problems in the higher velocity shallow units, small time steps are required. In numerical experiments, it was found that time steps on the order of days were required in order to obtain results with satisfactory convergence.

There is a balance between the accuracy of a solution, the length of time required for the system to reach a pseudo-equilibrium between energy potential, fluid flux and total dissolved solids distributions, and computer simulation time. In this report, a suitable balance was established by assuming that pseudo-equilibrium would be obtained one million years (1 Ma) after the imposed initial conditions. The impact of this assumption and cut-off time were investigated in a sensitivity analysis; the results support the use of a pseudo-equilibrium time of 1 Ma.

After 1 Ma, the model, having been allowed to reach pseudo-equilibrium, produces salinity profiles that are compatible with the geological framework, boundary conditions and hence the flow domain. In the north-eastern part of the model domain, the brine will be flushed because of a combination of the absence of a source term for brine and the effect of meteoric recharge near Georgian Bay where the Ordovician formations outcrop. This is contrasted to the deeper Ordovician shale and limestones units in the western portion of the domain which, because of the absence of a velocity to transport the brine from the system, will maintain a high salinity concentration. The location of the proposed DGR repository is located within this area. At such a location, stagnation of the groundwater is expected due to both the low permeability of the Ordovician units and the effect that density will have on reducing the flow velocity.

4.3 Regional-Scale Base-Case Analysis

The regional-scale conceptual model (refer to Chapter 2) for the base-case analysis describes the present day state of the groundwater system. The geological framework model, hydraulic parameters, transport parameters, pore water concentrations and boundary conditions are all based on observations, analyses and interpretations of this state. The initial conditions of TDS concentration and equivalent freshwater heads assumed for the conceptual model evolve to a

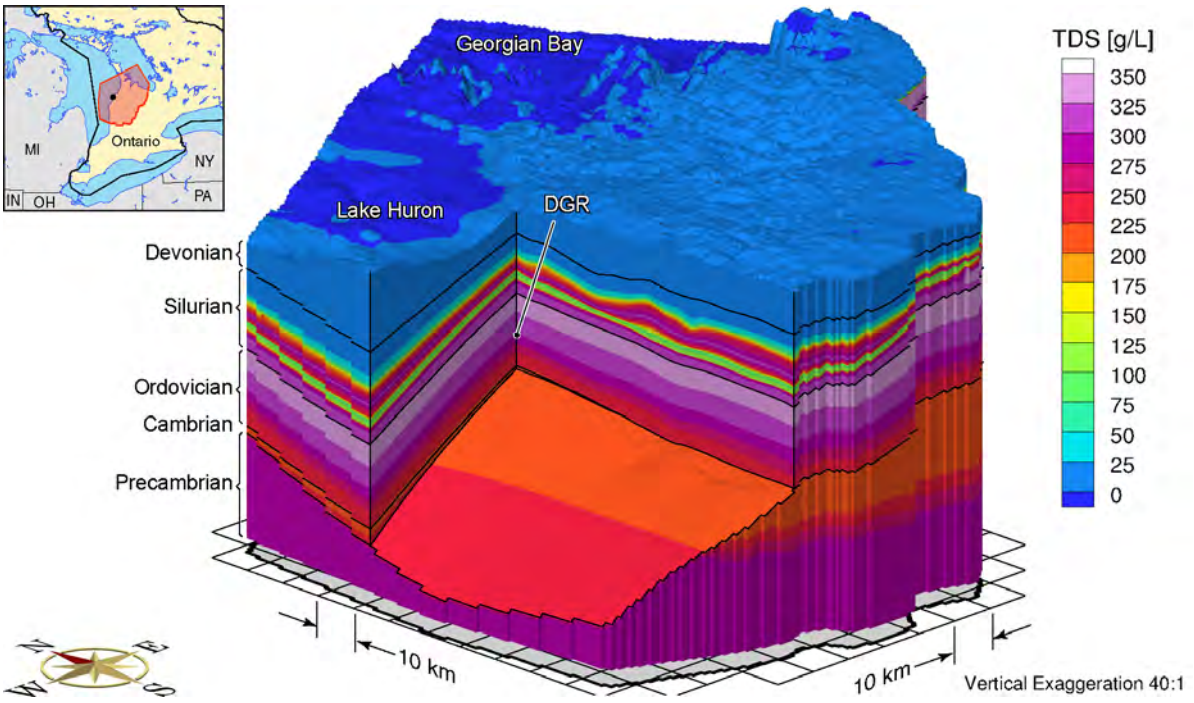

Figure 4.4: Block Cut View of Initial Total Dissolved Solids Concentration Distribution

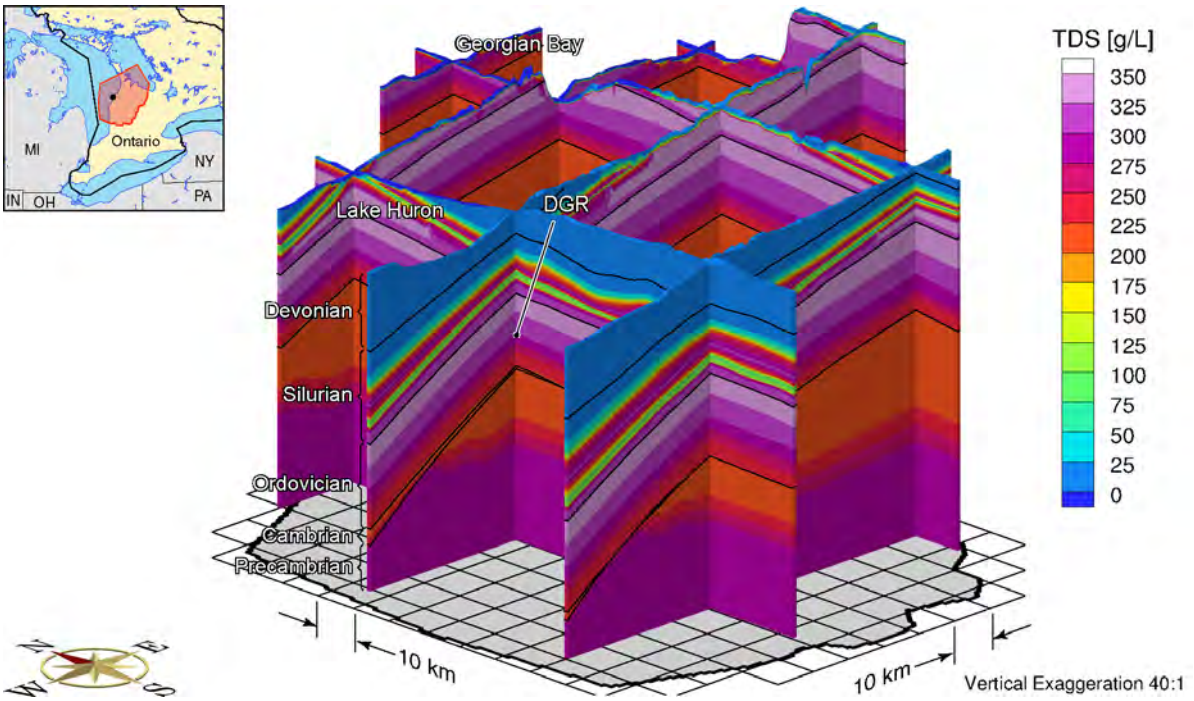

Figure 4.5: Fence View of Initial Total Dissolved Solids Concentration Distribution

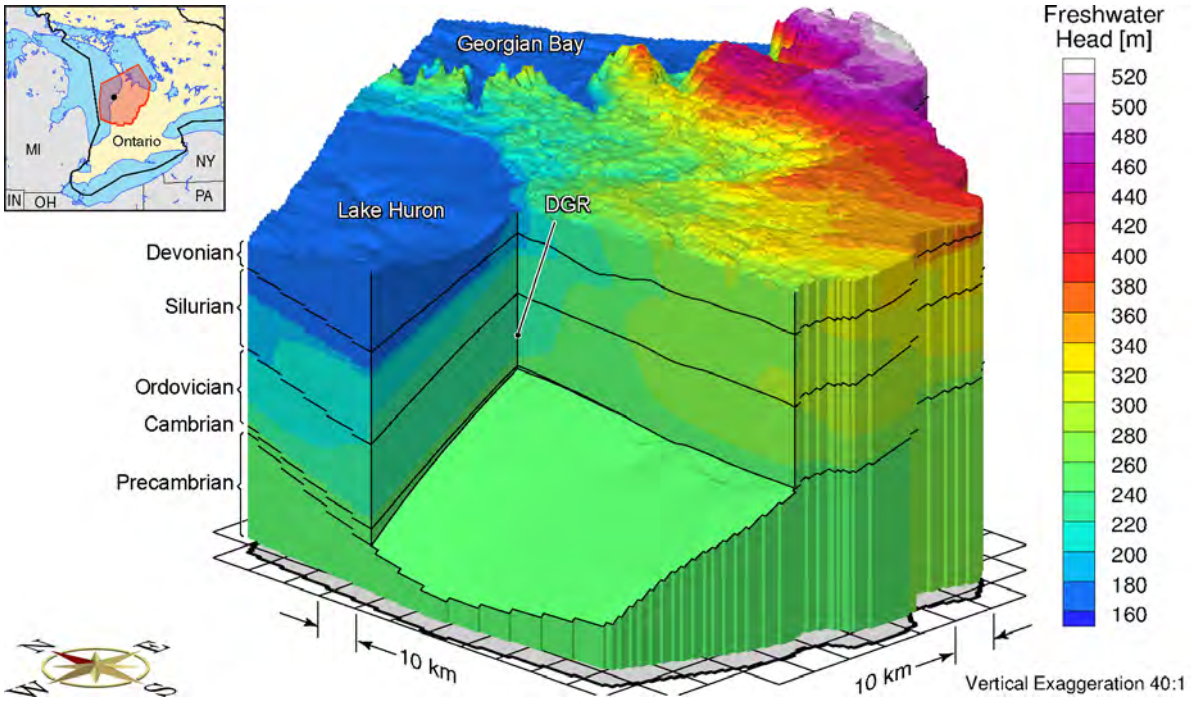

Figure 4.6: Block Cut View of Steady-State Density-Independent Freshwater Heads

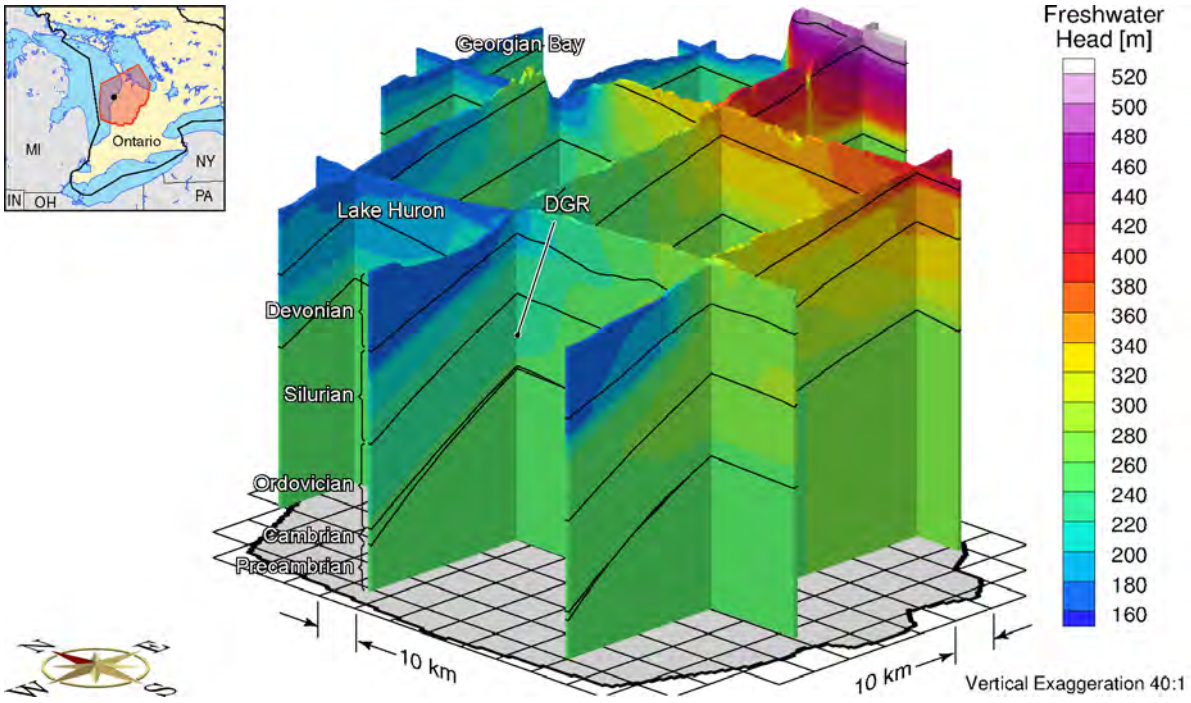

Figure 4.7: Fence Cut View of Steady-State Density-Independent Freshwater Heads

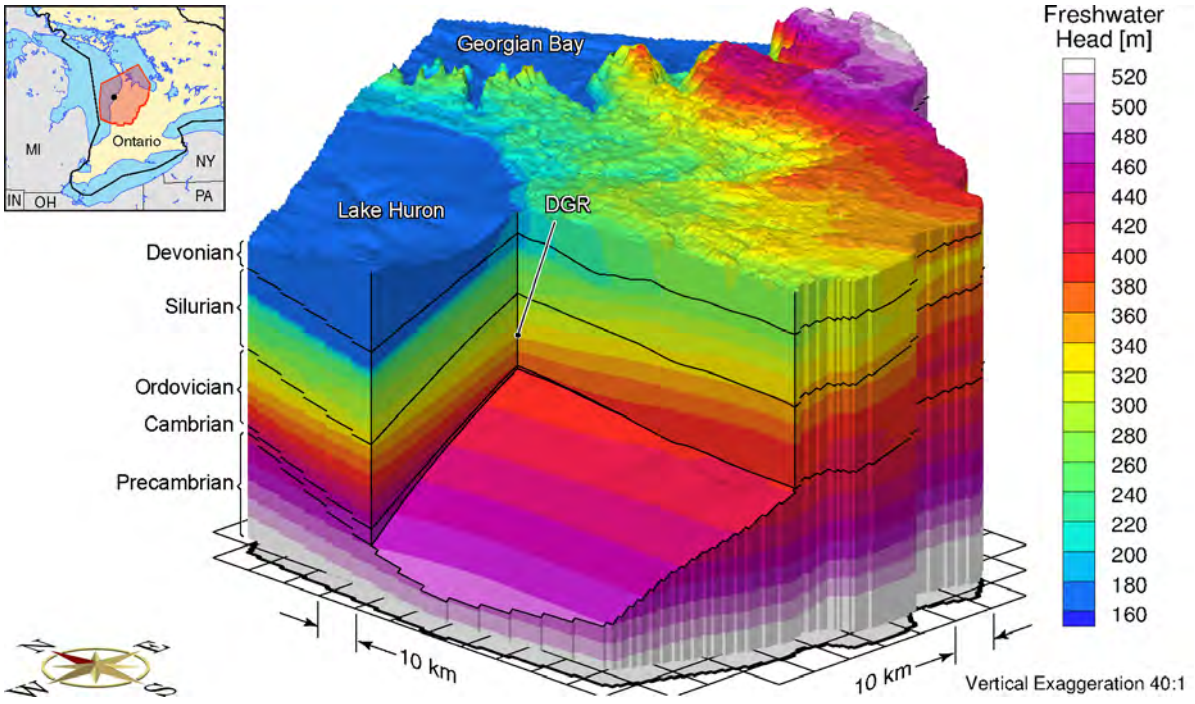

Figure 4.8: Block Cut View of Freshwater Heads That Have Equilibrated to the Static TDS Distribution

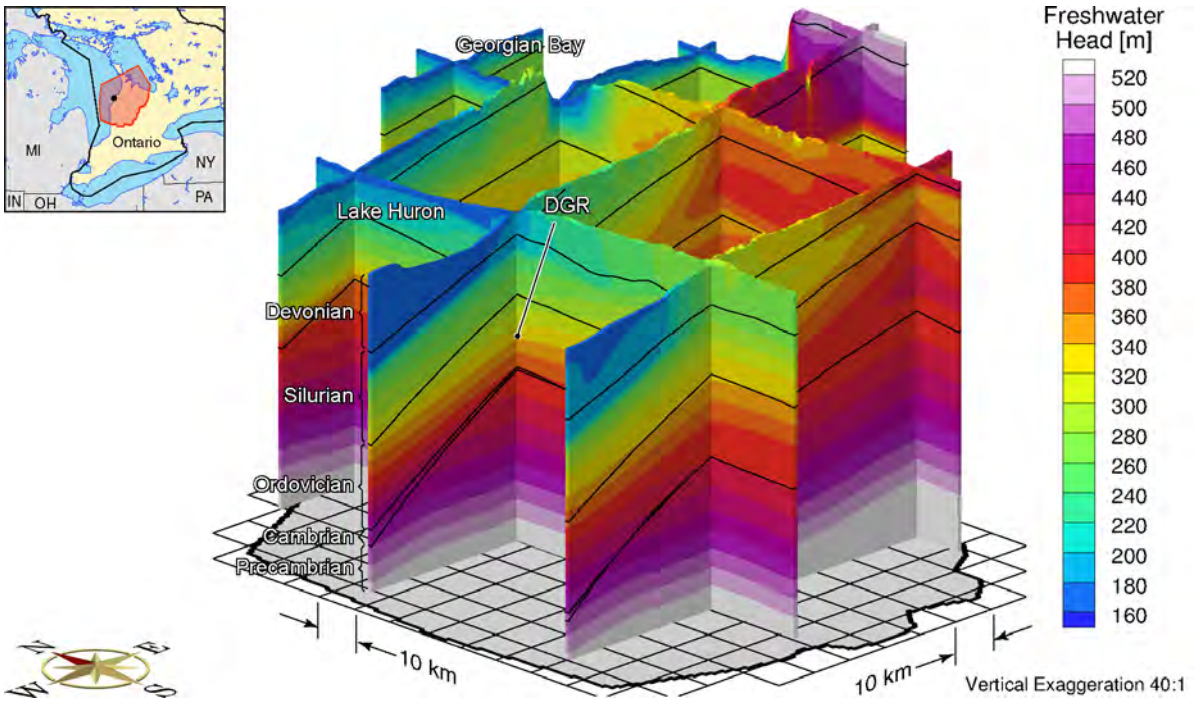

Figure 4.9: Fence View of Freshwater Heads That Have Equilibrated to the Static TDS Distribution

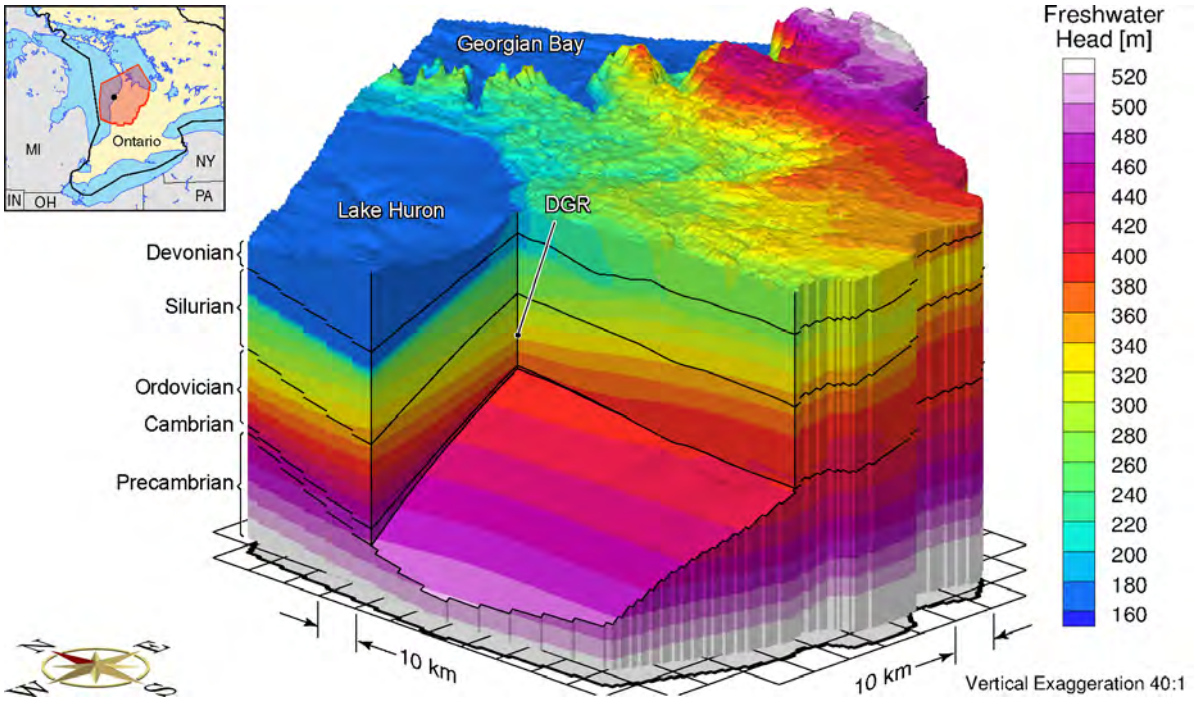

Figure 4.10: Block Cut View of Freshwater Heads That Have Equilibrated at 1 Ma to the Temporally Varying TDS Distribution

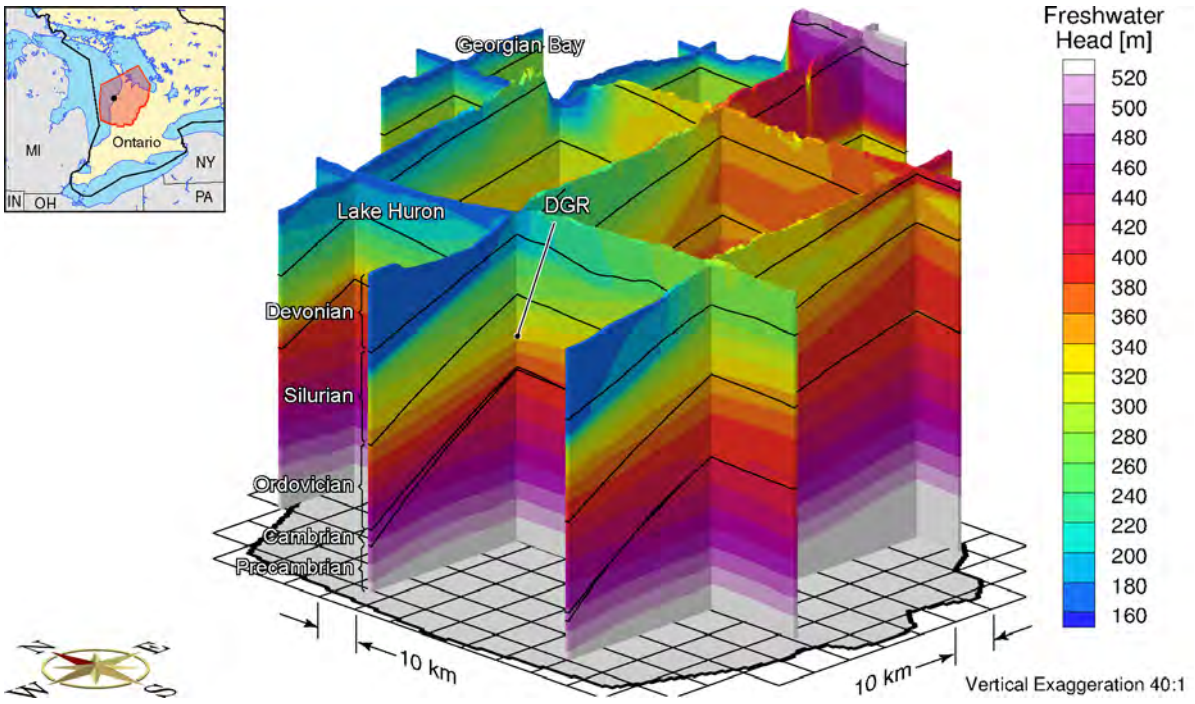

Figure 4.11: Fence View of Freshwater Heads That Have Equilibrated at 1 Ma to the Temporally Varying TDS Distribution

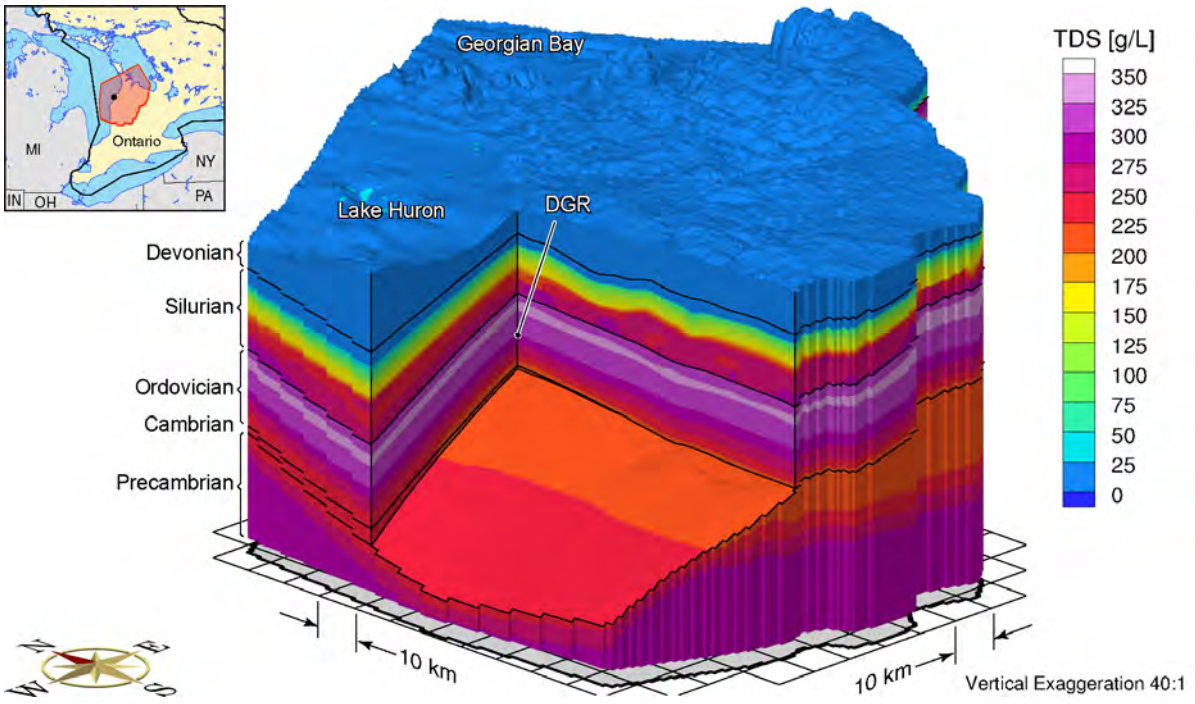

Figure 4.12: Block Cut View of Total Dissolved Solids Concentration Distribution that has Equilibrated at 1 Ma to the Freshwater Heads

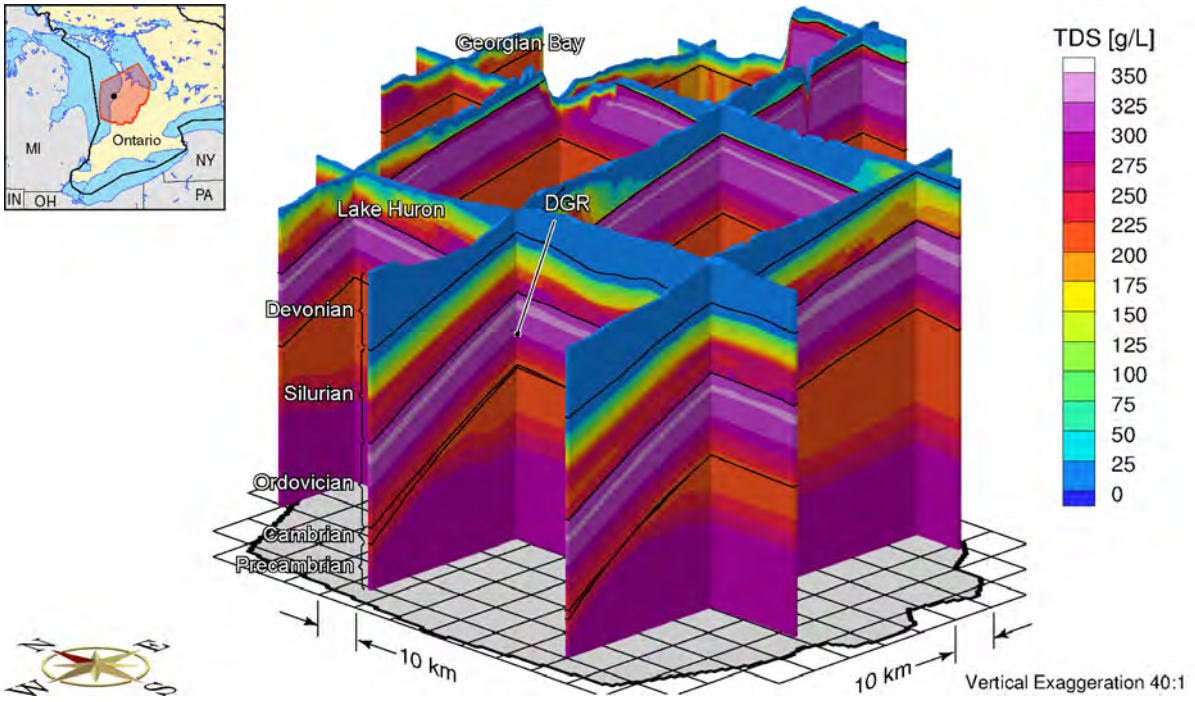

Figure 4.13: Fence View of Total Dissolved Solids Concentration Distribution that has Equilibrated at 1 Ma to the Freshwater Heads

pseudo-equilibrium solution for this state. The objective of the analysis, in part, is to reveal system behaviour and to identify observed attributes that may be the signature of a different state.

Based on a surface water level for Lake Huron of 176 mASL, the observed fluid under-pressures in the Ordovician and Lower Silurian units at the DGR boreholes (refer to Figure 2.15 in Section 2.5.3) is a consequence of a different state than that described by the base-case conceptual model. The pressures may be the result of rock dilation, from either glacial unloading or significant removal of mass through erosion that was at a rate that is greater than that of water influx to these low permeability units from the over and under-lying units with higher pressure; the pressure distribution is still evolving. Alternatively, the low pore fluid pressures may indicate the presence of a trapped non-wetting gas phase or the impact of osmosis or they may be the result of crustal flexure. The analysis of the pressure profile at the DGR boreholes can be approached from two perspectives: an assessment of the cause of the under-pressures of the Ordovician and Lower Silurian and the over-pressures of the Cambrian; and the evolution of the pressures from their current state. The former analysis would require either realizations of the previous state of the regional-scale system or the simulation of immiscible, two-phase flow of gas and water. The analysis of two-phase water and gas flow using the model TOUGH2-MP is developed in Section 6.3 for a one-dimensional column. The assessment of the evolution of the pressures cannot be undertaken at the regional scale due to a lack of data on the pressures at other locations in the domain; however, the analysis can be developed at the site scale (refer to Chapter 4.5).

The equivalent freshwater head distribution for the base-case simulation after 1 Ma (pseudo-equilibrium time) is shown in block-cut form in Figure 4.10 and as a fence diagram in Figure 4.11. The environmental head distribution for the base case parameters and boundary conditions is shown in Figure 4.14 and Figure 4.15. As explained in Section 3.5, plots of equivalent freshwater heads can be used to interpret horizontal flow gradients but not vertical gradients; conversely, the plots of environmental heads can be used to interpret vertical gradients but not horizontal gradients. At the location of the proposed DGR, the model calculated equivalent freshwater head in the Niagaran from the regional-scale base-case analysis is 263.1 m as compared to the August 24, 2009 measured equivalent freshwater head at the DGR-4 borehole that ranges from 210.4 m to 282.3 m for the units of the Niagaran that include the Guelph, Goat Island, Gasport and Lions Head. The model calculated environmental head in the Niagaran from the regional-scale base-case analysis is 238.9 m as compared to the August 24, 2009 estimated environmental head in the DGR-4 borehole that ranges from 186.3 m to 252.7 m. For the Cambrian, the base-case model estimated equivalent freshwater head is 380.6 m as compared to a measured value of 422.1 m while the base-case model environmental head is 268.3 m compared to an estimated value in the DGR-4 borehole of 317.6 m. The data for the Niagaran and Cambrian are included in the summary of the model calculated and DGR-4 estimated or measured values listed in Table 4.13 of Section 4.4.1. A comparison of the data indicates that the base-case regional-scale model under predicts the DGR-4 measured or estimated heads. However, the model does correctly predict the upward gradient that is observed in the DGR-4 borehole between the Cambrian and the Niagaran.

The shallow flow regime is the region above the Salina. It is dominated by flow that mimics topography. Beneath the shallow groundwater zone, the heads are not controlled to the same extent by the local elevation of the surface. The main control for the horizontal component of the density-dependent energy gradient at depth is the elevation difference between Lake Huron and the topographic high at the Niagara Escarpment. The head signature will be transmitted from the outcrop area and will be dissipated, depending on the energy gradient, across the domain (refer

to Figure 4.11). At a given location, the vertical component of the energy gradient is controlled by the difference in the environmental heads between the more permeable units that are separated by low permeability units (refer to Figure 4.15). For the regional domain, the higher permeability Cambrian, where present, and Niagaran Group are separated by the low permeability units of the Ordovician and Lower Silurian. The Niagaran is confined in the south-western part of the domain by the overlying low permeability units of the Salina. Flow in the Niagaran where it is unconfined (refer to Figure 2.28) is controlled by surface topography.

The environmental heads observed in the Cambrian at the DGR-4 borehole (Figure 2.15) are over-pressured but under predicted in the pseudo steady-state analysis with the base-case parameters, initial conditions and boundary conditions. Several causes can be postulated for the elevated Cambrian pressures. They may reflect a pressure distribution from a state of thermal, hydraulic and geomechanical conditions that were significantly different from that simulated by the base-case analysis; this would imply that the pressures are slowly evolving to a distribution that is compatible with the current state and boundary conditions of the groundwater system. The elevated environmental heads also may reflect conditions at the centre of the Michigan Basin where the Cambrian is several kilometres deep with a significant column of higher density saline fluids above; this would require continuity of the Cambrian's permeability from the centre to the margins of the basin. The pressures also may be the result of the presence of a gas phase that provides pressure support for the unit. Clearly, for the high pressures in the relatively thin permeable Cambrian to be sustained over the period of the analysis (1 Ma), both the effective vertical fluid permeability (or mobility) for the overlying Ordovician units must be significantly lower than that used in the base-case simulation, and either the Cambrian must be discontinuous in some manner such that the fluids in it are trapped, or the Cambrian may be connected to deeper portions of the Michigan Basin. The over-pressurization of the Cambrian is further investigated in subsequent analyses presented in this report.

In addition to the elevation component of the gravitational gradient imposed by the topographic high at the Niagara Escarpment, the density of the brine in the deep groundwater zone will have an impact on the energy gradients. The salinity profile for the base-case at a pseudo-equilibrium time of 1 Ma (Figure 4.12) consists of relatively fresh groundwater for the shallow groundwater zone and an area with much higher TDS concentrations for the intermediate and deep groundwater zone (below the Salina where present). The shallow groundwater zone will remain devoid of salinity because the continual inflow of meteoric water through recharge to the zone will dilute any salinity that diffuses upward through the Silurian or Ordovician. The brine concentrations in the low permeability Ordovician units at the Niagara Escarpment, where the Silurian is absent, will also experience some flushing as well; however, the higher density groundwater found in the deeper zone that has a higher energy than water with low total dissolved solids will prevent any significant penetration of freshwater. The TDS transition zone occurs across the Salina; variations in the upward flow through this unit in combination with the high longitudinal dispersivity result in the spatial oscillations in the salinity that is apparent in the figure (note the interface between the 200 g/L and the 100 g/L contours).

The base-case pore water velocity magnitudes are presented in Figure 4.16 and Figure 4.17. The highest velocities occur in the more permeable shallow groundwater zone. The lower velocities beneath Lake Huron and Georgian Bay are the result of the absence of a horizontal gradient. The reduction of the velocities in the Salina Group is clearly evident in the figure as are the higher velocities of the Niagaran in the Silurian (these velocities appear as the orange/red band above the Ordovician-Silurian interface). Above the Niagaran, higher velocities are also evident in the A1-Carbonate of the Silurian. Within the Ordovician in the vicinity of the proposed DGR, the groundwater pore velocities are less than 1×10^{-6} m/a; the pore water velocity

estimated for the Cobourg is 2.29×10^{-7} m/a. The estimated Péclet number (refer to Section 3.6.1) for the Cobourg for the base-case analysis is 2.91×10^{-4}. Based on the estimated low velocities and relative to a diffusion coefficient of 1.484×10^{-9} m^2/s, solute transport in the Ordovician will be diffusion dominated.

The ratio of vertical component of velocity to velocity magnitude for the regional-scale domain is plotted in block cut view in Figure 4.18 and in fence view in Figure 4.19. The figure can be used to determine the predominant direction of the calculated velocity vectors in the hydrostratigraphic units of the regional-scale model. The vertical component of the velocity vector will equal the velocity magnitude only when there are no horizontal components to the velocity vector; the ratio of the vertical component of the velocity vector to the velocity magnitude will be plus one for solely upward velocity and negative one for solely downward velocity. In the figure, blue corresponds to zones where the vertically downward velocity components dominate, white to zones where horizontal velocity components dominate the velocity vector and red to zones where the velocity vectors are dominated by the vertically upward component. Transition zones also are evident in the figure. It is important to note that the figures cannot be used to interpret velocity magnitude, they can only be used to interpret the direction of the calculated velocity vectors at a given location. It should also be noted that the velocity vectors in the Precambrian rock are characterized by sharp transitions over relatively short distances from upward to downward to horizontal flow. The pattern is a reflection of stagnant flow where subtle changes in topography and total dissolved solids concentration impact the direction of the velocity vectors. The magnitude of the pore water velocity in the Precambrian rock is shown in Figure 4.16.

For the base-case parameters and a pseudo-equilibrium time of 1 Ma, flow in the shallow groundwater zone is predominantly horizontal as is the flow in the more permeable units such as the Cambrian, Niagaran, and A1 upper carbonate. These units can be identified by the horizontal white bands in Figure 4.18 and in the fence diagram of Figure 4.19. The direction of the velocity vectors in the Salina are strongly vertical. The direction of velocity vectors in the Ordovician and Lower Silurian are predominantly vertical. The explanation of the predominant direction of the velocity vectors in the Ordovician sediments is more readily revealed in the fence diagram shown in Figure 4.19. The direction of a velocity vector in the Ordovician sediments at a given location is dependent on both whether the Cambrian sandstone is present at that location and on surface topography. Where the sandstone is present and surface elevations are low such as locations beneath Lake Huron, the predominant direction of the velocity vectors in the Ordovician sediments is generally upward (refer to the red zones in the figures). Where the Cambrian is absent or the surface elevation is higher than that of the water level in Lake Huron, the direction of the velocity vectors in the Ordovician sediments is generally downward (refer to the blue zones in the figure). Based on the regional-scale results, it can be concluded that the direction of velocities in the Ordovician sediments are controlled by both surface topography and the presence of an underlying permeable unit that is over-pressured.

The performance measure selected for the evaluation of the groundwater system is the mean life expectancy (Figure 4.20). The general trend for the mean life expectancy is similar to that found in the head and velocity distributions. The shallow groundwater zone has significantly shorter mean life expectancies compared to the deep groundwater zone. The areas of recharge versus discharge can be noted in the figure as the recharge areas have a high MLE while the discharge areas have low MLEs. The groundwater area surrounding the proposed DGR (shown in a fence diagram, Figure 4.21) is calculated to have a mean life expectancy of 164 Ma for the base-case regional-scale conceptual model.

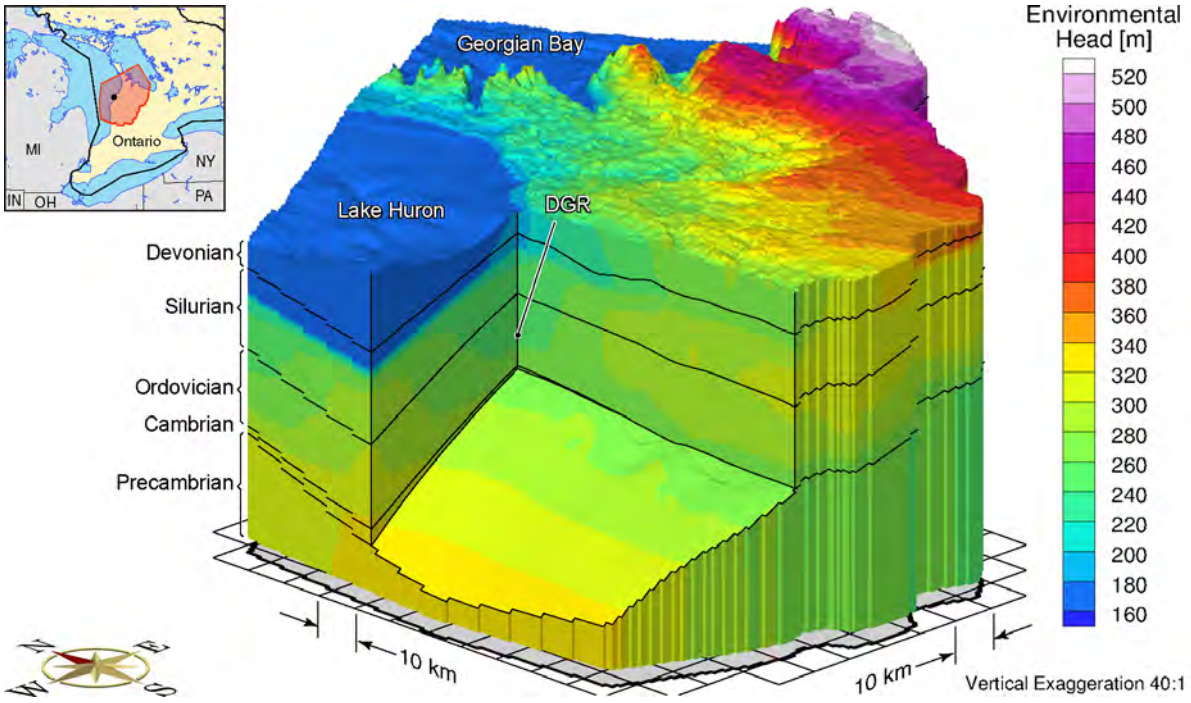

Figure 4.14: Base-Case Environmental Head Distribution

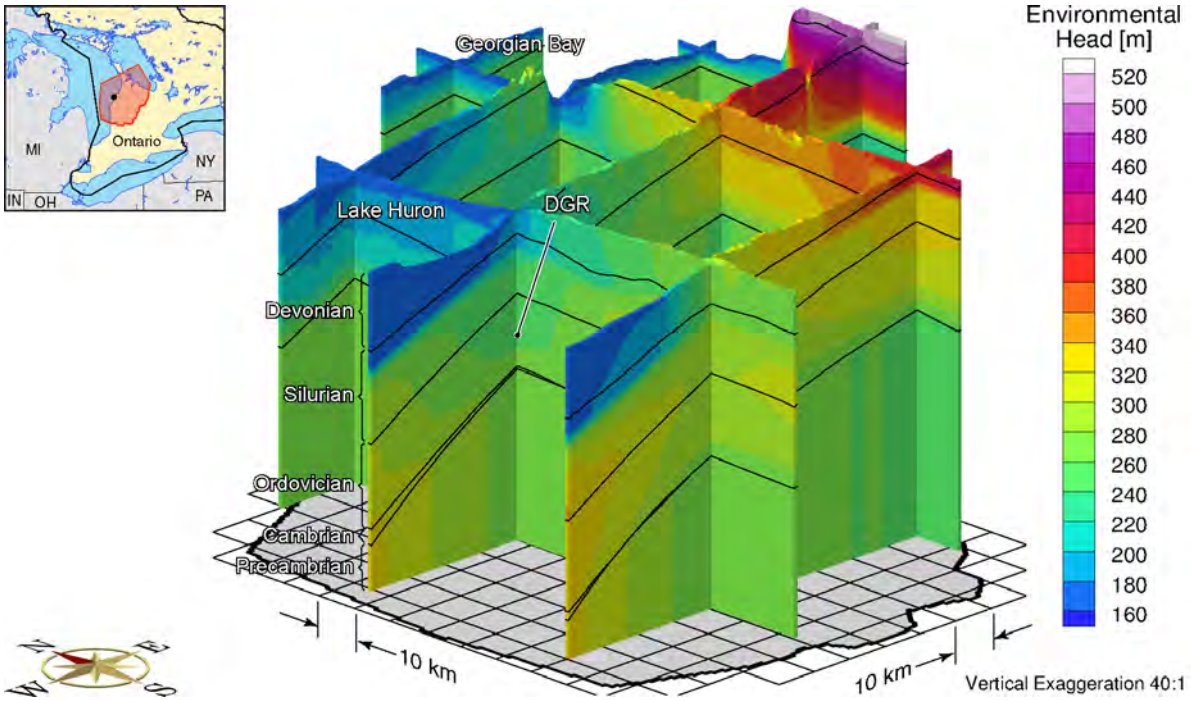

Figure 4.15: Fence View of the Base-Case Environmental Head Distribution

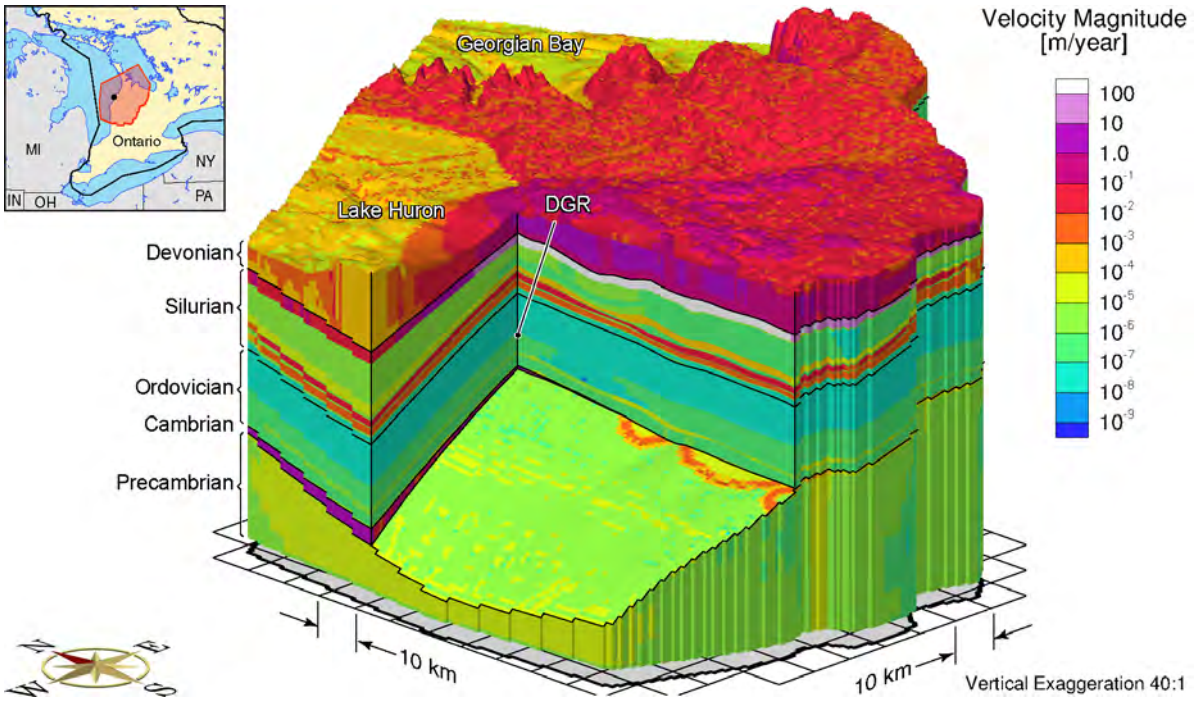

Figure 4.16: Block Cut View of Base-Case Pore Water Velocity Magnitude

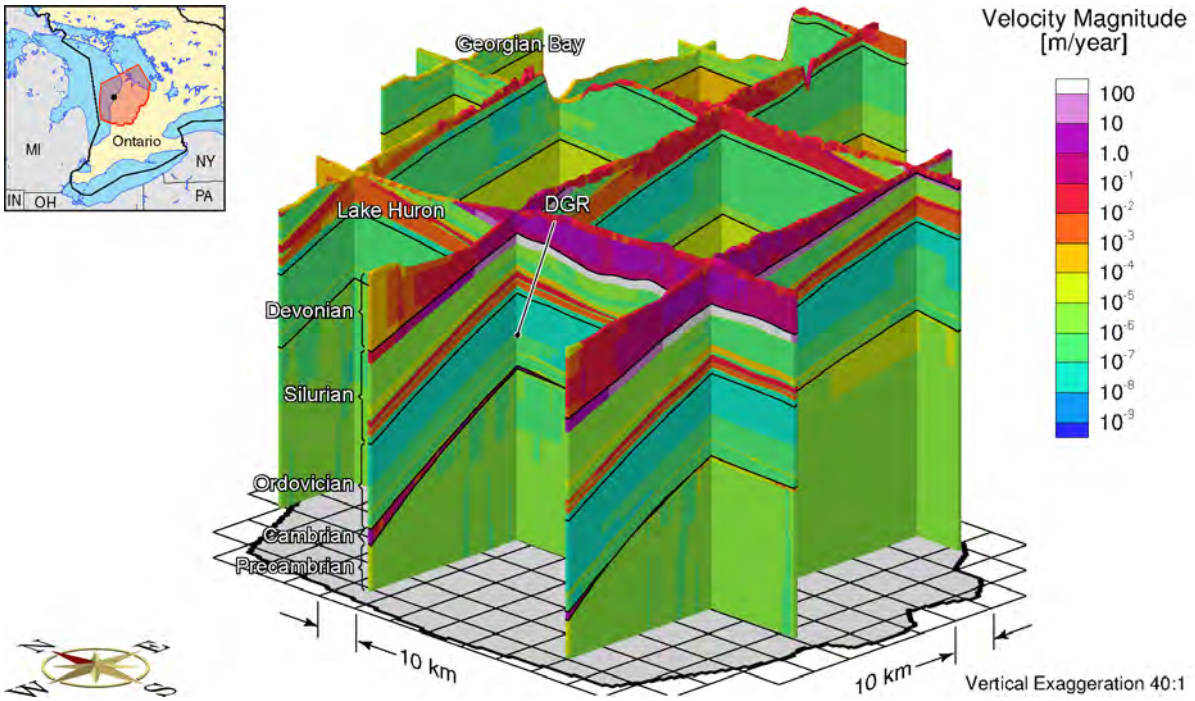

Figure 4.17: Fence View of Base-Case Pore Water Velocity Magnitude

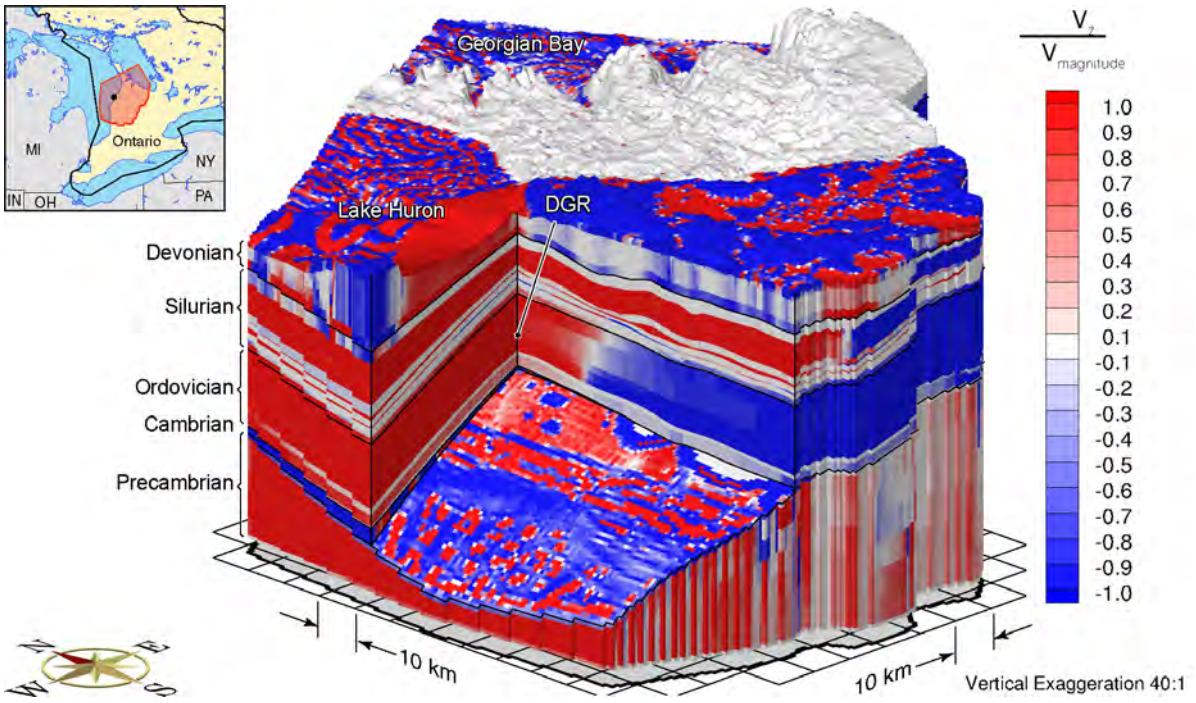

Figure 4.18: Block Cut View of Base-Case Ratio of Vertical Velocity to Velocity Magnitude

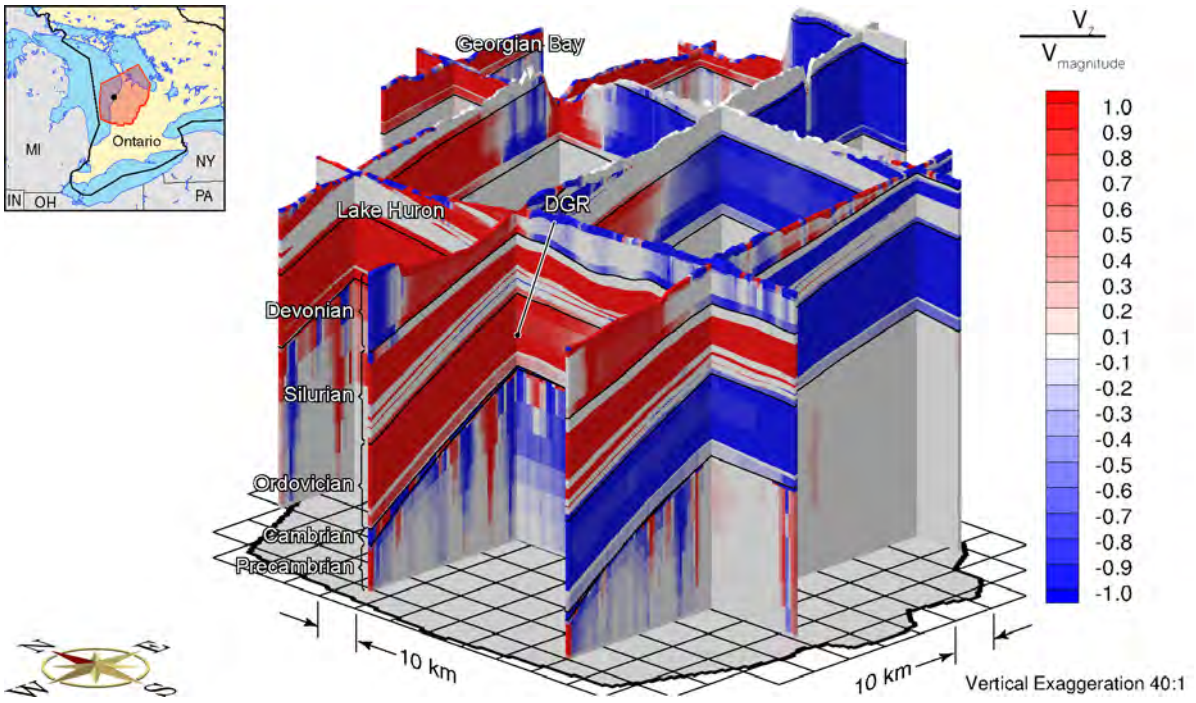

Figure 4.19: Fence View of Base-Case Ratio of Vertical Velocity to Velocity Magnitude

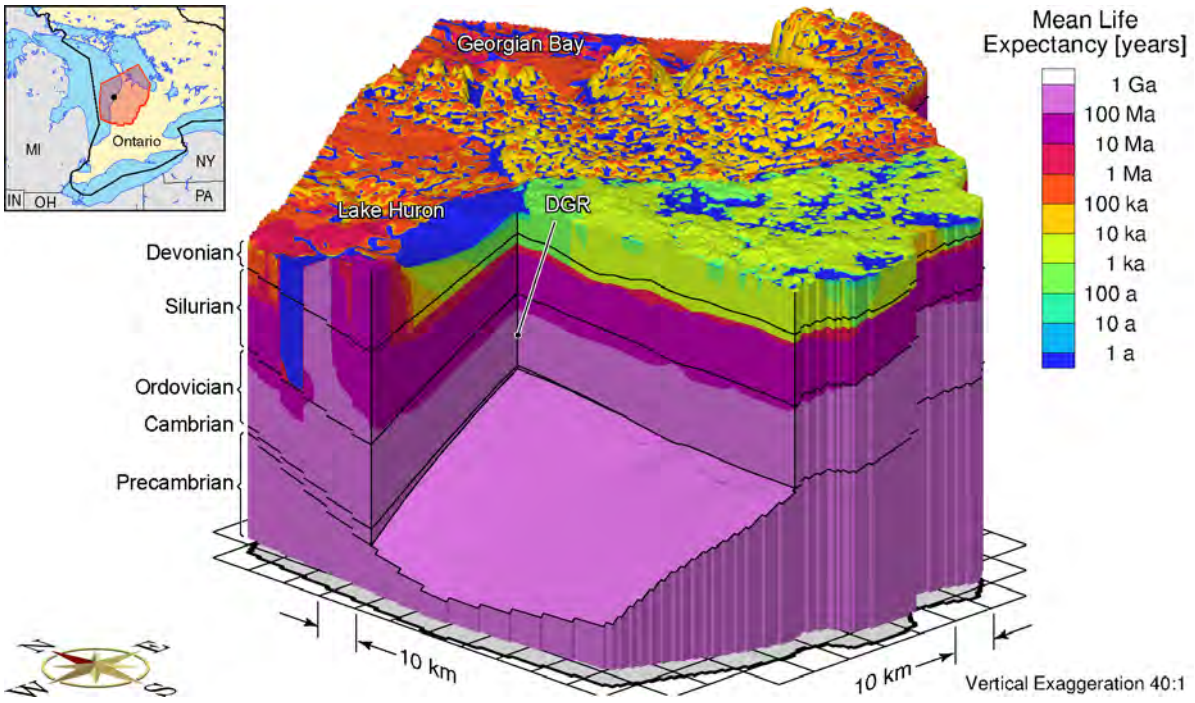

Figure 4.20: Block Cut View of Base-Case Mean Life Expectancy

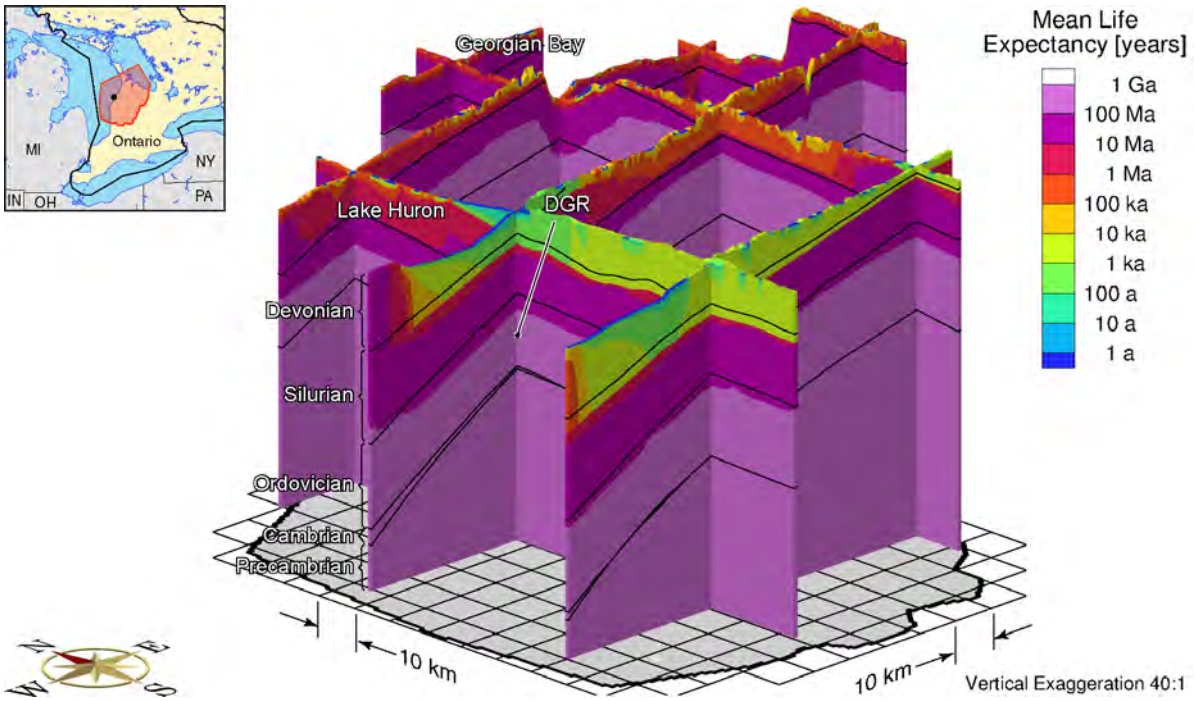

Figure 4.21: Fence View of Base-Case Mean Life Expectancy

4.4 Alternate Scenarios for the Regional-Scale System

The geological framework, flow boundary and initial conditions, TDS boundary and initial conditions and system parameters for the base-case conceptual model have been defined in the preceding sections of this report. The solution methodology for the simulation of isothermal, density-dependent flow and TDS migration at the regional-scale also has been presented. This section develops alternate cases or scenarios for the conceptual model; the genesis of the scenarios listed in Table 4.10 are issues raised in the development of the base-case model and the hypotheses of the geosynthesis program for the DGR. The objectives are: to reveal the attributes of the flow system that are important in the development of a safety case for a deep geologic repository; and, to investigate the sensitivity of the numerical solution to selected parameters. The performance measure for the analyses is MLE. The investigation of the attributes of the conceptual model and its parameters, boundary conditions and geological framework can also be approached with user defined performance measures and sensitivity coefficients.

The scenario names in Table 4.10 correspond to the prefix of the file names for the computer runs. The ‘f’ designates the FRAC3DVS-OPG computational model, the ‘r’ designates the regional-scale model, the middle descriptor of ‘base’ designates that the analysis is a perturbation of the base-case regional-scale model, while the third and forth descriptors designate the scenario. The third descriptor ‘paleo’ designates that the analysis is a paleohydrogeologic scenario with these being described in Chapter 5.

4.4.1 Summary of Scenario Analyses

Table 4.11 presents a summary of the vertical pore water or linear velocities in the Cobourg calculated for the regional-scale scenarios of this study. The velocities for all scenarios were estimated to be less than 1.0×10^{-6} m/a. The presence of a gas phase would result in the reduction of the estimated pore water velocities as a result of the impact of the relative permeability term that is dependent on the water saturation. Also shown in Table 4.11 are the Péclet numbers calculated using Equation (3.20) with a characteristic length ℓ of 1 m. The diffusion coefficient for NaI listed in the table has been revised by a factor of 0.5 to account for the diffusion accessible porosity of NaI. Bear (1988) states that the characteristic length is the mean grain size or any other characteristic medium length. Because of the many definitions in literature of the characteristic length, see for example Huysmans and Dassargues (2005), a value of 1 m is selected in this study. The Péclet numbers for the Cobourg, estimated in the regional-scale analyses, are less than 1.0×10^{-3} therefore clearly supporting the hypothesis that solute transport in the Ordovician sediments is diffusion dominant. Bear (1988) indicates a threshold for the predomination of diffusion is a Péclet number less than 0.4.

Table 4.12 summarizes the MLE at the location of the proposed DGR for the various scenarios (refer to Table 4.10) presented in this section. The MLE for the base-case regional-scale model is 164 Ma. The lowest value of 44 Ma was estimated for the case in which both the Niagaran and the Cambrian are assumed to fully communicate with the surface at the domain boundaries (refer to Section 4.4.4). Table 4.13 lists the equivalent freshwater heads and environmental heads in the Niagaran and the Cambrian at the location of the DGR-4 borehole for the various scenarios calculated using the regional-scale model. Also listed in the table are the measured freshwater heads and estimated environmental heads for the units based on the pressures measured on August 24, 2009 in the DGR-4 borehole (INTERA 2011). The site investigation measured the pressures in the four units of the Niagaran which are the Guelph, Goat Island, Gasport and Lions Head. The range of the measured or estimated values is given in Table 4.13.

Table 4.10: Table of Regional-Scale Simulations

		fr-base	fr-base-up	fr-base-camb-x0	fr-base-camb-x90	fr-base-hkp	fr-base-hbc	fr-base-rech	fr-base-paleo†	fr-base-paleo-biot	fr-base-paleo-gas	fr-base-paleo-head80	fr-base-paleo-head30	fr-base-paleo-zero-head	fr-base-paleo-le-zero	fr-base-paleo-nn9921	fr-base-paleo-openbnd
Precambrian Conductivity	Uniform		•	•	•												
	Vary with depth	•				•	•	•	•	•	•	•	•	•	•	•	•
Weathered Precambrian Conductivity	At least 1×10^{-10} m/s	•	•	•	•		•	•	•	•	•	•	•	•	•	•	
	At least 1×10^{-8} m/s					•											•
Cambrian Conductivity	$K_x = K_y$	•	•			•	•	•	•	•	•	•	•	•	•	•	•
	$K_x > K_y$			•													
	$K_x < K_y$				•												
Lateral Boundary Conditions	Neumann Zero Flux	•	•	•	•	•	•	•	•	•	•	•	•	•	•	•	
	Dirichlet heads for Cambrian, Niagaran, and A1-Carbonate																•
Surface Boundary Conditions	Dirichlet	•	•	•	•	•	•										
	Neumann							•									
Paleo Surface Boundary Conditions	Dirichlet 100% ice thickness								•	•	•				•	•	•
	Dirichlet 80% ice thickness											•					
	Dirichlet 30% ice thickness												•				
	Dirichlet 0% ice thickness													•			
Paleo Simulation	nn9930								•	•	•	•	•	•	•		•
	nn9921															•	
Hydromechanical Coupling	Biot coefficient = 1.0								•		•	•	•	•	•	•	•
	Biot coefficient = 0.5									•							
Presence of Gas Phase	No gas phase								•	•		•	•	•	•	•	•
	Partial gas phase										•						
Loading Efficiency	Actual								•	•	•	•	•	•		•	•
	Zero														•		
Paleo Cycles	1 - 120 ka								•	•	•	•	•	•	•	•	•
	2 - 240 ka								•								

Note: † Includes fr-base-paleo-2

Table 4.11: Vertical Linear Velocities (Without Roundoff) and Péclet Numbers for the Cobourg from the Regional-Scale Analyses

Simulation	Linear Velocity [m/a]	Tortuosity [/]	D_m [m^2/a]	Péclet Number [ℓ = 1 m]
fr-base (no density)	1.708277×10^{-7}	3.0×10^{-2}	0.0262	2.17×10^{-4}
fr-base	2.286102×10^{-7}	3.0×10^{-2}	0.0262	2.91×10^{-4}
fr-base-camb-x0	2.159643×10^{-7}	3.0×10^{-2}	0.0262	2.75×10^{-4}
fr-base-camb-x90	2.37826×10^{-7}	3.0×10^{-2}	0.0262	3.02×10^{-4}
fr-base-hbc	-5.96232×10^{-7}	3.0×10^{-2}	0.0262	7.59×10^{-4}
fr-base-hkp	2.466058×10^{-7}	3.0×10^{-2}	0.0262	3.13×10^{-4}
fr-base-rech	2.137599×10^{-7}	3.0×10^{-2}	0.0262	2.72×10^{-4}
fr-base-up	2.394118×10^{-7}	3.0×10^{-2}	0.0262	3.04×10^{-4}

Table 4.12: Mean Life Expectancy at the Location of the Proposed DGR from the Scenarios

Simulation	Cobourg MLE [Ma]
fr-base (no density)	155
fr-base	164
fr-base-camb-x0	166
fr-base-camb-x90	148
fr-base-hbc	44
fr-base-hkp	164
fr-base-rech	172
fr-base-up	161

Table 4.13: Model Calculated Equivalent Freshwater Heads and Environmental Heads at the DGR-4 Borehole and the Measured or Estimated Values from the Site Investigation

Simulation	Niagaran		Cambrian	
	Freshwater Heads [m]	Environmental Heads [m]	Freshwater Heads [m]	Environmental Heads [m]
Measured (24-Aug-2009)	210.4–282.3	186.3–252.7	422.1	317.6
fr-base (no density)	224.0	224.0	245.4	245.4
fr-base (init)	268.0	246.2	380.6	268.6
fr-base	263.1	238.9	380.6	268.3
fr-base-camb-x0	263.2	238.9	379.1	266.8
fr-base-camb-x90	263.2	238.9	381.8	269.5
fr-base-hbc	224.2	200.0	238.5	126.3
fr-base-hkp	263.2	239.0	382.9	270.6
fr-base-rech	265.2	241.3	380.8	268.8
fr-base-up	263.1	238.9	382.0	269.7

Note: Measured or estimated values from INTERA (2011).

4.4.2 Density-Independent Flow

The analysis of this section (scenario fr-base (no density) in Table 4.12) investigates the impact of assuming that groundwater flow is independent of density. The base-case parameters and boundary conditions are used for the analysis. As described in Section 4.2, the solution methodology for density-independent flow is considerably simplified from that of the density-dependent case as flow is determined from a steady-state solution with the TDS concentration set to zero throughout the domain. The MLE analysis also is simplified as it is based on the steady-state velocities rather than a solution that changes with the pseudo-equilibrium time as occurs in the analysis of density-dependent flow. The TDS distribution varies over a considerable range at the DGR boreholes. The shallow groundwater zone above the Salina is characterized by low, near freshwater TDS concentrations while the intermediate and deep groundwater zones have TDS concentrations that can be up to 300 g/L. To reflect the TDS distribution, the regional-scale base-case analysis simulates density-dependent flow. The importance of fluid density in impacting the calculated freshwater heads is revealed in a comparison of the results obtained for steady state density-independent flow (Figure 4.6) with those developed where the freshwater heads are allowed to equilibrate to an invariant or locked in TDS distribution (Figure 4.8) and to those of the final step in the solution methodology where both the freshwater heads and the TDS concentration distribution are allowed to vary to a pseudo-equilibrated state (Figure 4.10). There is an increase in the freshwater heads for the deeper zones in each successive step of the solution methodology. Clearly, the description of the over-pressures in the Cambrian improves with the solution of density-dependent flow. This conclusion is further investigated in the analysis of a cross-section of the Michigan Basin developed in Section 6.2.

The regional-scale pore water velocity magnitude plots, ratio of vertical velocity to velocity magnitude plots and mean life expectancy plots for the analysis of density-independent flow are presented in Figure B.1 to Figure B.6 of Appendix B. In comparing the figures and the data in Table 4.11 for the two cases of density-independent flow and the density-dependent base-case analysis, a notable difference is in the estimated vertical gradients. The difference is evident beneath Lake Huron in a comparison of the piezometric heads of Figure 4.7 with the environmental heads of Figure 4.15. For density-independent flow, the velocities in the Ordovician and Lower Silurian at the location of the DGR are approximately 66% of that calculated for the density-dependent case. For both cases however, the calculated vertical velocities calculated are small and support the hypothesis that solute transport in the Ordovician sediments is diffusion dominant.

At the location of the proposed DGR, a MLE of 155 Ma was estimated for the case of density-independent flow (refer to Table 4.12) while a Péclet number for the Cobourg was estimated to be 2.17×10^{-4} based on a vertical pore water velocity of 1.71×10^{-7} m/a. Solute transport in the Ordovician sediments is diffusion dominant for the case of density-independent flow. The path followed by average water particles released from the vicinity of the proposed DGR differ for the case from that determined for density-dependent flow for which the MLE at the location of the proposed DGR was calculated to be 164 Ma for the base-case velocity field at a pseudo-equilibrium time of 1 Ma. The difference in the MLE for the two cases is less than that calculated for other scenarios investigated in this study. It appears that MLE may not be a reliable metric to assess the impact of varying fluid density on the flow domain, particularly for a system in which transport is dominated by diffusion. For a system dominated by low permeability units, the MLE may have a greater sensitivity to the geological framework model, unit properties, boundary conditions and model constrained dispersion coefficients.

4.4.3 Analysis of the Surface Boundary Condition

A Dirichlet boundary condition defining either the regional water table or the elevation of Lake Huron is used for the surface of the base-case regional-scale model. The influx and efflux of water across the surface is controlled, in part, by the hydraulic conductivity of the top layer of the model as well as topographic gradients. It is assumed that, on average, the water table is located 3 m below the ground surface and that, to reflect weathering, the upper 20 m has a higher hydraulic conductivity than the underlying units. This scenario (fr-base-rech in Table 4.10) set prescribed heads for grid block nodes coinciding with regional rivers (refer to Figure 1.1) and prescribed a recharge boundary condition elsewhere. Figures are included in Appendix C.

This scenario investigates the use of areally constant net recharge flux boundary condition zones in conjunction with prescribed equivalent freshwater heads at the major rivers of the regional-scale spatial domain. In this study, net recharge is defined as the amount of water that contributes to the base flow of the rivers defined by prescribed equivalent freshwater heads. As shown in Figure 1.1, the network of rivers at the regional-scale excludes many of the small rills, gullies, ditches, creeks, brooks and streams that are important in the surface flow system. For grid blocks that are 900.9 m by 762.8 m, a large fraction of the recharge that occurs at a point will be interflow that contributes to the base flow of these smaller scale features. Thus, the impact of upscaling of point recharge in a model that includes only regional-scale rivers is to significantly reduce the net recharge. This reduction is particularly significant for the part of the drift that is underlain by the Silurian. The parameters for the base-case conceptual model were used for the analysis of this scenario. Through a sensitivity analysis, the upscaled, areal average, net recharge for the Scenario was determined to be 10 mm/a for the area underlain by the Devonian and 0.01 mm/a for the area underlain by the Silurian. The constraint used in the estimation of the value was the location of the model-determined water table relative to the elevation of the ground surface of the spatial domain. The low recharge value is a reflection of the fact that most point groundwater recharge will discharge to the surface at a scale that is considerably smaller than that of a regional-scale grid block. The results for the analysis are given in Figure C.1 to Figure C.8 of Appendix C. As compared to the base-case analysis (refer to Section 4.3), the model results with a prescribed recharge present a smoother shallow groundwater system. The difference is most obvious with a comparison of the MLE of Figure C.7 and Figure 4.20. For the case with recharge, the higher MLE at surface water divides (red and yellow in Figure C.7) and lower values at rivers (blue) are clearly apparent. The regional-scale rivers are obvious in the figure. The base-case analysis is considerably more complex as water that recharges at one block can discharge at an immediately adjacent block. However, the impact of the different conceptualizations of the surface boundary condition is dampened significantly by the low permeability of the Salina. At the location of the proposed DGR, a MLE of 172 Ma was estimated for a pseudo-equilibrium time of 1 Ma. Referring to Table 4.12 it is noted that the pore water velocities in the Niagaran and the Cambrian are marginally higher for this case than those calculated for the base case The Péclet number calculated for the Cobourg is 2.72×10^{-4} based on a vertical pore water velocity in the unit of 2.14×10^{-7} m/a; solute transport in the Ordovician sediments for the scenario is diffusion dominant. In this study, the use of a prescribed water table rather than a recharge boundary condition was selected for the base case due to its reduced computational time.

4.4.4 Analysis of the Lateral Boundary Condition

The regional-scale spatial domain is a subset of the Michigan Basin. For the more permeable units of the intermediate and deep groundwater zones such as the Niagaran and the Cambrian, it is possible that the use of a no-flow boundary condition for the lateral edges of the domain could

have an impact on the flow in the units and on the estimate of MLE at the location of the proposed DGR. The objective of the scenario of this section (fr-base-hbc) is to relax the constraint on lateral flow imposed by the no-flow boundary condition. This was achieved by assigning a vertical hydraulic conductivity of 1×10^{-5} m/s from the surface to the Precambrian at the perimeter of the domain. The upper boundary condition was identical to that of the base-case analysis. The described zone at the boundary allows communication at the domain edges between all of the deeper units and the surface where the equivalent freshwater heads were assigned based on either surface topography or the water elevation of Lake Huron and Georgian Bay. The hydraulic parameters for the analysis were the same as those of the base-case analysis. However, the solution methodology had to be altered as the high permeability perimeter zone allowed freshwater to penetrate to depth flushing TDS from units such as the Cambrian. To overcome this problem, the TDS concentration distribution of the base-case analysis at a pseudo-equilibrium time of 1 Ma was assigned to all grid blocks of the regional-scale domain and the transport solution turned off in FRAC3DVS-OPG. The resulting flow equation would thus include the impact of density as determined by the TDS concentration distribution but would not be able to alter the concentration as flow occurred.

The environmental head distribution for the Scenario is shown in Figure 4.22 and Figure 4.23, the velocity magnitude is shown in Figure 4.24 while the ratio of vertical velocity to the velocity magnitude is given in Figure 4.25. Finally, the calculated MLE for the scenario is given in Figure 4.26 and Figure 4.27. The impact of the communication zone at the domain perimeter on velocities is evident in both Figure 4.22 and Figure 4.24 with high velocities apparent in the boundary zone in the latter. A comparison of the results with those of the base-case analysis (Figure 4.14) shows that the lateral boundary zone, that permits communication between all layers and the surface, results in small vertical environmental head gradients between the deeper zones and the surface. This finding is clearly supported by the data at the location of the DGR boreholes presented in Table 4.13. The modelled vertical gradients across the Ordovician sediments and based on the environmental heads do not reflect those measured in the DGR boreholes (refer to Figure 2.15). As shown in Figure 4.25, when the Cambrian is open to the surface rather than being confined, the direction of velocity vectors across the Ordovician sediments is downward (refer to the blue zone in the figure) rather than upward as observed in the DGR boreholes. It is concluded that the observed vertical gradient can only occur if there is either limited or no vertical communication between the Cambrian and the shallower permeable units such as the Niagaran and the Devonian. For the results of this scenario, horizontal flow in units such as the Niagaran and Cambrian is topographically driven (refer to Figure 4.22 and Figure 4.25 and to Table 4.12). As expected, the MLE in the perimeter communication zone is low; however, the MLE values for the Ordovician units in the internal part of the domain are greater than 10 Ma. At the location of the proposed DGR, the MLE was estimated to be 44 Ma (refer to fr-base-hbc in Table 4.12). It is noted that the path either downward through the Ordovician to the Cambrian or upwards to the Niagaran Group and then to the domain boundary is long. Based on the analyses of this section that yielded a Péclet number of 7.59×10^{-4} in the Cobourg for a downward vertical velocity of 5.96×10^{-7} m/a, it can be concluded that solute transport in the Ordovician sediments is diffusion dominant and insensitive to a boundary condition that permits communication between the Cambrian and the surface layers.

4.4.5 Higher Hydraulic Conductivity Upper Precambrian

The permeability or hydraulic conductivity versus depth model for the Precambrian rock of Equation (4.1) and as shown graphically in Figure 4.1 (Normani 2009) reflects a weathered zone for rock near the ground surface. At the DGR, it is not known whether the upper zone of the Precambrian rock at depth has a higher hydraulic conductivity than the underlying deeper rock.

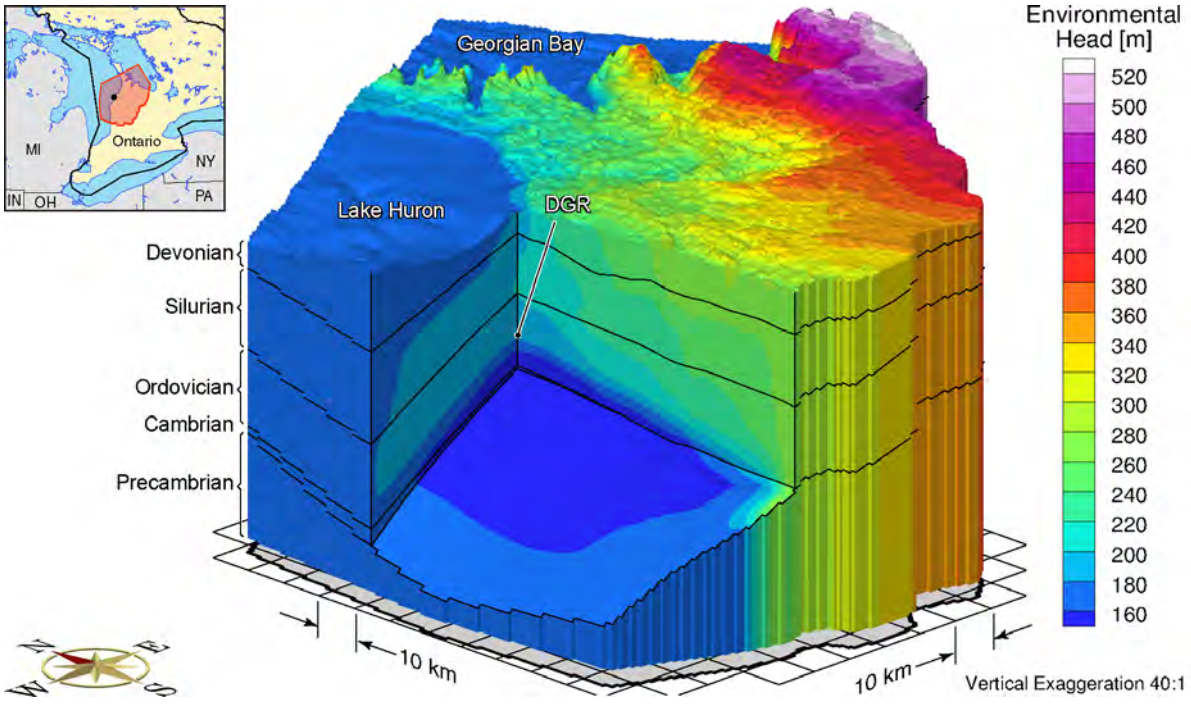

Figure 4.22: Environmental Head Distribution for Base-Case Parameters with High Permeability Zone Along Domain Boundaries

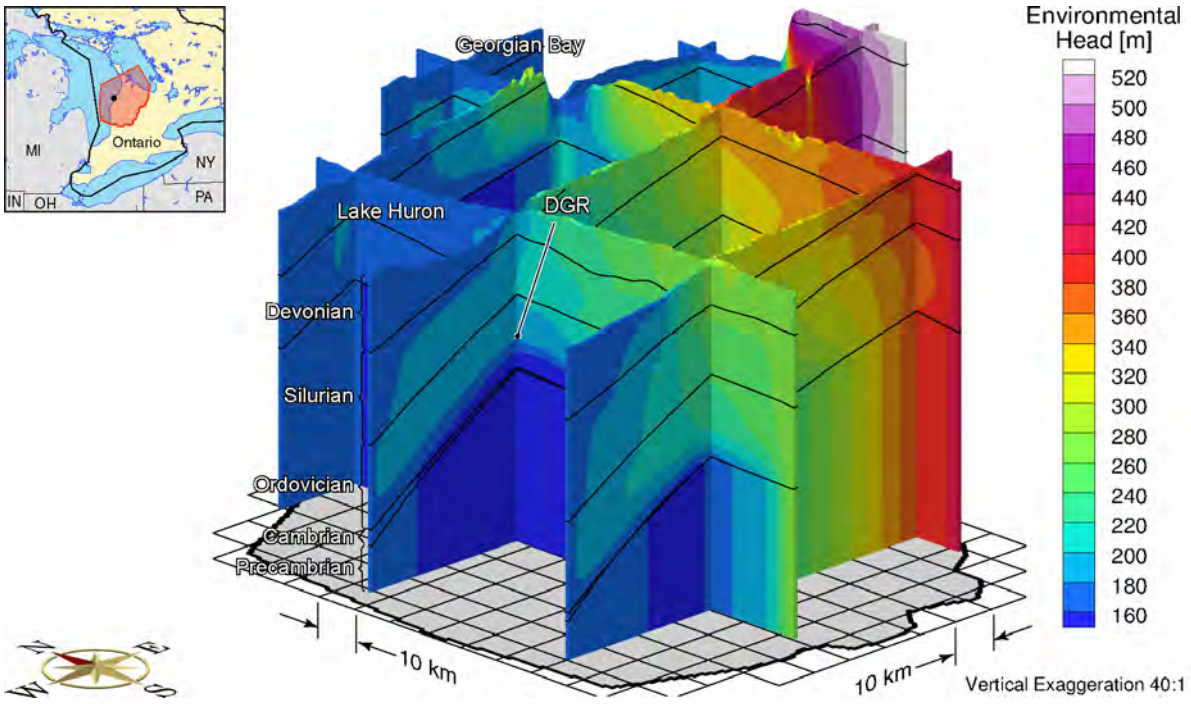

Figure 4.23: Fence View of Environmental Head Distribution for Base-Case Parameters with High Permeability Zone Along Domain Boundaries

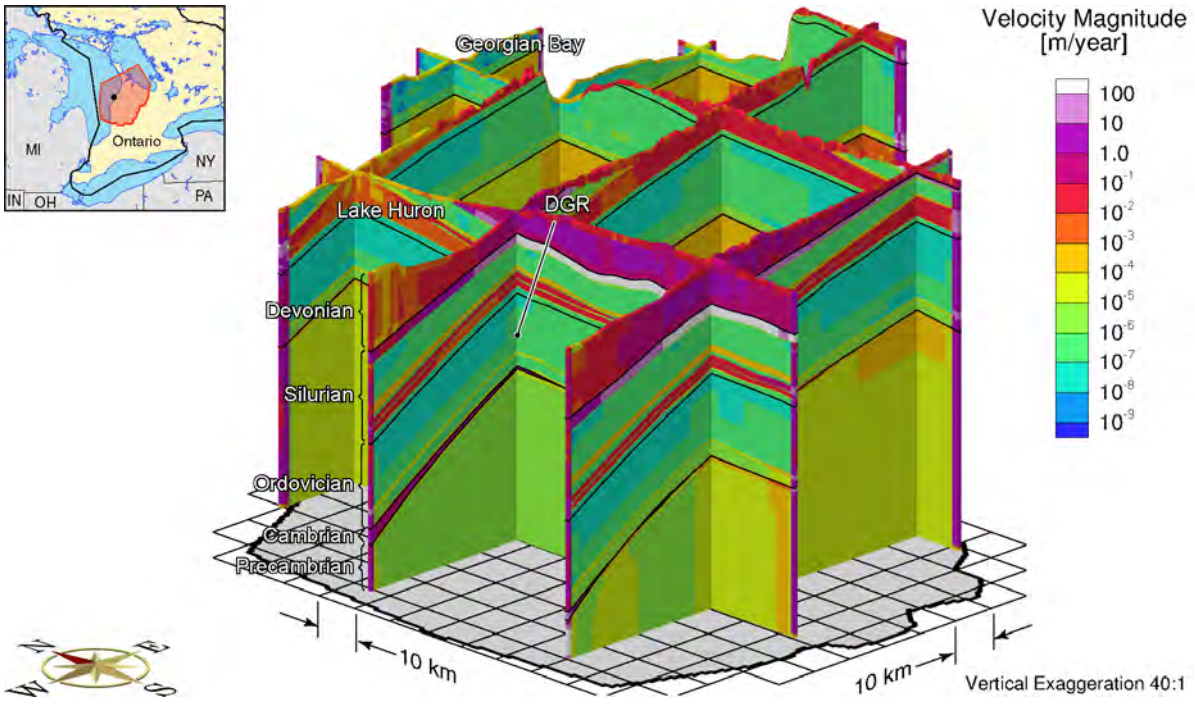

Figure 4.24: Velocity Magnitude for Base-Case Parameters with High Permeability Zone Along Domain Boundaries

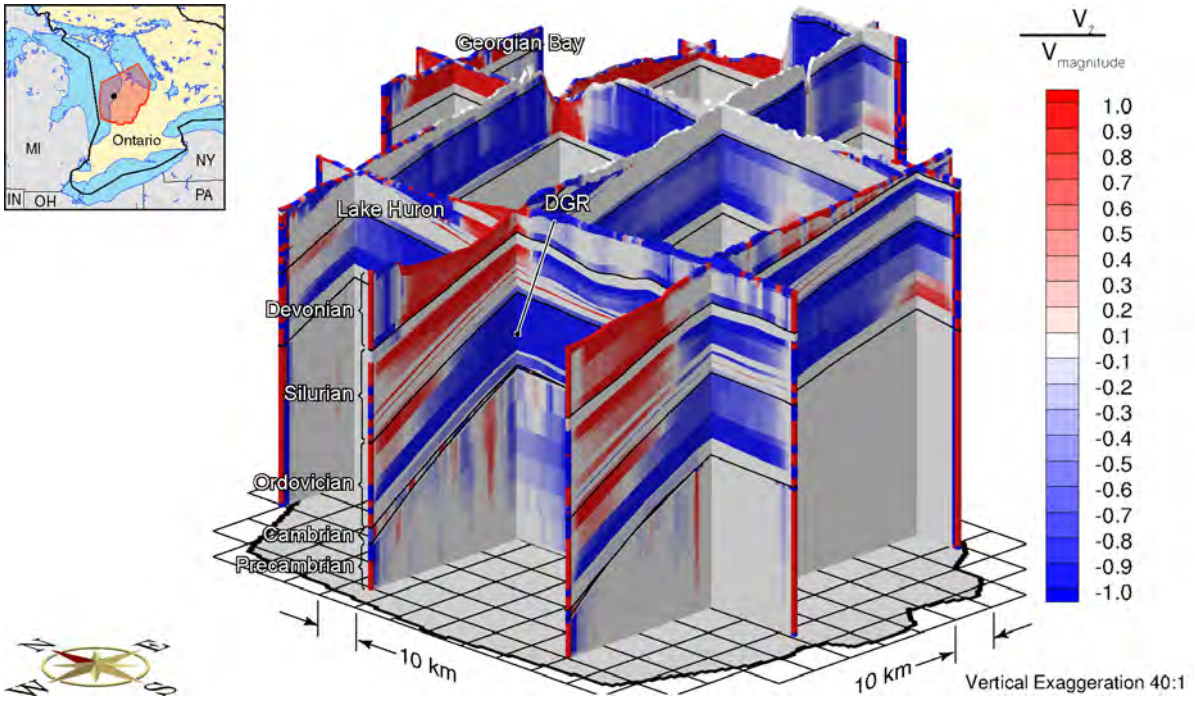

Figure 4.25: Fence Diagram of Ratio of Vertical Velocity to Velocity Magnitude for Base-Case Parameters with High Permeability Zone Along Domain Boundaries

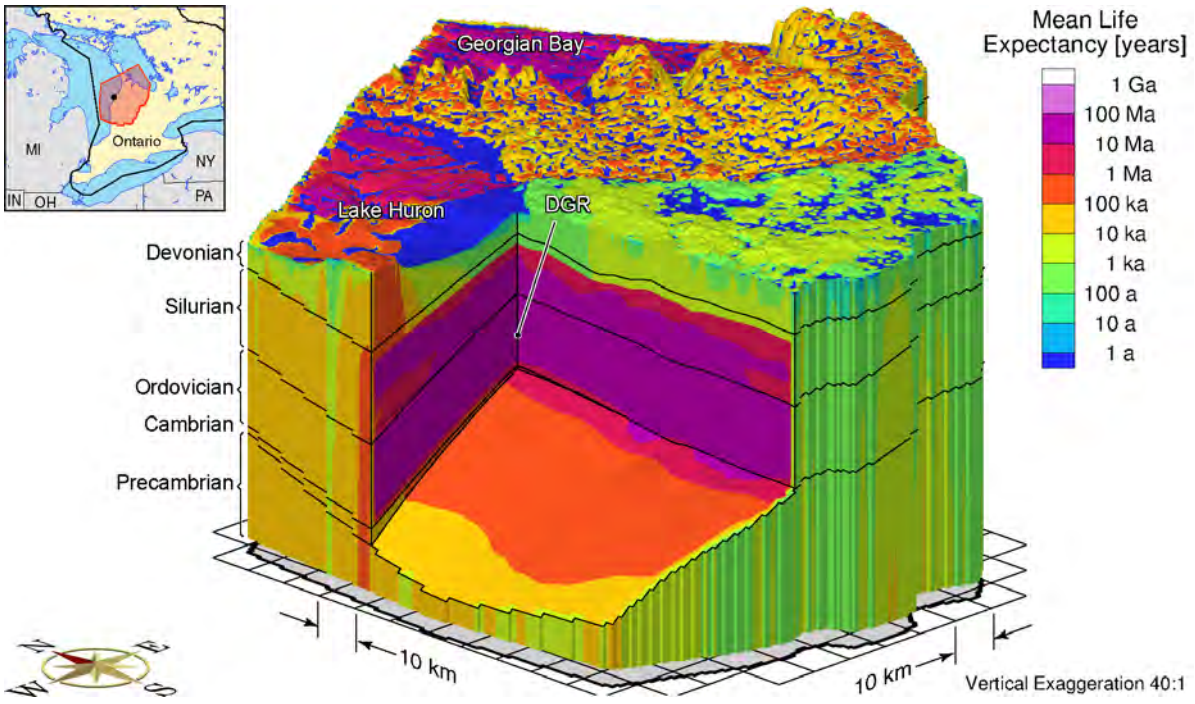

Figure 4.26: Mean Life Expectancy Distribution for Base Case Parameters with High Permeability Zone Along Domain Boundaries

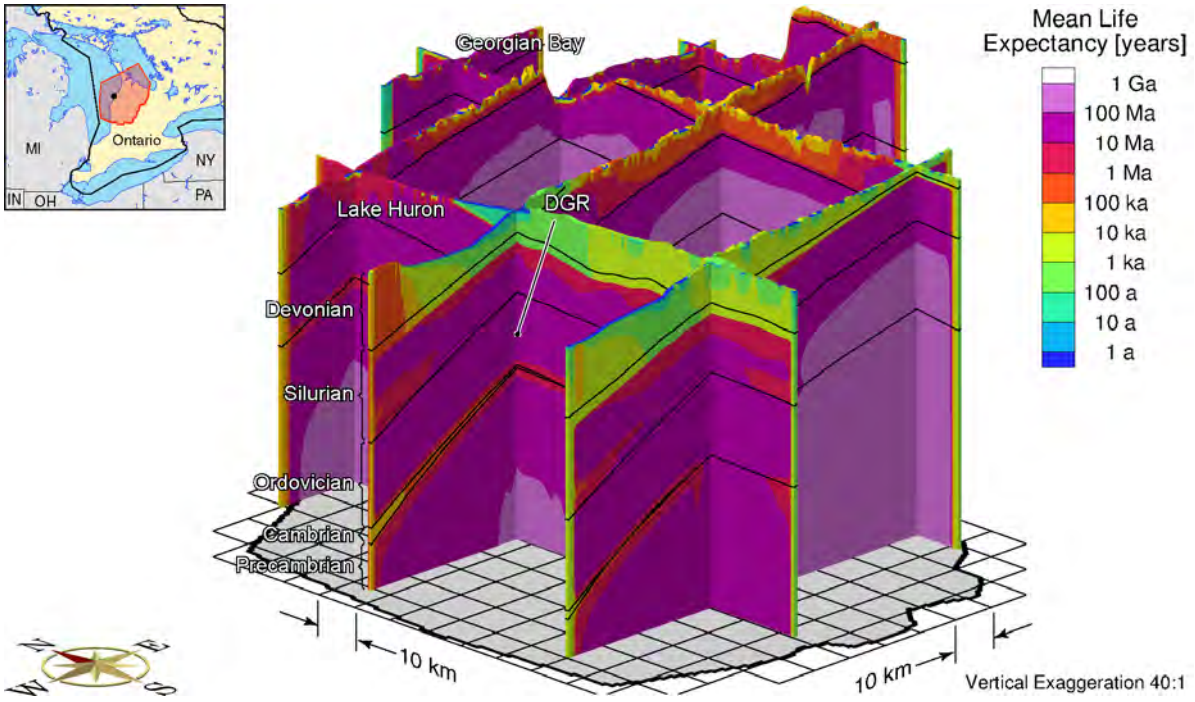

Figure 4.27: Fence Diagram of Mean Life Expectancy Distribution for Base-Case Parameters with High Permeability Zone Along Domain Boundaries

To investigate the impact of this uncertain layer on deep groundwater flow, the hydraulic conductivity of the upper Precambrian of the regional-scale numerical model was increased from that of the base-case analysis. The weathered layer was assumed to have a thickness of 20 m and a hydraulic conductivity of a minimum of 1×10^{-8} m/s (scenario fr-base-hkp). If the hydraulic conductivity versus depth model of Equation (4.1) yielded a greater value, it was assigned to the weathered upper Precambrian zone at that location. Note that the hydraulic conductivity of the assumed weathered zone is nearly two orders-of-magnitude lower than the base-case hydraulic conductivity for the Cambrian. However, the assumed hydraulic conductivity for the weathered zone is approximately 4 orders of magnitude higher than the value assigned to the Precambrian at the location of the DGR boreholes in the base-case analysis.

The freshwater heads for the analysis are shown in Figure E.1 and Figure E.2 while the environmental heads are shown in Figure E.3 and Figure E.4 of Appendix E. A comparison of the results to those of the base-case analysis shown in Figure 4.10 and Figure 4.14 reveals that the heads in the upper portion of the Precambrian are lower. The TDS shown in Figure E.5 and Figure E.6 is very similar to Figure 4.10 and Figure 4.11 from the base case analysis. Although the TDS is very similar, the differences in heads are likely attributed to the greater mobility in the upper Precambrian, due to a higher hydraulic conductivity, allowing heads to equilibrate quicker than in the base case.

Pore velocity magnitudes are shown in Figure E.7 and Figure E.8 and can be compared with the base case shown in Figure 4.16 and Figure 4.17. The block cut view shows the upper Precambrian surface, which exhibits a much higher velocity magnitude of approximately two orders of magnitude. In contrast, the velocities in the Precambrian below the upper Precambrian, are lower; since the transmissivity of the upper Precambrian is higher, less flux occurs in the Precambrian. The ratio of vertical velocity to the velocity magnitude is shown in Figure E.9 and Figure E.10. When compared to Figure 4.18 and Figure 4.19, the upper portion of the Precambrian exhibits more downward flow, but at lower velocity than the base case which is predominantly horizontal, but with higher velocity magnitudes.

The impact of a weathered upper Precambrian on the heads in the Niagaran and the Cambrian at the location of the proposed DGR is revealed in Table 4.13 through a comparison of the results for simulation fr-case hkp and those obtained for the base-case simulation fr-base. The difference in the heads of 0.1 m for the Niagaran between the two cases is insignificant. The heads for the Cambrian for the case with a weathered upper Precambrian are greater than those calculated for the base case. The explanation of the increase in head is that the impact of surface topography and the higher surface elevations at the Niagara Escarpment is greater with the higher transmissivity of the weathered upper Precambrian.

Mean life expectancy plots are shown in Figure E.11 and Figure E.12 and can be compared to the base case Figure 4.20 and Figure 4.21; both analyses result in nearly identical mean life expectancies. The MLE at the DGR site is approximately 164 Ma (refer to Table 4.12) and is unchanged from the base-case analysis. Based on the analysis of this section and a Péclet number in the Cobourg of 3.13×10^{-4} for a vertical pore water velocity in the unit of 2.47×10^{-7} m/a, it is concluded that solute transport in the Ordovician sediments is insensitive to the hydraulic conductivity assigned to the upper Precambrian. It is also concluded that the mean life expectancy for the location of the proposed DGR in the Cobourg is insensitive to the possible presence of weathered rock, as conceptualized in this study, in the upper Precambrian.

4.4.6 Uniform Hydraulic Conductivity for the Precambrian

The regional-scale base-case analysis assumes the permeability or hydraulic conductivity versus depth model for the Precambrian rock of Equation (4.1), and shown graphically in Figure 4.1 (Normani 2009). The simulation described in this section investigates the impact on groundwater flow of a conceptual model for the Precambrian in which the rock is assumed to be homogeneous with an isotropic hydraulic conductivity of 1.0×10^{-12} m/s (scenario fr-base-up). The results for the analysis are given in Figure E.13 to Figure E.20 of Appendix E. The data at the location of the DGR for the analysis are shown as simulation fr-base-up in Table 4.12 and Table 4.13. A comparison of the analysis of this section to the base-case results indicates that the description of flow in the Ordovician shale and limestone and in the shallower Niagaran at the location of the DGR is insensitive to the hydraulic conductivity distribution assigned to the Precambrian. The explanation of this lack of sensitivity is that the hydraulic conductivity versus depth model of Equation (4.1) is most important for the description or characterization of the shallow Precambrian rock. At the location of the DGR, the Precambrian rock is deep enough such that flow in the Ordovician and shallower units is insensitive to the description of the shallow Precambrian that is at a distance up dip from the site. The lack of sensitivity is also related to the hydraulic conductivity of the Shadow Lake formation that directly overlies the Precambrian for the eastern half of the domain. The Shadow Lake formation, with a horizontal hydraulic conductivity that is approximately 3 orders-of-magnitude greater than that of the Precambrian, has a significantly greater impact on fluid flux than the Precambrian. The pore water velocities and gradients in the Cambrian are also insensitive to the differences between the two conceptual models of the hydraulic conductivity for the Precambrian. The heads in the Cambrian for the uniform model of this section (refer to Table 4.13) are slightly higher than those of the base-case model. The increase in heads may be related to the use of the same pseudo-equilibrium time of 1.0 Ma for both cases. Specifically, the flushing of TDS in the shallow Precambrian will take longer time for the case of the uniform hydraulic conductivity for the Precambrian than it will using the model of Equation (4.1). This implies that the heads in the Cambrian at the location of the DGR are sensitive to the TDS distribution of the rock up dip of the site. The importance of the regional-scale distribution of TDS concentration and fluid density is further explored in Section 6.2.

The scenario MLE, Péclet number and vertical pore water velocity in the Cobourg at the location of the proposed DGR are estimated to 161 Ma, 3.04×10^{-4} and 2.39×10^{-7} m/a, respectively. Based on the results, solute transport in the Ordovician sediments is estimated to be diffusion dominant.

4.4.7 Analysis of the Cambrian: Investigation of the Impact of Horizontal Hydraulic Conductivity Anisotropy

The measured pressure data at the DGR boreholes and TDS concentration distribution for the units intersected by the borehole yields an estimate of the environmental head for the Cambrian that is greater than the environmental head at the water table (refer to Figure 2.15). The Cambrian pressures are also considerably greater than those of the Ordovician units; the environmental head profile at the DGR-4 borehole indicates that the energy gradient is upward from the Cambrian to the overlying Ordovician units. A theme of this study is the investigation of the numerical model attributes that are important in the assessment of regional-scale groundwater flow for a domain centred of the location of the proposed DGR. The groundwater flow for the domain is described by the base-case analysis. The attribute investigated in this section is the hydraulic conductivity model used for the Cambrian and its impact on the estimation of heads in that unit.

At the location of the DGR, the Cambrian is a relatively thin, permeable unit in which flow could be impacted by the horizontal hydraulic conductivity anisotropy model used to describe the unit. The overlying Shadow Lake Formation and the underlying Precambrian have significantly lower permeability than the Cambrian sandstone. This section investigates the impact on flow in the Cambrian of different principal directions of the hydraulic conductivity tensor. A homogeneous anisotropic hydraulic conductivity model is assumed. For all cases investigated, the K_1 component for the Cambrian has a value of 3×10^{-6} m/s with this being the same as the isotropic horizontal hydraulic conductivity used in the base-case analysis. The K_2 component was arbitrarily assigned a value of 3×10^{-8} m/s. The K_3 component of the hydraulic conductivity tensor has a principal direction that is vertical; the base-case value was used. For this study, the orientation of the principal directions of hydraulic conductivity were assumed to be uncertain. Two cases with different directions of the principal components of the hydraulic conductivity tensor were considered. Scenario fr-base-camb-x0 sets the higher hydraulic conductivity K_1 parallel to an east-west direction while scenario fr-base-camb-x90 sets K_1 parallel to a north-south direction. The parameters for the other units and the boundary conditions are the same as that of the base-case analysis. The results of the two simulations, presented in Appendix D, are similar to that of the base-case analysis with the exception of the direction of the horizontal gradients in the Cambrian and underlying Precambrian. These can be noted by a comparison of the plots of equivalent freshwater heads. Clearly, the direction of flow in the Cambrian is sensitive to the orientation of the principal directions of the hydraulic conductivity tensor used to describe the Cambrian.

The MLE values at the location of the proposed DGR are (refer to Table 4.12): fr-base-camb-x90 is 148 Ma and fr-base-camb-x0 is 166 Ma. The orientation of K_1 in a west to east direction (fr-base-camb-x0) has an MLE that is similar to that of the base-case analysis. When the low K_2 value is oriented in the west to east direction (fr-base-camb-x90), the MLE is predicted to decrease by approximately 16 Ma as compared to the MLE from the base-case . The MLE is thus sensitive to the hydraulic conductivity model for the Cambrian. It is likely that the rate of possible dissipation of the elevated pressures in the Cambrian, as may occur with a well that produces water from the unit, will also be sensitive to the hydraulic conductivity model and the nature of possible discontinuities of the Cambrian. The vertical pore water velocities and estimated Péclet number for the Cobourg for the analyses of this section are shown in Table 4.11; the scenario also supports the conclusion that solute transport in the Ordovician sediments is diffusion dominant.

4.5 Site-Scale Analyses

The objective of the site-scale hydrogeologic modelling of the proposed DGR is to provide a refined spatial discretization that will allow the simulation of features, events and processes that cannot be appropriately investigated with the regional-scale model. The use of a refined mesh over the entire regional-scale domain would be computationally intensive. Mehl and Hill (2002) indicate that such discretizations can lead to intractable solutions. The need for a locally refined mesh generally is due to three practical requirements (Mehl and Hill 2002):

- To capture accurately steep hydraulic gradients near pumping, injecting wells and the features of facilities such as the DGR;
- To capture accurately sharp fronts in contaminant transport; and
- To represent local-scale hydrogeologic features (e.g., fractures, stratigraphy, pinnacle reefs) as accurately as practicable.

There are three general approaches used in local mesh refinement: variably spaced meshes, model-in-model and direct embedment. Variably spaced meshes, as commonly used with

discretizations of the finite difference method, can lead to grid blocks with large aspect ratios and refinement in areas where such detail is not needed. A model-in-model approach used by Ward et al. (1987) (also referred to as a telescopic mesh refinement) entailed the use of three successively smaller-scale models: regional, local, and site models. In this case the approach for inter-scale information transfer has involved linear interpolation from the coarser scale to the finer scale with this being associated with several disadvantages. Firstly, coupling between two model meshes occurs only in one direction: from the large mesh to the small mesh. Because there is no feedback from the small mesh to the large mesh, non-linear analyses based on iterative solution techniques are not possible, and significant discrepancies can occur in fluxes or state variables (whichever are not used to couple the meshes) at the model interface. Secondly, the interpolation methods may not conserve mass with the result that short-circuiting, where there is fluid influx and efflux at adjacent boundary grid blocks, can occur at the boundaries of the smaller-scale system. The local mesh refinement or spatial sub-discretization approach developed for FRAC3DVS-OPG is based on the direct embedment approach (Guvanasen 2007). The spatial sub-discretization (sub-gridding) methodology that has been developed allows analysts to refine or coarsen an existing three-dimensional FRAC3DVS-OPG finite-element mesh in an efficient manner. Using a non-adaptive sub-discretization approach all the information for the sub-discretized elements is generated externally. The method is applicable to solid and plate elements only. An existing line element can be simply subdivided into several line elements by introducing additional nodes between the existing two nodes. Each new line element is treated exactly the same as the pre-sub-discretized element in FRAC3DVS-OPG; the solid and plate elements are treated differently at the transition zones between the densely and sparsely discretized areas (Guvanasen 2007).

In this study, the direct embedment approach is developed to provide initial and boundary conditions for site-scale analyses. Each node in the site-scale model has a counterpart with exactly the same coordinates in the regional-scale model with the direct embedment approach. No interpolation is needed to extract the initial and boundary conditions from the regional-scale model. The site-scale conceptual model is described in Section 4.5.1. The site-scale model is used to investigate the measured pressure profile in the composite DGR boreholes, the impact of hypothetical discrete fracture zones and the evolution of the tracer plume originating from the proposed DGR site. Table 4.14 presents a summary of the site-scale scenarios developed in this study.

4.5.1 Site-Scale Conceptual Model

The site-scale spatial domain relative to that of the regional-scale domain is depicted in Figure 4.28. The domain has a spatial extent of 19.078 km in the west-to-east direction and 18.918 km in the south-to-north direction centred on borehole DGR-2. The site-scale domain was discretized by using 6 columns (west-to-east sub-gridding) for each regional-scale column and 8 rows (south-to-north sub-gridding) for each regional-scale row. The resulting site-scale domain has 150 columns and 168 rows with each grid block being 127 m in the west-to-east direction and 112.6 m in the south-to-north direction. The areal discretization is shown in Figure 4.29. Sub-gridding was also used to refine the discretization of the Cobourg Formation with three layers being used in the site-scale model to represent the single regional-scale layer. As shown in Figure 4.30, the overlying Collingwood/Blue Mountain, Queenston and Niagaran Formations were subdivided into 8, 4 and 3 layers respectively. The underlying Gull River, Kirkfield and Sherman Fall Formations were further subdivided into 4, 2 and 3 layers in the site-scale model. Also evident in Figure 4.30 are the transition elements between the larger regional-scale elements and the site-scale mesh.

Table 4.14: Parameters and Initial Conditions for Site-Scale Analyses

		fs-base	fs-base-hkp	fs-1km	fs-5km	fs-base-under-pressure	fs-10kv-under-pressure	fs-100kv-under-pressure	fs-1km-under-pressure
Initial Heads	Steady State	•	•	•	•				
	Under-pressured					•	•	•	•
Hydraulic Conductivity of the Upper Precambrian	1×10^{-8} m/s		•						
	1×10^{-10} m/s	•		•	•	•	•	•	•
Fracture Zone Distance from DGR Site	1 km			•					•
	5 km				•				
Anisotropy in the Black River Group (K_H:K_V)	10:1						•		
	100:1							•	
	1,000:1	•	•	•	•	•			•

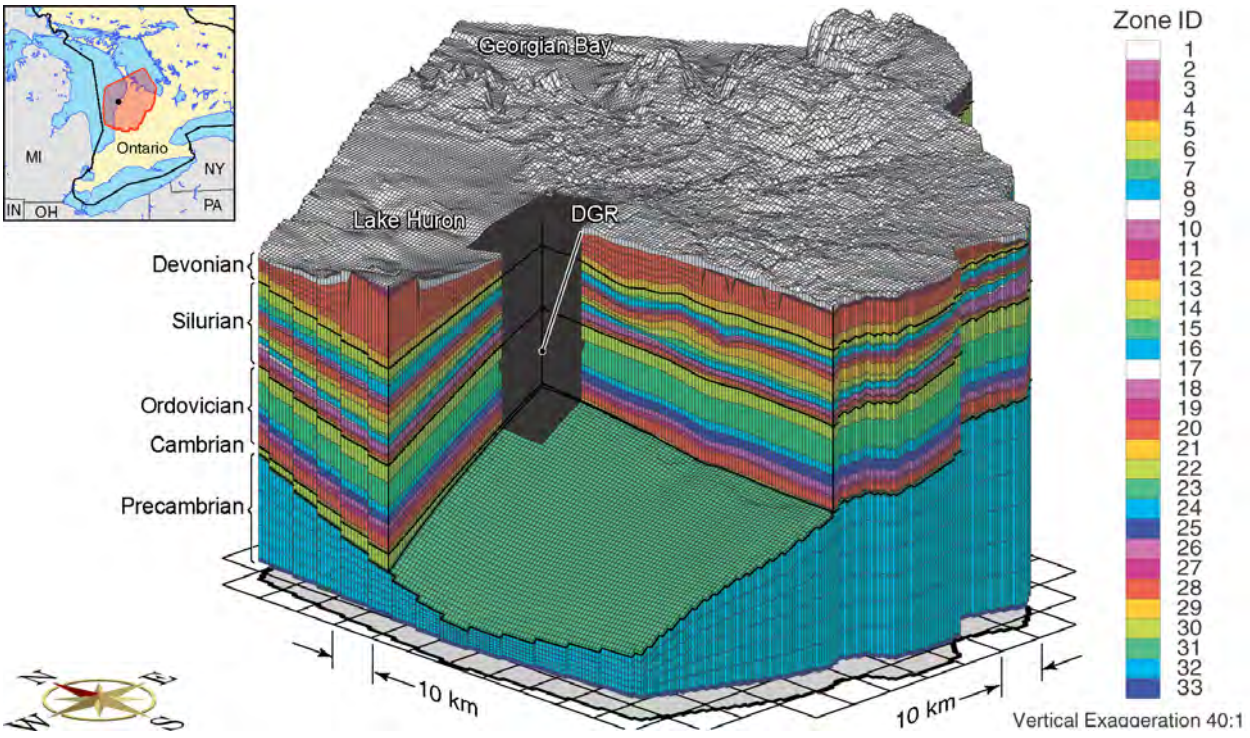

Figure 4.28: Regional-Scale Discretization Showing Location of Site-Scale Spatial Domain

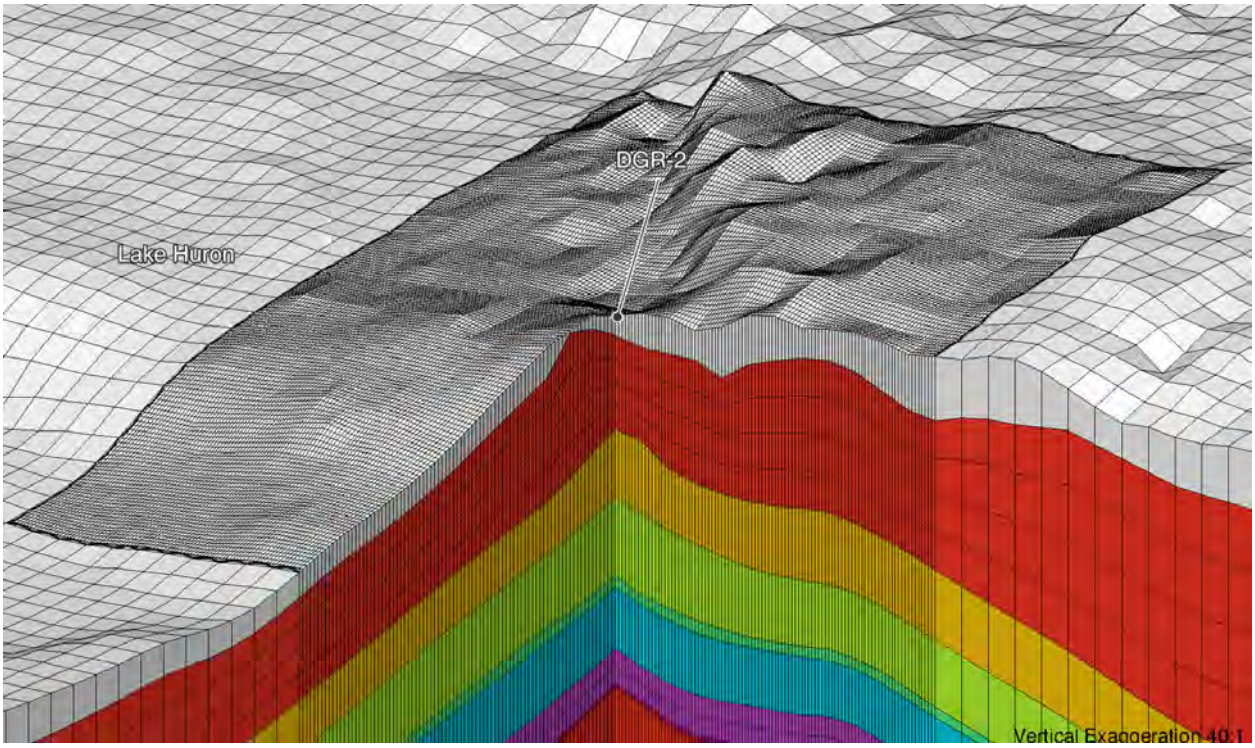

Figure 4.29: Regional-Scale Discretization Showing Site-Scale Discretized Spatial Domain

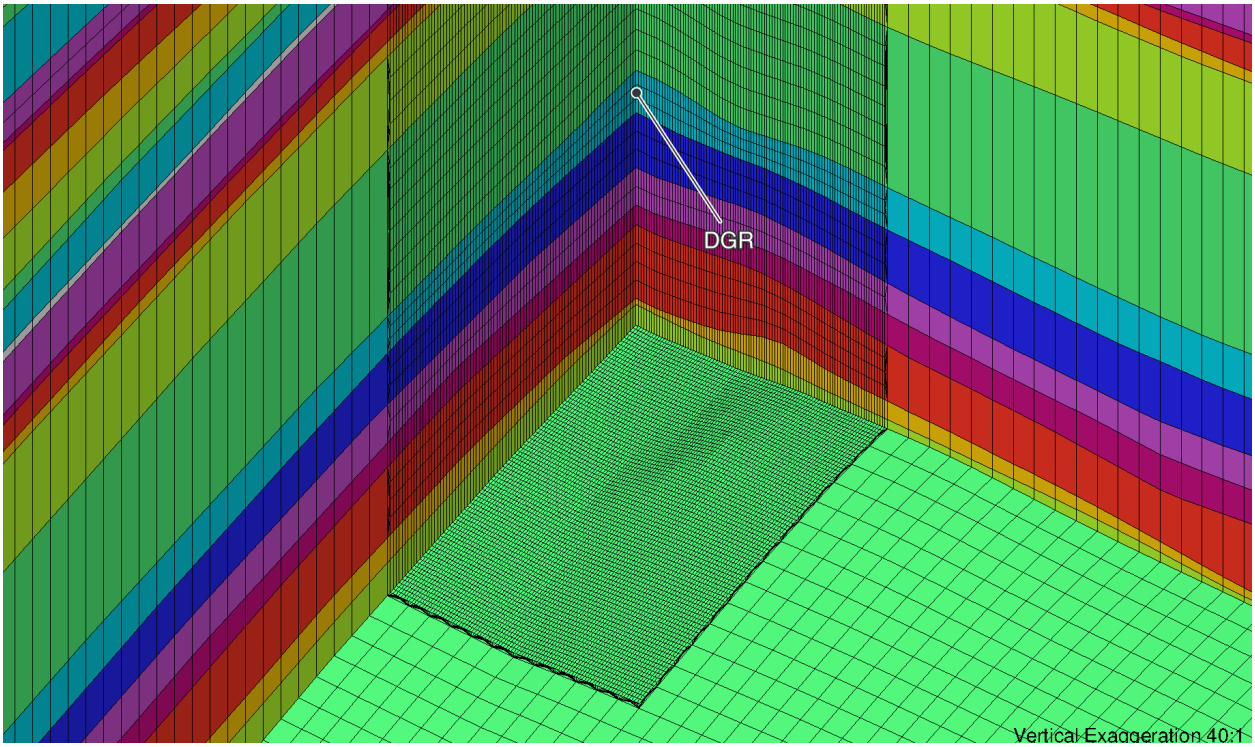

Figure 4.30: Regional-Scale Discretization Showing Vertical Details of Site-Scale Discretized Spatial Domain

The hydraulic properties used for the site-scale analyses and the verification of the embedment approach are the values developed in the site investigation (INTERA 2011) as presented in Section 2.5 of this report. The hydraulic and transport parameter values for each formation, unit or group are listed in Table 4.3. Each model layer was assigned unique but homogeneous properties. The parameters for the transport analysis are provided in Section 4.1.2. Using a grid Péclet number constraint, the longitudinal dispersivity coefficient was selected as approximately one half of the maximum length of the side of a site-scale grid block. The diffusion coefficients are listed in Table 4.9; temperature effects were not considered.

A caveat to the embedment approach in its current formulation in FRAC3DVS-OPG is that the selected longitudinal dispersivities used in the solute transport equation (refer to Equation (3.12) and Equation (3.13)) must satisfy the grid or cell Péclet and Courant constraints imposed by the coarser regional-scale elements or grid blocks. Thus, the embedment approach cannot take advantage of the finer site-scale discretization and use smaller values of the longitudinal dispersivity. As a consequence, the contribution to solute migration of mechanical dispersion may be overestimated. The boundary conditions for the embedment approach are those imposed on the regional-scale domain; the solution methodology is the same as that followed in the regional-scale analyses.

4.5.2 Saturated Flow: Base Case

The methodology used to determine solutions for the site-scale model are as follows:

i) A converged, temporally invariant, density-dependent solution for the regional-scale numerical model with the site-scale discretization embedded in it is obtained following the procedure described in Section 4.2.
ii) For the transient analyses with solely the site-scale numerical model, the initial conditions are the results for the equilibrated solution (pseudo-equilibrium at 1 Ma) for freshwater heads and total dissolved solids obtained in the preceding step. Dirichlet boundary conditions for the site-scale domain sides and bottom are based on the initial state (i.e., the solution from the preceding step). A Dirichlet boundary condition related to surface topography was used to represent the water table at the top of the site-scale domain. The zones for properties are identical to those used for the regional-scale analysis; this requirement is a constraint of the use of the embedment approach in FRAC3DVS-OPG.
iii) Transient site-scale analyses are obtained for freshwater head with brine transport disabled. This maintains a time-invariant TDS concentration distribution equal to the initial condition. The freshwater heads are dependent on the TDS distribution. The transient analyses assume saturated flow with the base-case parameters outlined in Table 4.3.

The base-case site-scale (scenario fs-base) solution for freshwater heads is depicted in blockcut view in Figure 4.31. Note that the vertical exaggeration for the site-scale blockcut views is 10:1. To clearly display the solution for freshwater heads at a pseudo-equilibrium time of 1 Ma, the results are presented in cross-section form in Figure 4.32. The upper figure is the north to south cross-section through the location of the DGR. The lower figure is the west to east cross-section through the DGR. The base-case site-scale pseudo-equilibrium solution for environmental heads are presented in blockcut view in Figure 4.33 and in cross-section view in Figure 4.34. Recall that environmental heads can be used to estimate vertical gradients while the freshwater heads can be used to estimate horizontal gradients.

The migration of a conservative tracer released to the Cobourg limestone at the proposed DGR site was investigated for the saturated base-case site-scale flow case. The source term for the

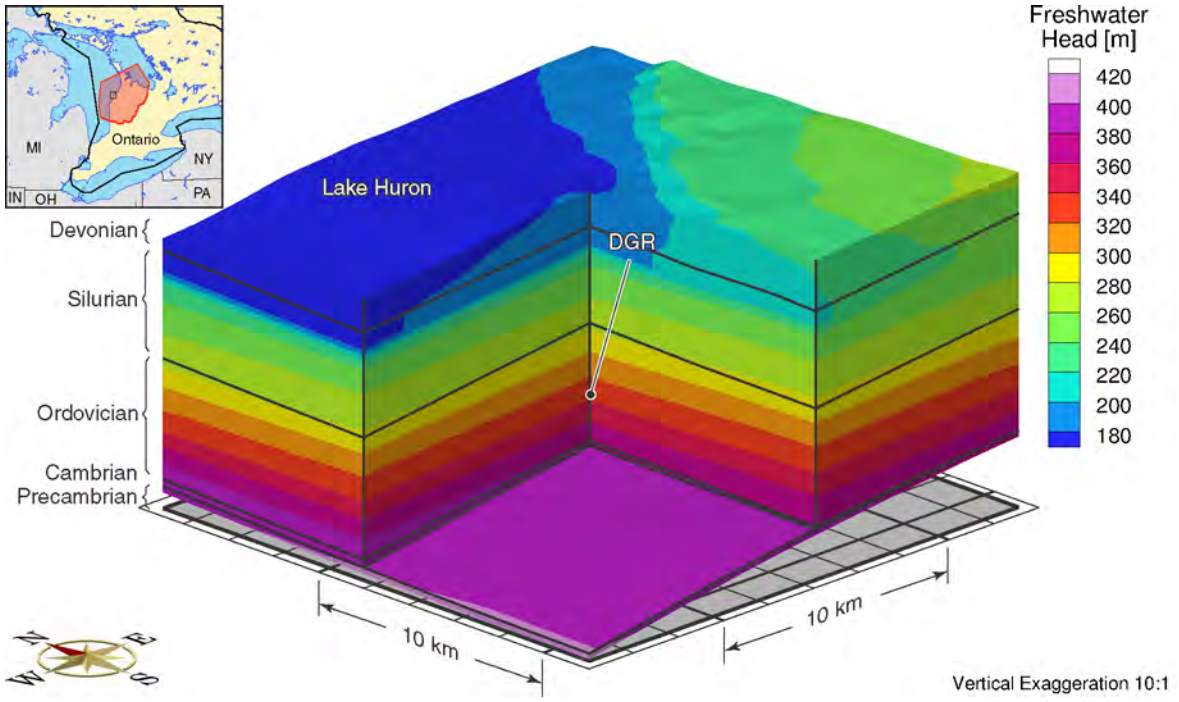

Figure 4.31: Freshwater Heads for the Base-Case Site-Scale Analysis with Equilibrated Regional-Scale Heads as the Initial Condition

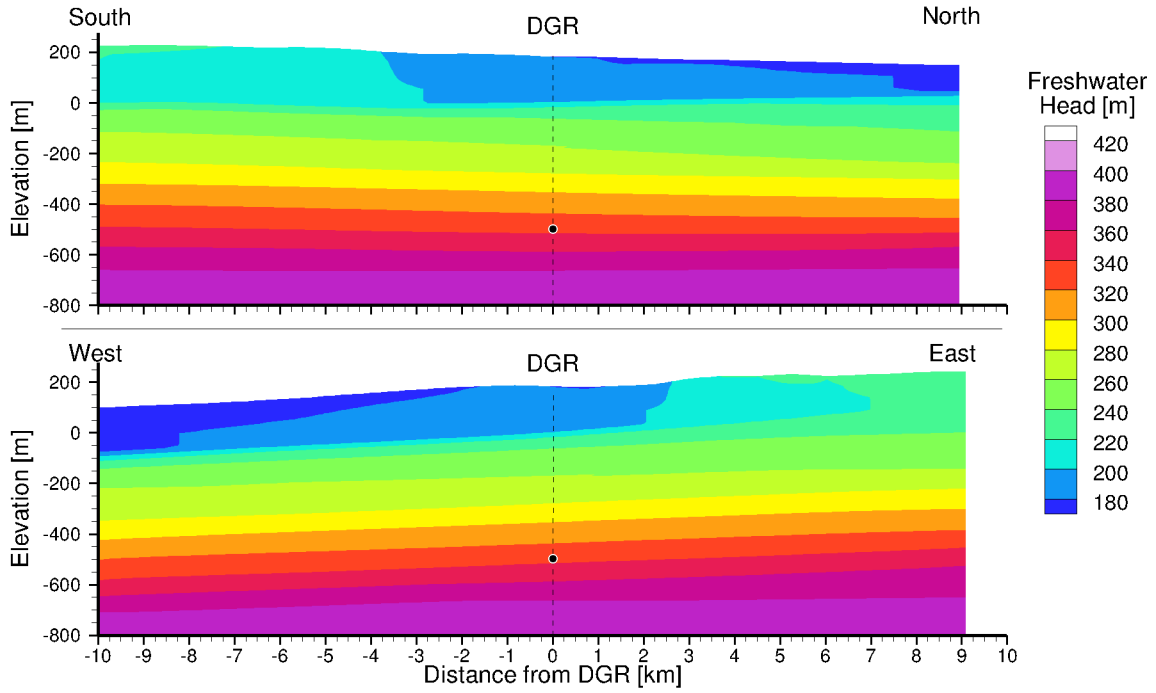

Figure 4.32: Cross Sections of Freshwater Heads for the Base-Case Site-Scale Analysis with Equilibrated Regional-Scale Heads as the Initial Condition

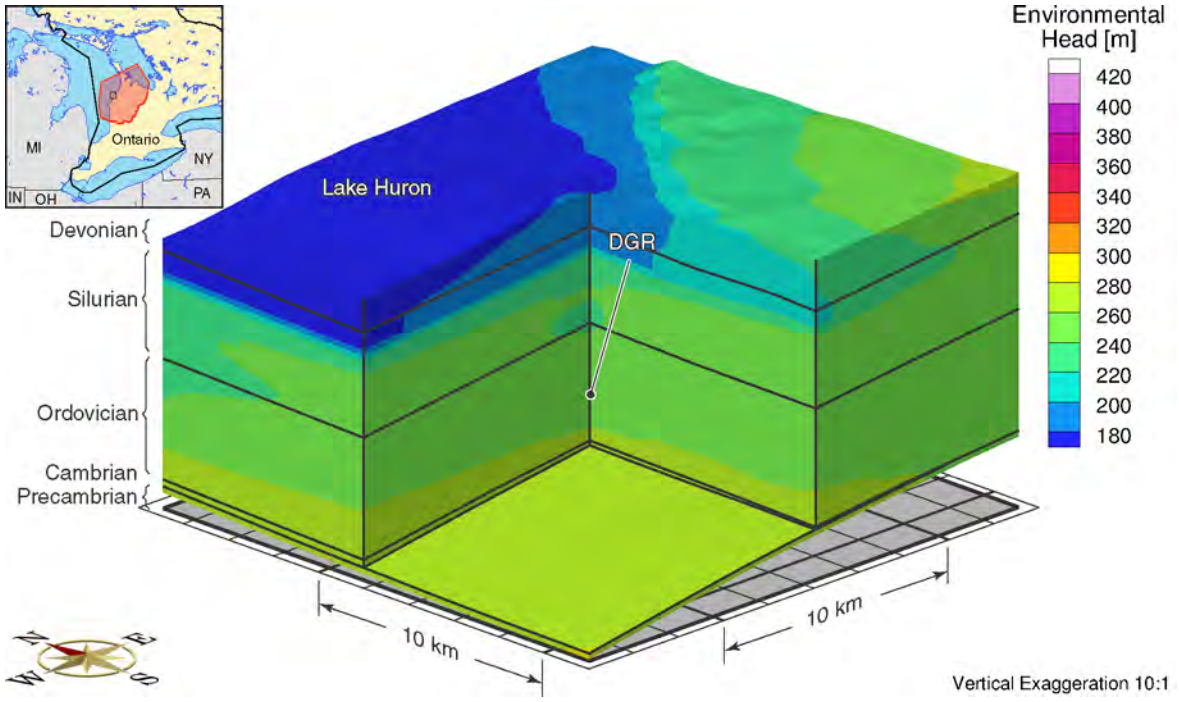

Figure 4.33: Environmental Heads for the Base-Case Site-Scale Analysis with Equilibrated Regional-Scale Heads as the Initial Condition

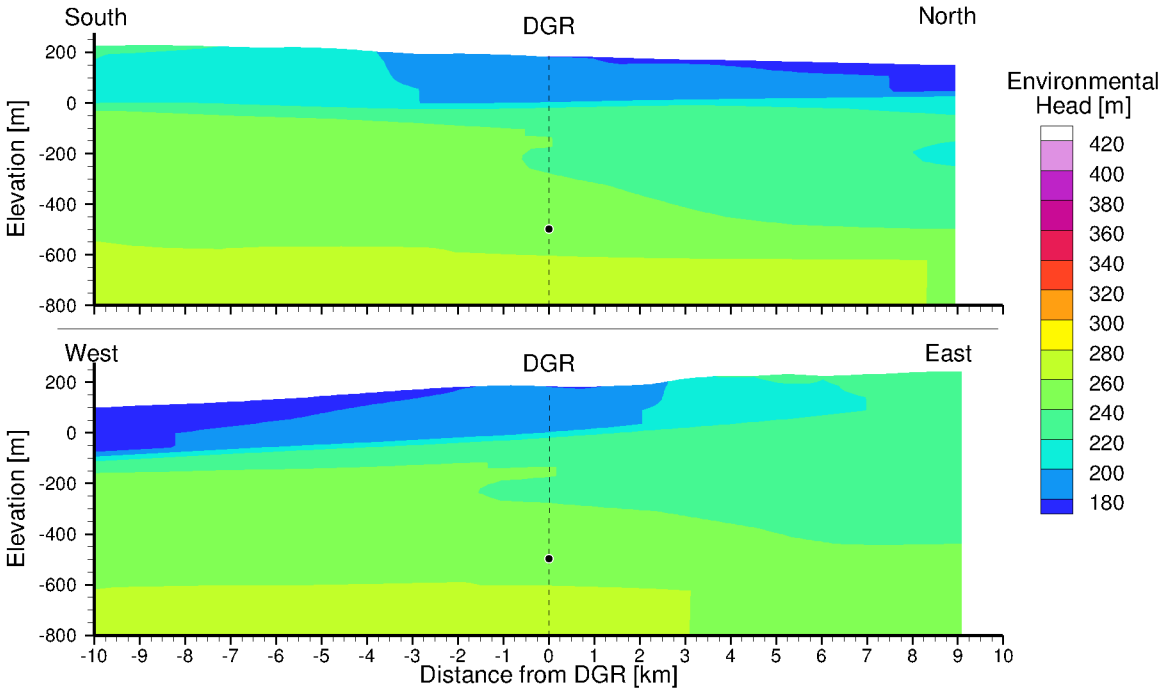

Figure 4.34: Cross Sections of Environmental Heads for the Base-Case Site-Scale Analysis with Equilibrated Regional-Scale Heads as the Initial Condition

conservative tracer was defined using prescribed concentrations of unity for the 8 nodes of a grid block at the horizontal direction centre of the site-scale grid in the middle layer of the 3 layers used to discretize the Cobourg. The analysis assumes that there is no decay of the source and that the solute neither decays nor adsorbs as it migrates. The transport parameters used for the analysis are given in Table 4.9. Unless otherwise specified, these settings will apply to all the subsequent site-scale analyses.

The spatial distributions of the tracer concentration for the base case and the pseudo-equilibrium flow state are plotted in cross-section form at 100 ka in Figure 4.35 and 1 Ma in Figure 4.36. The result of Figure 4.36 shows that the model simulated direction of flow in the Niagaran is towards the northwest. Advective transport is a mechanism for the tracer plume migration in the permeable Niagaran Group and Cambrian, and diffusive transport plays a key role in the other units with low permeability.

Figure 4.37 presents a log-log plot of the simulated breakthrough curve in the Niagaran Group and the Cambrian at the horizontal centre of the site-scale grid for the base case analysis. Breakthrough to the Cambrian occurs sooner than breakthrough to the Niagaran as the Cambrian is closer to the tracer source at the centre of the Cobourg limestone.

Cross-section views of the concentration for the same case but with the incorporation of a weathered zone in the upper Precambrian (scenario fs-base-hkp) are shown at 100 ka in Figure 4.38 and 1 Ma in Figure 4.39. A comparison of the results at 1 Ma for Figure 4.36 with those of the weathered zone case of Figure 4.39 demonstrates no obvious difference as the permeable Cambrian unit tends to diminish the impact of the weathered zone on the migration of the tracer plume.

4.5.3 Analysis of Measured Pressure Profile at the DGR Boreholes

The environmental head distribution versus depth for the DGR-4 borehole is plotted in Figure 2.15. The data in the figure are based on the pressure measurements DGR-4 on June 6, 2008, August 24, 2009, November 15, 2009, and February 25, 2010. Relative to the ground surface at DGR-4 of 181.6 mASL, the profile indicates that the Cambrian is over-pressured while units in the upper Ordovician are significantly under-pressured thus reflecting a water deficit relative to the amount of water that would be in the pores for pressures that are hydrostatic relative to the elevation of the ground surface. This section does not address whether the water deficit is related to either the presence of a separate gas phase in the pores or is a result of a stress effect and the dilation of the pores. The evolution of these pressures as they equilibrate to the present day boundary conditions is investigated in this study using the saturated site-scale model (scenario fs-base-under-pressure); this section presents an analysis using DGR-3 and DGR-4 borehole data (INTERA 2011). Instead of the pseudo-equilibrium state, the modelling methodology undertakes transient saturated site-scale analyses of flow with the August 24, 2009 measured pressure profile at the DGR-4 borehole defining the initial condition. The environmental head profile of Figure 2.15 indicates an upward gradient from the Cambrian to the Ordovician and a downward gradient from the Niagaran to the Ordovician. To simulate the evolution of the measured pressure gradient using the site-scale model, the initial heads for each site-scale layer are calculated from the pseudo-equilibrium heads from the sub-gridded regional-scale model by subtracting the difference between the pseudo-equilibrium and measured heads at the DGR-4 borehole for a given layer. The procedure ensures that the gradients in each model layer of the adjusted model are the same as those calculated for the base-case site-scale model.

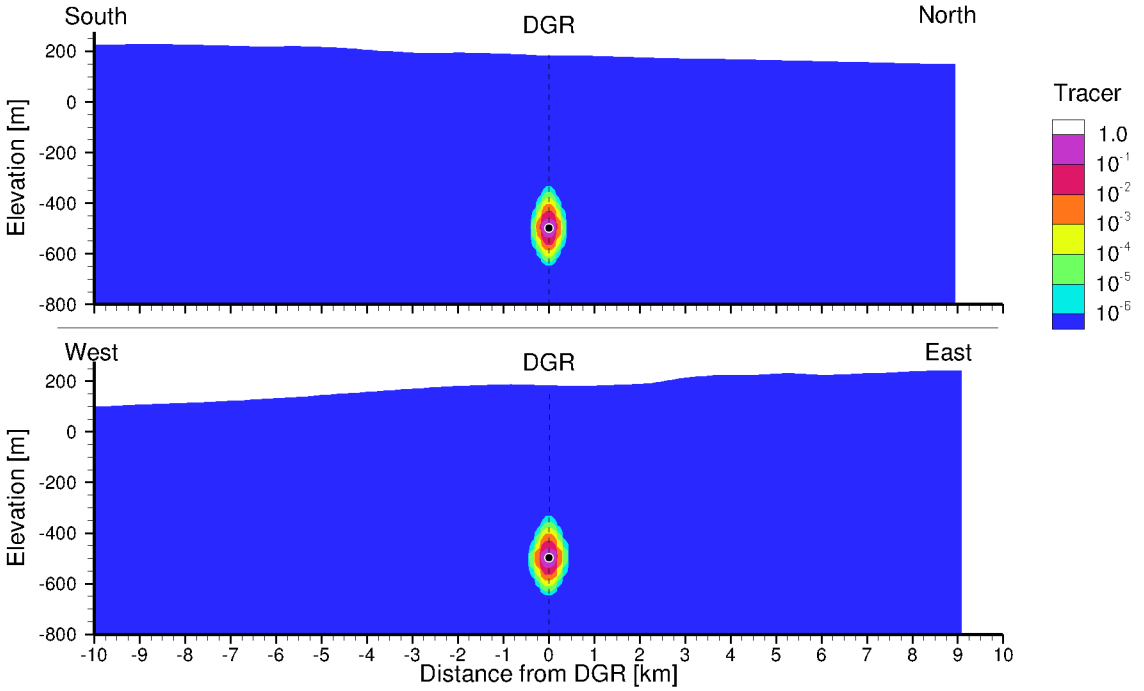

Figure 4.35: Cross-Section View of the Spatial Distribution of a Tracer at 100 ka with Equilibrated Regional-Scale Heads as the Initial Condition

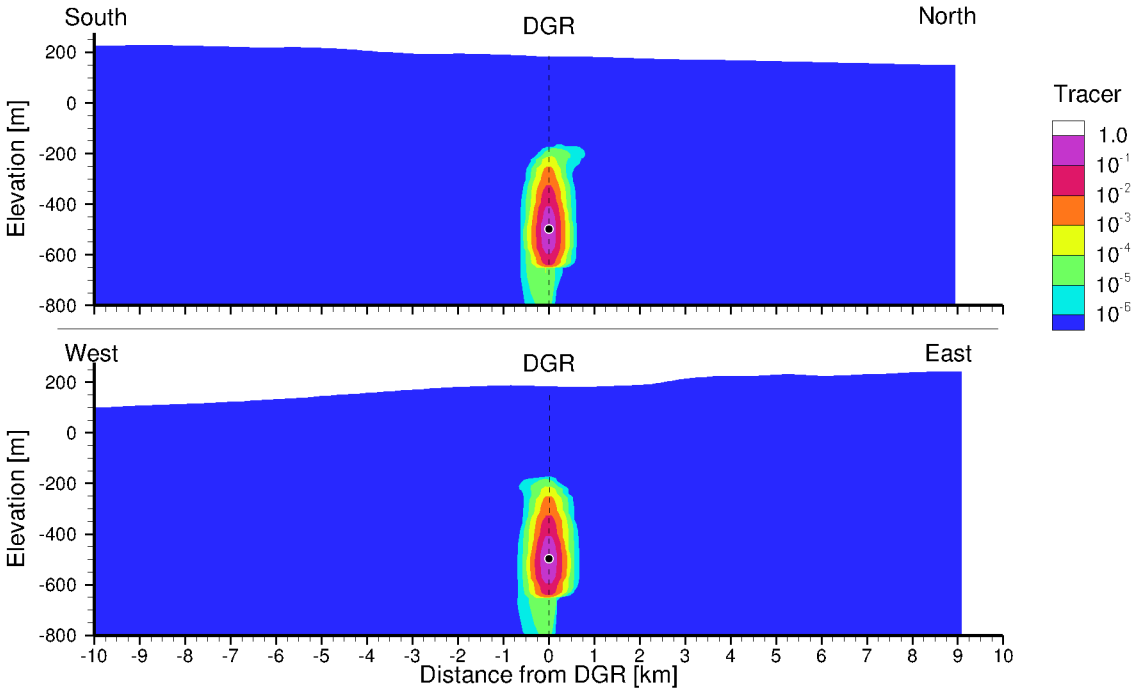

Figure 4.36: Cross-Section View of the Spatial Distribution of a Tracer at 1 Ma with Equilibrated Regional-Scale Heads as the Initial Condition

Instead of Dirichlet lateral boundary conditions for the base-case site-scale analysis, the lower Silurian (except the Niagaran), Ordovician and Cambrian units are assigned as zero flux Neumann boundary condition. Pressure support for the Cambrian is provided by using a Dirichlet boundary condition for all layers of the Precambrian with the freshwater head level being determined by the measured head for the Cambrian in the DGR-4 borehole. It is noted that the Cambrian sandstone is not continuous across the site-scale model domain. The gradient across the Precambrian was maintained to that of the base-case site-scale analysis.

The issue investigated in this section is: the assessment of the vertical hydraulic conductivities for the units of the Black River Group in the Ordovician sediments. Referring to Table 4.3, these units are the Shadow Lake, Gull River and Coboconk. A vertical to horizontal hydraulic conductivity anisotropy ratio of 0.001 was assumed for the Coboconk, Gull River and Shadow Lake Formations for both the regional-scale and site scale base-case modelling results.

In addition to the base-case vertical to horizontal hydraulic conductivity anisotropy ratio of 0.001 for the lower Ordovician units, to further assess the sensitivity of the head profile to the anisotropy ratios, ratios of 0.1 (scenario fs-10kv-under-pressure) and 0.01 (scenario fs-100kv-under-pressure) for the Black River Group also were investigated; thus, the horizontal hydraulic conductivities for the Ordovician units were constant for all analyses while the vertical hydraulic conductivities were determined from the horizontal values using the given factors.

The results for the three cases are plotted in Figure 4.40, Figure 4.41 and Figure 4.42. For all 3 cases, the results indicate that at 300 ka there is still a downward gradient from the Niagaran to

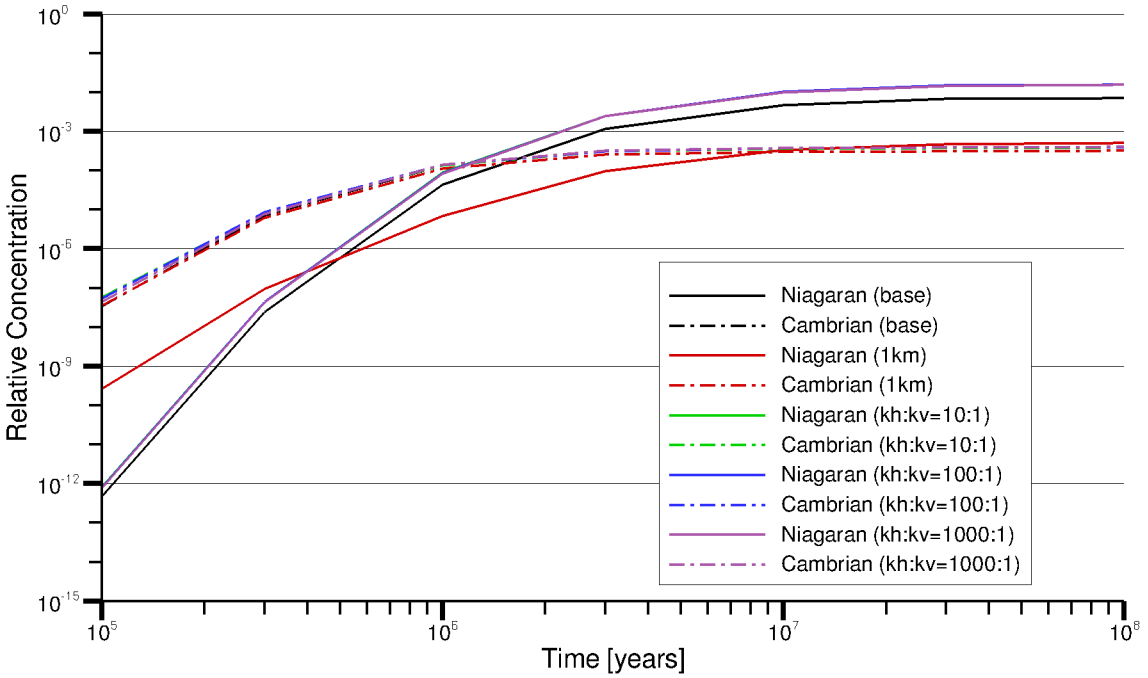

Note: The base case uses the initial condition derived from the regional-scale simulation; all other curves are based on the under-pressured initial condition.

Figure 4.37: Tracer Breakthrough Curves at the Niagaran Group and Cambrian for the Site-scale Analyses

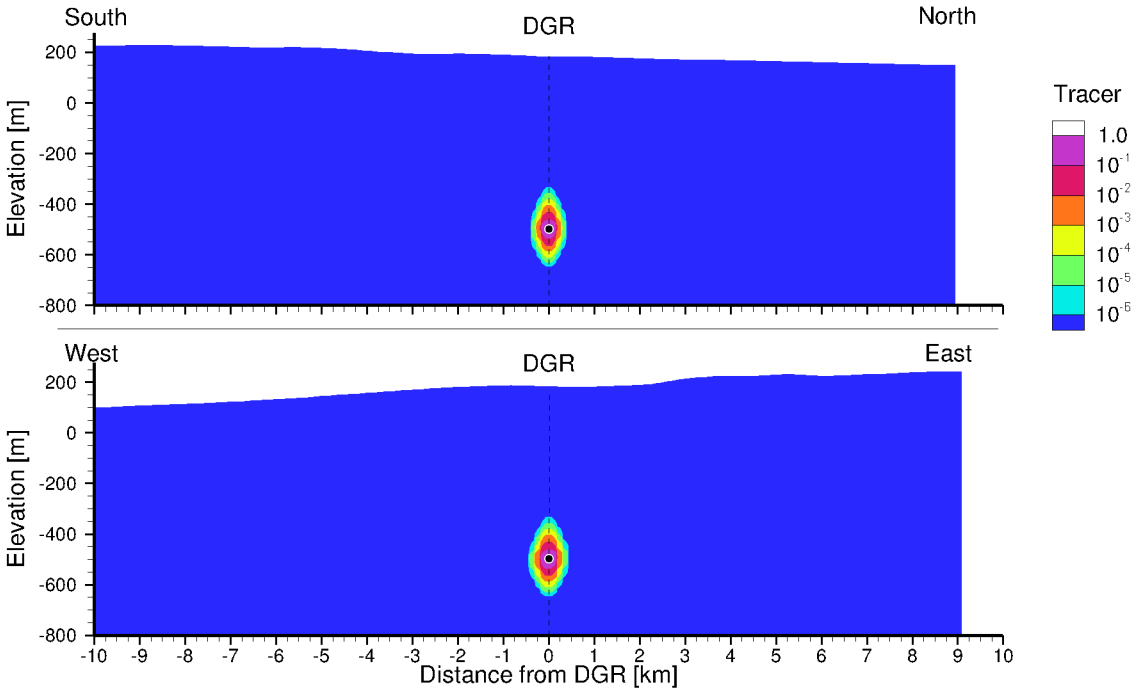

Figure 4.38: Weathered Zone in the Precambrian: Cross-Section View of the Spatial Distribution of a Tracer at 100 ka with Equilibrated Regional-Scale Heads as the Initial Condition

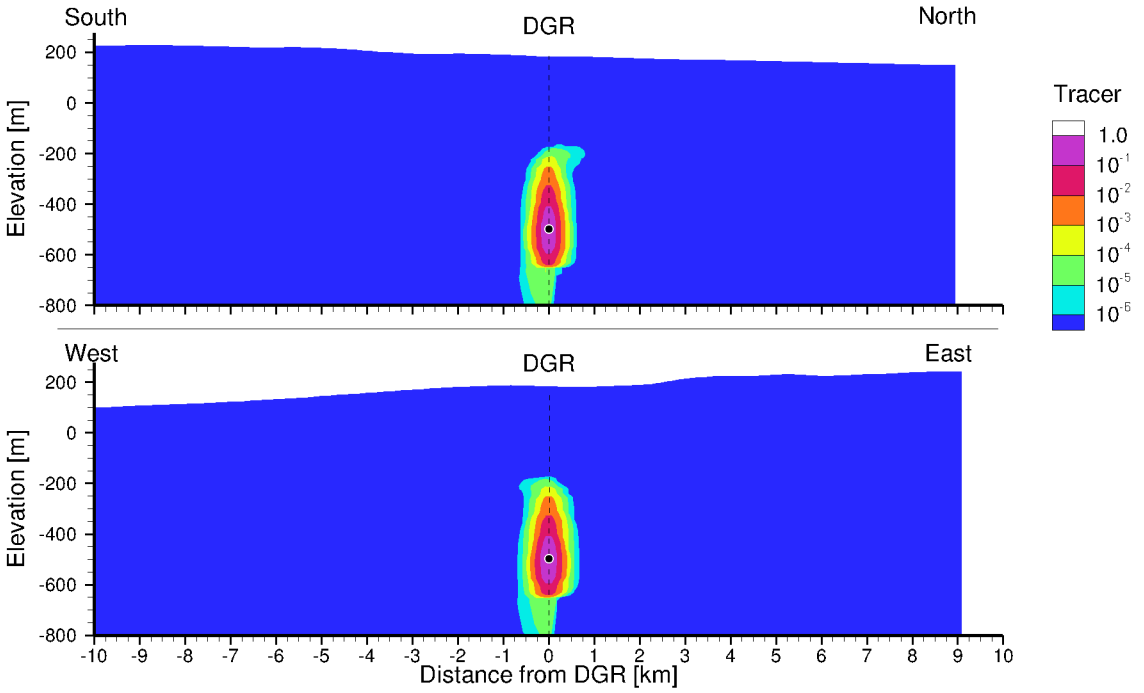

Figure 4.39: Weathered Zone in the Precambrian: Cross-Section View of the Spatial Distribution of a Tracer at 1 Ma with Equilibrated Regional-Scale Heads as the Initial Condition

the Ordovician. The pressure and related water deficit in the Ordovician has been met by approximately 1 Ma. Steady-state pressures are reached by 3 Ma with an upward gradient developing from the Cambrian to the surface. In the second case where the Shadow Lake, Gull River and Coboconk units of the Ordovician Black River Group have hydraulic conductivity anisotropy ratios of 0.1, the environmental head profiles of Figure 4.41 indicate that the over-pressurization of the Cambrian propagates quickly in these units such that the hydrostatic state with minimal vertical hydraulic gradient is reached by 10 ka. For all 3 cases, the water deficit in the Ordovician is met by the very slow influx from either the Cambrian or the Niagaran Group.

The spatial distributions of the tracer concentration for the base case with the measured under-pressure profile imposed as the initial condition are plotted in cross-section form at 100 ka in Figure 4.43 and 1 Ma in Figure 4.44. Comparing to the tracer distributions for the base case with pseudo-equilibrium state in Figure 4.35 and Figure 4.36, the same contour pattern of tracer evolution is observed. As opposed to the original pseudo-equilibrium state as the initial condition, using the under-pressure profile with steep hydraulic gradients has no apparent impact on both the timing and the pathway for the plume migration, which indicates that the tracer migration in the Ordovician is diffusion dominant.

The tracer breakthrough curves for the Niagaran and the Cambrian for the two different anisotropy cases for the Black River Group are plotted in Figure 4.37. The base-case breakthrough curves are also shown in the figure. It is noted that the curves for the three cases overlap. The similarity of the breakthrough curves confirms the conclusion that solute transport in the Ordovician is dominated by diffusion and that the impact on solute transport of pore velocity in the deep Ordovician limestone is negligible.

4.5.4 Analysis of Hypothetical Discrete Fracture Zones

The impact on both the pressure evolution in the Ordovician limestone and shale and the migration of a tracer from the Cobourg limestone was investigated for cases in which a hypothetical discrete fracture zone connecting the Cambrian sandstone and the Niagaran Group is located at an arbitrary distance from the tracer source grid block. The plane of the vertical discrete fracture zone was oriented in the north-south direction at a distance west of the tracer grid block. This provides a conservative analysis as the impact of a fracture zone east of the site is lessened by possible absence of the Cambrian. An equivalent porous media approach was used to characterize the 2 km long fracture zone that was assigned a hydraulic conductivity of 3.0×10^{-6} m/s and a fracture zone width of 1 m. The site-scale base-case parameters were used for the analysis. The configurations investigated include a hypothetical discrete fracture zone 1 km west (scenario fs-1km) of the tracer source zone grid block and a fracture zone 5 km west (scenario fs-5km).

The first analyses use the flow boundary conditions, initial pressure distribution and solution methodology of the base-case site-scale analysis. Cross-section views of the tracer concentration for the base-case site-scale fracture simulations are plotted at 100 ka and 1 Ma in Figure 4.45 to Figure 4.48. The upward hydraulic gradient from the Cambrian to the Niagaran for the base-case site-scale model forces an upward groundwater flow via the fracture zone reducing the heads in the Cambrian at the fracture creating a small sink and raising the heads in the Niagaran at the fracture creating a mound. The result is a reduced vertical gradient at the fracture as compared to that estimated for the Ordovician without a fracture. A review of the discrete fracture cases reveals that for the case with the fracture zone 1 km west of the proposed DGR site, the pathway for the solute tracer is migration by diffusion upward to the Niagaran Group and downward to the Cambrian. Some tracer in the Cambrian also migrates by advection and

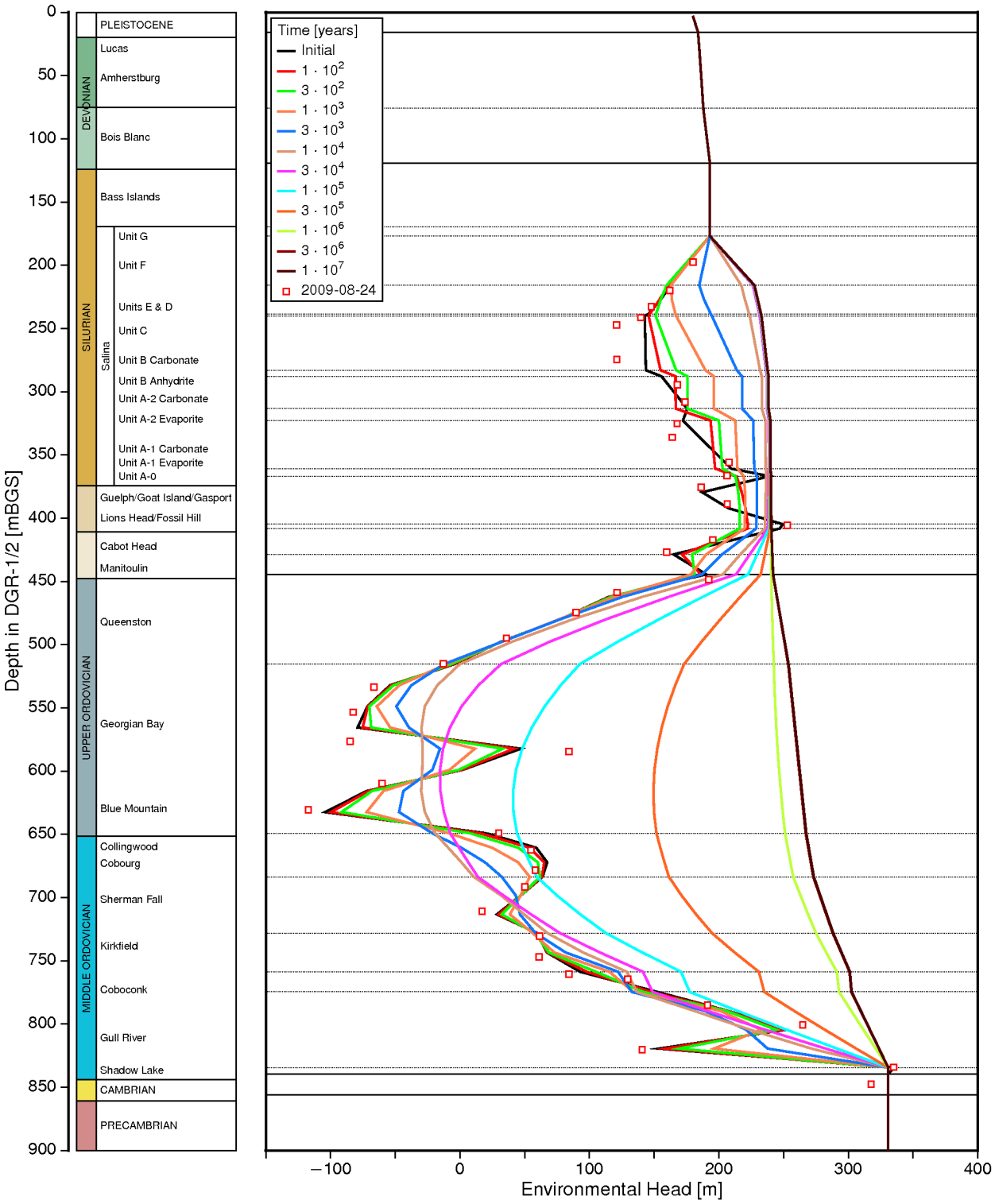

Figure 4.40: Predicted Evolution of Environmental Heads with Pressure Support in Both the Niagaran Group and Cambrian

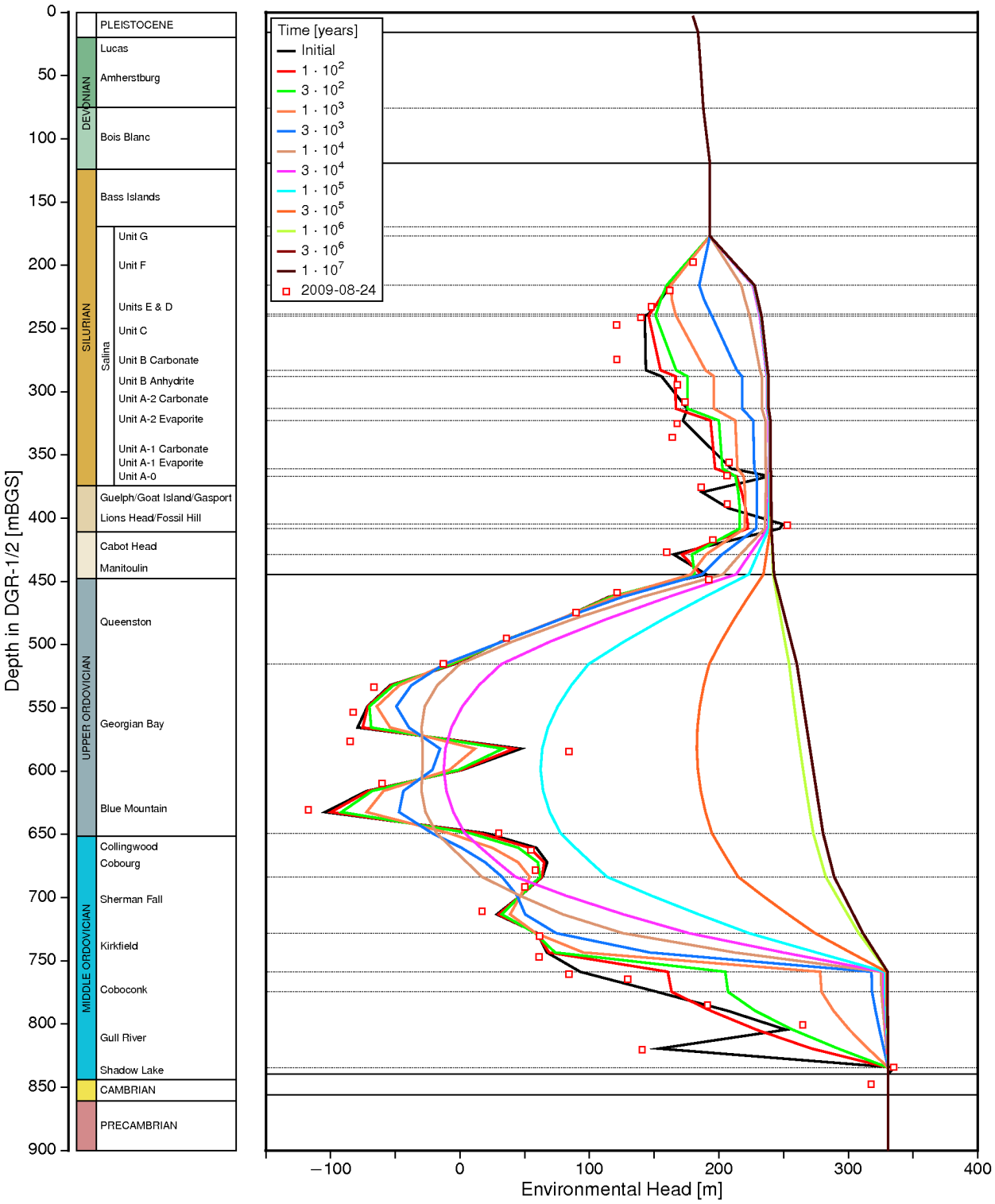

Figure 4.41: Anisotropy Ratio of 0.1 for the Black River Group: Predicted Evolution of Environmental Heads with Pressure Support in Both the Niagaran Group and Cambrian

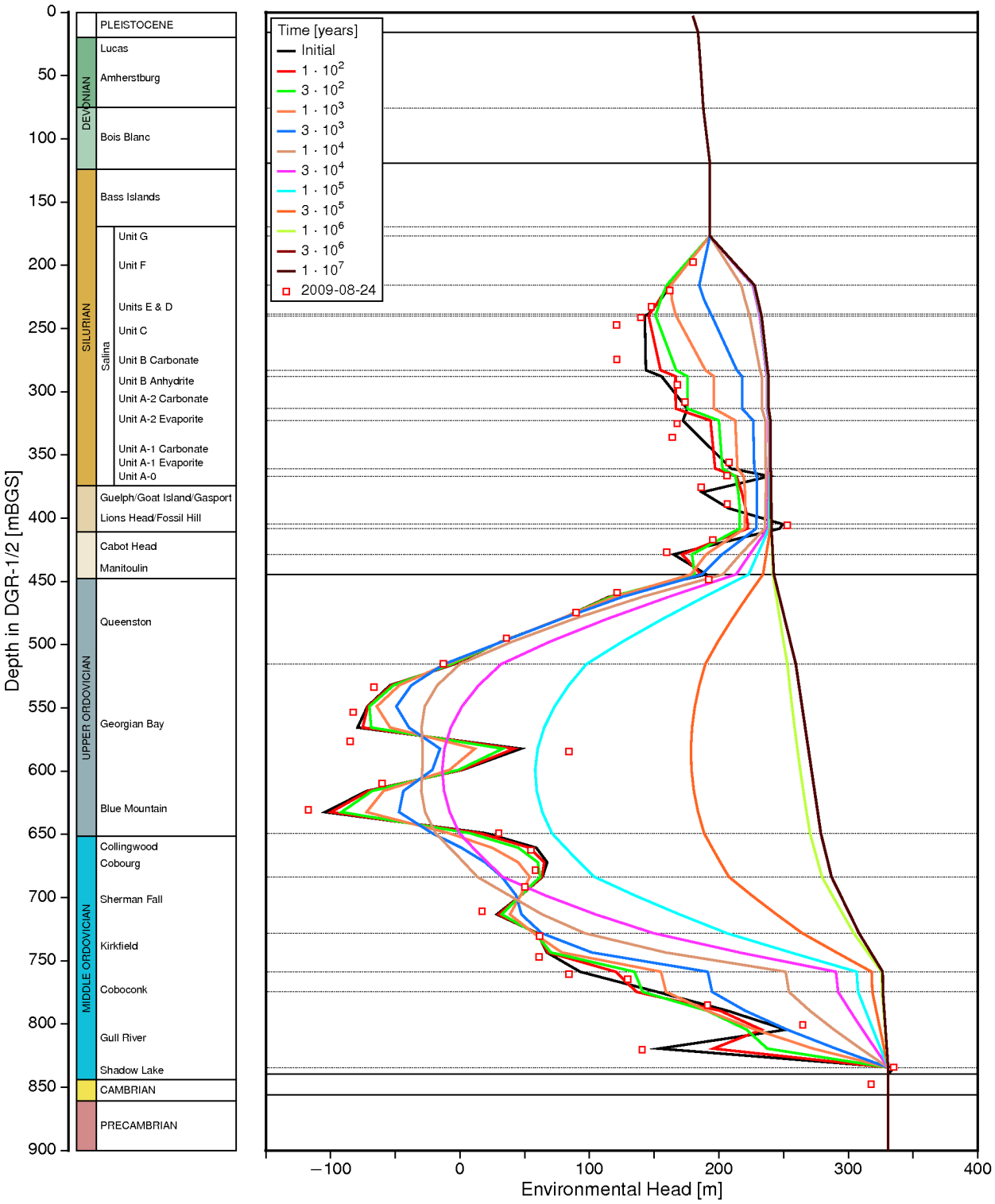

Figure 4.42: Anisotropy Ratio of 0.01 for the Black River Group: Predicted Evolution of Environmental Heads with Pressure Support in Both the Niagaran Group and Cambrian

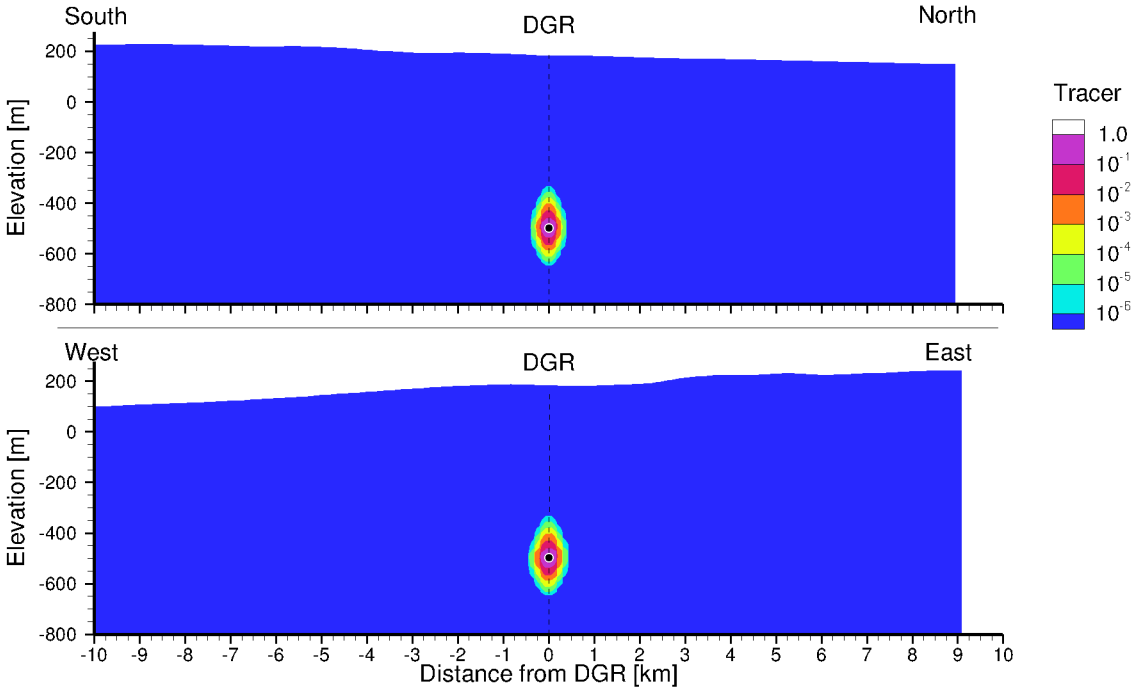

Figure 4.43: Under-Pressure in the Ordovician: Cross-Section View of the Spatial Distribution of a Tracer at 100 ka for Pressure Support in the Cambrian and Niagaran

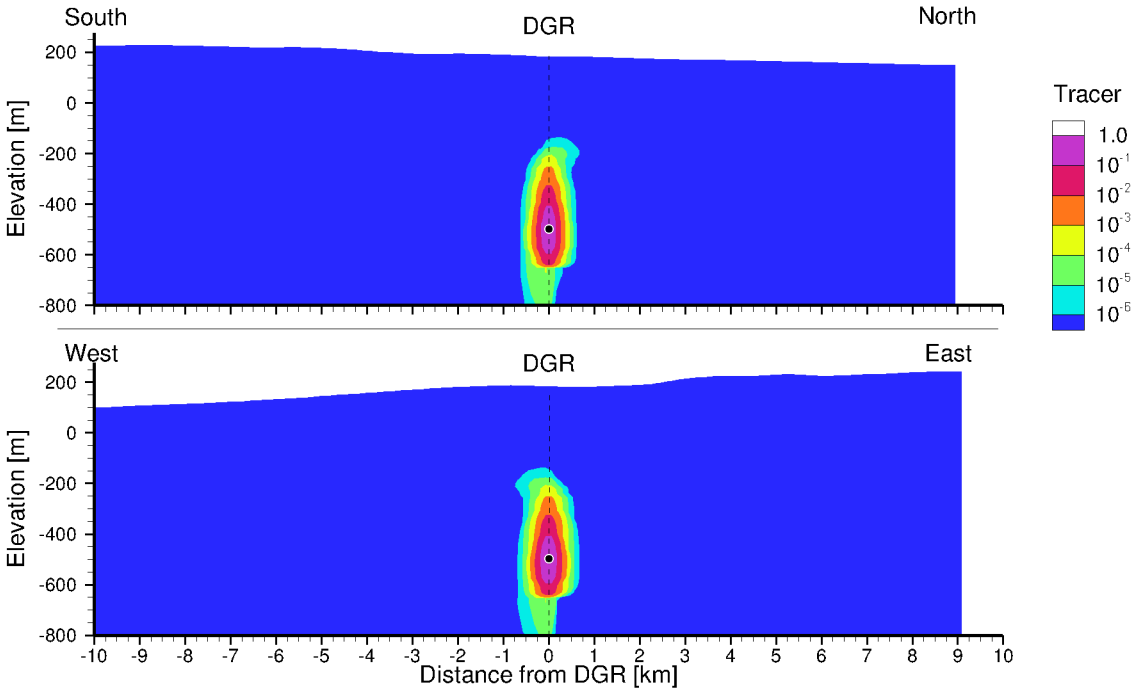

Figure 4.44: Under-Pressure in the Ordovician: Cross-Section View of the Spatial Distribution of a Tracer at 1 Ma for Pressure Support in the Cambrian and Niagaran

hydrodynamic dispersion towards the sink associated with the 1 km distant fracture and then vertically upward by advection from the Cambrian to the Niagaran through the fracture yielding the tracer distribution shown in Figure 4.46.

For the case with a fracture zone 5 km west of the DGR, the plume at 1 Ma shown in Figure 4.48 is similar to that of the base case without a fracture shown in Figure 4.36. The fact that there is only a slight difference in the tracer distribution in the Niagaran indicates that a fracture 5 km west of the proposed DGR site is too far from the DGR to have a significant impact on the evolution of the tracer plume in the Cambrian. There is no component of the tracer drawn toward the fracture and no upward migration of the tracer through the fracture from the Cambrian to the Niagaran Group for the 5 km fracture case.

In the second case, the impact of fracture zone configurations on the pressure distribution observed in the DGR-4 borehole was investigated. The parameters, boundary conditions and initial conditions are the same as that used for the analyses in Section 4.5.3. The evolution of the environmental heads observed in the DGR-4 borehole for the case with a discrete fracture zone 1 km west of the tracer source grid block is shown in Figure 4.49. A comparison of the analyses with the base-case results without a discrete fracture zone (Figure 4.40) reveals that the fracture zone significantly perturbs the pressure in the Niagaran Group by propagating the over-pressure of the Cambrian to the Niagaran Group through the hypothetical discrete fracture. It still takes 3 Ma for the pressures in the Ordovician limestone and shale to reach steady-state.

Cross-section views of the tracer concentration for the case with a fracture zone 1 km west and the measured DGR-4 under-pressure profile (scenario fs-1km-under-pressure) assigned as the initial condition are plotted in block-cut form at 100 ka in Figure 4.50 and 1 Ma in Figure 4.51. The imposed hydraulic gradient between the Niagaran and Cambrian units forces an upward groundwater flow via the fracture zone. For Figure 4.51, the pathway for the solute tracer is vertically downward by diffusion to the Cambrian and then horizontal migration occurs in the Cambrian to the fracture. The higher vertical gradient for this case, as compared to the base-case site-scale analysis of Figure 4.45 to Figure 4.46, results in the migration of all solute reaching the Cambrian towards the sink created by the hypothetical fracture. The tracer subsequently migrates up the fracture to the Niagaran Group where it can spread out by advection, mechanical dispersion and diffusion. Vertically upward migration from the tracer source to the Niagaran Group also occurs by diffusion. The tracer plume doesn't spread out in the Cambrian. The distributions of the hydraulic heads at 1 Ma for this case are shown in Figure 4.52 for the freshwater heads and Figure 4.53 for the environmental heads. The results indicate there exists an upward hydraulic gradient at the proposed DGR site and the fracture zone serves as the conduit connecting two permeable units, the Niagaran Group and Cambrian. At the fracture zone the heads in the Cambrian are reduced creating a sink while heads in the Niagaran at the fracture are increased creating a mound. The result is a reduced vertical gradient at the fracture as compared to that estimated for the Ordovician without a fracture.

4.5.5 Summary of Under-pressured Ordovician Sequence

This Section has investigated the evolution of the under-pressured Ordovician limestone and shale using transient site-scale saturated flow analyses that have boundary conditions for the permeable units that are derived from the regional-scale base-case analysis using the embedment approach. The initial condition for the environmental heads of the Ordovician sediments are the base-case regional-scale values and in a second case, the values estimated for the measured August 24, 2009 pressures in the DGR-4 borehole. The hydraulic parameters for the analyses are shown in Table 4.3. Based on the analyses it is concluded that it will take

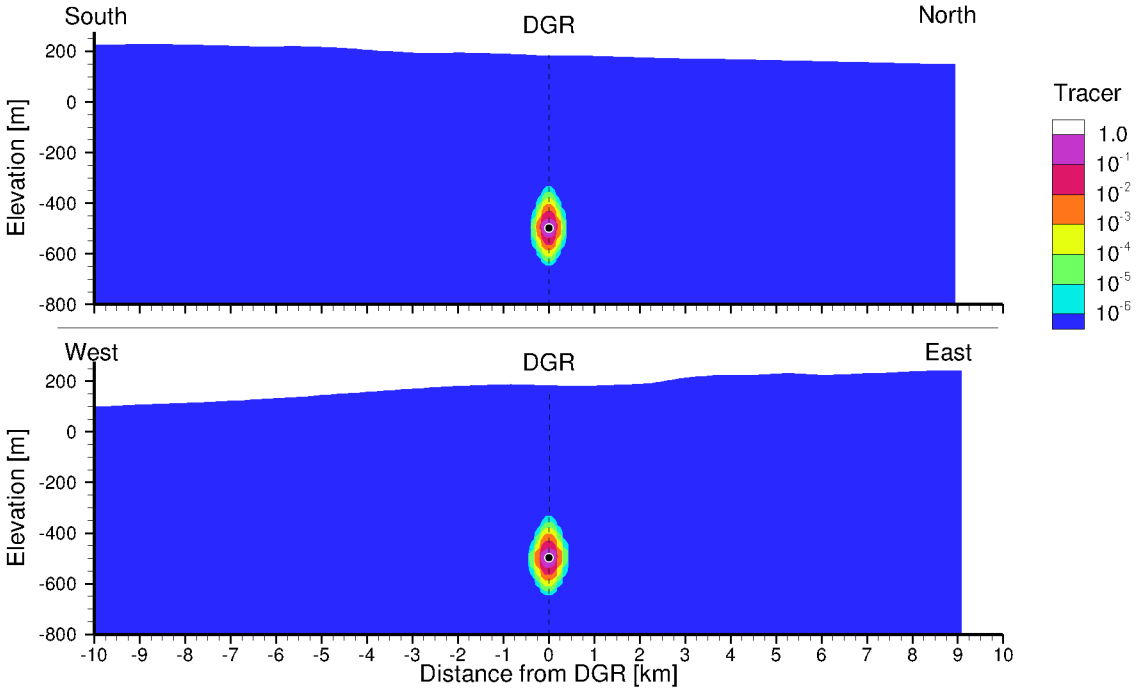

Figure 4.45: Fracture Zone 1 km from DGR: Cross-Section View of the Spatial Distribution of a Tracer at 100 ka with the Pseudo-Equilibrium State as Initial Condition

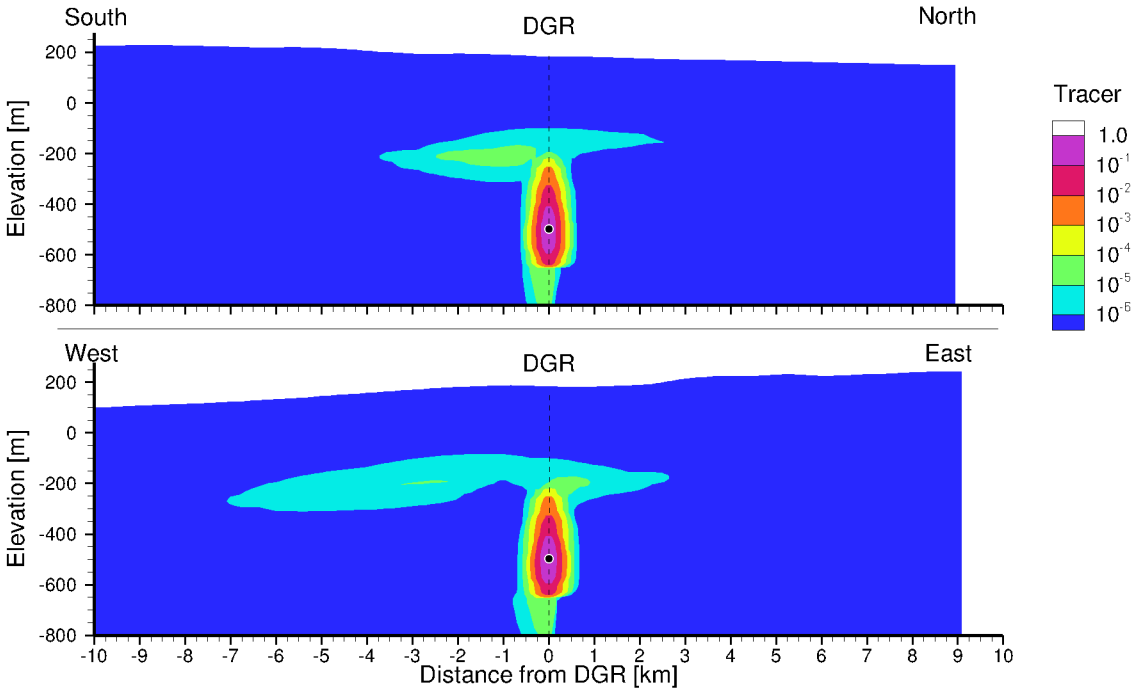

Figure 4.46: Fracture Zone 1 km from DGR: Cross-Section View of the Spatial Distribution of a Tracer at 1 Ma with the Pseudo-Equilibrium State as Initial Condition

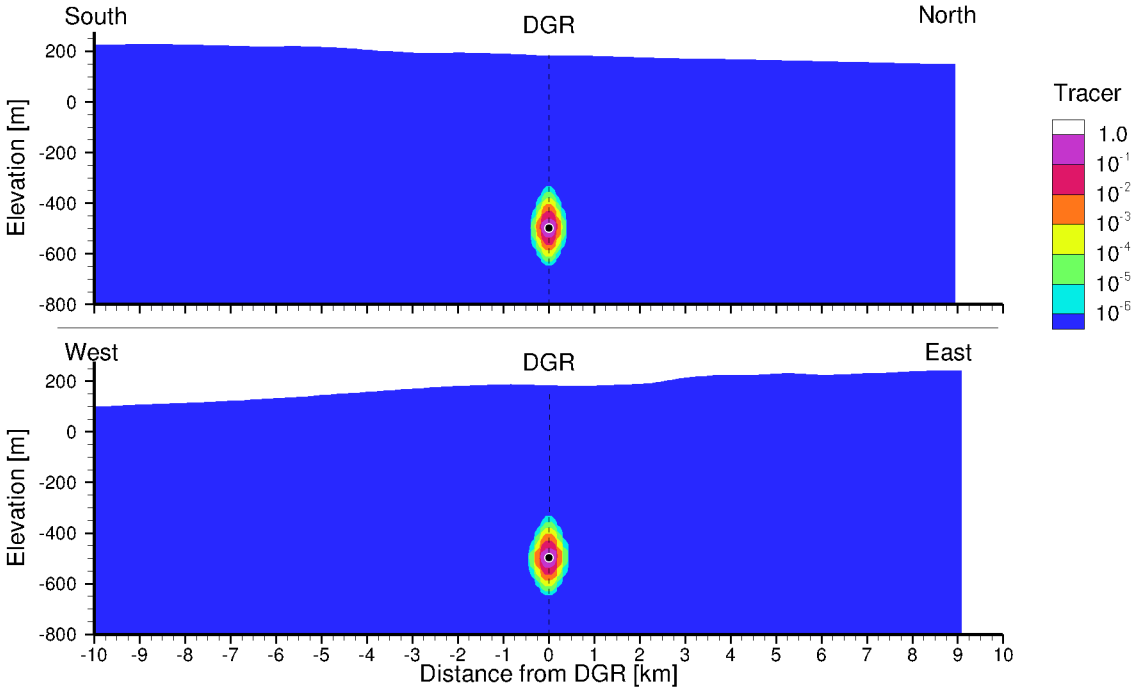

Figure 4.47: Fracture Zone 5 km from DGR: Cross-Section View of the Spatial Distribution of a Tracer at 100 ka with the Pseudo-Equilibrium State as Initial Condition

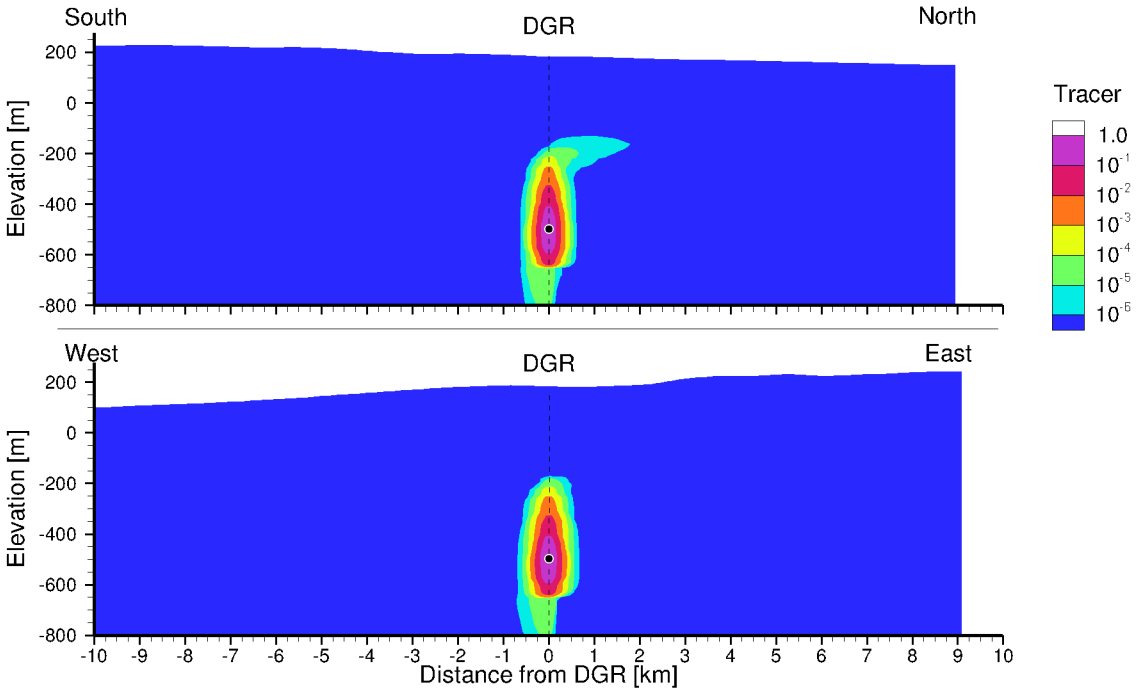

Figure 4.48: Fracture Zone 5 km from DGR: Cross-Section View of the Spatial Distribution of a Tracer at 1 Ma with the Pseudo-Equilibrium State as Initial Condition

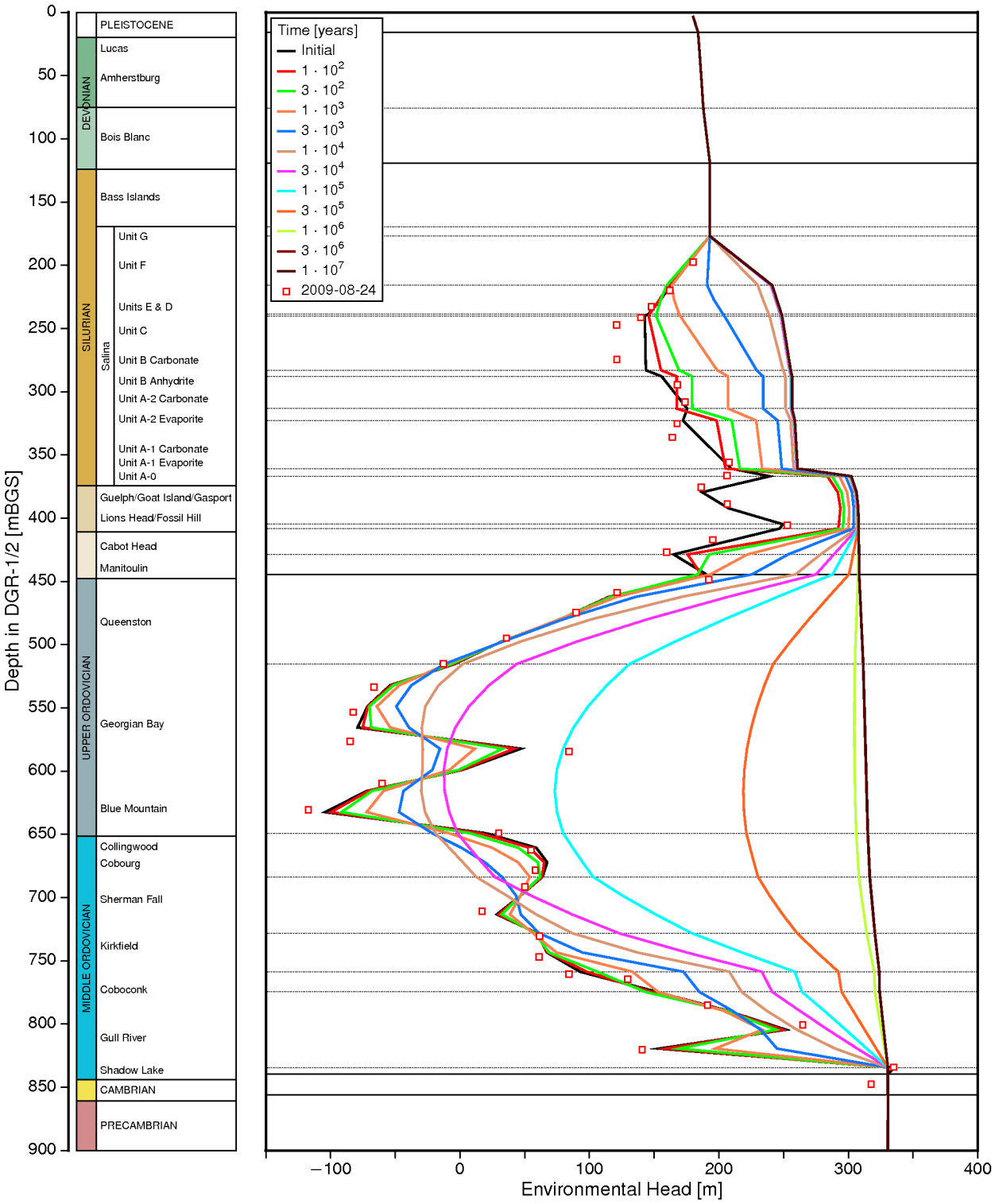

Figure 4.49: Fracture Zone 1 km from DGR: Predicted Evolution of Environmental Heads with Pressure Support in Both the Niagaran Group and the Cambrian

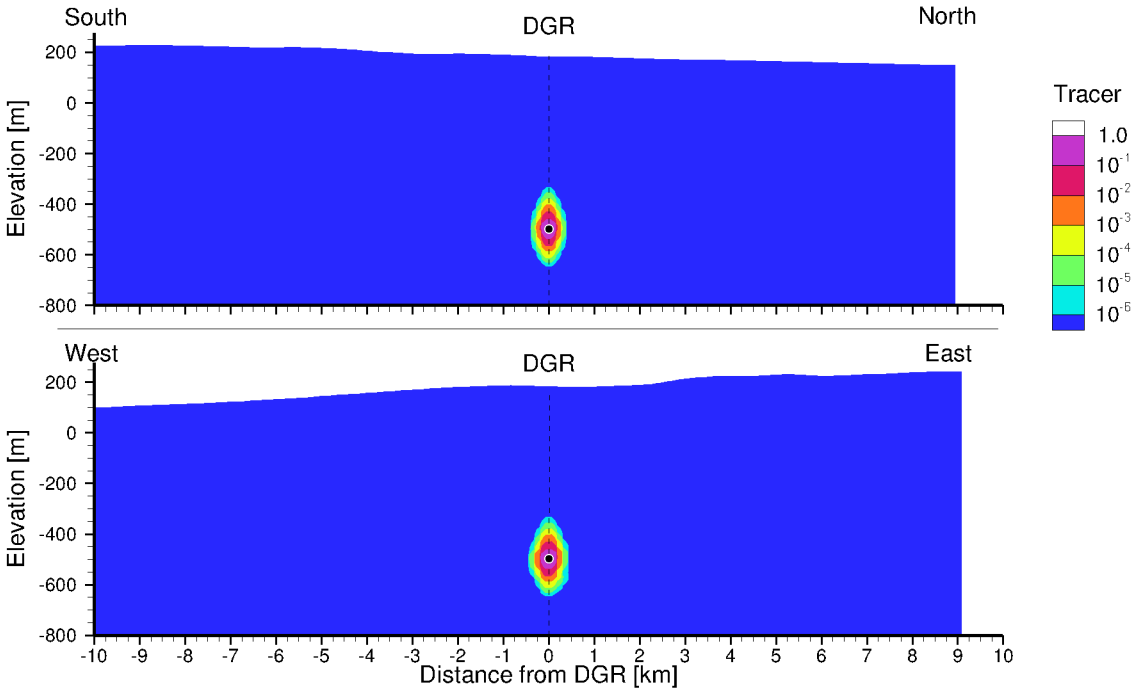

Figure 4.50: Fracture Zone 1 km from DGR and Under-Pressure in the Ordovician: Cross-Section View of the Tracer at 100 ka for Pressure Support in the Cambrian and Niagaran Group

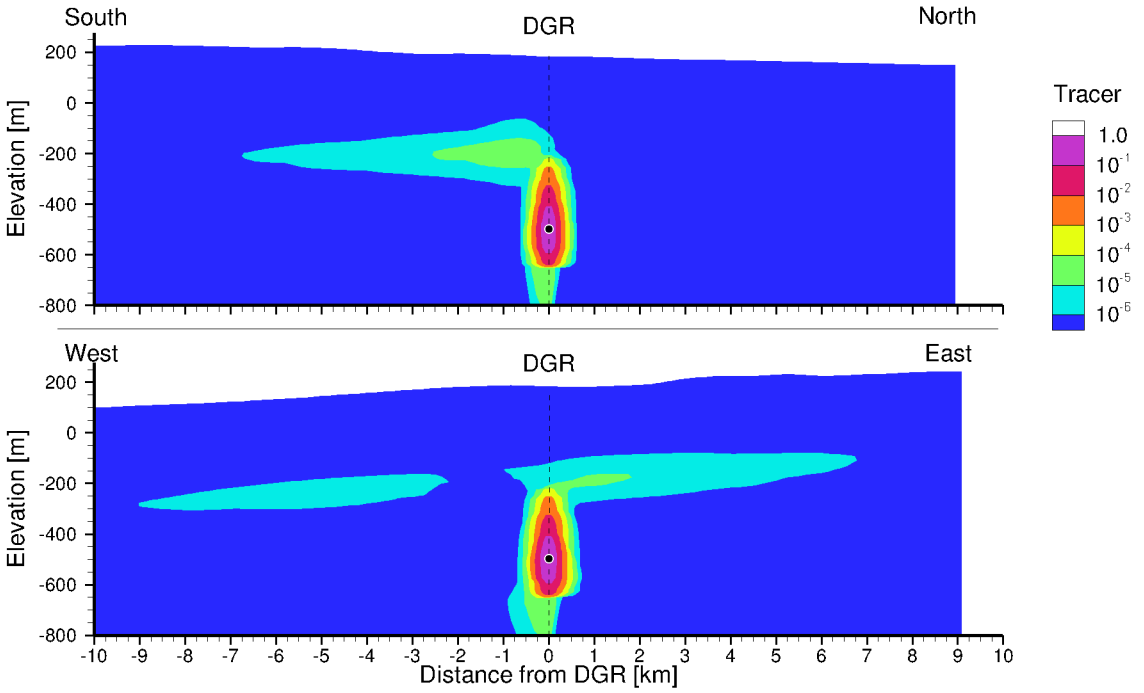

Figure 4.51: Fracture Zone 1 km from DGR and Under-Pressure in the Ordovician: Cross-Section View of the Tracer at 1 Ma for Pressure Support in the Cambrian and Niagaran Group

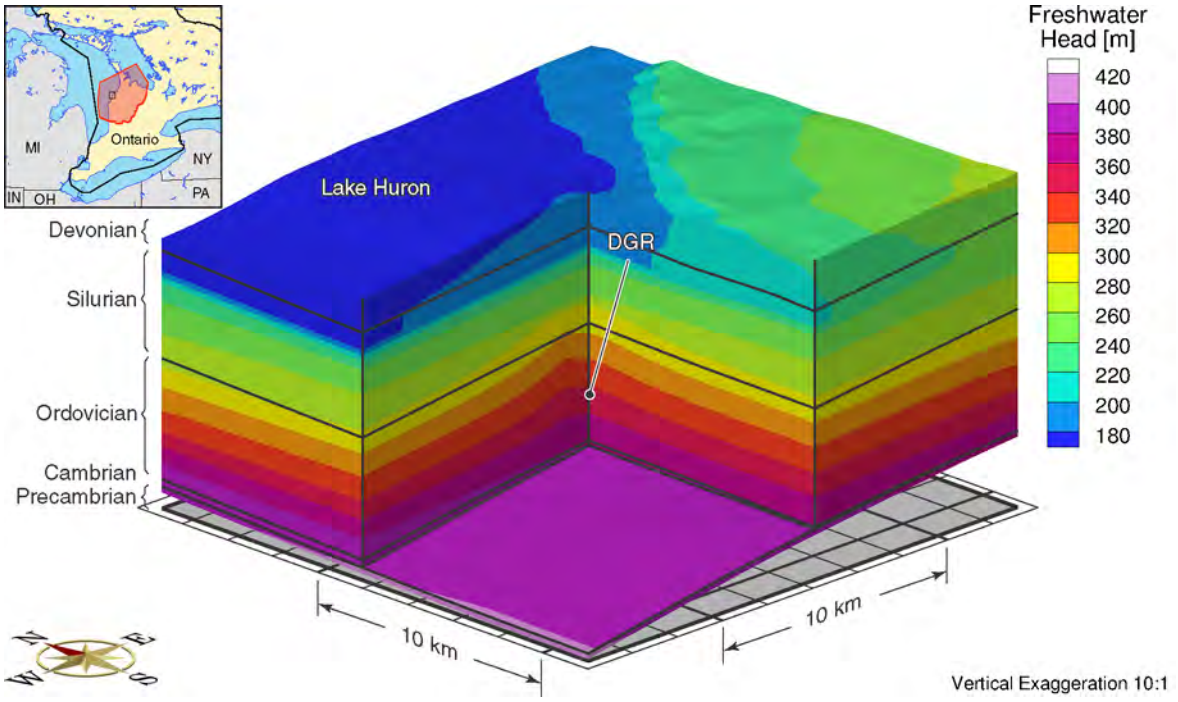

Figure 4.52: Fracture Zone 1 km from DGR and Under-Pressure in the Ordovician: Freshwater Heads at 1 Ma for Pressure Support in the Cambrian and Niagaran Group

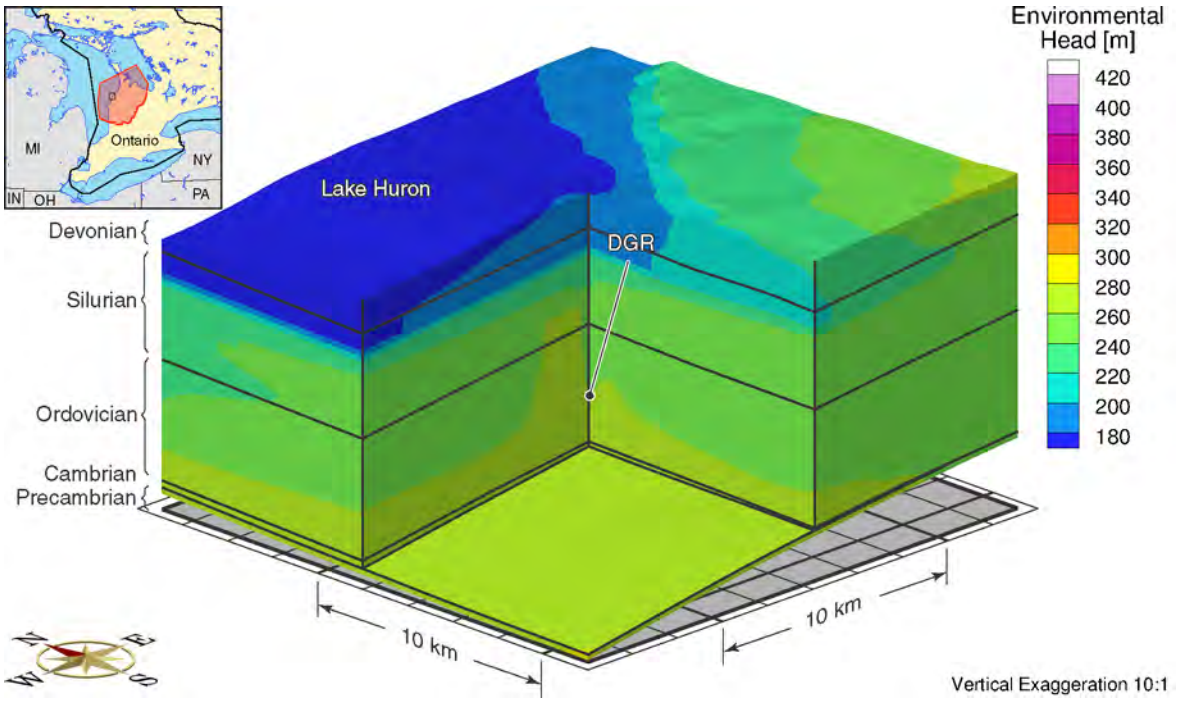

Figure 4.53: Fracture Zone 1 km from DGR and Under-Pressure in the Ordovician: Environmental Heads at 1 Ma for Pressure Support in the Cambrian and Niagaran Group

more than 3 Ma for the pressures in the Ordovician to reach steady-state values. The analysis of solute transport in the Ordovician shale and limestone confirms the conclusion of this hydrogeologic modelling study that transport is diffusion dominant. The impact on transport of pore water advection is negligible. The presence of a permeable discrete fracture zone 1 km from the tracer source that provides a preferential pathway between the Cambrian and the Niagaran Group does not alter the conclusion that solute transport in the Ordovician is diffusion dominant.

5. PALEOHYDROGEOLOGIC ANALYSES

5.1 Climate Change and Glaciation

Approximately nine episodes of complete glaciation have occurred during the past 1 Ma over the Canadian Shield (Peltier 2002). During these 1 Ma, Canada has been covered by a series of continental ice-sheets. These ice-sheets could reach a maximum thickness of 4 km and extend onto the northern portions of the United States (Peltier 2002, 2011). A single glaciation-deglaciation episode is comprised of multiple glacial advances and retreats, with deglaciation and isostatic depression leading to the formation of large proglacial lakes. Peltier (2002) states that it is "now well understood that this process of recurrent continent scale glaciation is a consequence of the small changes in the effective solar insolation incident upon the Earth that occur as a consequence of the changing geometry of Earth's orbit around the Sun due to gravitational 'n-body effects' in the solar system."

Climate change and glaciation are of concern for the Canadian, Swedish (Provost et al. 1998, Boulton et al. 2001a) and Finnish deep geologic disposal concepts (Cedercreutz 2004). Peltier (2002) and Marshall et al. (2000) have developed glaciological reconstructions of the Laurentide Ice-sheet over the North American continent using numerical models. According to Peltier (2002), these reconstructions of the Pleistocene ice-sheet history are based on three areas of study: (1) geological and paleogeological records; (2) the isostatic record of crustal deformation; and (3) the behaviour of modern day glaciers and ice-sheets. During ice-sheet advance the Bruce DGR repository site would evolve from periglacial to subglacial conditions and eventually be overlain by up to 3 km of ice. Permafrost develops below ground surface in advance of the ice-sheet. The thermal conditions at the base of the ice could be above or below the pressure melting point of the ice; a temperature above this point could result in sub-glacial flow of water or the development of streams, while colder temperatures could freeze the ice-sheet to bedrock (Hooke 2005). The ice-sheet provides a thermal break between the atmosphere and the bedrock; allowing the geothermal heat flux radiating towards the ground surface to reduce the depth of permafrost (Peltier 2002).

The weight of an ice-sheet depresses the Earth's surface up to 1 km or more, eventually rebounding once the ice-sheet retreats. The rate of rebound decreases with time, but it is, to this day, over 6 mm/a around Hudson Bay. The rate of rebound declines with distance away from Hudson Bay and approaches zero at the southern edge of the Canadian Shield (Peltier 2002, Davison et al. 1994). The relatively rapid melting of the ice-sheet leads to the formation of very large proglacial lakes at the southern margin of the Laurentide Ice-sheet. The magnitude of the freshwater fluxes were such that they are known to have had a strong impact on the thermohaline circulation of the oceans (Peltier 2002).

Although a future glaciation scenario is of interest, a Bayesian approach is applied to examine a range of models for the most recent North American glaciation event, constrained by various long-term observations in sea level, ice core oxygen isotope ratios, maximal extent of glaciation, and continental isostatic rebound, among others. The physical model used for these simulations is the University of Toronto (UofT) Glacial Systems Model (GSM) (Peltier 2011). The GSM is a physically based model, employing a *shallow ice approximation* whereby the vertical length scale is much smaller than the horizontal length scale. The model is subject to the equations of conservation of mass, momentum, and internal energy, represented as a set of non-linear coupled diffusion equations in essentially two dimensions, applied to a spherical Earth. A detailed description of the equations and model development can be found in Deblonde and Peltier (1991, 1993), and more recently in Tarasov and Peltier (1997, 1999, 2002, 2004, 2005, 2006).

The GSM is used for modelling ice-sheet evolution in a transient manner over a period of 120 ka. The model performs its calculations on a geographic grid measuring 1.0° in longitude by 0.5° in latitude. Various model outputs include normal stress on the ground surface due to an ice-sheet, permafrost depth, basal temperature relative to the pressure melting point of ice, surface lake depth, basal meltwater production, basal surface elevation subject to isostatic adjustment, surface elevation of ice-sheet, and ice-sheet thickness.

5.2 Glacial Meltwater

The water pressure at the base of a glacier is an important factor in assessing the impact of glaciation on a groundwater system. Beneath warm-based glaciers, free water can exist at the ice-bed contact and interstitially in subglacial sediment. Water at the contact can include porewater that has exfiltrated as a result of mechanical loading, basal meltwater and surface meltwater that has penetrated or flowed englacially to the base through ice-walled conduits that include fractures, fissures, crevices and moulins when they occur (Clarke 2005, Zwally et al. 2002, Fountain and Walder 1998). Surface melting is typically one to four orders of magnitude larger than basal melting and when it reaches the bed, it can supply sufficient water to require drainage at the ice-bed interface even when there are underlying aquifers (Arnold and Sharp 2002, Boulton et al. 1995). The presence of water at the ice-bed contact contributes to increased water pressure at the boundary with a corresponding reduction of the effective pressure given as $P_e = P_i - P_w$ (Clarke 2005) where P_w is the pressure of the subglacial water, and $P_i = \rho_i g h_i$ is the overburden ice pressure in which ρ_i is the ice density, g is the gravity acceleration and h_i is the ice thickness. The subglacial water also can penetrate into the subsurface.

Subglacial processes, including meltwater penetration into the subsurface and subglacial water drainage, are important because they determine the large-scale behaviour of glaciers and ice-sheets, yet upscaling from point-scale processes to macro-scale products remains uncertain (Clarke 2005, Marshall 2005). The pressure P_w of the subglacial water can vary temporally and spatially in a complicated manner that is determined by a balance between influx and efflux of water, the geometry of the subglacial system, the physical properties of the sediments underlying the glacier, thermodynamic conditions near the ice-bed interface, and the ice overburden pressure P_i (Clarke 2005, Boulton et al. 2007a,b). Glaciers are buoyantly supported by the pressure of the subglacial water and the magnitude of the support is given by the effective pressure P_e and the flotation ratio $f = P_w/P_i$. Clarke (2005) indicates that the water pressure beneath the fast-flowing West Antarctic ice streams is very close to the ice flotation pressure with point measurements yielding $f = 0.997$ and $P_e = 30$ kPa. High subglacial water pressures can decouple the ice from the underlying geologic sediments, reducing or eliminating basal friction by drowning geologic and topographic pinning points (Marshall 2005). Under the high water pressures, high rates of basal ice flow can occur (10^2 to 10^4 m/a). Marshall (2005) states that although localized, intermittent, or slow basal motion have been reported in cold-based ice masses, large scale basal flow requires warm-based conditions, where basal ice is at the pressure-melting point and liquid water can pond and accumulate at the ice-bed contact. Warm-based conditions prevail in most glacial environments including Antarctica and Greenland. Zwally et al. (2002) observed summer acceleration approximately 50 km from the ice margin in west Greenland at a location where ice thickness exceeds 1,200 m. The seasonal speedups were proportional to the total amount of meltwater generated each summer over a four-year period, thus implying penetration of surface meltwater to the base of the ice-sheet, where it facilitates basal flow. Zwally et al. (2002) indicate that the flow of the ice-sheet is capable of responding to summer surface melt within days to months rather than centuries to millennia. Arnold and Sharp (2002) indicate that the occurrence of high water pressure is critical, as it allows rapid basal motion by sliding, deformation of weak subglacial sediments, or some

combination of these processes. The flow of subglacial water is driven by the topography of the upper glacial surface and only weakly influenced by bed topography; the subglacial water pressure can vary over a wide range as a result of diurnal and seasonal cycling (Clarke 2005).

Water flows at the glacial bed in one or both of two qualitatively different flow systems commonly termed “channelized” and “distributed” (Fountain and Walder 1998, Boulton et al. 2007a,b). In a channelized drainage system, water fluxes are discharged by strongly turbulent flows in which water flow draws down water pressure resulting in channel pressures that are relatively low compared to ice pressures (Boulton et al. 2007a). However, an isolated, water-filled void or channel in a glacier will tend to be closed by inward ice flow unless the water pressure P_w equals the ice overburden pressure P_i. Englacial or subglacial channels may exist with $P_w < P_i$ if the flowing water dissipates enough energy as heat to melt the ice and thereby keep the channel open (Fountain and Walder 1998). Between channels, water pressure P_w increases approaching, and in some cases exceeding, the ice overburden pressure (Boulton et al. 2007a). For distributed drainage systems, flow is relatively slow and inefficient and water pressures increase, approaching the ice overburden pressure as the water flux increases (Boulton et al. 2007a). For both the “channelized” and “distributed” flow systems, a water pressure P_w of zero beneath a warm-based glacier would be inconsistent with the analyses and modelling of Fountain and Walder (1998) and Boulton et al. (2007a,b).

The presence of subglacial water is also critical as the depth of glacial meltwater penetration into the subsurface is of interest because dissolved oxygen O_2 can be transported to depth by infiltrating meltwater (Guimerà et al. 1999). In sedimentary basins, water can migrate from the basin margins to depth through the more permeable layers (McIntosh and Walter 2006).

5.3 Linking to the Glacial Systems Model

The modelling domain is restricted to southwestern Ontario, and the GSM developed by Peltier (2011) covers most of North America; vertical stress due to ice, and permafrost depth were spatially interpolated as shown in Figure 5.1. A TIN was created, whose nodes lie at the midpoint of each paleo grid block; the value of vertical stress or permafrost depth is taken at the midpoint of each paleo grid block, and linearly interpolated across each triangular facet of the TIN. Hydraulic boundary condition values for vertical stress corresponding to the FRAC3DVS-OPG grid are interpolated from the TIN for each 500 year time step in the 120 ka GSM simulation.

Peltier (2011) describes eight (8) models that “span the apparent range of model characteristics that provide acceptable fits to the totality of the observational constraints.” Of these eight models, nn9921 and nn9930 are two of the best models based on aggregate misfit, and both include high resolution permafrost development. Less permafrost leads to deeper recharge meltwater penetration into the subsurface (see Normani et al. 2007); of the two models, nn9921 and nn9930, model nn9930 had less permafrost than nn9921, yet both are selected for the paleohydrogeologic simulations presented herein.

A plot of various nn9930 and nn9921 GSM model outputs for the grid cell at the DGR site are shown in Figure 5.2 and Figure 5.3 respectively. These outputs include ice thickness, meltwater production rate, lake depth, permafrost depth, ground elevation, and ice-sheet basal temperature relative to the pressure melting point of ice. Only the ice thickness, lake depth, and permafrost depth outputs are applied to the paleohydrogeologic groundwater flow simulations.

The isostatic movement of the ground surface due to ice loading is not considered; applied hydraulic boundary conditions are stated in terms of elevation, assuming the grid does not move vertically. The application of lake depth is also a relative term independent of isostatic movement,

although isostatic depression is required for a proglacial lake to form. Although lake depth could be interpolated across the TIN in a similar manner to permafrost depth and vertical stress due to ice, since isostatic movement is not considered, large gradients could be created across the site which would not exist in the presence of a large proglacial body of water. Due to this, lake depth is added to the existing lake elevation and hydraulic boundary conditions are adjusted accordingly. Changes in surface topography due to glacial stripping of sediments is not considered.

5.4 Permafrost

Permafrost develops in advance of the ice-sheet since the ground surface is directly exposed to climate variations, while ice-sheets thermally insulate the geosphere from climate influences (Peltier 2002). Permafrost is also responsible for frost heaving of bedrock, where the displacement of blocks, panels and domes is caused by high pore water pressures that are unable to escape due to a downward advancing permafrost front of lower permeability; field measurements of pore water pressures within confined zones indicate pressures of 400 kPa at depths of 2 m, considerably in excess of overburden pressures (Dyke 1984). Ejected blocks of

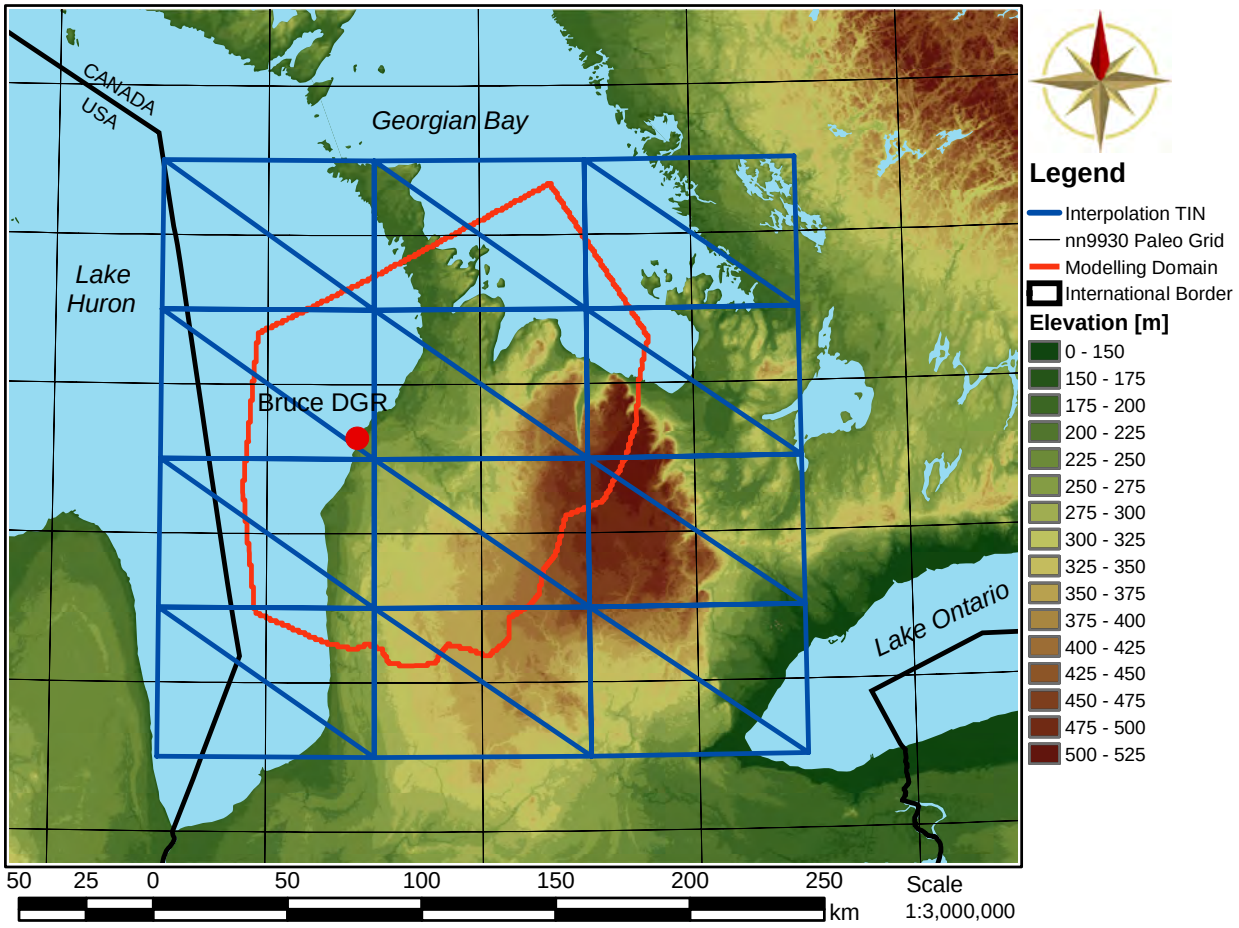

Note: nn9930 and nn9921 are from Peltier (2011).

Figure 5.1: TIN Used to Interpolate Properties for the Regional-Scale Spatial Domain from Grid Blocks of the nn9930 and nn9921 Glacial Systems Models

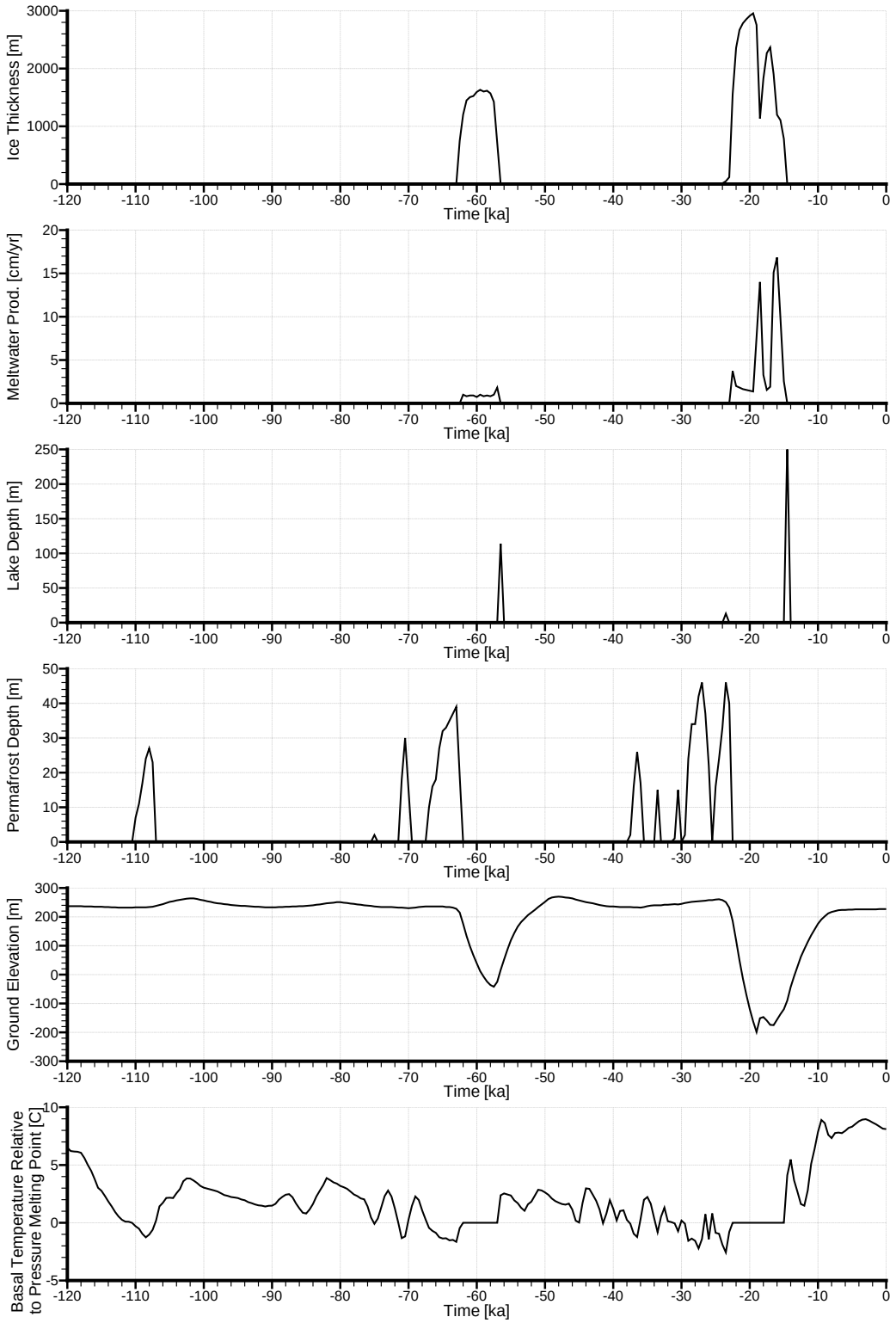

Note: Data from Peltier (2011). Plots of ice thickness, meltwater production rate, lake depth, permafrost depth, ground elevation, and ice-sheet basal temperature relative to pressure melting point versus time are shown.

Figure 5.2: Temporal Plots of Various Output Parameters from the nn9930 GSM Grid Block at the DGR Site

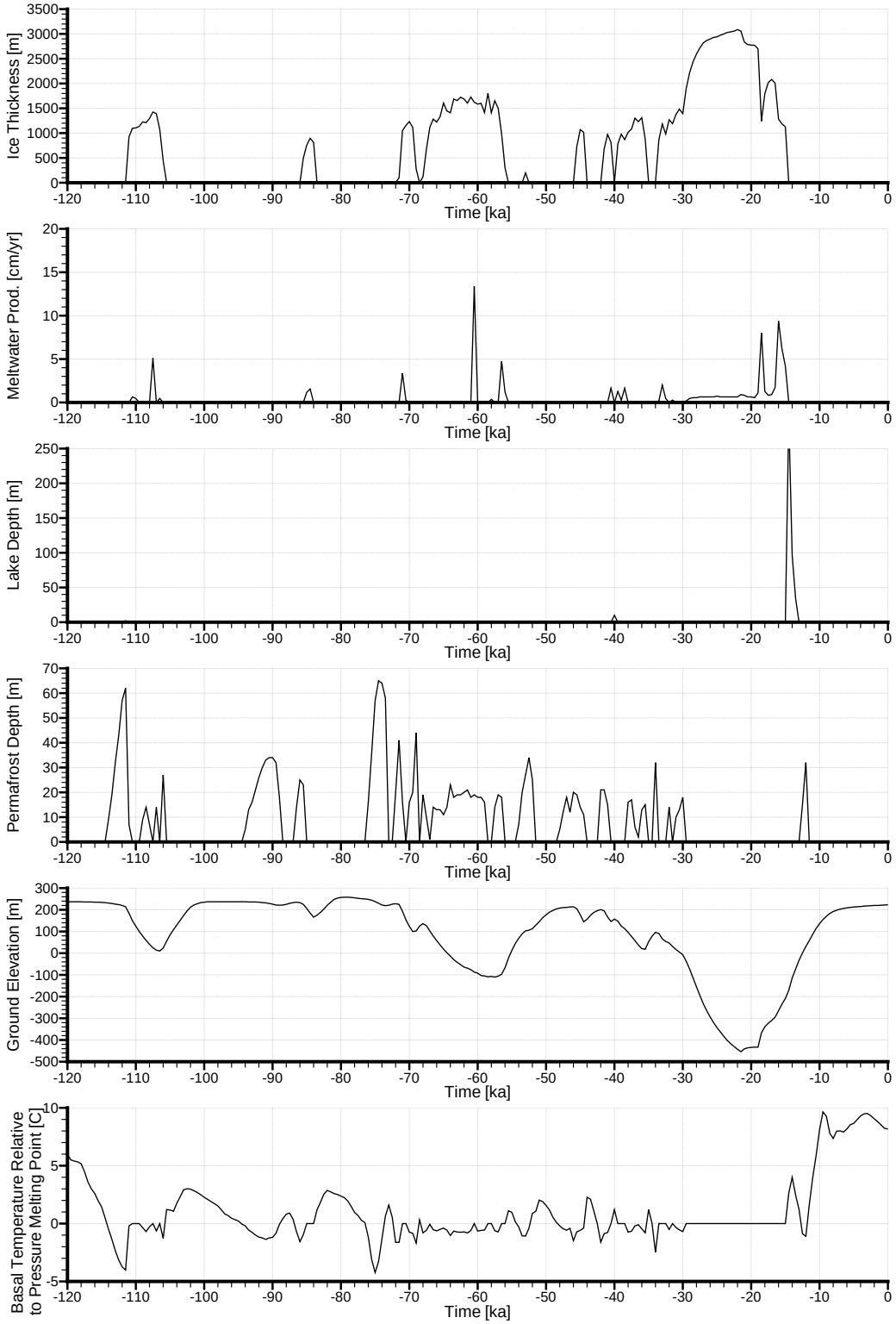

Note: Data from Peltier (2011). Plots of ice thickness, meltwater production rate, lake depth, permafrost depth, ground elevation, and ice-sheet basal temperature relative to pressure melting point versus time are shown.

Figure 5.3: Temporal Plots of Various Output Parameters from the nn9921 GSM Grid Block at the DGR Site

quartzite near Churchill, Manitoba can stand 3 m above surrounding terrain, with yearly vertical movements of 5 cm quite common.

In freezing pore waters, the connected flowing porosity is reduced, resulting in a much lower hydraulic conductivity. McCauley et al. (2002) conducted numerous experiments measuring hydraulic conductivity and permeability in frozen and unfrozen soils, including organic rich silty sand, sandy silt, and silty sand fill. For a 100% ice saturated sample, the hydraulic conductivity of the frozen soil sample was approximately 5×10^{-11} m/s. For each time step in FRAC3DVS-OPG, if the depth of permafrost extends below the top of an element, calculated at the centroid of the top face, that element will be assigned the permafrost hydraulic conductivity isotropically. FRAC3DVS-OPG can vary time steps to suit groundwater flow and solute transport maximum change criteria ($\Delta h, \Delta C$), as well as linearly interpolate permafrost values between successive time steps. Porosity is not adjusted in permafrost zones from its base values.

5.5 Paleohydrogeologic Boundary Conditions

Glaciogeomorphological evidence and numerical simulations (Tarasov and Peltier 2004, Bense and Person 2008) indicate that it is likely that thawed bed conditions persisted during the last glacial maximum across the Michigan Basin. Under such conditions, the mechanical loading upon ground surface due to the presence of an ice-sheet can be implemented as a hydraulic boundary condition in a groundwater flow model assuming the height of the ice-sheet can be replaced with an equivalent height of freshwater resulting in the same pressure or stress at its base. This approach has been applied by Boulton et al. (1995), Person et al. (2003, 2007), and Bense and Person (2008) for two-dimensional cross-sectional groundwater flow models. A groundwater flow model without hydromechanical coupling for glaciation processes ignores a significant factor which affects horizontal and vertical gradients during glacial advance and retreat. Mechanical loading at surface can increase insitu pore fluid pressures, thereby reducing or completely cancelling a vertical gradient that results from a specified head boundary condition; the degree of pore pressure increase is directly tied to the value of the one-dimensional loading efficiency ζ, as described in Section 3.2. The mechanical loading is not only important for the ice-sheet, but also for proglacial lakes. Any change to water levels will also impart a change to the mechanical surface loading of the system in addition to the change in hydraulic boundary conditions. This is formulated in the following equations:

$$\sigma_{zz} = \begin{cases} \rho_I \, g \, h_I & \text{if } h_W < \dfrac{\rho_I}{\rho_w} h_I, \\ \rho_W \, g \, h_W & \text{if } h_W \geq \dfrac{\rho_I}{\rho_w} h_I \end{cases} \tag{5.1}$$

$$\hat{h} = h_W \tag{5.2}$$

where ρ_I is the density of ice-sheet [M/L^3]; h_I is the height of ice-sheet [L]; ρ_W is the density of water [M/L^3]; h_W is the height of water [L]; and $\hat{h}$ is the specified head boundary condition [L]. The FRAC3DVS-OPG option of linearly interpolating specified heads to smoothly adjust time steps is used to mitigate abrupt changes in ice height, which could lead to unnecessarily small time steps or an unstable numerical solution.

An alternate approach for the paleohydrogeologic boundary condition is to apply glacial meltwater as recharge to the top of the groundwater model, which will increase heads beneath the ice-sheet. If the heads increase sufficiently such that the ice-sheet will begin to float, then the

system is considered unstable and a pressure limited specified head is applied as $\hat{h} = (\rho_I/\rho_W)h_I$ (Lemieux et al. 2008b,c,a). The authors only considered basal meltwater in their analysis; the contribution of surface meltwater to water at the ice-bed contact was ignored. The recharge was applied if permafrost does not exist below ground surface at that location. As discussed in the preceding section, in glaciation studies and two-dimensional groundwater flow modelling of northwest Europe by Boulton et al. (1995) and van Weert et al. (1997), meltwater that cannot be discharged as groundwater by a head less than the ice pressure, is otherwise drained at the base of the ice-sheet. The drainage mechanism can include flow in a thin sheet at the ice/bed interface, flow in relatively stable channels at the ice/bed interface, or flow in canals in deformed subglacial sediments beneath the ice/bed interface (Boulton et al. 1996). Further work by Boulton et al. (2001b, 2007a,b) extends the modelling to three dimensions to investigate the role of tunnels forming beneath ice-sheets.

(Selvadurai and Nguyen 1995) assumed a free draining (i.e., $P_W = 0$) boundary condition at the ice-bed contact in their analysis of the impact of glaciation on the mechanical behaviour of the underlying rock. The use of this boundary condition is inconsistent with literature on water pressures that develop at the ice-bed contact under warm based glaciers (refer to the preceding section). The assumption of this boundary condition will result in erroneous conclusions regarding the redistribution of pore water during rock compression in glaciation and rock dilation in deglaciation.

5.6 Paleohydrogeologic Simulations

The appropriate pseudo steady-state simulation was used as the initial conditions for each paleohydrogeologic simulation. These simulations are listed in Table 4.10. Most of the figures related to the paleohydrogeologic simulations are found in Appendix F, while others are provided in the following sections.

5.6.1 Base-case Paleohydrogeologic Simulation

The first paleohydrogeologic simulation (scenario fr-base-paleo) uses the parameters listed in Table 4.3 and Table 4.8, and represents the base-case analysis. The remaining paleohydrogeologic analyses represent variations on the base-case to investigate the influence of changes to the base-case parameters on the modelling results. The simulation results at the end of the paleohydrogeologic simulation are presented in this section, while fence view figures at 90 ka, 60 ka, 30 ka, and 0 ka before present for environmental heads, pore water velocity magnitudes, ratio of vertical pore water velocity to pore water velocity magnitude, and recharge water tracer migration are shown in Appendix F from Figure F.1 to Figure F.18, and are summarized in Table 5.1.

Table 5.1: Figure Numbers in Appendix F for the Base-Case Paleohydrogeologic Scenario

Parameter	Time before present			
	90 ka	60 ka	30 ka	Present
Freshwater Head	—	—	—	Figures F.1 & F.2
Environmental Head	Figure F.3	Figure F.4	Figure F.5	Figure F.6
Pore Water Velocity Magnitude	Figure F.7	Figure F.8	Figure F.9	Figure F.10
Ratio of Vertical Pore Water Velocity to Pore Water Velocity Magnitude	Figure F.11	Figure F.12	Figure F.13	Figure F.14
Tracer Concentration	Figure F.15	Figure F.16	Figure F.17	Figure F.18

Freshwater heads at the end of the paleohydrogeologic simulation (0 ka), representing the present time, are shown in Figure 5.4 and Figure 5.5, while environmental heads are shown in Figure 5.6 and Figure 5.7. The paleohydrogeologic boundary conditions using nn9930 represent the most recent 120 ka glacial episode over the Canadian landscape. In comparing Figure 5.6 to the paleohydrogeologic initial conditions shown in Figure 4.14, the environmental heads are higher throughout most of the Silurian and at the top of the Ordovician, namely the Queenston Formation. This elevated head is also shown in Figure 5.8, whereby the vertical profile of freshwater head, environmental head, and TDS are plotted versus depth at the DGR location. In Figure 5.8, the red lines represent the initial condition at −120 ka, and the black lines represent the end of the paleohydrogeologic simulation at 0 ka. The residual elevated heads persist even 14 ka after deglaciation, and is due to a high hydraulic diffusivity, characterized by a low hydraulic conductivity and a high storage coefficient. The high heads associated with the paleoclimate surface boundary condition propagate into the Salina and the Queenston Formation, and are slow to dissipate. According to Table 4.3, the Salina is characterized by slightly higher specific storage values and lower one-dimensional loading efficiencies than the Ordovician, leading to a greater storage capacity, and higher gradients due to a reduced insitu pore pressures resulting from hydro-mechanical coupling.

In comparing the freshwater and environmental heads to measured pressures in DGR-4 (see Figure 5.8), a clear mismatch exists for both the under-pressured Ordovician and over-pressured Cambrian relative to ground surface. The use of FRAC3DVS-OPG assumes that the entire modelling domain is fully saturated, while a possible cause for the under-pressurization in the Ordovician units can be explained by the presence of a gas phase, resulting in a partially saturated porous media. The over-pressure in the Cambrian can be related to higher density fluids in the central portion of the Michigan Basin, coupled with a high hydraulic conductivity of the Cambrian itself. The simulated heads at the Niagaran Group match very well with the measured heads in DGR-4.

Brine concentrations at the end of the paleohydrogeologic simulation period are presented in Figure 5.9 and Figure 5.10, while the initial conditions for the simulation are shown in Figure 4.12 and Figure 4.13. The TDS concentration profile in Figure 5.8c is only slightly affected by the paleoclimate loading, with most of the change occurring near the top of the Salina and in the vicinity of the Niagaran Group.

Pore water velocity magnitudes at the end of the paleohydrogeologic simulation are shown in Figure 5.11 and Figure 5.12. These plots clearly show the higher velocity zones associated with higher hydraulic conductivity, namely, the zones above the Salina, the A-1 Carbonate, the Niagaran Group, and the Cambrian. The ratio of vertical pore water velocity to pore water velocity magnitudes are shown in Figure 5.13 and Figure 5.14. These plots show the predominant direction of flow: vertically upward shown in red, vertically downward shown in blue, and horizontal shown in white. Due to the transient nature of the paleohydrogeologic simulation, flow is predominantly vertically downward through the Ordovician. This downward migration at the end of the paleohydrogeologic simulation can also be seen in the environmental head plot of Figure 5.8b. As more time passes since the paleoclimate forcing is applied, these downward velocities will reverse. Analysis that honours parameters from field and laboratory tests of the site characterization program does not yield results that match the pressures observed in the DGR boreholes, notably in the Ordovician. It is concluded that glaciation and deglaciation is not a cause of the observed pressures.

A tracer of unit concentration is applied as a Cauchy boundary condition to all surface nodes at the beginning of the paleohydrogeologic simulation. This tracer is used to characterize the

migration, from the surface, of recharge water that occurs during the paleohydrogeologic simulation; the recharge water includes glacial meltwater, whose importance was discussed in Section 5.2. Tracer concentrations for the modelling domain are presented in Figure 5.15. The 5% isochlor migrates approximately 1/3 into the Silurian sediments and is nearly in the same location as the top of the pore pressure transition in Figure 5.6. Furthermore, Figure 5.8d shows the tracer concentration with depth at the DGR location. Lithologic units from ground surface to the Bass Islands are characterized by higher hydraulic conductivities, while the units in the Salina are of comparatively lower conductivity. The downward migration of the tracer in Figure 5.8d is retarded by the Salina and demonstrates diffusion as the dominant transport mechanism.

5.6.2 Surface Boundary Condition Based on 80% of Ice Thickness

This scenario applies a hydraulic boundary condition to the surface of the modelling domain that is 80% of the ice thickness to allow for some reduction in heads beneath the ice sheet (scenario fr-base-paleo-head80). Fence view figures at 90 ka, 60 ka, 30 ka, and 0 ka before present for environmental heads, pore water velocity magnitudes, ratio of vertical pore water velocity to pore water velocity magnitude, and recharge water tracer migration are shown in Appendix F from Figure F.19 to Figure F.36, and are summarized in Table 5.2.

Table 5.2: Figure Numbers in Appendix F for Surface Boundary Condition Based on 80% of Ice Thickness

Parameter	Time before present			
	90 ka	60 ka	30 ka	Present
Freshwater Head	—	—	—	Figures F.19 & F.20
Environmental Head	Figure F.21	Figure F.22	Figure F.23	Figure F.24
Pore Water Velocity Magnitude	Figure F.25	Figure F.26	Figure F.27	Figure F.28
Ratio of Vertical Pore Water Velocity to Pore Water Velocity Magnitude	Figure F.29	Figure F.30	Figure F.31	Figure F.32
Tracer Concentration	Figure F.33	Figure F.34	Figure F.35	Figure F.36

The freshwater heads at the end of the paleohydrogeologic simulation are shown in Figures F.19 and F.20, while the environmental fence plots are shown in Figure F.21 to Figure F.24. Figure 5.17 also presents the freshwater and environmental heads at the end of the paleohydrogeologic simulation with a comparison to the initial condition. A slight over-pressure results from the Salina through to the Queenston Formation, and a slight under-pressure at the Kirkfield Formation. The measured pattern of under-pressures in the Salina and the Ordovician are not matched by the simulated results, indicating that the under-pressures are not a result of the imposed pattern of glacial loading and unloading. In addition, the over and under-pressures are similar in pattern to the base-case as shown in Figure 5.8, but with reduced magnitude, owing to the reduced surface boundary heads.

The TDS profile in Figure 5.17c changes slightly between the beginning and end of the paleohydrogeologic simulation, and occurs mainly at the top of the Salina and near the Niagaran Group. Otherwise, the TDS profile is essentially unchanged through the course of the simulation.

Pore water velocity magnitudes for the paleohydrogeologic simulation are shown in Figure F.25 to Figure F.28, while the ratio of vertical pore water velocity to pore water velocity magnitudes are shown in Figure F.29 to Figure F.32. Visually, these plots are very similar to the base-case

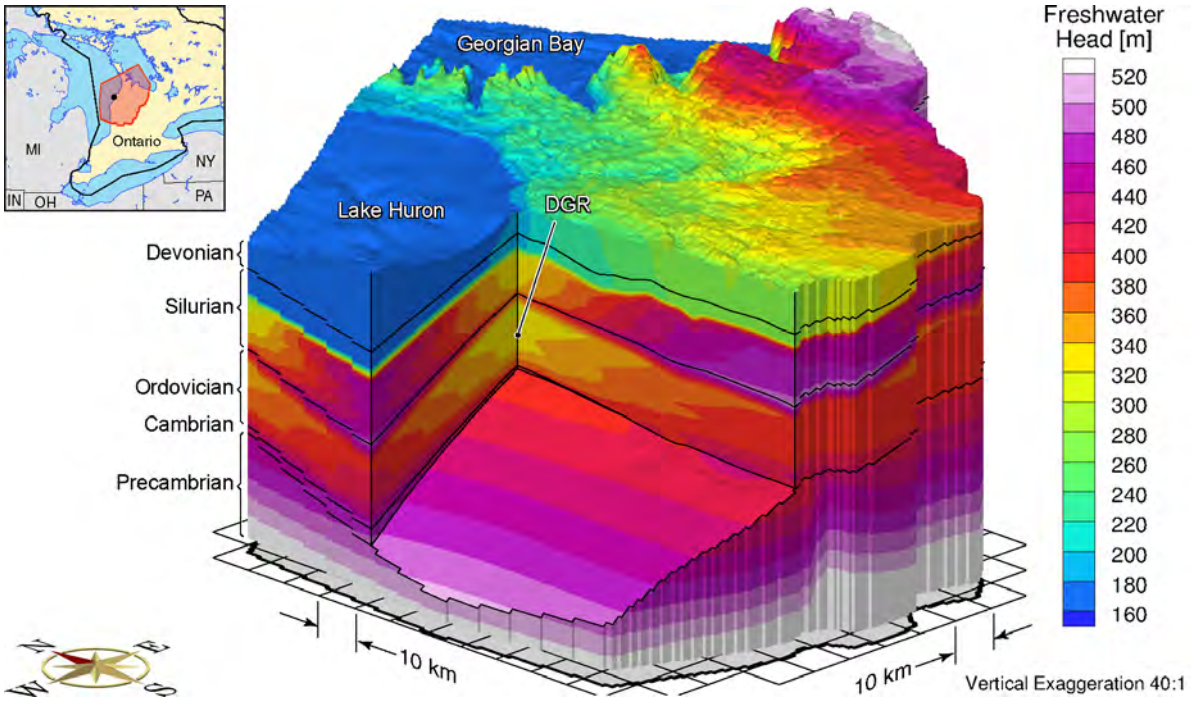

Figure 5.4: Block Cut View of Freshwater Heads at Present for the Base-Case Paleohydrogeologic Scenario

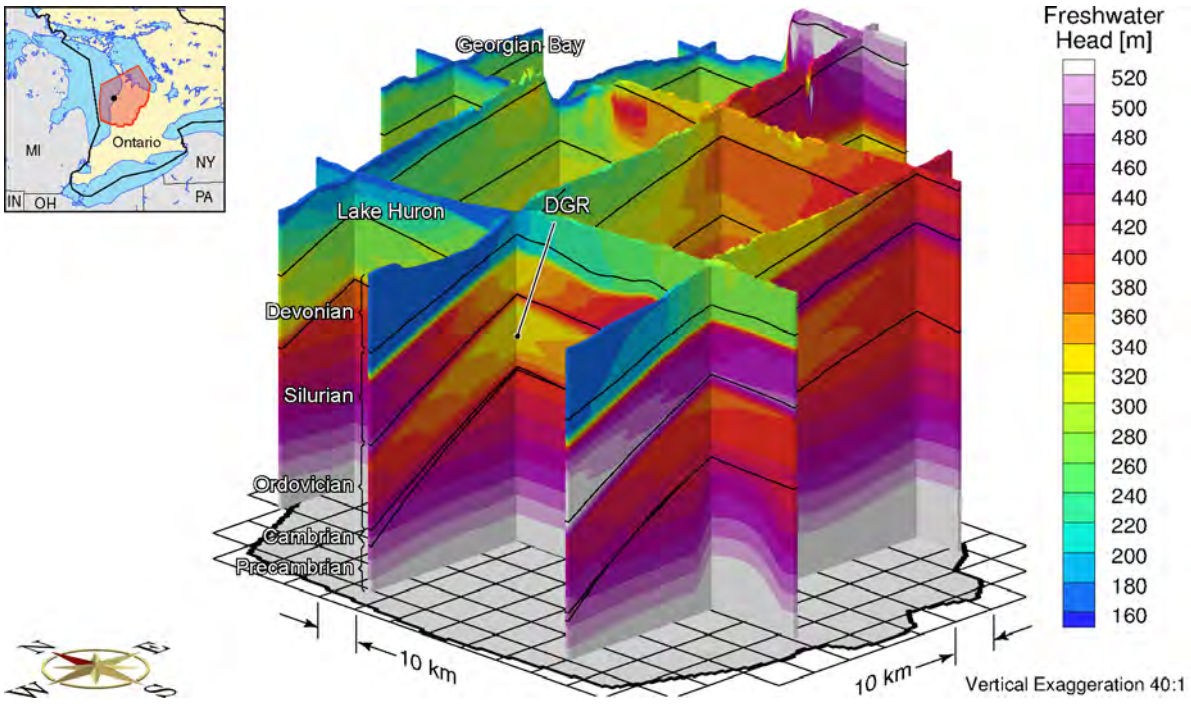

Figure 5.5: Fence View of Freshwater Heads at Present for the Base-Case Paleohydrogeologic Scenario

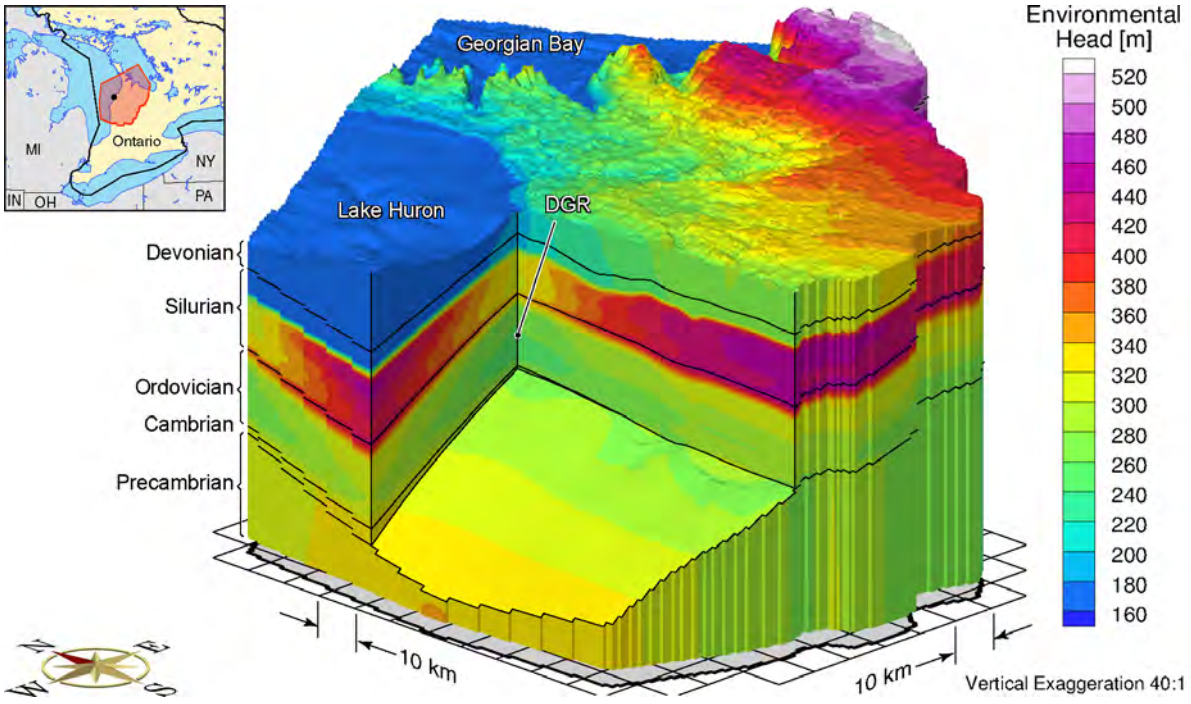

Figure 5.6: Block Cut View of Environmental Heads at Present for the Base-Case Paleohydrogeologic Scenario

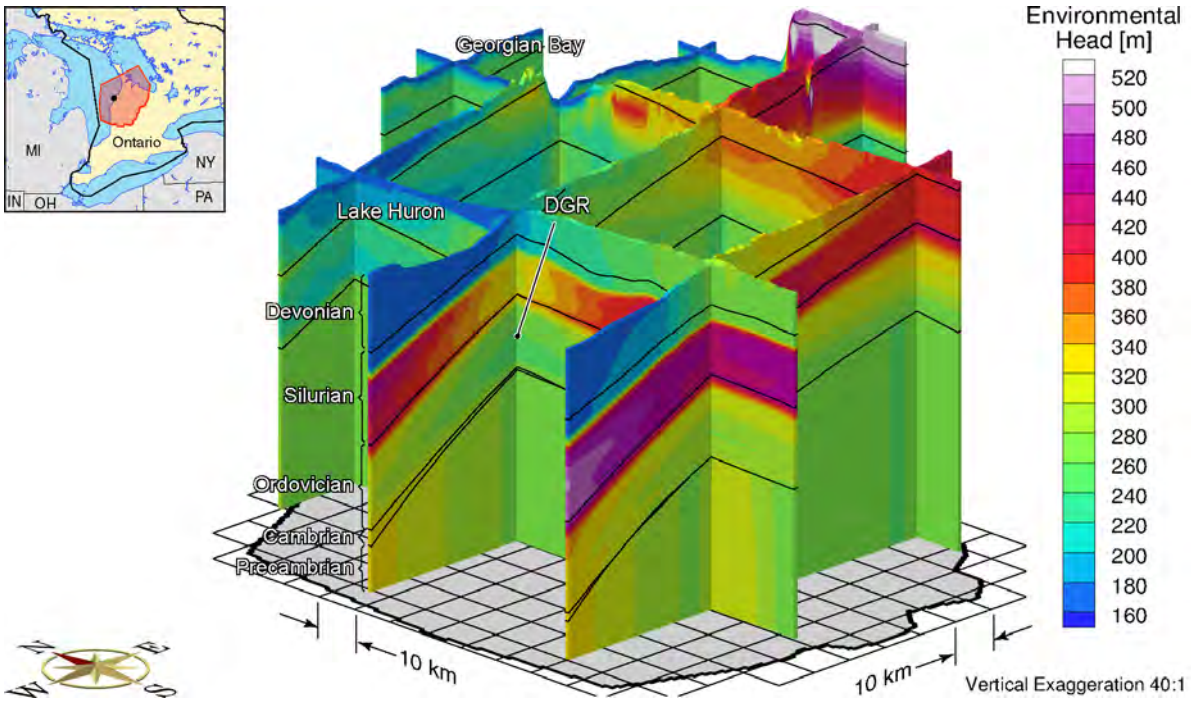

Figure 5.7: Fence View of Environmental Heads at Present for the Base-Case Paleohydrogeologic Scenario

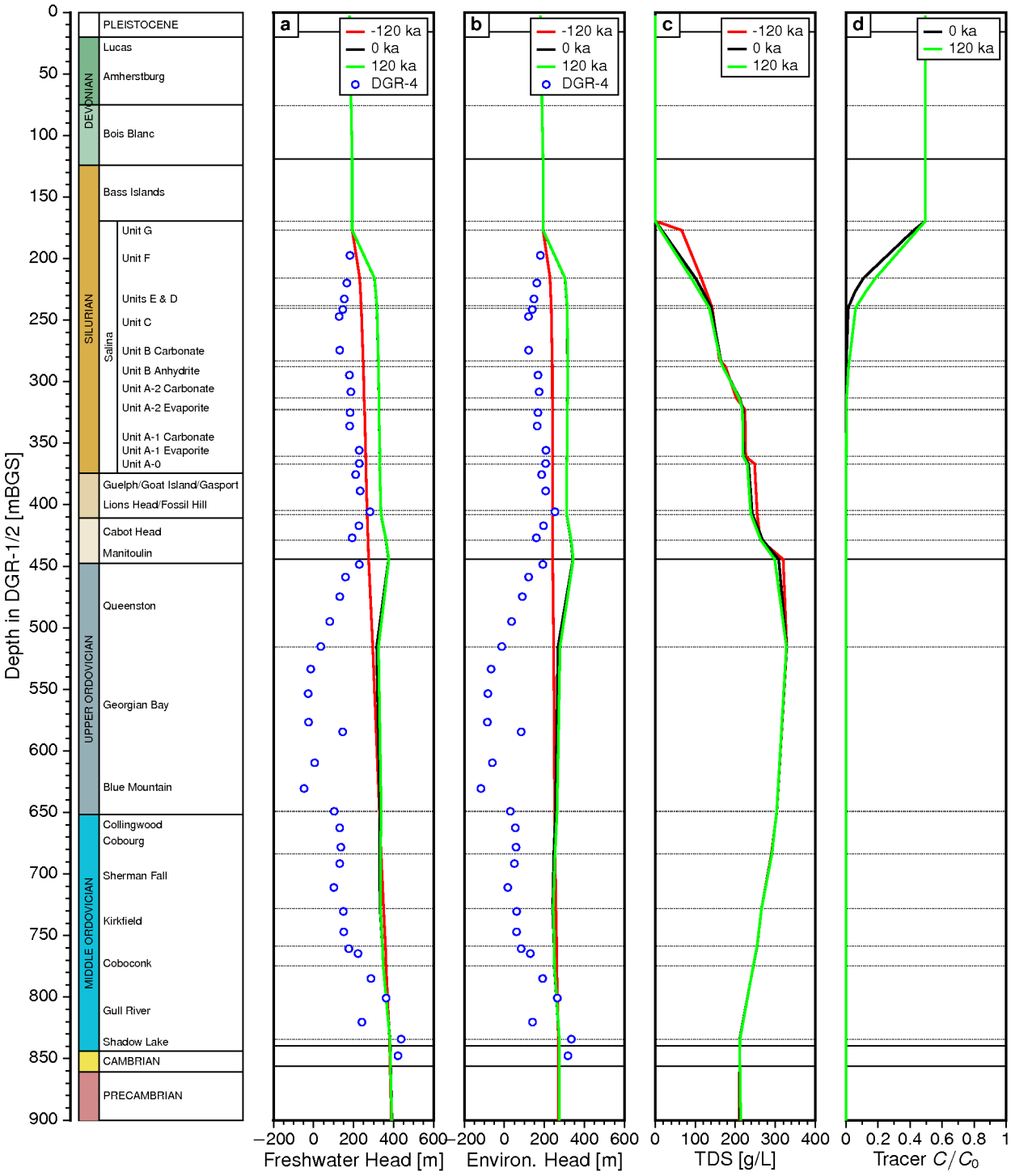

Note: (a) freshwater head, (b) environmental head, (c) total dissolved solids concentration, and (d) tracer concentration versus depth are plotted at beginning (−120 ka) and end (0 ka) of a paleohydrogeologic cycle. The end of a second paleohydrogeologic cycle is shown at 120 ka. Freshwater and environmental heads for DGR-4 are shown as measured on August 24, 2009.

Figure 5.8: Vertical Profile Plots for Base Paleohydrogeologic Simulation at the DGR Site

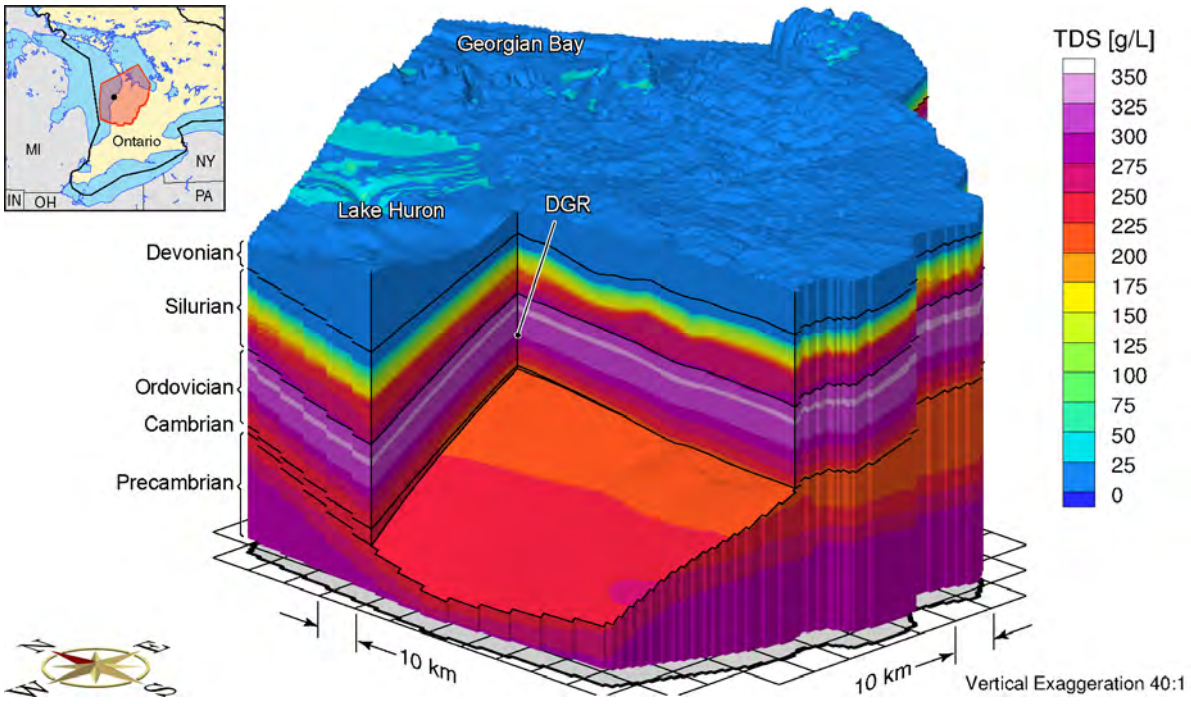

Figure 5.9: Block Cut View of Total Dissolved Solids at Present for the Base-Case Paleohydrogeologic Scenario

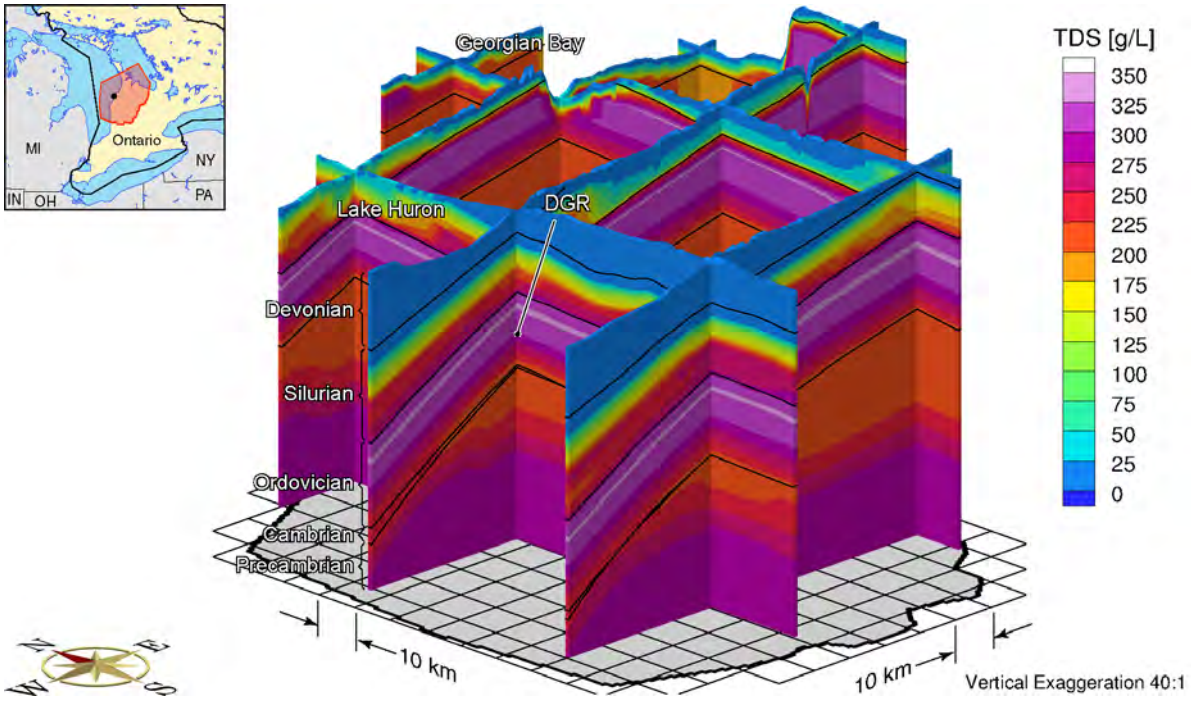

Figure 5.10: Fence View of Total Dissolved Solids at Present for the Base-Case Paleohydrogeologic Scenario

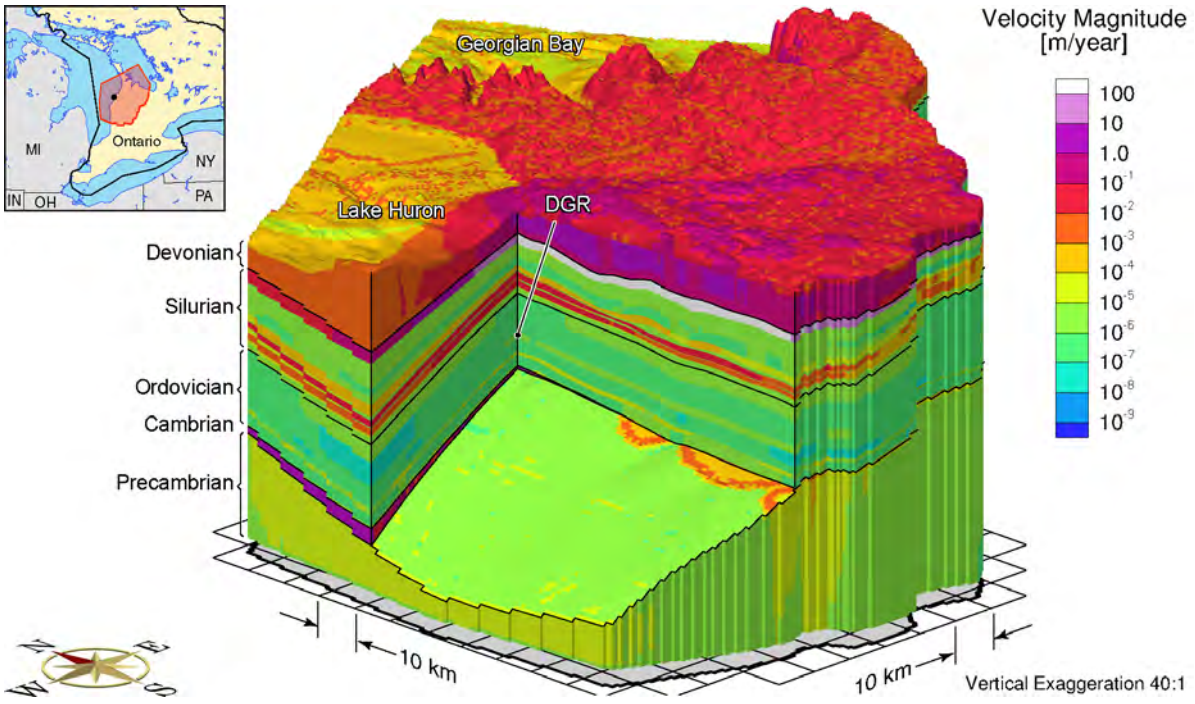

Figure 5.11: Block Cut View of Pore Velocity Magnitude at Present for the Base-Case Paleohydrogeologic Scenario

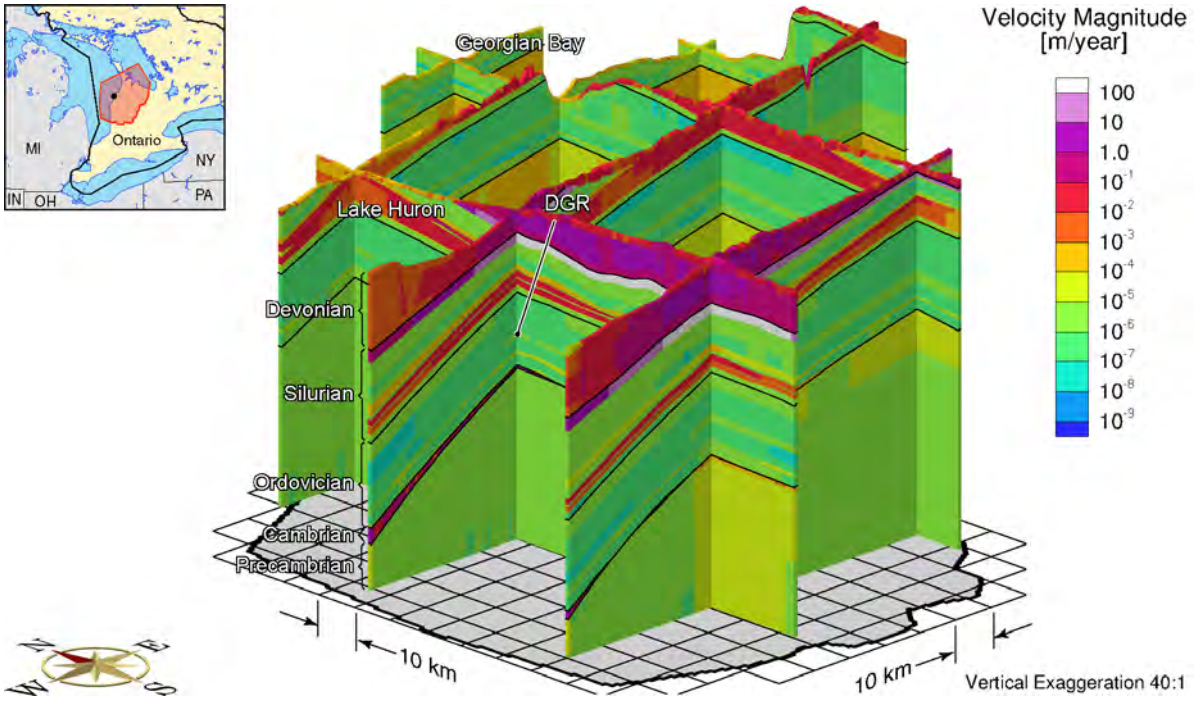

Figure 5.12: Fence View of Pore Velocity Magnitude at Present for the Base-Case Paleohydrogeologic Scenario

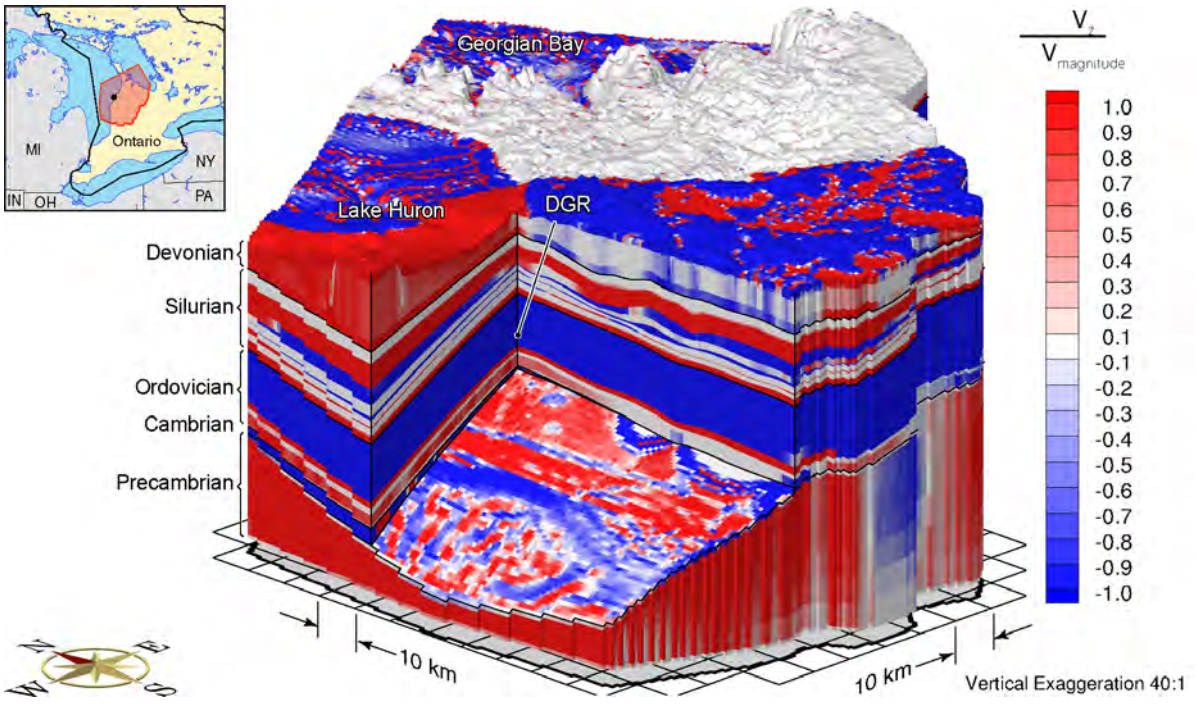

Figure 5.13: Block Cut View of Ratio of Vertical Pore Velocity to Pore Velocity Magnitude at Present for the Base-Case Paleohydrogeologic Scenario

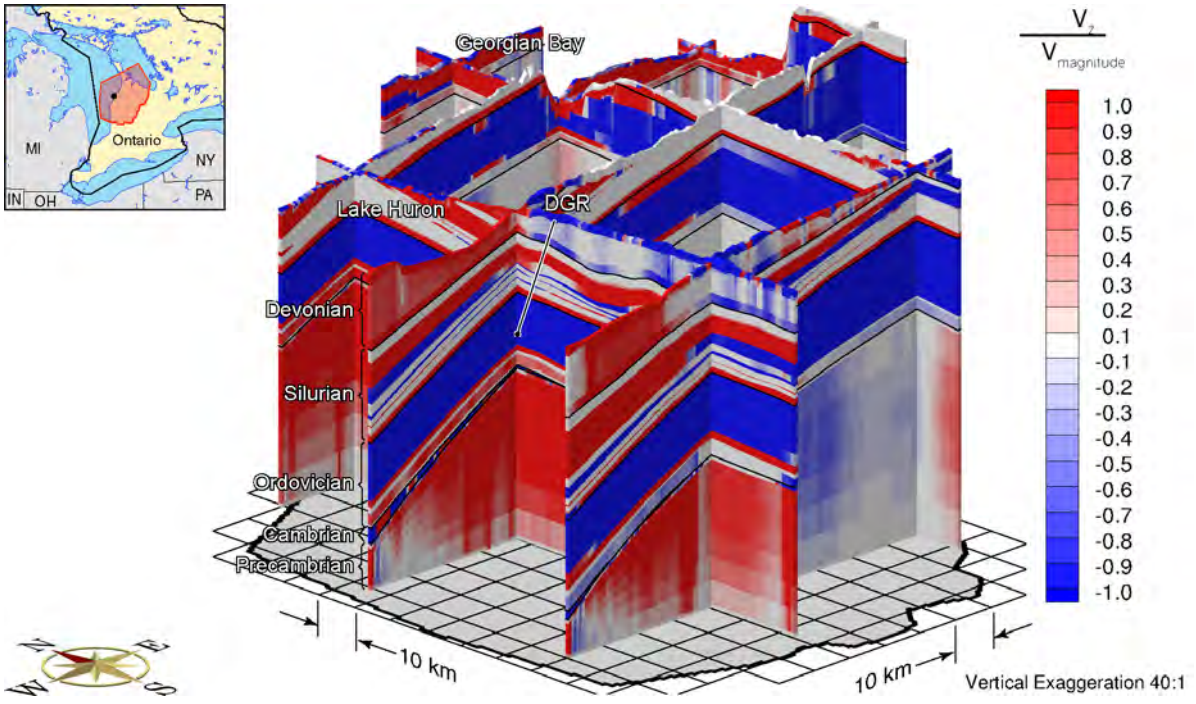

Figure 5.14: Fence View of Ratio of Vertical Pore Velocity to Pore Velocity Magnitude at Present for the Base-Case Paleohydrogeologic Scenario

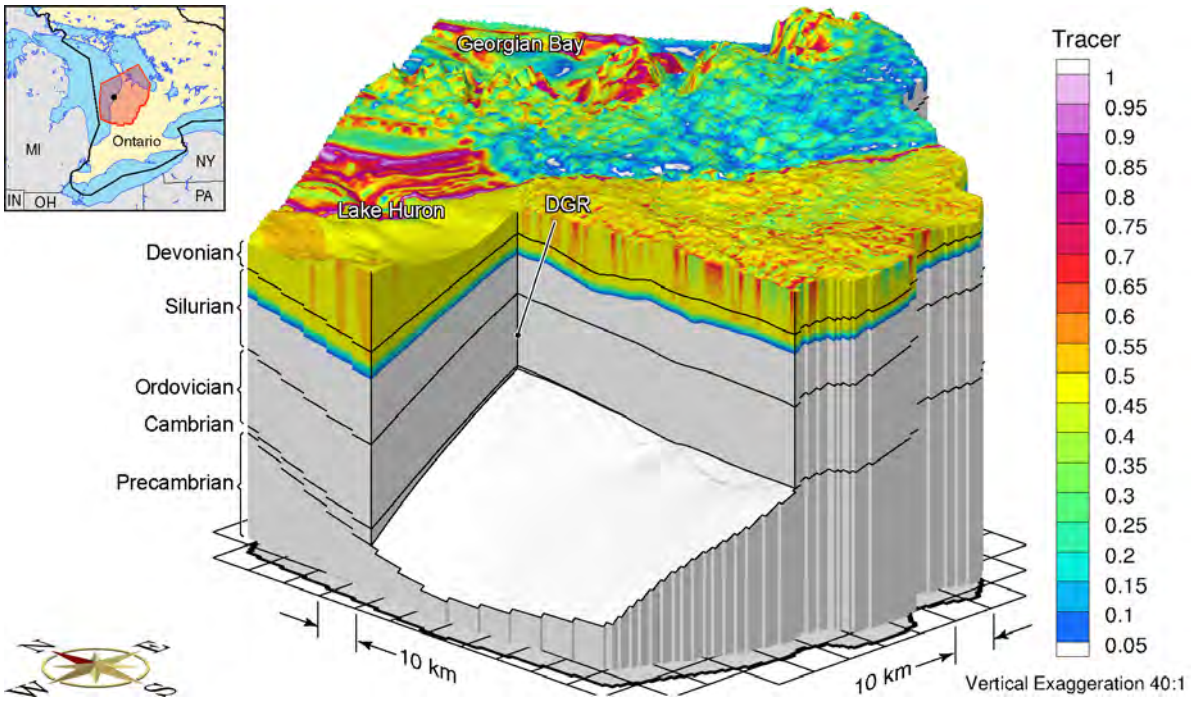

Figure 5.15: Block Cut View of Tracer Concentrations at Present for the Base-Case Paleohydrogeologic Scenario

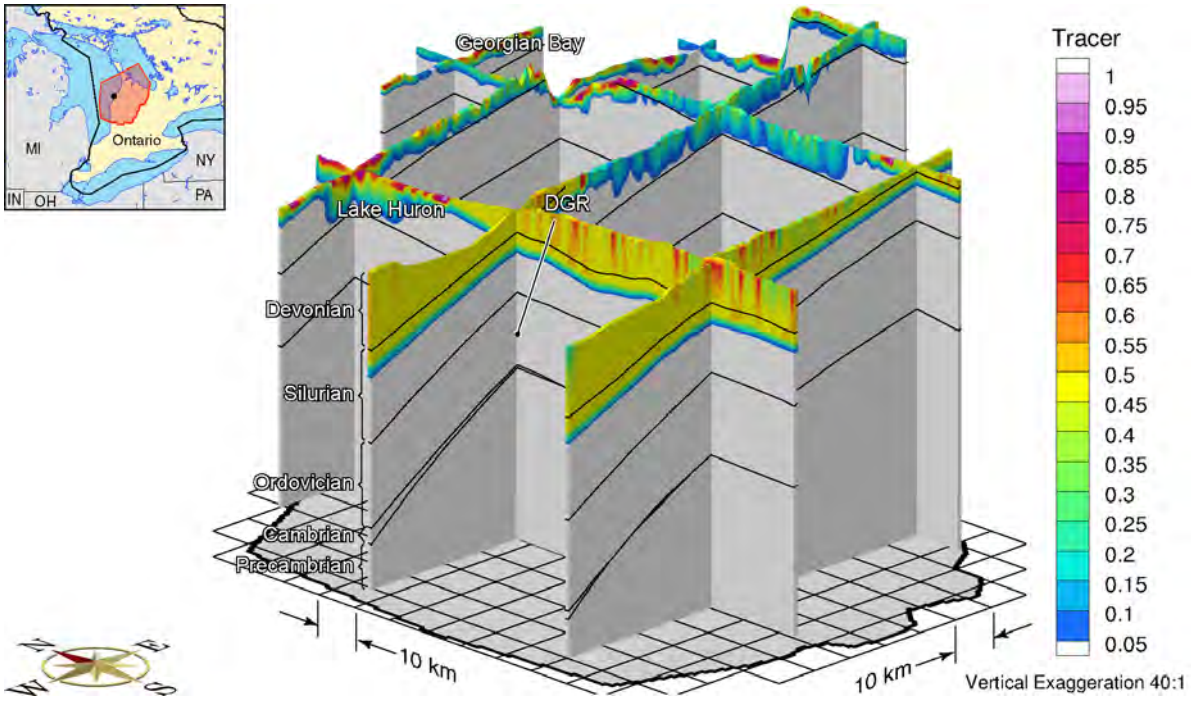

Figure 5.16: Fence View of Tracer Concentrations at Present for the Base-Case Paleohydrogeologic Scenario

figures, except for the ratio plots at the end of the simulation which indicate both upward and downward flow, while the base-case indicates downward flow in the Ordovician. This is due to the reduced heads applied at the surface boundary.

Tracer concentrations for the modelling domain are presented in Figure F.33 to Figure F.36. Figure 5.17d shows the migration of the tracer into the subsurface. Similar to the base-case, the tracer only migrates into the top of the Salina by the end of the paleohydrogeologic simulation, however, the tracer migrates shallower in this simulation as compared to the base-case in Figure 5.8d due to the reduced vertical gradients from a reduced surface hydraulic boundary condition. The downward migration of the tracer is retarded by the Salina and demonstrates diffusion as the dominant transport mechanism.

5.6.3 Surface Boundary Condition Based on 30% of Ice Thickness

This scenario applies a hydraulic boundary condition to the surface of the modelling domain that is 30% of the ice thickness to allow for some reduction in heads beneath the ice sheet (scenario fr-base-paleo-head30). Fence view figures at 90 ka, 60 ka, 30 ka, and 0 ka before present for environmental heads, pore water velocity magnitudes, ratio of vertical pore water velocity to pore water velocity magnitude, and recharge water tracer migration are shown in Appendix F from Figure F.37 to Figure F.54, and are summarized in Table 5.3.

Table 5.3: Figure Numbers in Appendix F for Surface Boundary Condition Based on 30% of Ice Thickness

Parameter	Time before present			
	90 ka	60 ka	30 ka	Present
Freshwater Head	—	—	—	Figures F.37 & F.38
Environmental Head	Figure F.39	Figure F.40	Figure F.41	Figure F.42
Pore Water Velocity Magnitude	Figure F.43	Figure F.44	Figure F.45	Figure F.46
Ratio of Vertical Pore Water Velocity to Pore Water Velocity Magnitude	Figure F.47	Figure F.48	Figure F.49	Figure F.50
Tracer Concentration	Figure F.51	Figure F.52	Figure F.53	Figure F.54

The freshwater heads at the end of the paleohydrogeologic simulation are shown in Figures F.37 and F.38, while the environmental fence plots are shown in Figure F.39 to Figure F.42. As compared to the base-case, the Silurian is under-pressured due to the reduced surface heads. Figure 5.18 also presents the freshwater and environmental heads at the end of the paleohydrogeologic simulation with a comparison to the initial condition. A slight under-pressure results from the Salina through to the Queenston Formation, and a slight under-pressure at the Kirkfield Formation, this latter portion is similar to the base-case. The measured pattern of under-pressures in the Salina are approximately matched by the simulated results, however, the greater under-pressures in the Ordovician are not matched at all indicating that the under-pressures in this portion of the system are not a result of the imposed pattern of glacial loading and unloading.

The TDS profile in Figure 5.18c changes slightly between the beginning and end of the paleohydrogeologic simulation, and occurs mainly at the top of the Salina and near the Niagaran Group. Otherwise, the TDS profile is essentially unchanged through the course of the simulation, as occurred in the base-case paleohydrogeologic analysis.

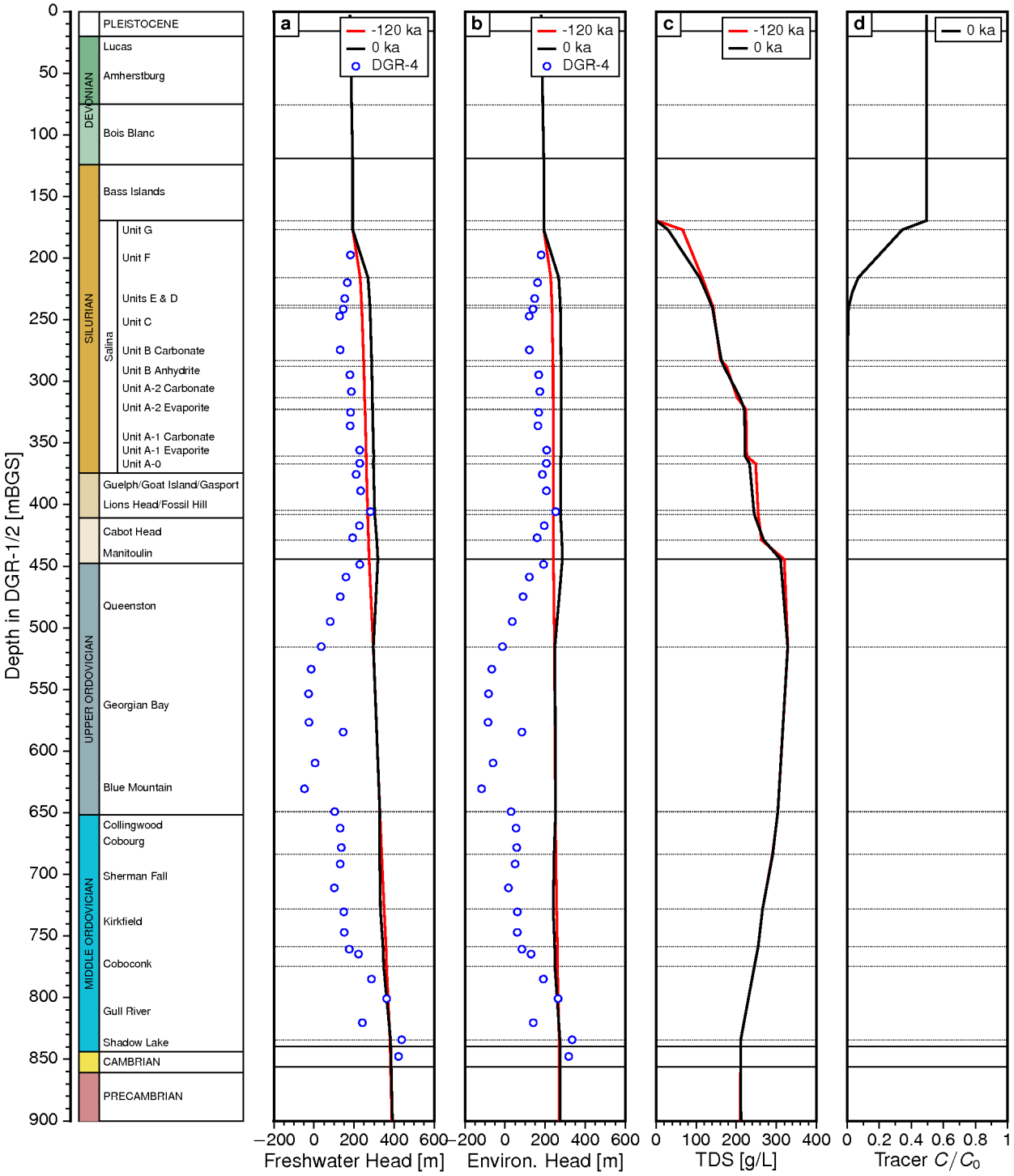

Note: (a) freshwater head, (b) environmental head, (c) total dissolved solids concentration, and (d) tracer concentration versus depth are plotted at beginning (−120 ka) and end (0 ka) of a paleohydrogeologic cycle. Freshwater and environmental heads for DGR-4 are shown as measured on August 24, 2009.

Figure 5.17: Vertical Profile Plots for Paleohydrogeologic Scenario at the DGR Site with the Surface Boundary Condition Based on 80% of Ice Thickness

Pore water velocity magnitudes for the paleohydrogeologic simulation are shown in Figure F.43 to Figure F.46, while the ratio of vertical pore water velocity to pore water velocity magnitudes are shown in Figure F.47 to Figure F.50. Visually, these plots are very similar to the base-case figures, except for the ratio plots at the end of the simulation which indicate upward flow, while the base-case indicates downward flow in the Ordovician. This is due to the reduced heads applied at the surface boundary and are transient.

Tracer concentrations for the modelling domain are presented in Figure F.51 to Figure F.54. Figure 5.18d shows the migration of the tracer into the subsurface. Similar to the base-case, the tracer only migrates into the top of the Salina by the end of the paleohydrogeologic simulation and to a similar, yet slightly shallower depth as compared to the base-case in Figure 5.8d. The downward migration of the tracer is retarded by the Salina and demonstrates diffusion as the dominant transport mechanism.

5.6.4 Free Draining Surface Boundary Condition

This scenario investigates the effect of choosing a zero pressure hydraulic surface boundary condition for the paleohydrogeologic simulation; this choice of boundary condition creates a free draining surface boundary condition where water can enter or exit the boundary as needed (scenario fr-base-paleo-zero-head). The exiting water effectively “disappears” and is not accumulated or routed in a subglacial hydrology sense. In Section 5.2, the subglacial hydraulic conditions were discussed and field evidence was presented to state that subglacial water pressures are not zero, nor that the subglacial flow system is free draining everywhere.

Fence view figures at 90 ka, 60 ka, 30 ka, and 0 ka before present for environmental heads, pore water velocity magnitudes, ratio of vertical pore water velocity to pore water velocity magnitude, and recharge water tracer migration are shown in Appendix F from Figure F.55 to Figure F.72, and are summarized in Table 5.4.

Table 5.4: Figure Numbers in Appendix F for a Free Draining Surface Boundary Condition

Parameter	Time before present			
	90 ka	60 ka	30 ka	Present
Freshwater Head	—	—	—	Figures F.55 & F.56
Environmental Head	Figure F.57	Figure F.58	Figure F.59	Figure F.60
Pore Water Velocity Magnitude	Figure F.61	Figure F.62	Figure F.63	Figure F.64
Ratio of Vertical Pore Water Velocity to Pore Water Velocity Magnitude	Figure F.65	Figure F.66	Figure F.67	Figure F.68
Tracer Concentration	Figure F.69	Figure F.70	Figure F.71	Figure F.72

The freshwater heads at the end of the paleohydrogeologic simulation are shown in Figures F.55 and F.56, while the environmental fence plots are shown in Figure F.57 to Figure F.60. Vertical profiles of freshwater and environmental heads at the DGR location are shown in Figure 5.19. In comparing Figure 5.19 to Figure 5.8, the over-pressures in the base-case are now under-pressures in a very similar, yet opposite sense. There appears to be some agreement between the under-pressures in the DGR-4 borehole through the upper half of the Silurian, but disagreement in the Ordovician. In fact, the generated under-pressures due to a free draining hydraulic surface boundary condition do not permit a matching residual under-pressure to exist at the end of the paleohydrogeologic simulation within the Ordovician. The over-pressures in the

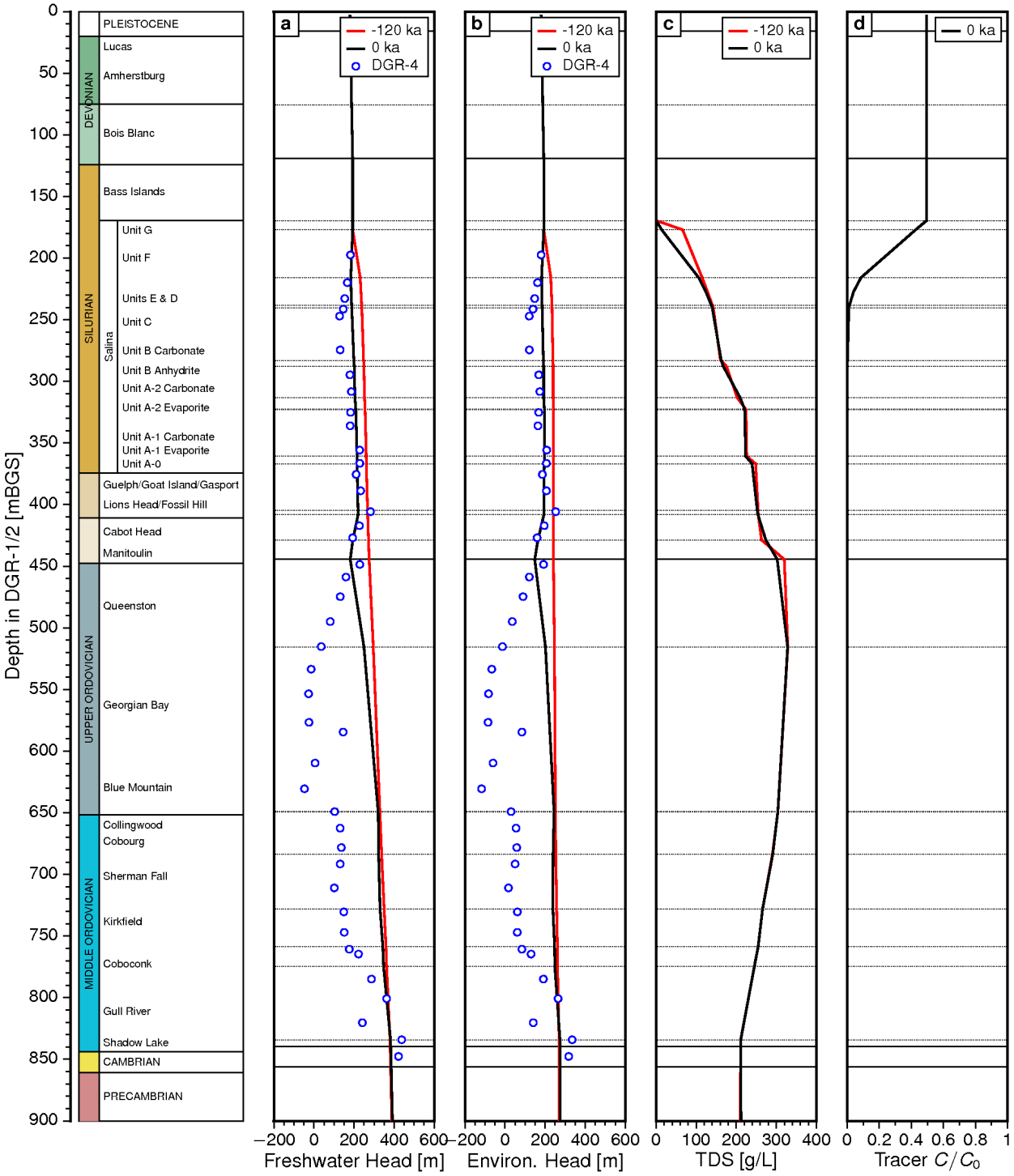

Note: (a) freshwater head, (b) environmental head, (c) total dissolved solids concentration, and (d) tracer concentration versus depth are plotted at beginning (−120 ka) and end (0 ka) of a paleohydrogeologic cycle. Freshwater and environmental heads for DGR-4 are shown as measured on August 24, 2009.

Figure 5.18: Vertical Profile Plots for Paleohydrogeologic Scenario at the DGR Site with the Surface Boundary Condition Based on 30% of Ice Thickness

Cambrian Formation are also not matched. Although the hydraulic conductivity of the units above the Silurian are quite permeable, the presence of permafrost acts to significantly reduce the near surface hydraulic conductivity, thereby reducing vertical drainage fluxes that would occur during glacial loading.

The TDS concentration profile in Figure 5.19c is nearly unchanged from its initial conditions and is also very similar to the profile in the base-case (see Figure 5.8c).

Pore water velocity magnitudes for the paleohydrogeologic simulation are shown in Figure F.61 to Figure F.64, while the ratio of vertical pore water velocity to pore water velocity magnitudes are shown in Figure F.65 to Figure F.68. Visually, these plots are very similar to the base-case figures, except for the ratio plots at the end of the simulation which indicate upward flow, while the base-case indicates downward flow in the Ordovician. This is due to the free draining surface boundary condition.

Tracer concentrations for the modelling domain are presented in Figure F.69 to Figure F.72. Figure 5.19d shows the migration of the tracer into the subsurface, and appears very similar to the base-case. The position of the 5% isochlor is slightly shallower on the western face of the domain as compared to the base-case, but is otherwise very similar to the base-case. Instead of surface waters entering the system during a glacial loading event, as in the base-case, the waters will enter the system upon glacial unloading due to water being pulled back into the domain. The cumulative effect over the course of a paleohydrogeologic simulation is that glacial waters do enter the system regardless of how the geosphere hydraulic surface boundary condition is applied.

5.6.5 Zero Loading Efficiency ($\zeta = 0$)

This paleohydrogeologic scenario investigates the role of neglecting hydromechanical coupling by setting the one-dimensional loading efficiency ζ to zero (scenario fr-base-paleo-le-zero). Fence view figures at 90 ka, 60 ka, 30 ka, and 0 ka before present for environmental heads, pore water velocity magnitudes, ratio of vertical pore water velocity to pore water velocity magnitude, and recharge water tracer migration are shown in Appendix F from Figure F.73 to Figure F.90, and are summarized in Table 5.5.

Table 5.5: Figure Numbers in Appendix F for a Loading Efficiency of Zero

Parameter	Time before present			
	90 ka	60 ka	30 ka	Present
Freshwater Head	—	—	—	Figures F.73 & F.74
Environmental Head	Figure F.75	Figure F.76	Figure F.77	Figure F.78
Pore Water Velocity Magnitude	Figure F.79	Figure F.80	Figure F.81	Figure F.82
Ratio of Vertical Pore Water Velocity to Pore Water Velocity Magnitude	Figure F.83	Figure F.84	Figure F.85	Figure F.86
Tracer Concentration	Figure F.87	Figure F.88	Figure F.89	Figure F.90

The freshwater heads at the end of the paleohydrogeologic simulation are shown in Figures F.73 and F.74, while the environmental fence plots are shown in Figure F.75 to Figure F.78. Vertical profiles of freshwater and environmental heads at the DGR location are shown in Figure 5.20. In comparing Figure 5.20 to Figure 5.8, the vertical gradients for this simulation are greater than for

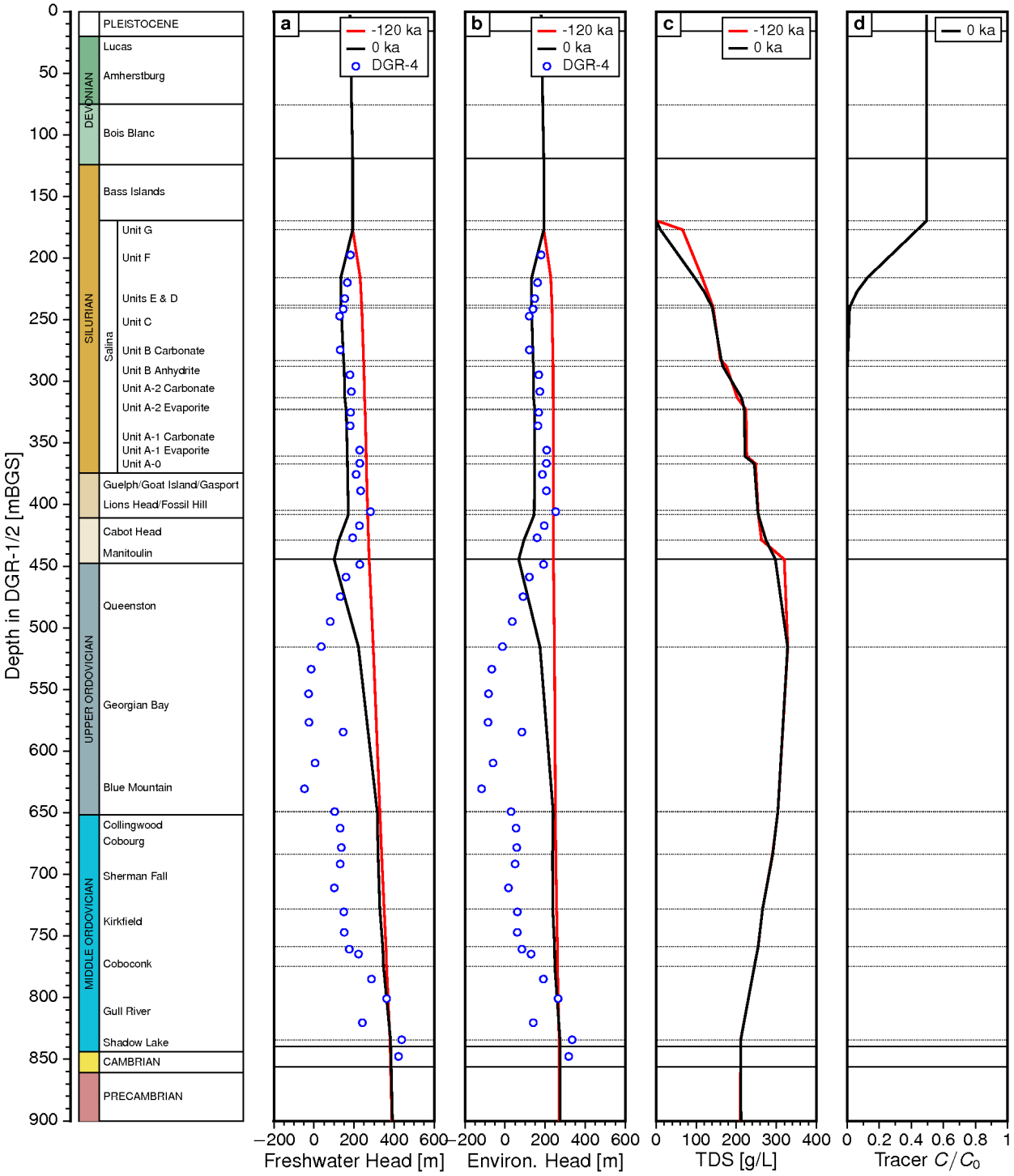

Note: (a) freshwater head, (b) environmental head, (c) total dissolved solids concentration, and (d) tracer concentration versus depth are plotted at beginning (−120 ka) and end (0 ka) of a paleohydrogeologic cycle. Freshwater and environmental heads for DGR-4 are shown as measured on August 24, 2009.

Figure 5.19: Vertical Profile Plots for Paleohydrogeologic Scenario at the DGR Site with a Free Draining Boundary Condition at the Ice Base

the base-case. The lack of hydromechanical coupling results in larger vertical gradients since the hydromechanical term, described in Section 3.2 and behaving as a fluid source/sink term, does not allow for an increase in pore pressure throughout the domain due to glacially induced mechanical loading. For a non-zero loading efficiency, the increase in pore pressure thereby reduces the vertical fluid energy gradient. Both freshwater heads and environmental heads are higher at depth at the end of the paleohydrogeologic simulation as compared to the base-case. The increased gradients in this simulation lead to higher residual heads at the end of the simulation, but with a similar pattern to the base-case. The exception is that higher pore pressures are evident also in the Georgian Bay and Blue Mountain Formations. The pattern of under-pressures throughout the Silurian and Ordovician are not represented in the simulation results; in fact, the entire profile is significantly over-pressured.

The TDS concentration profile in Figure 5.20c is nearly unchanged from its initial conditions and is also very similar to the profile in the base-case. The TDS profile shows some downward migration or adjustment among the Niagaran Group to the Queenston Formation, likely due to higher vertical gradients and their resulting velocities.

Pore water velocity magnitudes for the paleohydrogeologic simulation are shown in Figure F.79 to Figure F.82, while the ratio of vertical pore water velocity to pore water velocity magnitudes are shown in Figure F.83 to Figure F.86. Visually, these pore water velocity magnitudes are very similar to the base-case figures. The ratio plots are quite different and illustrate the movement of groundwater in the Precambrian during the first glacial loading event at 60 ka before present which indicate upward flow in the base-case, and horizontal movement for this simulation. At the end of the paleohydrogeologic simulation, groundwater flow in the Precambrian is essentially horizontal, while in the base-case, the movement is strongly upward in the portion of the Precambrian that is beneath the Cambrian.

Tracer concentrations for the modelling domain are presented in Figure F.69 to Figure F.72. The position of the 5% isochlor is slightly deeper than in the base-case and is due to the increased vertical gradients and vertical velocities resulting from a lack of hydromechanical coupling. Figure 5.19d shows the migration of the tracer into the subsurface. This migration is slightly deeper into the domain than the base-case, but is still contained within the upper Salina.

5.6.6 Biot Coefficient of 0.5

This paleohydrogeologic simulation investigates the role of assuming a compressible grain modulus with a Biot coefficient of 0.5; resulting in a grain modulus which is twice the bulk modulus (scenario fr-base-paleo-biot). This change lowers the calculated storage coefficient and loading efficiency. The updated table of parameters for this case is provided in Table 4.5. Fence view figures at 90 ka, 60 ka, 30 ka, and 0 ka before present for environmental heads, pore water velocity magnitudes, ratio of vertical pore water velocity to pore water velocity magnitude, and recharge water tracer migration are shown in Appendix F from Figure F.91 to Figure F.108, and are summarized in Table 5.6.

The freshwater heads at the end of the paleohydrogeologic simulation are shown in Figures F.91 and F.92, while the environmental fence plots are shown in Figure F.93 to Figure F.96. The heads are generally higher at the end of this simulation as compared to the base-case. Figure 5.21 also presents the freshwater and environmental heads at the end of the paleohydrogeologic simulation with a comparison to the initial head condition at −120 ka. Similarly at the DGR site, the heads are higher at the end of the simulation when compared to the base-case. These simulation results do not mimic the under-pressures in either the Silurian or Ordovician. The

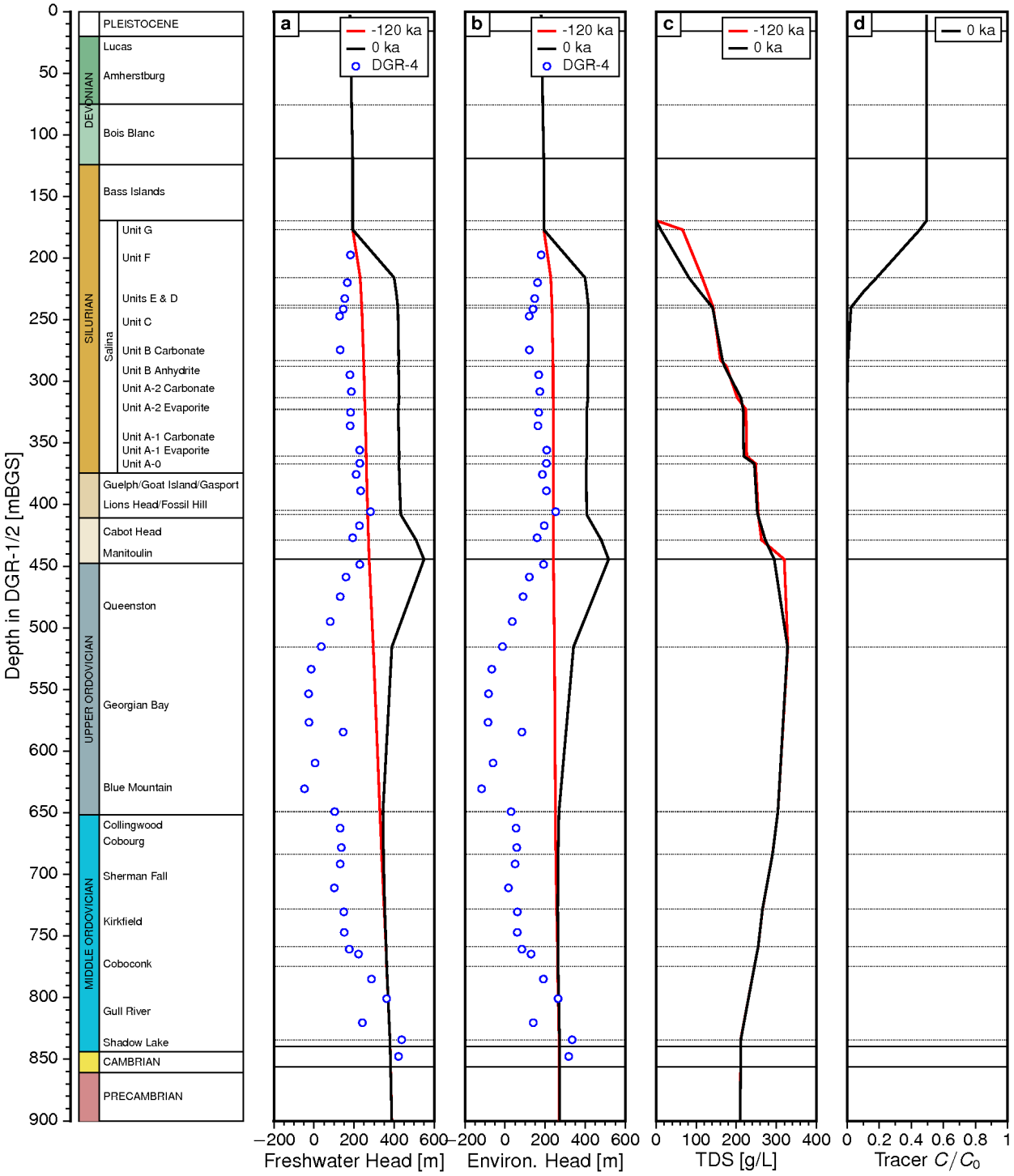

Note: (a) freshwater head, (b) environmental head, (c) total dissolved solids concentration, and (d) tracer concentration versus depth are plotted at beginning (−120 ka) and end (0 ka) of a paleohydrogeologic cycle. Freshwater and environmental heads for DGR-4 are shown as measured on August 24, 2009.

Figure 5.20: Vertical Profile Plots for Paleohydrogeologic Scenario at the DGR Site with a One-Dimensional Loading Efficiency of Zero

Table 5.6: Figure Numbers in Appendix F for a Biot Coefficient of 0.5

Parameter	Time before present			
	90 ka	60 ka	30 ka	Present
Freshwater Head	—	—	—	Figures F.91 & F.92
Environmental Head	Figure F.93	Figure F.94	Figure F.95	Figure F.96
Pore Water Velocity Magnitude	Figure F.97	Figure F.98	Figure F.99	Figure F.100
Ratio of Vertical Pore Water Velocity to Pore Water Velocity Magnitude	Figure F.101	Figure F.102	Figure F.103	Figure F.104
Tracer Concentration	Figure F.105	Figure F.106	Figure F.107	Figure F.108

over-pressure propagates deeper into the domain to the top of the Cobourg Formation. Lower storage coefficients will tend to allow pressure pulses to propagate deeper into the system and the ability to store changes in pore pressure is diminished.

The TDS concentration profile in Figure 5.21c is nearly unchanged from its initial conditions and is also very similar to the profile in the base-case. The TDS profile shows some downward migration or adjustment at the top of the Salina, the Niagaran Group, and the top of the Queenston Formation as compared to the initial condition.

Pore water velocity magnitudes for the paleohydrogeologic simulation are shown in Figure F.97 to Figure F.100, while the ratio of vertical pore water velocity to pore water velocity magnitudes are shown in Figure F.101 to Figure F.104. Visually, these pore water velocity magnitudes are very similar to the base-case figures. The ratio plots are also quite similar to the base-case plots.

Tracer concentrations for the modelling domain are presented in Figure F.105 to Figure F.108. Figure 5.21d shows the migration of the tracer into the subsurface. This migration is nearly identical to the base-case, and is still contained within the upper Salina.

5.6.7 Analysis of the Effect of a Gas Phase

This paleohydrogeologic simulation investigates the role of partially saturated porous media from the perspective of mechanical and storage effects and not from a two-phase analysis (scenario fr-base-paleo-gas). This change significantly raises the storage coefficient while decreasing the loading efficiency for those layers with a pore space that contains both a brine and a gas. In this case, the fluid compressibility is the saturation weighted ratio of the brine and gas individual compressibilities. The gas phase is characterized by air at an insitu pressure of 12.5 MPa with the gas saturations for the various layers being defined in Table 2.16. The updated table of parameters is provided in Table 4.7. Fence view figures at 90 ka, 60 ka, 30 ka, and 0 ka before present for environmental heads, pore water velocity magnitudes, ratio of vertical pore water velocity to pore water velocity magnitude, and recharge water tracer migration are shown in Appendix F from Figure F.109 to Figure F.126, and are summarized in Table 5.7.

The freshwater heads at the end of the paleohydrogeologic simulation are shown in Figures F.91 and F.92, while the environmental fence plots are shown in Figure F.93 to Figure F.96. The heads are generally higher at the end of this simulation as compared to the base-case, and are also higher than for the paleohydrogeologic simulation with a Biot coefficient of 0.5. Figure 5.21 also presents the freshwater and environmental heads at the end of the paleohydrogeologic simulation with a comparison to the initial head condition at −120 ka. The higher storage coefficients through most of the Silurian lead to an enhanced ability to retain elevated pore pressures arising from the paleoclimate surface boundary conditions. These simulated

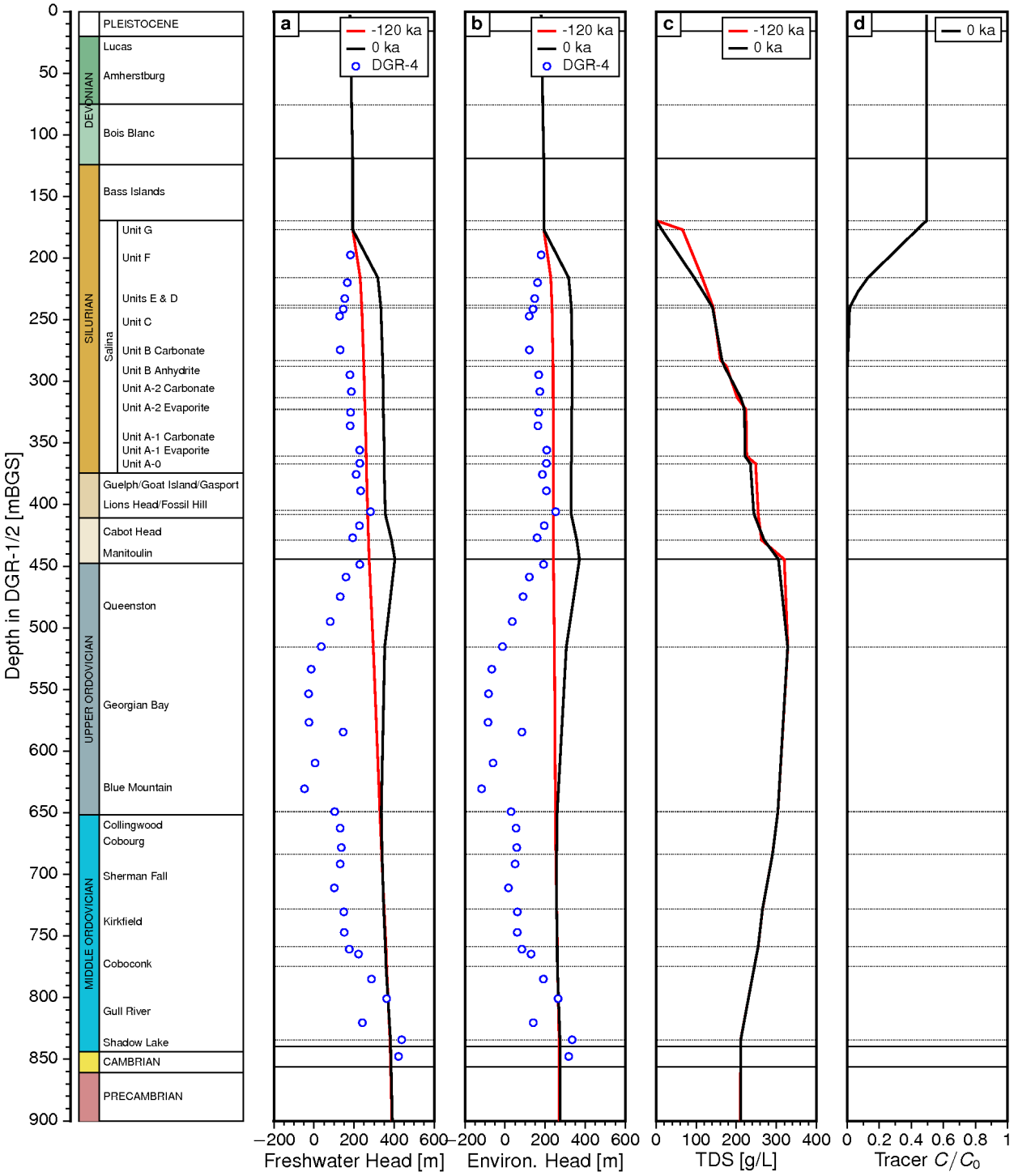

Note: (a) freshwater head, (b) environmental head, (c) total dissolved solids concentration, and (d) tracer concentration versus depth are plotted at beginning (−120 ka) and end (0 ka) of a paleohydrogeologic cycle. Freshwater and environmental heads for DGR-4 are shown as measured on August 24, 2009.

Figure 5.21: Vertical Profile Plots for Paleohydrogeologic Scenario at the DGR Site with the Base-Case Parameters and a Biot Coefficient of 0.5

Table 5.7: Figure Numbers in Appendix F Reflecting the Presence of a Gas Phase

Parameter	Time before present			
	90 ka	60 ka	30 ka	Present
Freshwater Head	—	—	—	Figures F.109 & F.110
Environmental Head	Figure F.111	Figure F.112	Figure F.113	Figure F.114
Pore Water Velocity Magnitude	Figure F.115	Figure F.116	Figure F.117	Figure F.118
Ratio of Vertical Pore Water Velocity to Pore Water Velocity Magnitude	Figure F.119	Figure F.120	Figure F.121	Figure F.122
Tracer Concentration	Figure F.123	Figure F.124	Figure F.125	Figure F.126

over-pressures, which are on the order of 200 m are not representative of the measured under-pressures in both the Silurian and Ordovician. Below the Queenston, very little difference is noted between the initial heads and the heads at the end of the simulation. During the first loading phase at 60 ka before present, the effect of a gas on the Silurian and Ordovician are evident in that flow is toward the units with lower loading efficiencies, characterized in this simulation as layers containing a gas phase. The TDS concentration profile in Figure 5.22c is nearly unchanged from its initial conditions and is also very similar to the profile in the base-case. The TDS profile shows some downward migration or adjustment at the top of the Salina, the Niagaran Group, and the top of the Queenston Formation as compared to the initial condition.

Pore water velocity magnitudes for the paleohydrogeologic simulation are shown in Figure F.115 to Figure F.118, while the ratio of vertical pore water velocity to pore water velocity magnitudes are shown in Figure F.119 to Figure F.122. Visually, these pore water velocity magnitudes are very similar to the base-case figures. The ratio plots are also quite similar to the base-case plots, except for layers that have a reduced loading efficiency as pore fluids tend to flow towards these layers since adjacent fully brine saturated layers have less storage and a higher loading efficiency which will tend to expel pore fluid, and collect in those partially saturated layers exhibiting high storage and low loading efficiencies.

Tracer concentrations for the modelling domain are presented in Figure F.123 to Figure F.126. Figure 5.22d shows the migration of the tracer into the subsurface. This migration is deeper than the base-case, but is still contained within the upper Salina.

5.6.8 Analysis of Two Paleohydrogeologic Cycles of 120 ka Each

This paleohydrogeologic simulation investigates the role of two consecutive paleohydrogeologic cycles using the nn9930 paleoclimate model (scenario fr-base-paleo-2). The initial conditions for the second paleohydrogeologic cycle use the final freshwater heads, brine and tracer concentrations from the first paleohydrogeologic cycle. Fence view figures at 90 ka, 60 ka, 30 ka, and 0 ka before present for environmental heads, pore water velocity magnitudes, ratio of vertical pore water velocity to pore water velocity magnitude, and recharge water tracer migration are shown in Appendix F from Figure F.127 to Figure F.144, and are summarized in Table 5.8.

The freshwater heads at the end of the paleohydrogeologic simulation are shown in Figures F.127 and F.128, while the environmental fence plots are shown in Figure F.129 to Figure F.132. The heads are generally higher at the end of this simulation as compared to the base-case, however the environmental heads are slightly higher as compared to the base-case. Figure 5.8 also presents the freshwater and environmental heads at the end of the paleohydrogeologic simulation with a comparison to the initial head condition at −120 ka and the previous

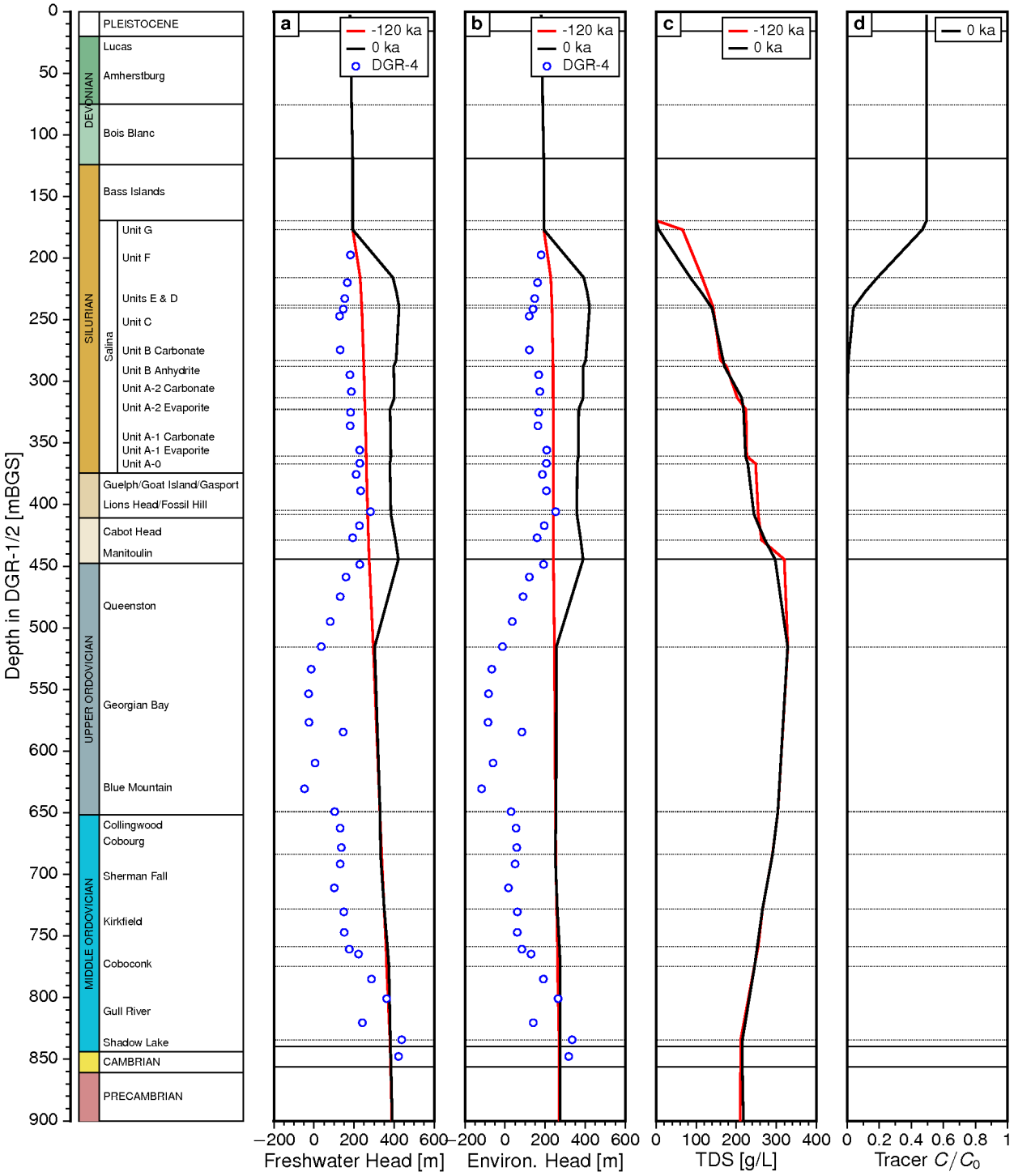

Note: (a) freshwater head, (b) environmental head, (c) total dissolved solids concentration, and (d) tracer concentration versus depth are plotted at beginning (−120 ka) and end (0 ka) of a paleohydrogeologic cycle. Freshwater and environmental heads for DGR-4 are shown as measured on August 24, 2009.

Figure 5.22: Vertical Profile Plots for Paleohydrogeologic Scenario at the DGR Site with the 1-D Loading Efficiencies and Storage Coefficients Reflecting the Presence of a Gas Phase

Table 5.8: Figure Numbers in Appendix F for Two Consecutive Paleohydrogeologic Cycles of 120 ka

Parameter	Time before present			
	90 ka	60 ka	30 ka	Present
Freshwater Head	—	—	—	Figures F.127 & F.128
Environmental Head	Figure F.129	Figure F.130	Figure F.131	Figure F.132
Pore Water Velocity Magnitude	Figure F.133	Figure F.134	Figure F.135	Figure F.136
Ratio of Vertical Pore Water Velocity to Pore Water Velocity Magnitude	Figure F.137	Figure F.138	Figure F.139	Figure F.140
Tracer Concentration	Figure F.141	Figure F.142	Figure F.143	Figure F.144

paleohydrogeologic cycle at 0 ka. The heads profile at the DGR site is nearly the same at the end of each paleohydrogeologic cycle, although slightly higher through the Upper Ordovician. Such little change can be attributed to the long period of time prior to the first glacial advance and retreat, which allows sufficient time to equilibrate heads to a state close to the initial conditions for the base-case. In either case, both the freshwater heads and the environmental heads are higher throughout the Silurian and the Upper Ordovician, and do not represent the under-pressures measured in the Silurian and Ordovician.

The TDS concentration profile in Figure 5.8c is nearly unchanged from its initial conditions and is also very similar to the profile in the base-case. The TDS profile shows some downward migration or adjustment at the top of the Salina, the Niagaran Group, and the top of the Queenston Formation as compared to the initial condition, however the TDS adjustment during the second paleohydrogeologic cycle is less than the amount which occurred during the first paleohydrogeologic cycle.

Pore water velocity magnitudes for the paleohydrogeologic simulation are shown in Figure F.133 to Figure F.136, while the ratio of vertical pore water velocity to pore water velocity magnitudes are shown in Figure F.137 to Figure F.140. Visually, these pore water velocity magnitudes are very similar to the base-case figures. The ratio plots at 90 ka before present show downward flow in the Ordovician due to the last glacial maximum which occurred towards the end of the previous paleohydrogeologic cycle. By 60 ka before present, the flow patterns are nearly the same. Towards the end of the paleohydrogeologic simulations, the flow patterns are also very similar.

Tracer concentrations for the modelling domain are presented in Figure F.141 to Figure F.144. Figure 5.8d shows the migration of the tracer into the subsurface after a second paleohydrogeologic cycle. This migration is deeper than what occurred at the end of the first paleohydrogeologic cycle, but is still contained within the upper Salina.

5.6.9 Analysis Using Paleoclimate Model nn9921

This paleohydrogeologic simulation investigates the role of using an alternate paleoclimate model, namely nn9921 instead of nn9930 which was used in the base-case (scenario fr-base-paleo-nn9921). In comparing Figure 5.3 to Figure 5.2, nn9921 exhibits more glaciation episodes, with the major episodes centred at approximately −60 ka and −25 ka of nearly double the temporal duration over the DGR site. The duration over which permafrost is present is also greater in nn9921. Lake depth at approximately −14 ka is also greater in nn9921 than in nn9930. Fence view figures at 90 ka, 60 ka, 30 ka, and 0 ka before present for environmental heads, pore water velocity magnitudes, ratio of vertical pore water velocity to pore water velocity magnitude,

and recharge water tracer migration are shown in Appendix F from Figure F.145 to Figure F.162, and are summarized in Table 5.9.

Table 5.9: Figure Numbers in Appendix F for Alternate Paleoclimate Model nn9921

Parameter	Time before present			
	90 ka	60 ka	30 ka	Present
Freshwater Head	—	—	—	Figures F.145 & F.146
Environmental Head	Figure F.147	Figure F.148	Figure F.149	Figure F.150
Pore Water Velocity Magnitude	Figure F.151	Figure F.152	Figure F.153	Figure F.154
Ratio of Vertical Pore Water Velocity to Pore Water Velocity Magnitude	Figure F.155	Figure F.156	Figure F.157	Figure F.158
Tracer Concentration	Figure F.159	Figure F.160	Figure F.161	Figure F.162

The freshwater heads at the end of the paleohydrogeologic simulation are shown in Figures F.145 and F.146, while the environmental fence plots are shown in Figure F.147 to Figure F.150. Both freshwater and environmental heads are greater at the end of this simulation as compared to the base-case. The environmental heads are also higher at 90 ka before present due to the first glaciation episode beginning at approximately −112 ka in nn9921, and at −63 ka in nn9930. Figure 5.23 also presents the freshwater and environmental heads at the end of the paleohydrogeologic simulation with a comparison to the initial head condition at −120 ka at the DGR site. Both the freshwater and environmental heads are over-pressured relative to the initial heads, and are significantly different than the measured under-pressures in the Silurian and Ordovician. An under-pressure relative to initial conditions is generated within the Kirkfield and Coboconk Formations.

The TDS concentration profile in Figure 5.23c is nearly unchanged from its initial conditions and is also very similar to the profile in the base-case. The TDS profile shows some downward migration or adjustment at the top of the Salina, the Niagaran Group, and the top of the Queenston Formation as compared to the initial condition.

Pore water velocity magnitudes for the paleohydrogeologic simulation are shown in Figure F.151 to Figure F.154, while the ratio of vertical pore water velocity to pore water velocity magnitudes are shown in Figure F.155 to Figure F.158. Visually, these pore water velocity magnitudes are very similar to the base-case figures, except that velocities can be several orders of magnitude greater than the base-case during glaciation episodes which occur in nn9921, but not in nn9930, as occurs at −90 ka. The ratio plots at present are very similar to the base-case with downward flow in the Ordovician, whereas at other times, the flow directions are dependent on the timing of glacial loading and unloading specific to each paleohydrogeologic simulation.

Tracer concentrations for the modelling domain are presented in Figure F.159 to Figure F.162. Figure 5.23d shows the migration of the tracer into the subsurface at the end of the paleohydrogeologic simulation. This migration is slightly deeper than what occurred at the end of the base-case paleohydrogeologic simulation, but is still contained within the upper Salina.

5.6.10 Analysis of Open Boundary Paleohydrogeologic Model

This paleohydrogeologic simulation investigates the role of open lateral boundaries for high conductivity units such as the A-1 Carbonate, Niagaran Group, and the Cambrian Formation

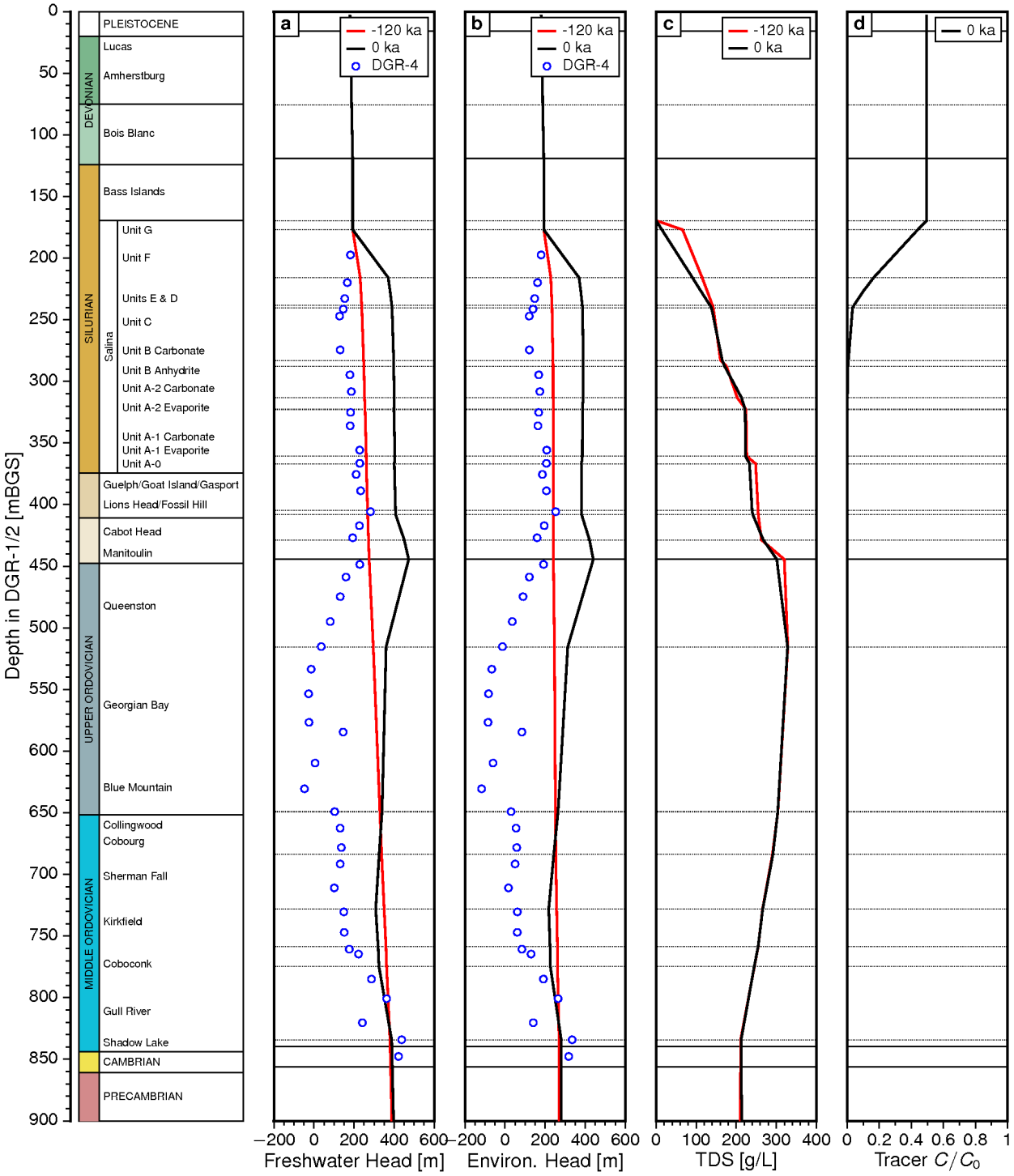

Note: (a) freshwater head, (b) environmental head, (c) total dissolved solids concentration, and (d) tracer concentration versus depth are plotted at beginning (−120 ka) and end (0 ka) of a paleohydrogeologic cycle. Freshwater and environmental heads for DGR-4 are shown as measured on August 24, 2009.

Figure 5.23: Vertical Profile Plots for Alternate Paleoclimate Model nn9921 at the DGR Site with Base-Case Parameters

(scenario fr-base-paleo-open-bnd). This approach applies a specified head boundary condition and a specified TDS concentration equal to their respective initial conditions for the entire 120 ka to nodes which meet all of the following conditions:

- Node is located on the lateral outer boundary of the modelling domain;
- Node is located on the top of each of the following lithologic units: A-1 Carbonate, Niagaran Group, and Cambrian. Only nodes along the top of a layer are used to prevent short circuiting between node pairs that would define both the top and bottom of a unit as the TDS changes; and
- Node is at or below an elevation of zero metres. This is important to prevent short circuiting of flow, and generating high velocities, with the high heads that are applied to the surface of the modelling domain during a paleohydrogeologic cycle.

In addition, a high hydraulic conductivity of 1×10^{-8} m/s is applied to the Upper Precambrian. The goal of this simulation is to provide a high conductivity pathway through the Cambrian and Upper Precambrian, to apply the highest possible heads during a paleohydrogeologic cycle, and to create the highest possible gradient through the high conductivity units by maintaining the boundary heads for these units at their pre-glaciation levels throughout the paleohydrogeologic cycle. It is unrealistic to expect that these units would be free draining, In the case of the Cambrian, it is connected to the centre of the Michigan Basin which would provide a pathway for migration as well as providing pressure support during a glacial event. This pressure support is likely between 0%, as represented in this paleohydrogeologic simulation, and 100% as represented in the base-case, resulting in zero flux across the model boundary. A tracer is applied to all recharge waters to determine if this tracer can migrate under these high gradients, and hence high pore water velocities, to the DGR site during the course of a paleohydrogeologic simulation.

Fence view figures at 90 ka, 60 ka, 30 ka, and 0 ka before present for environmental heads, pore water velocity magnitudes, ratio of vertical pore water velocity to pore water velocity magnitude, and recharge water tracer migration are shown in Appendix F from Figure F.163 to Figure F.180, and are summarized in Table 5.10.

Table 5.10: Figure Numbers in Appendix F for the Open Boundary Paleohydrogeologic Model

Parameter	Time before present			
	90 ka	60 ka	30 ka	Present
Freshwater Head	—	—	—	Figures F.163 & F.164
Environmental Head	Figure F.165	Figure F.166	Figure F.167	Figure F.168
Pore Water Velocity Magnitude	Figure F.169	Figure F.170	Figure F.171	Figure F.172
Ratio of Vertical Pore Water Velocity to Pore Water Velocity Magnitude	Figure F.173	Figure F.174	Figure F.175	Figure F.176
Tracer Concentration	Figure F.177	Figure F.178	Figure F.179	Figure F.180

The freshwater heads at the end of the paleohydrogeologic simulation are shown in Figures F.163 and F.164, while the environmental fence plots are shown in Figure F.165 to Figure F.168. The heads at the end of the paleohydrogeologic simulation are quite different than in the base-case (see Figure F.3 to Figure F.6). Heads in the Silurian are lower while heads in the Precambrian are much lower. At −60 ka, the effect of not allowing the heads at the boundary

nodes to change can be seen. The Cambrian is under-pressured relative the surrounding units, and the Niagaran Group and A-1 Carbonate are also under-pressured near the boundary. The Cambrian is at least two orders of magnitude higher conductivity than the A-1 Carbonate, and nearly three orders of magnitude higher than the Niagaran Group. The reduction in heads within the Cambrian is more pronounced than with either the A-1 Carbonate or the Niagaran Group. At the end of the paleohydrogeologic simulation, the Precambrian is significantly under-pressured relative to the base-case. The Silurian is also under-pressured relative to the base-case. Figure 5.24 also presents the freshwater and environmental heads at the end of the paleohydrogeologic simulation with a comparison to the initial head condition at −120 ka. At the DGR site, the heads are slightly under-pressured relative to the initial condition from the Salina through to the Cobourg. Below the Cobourg Formation, the heads drop to create an under-pressure and match a few of the measured DGR-4 data from the Coboconk to the Cambrian. Most of the under-pressures measured for the Silurian and Ordovician are not matched by the heads resulting from this paleohydrogeologic simulation.

The TDS concentration profile in Figure 5.24c is nearly unchanged from its initial conditions and is also very similar to the profile in the base-case. The TDS profile shows some downward migration or adjustment at the top of the Salina, the Niagaran Group, and the top of the Queenston Formation as compared to the initial condition.

Pore water velocity magnitudes for the paleohydrogeologic simulation are shown in Figure F.169 to Figure F.172, while the ratio of vertical pore water velocity to pore water velocity magnitudes are shown in Figure F.173 to Figure F.176. At −60 ka during the first glacial episode, pore velocities are approximately two orders of magnitude higher in the Precambrian as compared to the base-case, due to the much lower heads in the Cambrian. The high heads in the surrounding formations are due to hydromechanical coupling increasing pore pressures, which dissipate in the direction of the Cambrian. At the end of the paleohydrogeologic simulation, pore velocities in the Precambrian continue to be high as the flow system transitions towards equilibrium. The ratio plots at present are somewhat different as compared to the base-case. In this simulation, the Ordovician exhibits both upward and downward velocities, whereas in the base-case, the Ordovician exhibits primarily downward flow. In the base-case, the Precambrian exhibits upward flow while in this simulation, the Precambrian exhibits mostly downward flow.

Tracer concentrations for the modelling domain are presented in Figure F.177 to Figure F.180. At the end of the paleohydrogeologic simulation, the tracer has migrated into the subsurface, but when compared to the base-case, the depth of migration is nearly the same. The tracer has not propagated deeply enough during the paleohydrogeologic simulation to enter into the high conductivity units and migrate westward towards the DGR site. Figure 5.24d shows the migration of the tracer into the subsurface at the end of the paleohydrogeologic simulation. This migration is nearly identical to what occurred at the end of the base-case paleohydrogeologic simulation, and is still contained within the upper Salina.

5.6.11 Summary of Paleohydrogeologic Simulations

A summary figure of freshwater and environmental head vertical profiles for all paleohydrogeologic simulations is shown in Figure 5.25, while a summary figure of TDS and tracer concentration vertical profiles for all paleohydrogeologic simulations is shown in Figure 5.26. Also shown in Figure 5.25 and Figure 5.26 are the paleohydrogeologic initial conditions shown as a dashed line for fr-base. As can be seen in Figure 5.25, the heads at the end of any simulation (0 ka) are not able to match the under-pressures in the Ordovician. In Figure 5.26a, the TDS profile with depth changes very little from one simulation to the next. The

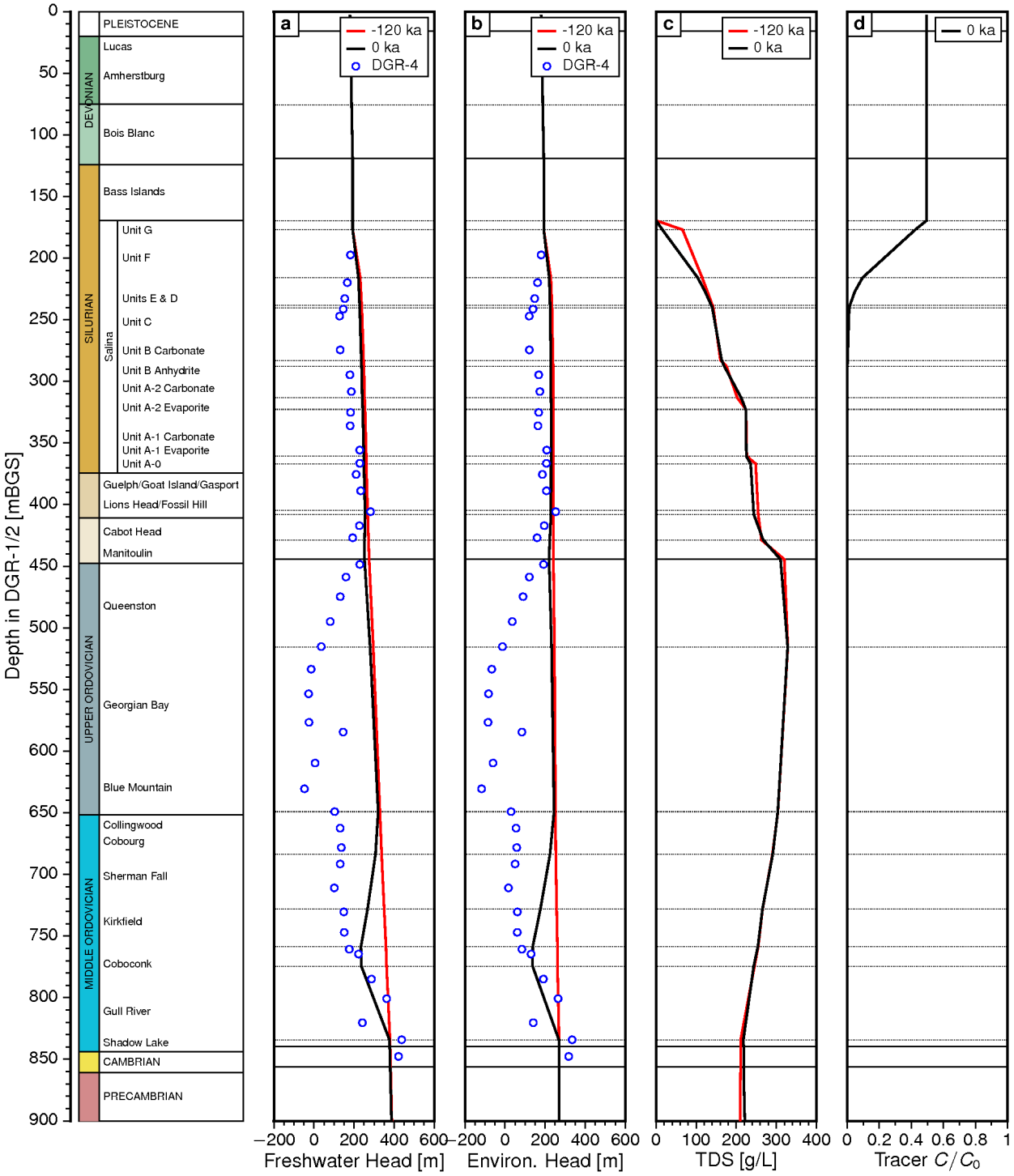

Note: (a) freshwater head, (b) environmental head, (c) total dissolved solids concentration, and (d) tracer concentration versus depth are plotted at beginning (−120 ka) and end (0 ka) of a paleohydrogeologic cycle. Freshwater and environmental heads for DGR-4 are shown as measured on August 24, 2009.

Figure 5.24: Vertical Profile Plots for Open Boundary Paleohydrogeologic Model at the DGR Site with Base-Case Parameters

tracer migration from surface, shown in Figure 5.26b, also demonstrates that diffusion is the dominant transport mechanism through the Salina formations.

5.6.12 Paleoclimate Effects on Pore Water Velocities in the Cobourg Formation

The horizontal magnitude of pore water velocities and the vertical pore water velocities in the Cobourg Formation at the DGR site during each paleohydrogeologic simulation are presented collectively in Figure 5.27, Figure 5.28, and Figure 5.29. Paleohydrogeologic simulations based on nn9930 are shown in Figure 5.27 and Figure 5.28, while the simulation based on nn9921 is shown in Figure 5.29. Both ice-sheet thickness and permafrost depth as a function of time for the 120 ka simulations are also shown to provide an indication of the mechanical, hydraulic and thermal loads at any time during the various paleoclimate cycles. As can be seen in the figures, horizontal pore water velocity magnitudes are normally less than 10^{-7} m/a while vertical pore water velocities are normally less than 10^{-5} m/a, either upward or downward, except during the ice loading event at approximately -20 ka in the nn9930 GSM, for which the maximum vertical velocities are slightly greater than 10^{-5} m/a. The velocities are also predominantly vertical, as compared to the horizontal pore water velocity magnitude, due to the much larger vertical gradients created during glacial advance or retreat.

Figure 5.27 plots the horizontal and vertical pore water velocities for the base-case, the second paleohydrogeologic cycle, a surface hydraulic boundary equal to 0%, 30%, and 80% of equivalent ice-sheet height as freshwater, and a loading efficiency of zero. The second paleohydrogeologic cycle of the base-case (red line) is very similar to the base-case once the first ice-sheet advance occurs at approximately -60 ka. Some deviation in velocities between -50 ka and -25 ka occurs due to excess heads being stored in units above, taking more time to reduce pore water velocities. The vertical pore water velocity at the end of the paleohydrogeologic simulation is nearly the same at the end of the second cycle as at the end of the first paleohydrogeologic cycle. The variation in surface hydraulic boundary condition leads to a vertical pore water velocity reversal at different times due to the reduced hydraulic gradients that occur as the surface hydraulic boundary condition is reduced; in addition, the reversal occurs sooner as the surface hydraulic boundary condition is reduced. The role of hydromechanical coupling is evident when considering the zero loading efficiency case. There is no change in the vertical pore water velocity until the effects of a change in the surface boundary condition are able to propagate through the overlying layers and into the Cobourg Formation at approximately -36 ka.

Figure 5.28 plots the horizontal and vertical pore water velocities for the base-case, setting the Biot coefficient to 0.5, changing fluid compressibilities due to the presence of a gas phase, and the open lateral boundary case. The Biot coefficient paleohydrogeologic simulation shows reduced upward vertical pore water velocities from the base-case of approximately one order of magnitude when the ice-sheet is present over the site and is attributed to the reduced one-dimensional loading efficiency throughout the domain. Storage coefficients are also reduced for a Biot coefficient of 0.5 as compared to the base-case. The paleohydrogeologic simulation with the presence of a gas phase is quite similar to the base-case, although the maximum vertical pore water velocities are reduced due to lower one-dimensional loading efficiencies, primarily in the Ordovician and approximately half of the Silurian formations. Storage coefficients for formations comprising a gas phase are also increased owing to the increased compressibility of the gas. The open boundary case is nearly identical to the base-case velocity profile, except for the period of time preceding the final glacial advance and retreat and is related to a lack of sustaining higher pore pressures in the deeper units.

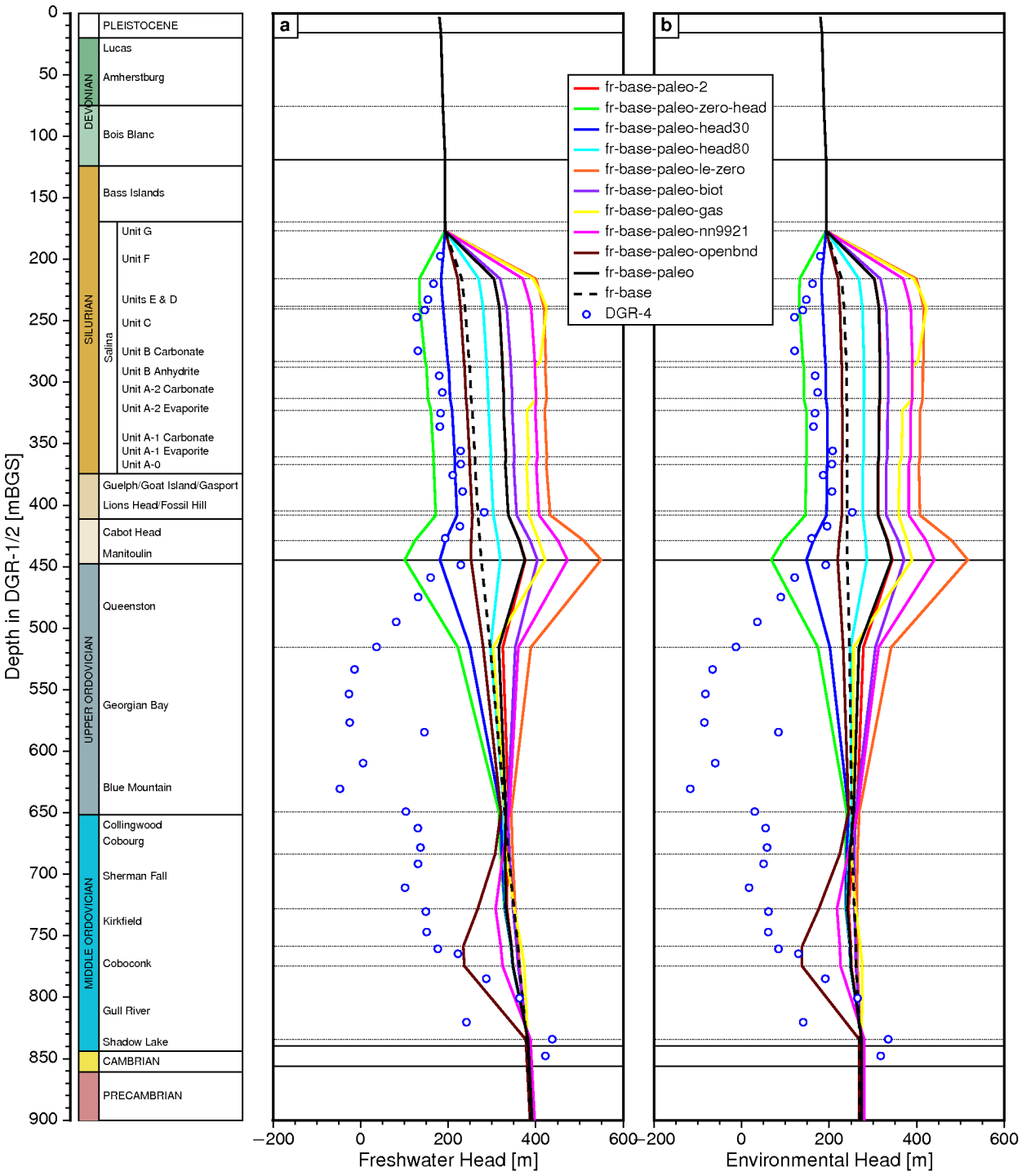

Note: (a) freshwater head, and (b) environmental head versus depth are plotted at for all paleohydrogeologic simulations. Freshwater and environmental heads for DGR-4 are shown as measured on August 24, 2009.

Figure 5.25: Summary of Freshwater and Environmental Heads Vertical Profile Plots for All Paleohydrogeologic Simulations

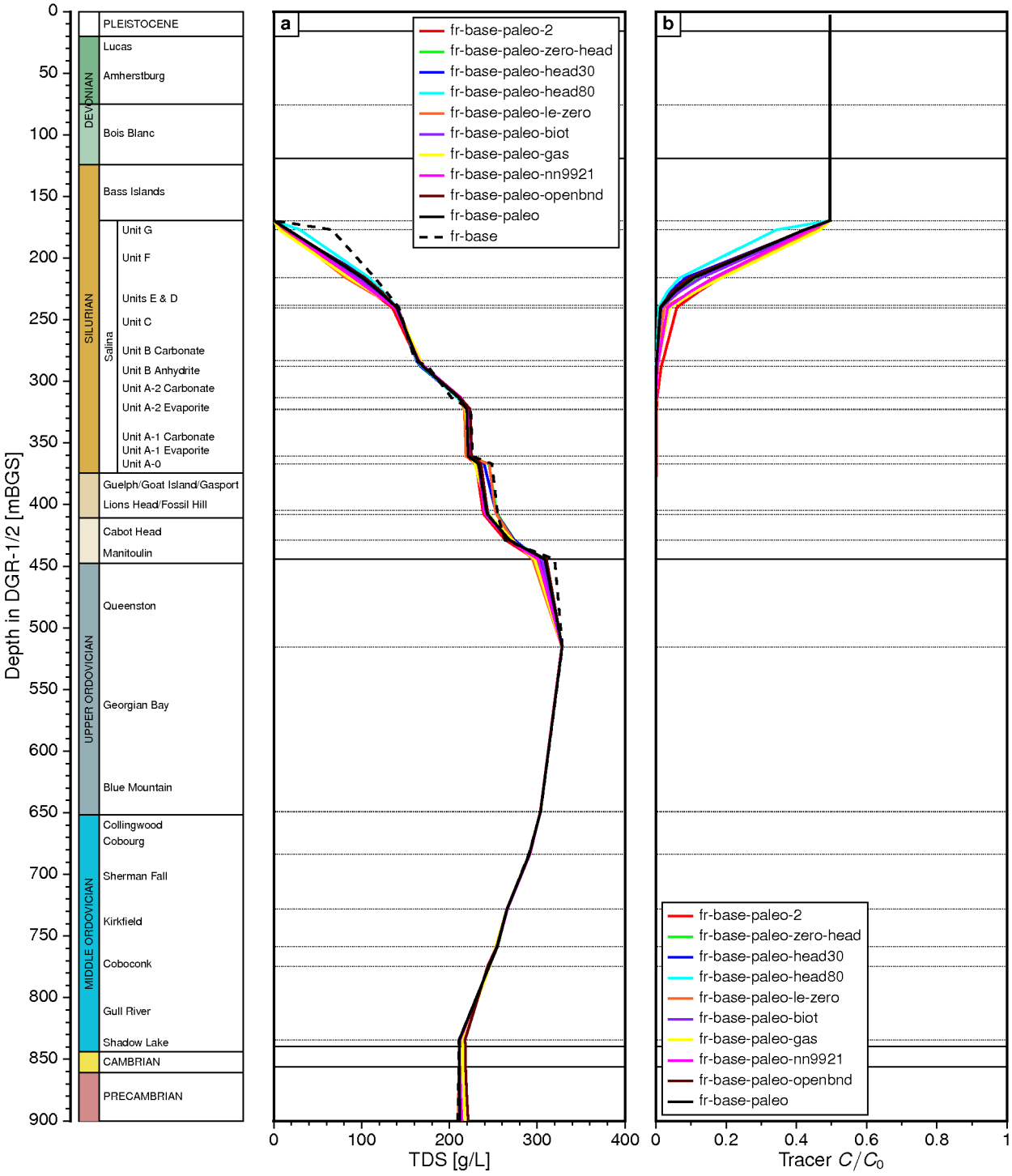

Note: (a) total dissolved solids concentration, and (d) tracer concentration versus depth are plotted for all paleohydrogeologic simulations.

Figure 5.26: Summary of TDS and Tracer Concentration Vertical Profile Plots for All Paleohydrogeologic Simulations

Figure 5.29 plots the horizontal and vertical pore water velocities for the paleohydrogeologic simulation using the nn9921 GSM. The velocities show more transitions between upward and downward velocities primarily based on the transient and multiple ice-sheet loading and unloading events. The presence of an ice-sheet results in upward velocities, while absence results in downward velocities. This behaviour is due to the hydromechanical coupling, the resulting changes in pore water pressures, and hydraulic gradients.

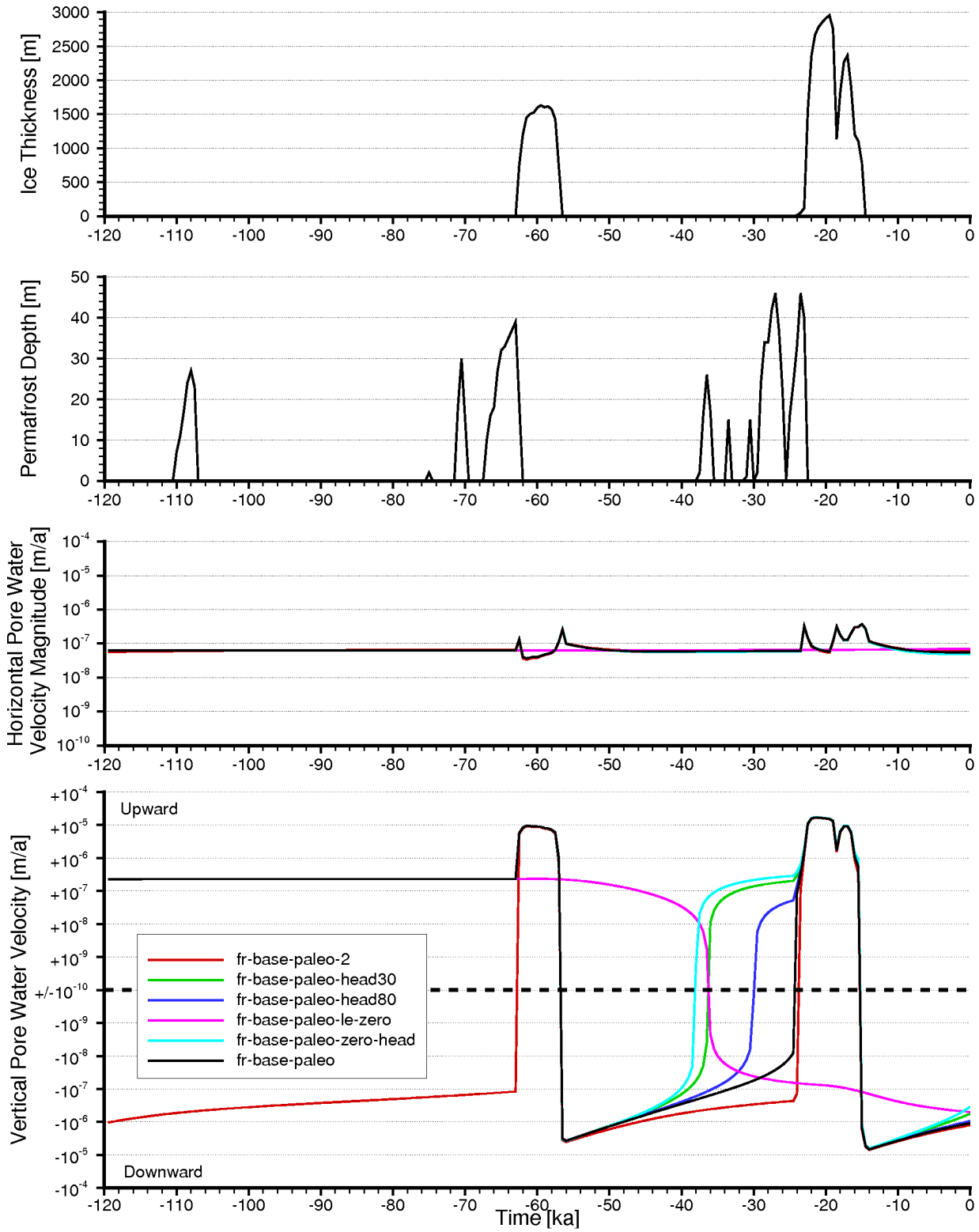

Note: Ice thickness and permafrost depth are also plotted.

Figure 5.27: Plot of Horizontal and Vertical Pore Water Velocities in Cobourg Formation at the DGR Site Versus Time for Six nn9930 Paleoclimate Simulations

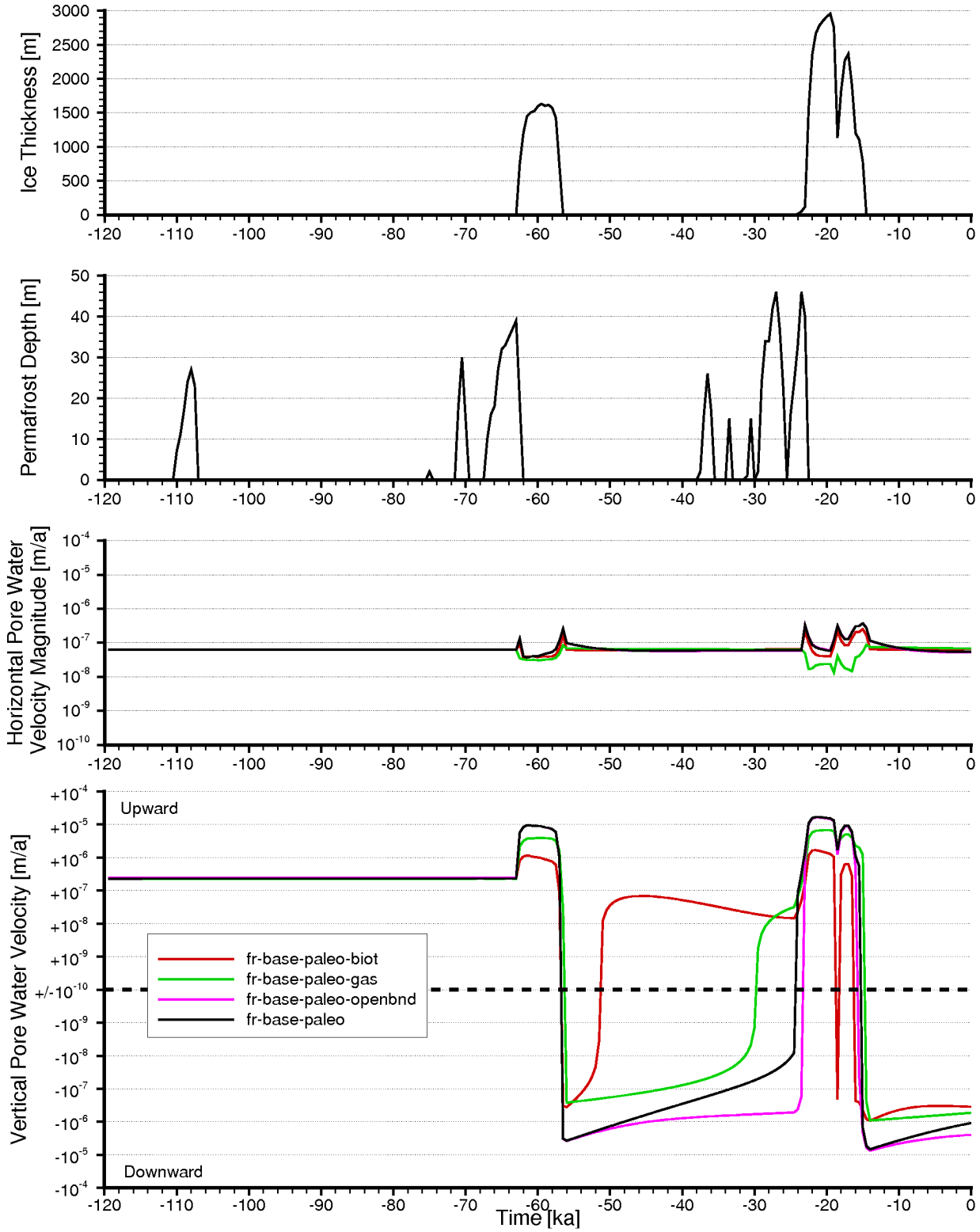

Note: Ice thickness and permafrost depth are also plotted.

Figure 5.28: Plot of Horizontal and Vertical Pore Water Velocities in Cobourg Formation at the DGR Site Versus Time for Four nn9930 Paleoclimate Simulations

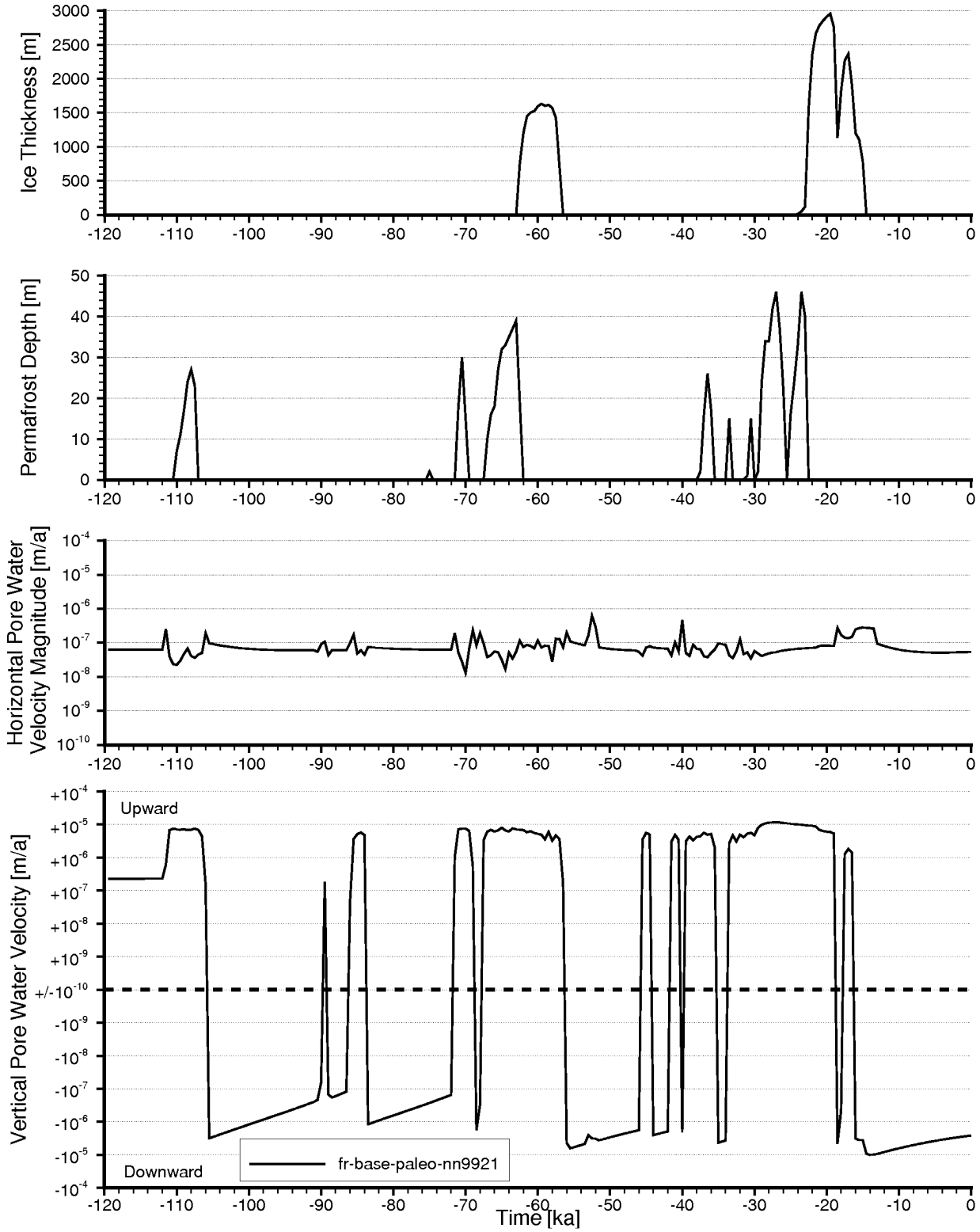

Note: Ice thickness and permafrost depth are also plotted.

Figure 5.29: Plot of Horizontal and Vertical Pore Water Velocities in Cobourg Formation at the DGR Site Versus Time for the nn9921 Paleoclimate Simulation

6. ABNORMAL PRESSURES

6.1 Assessment of Abnormal Pressures

Pressure data for the DGR boreholes indicate that the Cambrian sandstone and the Niagaran Group are over-pressured relative to density corrected hydrostatic levels relative to the ground surface. The Ordovician limestone and shale is significantly under-pressured. There are numerous hypotheses in the literature on the cause of abnormal pressures in sedimentary rock. Sedimentary basins, when at hydrological equilibrium, normally show a near-hydrostatic pressure distribution. Under certain conditions some excess pressure or pressure greater than hydrostatic can develop in low-permeability layers or other hydraulically isolated parts of systems. The processes commonly invoked to explain these over-pressures are compaction, hydrocarbon migration, diagenesis, tectonic stress or more simply topographic effects (Gonçalvès et al. 2004). Explanations of abnormal under-pressures include osmosis, exhumation, glaciation unloading, crustal flexure, and the presence of a non-wetting gas phase in pores (Neuzil 2000, Bader and Kooi 2005, Neuzil 2003, Johnston et al. 1998, Vinard 1998). A requirement of both abnormal over-pressures and under-pressures is low hydraulic conductivity in either the formation in which the abnormal pressures are observed or in the overlying and underlying formations. The inference on hydraulic conductivity of, and the hypotheses for, abnormal pressures are discussed in either the following paragraphs or the remaining sections of this chapter.

6.1.1 Inference on Hydraulic Conductivity of Abnormal Pressures

The abnormal pressures for the Cambrian sandstones and carbonates measured in the DGR borehole (refer to Figure 2.15) support the conceptual model that the Cambrian may be connected to deeper portions of the Michigan Basin to the west and that overpressures result from higher density fluids. The preservation of the high pressures requires the presence of extensive low-permeability bounding strata (Neuzil 1995) such as those of the Ordovician formations. Neuzil (1995) indicates that an abnormal pressure state may be a relic feature preserved by a virtual absence of fluid flow over geologic time. From a hydrodynamic perspective, flow can also play an important role in the development of abnormal pressures with the flow regime being either equilibrated or disequilibrated. Equilibrated-type pressures generally develop from topographically-driven flow but may also occur as a result of fluid density contrasts. The disequilibrium-type abnormal pressures are caused by natural geologic processes such as compaction, diagenesis, and deformation. Both types require the presence of extensive low-permeability strata (Neuzil 1995) such as those of the Ordovician formations and Precambrian.

6.1.2 Glacial Loading and Unloading

Vinard (1998) and Vinard et al. (1993) report that a 900 m marl-shale aquitard at the Wellenberg site in Switzerland is under-pressured. They hypothesize that the under-pressures could be related to stress relief due to deglaciation, extensive erosion or tectonic-thrusting scenarios that results in the dilation of the rock. They also state that the under-pressurization could result from the presence of a gas-phase in the aquitard. They investigated their preferred scenario of the deglaciation process using a geomechanical model. However, they did not investigate the pore pressure distribution during the stress loading stage of glaciation. The argument that the pressure profile in the Ordovician units is based on a glaciation scenario must be based on the evolution of pressures during both the rock compression stage of glaciation and the rock dilation stage of deglaciation. For the paleoclimate scenario nn9930 of Peltier (2011) investigated in this hydrogeologic modelling study, this is critical since the glaciation time is shorter than the

deglaciation stage. Based on the regional-scale numerical model for the proposed DGR site, a comprehensive analysis of the impact of glacial loading and unloading on the estimated pressure distribution at the DGR borehole is presented in Chapter 5.

6.1.3 Osmosis

Low permeability sediments such as clay may exhibit membrane behaviour resulting in the restriction of solute transport relative to the flow of water. This property of clay gives rise to chemical osmosis: fluid flow in response to a chemical gradient (Bader and Kooi 2005). In media with membrane properties, osmosis drives fluid flow from regions of low solute concentration to where it is high, thereby tending to raise fluid pressure where concentrations are high and to decrease them where they are low. The pressure changes create a countering hydraulic flow and osmotic equilibrium is reached when these opposing flows are matched. In such a case the net fluid flow is zero (Garavito et al. 2006). Chemical gradients will also reduce osmotic pressures. However, whether osmosis can have a significant effect on the pressure of fluids in geological environments has been controversial, because the membrane properties of geological media are poorly understood (Neuzil 2000). The results of a nine-year in situ measurement of fluid pressures and solute concentrations in shale that are consistent with the generation of large (up to 20 MPa) osmotic-pressure anomalies which could persist for tens of millions of years is presented by (Neuzil 2000). The cited abnormal pressures require small shale porosity and large contrasts in the amount of dissolved solids in the pore waters - criteria that may help to distinguish between osmotic and crustal-dynamic origins of anomalous pressures. For the over-pressures observed in the Cambrian and Niagaran at the DGR boreholes, an osmotic explanation was not considered as the over-pressures occur in sandstone and dolomite rather than a shale and the total dissolved solids gradient is inconsistent with osmosis. It can be hypothesized that the under-pressures in the Ordovician sediments is caused by osmosis. Having less saline water in the borehole than the formation is consistent with osmotic flow out of the borehole if the formation has membrane properties. Causing flow out of the borehole, osmosis would tend to lower pressure and keep it low until diffusion cancels salinity differences. Arguing against osmosis is the lithology. The under-pressures are observed in the DGR boreholes equally in the shale of the upper Ordovician and the carbonates of the lower Ordovician (refer to Figure 2.15). Carbonates do not function as membranes in the same manner as shales. Also arguing against an osmotic explanation of the under-pressures is the prediction of the significant under-pressures in the short-term straddle packer hydraulic tests in the DGR boreholes (refer to the vertical bars in the right panel of Figure 2.15). Since the osmotic process in a low hydraulic conductivity medium is dynamic, the under-pressures predicted by the straddle packer tests would not be expected. In summary, it is a conclusion of this study that osmotic processes cannot explain the abnormal pressures observed in the DGR boreholes. Further support for this conclusion is provided in the analyses of Neuzil in Appendix A.

6.1.4 Exhumation

In conceptual models positing only a liquid water fluid phase, the common thread in all the processes considered for underpressuring is changes in external mechanical loads. The most obvious candidates are long-term overburden removal, ice-load changes, and flexure related to the latter. The volumetric strains in the rock matrix and matrix solids that accompany the load or stress changes are a forcing that can perturb fluid pressure. At the DGR site, stress relief has occurred as a result of mass erosion of the formations of the Phanerozoic, Mesozoic and Cenozoic Eras above the Devonian Period sediments. For exhumation to be a credible explanation for the under-pressures, the rate of stress relief must be greater than the rate of water influx required to meet the water deficit caused by the dilation of the rock. Based on the

analyses of Chris Neuzil of the United States Geologic Survey in Reston, Virginia included in Appendix A of this report, long-term unburdening by downwasting is far too slow to contribute in any significant way to the under-pressures observed in the DGR boreholes.

6.1.5 Crustal Flexure

Johnston et al. (1998) examined the incremental stress caused by glacial loads using a number of different models. Assuming a circular ice sheet load on a lithosphere - asthenosphere with a spherical geometry and represented as a thick elastic plate overlying an inviscid mantle, they calculated horizontal stress increments from crustal flexure that can be as much as five times the vertical stress increment from the ice weight itself. The lateral stress changes are greatest at the top and bottom edges of the 100 km thick lithosphere. The magnitude of the horizontal incremental stress depended on the lateral extent of the glacial load and significant stress can occur at considerable distances beyond the ice margin. The glaciation scenario nn9930 developed by Peltier (2011) and shown in Figure 5.2 illustrates this conclusion as changes in ground elevation and hence deformation are predicted to occur in the absence of ice at the DGR site. Flexural stress change rates asymptotically approach zero as rebound progresses. The loading related to flexure does not track the ice load, instead lagging it.

The fluid pressure is dependent on the total stress and with dynamic loading and flexure, the total stress will vary between compression and tension over a glacial episode. While tension will occur above the neutral axis in the fore bulge of the glacier, compression will occur at the ice margin. The relationship between total stress and pressure as affected by flexure will be dependent on stratigraphy, lithology, mechanical properties and the geometry of sedimentary layers. For example, salt layers will behave as a viscous plastic media whereas elastic behaviour will better represent the deformation and stress in dolomites and sandstones. Depending on the state of the system when deglaciation occurs, flexural dilatation after deglaciation may be sufficient to significantly contribute to underpressuring. However, the stress-strain relationship in flexure will not likely be able to account for the pressure anomalies that occur, for example, at the 585 m depth in the DGR borehole. The quantitative analysis of crustal flexure using numerical models was not developed in this study.

The hypotheses that are quantitatively tested in this study to explain the abnormal pressures in the DGR boreholes are that: (1) the over-pressures in the Cambrian and Niagaran Group and the under-pressures in the Ordovician shale and limestone are a consequence of glaciation and deglaciation; (2) the over-pressures in the Cambrian and Niagaran Group are related to the dynamics of density-dependent saturated flow in the Michigan Basin; (3) the under-pressures in the Ordovician are the result of the presence of a non-wetting gas phase in the limestone and shale. The first hypothesis is explored in this study using paleohydrogeologic analyses of density-dependent saturated flow with the regional-scale conceptual model. It is a conclusion of this study through the analyses of Chapter 5 that the abnormal pressures could not be explained by glaciation loading and unloading. The second hypothesis is investigated through the simulation of density-dependent saturated flow in a cross-section of the Michigan Basin that extends from west of Lake Michigan to Georgian Bay. The Michigan Basin cross-section analyses are presented in Section 6.2. The third hypothesis is investigated in this report through the analysis of one-dimensional vertical two-phase air and water flow. The model TOUGH2-MP is used for the analyses presented in Section 6.3 of this study.

6.2 Michigan Basin Cross-Section

The analyses of the Michigan Basin cross-section are designed to meet two objectives:

- To investigate the abnormal over-pressures measured in the Cambrian at the DGR site; and
- To investigate the hypothesis that at a point in all units/formations beneath Lake Huron either a divide for groundwater flow occurs or density-dependent horizontal flow is negligible.

The first objective was also investigated in the regional-scale, saturated, density-dependent analyses of Section 4. The base-case regional-scale model results developed in Section 4.3 and depicted in Figure 4.14 replicate an over-pressure in the Cambrian and upward flow through the Ordovician sediments to the Niagaran. The over-pressures for the Cambrian were under predicted using the regional-scale model as compared to the pressures measured in the DGR boreholes. The second objective is tested in this section. However, the sensitivity of solute transport in the Ordovician sediments to the hypothesis and the assumption of a zero flux boundary condition for the Cambrian beneath Lake Huron was evaluated in Section 4.4.4. The analyses clearly show that solute transport in the Ordovician is diffusive and that this conclusion does not depend on the lateral boundary condition conceptualized for the Cambrian.

The Michigan Basin cross-section was also used to evaluate different conceptual models for the distribution of total dissolved solids concentration versus depth for the Precambrian rock, and different models for the change in fluid density for a change in TDS concentration. The impact of the hypothesis that there is a weathered zone with increased hydraulic conductivity at the top of the Precambrian was also evaluated. The scenarios or cases investigated using the Michigan Basin cross-section numerical model are summarized in Table 6.1. Note that the scenario names correspond to the prefix of the file names for the computer runs. The ‘f’ designates the FRAC3DVS-OPG computational model, the ‘c’ designates cross-section model, the middle designation is a descriptor of the scenario, and ‘litds’ designates that the total dissolved solids concentration distribution is fixed or locked-in.

Table 6.1: Model Scenarios for the Analysis of the Michigan Basin Cross-Section

Scenario	Description
fc-base-litds	Base-case analysis with the (Frape and Fritz 1987) TDS model for the Precambrian
fc-hanor-litds	Base-case parameters with the Hanor (1979) TDS model for the Precambrian
fc-hkp-litds	Impact of a weathered zone at the top of the Precambrian rock
fc-intera-litds	Investigation of the INTERA (2011) TDS versus fluid density model
fc-usgs-litds	Investigation of the Lampe (2009) TDS versus fluid density model

6.2.1 Base Case Conceptual Model of Michigan Basin

6.2.1.1 Model Domain and Mesh Generation

The Michigan Basin cross-section model is a computationally efficient approach with a dimensionally simplified representation of the system. The Michigan Basin cross-section, shown in Figure 6.1, extends laterally from southwestern Ontario to Wisconsin across Lake Huron, Michigan state and Lake Michigan. It occupies an extent of approximately 677 km.

The vertical elevations range from −5,000 m at the lowest point in the Precambrian to 509 m at the highest point on the Niagara Escarpment. The Cambrian sandstone outcrops in Wisconsin, refer to Figure 6.2, and it is absent at the Algonquin Arch. As shown in Figure 6.2, the Cambrian also outcrops north of Sault Ste. Marie, Ontario.

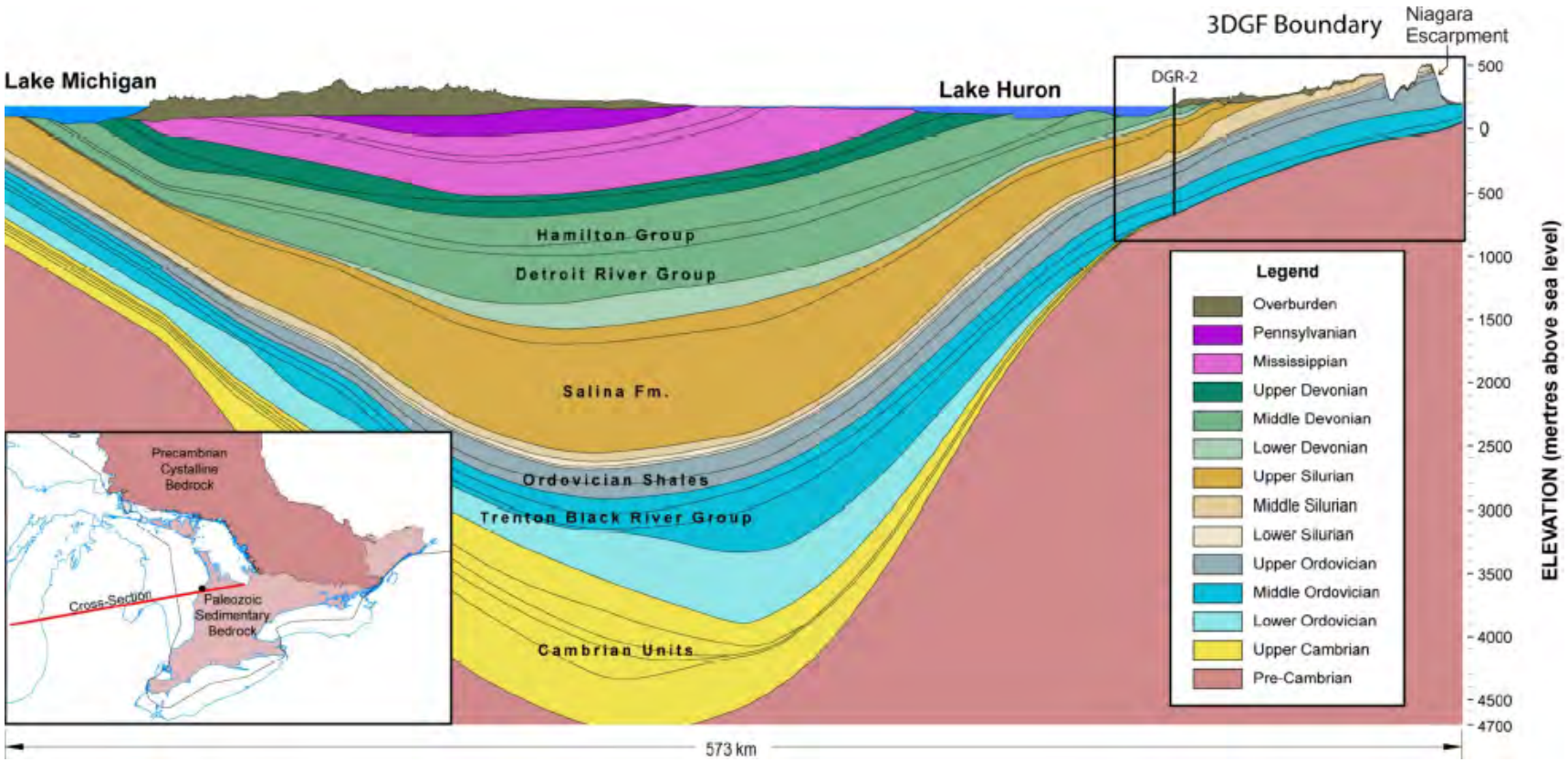

Note: From AECOM and ITASCA CANADA (2011). Vertical axis is elevation in metres relative to sea level. Boundary of the regional 3D geologic framework is indicated by black outline in top left corner of the cross-section. Mesozoic rocks overlying the Pennsylvanian sediments are too thin and discontinuous to be shown on cross-section. DGR-2 borehole is projected on to geological cross-section. Vertical exaggeration approximately x45.

Figure 6.1: Geological Cross-Section of the Michigan Basin

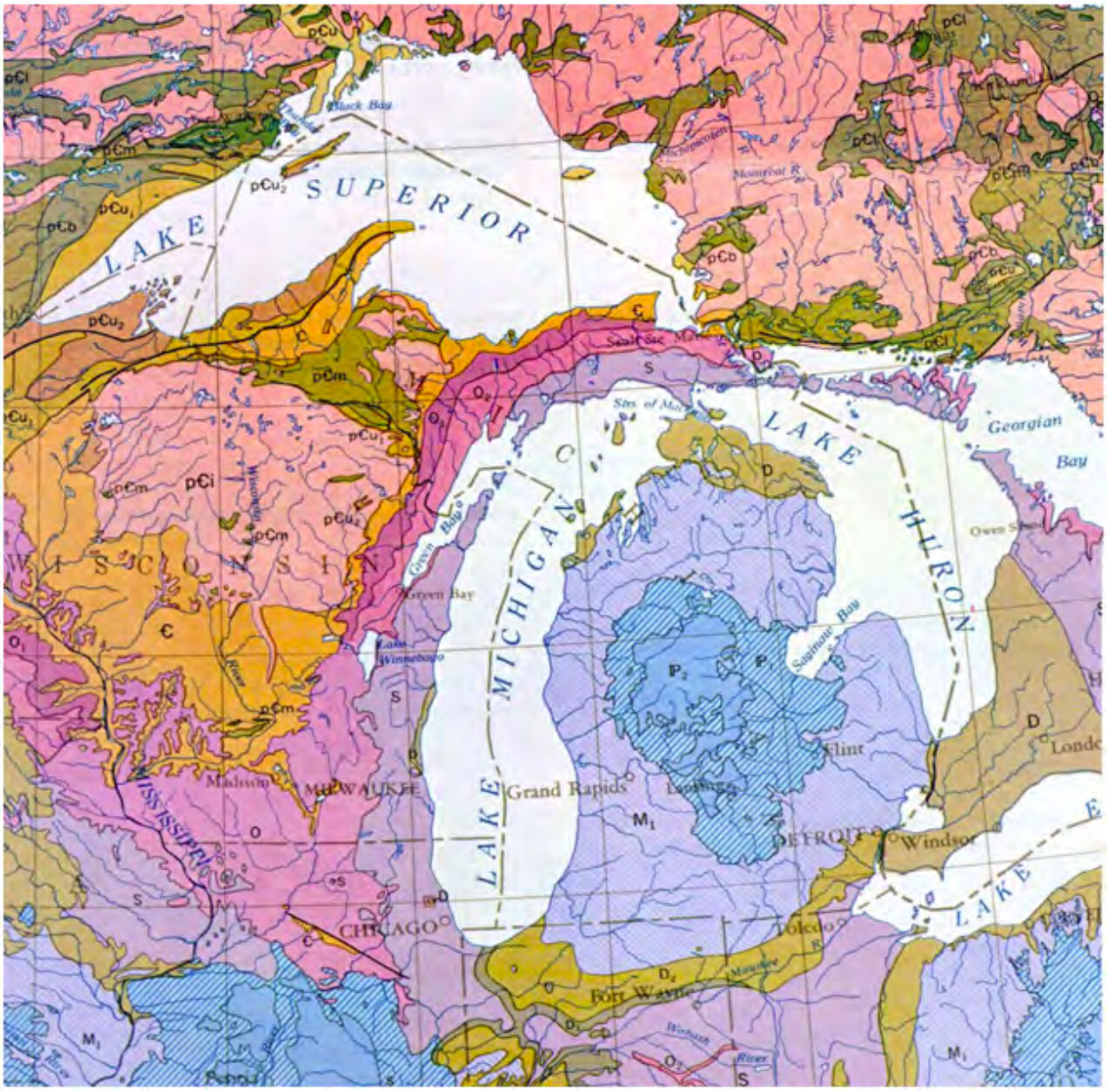

Note: Cambrian coloured orange and labelled as 'C'.

Figure 6.2: Geologic Map of the Michigan Basin Showing the Outcrop for the Cambrian in Wisconsin and North of Sault Ste. Marie, Ontario

The domain under zero elevation aMSL, where a density-dependent flow simulation was necessary due to the high salinity in the Michigan Basin groundwater system, was finely discretized into a planar hexahedral mesh with 1,355 columns, 600 rows, and 1 block in thickness to create a vertical two-dimensional mesh. These hexahedral elements have sides of 500 m in the horizontal direction by 10 m in the vertical direction by 1 m in thickness. The non-orthogonal mesh above sea level has 100 evenly distributed layers with 1,355 nodes each. The elevation of the nodes for each layer were determined from the geological framework model. Given the fact

that the continuity of each geologic unit was strictly maintained, 30 stratigraphic units for the Michigan Basin cross-section in Figure 6.3 were mapped to the mesh based on the centroid location of each hexahedral element so that the numerical model closely resembles the geological framework model. In other words, grid block properties were assigned according to the properties of the centroid of the grid block. The Michigan Basin figures shown in this report have a vertical exaggeration of 50:1.

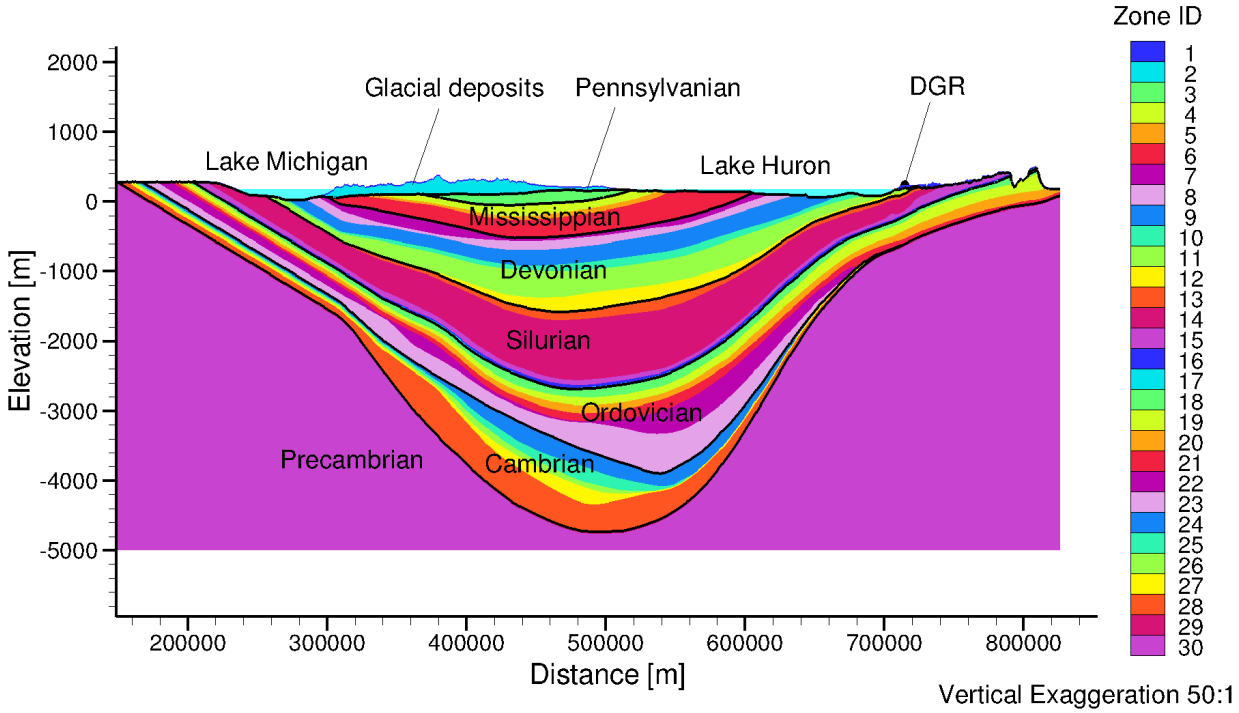

Figure 6.3: FRAC3DVS-OPG Zones for Michigan Basin Cross-Section Model

6.2.1.2 Flow Boundary and Initial Conditions

The eastern side boundary of the domain is the water divide for the surface water system, and conceptualized as a Neumann no-flow boundary condition. Due to the lack of geologic data for the western portion, the boundary condition cannot be properly determined. However, as shown in Figure 6.3, the impact of the conceptual model for the western boundary on the proposed DGR repository site will be greatly reduced by its distance from the western boundary. The western portion boundary can be conceptualized as a Neumann no-flow boundary condition as well. The bottom of the Michigan Basin cross-section model is comprised of the Precambrian granitic gneiss with very sparse fractures (INTERA 2011). Therefore, the bottom boundary condition of the model was assumed as a Neumann no-flow boundary condition. The elevation of the nodes at the top of the model domain are defined by either the DEM or the lake bathymetry. For surface nodes including those occupied by Lake Huron and Lake Michigan, the assigned prescribed head was set as the elevation minus 3 m but not less than the 176 m Lake Huron and Lake Michigan water elevation. The imposed surface boundary condition permits recharge and discharge to occur as determined by the surface topography and the hydraulic conductivity of the top model

layer. The assigned head represents a water table occurring at an assumed depth of 3 m below ground surface. Because of the resolution of the DEM (grid blocks that are 500 m, stream channels are conceptualized to have a depth to water that is 3 m less than defined by the DEM.

6.2.1.3 Hydraulic and Transport Parameters

The base-case data set for the conceptual model consists of 30 model zones (layers), with each zone corresponding to a unit in a stratigraphic section. Table 6.2 shows the layers and their associated hydraulic conductivities, anisotropy ratios, porosities, and specific storage coefficients. For those geologic units existing at the DGR site, the hydraulic parameter values were inherited from the regional scale model in Section 4.1. The variation of the hydraulic conductivity in the Precambrian with depth were calculated using Equation (4.1) and Equation (4.2). Other Michigan Basin geologic units, such as Saginaw, Marshall, the Ancell Group, and Prairie Du Chien, pinch out to the west of the proposed DGR site. These units are not observed in the DGR field program. Their values were either derived from the literature or estimated by appropriate assumptions shown in Table 6.3, Table 6.4, Table 6.5, and Table 6.6.

Contrary to the horizontal conductivity, the effective vertical conductivity of a horizontally bedded formation is largely determined by the low conductivity beds or sub-layers. In addition, the orientation of mineral grains of sedimentary rock will contribute to an even lower vertical hydraulic conductivity. Anisotropy ratios of 10:1 for most units with low permeability is considered conservative in Table 6.4, but are selected for consistency with the regional-scale simulations. Similarly, anisotropy ratios for units with high permeability such as sandstone are set to 1:1 in Table 6.4. The specific storage coefficients in Table 6.6 were estimated by Equation (3.9), where the compressibility for the Michigan Basin geologic units were derived from Domenico and Schwartz (1990). The analyses of this section do not include the very substantial withdrawal of water in Illinois and Wisconsin from the shallow Cambrian and Ordovician aquifer complex in those states.

Table 4.8 gives the parameters assumed for the migration of total dissolved solids. Using a grid Péclet number constraint, the longitudinal dispersivity coefficient was selected as approximately the maximum length of the side of a Michigan Basin scale grid block of 500 m. The diffusion coefficient is listed in the table; temperature effects were not considered.

6.2.1.4 Total Dissolved Solids

Salinity plays an important role with regard to a density-dependent groundwater flow system. An increase in the concentration of TDS will result in an increase in the fluid density, and act as an inhibiter of active groundwater flow. For the base-case scenario, the initial prescribed TDS distribution was developed as follows. The TDS versus depth relationship from the Canadian Shield in Equation (4.3) (Frape and Fritz 1987) was used to describe the initial TDS distribution for the Precambrian. The TDS distribution for the sedimentary stratigraphic units in the Michigan Basin was determined by the TDS versus depth relationship given in Hanor (1979) and shown in Figure 6.4, where the maximum TDS concentration is 432 g/L. The TDS concentration for the Michigan, Marshall and Coldwater units (refer to Table 6.2 were set to 50 g/L, 100 g/L, and 300 g/L respectively following Lampe (2009). The shallower geologic units were assigned zero TDS concentration. The resulting base-case TDS concentration distribution is shown in Figure 6.5. As can be noted in the figure, the described TDS concentration distribution model results in a discontinuity in the concentration at the top of the Precambrian.

The conceptual model for TDS used in the Michigan Basin cross-section analysis is the same as that of the regional-scale analysis: there are no TDS inflows and no sources were used to

Table 6.2: Summary of Formation Parameters for Michigan Basin Cross-Section Numerical Models

Period	Formation	K_H [m/s]	K_V [m/s]	K_H:K_V	θ	S_s [m^{-1}]
Quaternary	Drift	1.0×10^{-8}	5.0×10^{-9}	2:1	0.200	9.9×10^{-5}
Pennsylvanian	Saginaw	1.0×10^{-5}	1.0×10^{-8}	1,000:1	0.100	9.9×10^{-5}
Mississippian	Michigan	1.0×10^{-11}	1.0×10^{-12}	10:1	0.100	9.9×10^{-5}
	Marshall	5.0×10^{-7}	5.0×10^{-7}	1:1	0.100	9.9×10^{-5}
	Coldwater	1.0×10^{-9}	1.0×10^{-10}	10:1	0.100	9.9×10^{-5}
Devonian	Berea Bedford	1.0×10^{-7}	1.0×10^{-8}	10:1	0.100	9.9×10^{-5}
	Kettle Point	3.0×10^{-9}	3.0×10^{-10}	10:1	0.100	1.5×10^{-6}
	Hamilton Group	2.2×10^{-11}	2.2×10^{-12}	10:1	0.100	1.5×10^{-6}
	Dundee	8.4×10^{-8}	8.4×10^{-9}	10:1	0.100	1.5×10^{-6}
	Detroit River Group	5.9×10^{-7}	2.0×10^{-8}	30:1	0.077	1.4×10^{-6}
	Bois Blanc	1.0×10^{-7}	1.0×10^{-8}	10:1	0.077	1.4×10^{-6}
Silurian	Bass Islands	5.0×10^{-5}	1.7×10^{-6}	30:1	0.056	2.0×10^{-6}
	F Unit	5.0×10^{-14}	5.0×10^{-15}	10:1	0.100	9.5×10^{-7}
	Niagaran	3.6×10^{-9}	2.5×10^{-13}	14,431:1	0.026	2.7×10^{-7}
	Cabot Head	9.0×10^{-14}	9.0×10^{-15}	10:1	0.116	1.1×10^{-6}
	Manitoulin	9.0×10^{-14}	9.0×10^{-15}	10:1	0.028	7.5×10^{-7}
Ordovician	Queenston	2.0×10^{-14}	2.0×10^{-15}	10:1	0.073	9.0×10^{-7}
	Georgian Bay/Blue Mtn.	3.5×10^{-14}	3.2×10^{-15}	11:1	0.070	1.2×10^{-6}
	Trenton Group†	1.2×10^{-14}	1.0×10^{-15}	12:1	0.018	4.3×10^{-7}
	Black River Group‡	6.5×10^{-11}	9.9×10^{-16}	65,657:1	0.023	5.0×10^{-7}
	Ancell Group	3.5×10^{-5}	3.5×10^{-5}	1:1	0.020	1.3×10^{-6}
	Prairie du Chien Group	3.5×10^{-5}	3.5×10^{-5}	1:1	0.020	1.3×10^{-6}
Cambrian	Trempealeau Fm	3.5×10^{-10}	3.5×10^{-11}	10:1	0.020	1.3×10^{-6}
	Francania Fm	3.5×10^{-10}	3.5×10^{-11}	10:1	0.020	1.3×10^{-6}
	Galesville Sandstone	3.0×10^{-6}	3.0×10^{-6}	1:1	0.071	3.7×10^{-7}
	Eau Claire Fm	3.0×10^{-6}	3.0×10^{-6}	1:1	0.071	3.7×10^{-7}
	Mount Simon Fm	3.0×10^{-6}	3.0×10^{-6}	1:1	0.071	3.7×10^{-7}
Precambrian	Upper Precambrian	1.0×10^{-10}	1.0×10^{-10}	1:1	0.038	2.6×10^{-7}
	Precambrian	1.0×10^{-12}	1.0×10^{-12}	1:1	0.005	1.5×10^{-7}

Note: † K_V is the thickness weighted harmonic mean of Cobourg, Sherman Fall and Kirkfield formations; ‡ K_V is the thickness weighted harmonic mean of Coboconk, Gull River, and Shadow Lake formations.

Table 6.3: Horizontal Hydraulic Conductivity K_H of Formations for Michigan Basin Cross-Section Numerical Models

Period	Formation	K_H [m/s]	Reference	Note
Quaternary	Drift	1.00×10^{-8}	Regional-scale dataset	
Pennsylvanian	Saginaw	1.00×10^{-5}	Hoaglund et al. (2002), Table 1	
Mississippian	Michigan	1.00×10^{-11}	Hoaglund et al. (2002), Table 1	
	Marshall	5.00×10^{-7}	Hoaglund et al. (2002), Table 1	
	Coldwater	1.00×10^{-9}	Westjohn and Weaver (1996), Page 16	
Devonian	Berea Bedford	1.00×10^{-7}	Freeze and Cherry (1979), Table 2.2	
	Kettle Point	3.00×10^{-9}	Regional-scale dataset	
	Hamilton Group	2.20×10^{-11}	Regional-scale dataset	
	Dundee	8.40×10^{-8}	Regional-scale dataset	
	Detroit River Group	5.90×10^{-7}	Regional-scale dataset	
	Bois Blanc	1.00×10^{-7}	Regional-scale dataset	
Silurian	Bass Islands	5.00×10^{-5}	Regional-scale dataset	
	F Unit	5.00×10^{-14}	Regional-scale dataset	
	Niagaran	3.60×10^{-9}	Regional-scale dataset	
	Cabot Head	9.00×10^{-14}	Regional-scale dataset	
	Manitoulin	9.00×10^{-14}	Regional-scale dataset	
Ordovician	Queenston	2.00×10^{-14}	Regional-scale dataset	
	Georgian Bay/Blue Mtn.	3.50×10^{-14}	Regional-scale dataset	
	Trenton Group†	1.19×10^{-14}	Regional-scale dataset	See footnote
	Black River Group‡	6.52×10^{-11}	Regional-scale dataset	See footnote
	Ancell Group	3.53×10^{-5}	Emmons (1987), Page 18	
	Prairie du Chien Group	3.53×10^{-5}	Emmons (1987), Page 18	
Cambrian	Trempealeau Fm	3.53×10^{-10}	Emmons (1987), Page 19	
	Francania Fm	3.53×10^{-10}	Emmons (1987), Page 19	
	Galesville Sandstone	3.00×10^{-6}	Regional-scale dataset	Set to Cambrian
	Eau Claire Fm	3.00×10^{-6}	Regional-scale dataset	Set to Cambrian
	Mount Simon Fm	3.00×10^{-6}	Regional-scale dataset	Set to Cambrian
Precambrian	Upper Precambrian	1.00×10^{-10}	Regional-scale dataset	
	Precambrian	1.00×10^{-12}	Regional-scale dataset	

Note: † thickness weighted arithmetic mean of Cobourg, Sherman Fall and Kirkfield formations; ‡ thickness weighted arithmetic mean of Coboconk, Gull River, and Shadow Lake formations.

Table 6.4: Horizontal to Vertical Anisotropy for Hydraulic Conductivity K_H:K_V of Formations for Michigan Basin Cross-Section Numerical Models

Period	Formation	K_H:K_V	Reference	Note
Quaternary	Drift	2:1	Regional-scale dataset	
Pennsylvanian	Saginaw	1,000:1	Hoaglund et al. (2002), Table 1	
Mississippian	Michigan	10:1	—	Assumed
	Marshall	1:1	Hoaglund et al. (2002), Table 1	
	Coldwater	10:1	—	Assumed
Devonian	Berea Bedford	10:1	—	Assumed
	Kettle Point	10:1	Regional-scale dataset	
	Hamilton Group	10:1	Regional-scale dataset	
	Dundee	10:1	Regional-scale dataset	
	Detroit River Group	30:1	Regional-scale dataset	
	Bois Blanc	10:1	Regional-scale dataset	
Silurian	Bass Islands	30:1	Regional-scale dataset	
	F Unit	10:1	Regional-scale dataset	
	Niagaran	14,431:1	Regional-scale dataset	
	Cabot Head	10:1	Regional-scale dataset	
	Manitoulin	10:1	Regional-scale dataset	
Ordovician	Queenston	10:1	Regional-scale dataset	
	Georgian Bay/Blue Mtn.	11:1	Regional-scale dataset	
	Trenton Group†	12:1	Regional-scale dataset	See footnote
	Black River Group†	65,657:1	Regional-scale dataset	See footnote
	Ancell Group	1:1	—	Assumed
	Prairie du Chien Group	1:1	—	Assumed
Cambrian	Trempealeau Fm	10:1	—	Assumed
	Francania Fm	10:1	—	Assumed
	Galesville Sandstone	1:1	Regional-scale dataset	Set to Cambrian
	Eau Claire Fm	1:1	Regional-scale dataset	Set to Cambrian
	Mount Simon Fm	1:1	Regional-scale dataset	Set to Cambrian
Precambrian	Upper Precambrian	1:1	Regional-scale dataset	
	Precambrian	1:1	Regional-scale dataset	

Note: † K_H:K_V anisotropy ratio is calculated using K_H in Table 6.3 and K_V in Table 6.2.

Table 6.5: Porosity θ of Formations for Michigan Basin Cross-Section Numerical Models

Period	Formation	θ	Reference	Note
Quaternary	Drift	0.200	Regional-scale dataset	
Pennsylvanian	Saginaw	0.100	—	Assumed
Mississippian	Michigan	0.100	—	Assumed
	Marshall	0.100	—	Assumed
	Coldwater	0.100	—	Assumed
Devonian	Berea Bedford	0.100	—	Assumed
	Kettle Point	0.100	Regional-scale dataset	
	Hamilton Group	0.100	Regional-scale dataset	
	Dundee	0.100	Regional-scale dataset	
	Detroit River Group	0.077	Regional-scale dataset	
	Bois Blanc	0.077	Regional-scale dataset	
Silurian	Bass Islands	0.056	Regional-scale dataset	
	F Unit	0.100	Regional-scale dataset	
	Niagaran	0.026	Regional-scale dataset	
	Cabot Head	0.116	Regional-scale dataset	
	Manitoulin	0.028	Regional-scale dataset	
Ordovician	Queenston	0.073	Regional-scale dataset	
	Georgian Bay/Blue Mtn.	0.070	Regional-scale dataset	
	Trenton Group†	0.018	Regional-scale dataset	See footnote
	Black River Group‡	0.023	Regional-scale dataset	See footnote
	Ancell Group	0.020	—	Assumed
	Prairie du Chien Group	0.020	—	Assumed
Cambrian	Trempealeau Fm	0.020	—	Assumed
	Francania Fm	0.020	—	Assumed
	Galesville Sandstone	0.071	Regional-scale dataset	Set to Cambrian
	Eau Claire Fm	0.071	Regional-scale dataset	Set to Cambrian
	Mount Simon Fm	0.071	Regional-scale dataset	Set to Cambrian
Precambrian	Upper Precambrian	0.038	Regional-scale dataset	
	Precambrian	0.005	Regional-scale dataset	

Note: † thickness weighted arithmetic mean of Cobourg, Sherman Fall and Kirkfield formations; ‡ thickness weighted arithmetic mean of Coboconk, Gull River, and Shadow Lake formations.

Table 6.6: Specific Storage Coefficient of Formations for Michigan Basin Cross-Section Numerical Models

Period	Formation	S_s [m^{-1}]	Reference	Note
Quaternary	Drift	9.85×10^{-5}	Regional-scale dataset	
Pennsylvanian	Saginaw	9.85×10^{-5}	Domenico and Schwartz (1990), Table 4.1	
Mississippian	Michigan	9.85×10^{-5}	Domenico and Schwartz (1990), Table 4.1	
	Marshall	9.85×10^{-5}	Domenico and Schwartz (1990), Table 4.1	
	Coldwater	9.85×10^{-5}	Domenico and Schwartz (1990), Table 4.1	
Devonian	Berea Bedford	9.85×10^{-5}	Domenico and Schwartz (1990), Table 4.1	
	Kettle Point	1.50×10^{-6}	Regional-scale dataset	
	Hamilton Group	1.50×10^{-6}	Regional-scale dataset	
	Dundee	1.50×10^{-6}	Regional-scale dataset	
	Detroit River Group	1.40×10^{-6}	Regional-scale dataset	
	Bois Blanc	1.40×10^{-6}	Regional-scale dataset	
Silurian	Bass Islands	2.00×10^{-6}	Regional-scale dataset	
	F Unit	9.50×10^{-7}	Regional-scale dataset	
	Niagaran	2.70×10^{-7}	Regional-scale dataset	
	Cabot Head	1.10×10^{-6}	Regional-scale dataset	
	Manitoulin	7.50×10^{-7}	Regional-scale dataset	
Ordovician	Queenston	9.00×10^{-7}	Regional-scale dataset	
	Georgian Bay/Blue Mtn.	1.20×10^{-6}	Regional-scale dataset	
	Trenton Group†	4.26×10^{-7}	Regional-scale dataset	See footnote
	Black River Group‡	4.97×10^{-7}	Regional-scale dataset	See footnote
	Ancell Group	1.28×10^{-6}	Domenico and Schwartz (1990), Table 4.1	
	Prairie du Chien Group	1.28×10^{-6}	Domenico and Schwartz (1990), Table 4.1	
Cambrian	Trempealeau Fm	1.28×10^{-6}	Domenico and Schwartz (1990), Table 4.1	
	Francania Fm	1.28×10^{-6}	Domenico and Schwartz (1990), Table 4.1	
	Galesville Sandstone	3.70×10^{-7}	Regional-scale dataset	Set to Cambrian
	Eau Claire Fm	3.70×10^{-7}	Regional-scale dataset	Set to Cambrian
	Mount Simon Fm	3.70×10^{-7}	Regional-scale dataset	Set to Cambrian
Precambrian	Upper Precambrian	2.60×10^{-7}	Regional-scale dataset	
	Precambrian	1.50×10^{-7}	Regional-scale dataset	

Note: † thickness weighted arithmetic mean of Cobourg, Sherman Fall and Kirkfield formations; ‡ thickness weighted arithmetic mean of Coboconk, Gull River, and Shadow Lake formations.

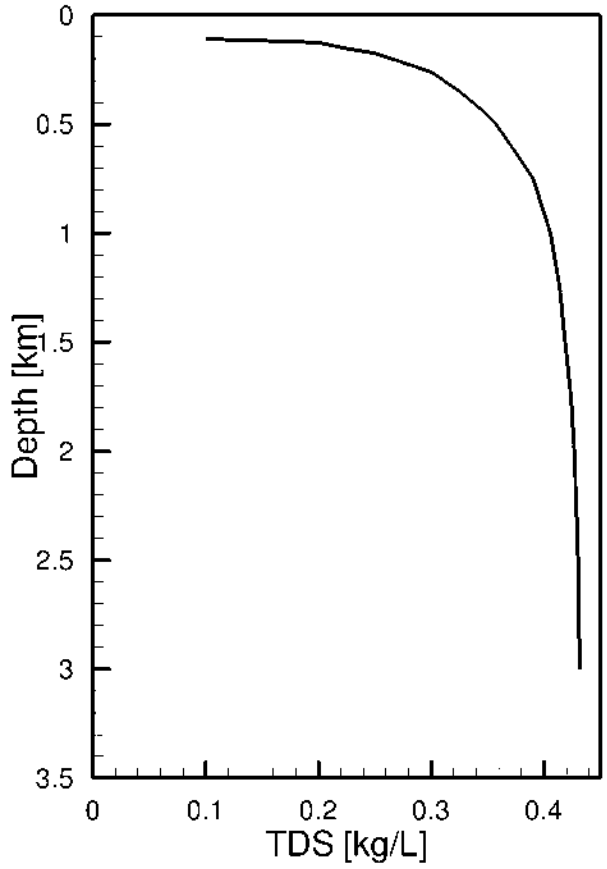

Note: Adapted from Hanor (1979).

Figure 6.4: Plot of TDS Versus Depth for Groundwaters from the Michigan Basin

generate total dissolved solids in the domain as the simulation time progressed. As a consequence, the dissolved solids will gradually reduce in a temporal analysis as the groundwater discharges from the system. To resolve this, the calculational procedure for the analysis of density-dependent flow is as follows:

i) determine the distribution of freshwater heads for steady state density-independent flow
ii) assign a temporally invariant distribution for the total dissolved solids concentration in the cross section based on literature data
iii) with the TDS transport module in FRAC3DVS-OPG turned off, and the freshwater head distribution of the first step as an initial condition, determine a solution for the freshwater heads that has equilibrated to the defined TDS concentration distribution

For the analysis with the TDS transport module disabled, theoretically, the equilibrium freshwater head distribution could be obtained directly by running the model in the steady-state mode. However, the direct approach was unfeasible, as computational difficulties and convergence issues for the simulation and analysis of density-dependent flow using FRAC3DVS-OPG are significant. The equilibrium solution for the described transient analysis was reached at 10 Ma; no change was observed in the equivalent freshwater head distribution after this time.

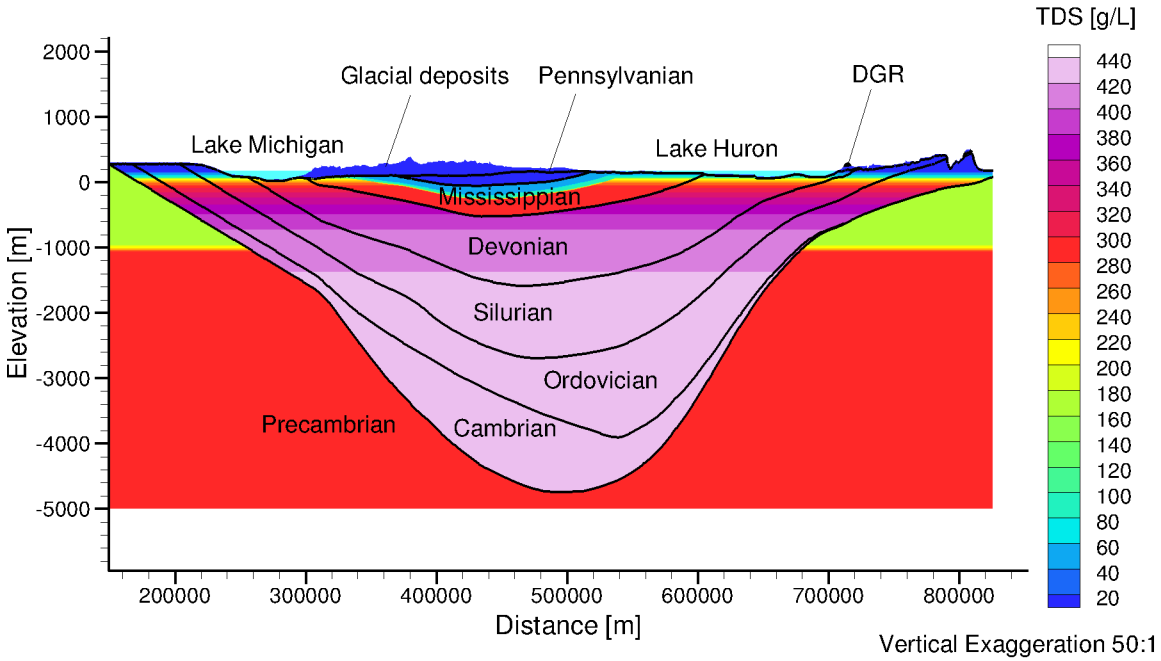

Figure 6.5: Initial Total Dissolved Solids Distribution

6.2.2 Base-Case Analysis of Michigan Basin Cross-Section

The scenario fc-base-litds represents the base-case analysis for the Michigan Basin cross-section. The distribution of heads from the Michigan Basin cross-section simulation of steady-state density-independent flow with the base-case parameters is shown in Figure 6.6. The pattern of flow in the Cambrian is generally eastward from the units outcrop in Wisconsin (refer to Figure 6.2) to its pinch out immediately east of the DGR site. Beneath the east part of Lake Huron the pore water velocity in the Cambrian is less than 0.001 m/a. The simulated environmental head in the Cambrian for the analysis at the location of the DGR is 305.3 m (refer to Table 6.7). The August 24, 2009 measured freshwater head and estimated environmental head in the Cambrian at the DGR-4 borehole are 422.1 m and 317.6 m respectively. The importance of density-dependent flow is revealed by the comparison; however, even with a density-independent simulation, the Cambrian is over-pressured throughout the domain relative to the pressure in the overlying Ordovician carbonates and shales. Because the Cambrian is bounded by low hydraulic units below (Precambrian) and above (Ordovician), the fluids in it are trapped with slow dissipation upward through the Ordovician. The high hydraulic conductivity of the Cambrian results in only a small loss of energy across the domain: the horizontal hydraulic gradient in the Cambrian is negligible.

The equivalent freshwater and environmental head distributions for the base-case and TDS concentration distribution of Figure 6.5 are shown in Figure 6.7 and Figure 6.8 respectively. For the Michigan Basin cross-section model, the shallow flow regime, which includes glacial deposits, Pennsylvanian period and Mississippian period sediments, is dominated by flow that mimics topography. Beneath the shallow groundwater zone, the heads are not controlled to the same extent by the local elevation of the surface, as the downward transmission of the head signature is dissipated by the Devonian period low permeability units. The lower flow regime in the

Devonian period and the Bass Islands units is controlled by the horizontal gradients towards Lake Michigan to the west and Lake Huron to the east. The Silurian period sediments are the transition regime, where the dominant vertical flow is caused by the difference in the environmental heads between the Devonian and Ordovician periods (refer to Figure 6.8). The deep flow regime in the Ordovician and Cambrian period rock reaches hydrostatic equilibrium, as there is no horizontal gradient in the freshwater head distribution and no vertical gradient in the environmental head distribution. A negligible vertical environmental head gradient was observed in the Precambrian unit. The horizontal fresh water head gradient in the Precambrian, indicating the horizontal flux to the margins of the Michigan Basin, is caused by the fact that the brine in the sedimentary basin has a higher TDS concentration than that in the Precambrian. The highly permeable units in the Cambrian period including the Ancell Group, Prairie Du Chien, Galesville, Eau Claire, and Mount Simon, are confined by the overlying and underlying low permeability units of the Ordovician and Precambrian.

The pore water velocity magnitudes are presented in Figure 6.9; note that the direction of flow is not shown in the figure. A review of the velocity data from the simulation indicates that a divide occurs in the Bass Island and all shallower units at approximately the centre of Lake Huron. The pore velocities in the Niagaran are less than 0.001 m/a and the horizontal pore velocities in the Cambrian are generally less than 0.1 m/a beneath approximately the centre of Lake Huron. A large contrast in pore fluid density occurs between the Cambrian and the Precambrian whereby the TDS in the Cambrian at that location is approximately 425 g/L and in the Upper Precambrian is 300 g/L. This fluid density contrast induces strong vertical velocities between the Cambrian and the Upper Precambrian due to the fixed TDS distribution. In a case where TDS is allowed to redistribute due to advection and diffusion, this density contrast, and the resulting vertical velocities would be reduced. In scenario fc-hanor-litds where the density contrast does not exist, pore fluid velocities are greatly reduced as compared to the base-case. The pore water velocities in the low permeability units such as those in the Silurian and in the Ordovician sediments are significantly lower. The horizontal pore water velocity data for the Michigan Basin base-case cross-section analysis confirms the hypothesis of this study that at a point in all units/formations beneath Lake Huron either a divide for groundwater flow occurs or horizontal flow is negligible. It is noted that a pore velocity of 0.001 m/a equates to a velocity of 1 km/Ma.

The freshwater and environmental head distribution versus depth for the DGR-4 borehole has been extracted from the base-case model and plotted against the heads estimated from the pressures measured on August 24, 2009 in Figure 6.10. An environmental head gradient reflecting upward flow is predicted in the steady-state analysis. Relative to the ground surface at 181.6 mASL, the measured over-pressures in the Cambrian and Niagaran unit are reconstructed by the Michigan Basin cross-section model. The under-pressure observed in the upper Silurian and Ordovician at the DGR-4 borehole are not predicted in the saturated steady-state analysis with pre-defined TDS distribution, base-case parameters, and boundary conditions. The significantly under-pressured head profile indicating the possible presence of a gas phase will be explored and discussed in a following section.

6.2.3 Alternate Density and TDS Concentration Distributions

An alternate approach to the base-case TDS characterization, applies the TDS versus depth relationship given in Hanor (1979) to both the sedimentary and the Precambrian rock (scenario fc-hanor-litds). The TDS concentration for this case is shown in Figure 6.11. For the Devonian and the lower periods, the TDS concentration is strictly depth dependent. The equilibrium solution for freshwater heads was reached at 10 Ma. Figure 6.12 and Figure 6.13 show the equivalent freshwater and environmental head distributions for the base-case parameters and

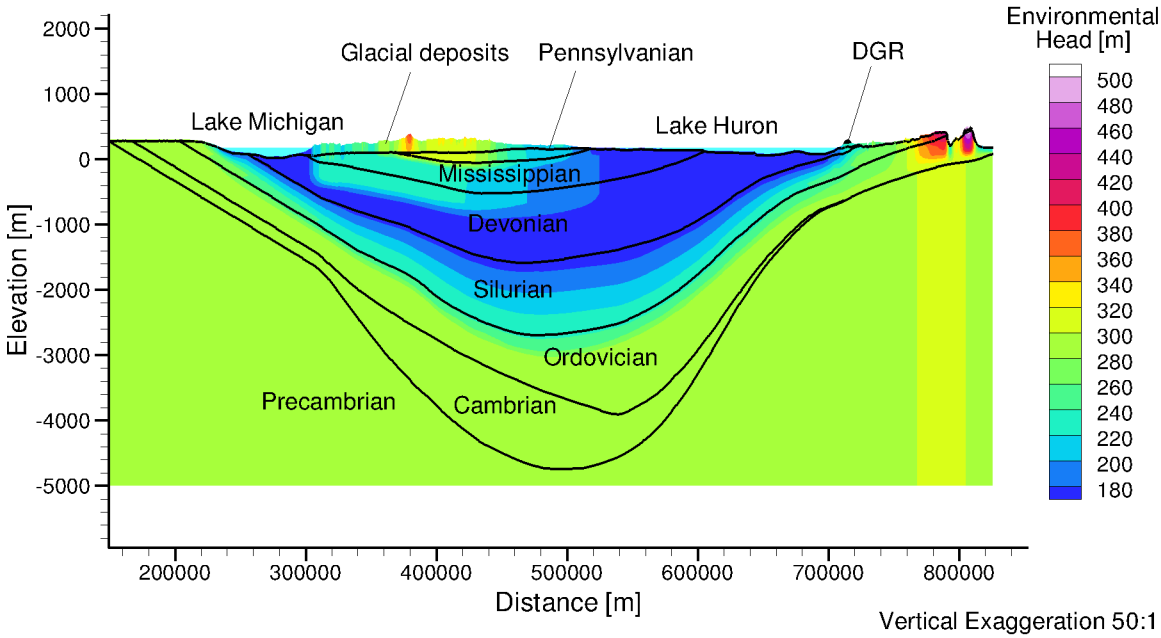

Figure 6.6: Distribution of Heads for Steady-State Density-Independent Flow

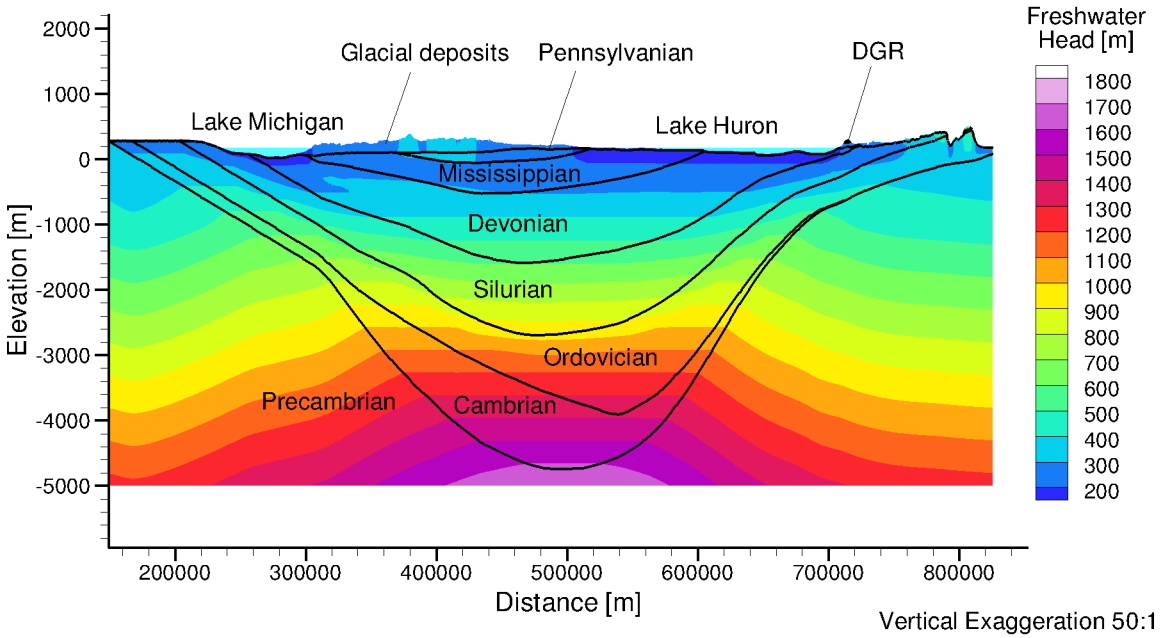

Figure 6.7: Base-Case Analysis of Michigan Basin Cross-Section: Equilibrium Freshwater Heads for Defined TDS Distribution

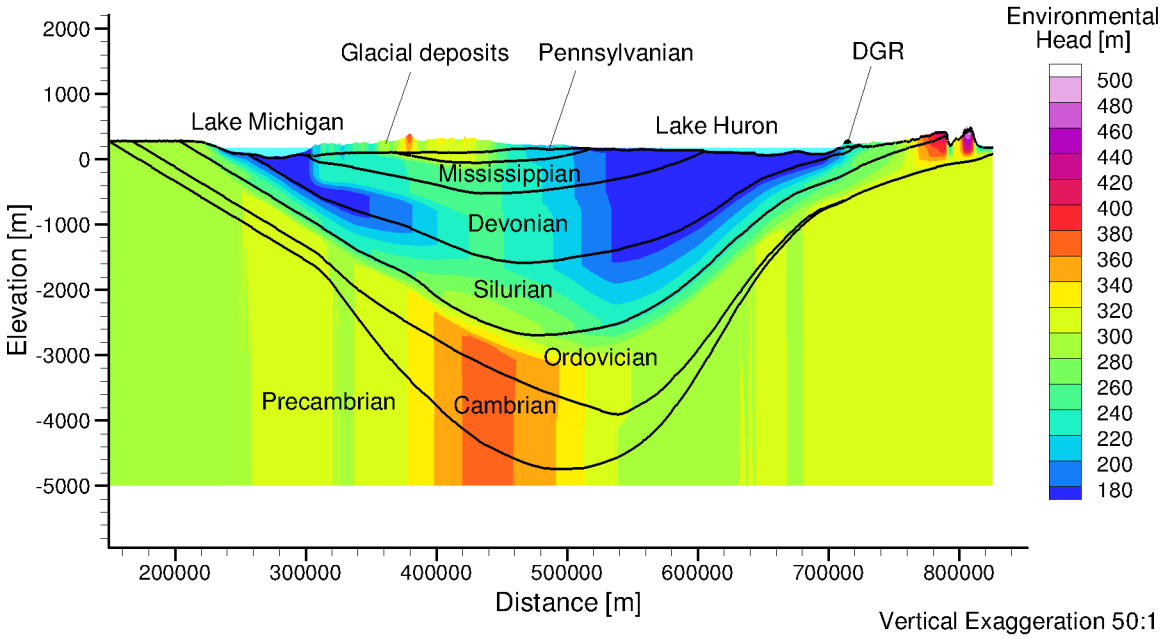

Figure 6.8: Base-Case Analysis of Michigan Basin Cross-Section: Equilibrium Environmental Heads for Defined TDS Distribution

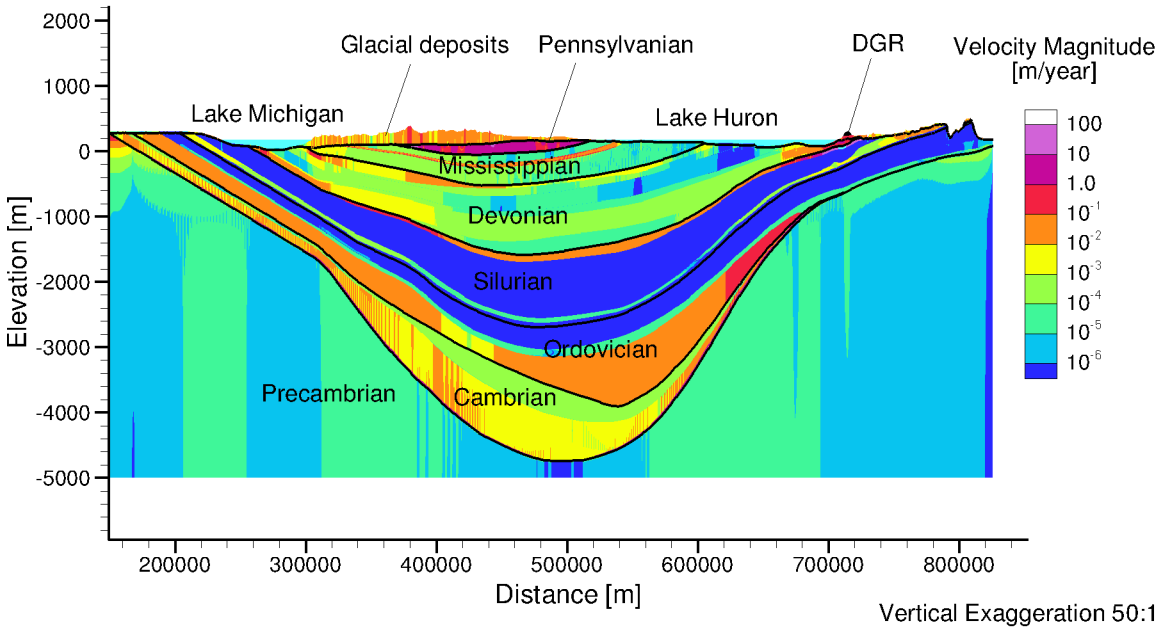

Figure 6.9: Base-Case Analysis of Michigan Basin Cross-Section: Pore Water Velocity Magnitude for Michigan Basin Cross-Section Analysis and Defined TDS Distribution

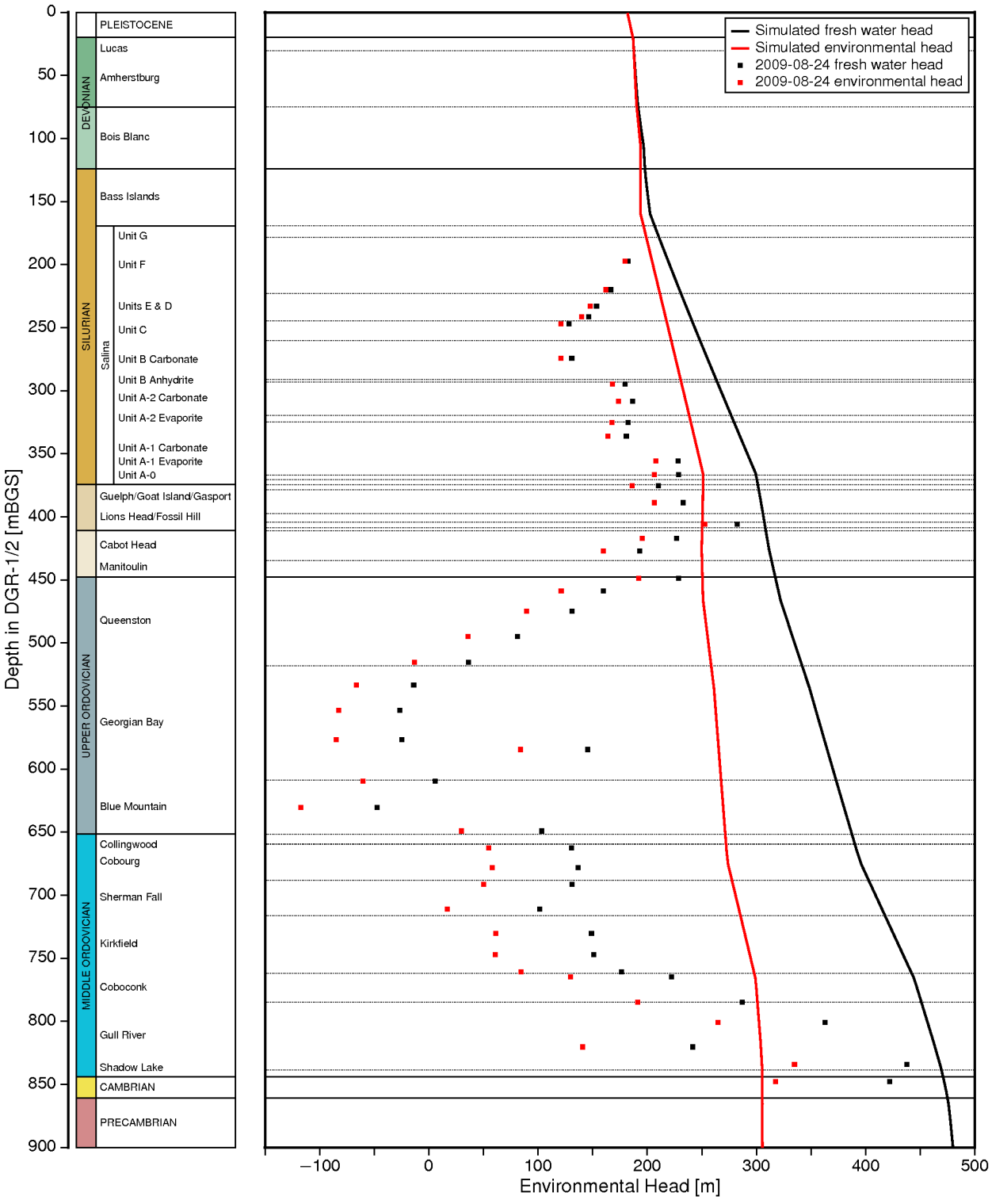

Figure 6.10: Base-Case Analysis of Michigan Basin Cross-Section: Comparison of Simulated and Measured August 24, 2009 DGR-4 Heads

boundary conditions at 10 Ma starting from the density-dependent hydrostatic initial condition. Except for some disturbance caused by slightly uneven TDS distribution in the upper units, these two head distribution plots indicate that the deep flow regime in the Ordovician, Cambrian, and Precambrian is stagnant.

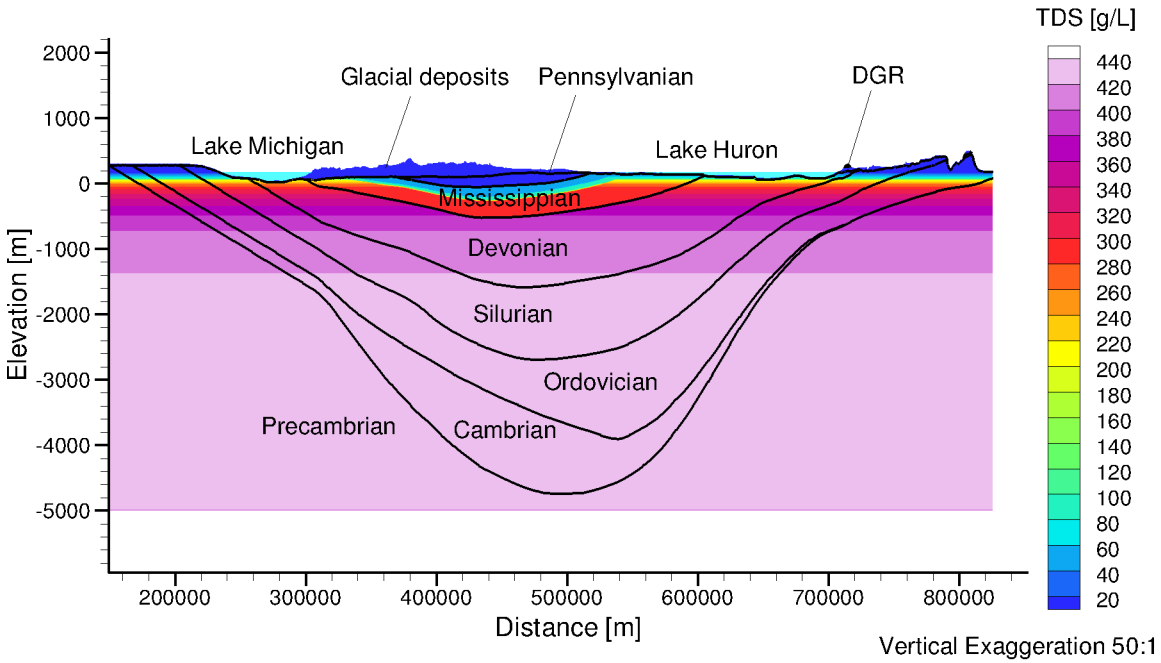

Figure 6.11: Initial Total Dissolved Solids Distribution for Michigan Basin Cross-Section Analysis and Alternate Defined TDS Distribution

The pore water velocity magnitudes for the analysis described in the preceding paragraph is presented in Figure 6.14. The velocity data for the simulation indicate that a divide occurs in the Bass Island at approximately the centre of Lake Huron. For the Niagaran, a divide occurs at approximately the west side of the lake. The pore water velocity magnitude in the Cambrian is less than 10^{-5} m/a beneath approximately the centre of Lake Huron and decreases to the east. The pore water velocity magnitude in the Precambrian is generally less than 10^{-6} m/a. The pore water velocity data for this alternate Michigan Basin cross-section analysis also confirms the hypothesis of this study that at a point in all units/formations beneath Lake Huron either a divide for groundwater flow occurs or horizontal flow is negligible. A comparison of the results for this case to those of the base-case described in preceding paragraphs indicates that density-dependent groundwater flow in the Michigan Basin is sensitive to the description of the TDS concentration distribution in the Precambrian.

Figure 6.15 compares the simulated freshwater and environmental heads for the alternate case to the head profile based on the measured pressures in borehole DGR-4. The simulation describes the upward environmental head gradient in the Ordovician and the quality of the fit between estimated and calculated heads provides strong evidence that the over-pressure in the Cambrian is caused by geometry and differences in fluid density in the units of the basin.

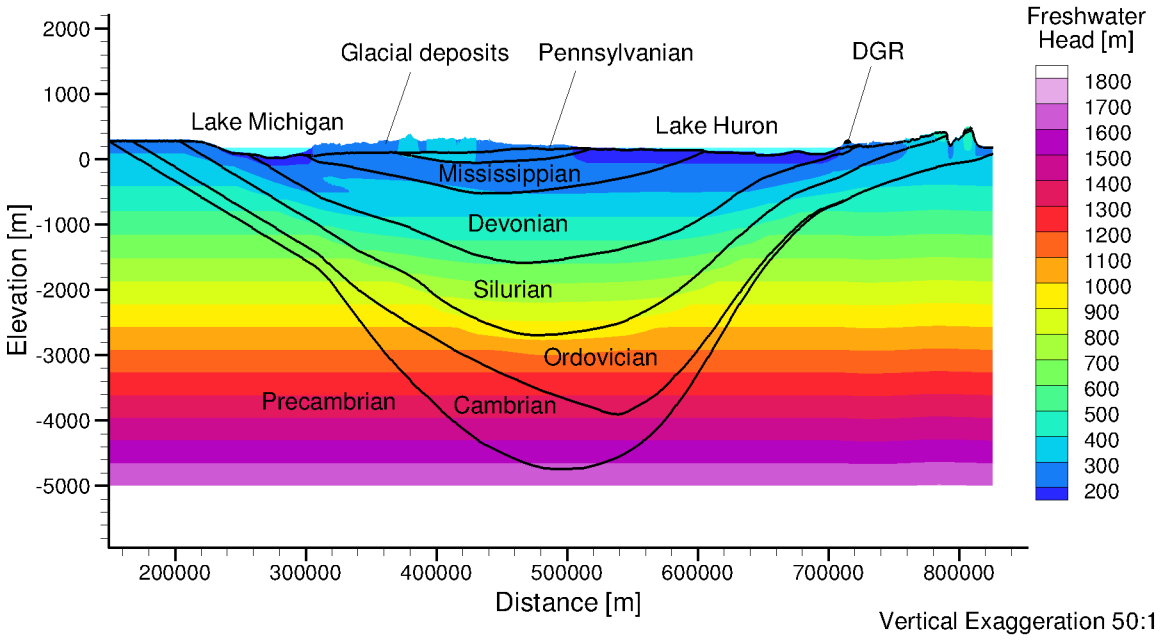

Figure 6.12: Equilibrium Freshwater Heads for Michigan Basin Cross-Section Analysis and Alternate Defined TDS Distribution

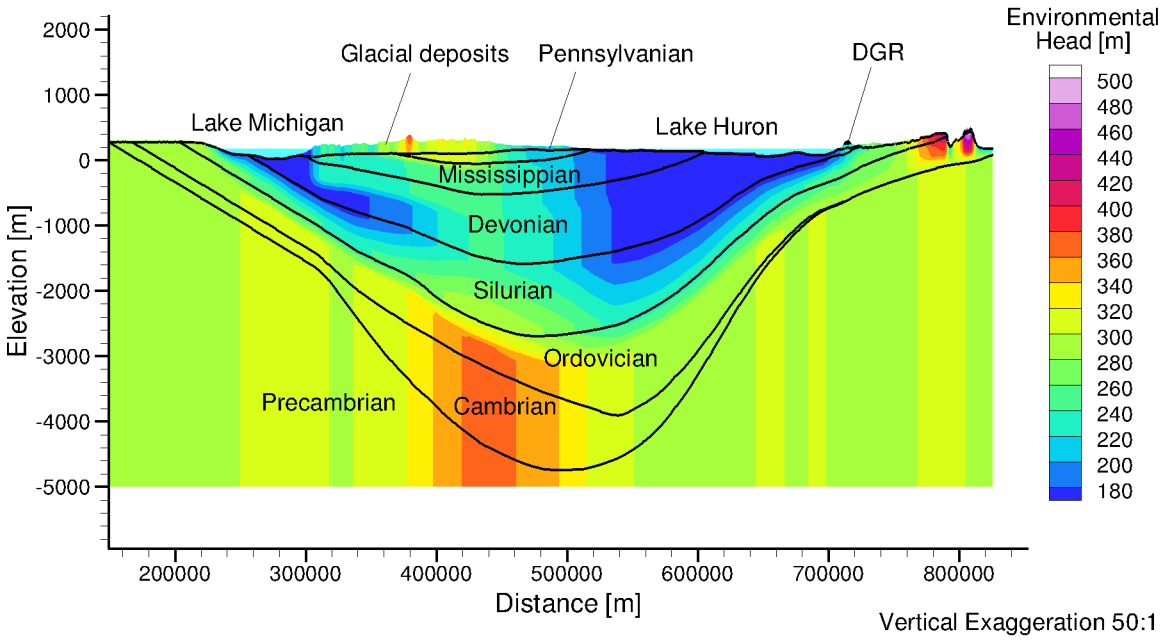

Figure 6.13: Equilibrium Environmental Heads for Michigan Basin Cross-Section Analysis and Alternate Defined TDS Distribution

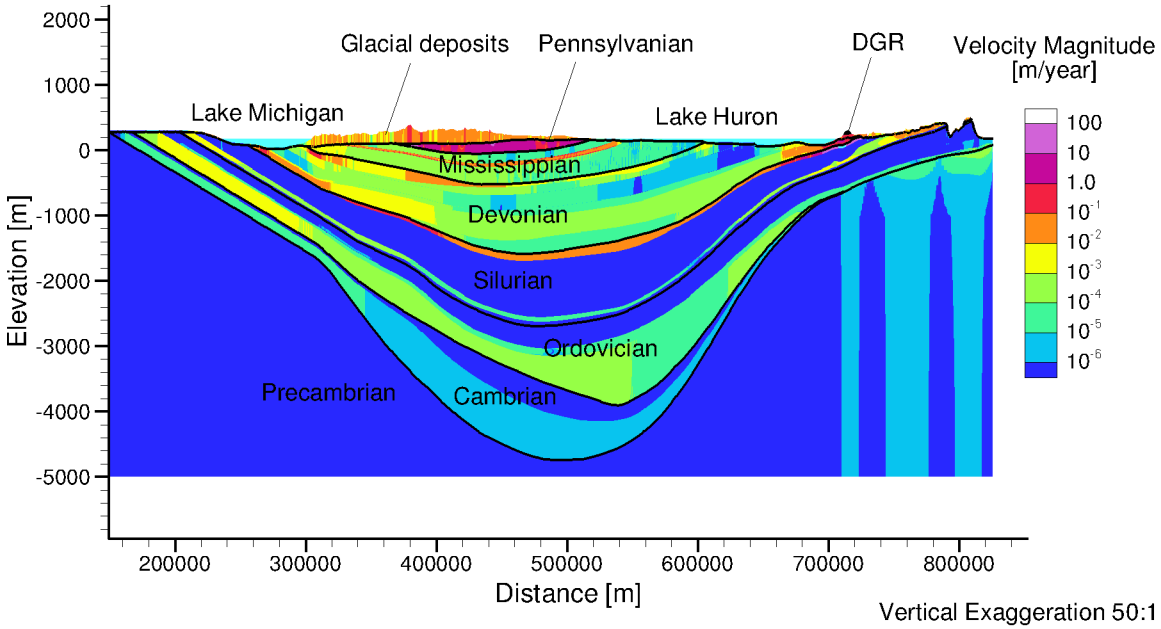

Figure 6.14: Pore Water Velocity Magnitude for Michigan Basin Cross-Section Analysis and Alternate Defined TDS Distribution

Section 4.1.4 presents three different models for the relationship between total dissolved solids concentration and water density: Equation (4.6) is used in this study; Equation (4.5) is used by INTERA (2011) to estimate water densities from TDS concentrations in borehole porewater at the DGR site (scenario fc-intera-litds); and, Equation (4.4) is the model developed by Lampe (2009) (scenario fc-usgs-litds) from data compiled by Gupta (1993). The calculated equivalent freshwater head and environmental head profiles of Figure 6.10 were obtained using the base-case parameters and the TDS versus density relationship developed for this study (refer to Equation (4.6)). The sensitivity of the head profiles for the Michigan Basin cross-section analysis to the model of TDS versus density was assessed using the base-case parameters and the models of INTERA (2011) and Lampe (2009). The TDS concentration distribution, equivalent freshwater heads, environmental heads and velocity magnitude plots for the results using the model of INTERA (2011) are presented in Figure G.3, Figure G.5, Figure G.6 and Figure G.4 respectively of Appendix G. The TDS concentration distribution, equivalent freshwater heads, environmental heads and velocity magnitude plots for the results using the model of Lampe (2009) are presented in Figure G.7, Figure G.8, Figure G.9, and Figure G.10 respectively of Appendix G. The head profiles for the INTERA (2011) and Lampe (2009) cases, presented in Figure 6.16 and Figure 6.17 respectively, can be compared to the base-case analysis head profile shown in Figure 6.10. A comparison of the three plots reveals that the equivalent freshwater head profiles show a greater sensitivity to the TDS versus density model than do the environmental heads. The environmental head profiles for the three analyses are virtually identical. The lack of sensitivity of the environmental heads to the TDS versus density model is related to the fact that the environmental heads have removed the effect of density by subtracting from the freshwater head the excess head due to a density greater than that of freshwater. The implication of the results is that while an adjustment of the TDS versus density model can improve the fit between the observed and measured freshwater heads, the adjustment will not

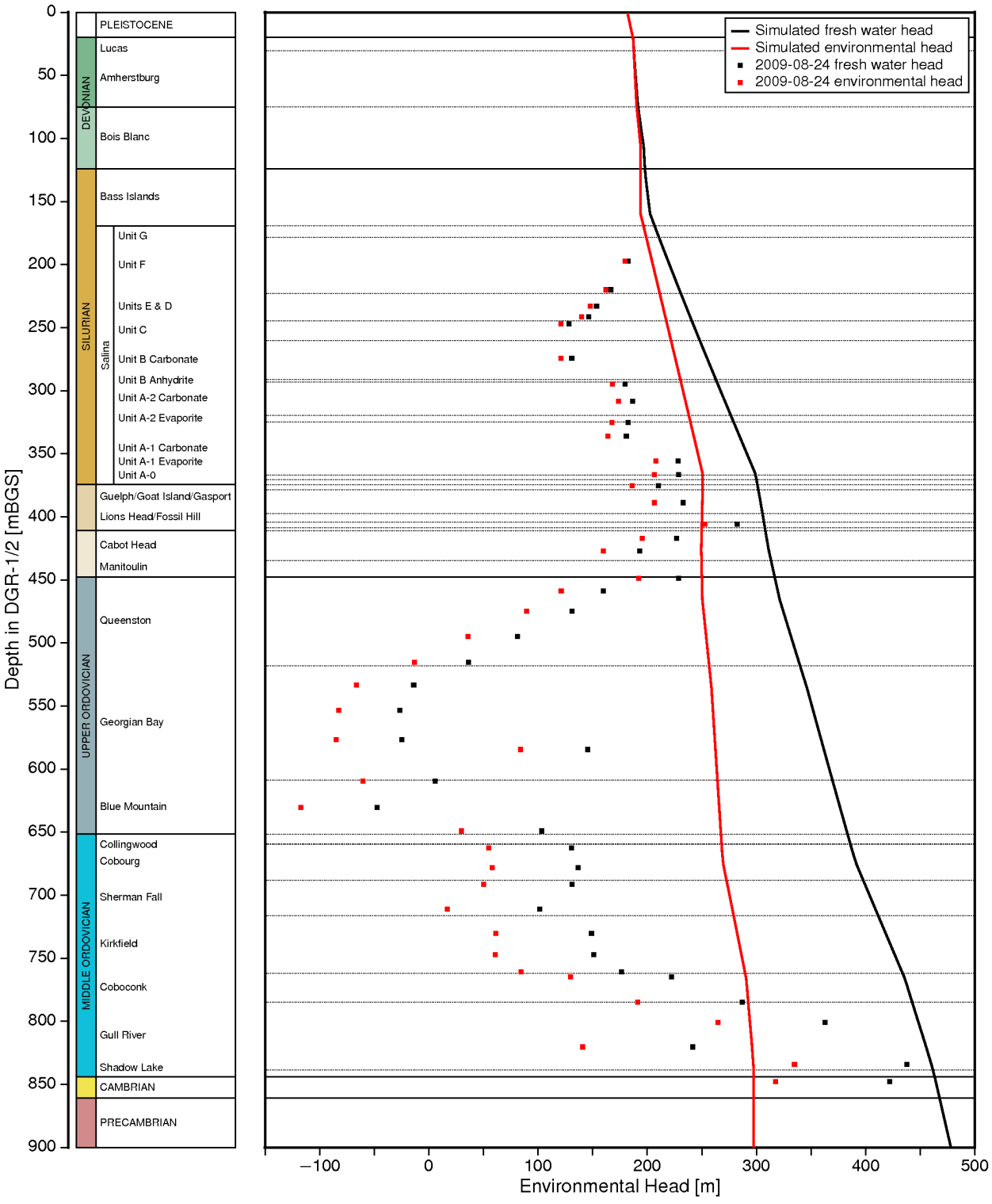

Figure 6.15: Comparison of Simulated and Measured August 24, 2009 DGR-4 Heads for Michigan Basin Cross-Section Analysis and Alternate Defined TDS Distribution

necessarily improve the fit for the environmental heads. Both the environmental heads and the freshwater heads will be sensitive to the spatial distribution of total dissolved solids concentration.

Of the three models for TDS concentration versus density discussed in the preceding paragraph, the smallest difference between the FRAC3DVS-OPG calculated freshwater heads and the freshwater heads estimated from the borehole pressure measurements of the Cambrian is obtained using the INTERA (2011) TDS concentration versus density model of Equation (4.5). However, a comparison at one point (the Cambrian) cannot be used to validate a model.

6.2.4 Impact on Flow of a Hypothetical Higher Permeability Zone in the Precambrian

The upper several metres of the Precambrian basement is often comprised of a weathered alteration zone (INTERA 2011). The conceptual model of this scenario (fc-hkp-litds) is designed to investigate the impact that a higher permeability zone in the Precambrian has on the Michigan Basin groundwater flow system, especially at the proposed DGR site. In this study, it was assumed that there is a 20 m weathered zone in the upper Precambrian across the whole Michigan basin from east to west. The parameters for the weathered layer were set to be the same as the regional-scale numerical model. The head distributions at the equilibrium solution of 10 Ma are given in Figure G.1 and Figure G.2. As compared to the base-case analysis, except for the west boundary, where the head signature is transmitted by the weathered zone in the upper Precambrian, no obvious difference in head distributions is observed. The thickness of the weathered Precambrian zone is too thin relative to its horizontal extent so that its impact on the head distributions is trivial. In addition, the bowl-shaped Michigan Basin with high salinity tends to dampen the energy gradient and stagnate the groundwater. By comparing the pore water velocity magnitudes in Figure 6.18 to the one in the base case analysis, the most notable difference is that the high velocity zone in the Cambrian and upper weathered Precambrian is continuous and unconfined at both sides. However, within the Ordovician in the vicinity of the proposed DGR, the groundwater pore velocities are still less than 0.001 m/a. The solute transport in the Ordovician is diffusion dominated. The outcrop of a highly permeable weathered Precambrian zone releases the over-pressure to some extent. The simulated heads for the deep geologic units at the proposed DGR in Figure 6.19 is slightly larger than those for the base-case study. The head gradient in the Ordovician is still upward. Therefore, based on the preceding comparisons, it can be concluded that the model results are insensitive to the inclusion of a weathered zone in the Upper Precambrian.

6.2.5 Discussion of the Michigan Basin Cross-Section Analyses

The analyses developed in this section for density-dependent groundwater flow in a cross-section of the Michigan Basin confirm the hypothesis that at a point in all units/formations of the Michigan Basin beneath Lake Huron either a divide for groundwater flow occurs or density-dependent horizontal flow is negligible. The analyses predict the occurrence of over-pressures in the Cambrian at the DGR site. Table 6.7 presents a summary of the equivalent freshwater and environmental heads measured on August 24, 2009 in the Niagaran and the Cambrian and the heads calculated in the scenarios developed in this section. In the DGR boreholes, the Niagaran is differentiated as the Guelph, Goat Island, Gasport and Lions Head; the range of measured heads in Table 6.7 is developed from the measured heads for these members. From the table, it can be concluded that all scenarios predict an upward gradient between the Cambrian and the Niagaran and that the difference between the measured and model calculated heads is less than the difference obtained with the regional-scale model (refer to the analyses of Section 4.4).

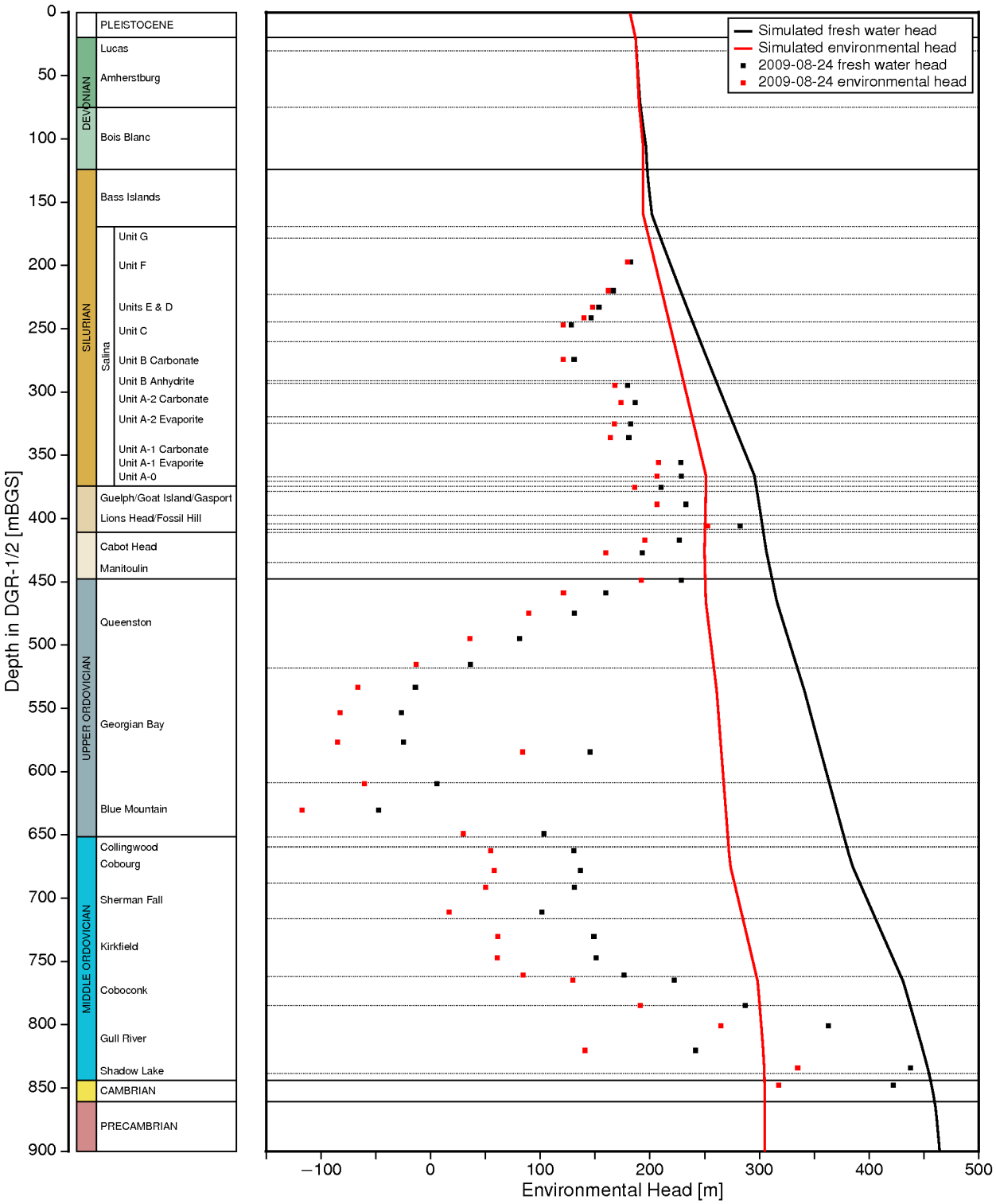

Note: Refer to Equation (4.5) for TDS concentration versus density relationship. Head measurements from August 24, 2009.

Figure 6.16: Comparison of Simulated and Measured DGR-4 Heads for the Base-Case Parameters and the (INTERA 2011) TDS Versus Density Relationship

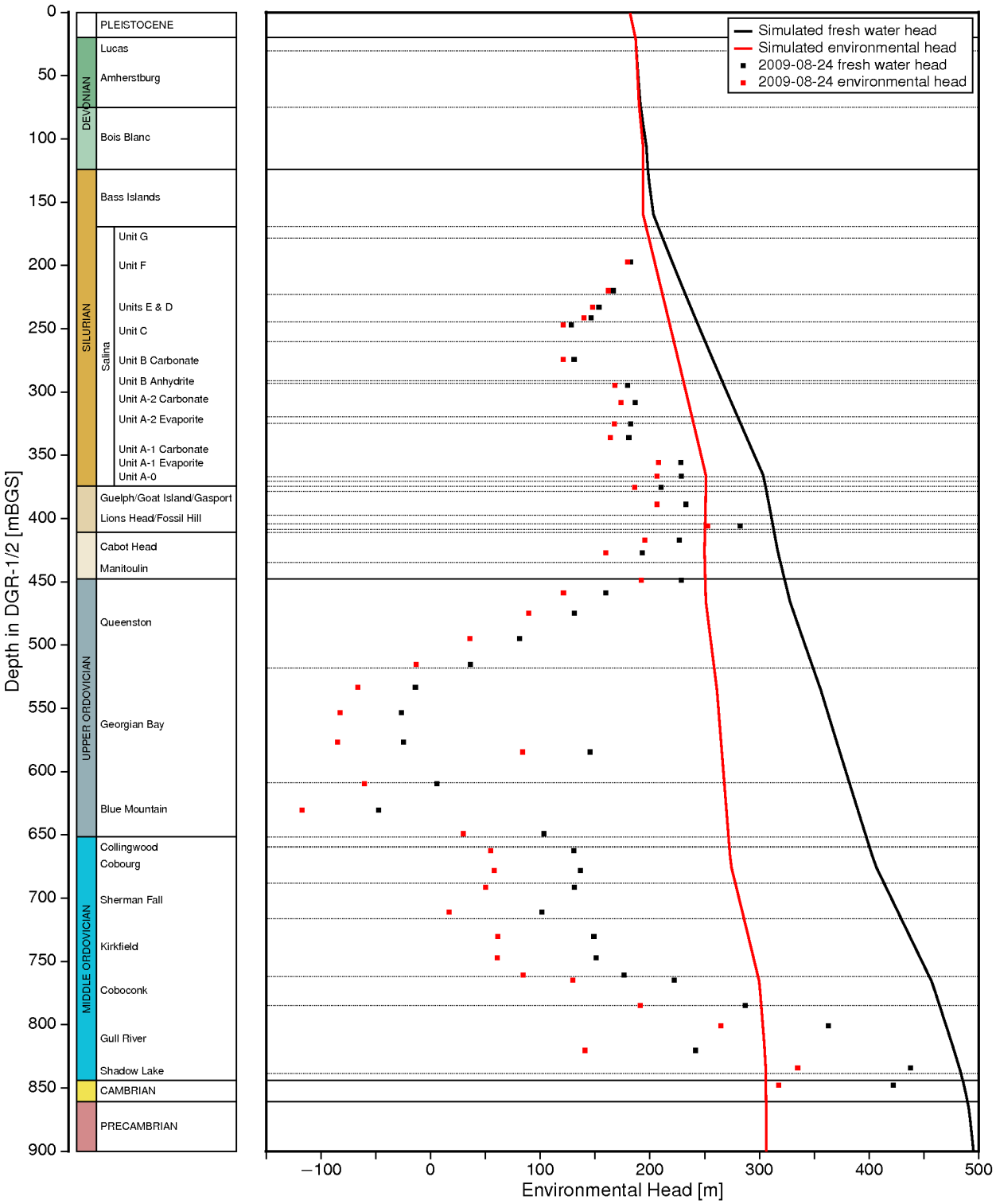

Note: Refer to Equation (4.4) for TDS concentration versus density relationship. Head measurements from August 24, 2009.

Figure 6.17: Comparison of Simulated and Measured DGR-4 Heads for the Base-Case Parameters and the Lampe (2009) TDS Versus Density Relationship

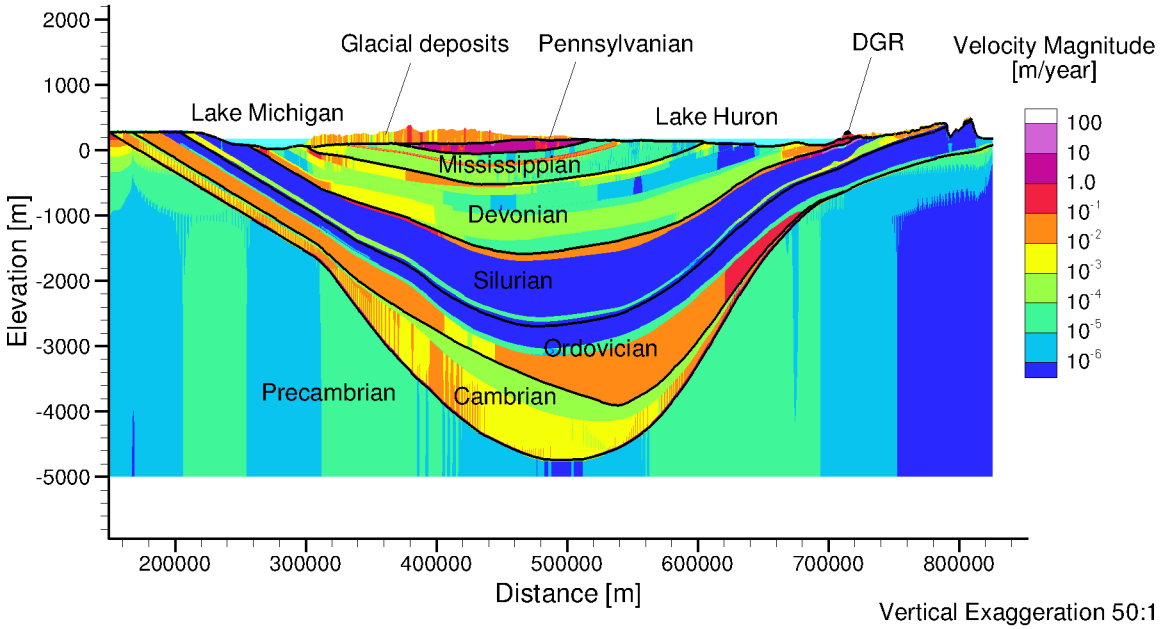

Figure 6.18: High Permeability Zone in the Precambrian: Pore Water Velocity Magnitude for Defined TDS Distribution

This study investigated only a single TDS concentration versus depth model for the sedimentary rock. An alternate TDS versus depth model for the sedimentary rock may result in an improved fit. Regardless, based on the results, it is concluded that the over-pressures in the Cambrian can be attributed to the spatial distribution of fluid density and the geometry of the various stratigraphic layers in the Michigan Basin.

Table 6.7: Comparison of DGR-4 Measured Heads in the Niagaran and the Cambrian with the Calculated Heads from the Scenarios for the Michigan Basin Cross-Section

Simulation	Niagaran		Cambrian	
	Freshwater Heads [m]	Environmental Heads [m]	Freshwater Heads [m]	Environmental Heads [m]
Measured (24-Aug-2009)	210.4–282.3	186.3–252.7	422.1	317.6
no density case	250.9	250.9	297.5	297.5
fc-base-litds	304.7	250.9	472.6	305.3
fc-hanor-litds	304.3	250.5	465.0	297.6
fc-hkp-litds	305.1	251.2	472.8	305.5
fc-intera-litds	300.1	250.9	457.6	304.6
fc-usgs-litds	309.2	250.9	487.2	306.0

The pore water velocities and gradients in the Niagaran and the Cambrian at the location of the DGR from the Michigan Basin cross-section scenarios are summarized in Table 6.8. The results

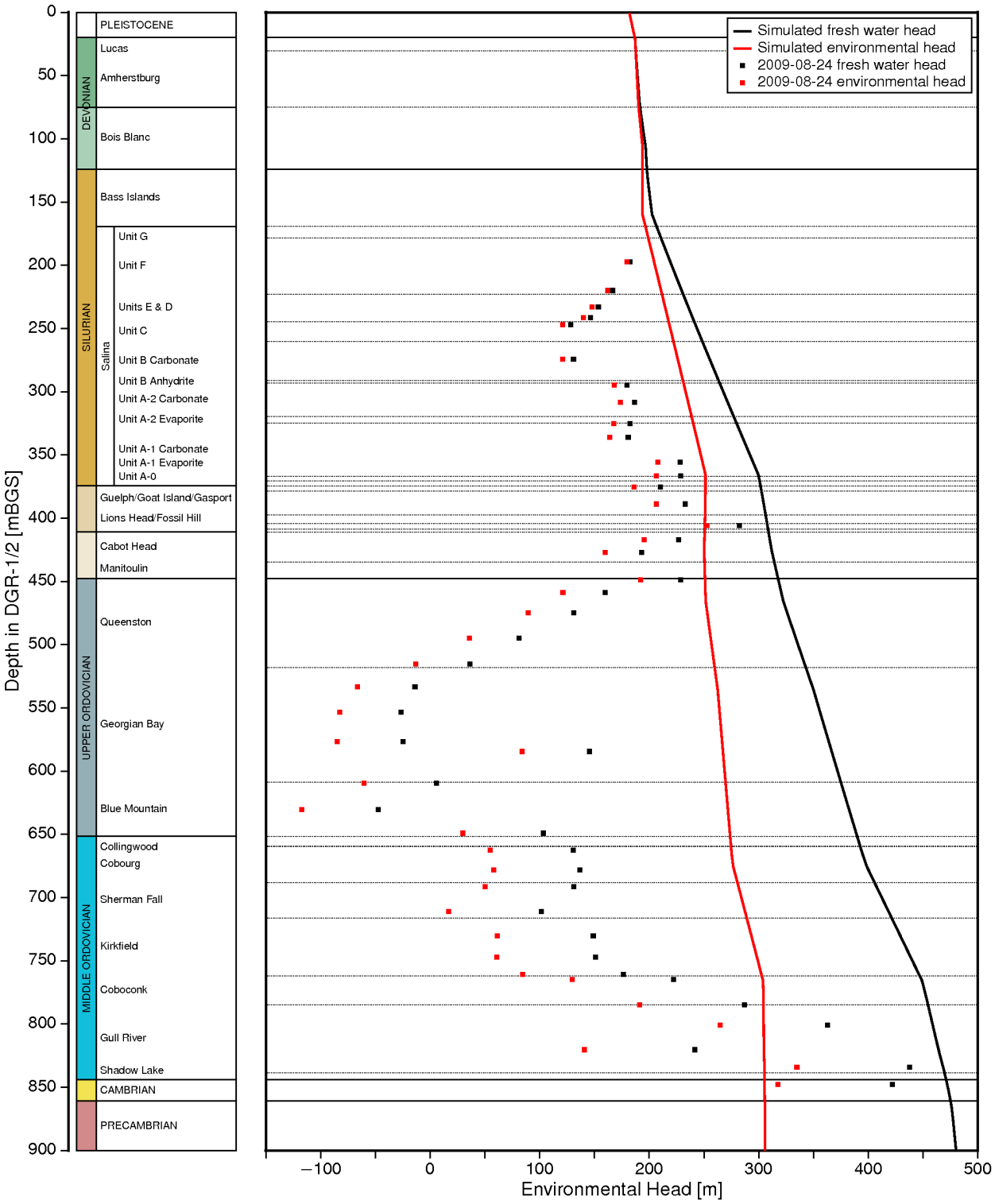

Figure 6.19: High Permeability Zone in the Precambrian: Comparison of Simulated and Measured August 24, 2009 DGR-4 Heads for Defined TDS Distribution

predict that the pore water velocity in the Niagaran is westerly and that it is insensitive to the TDS versus depth model for the Precambrian. The Niagaran velocities are also insensitive to the TDS versus fluid density model. The magnitude of the velocity yields a travel distance in the Niagaran of 1.3 km in 1 Ma. Except for the case with the weathered zone in the upper Precambrian, the predicted pore water velocities in the Cambrian are easterly and with negligible gradient they correspond to a travel distance ranging up to 0.3 km in 1 Ma. The results for both the Niagaran and Cambrian provide support for the hypothesis that flow in the deeper permeable units of the Michigan Basin is essentially stagnant. The sluggish velocities also support the hypothesis that the concentration of both the major ions and the environmental isotopes for the deep groundwater system are relatively insensitive to transport and that there is a greater dependence on local-scale rock water interaction.

Table 6.8: Calculated Gradients and Velocities in the Niagaran and Cambrian (Ancell Group) at the DGR-4 Borehole from the Scenarios for the Michigan Basin Cross-Section

Simulation	Niagaran (Horizontal)		Cambrian (Horizontal)	
	Velocity [m/a]	Gradient [m/m]	Velocity [m/a]	Gradient [m/m]
fc-base-litds	-1.3×10^{-3}	-3.0×10^{-4}	3.0×10^{-4}	2.3×10^{-7}
fc-hanor-litds	-1.4×10^{-3}	-3.2×10^{-4}	2.5×10^{-4}	1.9×10^{-7}
fc-hkp-litds	-1.4×10^{-3}	-3.2×10^{-4}	-1.5×10^{-2}	-1.1×10^{-5}
fc-intera-litds	-1.3×10^{-3}	-3.0×10^{-4}	3.0×10^{-4}	2.3×10^{-7}
fc-usgs-litds	-1.3×10^{-3}	-3.0×10^{-4}	3.0×10^{-4}	2.3×10^{-7}

6.3 Two-Phase Gas and Water Flow Analysis

The spatial domain for the analysis of two-phase immiscible flow is often limited by the requirements of vertical discretization. These requirements are revealed in the analysis of surface hydrology using Richards' Equation. The appropriate level of vertical discretization of the Richards' Equation required for simulating infiltration, evapotranspiration, and initiation of runoff can be determined through the analysis of a spatial convergence study as demonstrated by Downer and Ogden (2004). The outcome of a spatial convergence study reveals the resolution (i.e., cell size) required to achieve a solution that accurately represents the system. In order to obtain a meaningful, physically correct solution to the Richards' Equation under transient, variably saturated conditions a very fine vertical discretization is required to capture the non-linear response of the vadose zone, as illustrated by the soil characteristic curves (Downer and Ogden 2004). The results of their investigations show that a near surface vertical discretization coarser than 2 cm can result in significant misrepresentation of the hydrological process, (i.e., infiltration, evapotranspiration, and runoff). Downer and Ogden (2004) conclude that employing too coarse of a vertical discretization, especially at the ground surface, can result in a model that does not respond in an accurate, physically correct manner. In fact, this necessarily implies that too coarse of a discretization will result in the specification of physically unrealistic parameter values in order to achieve a solution that is consistent with observations. The requirement of a fine vertical discretization can be extended to the application of the TOUGH2 series of models where the computational requirements (for both storage and processing speed) are directly proportional to the level of discretization employed in the model. The vertical discretization required to achieve spatial convergence, which is necessary to properly represent the hydrological processes, may

be too burdensome; the compromise or simplifying assumption often invoked is to reduce the dimensionality of the problem.

The discretization that is required for a three-dimensional regional-scale model of the geosphere surrounding the Bruce DGR is too coarse for the modelling of two-phase gas and water flow. In addition, while there is evidence that a gas phase may exist in the Ordovician sediments, the spatial extent of a gas phase is unknown and the degree of saturation for the gas phase is uncertain. Two-phase gas and water flow is thus investigated in this study using a one-dimensional vertical column. It is assumed that both horizontal pressure gradients and horizontal solute concentration gradients are negligible in the Ordovician. The objective of the modelling is solely to ascertain whether the under-pressures measured in the Ordovician shale and limestone can be explained by the presence of a gas phase.

A one-dimensional two-phase air-water analysis was performed using TOUGH2-MP (Pruess et al. 1999) to investigate anomalous pressures in formations below the Niagaran Group. The following sections describe the methodology, conceptual model, and resulting analyses. The scope of the two-phase air-water analysis was limited to demonstrating that the presence of a gas phase in the Ordovician sediments could result in water phase pressures that are less than the hydrostatic pressures estimated from the surface elevation and water density profile observed in the DGR boreholes. The measured Westbay pressure and estimated head profile for the DGR-4 borehole (INTERA 2011) are shown in Figure 2.15. The scenarios or cases investigated using the one-dimensional two-phase air-water flow model are summarized in Table 6.9. Note that the scenario names correspond to the prefix of the file names for the computer runs. The ‘t’ designates the TOUGH2-MP computational model, and the remaining descriptors designate the scenario.

Table 6.9: Model Scenarios for the Analysis of the One-Dimensional Two-Phase Air-Water Flow

Scenario	Description
t-Sg-17	Initial gas saturation of 0.17 between Coboconk and Gasport formations
t-Sg-17-fracture	Scenario t-Sg-17 with a discontinuity at 585 m depth
t-MQ-highD	Air generation between Coboconk and Queenston formations
t-MQ-highD-fracture	Scenario t-MQ-highD with a discontinuity at 585 m depth

6.3.1 Modelling Methodology: TOUGH2-MP

The TOUGH2-MP computational model was selected for this study based on its capabilities, multi-phase flow attributes, the validation and verification reports for the model, and its broad use throughout the world. The target formations for the TOUGH2-MP analyses lie from the Guelph Formation to the Cambrian Formation, inclusive. Although brines exist within these formations, the TOUGH2-MP analyses applied the EOS3 (Equation Of State 3 - Air/Water) module. Although the fluids within the modelled formations have a density greater than freshwater, the pore fluid is modelled as freshwater, and the gas is modelled as air as a first approximation. The formation permeability is calculated from the formation hydraulic conductivity, formation fluid density, and fluid viscosity. The environmental head of insitu pressure measurements are used in this section

to remove the effects of pore fluid density on the comparison of heads calculated using the TOUGH2-MP compositional model.

The attributes of the TOUGH2-MP model are described in Pruess et al. (1999). For the analyses of this study, the van Genuchten model (van Genuchten 1980) was used to describe the capillary pressure versus saturation relationship. The van Genuchten-Mualem model (van Genuchten 1980, Mualem 1976) was used to describe the relative permeability versus saturation relationship. The parameters for the models include the irreducible water saturation S_{lr}, the irreducible gas saturation S_{gr}, the maximum water saturation S_{ls}, the maximum capillary pressure P_{max}, the fitting parameter $1/\alpha$ which is analogous to the air entry pressure, and the fitting parameter λ for the relative permeability model.

A hypothesis of this study and the Geosynthesis program is that solute transport in the low permeability Ordovician rock is dominated by diffusion. In the TOUGH2-MP compositional model, diffusive flux $\mathbf{f}$ of constituent κ can occur in both the gas phase and the water phase β with the model being:

$$\mathbf{f}_\beta^\kappa = -\phi \tau_\mathbf{0} \tau_\beta \rho_\beta \mathbf{d}_\beta^\kappa \nabla \mathbf{X}_\beta^\kappa \tag{6.1}$$

where ϕ is the porosity, $\tau_0 \tau_\beta$ is the tortuosity which includes a porous medium dependent factor τ_0 and a coefficient that depends on the phase saturation S_β, ρ_β is the phase density, d_β^κ is the diffusion coefficient of component κ, assumed to be air in this study, in bulk fluid phase β and X_β^κ is the mass fraction of component κ in phase β. Saturation dependent tortuosity models that are considered in this study include Millington and Quirk (1961):

$$\tau_0 \tau_\beta = \phi^{1/3} S_\beta^{10/3} \tag{6.2}$$

and an optional model included in TOUGH2-MP:

$$\tau_0 \tau_\beta = \tau_0 k_{r\beta}(S_\beta) \tag{6.3}$$

where $k_{r\beta}(S_\beta)$ is the saturation dependent relative permeability for phase β.

Both the TOUGH2-MP model version 2.0 and the EOS3 module version 3.0 were provided as source code, which needed to be compiled and linked to message passing libraries for parallel computing, the Aztec parallel solver, Metis graph partitioning library, the Netlib Y12M Fortran libraries for matrices, and the BLAS and LAPACK high performance matrix/vector libraries. The resulting executable can run on a super-computing cluster, or a multi-processor capable computer. The resulting execution time typically linearly scales to the inverse of the number of available processors.

6.3.2 Conceptual Model for Two-Phase Flow Analysis

The modelling domain is one-dimensional, comprised of 982 blocks with a thickness of approximately 0.5 m in height. The facies change in the Georgian Bay Formation at a depth of approximately 585 m, and labelled in Figure 6.20 as a possible gas-containing zone or discontinuity, was represented using a block with a height of 0.5 m.

The hydrogeologic parameters for the domain are shown in Table 6.10. The hydraulic conductivity values were converted to permeability by using the formation specific fluid densities (see Table 4.2) and a viscosity of 2×10^{-3} Pa s as described in INTERA (2011). The van

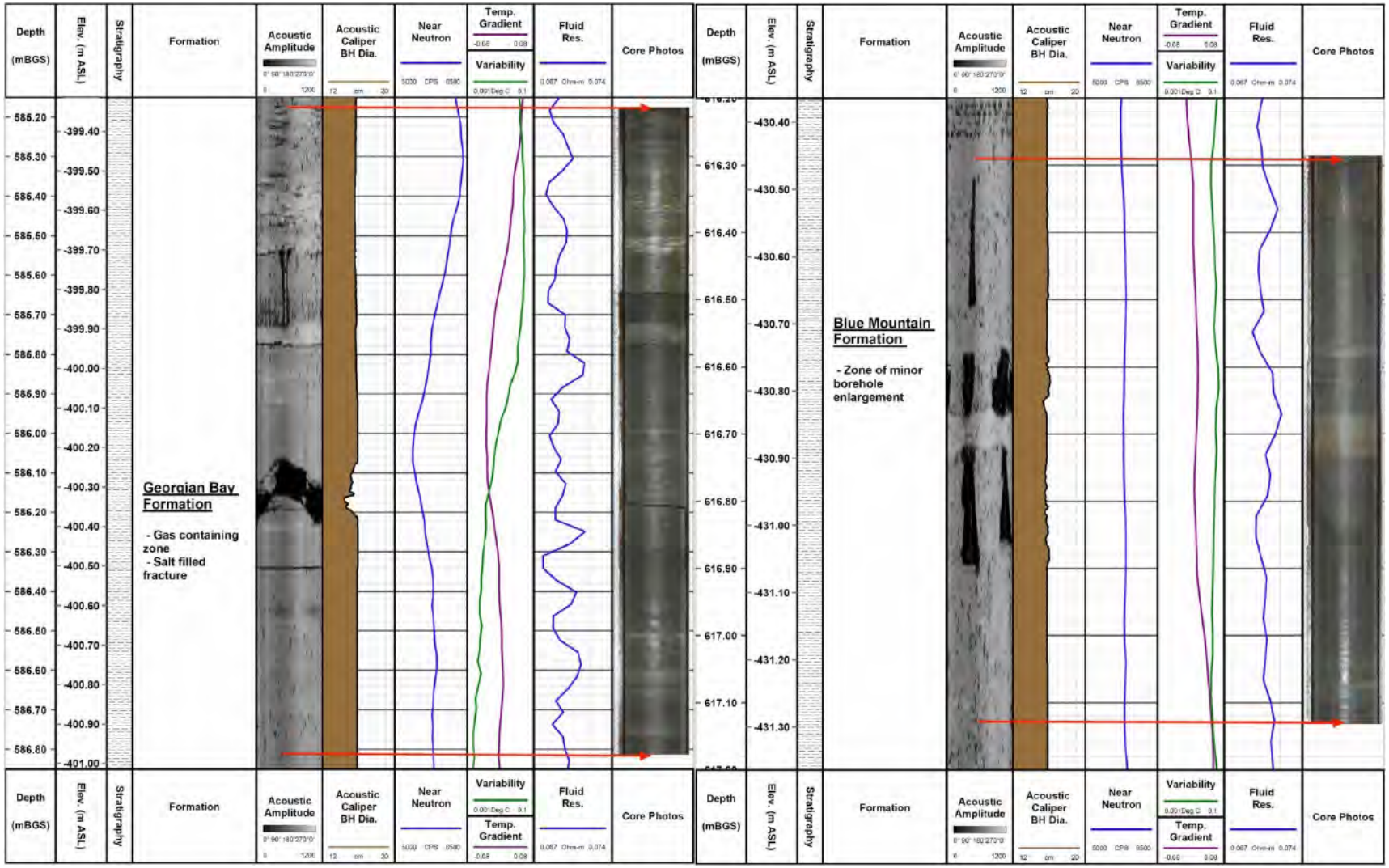

Note: From INTERA (2011).

Figure 6.20: ATV Logs, Selected Geophysical Logs and Core Photographs of Possible Gas-Containing Discontinuity (Left) in Georgian Bay Formation in DGR-2 and Zone of Minor Borehole Enlargement (Right) in Blue Mountain Formation in DGR-2

Genuchten (1980) parameters for the non-hysteretic capillary pressure and relative permeability curves for use in TOUGH2-MP are shown in Table 6.10. The capillary pressure versus water saturation curves for the formations listed in Table 6.10 are shown in Figure 6.21. The more permeable discontinuity is modelled using the capillary pressure curve labeled as FRACT in Figure 6.21. It should be noted that different capillary pressure versus water saturation curves will yield different pressures and saturations within the discontinuity. The full investigation of this aspect of two-phase flow will not materially affect the findings of this study and the assessment of the impact of a gas phase on water flow and the explanation of the abnormal pressures measured in the DGR boreholes.

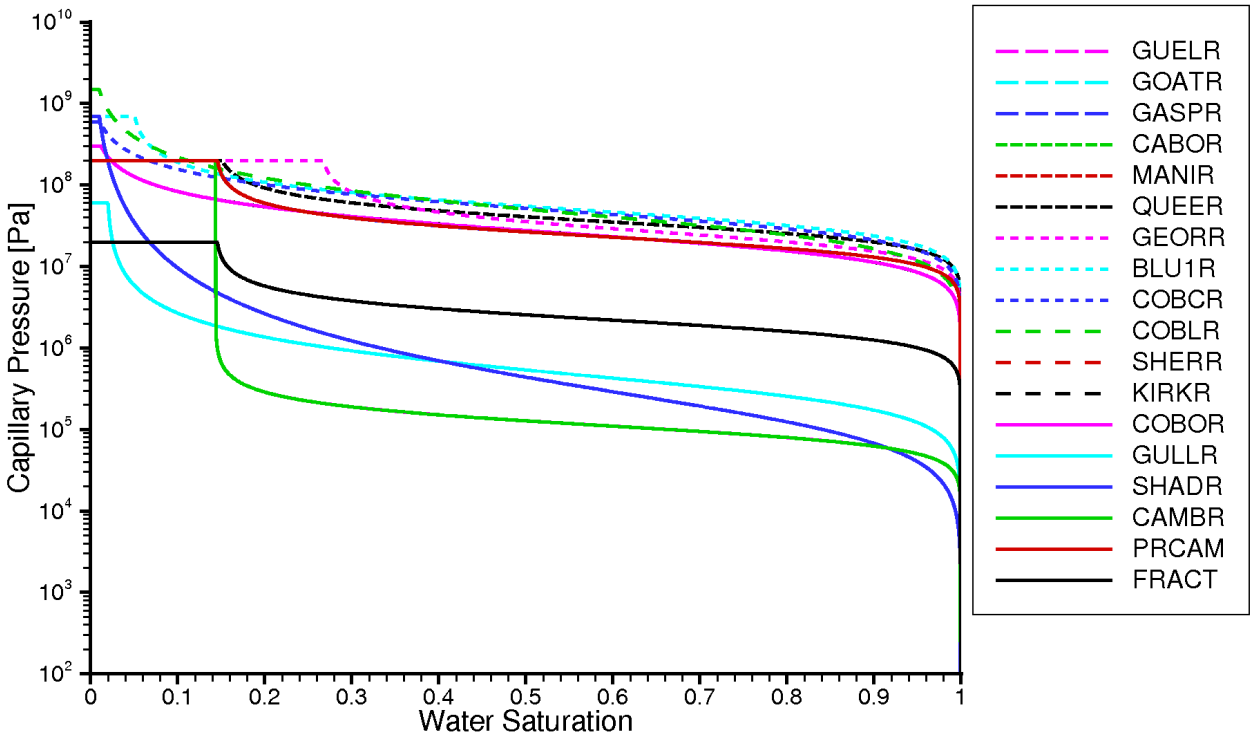

Figure 6.21: Capillary Pressure Versus Saturation Relationships for the Two-Phase Flow Analysis

6.3.3 Analysis With a Gas Phase Saturation Specified as an Initial Condition

6.3.3.1 Conceptual Model Without a Discontinuity at 585 m Depth

This simulation is identified as scenario t-Sg-17. The TOUGH2-MP model required boundary conditions to be set for the top and bottom blocks in the modelling domain representing the Guelph Formation and the Cambrian Formation respectively. Both blocks are set to specified gas pressure and gas saturation, the state variables solved for by TOUGH2-MP. A gas saturation of zero was assumed for both formations yielding a corresponding capillary pressure of zero. The initial gas saturation for the units between the Coboconk and the Gasport was set to 0.17, resulting in an initial water saturation of 0.83 as shown in Figure 6.22. The Gull River and Shadow Lake were assumed to have an initial gas saturation of zero.

Table 6.10: Hydrogeologic and Two-Phase Flow Properties for Each Geologic Unit

Formation	ID	Density	Porosity	Permeability			Relative Permeability Curves				Capillary Pressure Curves				
				k_x	k_y	k_z	λ	S_{lr}	S_{ls}	S_{gr}	λ	S_{lr}	$1/\alpha$	P_{max}	S_{ls}
		[kg/m^3]	[/]	[m^2]	[m^2]	[m^2]	[/]	[/]	[/]	[/]	[/]	[/]	[MPa]	[MPa]	[/]
Guelph	GUELR	2,810	0.057	4.91×10^{-15}	4.91×10^{-15}	4.91×10^{-15}	0.718	0.14	1.00	0.08	0.718	0.14	1.0×10^{5}	2.0×10^{8}	1.00
Goad Island	GOATR	2,730	0.020	3.40×10^{-19}	3.40×10^{-19}	3.40×10^{-20}	0.718	0.14	1.00	0.08	0.718	0.14	2.1×10^{7}	2.0×10^{8}	1.00
Gasport	GASPR	2,730	0.020	3.40×10^{-19}	3.40×10^{-19}	3.40×10^{-20}	0.718	0.14	1.00	0.08	0.718	0.14	2.1×10^{7}	2.0×10^{8}	1.00
Cabot Head	CABOR	2,790	0.116	1.52×10^{-20}	1.52×10^{-20}	1.52×10^{-21}	0.718	0.14	1.00	0.08	0.718	0.14	3.2×10^{7}	2.0×10^{8}	1.00
Manitoulin	MANIR	2,720	0.028	1.49×10^{-20}	1.49×10^{-20}	1.49×10^{-21}	0.718	0.14	1.00	0.08	0.718	0.14	3.2×10^{7}	2.0×10^{8}	1.00
Queenston	QUEER	2,770	0.073	3.38×10^{-21}	3.38×10^{-21}	3.38×10^{-22}	0.718	0.14	1.00	0.08	0.718	0.14	3.2×10^{7}	2.0×10^{8}	1.00
Georgian Bay	GEORR	2,760	0.071	5.08×10^{-21}	5.08×10^{-21}	5.08×10^{-22}	0.706	0.26	1.00	0.12	0.706	0.26	2.4×10^{7}	2.0×10^{8}	1.00
Blue Moutain	BLU1R	2,770	0.078	8.52×10^{-21}	8.52×10^{-21}	8.52×10^{-22}	0.656	0.05	1.00	0.00	0.656	0.05	4.3×10^{7}	7.0×10^{8}	1.00
Cobourg - Collingwood	COBCR	2,700	0.012	3.55×10^{-21}	3.55×10^{-21}	3.55×10^{-22}	0.626	0.00	1.00	0.13	0.626	0.00	4.0×10^{7}	6.0×10^{8}	1.00
Cobourg - Lower	COBLR	2,710	0.015	3.45×10^{-21}	3.45×10^{-21}	3.45×10^{-22}	0.549	0.00	1.00	0.00	0.549	0.00	3.3×10^{7}	1.5×10^{9}	1.00
Sherman Fall	SHERR	2,720	0.016	1.73×10^{-21}	1.73×10^{-21}	1.73×10^{-22}	0.626	0.00	1.00	0.14	0.626	0.00	2.1×10^{7}	3.0×10^{8}	1.00
Kirkfield	KIRKR	2,710	0.021	1.41×10^{-21}	1.41×10^{-21}	1.41×10^{-22}	0.626	0.00	1.00	0.14	0.626	0.00	2.1×10^{7}	3.0×10^{8}	1.00
Coboconk	COBOR	2,690	0.009	6.97×10^{-19}	6.97×10^{-19}	6.97×10^{-22}	0.626	0.00	1.00	0.14	0.626	0.00	2.1×10^{7}	3.0×10^{8}	1.00
Gull River	GULLR	2,730	0.022	1.26×10^{-19}	1.26×10^{-19}	1.26×10^{-22}	0.547	0.02	1.00	0.00	0.547	0.02	3.4×10^{5}	6.0×10^{7}	1.00
Shadow Lake	SHADR	2,760	0.097	1.80×10^{-16}	1.80×10^{-16}	1.80×10^{-19}	0.350	0.00	1.00	0.00	0.350	0.00	1.3×10^{5}	7.0×10^{8}	1.00
Cambrian	CAMBR	2,700	0.071	5.29×10^{-13}	5.29×10^{-13}	5.29×10^{-13}	0.718	0.14	1.00	0.08	0.718	0.14	1.0×10^{5}	2.0×10^{8}	1.00
Precambrian	PRCAM	2,590	0.038	1.70×10^{-17}	1.70×10^{-17}	1.70×10^{-17}	0.718	0.14	1.00	0.08	0.718	0.14	2.1×10^{7}	2.0×10^{8}	1.00
Fracture - P_c	FRACT	2,760	0.071	5.08×10^{-21}	5.08×10^{-21}	5.08×10^{-22}	0.718	0.14	1.00	0.08	0.718	0.14	2.0×10^{6}	2.0×10^{7}	1.00

Note: Two-phase flow properties are for the van Genuchten (1980) model.

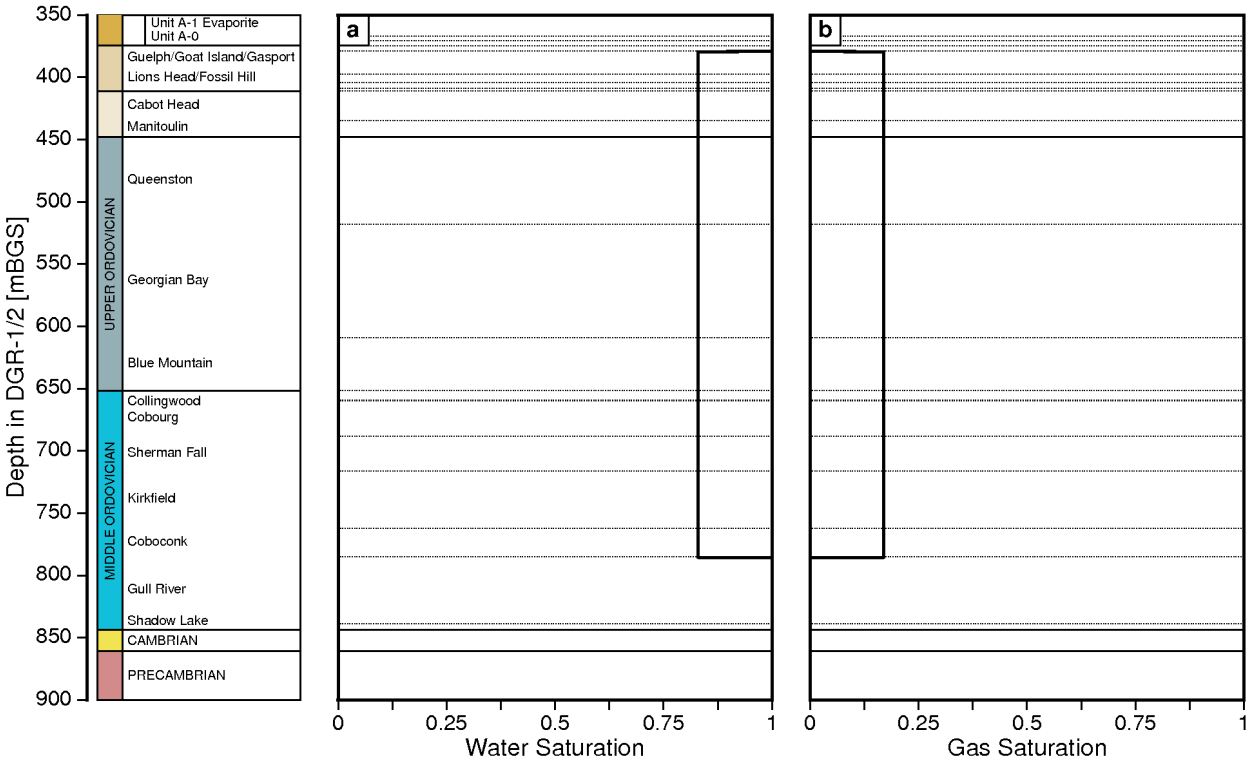

Note: (a) water saturation profile, and (b) gas saturation profile.

Figure 6.22: Initial Saturations for the Two-Phase Gas-Water Flow Analysis

The initial conditions for pressures are shown in Figure 6.23a. The equivalent freshwater heads, gas pressure and capillary pressure are also shown in Figure 6.23. The initial saturations are used to determine the capillary pressure within a formation. The initial water pressure is specified to account for hydrostatic conditions in the Guelph Formation, and hydrostatic conditions with 120 m over-pressure in the Gull River, Shadow Lake, Cambrian and the top of the Precambrian Formations. Initial water pressures are set to zero between the Guelph Formation and the Gull River Formation. The initial gas pressure is calculated from the water pressure minus the capillary pressure.

For the no discontinuity scenario, the water pressure, water head, gas pressure and capillary pressure at 400 ka are shown in Figure 6.24. Saturations at 400 ka are shown in Figure 6.25. As is shown, pressures are continuous from one formation to the next, but saturations are discontinuous. The pressure profiles are still evolving at this stage in the simulation. In Figure 6.24b, the water head is negative within the middle formations and remains over-pressured in the Gull River and Shadow Lake formations.

The water pressure, water head, gas pressure and capillary pressure at 1.25 Ma are shown in Figure 6.26 while the corresponding saturations at 1.25 Ma are shown in Figure 6.27. A comparison of the plots at 1.25 Ma with those presented at 400 ka reveals that the gas phase is dissipating with a corresponding increase in the water pressure (head) occurring. The dissipation of the gas phase occurs as a result of both gas transport as a separate phase from the domain as well as partitioning of the water vapour and air phases from the gas to the water phase and then diffusion in the solution phase to the bounding layers (Guelph and Cambrian). Migration of the

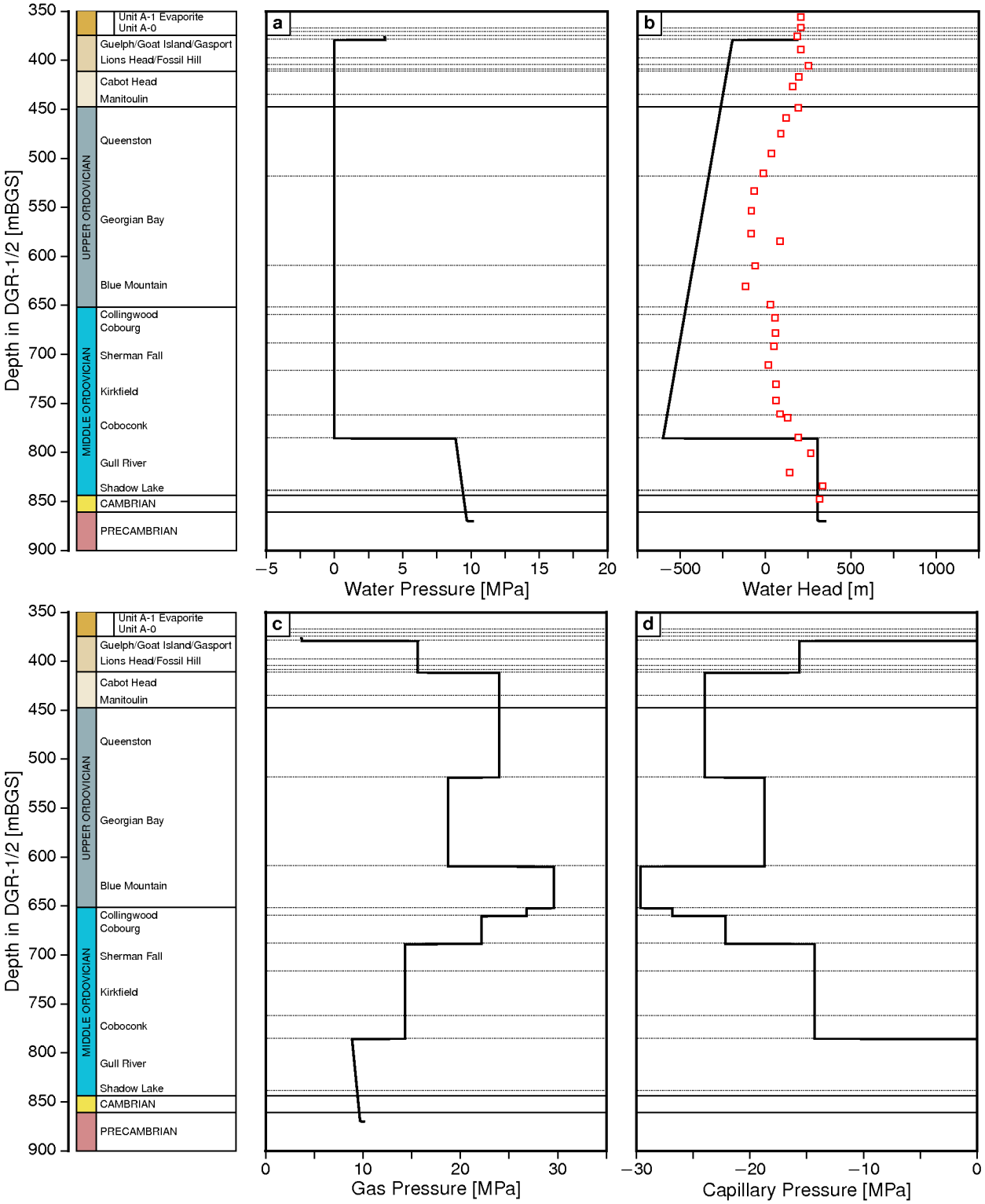

Note: (a) water pressure, (b) freshwater head, (c) gas pressure, and (d) capillary pressure.

Figure 6.23: Initial Conditions for the Two-Phase Gas-Water Flow Analysis with No Discontinuity at 585 m Depth

gas phase is sensitive to the relative permeability versus saturation curves for both the water phase and the gas phase, while diffusion of the air in the water phase is sensitive to the diffusion model used in the analysis. The simulations of this section are based on a diffusion coefficient in which the tortuosity is calculated using Equation (6.3) as the product of tortuosity for a formation (refer to Table 4.2) and the relative permeability for the water phase. The simulations using alternate diffusion models, such as that of Millington and Quirk (1961), are not included in base-case analysis presented in this study; however, the dissipation of the gas phase occurs more quickly with the Millington and Quirk (1961) model than that which occurs with the described tortuosity model of Equation (6.3). With the tortuosity model, the gas phase has completely dissipated by 3 to 4 Ma. Regardless, the results for the water head at 1.25 Ma as shown in Figure 6.26 indicate that the under-pressures in the Ordovician sediments can be described by the presence of a gas phase.

6.3.3.2 Conceptual Model With a Discontinuity at 585 m Depth

Similar to the previous section, the analysis in this section investigates a change to the capillary pressure versus water saturation curve, and its effect on pressures and saturations in a modelling domain that includes a discontinuity with higher permeability in the Georgian Bay Formation at a depth of 585 m (scenario t-Sg-17-fracture). The initial saturations are identical to that assumed for the base-case described in the preceding section and as shown in Figure 6.22. The initial water pressures are the same as those of the base-case (Figure 6.23).

At 300 ka, the presence of the discontinuity is seen in Figure 6.28 for pressures and in Figure 6.29 for saturations. Gas pressures are continuous throughout the formation. The discontinuity exhibits a high gas saturation and high water pressure relative to the adjacent Georgian Bay Formation. The water pressure in the discontinuity can be adjusted by choosing a different capillary pressure versus saturation curve for the zone. From a solute transport perspective, the higher gas phase saturation and lower water phase saturation in the discontinuity as compared to the adjacent rock will result in a reduction of the water phase diffusion in the discontinuity through its dependence on the water phase saturation. The implication is that water phase diffusion can be significantly reduced as a result of the presence of zones in the rock with higher gas saturation.

The distribution of pressures at 500 ka for the discontinuity case are shown in Figure 6.30 with the corresponding saturations being shown in Figure 6.31. The discontinuity is evident in Figure 6.30. No attempt was made to adjust the capillary pressure versus saturation curves or the relative permeability versus saturation curves in order to yield a better comparison between the modelled results and the measured pressures in the DGR-4 borehole. Regardless, the results again indicate that the under-pressures of the water phase in the Ordovician rock can be simulated by the presence of a gas phase. The results also support the argument that the water pressure is sensitive to the rock dependent capillary pressure versus saturation relationships. The results also demonstrate that the gas saturations are not expected to be continuous but will vary significantly throughout the rock column.

6.3.4 Two-Phase Flow Analysis With Air Generation

The preceding Section 6.3.3 investigated the evolution of an assumed initial gas saturation of 17% from the Coboconk to the Goat Island formations and an initial water pressure in the units assumed to be zero; the results of the analysis indicate that the under-pressures in the Ordovician rock can be described using the physics of two-phase gas and water flow. To provide strength to this conclusion, this section develops an alternate conceptual model to demonstrate that under-pressures can result if a gas phase is present in the Ordovician rock. Rather than

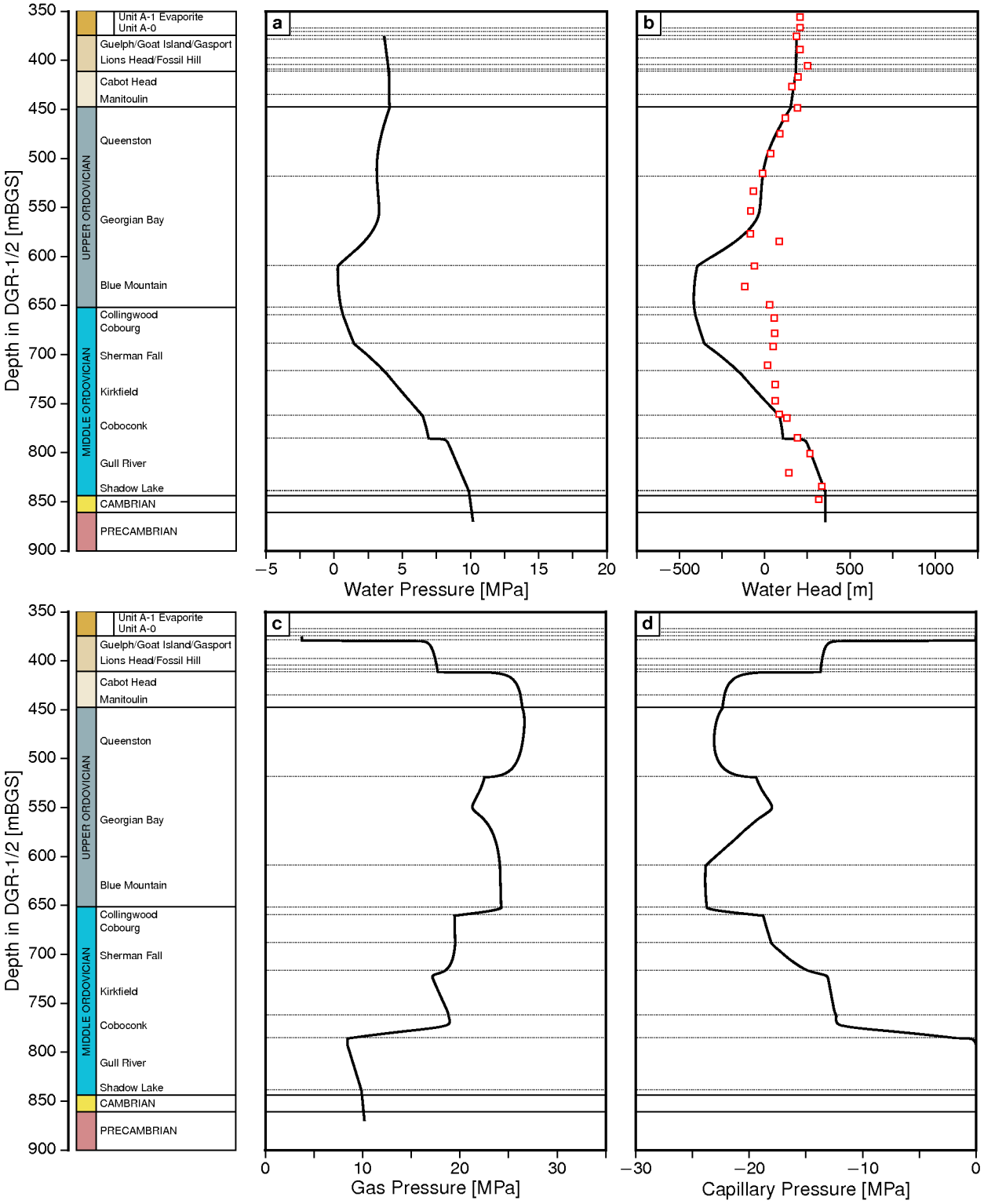

Note: (a) water pressure, (b) freshwater head with posted August 24, 2009 measurements in DGR-4, (c) gas pressure, and (d) capillary pressure.

Figure 6.24: Two-Phase Gas-Water Flow Analysis at 400 ka with No Discontinuity Zone at 585 m Depth

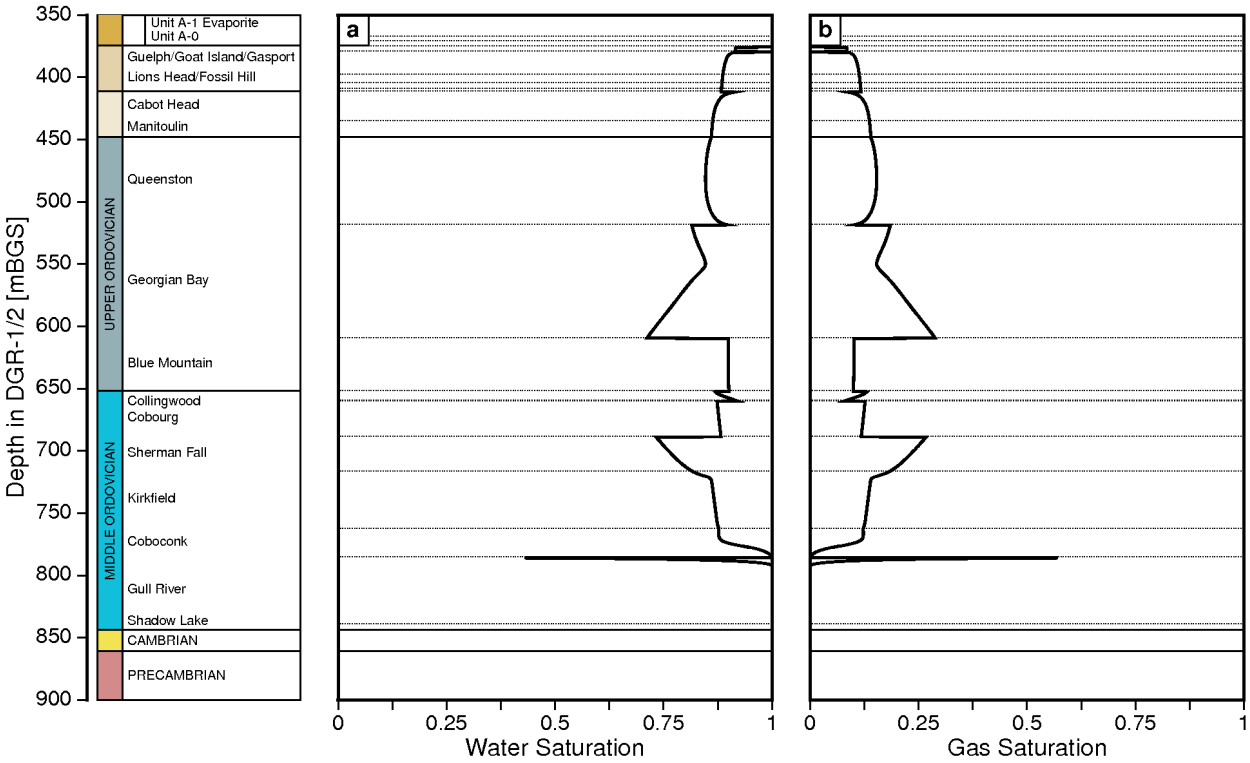

Note: (a) water saturation profile, and (b) gas saturation profile.

Figure 6.25: Saturations for the Two-Phase Gas-Water Flow Analysis at 400 ka with No Discontinuity at 585 m Depth

assuming an initial gas saturation and under-pressure in the Ordovician sediments, the second conceptual model assumes that gas is slowly introduced to the water saturated Ordovician rock that is initially in hydrostatic equilibrium to the DGR borehole measured water pressures in the Cambrian and the Niagaran. For the analysis, the initial water pressure and water head distribution shown in Figure 6.32 is assumed. It is also assumed that the rock is water saturated at time zero. As a gas source, air was introduced uniformly for 200 ka from the Coboconk to the Queenston inclusive. The total amount of air introduced per unit length of rock was assumed to be 98% of the air that would be contained in a volume of rock with a water saturation of 95% and a gas saturation of 5%. Alternate gas generation rates were not investigated in this study as the objective of the analysis was solely to demonstrate that the observed under-pressures could be described by the presence of a gas phase in the Ordovician sediments. The boundary conditions, properties and parameters for the analyses are identical to those used to obtain the results of the preceding section. The same two cases investigated in the preceding sections are also investigated using the second gas - water conceptual model.

6.3.4.1 Conceptual Model Without a Discontinuity at 585 m Depth

This section describes the impact on water pressures of the introduction of air in the Coboconk to the Queenston for 200 ka with no discontinuity at a depth of 585 m (scenario t-MQ-highD). After time zero, air generation greater than the amount that can be accommodated by the pore compressibility results in water pressures in the Ordovician that are over-pressured. The water that is being displaced by the gas phase migrates from the domain under the resulting efflux

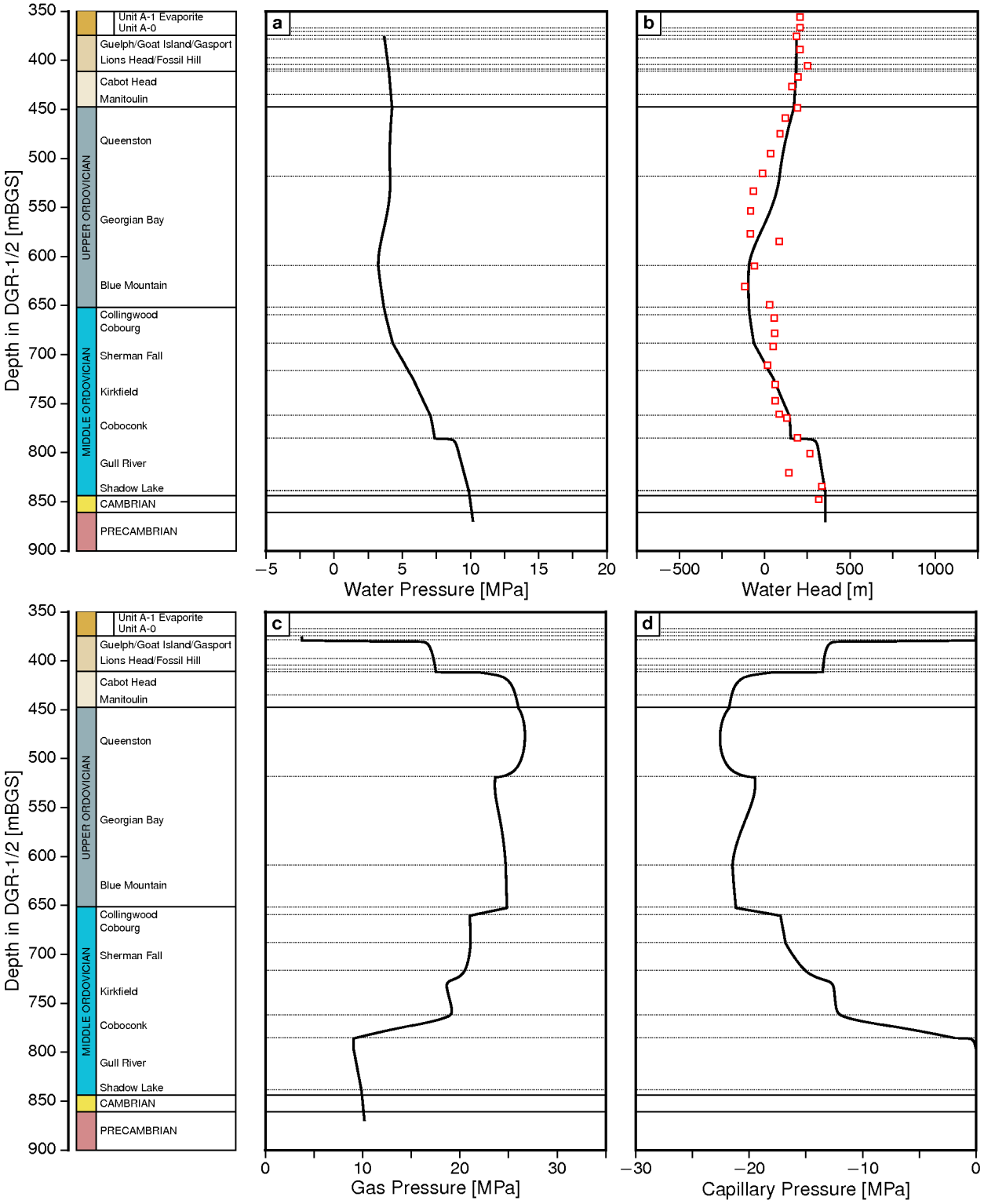

Note: (a) water pressure, (b) freshwater head with posted August 24, 2009 measurements in DGR-4, (c) gas pressure, and (d) capillary pressure.

Figure 6.26: Two-Phase Gas-Water Flow Analysis at 1.25 Ma with No Discontinuity at 585 m Depth

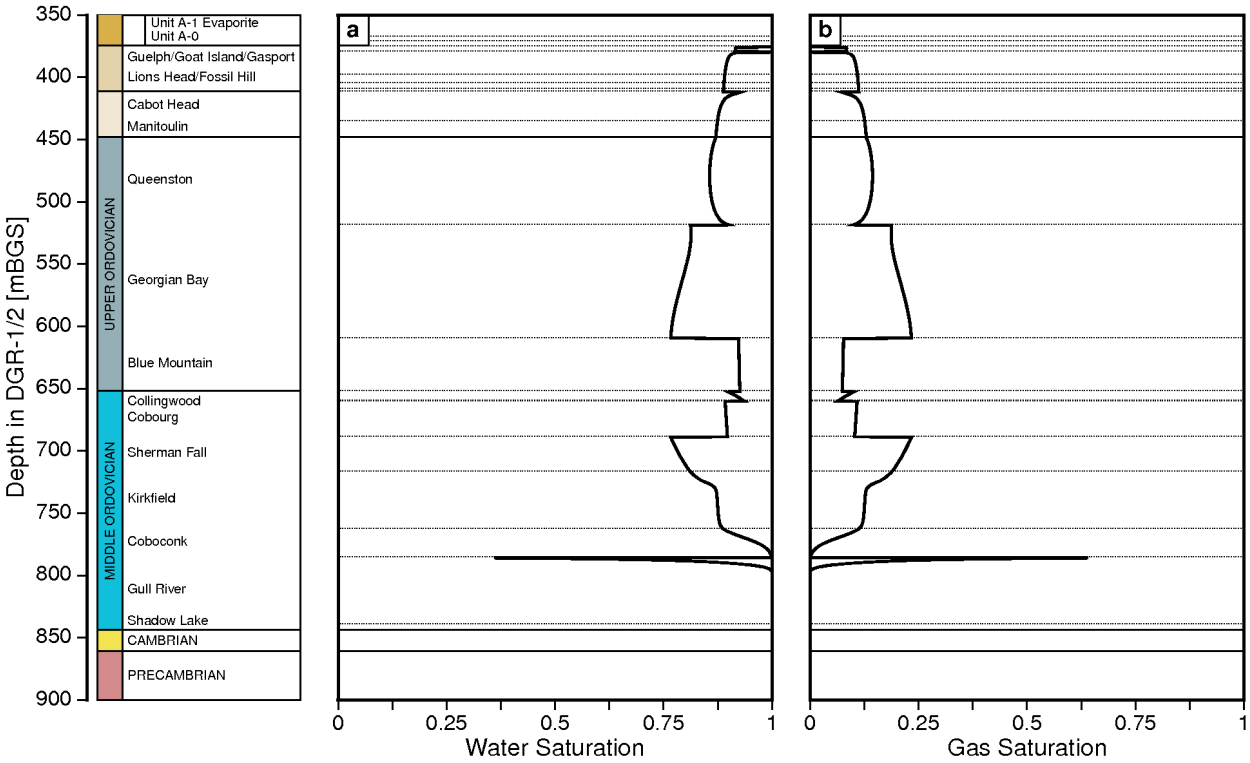

Note: (a) water saturation profile, and (b) gas saturation profile.

Figure 6.27: Saturations for the Two-Phase Gas-Water Flow Analysis at 1.25 Ma with No Discontinuity 585 m Depth

water gradients. The air in the gas phase partitions into the water phase and migrates from the domain through diffusion in the solution phase. The air also migrates from the domain as a separate phase. The dissipation of both the displaced water phase and the air phase results in a decrease in the water pressure after the termination of gas generation at 200 ka. Continued migration of the air in the gas phase and in the solution phase results in a water deficit that must be met by the development of under-pressures in the water phase and a water phase gradient into the domain from both boundaries. The water pressure is sensitive to the pore compressibility while the pore volume is sensitive to the high air entry gas pressure for the capillary pressure versus saturation curves for the Ordovician rock. The under-pressures that develop at 1.0 Ma are shown in Figure 6.33. The corresponding saturations are shown in Figure 6.34. The water pressures compare favourably with the measured pressures in the DGR-4 borehole. Continued diffusion of air in the solution phase results in the gradual dissipation of the air phase and a return of the water pressures to a hydrostatic state. The rate of return is sensitive to the diffusion coefficient. For the preceding analysis, diffusion of air in the water phase was modelled using the Millington and Quirk (1961) relationship and a free-phase diffusion coefficient of 1.25×10^{-8} m^2/s. The use of the tortuosity diffusion model of Equation (6.3) described in a preceding section resulted in a prolonged maintenance of a state of over-pressured water. The investigation of the relationship between air generation and air dissipation through diffusion was beyond the scope of this study; more research on this issue is required. However, based on the results of this section, it can be concluded that the presence of a gas phase can result in the development of

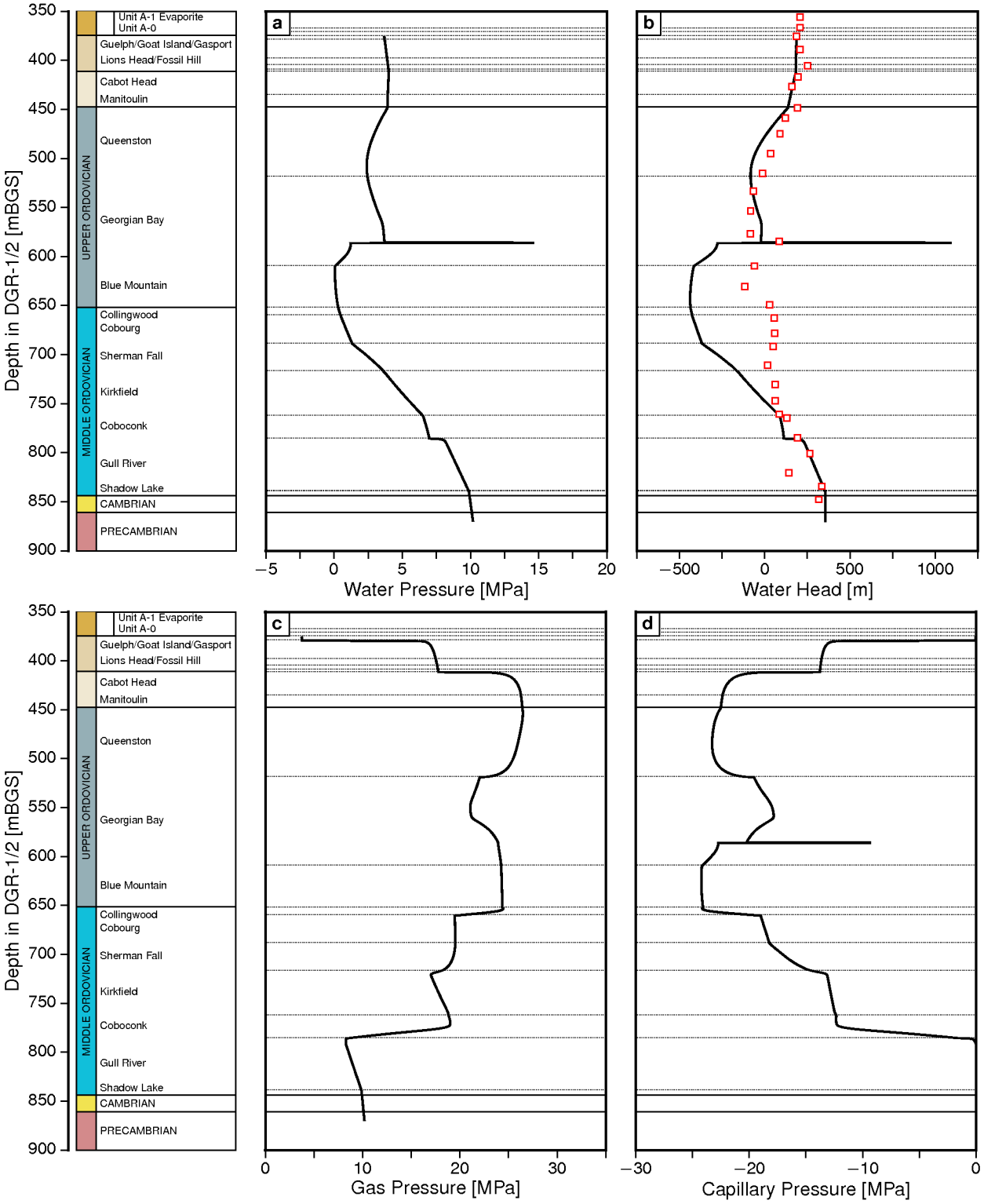

Note: (a) water pressure, (b) freshwater head with posted August 24, 2009 measurements in DGR-4, (c) gas pressure, and (d) capillary pressure.

Figure 6.28: Two-Phase Gas-Water Flow Analysis at 300 ka with a Discontinuity at 585 m Depth

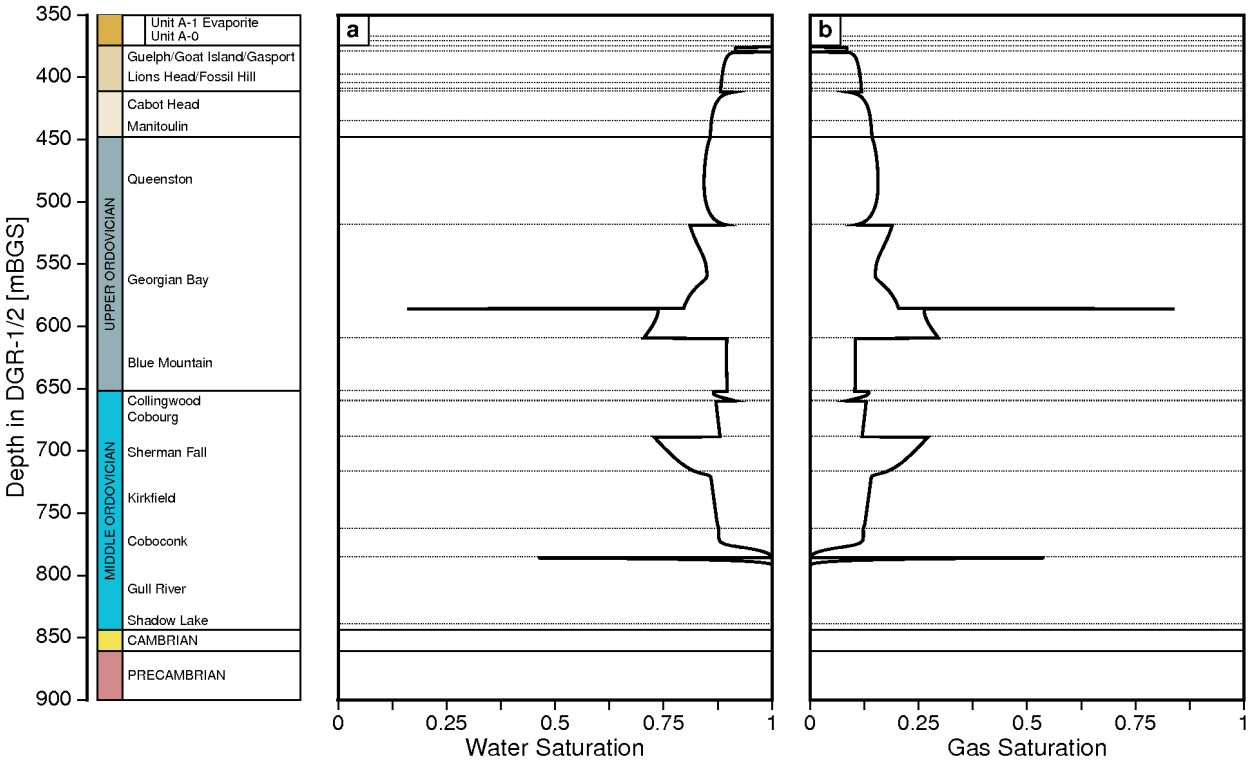

Note: (a) water saturation profile, (b) gas saturation profile.

Figure 6.29: Saturations for the Two-Phase Gas-Water Flow Analysis at 300 ka with a Discontinuity at 585 m Depth

under-pressures in the water phase. As shown in Figure 6.34, very little gas is required to generate the under-pressures.

6.3.4.2 Conceptual Model With a Discontinuity at 585 m Depth

This simulation is identified as scenario t-MQ-highD-fracture. Using the identical air generation conceptual model, boundary conditions, properties and parameters as the preceding case and a discontinuity in the Georgian Bay Formation at a depth of 585 m results in the pressure distributions shown in Figure 6.35 at 1.0 Ma. The saturations for the gas phase and water phase at 1.0 Ma are shown in Figure 6.36. The results confirm that the gas phase can cause under-pressures in the water phase. The results also support the conclusion that heterogeneities in the rock can cause significant discontinuities in the phase saturations. A reduction in the effective diffusion in a phase will also occur as the saturation for that phase decreases.

6.4 Abnormal Pressures Summary

This section has investigated hypotheses of the cause of the abnormal pressures observed in the DGR boreholes. The hypotheses are (1) the over-pressures in the Cambrian and Niagaran Group and the under-pressures in the Ordovician shale and limestone are a consequence of glaciation and deglaciation; (2) the over-pressures in the Cambrian and Niagaran Group are related to the dynamics of density-dependent saturated flow in the Michigan Basin; (3) the under-pressures in the Ordovician are the result of the presence of a non-wetting gas phase in the limestone and

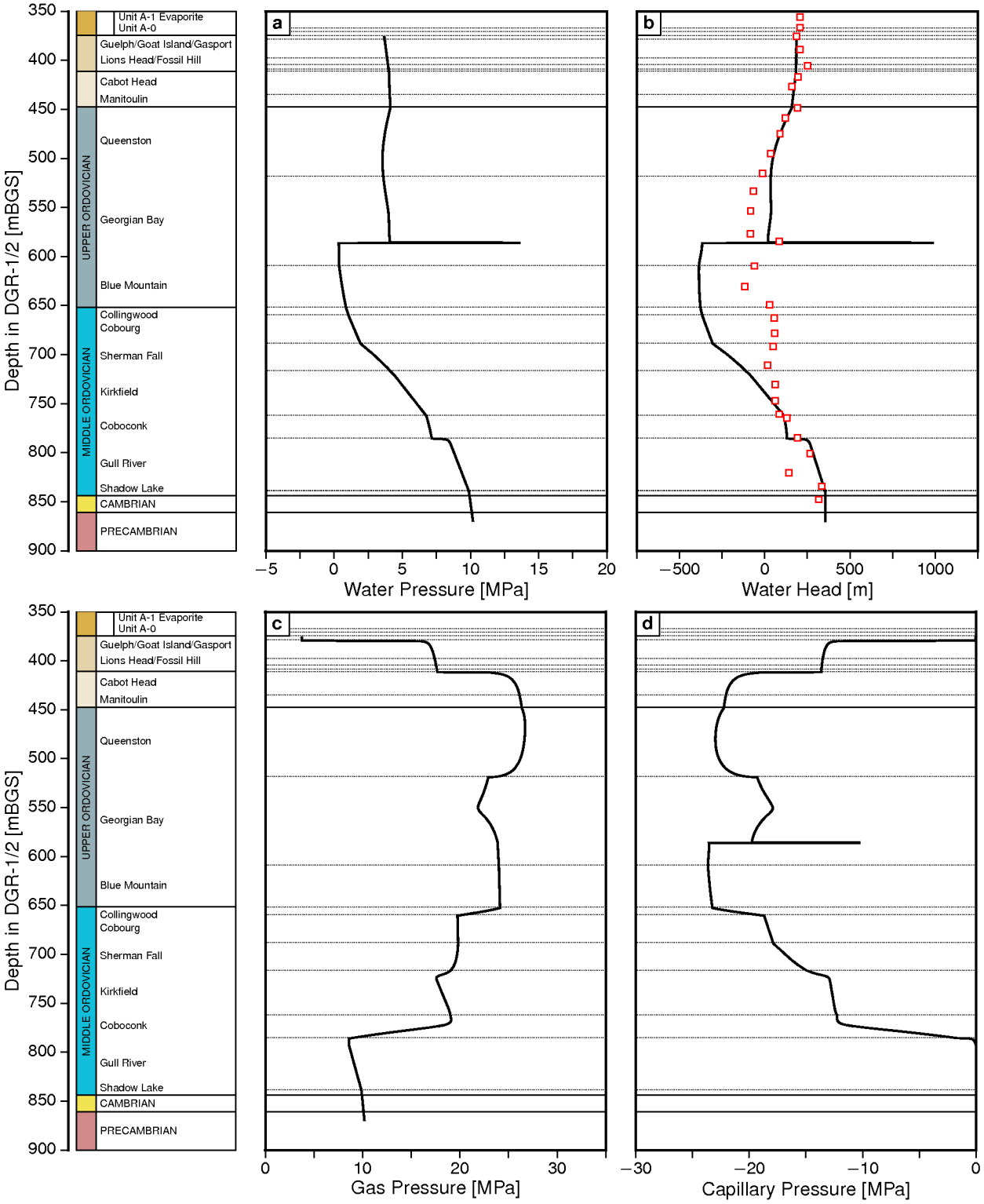

Note: (a) water pressure, (b) freshwater head with posted August 24, 2009 measurements in DGR-4, (c) gas pressure, and (d) capillary pressure.

Figure 6.30: Two-Phase Gas-Water Flow Analysis at 500 ka with a Discontinuity at 585 m Depth

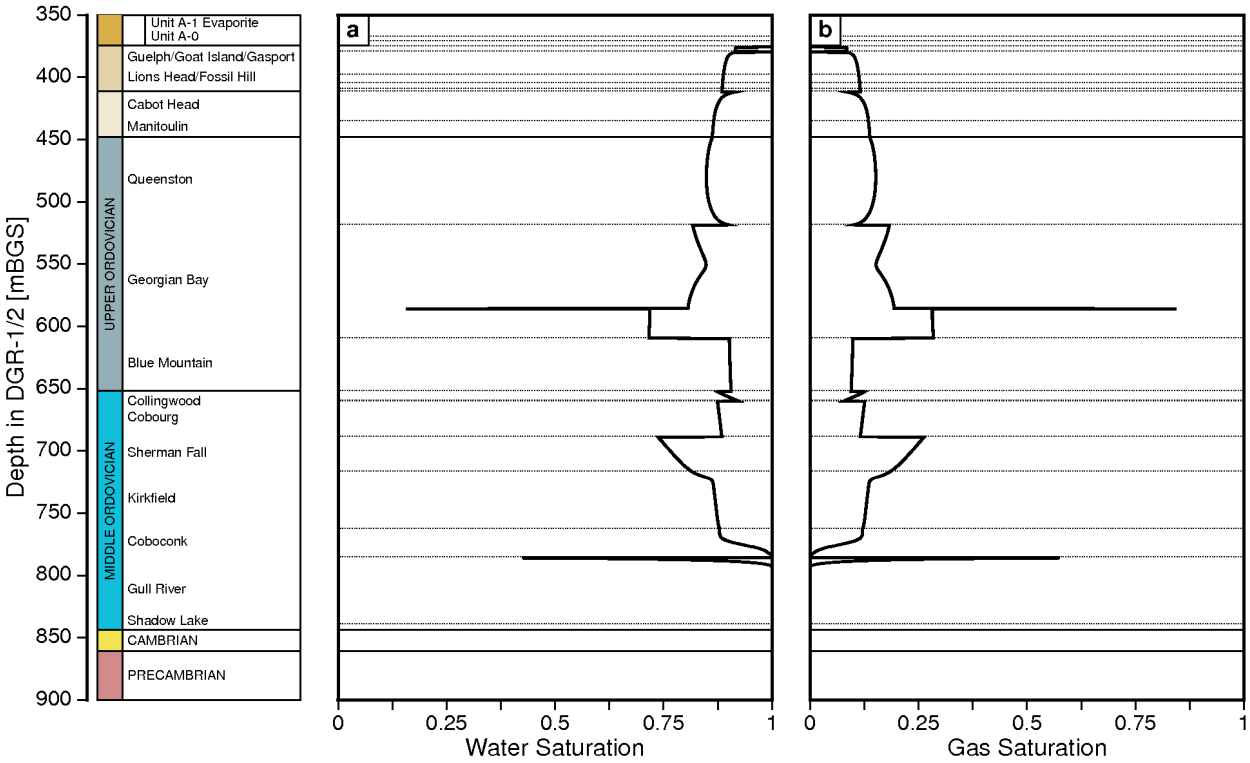

Note: (a) gas saturation profile, and (b) water saturation profile.

Figure 6.31: Saturations for the Two-Phase Gas-Water Flow Analysis at 500 ka with a Discontinuity at 585 m Depth

shale. Explanations of abnormal pressures also include exhumation, osmosis and crustal flexure. These explanations are discussed in Section 6.1. It is a conclusion of this study that it is unlikely that either exhumation or osmotic effects can explain the abnormal pressures observed in the DGR boreholes. While crustal flexure may provide a credible explanation, it is believed that it is unlikely that the anomalous pressures such as those observed at the 585 m depth of the DGR-2 borehole (refer to Figure 6.20) can be explained by the mechanical affects of crustal flexure.

The first hypothesis was investigated in Section 5.6 of this report. Based on the analyses of this study, it is concluded that glaciation and deglaciation can not explain the abnormal pressures observed at the DGR for appropriately modelled paleohydrogeologic scenarios. The requirements are a surface boundary condition that reflects the pressure of the ice thickness, mechanical parameters that correctly replicate rock dependent compression and dilation under glaciation and deglaciation respectively and paleoclimate scenarios from Peltier (2011).

The second hypothesis was addressed in Section 6.2. It can be concluded that based on saturated density-dependent flow analyses, the pore water in the formations of the Ordovician, Cambrian and Precambrian is stagnant. This state can be attributed to both the lack of a gravitational gradient across the Michigan Basin and the presence of total dissolved solids concentrations at depth in the basin that inhibit flow. The pore water is stagnant in the high permeable units of the Cambrian as well as in the low permeability shales and limestones of the Ordovician. Flow was also estimated to be negligible and the pore water stagnant in a hypothesized permeable shallow Precambrian layer (refer to Figure G.1 and Figure G.2). Finally,

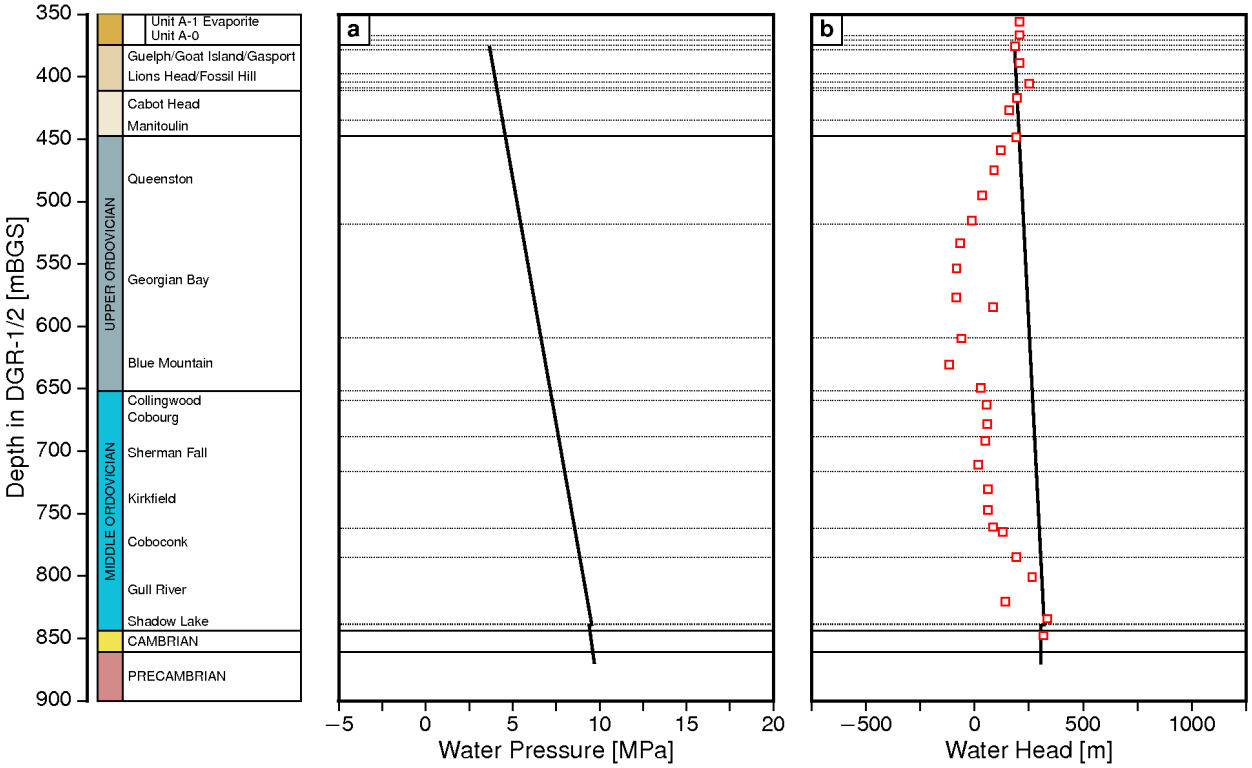

Note: (a) water pressure, and (b) freshwater head.

Figure 6.32: Initial Conditions for the Two-Phase Gas-Water Flow Analysis of the Cases with Air Generation

the saturated cross-sectional analyses explained the over-pressures observed in the Cambrian and the Niagaran Group (refer to Figure 6.10, Figure 6.15 and Figure 6.19 and the summary Table 6.7). The saturated cross-sectional analyses could not explain the under-pressures observed in the Ordovician at the DGR.

The under-pressures in the Ordovician limestone and shale were analysed in the third hypothesis (refer to Figure 6.3). Based on the two-phase air and water simulations using TOUGH2-MP, it is concluded that the under-pressures are consistent with the presence of a non-wetting gas phase in the Ordovician. The pressure in the discontinuity at the 585 m depth in the Georgian Bay Formation (refer to Figure 6.20) was also explained by the presence of a non-wetting gas phase. Specifically, the capillary pressure in the disccontinuity is lower than that in the adjacent rock matrix for a given water or gas saturation. Because pressures are continuous, this results in the accumulation of gas in the discontinuity and a higher fluid pressure at the horizon.

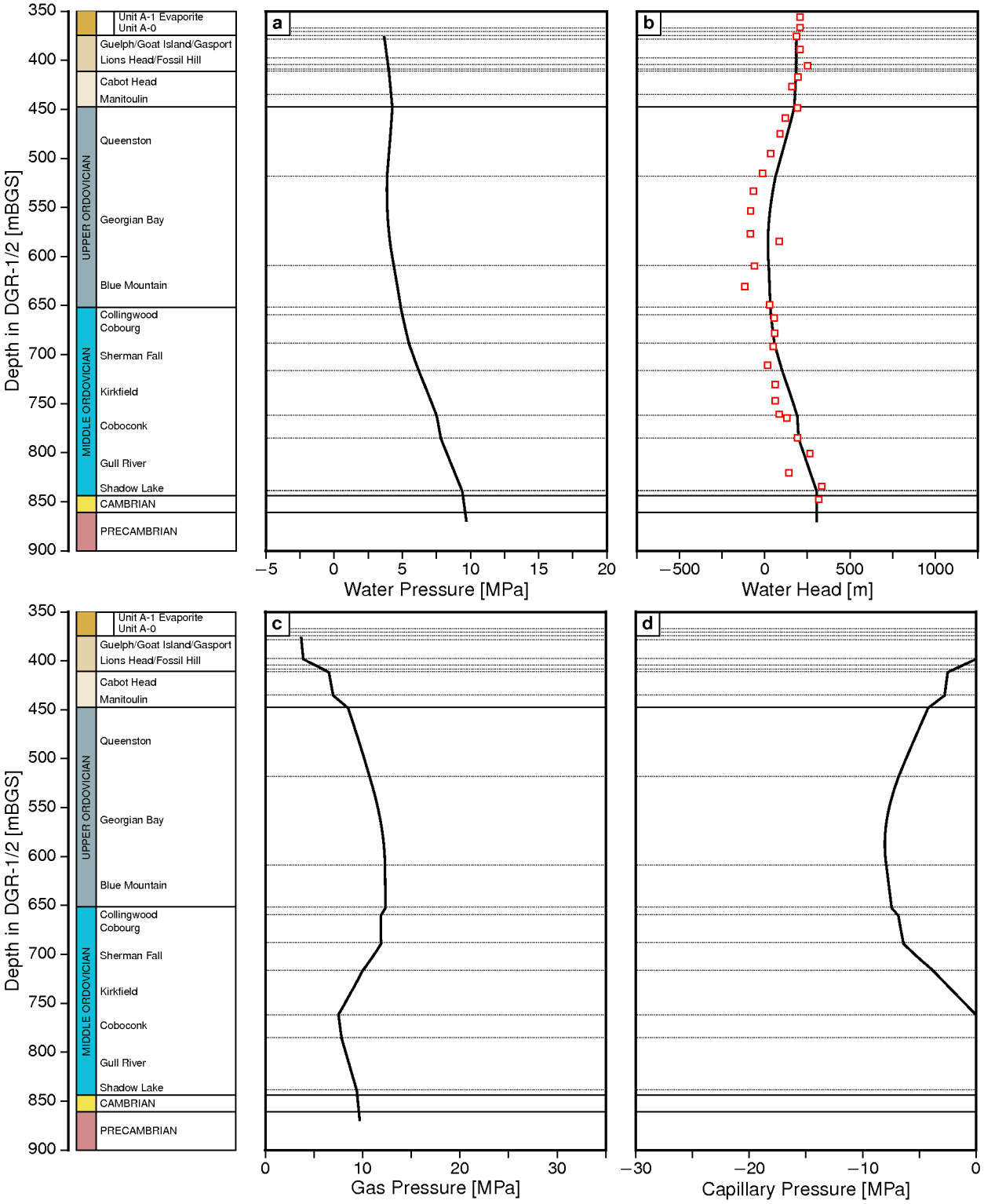

Note: (a) water pressure, (b) freshwater head with posted August 24, 2009 measurements in DGR-4, (c) gas pressure, and (d) capillary pressure.

Figure 6.33: Two-Phase Gas-Water Flow Analysis at 1 Ma Without a Discontinuity at 585 m Depth and Air Generation

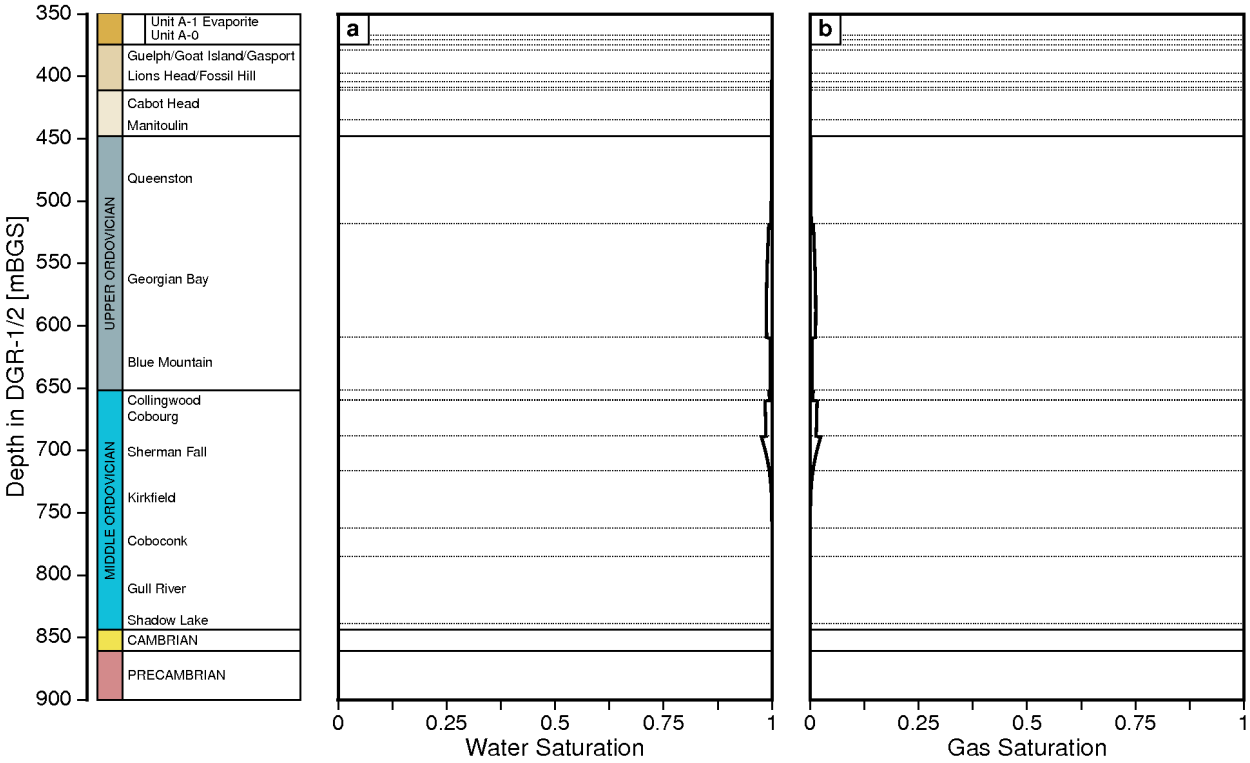

Note: (a) gas saturation profile, and (b) water saturation profile.

Figure 6.34: Saturations for the Two-Phase Gas-Water Flow Analysis at 1 Ma Without a Discontinuity at 585 m Depth and Air Generation

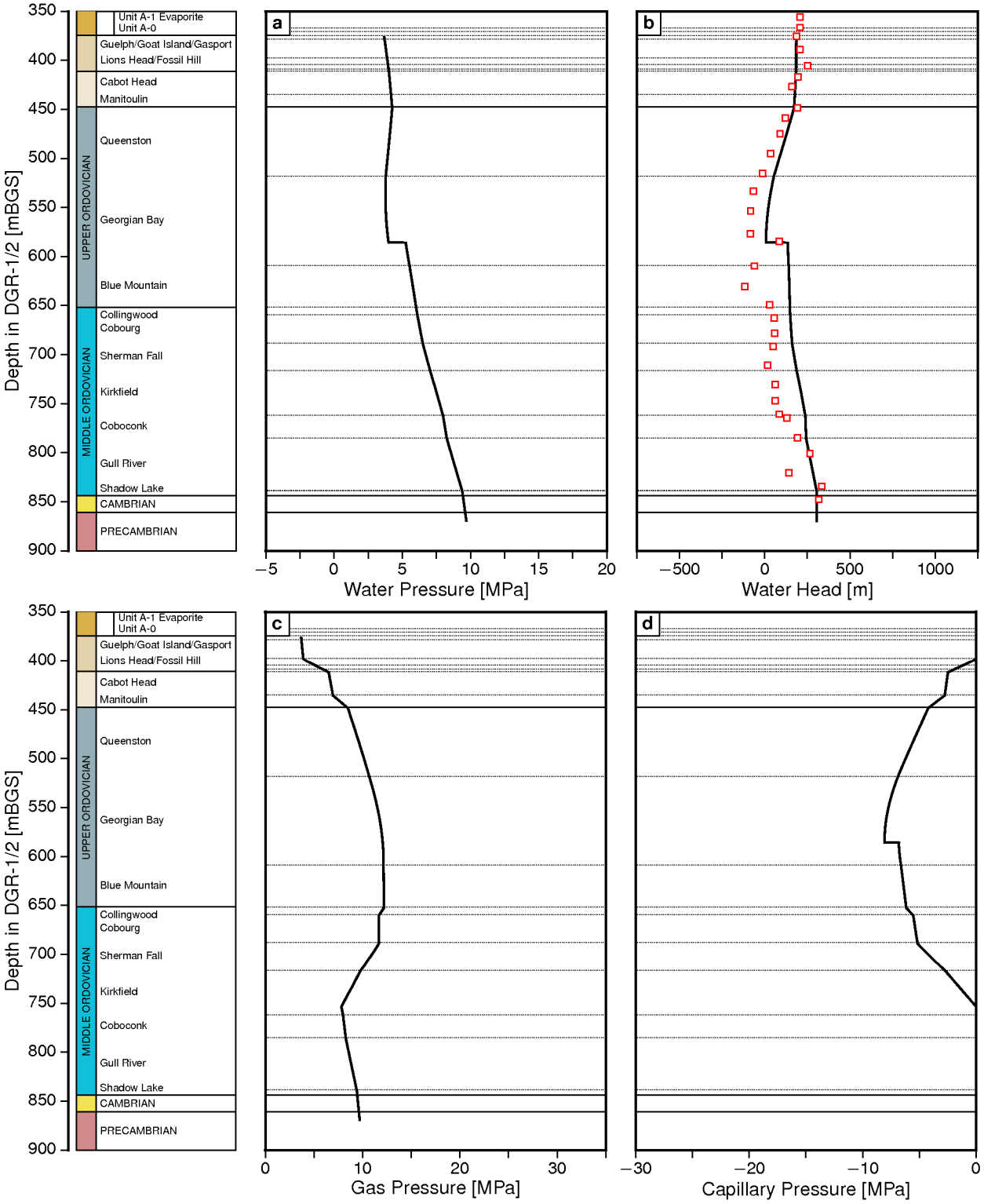

Note: (a) water pressure, (b) freshwater head with posted August 24, 2009 measurements in DGR-4, (c) gas pressure, and (d) capillary pressure.

Figure 6.35: Two-Phase Gas-Water Flow Analysis at 1 Ma with a Discontinuity at 585 m Depth and Air Generation

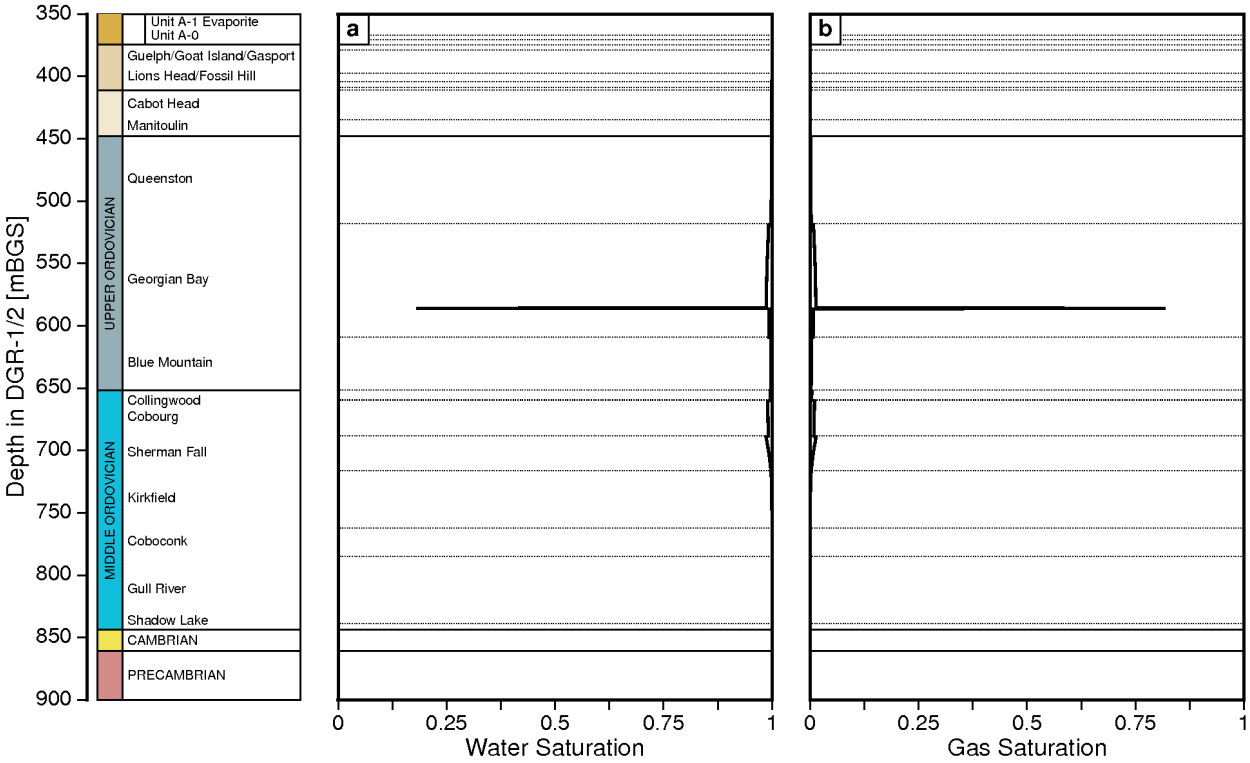

Note: (a) gas saturation profile, and (b) water saturation profile.

Figure 6.36: Saturations for the Two-Phase Gas-Water Flow Analysis at 1 Ma with a Discontinuity at 585 m Depth and Air Generation

7. DISCUSSION AND CONCLUSIONS

This hydrogeological modelling study is part of the Geosynthesis Program of the Deep Geologic Repository (DGR) (NWMO 2011). The analyses of this study, performed using the three-dimensional model FRAC3DVS-OPG and the two-phase gas and water flow model TOUGH2-MP with the equation-of-state module EOS3, were designed to gain insight on groundwater system hydrodynamics and evolution relevant to an understanding of groundwater pathways and solute migration from the location of the proposed DGR in the Cobourg Formation.

FRAC3DVS-OPG was used for three-dimensional regional-scale, three-dimensional site-scale and Michigan Basin two-dimensional cross-section analyses. The regional-scale extent is approximately 18,000 km^2 while the site-scale extent is approximately 400 km^2. The boundary conditions for the site-scale analysis were developed using an embedment approach (refer to Section 4.5) that better enables the treatment of transient simulations. The model TOUGH2-MP was used to investigate one-dimensional two-phase gas and water flow in a vertical domain that describes the stratigraphy, lithology and geometry observed in the DGR boreholes. The approach adopted for all of the analyses of this study is intent on remaining as faithful as possible to the site geometry and boundary conditions with direct linkages to the descriptive geosphere site model (INTERA 2011), geological framework model (AECOM and ITASCA CANADA 2011, ITASCA CANADA and AECOM 2011), hydrogeochemistry (Hobbs et al. 2011), site specific geomechanical stability analysis (ITASCA 2011) and glacial simulations of long-term climate change (Peltier 2011). The modelling permits an assessment of the influence of hydrostratigraphy, variable salinity, mechanical affects, glaciation, immiscible gas flow, parameter uncertainty and boundary conditions on the processes and mechanisms governing groundwater and solute migration.

The discussion and conclusions of this report are presented in the following main sections:

- Section 7.1 presents an overview of the regional-scale groundwater system;
- Section 7.2 discusses the issues that are investigated using hydrogeologic modelling;
- Section 7.3 summarizes some of the key conclusions from the analyses of this study; and
- Section 7.4 presents a confidence assessment of the hydrogeologic modelling.

In this study, an issues based approach based on reasoning and modelling lines of evidence was used for hypothesis testing. An important attribute of the Ordovician sediments as a host for a DGR is their very low permeability. From a groundwater perspective, the very slow rate of fluid migration results in travel times that are tens of millions of years for an average water particle to transit from the proposed horizon of the DGR to a point of interest such as the biosphere. The Mean Life Expectancy (MLE) (refer to Section 3.6.2) for the base-case regional-scale analysis is 164 Ma. It is a hypothesis of the DGR program that solute transport along this path in the Ordovician sediments is dominated by diffusion. To analyse transport over millions of years, both the evolution of groundwater flow and the investigation of perturbing factors such as continental glaciation were considered. Basin wide flow was investigated using a two-dimensional approximately west to east cross-section of the Michigan Basin. The specific factors and issues that were investigated in this study are discussed in Section 7.2. The issues include:

- Section 7.2.1 comments on issues relating to geologic structure;
- Section 7.2.2 discusses issues related to the selection of a regional-scale domain that is a subset of the Michigan Basin and the sensitivity of the performance measures including Péclet number and mean life expectancy for the Cobourg Formation to the regional-scale lateral boundary condition;

- Section 7.2.3 discusses and develops the salient conclusions of the numerous scenarios or parameter case studies that were investigated in the work of this report using the regional-scale numerical model;
- Section 7.2.4 presents a brief discussion of the paleohydrogeologic simulations undertaken in this study;
- Section 7.2.5 summarizes the support for the hypothesis that solute transport in the Ordovician sediments is diffusion dominant;
- Section 7.2.6 presents the conclusions on flow in the more permeable units observed in the DGR boreholes such as the Cambrian, Niagaran (includes the Guelph unit), A-1 Carbonates and near-surface sediments;
- Section 7.2.7 discusses the impact of alternate descriptions of the Precambrian on flow and solute transport at the DGR site;
- Section 7.2.8 discusses the implications of the observed pressure profile in the DGR boreholes on the estimation of permeability of the Ordovician units and on the far-field state of the groundwater system;
- Section 7.2.9 presents the conclusions from the analyses that were undertaken in the investigation of the abnormal pressures observed in the DGR boreholes; and
- Section 7.2.10 discusses the findings of this study relative to the impact of a hypothetical fault through the Ordovician sediments proximal to the DGR on solute transport.

An important aspect of this study is that it explores the solution space for the domain centred on the proposed DGR by varying parameters and boundary conditions over their feasible range. This approach honours both the geologic framework and the lithology of the groundwater system.

7.1 Overview of the Regional-Scale Groundwater System

The geological framework model for the regional-scale analysis of the proposed DGR at the Bruce nuclear site near Tiverton, Ontario was first developed by Sykes (2007) and then expanded upon and refined by AECOM and ITASCA CANADA (2011) and ITASCA CANADA and AECOM (2011). The models are significant in that they are the first regional-scale three-dimensional depictions of the stratigraphic units of southern Ontario. The geology in the regional domain was modelled using geostatistical and other interpolation methods to develop the correlation structure of the data and to facilitate interpolation of unit thicknesses and structural contours between boreholes. To ensure that the top of the model conformed to known surface elevations and lake bathymetries, additional data were added to the geologic model from Digital Elevation Models (DEMs) and bathymetry maps of Lake Huron and Georgian Bay. The geologic model, with corrections for proper topography and bathymetry, was used as the basis for the regional-scale and site-scale numerical models. The model of AECOM and ITASCA CANADA (2011) and ITASCA CANADA and AECOM (2011) includes 31 layers that are traceable and could be reliably interpreted within the study area (refer to Section 2.2). The hydrologic parameters of the model are informed, in part, by estimates obtained from the DGR boreholes.

The regional scale domain, with an area of approximately 18,000 km^2, can be divided into three major zones at the DGR site:

- The shallow zone with a thickness of 178 m;
- The intermediate zone with a thickness of 270 m; and
- The deep zone with a thickness of 413 m.

The shallow groundwater zone at the DGR site is characterized by layers with higher permeability and a groundwater composition with a relatively low total dissolved solids concentration

(Table 2.7). It includes the horizons above the base of the Bass Islands Formation (Figure 1.2) and the dolomite and limestone units of the Devonian formations. The glacially deposited sediments also are part of the shallow zone. The direction of groundwater flow in the shallow zone is strongly influenced by topography and has much shorter MLE than the deeper groundwater zone (the base-case results are given in Figure 4.20). With low total dissolved solids, the higher groundwater velocities in the shallow zone (Figure 4.17) are dependent on energy gradients that are relatively independent of fluid density. Solute transport in the shallow groundwater zone is dominated by advection and the related mechanical dispersion. From a regional-scale flow perspective, the estimated mean life expectancy for the horizon of the proposed repository in the Cobourg Formation is insensitive to the glacially deposited sediments of the shallow zone.

Separating the shallow and deep groundwater zones are the layers of the intermediate groundwater zone, which extends from the base of the Bass Islands Formation to the bottom of the Manitoulin Formation. Within this zone, the low permeability of aquitard units within the Salina Formation, where present, isolate the topographically driven shallow flow system from that of the underlying Ordovician shale and limestone formations. The Niagaran Group with a thickness at the DGR-1/2 borehole of 34.1 m and the A1 upper carbonate with a thickness of 41.5 m are the most permeable layers in the intermediate zone. The Guelph unit in the Niagaran Group has a thickness of approximately 4 m.

The deep groundwater zone comprises the layers beneath the Manitoulin of the Lower Silurian and includes the Ordovician limestones and shales, as well as the Cambrian sandstones and the crystalline Precambrian basement. Groundwater in the deeper zone can be characterized as being stagnant and has high Total Dissolved Solids (TDS) concentrations that can exceed 300 g/L with a corresponding specific gravity of approximately 1.2. In this study, the term stagnant is used to define groundwater in which solute transport is dominated by molecular diffusion. The deep groundwater zone has much lower velocities and high MLE (Figure 4.17 and Figure 4.20, respectively). Since the deep groundwater zone is isolated from any local topographic effects by the very low hydraulic conductivities of both the Salina Formation and the Lower Silurian carbonates and shales, the horizontal energy gradients in this zone will be very low and are strongly influenced by density gradients. The only place within the domain for a significant gravitational gradient will be at the Niagara Escarpment where some of the formations in the deep groundwater zone subcrop or outcrop. The most permeable formation in the deep zone is the Cambrian. This layer is relatively thin (17 m) at the DGR site, thickens and deepens towards the centre of the Michigan Basin and outcrops west of Lake Michigan as well as north of Sault Sainte Marie, Ontario (more than 300 km northwest of the DGR site).

Flow in the deep domain, as it may occur, most likely will be controlled by basin wide topography and potential formational facies changes. With the deep fluids having a specific gravity that is greater than the shallow groundwater, fluid density gradients may also influence regional flow. This issue is investigated, in part, through the basin-wide cross-sectional flow analyses of Section 6.2

7.2 Issues Explored Through Hydrogeological Modelling

An issues based approach was followed in this study. The following sections provide a brief description and summary of the work and present the main findings of the study.

7.2.1 Geologic Structure: Faulting

The geological framework model developed by AECOM and ITASCA CANADA (2011), ITASCA CANADA and AECOM (2011) presents an accurate three-dimensional description of the various units/formations/groups of the regional-scale domain. It forms the basis of the conceptual model investigated in this study. Sanford et al. (1985) postulates that faults may occur within this framework (refer to Figure 2.3) and that these faults explain the development of oil and gas traps, particularly in the Niagara Megablock. While this report cites the hypothesis of Sanford et al. (1985) and Carter et al. (1996), at the time of the writing of this report, there are no data from the Bruce DGR field program to indicate that vertical permeable faults are present in the Ordovician formations within the vicinity of the proposed site.

Based on the site-scale analyses of Section 4.5.4, the abnormal pressures measured in the DGR boreholes are inconsistent with the presence of permeable faults in the Ordovician sediments proximal to the proposed DGR site. Such permeable faults would enable the dissipation of both the elevated pressures in the Cambrian and the under-pressures of the Ordovician units; the abnormal pressures could not exist in the presence of permeable faults that enable flow through the Ordovician. The chemical characteristics of the water in the Niagaran Group, which includes the Guelph as compared to that of the Cambrian sandstone are also inconsistent with that expected if a fracture were present proximal to the location of the proposed DGR. The impact of possible faults in the Ordovician sediments is further discussed in Section 7.2.10.

In spite of the lack of evidence for the existence of faults, the analyses of the Cambrian of Section 4.4.7 were undertaken to determine the sensitivity of the flow in the Cambrian to the orientation of possible faults. Consistent with the conclusion that the Cambrian is not a significant pathway for solute migration from the vicinity of the proposed DGR in the Cobourg Formation, the results indicate that the orientation of faults has only a marginal impact on the conservative estimates of Péclet number and MLE at the DGR site (refer to Table 4.11 and Table 4.12).

7.2.2 The Spatial Extent of the Regional-Scale Domain

The regional-scale domain occupies an area of approximately 18,000 km^2; the domain is thin relative to its spatial extent. The approximate western and northern boundaries coincide with the deepest points in Lake Huron and the deepest points in Georgian Bay. It is a hypothesis of this study that at a point in units/formations beneath Lake Huron either a divide for groundwater flow occurs or horizontal flow is negligible. This hypothesis is tested using the two-dimensional west to east cross-section of the Michigan Basin. The analyses were undertaken, in part, to further strengthen the acceptability of the extent of the regional-scale domain for the resolution of issues (refer to Section 6.2).

The southern and eastern boundaries of the regional-scale spatial domain are set to coincide with the regional divides for the surface water system. The selected domain has a sufficient spatial extent for the appropriate characterization of groundwater flow in the shallow zone above the base of the Bass Islands Formation and flow in the sub- or outcrop portions of the Niagaran Group aquifer in the intermediate zone. The domain includes the outcrop for the Ordovician layers (refer to Figure 2.24). The analyses of the many regional-scale and site-scale scenarios undertaken in this study combined with the data from the DGR boreholes enabled the assessment of the adequacy of the regional-scale spatial extent for the simulation of flow in the units beneath the Silurian Salina Formation. The factors that contribute to the assessment of adequacy of the regional-scale spatial domain are characterized by the following points.

- Based on the analyses of Section 6.2 and a review of the pore water velocity data from the base-case simulation, a divide occurs in the Bass Islands and all shallower units at approximately the centre of Lake Huron. The pore water velocity data for the Michigan Basin base-case cross-section analysis strongly supports the hypothesis of this study that at a point in all units/formations beneath Lake Huron either a divide for groundwater flow occurs or horizontal flow is negligible.
- Park et al. (2009) show that for increasing TDS concentrations with depth there can be a static brine region because the surface driving forces cannot lift the brine located at depth. Within this region, the groundwater is essentially stagnant. Over the entire Michigan Basin, the gravitational driving force imposed by topography is minimal; the gradients attributed to the gravitational driving force are larger in the regional-scale domain as determined by the elevation difference between the Niagara Escarpment and Lake Huron than they are across the Michigan Basin (Lake Michigan and Lake Huron have the same elevation). From this perspective, the results of the regional-scale model can be deemed to be conservative.
- Within the low permeability units such as those of the Ordovician layers, the magnitude of vertical velocity results in solute transport being diffusion dominant; this finding is insensitive to the extent of the regional-scale domain.
- The direction of the flow in the low permeability units in the vicinity of the proposed DGR is strongly vertical with horizontal flow not being predicted for any of the scenarios investigated in this study. As indicated by Table 4.12, the path followed by water particles is vertically upward from the Ordovician to the more permeable shallower Niagaran Group (includes the Guelph unit) for all cases except the fr-base-hbc case that investigates the communication between the Cambrian sandstone and the surface layers. The direction of gradients in the Ordovician sediments at the location of the proposed DGR is insensitive to the extent of the regional-scale domain.
- The Niagaran Group has been characterized sufficiently such that the sub- and outcrop portions of the units are included in the regional-scale domain (refer to Figure 2.4 and to Figure 2.27). While the Niagaran Group has been truncated to the south by the selection of the regional-scale domain, the units of the group become deeper south of the domain and potential paths in a southward direction to the biosphere are significantly longer than those estimated by the analyses of this study.
- The Cambrian sandstones and carbonates are absent over the Algonquin Arch while the unit deepens both to the west and to the south; the Cambrian outcrop is north of the regional-scale domain. A MLE of 44 Ma was predicted in the assessment of the lateral boundary condition (refer to Section 4.4.4). The extension of the regional-scale domain to include the Cambrian outcrop would result in a longer flow path and hence a longer MLE; the analysis of Section 4.4.4, that includes permeable pathways to the biosphere at the domain boundary for both the Niagaran Group and the Cambrian, is thus very conservative.
- The paleohydrogeologic analysis of Section 5.6.10 investigated the role of open or freely draining lateral boundaries for high conductivity units such as the A-1 Carbonate, Niagaran Group, and the Cambrian Formation. The approach applied a specified head boundary condition equal to the initial condition for the entire 120 ka for select lateral boundary nodes. The tracer distribution for the analysis is undifferentiated from that of the base-case paleohydrogeologic simulation.

In summary, the regional-scale spatial domain is of sufficient extent since it fully includes the potential solute transport pathways at time and space scales relevant to DGR safety.

7.2.3 Analyses of the Regional-Scale Groundwater System

The analysis of the base-case represents the groundwater system, or state, that is predicted to develop after the elevated pressure in the Cambrian has dissipated and the water deficit (under-pressure) in the Ordovician formations has been eliminated. Depending upon values assigned to the hydrogeologic parameters for the Ordovician units, and the assumed boundary conditions, calculations suggest that it may take considerably more than 1 Ma for this state to be established. Until the currently observed disequilibrium pressures dissipate, groundwater will flow extremely slowly into the Ordovician formations; regardless of state, solute migration in the Ordovician will be diffusion dominant. While the parameters of the developed regional-scale model have not been calibrated in a formal sense, the analyses of this study support conclusions relevant to the flow and transport regime at the site of the proposed DGR. Solute transport in the Ordovician limestones and shales of the deep groundwater zone, because of the low velocities, will be dominated by diffusion. The model estimated velocities in the Ordovician shale and limestone are less than 1.0×10^{-6} m/a with Péclet numbers less than 0.001 for the units. The direction of the velocity is upward for the base case (Figure 4.19); significant horizontal velocity components were not calculated for the Ordovician formations enclosing the DGR location. This result supports the selection of a regional-scale domain that is a subset of the Michigan Basin as horizontal boundaries are less important in a groundwater system that is dominated by vertical gradients (refer to Section 7.2.2 for further discussion of this issue).

The regional-scale domain has topography that ranges from 176 m at Lake Huron and Georgian Bay to more than 500 m at the Niagara Escarpment. Through sensitivity analyses using the regional-scale model (refer to Section 4.4 and Table 4.11 to Table 4.13), the boundary conditions and extent of the domain were determined to be sufficient to allow the development of horizontal flow components, if they can occur, in the deeper Ordovician Formations at the proposed DGR site. However, the estimated velocities are more sensitive to the very low permeability of the units and the dampening impact of density on the energy gradients than they are to either the extent of the regional domain or the boundary conditions of the conceptual model.

The assessment of groundwater system behaviour involved numerous scenarios or parameter case studies. The results of these simulations are summarized in Table 7.1. Also given are the key study findings that when combined indicate a groundwater system in the Ordovician that is stagnant in the sense that it remained diffusion dominant for all simulations that respect field observations.

One of the performance measures used in the analysis of the regional-scale groundwater model was MLE, described in Section 3.6.2, which is an estimate of the average time required for water particles at a spatial position in a groundwater system to reach potential outflow points considering the advective and hydrodynamic dispersion transport processes. The independent variables for this probabilistic measure are the spatial distribution of the velocities and for the second-order term the dispersivity components and diffusion. The velocities are density-dependent and hence a fully coupled transient flow and brine transport analysis was required for their estimation. A pseudo-equilibrium solution was determined at 1 Ma after the imposition of an initial total dissolved solids distribution in the regional domain. The boundary conditions for the analysis were time invariant. For the base-case analysis, the MLE in the Cobourg Formation in the vicinity of the proposed repository was conservatively estimated to be more than 164 Ma (refer to Table 4.12). The high mean life expectancy is a result of the fact that the low permeability of the Ordovician sediments results in solute transport in the units that is diffusion dominant. The Péclet numbers for the Cobourg, as estimated in this study, are presented in Table 4.11.

Table 7.1: Key Findings from the Regional-Scale Analyses of This Study

Scenario	Description	Key Study Findings
Base Case (fr-base)	• parameters from Table 4.3 • present day boundary conditions • Release 1.1 3DGF	• shallow groundwater system topographically driven • fluids in low permeability intermediate and deep zone layers are stagnant (diffusion dominant) • indicates extremely low vertical velocities at repository horizon • no horizontal velocities at repository horizon
Surface Boundary Condition (fr-base-rech)	• base case parameters • compare Type I and Type II boundary conditions	• groundwater pathways from DGR unchanged
Geologic Model (fr-base-camb-x0) (fr-base-camb-x90)	• base-case parameters • anisotropic K for Cambrian	• orientation of faults has only a marginal impact on the conservative estimates of Péclet number and MLE at the DGR site
Density-Independent Flow (fr-base – no density)	• base-case parameters	• density gradients influence groundwater pathways • solute transport at DGR horizon remains diffusion dominant • density-dependent flow required for prediction of heads measured in DGR boreholes
Horizontal Boundary Condition (fr-base-hbc)	• base-case parameters • high permeability perimeter	• solute transport at DGR horizon remains diffusion dominant • extremely low vertical velocities at repository horizon
Weathered Shallow Precambrian (fr-base-hkp)	• base-case parameters • 20 m zone at top of Precambrian	• no change in the MLE from base case
Uniform Precambrian Permeability (fr-base-up)	• base-case parameters • Precambrian $K = 1.0 \times 10^{-12}$ m/s	• solute transport in Ordovician sediments remains diffusion dominant

7.2.4 Regional-Scale Paleohydrogeologic Analyses

The impact of glaciation and deglaciation on the groundwater system was investigated in paleohydrogeologic scenarios using the regional-scale model with the analyses being presented in Chapter 5. A summary of the paleohydrogeologic scenarios is presented in Table 4.10. A summary of the key findings of the paleohydrogeologic analyses is presented in Table 7.2. The results of the analysis indicate that basal meltwater should not penetrate below the units of the Salina at the DGR site. The most significant consequence of glacial loading is the generation of higher pressures during loading throughout the rock column, with the level dependent on the one-dimensional loading efficiency of the rock mass. Nine different paleohydrogeologic scenarios were investigated in this study. Based on these analyses it is concluded that glaciation and deglaciation is unable to yield the abnormal pressures observed in the DGR boreholes. Contributing to this conclusion is the strength of the rock, particularly the Ordovician sediments, and the resulting low storage coefficients that result. From the paleohydrogeologic analyses it is also concluded that flow in the more permeable units such as the Cambrian and Niagaran at the location of the proposed DGR is relatively insensitive to glaciation and deglaciation. Based on velocity magnitude and Péclet numbers, solute transport in the Ordovician sediments remained diffusion dominant for all of the paleohydrogeologic scenarios investigated.

7.2.5 Analysis of Solute Transport in the Ordovician Sediments

A hypothesis that has been investigated in this study is that solute transport in the Ordovician sediments is dominated by diffusion. This hypothesis is supported, in part, by the estimated Péclet numbers (refer to Section 3.6.1) for the Cobourg limestone that are significantly less than 0.4 (Bear 1988). The Péclet numbers that were calculated for the regional-scale scenarios are listed in Table 4.11. Based on a characteristic length ℓ = 1 m, the Péclet numbers are all less than 0.001. The vertical pore water velocity in the Cobourg limestone was estimated to be less than 1×10^{-6} m/a. This velocity is conservative as it does not account for the reduction of the velocity by the saturation dependent relative permeability that is associated with the presence of an immiscible gas phase in the unit.

The site-scale analyses also support the hypothesis that solute migration in the Ordovician sediments is diffusion dominant. The breakthrough curves to the Cambrian and the Niagaran for a conservative tracer released in the Cobourg at the horizon of the proposed DGR are shown in Figure 4.37. As shown in the figure, breakthrough to the closer Cambrian is predicted to occur prior to breakthrough to the Niagaran. The relative concentration to the Cambrian for the conservative tracer is less than 0.001 throughout the 100 million year simulation period.

Diffusion dominant solute transport in the Ordovician sediments was determined to be insensitive to glaciation and deglaciation. The porewater velocity magnitude plots for the various paleohydrogeologic scenarios illustrate this finding. The velocities in the Cobourg limestone at the horizon of the proposed DGR are less than 1×10^{-6} m/a, the same order-of-magnitude as that of the base-case analysis.

7.2.6 Analysis of Flow in the Higher Permeability Units

Based on both the hydraulic conductivities estimated from the straddle packer tests in the DGR boreholes presented in Table 4.3 and the analyses of this study, it is concluded that in the Ordovician sediments, in the lower Silurian units and in the low permeability units of the Salina, advective flow is minimal such that solute transport in these formations is dominated by diffusion. The direction of advective flow, if it occurs, is vertical. At the DGR site, horizontal flow can only

Table 7.2: Key Findings from the Regional-Scale Paleohydrogeologic Analyses of This Study

Scenario	Description	Key Study Findings
Base Case (fr-base-paleo)	• base case parameters • surface pressure based on ice sheet thickness	• no glacial meltwater penetration below Salina • glacial perturbation not cause of abnormal pressures at DGR boreholes • solute transport at DGR horizon remains diffusion dominant
Biot Coefficient of 0.5 (fr-base-paleo-biot)	• revise base-case parameters • revised storage coefficient and loading efficiency	• no glacial meltwater penetration below Salina • does not describe measured pressures in DGR boreholes • solute transport at DGR horizon remains diffusion dominant
Effect of a Gas Phase (fr-base-paleo-gas)	• revise base-case parameters • insitu gas pressure of 12.5 MPa • layer specific gas saturations	• no glacial meltwater penetration below Salina • does not describe measured pressures in DGR boreholes • solute transport at DGR horizon remains diffusion dominant
Pressure at Surface is 80% Ice Thickness (fr-base-paleo-head80)	• base-case parameters	• no glacial meltwater penetration below Salina • does not describe measured pressures in DGR boreholes • solute transport at DGR horizon remains diffusion dominant
Pressure at Surface is 30% Ice Thickness (fr-base-paleo-head30)	• base-case parameters	• no glacial meltwater penetration below Salina • does not describe measured pressures in DGR boreholes • solute transport at DGR horizon remains diffusion dominant
Free Drainage at Surface (fr-base-paleo-zero-head)	• base-case parameters • $P = 0$ at ice base	• no glacial meltwater penetration below Salina • does not describe measured pressures in DGR boreholes • solute transport at DGR horizon remains diffusion dominant
Loading Efficiency of Zero (fr-base-paleo-le-zero)	• revise base-case parameters • pressures independent of rock loading	• no glacial meltwater penetration below Salina • does not describe measured pressures in DGR boreholes • solute transport at DGR horizon remains diffusion dominant
Paleoclimate Model nn9921 (fr-base-paleo-nn9921)	• base-case parameters • alternate ice thickness and permafrost depth	• no glacial meltwater penetration below Salina • does not describe measured pressures in DGR boreholes • solute transport at DGR horizon remains diffusion dominant
Open Lateral Boundaries (fr-base-paleo-openbnd)	• base-case parameters • boundary heads invariant for selected layers	• no glacial meltwater penetration below Salina • does not describe measured pressures in DGR boreholes • solute transport at DGR horizon remains diffusion dominant

occur in the more permeable units such as the Cambrian, the Niagaran and the A1 upper carbonate in the Salina. Horizontal flow can also occur in the near surface Bass Islands and shallower units. For solute at the proposed horizon of the DGR in the Cobourg limestone, the pathway for migration is diffusion in the Ordovician sediments to the Niagaran and the Cambrian and then horizontal advective and dispersive transport in these units.

Important in the assessment of the impact of solute transport in either the Niagaran or the Cambrian is the time of breakthrough at the Niagaran or the Cambrian of a solute migrating from the proposed horizon of the DGR in the Cobourg limestone. For the base-case site-scale analysis, breakthrough of a conservative, constant source sodium iodide tracer will occur at a relative concentration of 0.0001 to the Niagaran and the Cambrian after 1 Ma (refer to Figure 4.37). The base-case results show that a relative concentration of 0.001 is reached in the Niagaran after 2 Ma and that this concentration is never reached in the Cambrian.

Travel distances in the Cambrian are long; the unit becomes deeper to the south and the west, it is absent over the Algonquin Arch and the closest outcrop is approximately 300 km to the northwest. Finally, the direction of flow in both the Cambrian and the Niagaran is sensitive to the regional scale distribution of TDS concentration versus depth.

Based on the analyses of this study, the A1 upper carbonate is not considered to be a significant pathway for horizontal migration of solute from a deeper horizon as it is isolated by overlying and underlying low permeability units of the Salina.

7.2.7 Analysis of Alternate Descriptions of the Precambrian

The base-case regional-scale conceptual model used the permeability versus depth relationship for the Precambrian developed by Normani (2009) given by Equation (4.1). The TDS concentration versus depth for the Precambrian using data from Frape and Fritz (1987) is shown in Figure 4.2. Alternate descriptions of the Precambrian that were investigated in this study include:

- A weathered layer for the upper Precambrian at depth with an assumed thickness of 20 m and a higher hydraulic conductivity was investigated using both the regional-scale model and the Michigan Basin cross-sectional model (refer to Section 4.4.5 and Section 6.2.4 respectively);
- A uniform permeability versus depth model for the Precambrian was investigated using the regional-scale numerical model (refer to Figure 4.4.6); and
- The TDS concentration versus depth relationship from Hanor (1979) was assumed for the Precambrian in an analysis using the Michigan Basin cross-sectional numerical model (refer to Figure 6.2.3).

Based on the results from both the regional-scale and the Michigan Basin cross-sectional numerical models, it is concluded that solute transport in the Ordovician sediments is insensitive to the conceptual model used for the Precambrian. The results of the Michigan Basin cross-sectional numerical model indicate that the heads in the Niagaran are insensitive to the TDS versus depth model used for the Precambrian while the heads in the Cambrian are sensitive to the TDS versus depth model for the Precambrian.

7.2.8 Inference of the Abnormal Pressures Observed in the DGR Boreholes on the Hydraulic Conductivity of the Ordovician Sediments

The environmental head profile from the measured TDS concentrations and pressures at the DGR boreholes (Figure 2.15) indicates that the Cambrian is over-pressured relative to the

elevation of the ground surface while the Ordovician shale and limestone units are significantly under-pressured. The Cambrian pinches out east of the DGR site (Figure 2.26); it is absent at the Algonquin Arch. An essential requirement of the abnormal high pressures of the Cambrian and their slow dissipation is overlying, extensive, low vertical hydraulic conductivity strata. The site-scale analyses of Section 4.5.3 indicate that the upscaled vertical hydraulic conductivity for the units of the Black River Group (Shadow Lake, Gull River and Coboconk) must be three or more orders-of-magnitude lower than the horizontal hydraulic conductivities.

The investigation of the evolution of the observed pressure profile was undertaken using the site-scale model. The analyses of this study indicate that the effective vertical hydraulic conductivity for the Ordovician units required to preserve the observed pressure distribution is most likely on the order of 1×10^{-14} m/s or possibly lower (refer to Figure 4.40). It is evident that the observed pressure profile is related to a state that is different from that investigated in the base-case regional-scale analysis of this study. In either an equilibrium or a disequilibrium model (Neuzil 1995), the profile is a result of past boundary conditions and stresses that are different from those observed today and used in the base-case analysis. Regardless of whether a gas phase is present, in the equilibrium model the pressures in the Cambrian and Ordovician are static and the pore waters stagnant. In the disequilibrium model, the pressures are slowly evolving, in a geologic time sense, to a distribution that is compatible with the boundary conditions and stresses of the currently observed state; flow will be converging on the Ordovician from the overlying Niagaran and the underlying Cambrian. Based on the vertical hydraulic conductivity of the Ordovician units used in this study, this process may take considerably more than one million years.

7.2.9 The Investigation of the Abnormal Pressures Observed in the DGR Boreholes

The cause of the abnormal pressures observed in the DGR boreholes (refer to Figure 2.15) was investigated in Chapter 6. The over-pressures measured in the DGR boreholes could not be described with a glaciation scenario. The analyses of saturated flow in a two-dimensional cross-section of the Michigan Basin strongly support the finding that the over-pressures in the Cambrian and Niagaran Group are related to the dynamics of density-dependent saturated flow in the Michigan Basin. The low flow rate in the Cambrian can be attributed to both the lack of a gravitational gradient across the Michigan Basin and the presence of total dissolved solids concentrations at depth in the basin that inhibit flow. The regional-scale analyses support the conclusion that the over-pressures in the Cambrian may be attributed to the dynamics of density-dependent flow, the geometry of the basin and the complexities of the stratigraphy in the basin.

Evidence suggests that the under-pressures in the Ordovician sediments cannot be described by osmosis. The support for this conclusion, provided in Section 6.1 and in Appendix A includes the prediction of under-pressures in the short term straddle packer hydraulic testing in the DGR boreholes, on the observation of similar under-pressures in both the Ordovician shale and the Ordovician limestone, and on the absence of any increase in the pressures as osmotic effects decline with time due to diffusion raising concentrations in the boreholes to match the formation concentration.

Further assessment indicates that the under-pressures in the Ordovician sediments are unlikely to be described by mass erosion of the formations of the Phanerozoic, Mesozoic and Cenozoic Eras above the Devonian Period sediments. Support for this conclusion is provided in Section 6.1 and in Appendix A; reasoning includes the slow rate of erosion and the relatively low storage coefficients for the Ordovician rock. Using the two-phase gas and water flow model TOUGH2-MP,

the 400 Ma evolution of an air (representing methane) saturated brine in a column from the Cambrian to the Niagaran was investigated. The initial water pressure reflected the presence of approximately 2 km of sediments above the Devonian; the gas saturation was initially set to zero. The water pressure was slowly reduced to levels measured in the DGR boreholes. Using both the Millington and Quirk (1961) diffusion model and the tortuosity model of Equation (6.3), the excess air (methane) in the solution phase was able to leave the system at a rate such that no separate gas phase formed as depressurization occurred. That is, the rate of methane transport out of the domain in the water phase exceeded the rate of formation of a gas phase. This finding accentuates the slow rate at which mass removal occurred. The finding also indicates the importance of solute transport by diffusion for two-phase flow analyses. It is probable that solute diffusion is being overestimated in this study, particularly for the case where a gas phase is present in the Ordovician rock.

It was hypothesized that crustal flexure could be an explanation of the under-pressures observed in the DGR boreholes. While the quantitative assessment of crustal flexure is not developed in this study, based on the experience gained in this study using the coupled hydrologic and mechanical model described in Section 3.2, it is concluded that depending on the state of the system when deglaciation occurs, flexural dilatation after deglaciation may be sufficient to significantly contribute to under-pressuring. However, the stress-strain relationship in flexure will not likely be able to account for the pressure anomalies that occur, for example, at the 585 m depth in the DGR borehole (see Figure 6.20).

The impact of glaciation and deglaciation as a cause of the under-pressures observed in the DGR boreholes was investigated in paleohydrogeologic scenarios. In the numerous simulations performed in this study, as detailed in Section 7.2.4, the observed under-pressures could not be described by the the mechanical loading during glaciation and unloading and consequent rock dilation during deglaciation.

The impact of the presence of an immiscible gas phase in the Ordovician sediments on flow and water pressures was simulated in this study using the computational model TOUGH2-MP (refer to Section 6.3). The gas phase components included air, representing methane, and water vapour. The objective of the analysis was solely to explore the relationship between the presence of an immiscible gas phase in the Ordovician sediments and the development of under-pressures. The work was based on literature models for solute diffusion in the water phase. Two conceptual models were investigated: (i) a model with an assumed initial gas saturation of 17% for the units between the Coboconk and the Gasport and an initial water pressure of zero; and, (ii) a model with air being introduced uniformly for 200 ka from the Coboconk to the Queenston inclusive and with an initial water pressure reflecting the gradient measured between the Cambrian and the Niagaran in the DGR boreholes. Both analyses resulted in pressure and hence head distributions that provided a reasonable fit with the observed pressures in the DGR boreholes. The comparison was particularly compelling for the Black River Group of Ordovician sediments that are proximal to the Cambrian and for the Lower Silurian units that are beneath the Niagaran. For both regions, the predicted gas saturations are low resulting in low capillary pressures and hence water pressures that are near those of the bounding aquifers. The cause of the low gas saturation is the partitioning of the air (methane) in the gas phase to the water phase and then the dissolved air (methane) migration from the system by diffusion in the solution or water phase. Thus the dissipation of the gas phase near the bounding aquifers was dominated by solute migration of the dissolved air rather than migration of the air in the gas phase towards either the Cambrian or the Niagaran. This finding accentuates the importance of solute diffusion in a two-phase gas and water system. It also strengthens the

importance of two-phase flow, phase partitioning and diffusion in a phase for the description of the environmental tracer distributions measured in the DGR boreholes (refer to Figure 2.13).

In conclusion, based on the analyses of this study, the under-pressures measured in the DGR boreholes are consistent with those expected with the presence of a gas phase in the low permeability Ordovician sediments. Depending on the gas saturation and the pressure dependent gas compressibility, mechanical effects may be minimized through a reduction of Skempton's coefficient (refer to Figure 3.1b). The analyses do not require that the gas phase be continuous as change in the gas saturation can occur by phase partitioning and diffusion of a component in the continuous water phase. Where the water phase is either discontinuous or stagnant as may occur at a feature with a lower capillary pressure than the adjacent rock for a given water saturation, then diffusion in the low saturation water phase of the feature may be significantly reduced from that which would occur in fully water saturated pores. Thus, spatial discontinuities in both gas saturation and water saturation can result in a system where solute transport by molecular diffusion has been overestimated in this study as a result of upscaling.

7.2.10 Assessment of Hypothetical Faults in the Ordovician Sediments

The impact on solute transport of a conservative sodium iodide tracer from the location of a proposed DGR in the Cobourg limestone of a permeable discrete vertical fracture zone between the Cambrian and the Niagaran Group was investigated in Section 4.5.4. The hypothetical fracture zones were located at arbitrary distances from the location of a proposed DGR of 1 km and 5 km. An equivalent porous media approach was used to characterize the 2 km long fracture zone that was assigned a hydraulic conductivity of 3.0×10^{-6} m/s and a fracture zone width of 1 m. As shown in Figure 4.37, the breakthrough of a conservative solute to the Niagaran and the Cambrian is insensitive to a hypothetical discrete fracture zone 1 km west of the location of the proposed DGR. Based on the analyses of this study, the presence of the fracture zone between the Cambrian and the Niagaran Group does not alter the conclusion that solute transport in the Ordovician is diffusion dominant. The hypothetical discrete fracture zone would alter the flow domain from that observed in the DGR boreholes. The observed hydraulic gradient between the Niagaran and Cambrian units forces an upward groundwater flow via the transmissive fracture zone reducing the heads in the Cambrian at the fracture creating a sink and raising the heads in the Niagaran at the fracture creating a mound. The result is a reduced vertical gradient at the fracture as compared to that estimated for the Ordovician without a fracture. The pathway for the solute tracer is vertically downward by diffusion to the Cambrian and then horizontal migration occurs in the Cambrian to the fracture. Because of the sink, the tracer plume does not spread out in the Cambrian. The tracer subsequently migrates up the fracture to the Niagaran Group where it can spread out radially by advection, mechanical dispersion and diffusion. Vertically upward migration from the tracer source to the Niagaran Group also occurs by diffusion.

In summary, the presence of a permeable vertical discrete fracture zone between the Cambrian and the Niagaran located 1 km or closer to the location of the proposed DGR is inconsistent with the vertical gradient observed in the DGR boreholes. If a fracture were present, it would lower the heads in the Cambrian and raise the heads in the Niagaran relative to the heads expected for the non-fractured rock. The chemical characteristics of the water in the Niagaran (Guelph) as compared to that of the Cambrian sandstone are also inconsistent with that expected if a fracture were present proximal to the location of the proposed DGR.

7.3 Summary of Key Study Findings

Some of the key findings of the work, analyses and interpretations of this study are summarized in the following points.

- The deep groundwater system is isolated; it is resilient to surface perturbations.
- The permeability of the Ordovician sediments is extremely low. This is a necessary requirement for the existence of the abnormal pressures and high gradients observed in the DGR boreholes.
- The sedimentary sequence at the DGR site provides multiple barriers in both the deep and intermediate zones; solute transport in the Ordovician layers is diffusion dominant as is transport in the Silurian Salina Formation.
- The calculated density-dependent fluid velocities in the Ordovician layers are extremely low and vertical; no horizontal velocities were predicted to occur at the DGR site.
- The analysis of density-dependent flow is required for the determination of groundwater pathways and the assessment of potential solute migration from the horizon of the proposed DGR to the biosphere.
- There is no evidence to support the existence of permeable connected pathways, proximal to the proposed DGR site, through the sedimentary sequence of the deep groundwater zone; the presence of permeable pathways is inconsistent with the abnormal pressures measured in the DGR boreholes and the chemistry of the pore waters.
- A solute released from the horizon of the proposed DGR in the Cobourg Formation would migrate by diffusion through the Ordovician sediments to the overlying Niagaran Group and to the thin underlying Cambrian layer. The extremely low fluid velocities in the Ordovician will have little impact on this diffusion dominated transport. Both advective and dispersive transport can occur in the Niagaran Group, however the pathway to the accessible biosphere is long resulting in estimated mean life expectancies for the DGR horizon that are likely considerably greater than 100 Ma.
- Based on density-dependent saturated analyses, it will take considerably longer than 1 Ma for the observed under-pressure in the Ordovician limestone and shale at the DGR site to equilibrate to the over-pressures observed in the underlying Cambrian sandstone and the overlying Niagaran Group.
- As a result of the lack of a topographical gradient across the Michigan Basin and the impact of the high total dissolved solids concentrations in the deep units inhibiting flow, energy gradients in the Cambrian are very low yielding pore water velocities that are estimated to be less than 1×10^{-2} m/a.
- Over-pressures observed in the Cambrian at the DGR boreholes can be explained by the stagnant density-dependent saturated flow analyses of the Michigan Basin cross-section.
- The under-pressure in the Ordovician could not be explained by the density-dependent saturated Michigan Basin cross-section analysis.
- The abnormal pressures observed in the DGR boreholes could not be explained by paleohydrogeologic analyses that use field and laboratory derived parameters, boundary conditions and glaciation/deglaciation scenarios.
- The under-pressure in the Ordovician limestone and shale can be explained by the presence of a non-wetting immiscible gas phase in the rock and two-phase air and water analyses using the model TOUGH2-MP.
- The water pressure in the discontinuity in the Georgian Bay Formation at a depth of 585 m can be explained by the presence in the rock of a non-wetting gas phase (see Figure 6.20).

The fundamental hypotheses of the safety case for the DGR site are:

(a) Predictable: horizontally layered, undeformed sedimentary shale and limestone formations of large lateral extent;
(b) Multiple Natural Barriers: multiple low permeability bedrock formations enclose and overlie the DGR;
(c) Contaminant Transport is Diffusion Dominated: deep groundwater regime is ancient showing no evidence of glacial perturbation or cross-formational flow;
(d) Seismically Quiet: comparable to stable Canadian Shield setting;
(e) Geomechanically Stable: selected DGR limestone formation will provide stable, virtually dry openings.
(f) Natural Resource Potential is Low: commercially viable oil and gas reserves are not present;
(g) Shallow Groundwater Resources are Isolated: near surface groundwater aquifers isolated; and

The analyses of this study support hypotheses (a), (b), (c) and (g). The basis of this support is summarized in the preceding paragraphs. It also is provided in the responses to the issues itemized in the text that follows. The analyses of this study do not address hypotheses (d), (e) and (f).

7.4 Confidence Assessment of the Hydrogeological Modelling Analyses

The design that was followed for this numerical modelling study of the Geosynthesis program was to use four numerical models with different scales and two computational models to evaluate Features, Events and Processes (FEP) that are relevant to the development of the safety case for the proposed DGR in the argillaceous limestone of the Cobourg Formation. A graphical overview of the design of the numerical modelling study is presented in Figure 1.3. The modelling strategy included parameter perturbation analyses and the use of multiple numerical models that honoured the field and laboratory data obtained in the DGR study. The numerical models also remained faithful to the geometry of the DGR site; the study design minimized upscaling.

The most important FEP investigated in this study was solute transport in the Ordovician sediments. There is *high confidence* that solute transport in the Ordovician sediments is dominated by diffusion. All analyses undertaken in this study support this assertion.

There is *high confidence* that the diffusion dominated solute transport in the Ordovician sediments is insensitive to glaciation and deglaciation, the presence of a hypothetical undetected transmissive fracture between the Cambrian and Niagaran Group located 1 km from the DGR site or a possible weathered zone at the top of the Precambrian rock.

There is *high confidence* that the pathway that a solute would follow to the biosphere in either the Niagaran Group or the Cambrian sandstone are long. The closest outcrop for the Cambrian sandstone is more than 300 km northwest of the proposed DGR site. The Cambrian is bounded above by the low permeability Ordovician sediments and below by the Precambrian rock. The Niagaran Group is bounded above by the low permeability units of the Salina where solute transport, if it occurs, is diffusion dominant. It is bounded below by the low permeable units of the Lower Silurian. There is *high confidence* that the travel time for a conservative solute to migrate in either the Niagaran Group or the Cambrian sandstone from the location of the proposed DGR to the accessible biosphere is millions of years.

There is *high confidence* that there are multiple barriers provided by the location of the DGR in the Cobourg limestone. These barriers include: the low permeability Ordovician sediments where solute transport is diffusion dominant; the long travel paths in the Cambrian and the Niagaran; the

low permeability of the Salina in which solute transport is diffusion dominant and which isolates the more permeable A1 upper carbonate; and, the high total dissolved solids concentration of the rock below the Bass Islands Formation, which contributes to a groundwater that is stagnant.

In characterizing the Black River Group in the lower Ordovician, there is *high confidence* that the vertical hydraulic conductivity for that group is significantly lower than the estimated horizontal hydraulic conductivity from the straddle-packer hydraulic tests in the DGR boreholes. The confidence assessment is based on the unrealistically rapid evolution of the observed pressure gradient that is predicted to occur when the vertical hydraulic conductivities approach the estimated horizontal hydraulic conductivity values for the Group.

There is *high confidence* that a transmissive fracture connecting the Cambrian and the Niagaran Group does not occur in immediate proximity to the location of the DGR. The measured pressures in the DGR boreholes are inconsistent with the occurrence of a transmissive fracture. The differences in the pore water chemistry of the Cambrian and the Niagaran Group would not be expected if a transmissive fracture connecting the units were present.

Over-pressures were measured in the permeable Cambrian sandstone at the DGR boreholes. Based on the Michigan Basin cross-section analysis and the regional-scale numerical model, there is *high confidence* that the over-pressures are the result of topography, the geometry of the hydrostratigraphic layers in the Michigan Basin and the total dissolved solids distribution in the units of the Michigan Basin.

Under-pressures were measured in the Ordovician sediments at the DGR boreholes. There is *high confidence* that these under-pressures are not caused by glaciation and deglaciation. There is *high confidence* that an immiscible gas phase and the physics of multi-phase fluid flow can result in under-pressures.

8. REFERENCES

Adams, J.J. and S. Bachu. 2002. Equations of state for basin geofluids: Algorithm review and intercomparison for brines. Geofluids 2(4), 257–271.

AECOM and ITASCA CANADA. 2011. Regional Geology – Southern Ontario. AECOM Canada Ltd. and Itasca Consulting Canada, Inc. report for the Nuclear Waste Management Organization, NWMO DGR-TR-2011-15 R000. Toronto, Canada.

Aravena, R., L.I. Wassenaar, and L.N. Plummer. 1995. Estimating ^{14}C groundwater ages in a methanogenic aquifer. Water Resources Research 31(9), 2307–2317.

Armstrong, D.K. and T.R. Carter. 2006. An Updated Guide to the Subsurface Paleozoic Stratigraphy of Southern Ontario. Ontario Geological Survey, Open File Report 6191. Sudbury, Canada.

Arnold, N. and M. Sharp. 2002. Flow variability in the Scandinavian ice sheet: Modelling the coupling between ice sheet flow and hydrology. Quaternary Science Reviews 21(4-6), 485–502.

Bader, S. and H. Kooi. 2005. Modelling of solute and water transport in semi-permeable clay membranes: Comparison with experiments. Advances in Water Resources 28(3), 203–214.

Bailey Geological Services Ltd. and R.O. Cochrane. 1984. Evaluation of the Conventional and Potential Oil and Gas Reserves of the Cambrian of Ontario. Ontario Geological Survey, Open File Report 5499. Sudbury, Ontario.

Barton, K.E., D.G. Howell, J.F. Vigil, J.C. Reed, and J.O. Wheeler. 2003. The North America tapestry of time and terrain. United States Geological Survey. Geologic Investigations Series I-2781, Version 1.0.

Batzle, M. and Z. Wang. 1992. Seismic properties of pore fluids. Geophysics 57(11), 1396–1408.

Bear, J. 1988. Dynamics of Fluids in Porous Media. Dover edition. Dover Publications Inc., New York, USA.

Bense, V. and M. Person. 2008. Transient hydrodynamics within intercratonic sedimentary basins during glacial cycles. Journal of Geophysical Research 113, 1–17.

Beven, K.J., M.J. Kirkby, N. Schofield, and A.F. Tagg. 1984. Testing a physically-based flood forecasting model (TOPMODEL) for three U.K. catchments. Journal of Hydrology 69(1-4), 119–143.

Birkholzer, J., Q. Zhou, K. Zhang, P. Jordan, J. Rutqvist, and C.F. Tsang. 2008. Research Project on CO_2 Geological Storage and Groundwater Resources: Large-Scale Hydrological Evaluation and Modeling of the Impact on Groundwater Systems. Earth Sciences Division, Lawrence Berkeley National Laboratory, Annual Report October 1, 2007 to September 30, 2008. Berkeley, California.

Bottomley, D.J., L.H. Chan, A. Katz, A. Starinsky, and I.D. Clark. 2003. Lithium isotope geochemistry and origin of Canadian Shield brines. Ground Water 41(6), 847–856.

Bottomley, D.J., R. Renaud, T. Kotzer, and I.D. Clark. 2002. Iodine-129 constraints on residence times of deep marine brines in the Canadian Shield. Geology 30(7), 587–590.

Boulton, G.S., P.E. Caban, and K. van Gijssel. 1995. Groundwater flow beneath ice sheets: Part I – Large scale patterns. Quaternary Science Reviews 14(6), 545–562.

Boulton, G.S., P.E. Caban, K. van Gijssel, A. Leijnse, M. Punkari, and F.H.A. van Weert. 1996. The impact of glaciation on the groundwater regime of Northwest Europe. Global and Planetary Change 12(1-4), 397–413.

Boulton, G.S., U. Kautsky, L. Moren, and T. Wallroth. 2001a. Impact of Long-term Climate Change on a Deep Geological Repository for Spent Nuclear Fuel. Swedish Nuclear Fuel and Waste Management Co. (SKB), Technical Report TR-99-05. Stockholm, Sweden.

Boulton, G.S., R. Lunn, P. Vidstrand, and S. Zatsepin. 2007a. Subglacial drainage by groundwater-channel coupling, and the origin of esker systems: Part 1 – glaciological observations. Quaternary Science Reviews 26(7-8), 1067–1090.

Boulton, G.S., R. Lunn, P. Vidstrand, and S. Zatsepin. 2007b. Subglacial drainage by groundwater-channel coupling, and the origin of esker systems: Part 2 – theory and simulation of a modern system. Quaternary Science Reviews 26(7-8), 1091–1105.

Boulton, G.S., S. Zatsepin, and B. Maillot. 2001b. Analysis of Groundwater Flow Beneath Ice Sheets. Swedish Nuclear Fuel and Waste Management Co. (SKB), Technical Report TR-01-06. Stockholm, Sweden.

Burnett, R.D. and E.O. Frind. 1987. Simulation of comtaminant transport in three dimensions 2. dimensionality effects. Water Resources Research 23(4), 695–705.

Carpenter, A.B. 1978. Origin and chemical evolution of brines in sedimentary basins. Oklahoma Geological Survey Circular 79, 60–77.

Carter, T.R., R.A. Trevail, and R.M. Easton. 1996. Basement controls on some hydrocarbon traps in southern Ontario, Canada. In Basement and basins of eastern North America (B.A. van der Pluijm and P.A. Catacosinos, eds.). Number 308 in Special Paper, Geological Society of America, 95–107.

Case, L.C. 1945. Exceptional Silurian brine near Bay City, Michigan. American Association of Petrololeum Geology Bulletin 29, 567–570.

Cedercreutz, J. 2004. Future Climate Scenarios for Olkiluoto with Emphasis on Permafrost. Posiva Oy, Technical Report 2004-06. Olkiluoto, Finland.

Chan, T., N.W. Scheier, and V. Guvanasen. 1999. MOTIF Code Version 3.2: Theory Manual. Ontario Hydro, Technical Report 06819-REP-01200-0091-R00. Toronto, Canada.

Chernicoff, S., H.A. Fox, and L.H. Tanner. 2002. Earth: Geologic Principles and History. Houghton Mifflin Company, Boston, USA.

Clark, I.D., T.A. Al, R.B. Jackson, and K. Raven. 2010. Influence of partial gas saturation on solute transport: Michigan Basin, southwest Ontario. In GeoCanada - Working with the Earth. Calgary, Canada, 4.

Clarke, G.K.C. 2005. Subglacial processes. Annual Review of Earth and Planetary Sciences 33, 247–276.

Cornaton, F. and P. Perrochet. 2006a. Groundwater age, life expectancy and transit time distributions in advective–dispersive systems: 1. Generalized reservoir theory. Advances in Water Resources 29(9), 1267–1291.

Cornaton, F. and P. Perrochet. 2006b. Groundwater age, life expectancy and transit time distributions in advective–dispersive systems: 2. Reservoir theory for sub-drainage basins. Advances in Water Resources 29(9), 1292–1305.

Davison, C.C., T. Chan, A. Brown, M. Gascoyne, D.C. Kamineri, G.S. Lodha, T.W. Melnyk, B.W. Nakka, P.A. O'Connor, D.U. Ophori, N.W. Scheier, N.M. Soonawala, F.W. Stanchell, D.R. Stevenson, G.A. Thorne, T.T. Vandergraaf, P. Wilks, and S.H. Whitaker. 1994. The Disposal of Canada's Nuclear Fuel Waste: The Geosphere Model for Postclosure Assessment. AECL Research, Whiteshell Laboratories, Technical Report AECL-10719, COG-93-9. Pinawa, Manitoba, Canada.

Deblonde, G. and W.R. Peltier. 1991. Simulations of continental ice sheet growth over the last glacial-interglacial cycle: Experiments with a one-level seasonal energy balance model including realistic geography. Journal of Geophysical Research 96(D5), 9189–9215.

Deblonde, G. and W.R. Peltier. 1993. Late Pleistocene ice age scenarios based on observational evidence. Journal of Climate 6(4), 709–727.

Desbarats, A.J., C.E. Logan, M.J. Hinton, and D.R. Sharpe. 2002. On the kriging of water table elevations using collateral information from a digital elevation model. Journal of Hydrology 255(1-4), 25–38.

Domenico, P.A. and F.W. Schwartz. 1990. Physical and Chemical Hydrogeology. John Wiley & Sons, New York, USA.

Downer, C.W. and F.L. Ogden. 2004. Appropriate vertical discretization of Richards' equation for two-dimensional watershed-scale modelling. Hydrological Processes 18(1), 1–22.

Duan, Z. and S. Mao. 2006. A thermodynamic model for calculating methane solubility, density and gas phase composition of methane-bearing aqueous fluids from 273 to 523 K and from 1 to 2000 bar. Geochimica et Cosmochimica Acta 70(13), 3369–3386.

Dyke, L.D. 1984. Frost heaving of bedrock in permafrost regions. Bulletin of the Association of Engineering Geologists 21(4), 389–405.

Ellis, G.D. 1969. Architecture of the Michigan Basin. In Studies of the Precambrian of the Michigan Basin, Michigan Basin Geological Society Annual Field Excursion Guidebook. 60–80.

Emmons, P.J. 1987. An Evaluation of the Bedrock Aquifer System in Northeastern Wisconsin. United States Geological Survey, Water-resources Investigations Report 4199. Madison, Wisconsin.

Fountain, A.G. and J.S. Walder. 1998. Water flow through temperate glaciers. Reviews of Geophysics 36(3), 299–328.

Frape, S.K., P.S. Dollar, B. Sherwood Lollar, and R.H. McNutt. 1989. Mixing of saline basinal fluids in southern Ontario: Implications of rock-water interaction, hydrocarbon emplacement and Canadian Shield brines. In Water-Rock Interaction, WRI-6. Proceedings of the 6th International Symposium on Water-Rock Interaction, Malvern, U.K. (D.L. Miles, ed.). A. A. Balkema, Rotterdam, The Netherlands, 223–226.

Frape, S.K. and P. Fritz. 1987. Geochemical trends for groundwaters from the Canadian Shield. In Saline Water and Gases in Crystalline Rocks (P. Fritz and S.K. Frape, eds.). Number 33 in Geological Association of Canada Special Paper, 19–38.

Freeze, R.A. and J. Cherry. 1979. Groundwater. Prentice Hall, Englewood Cliffs, USA.

Frind, E.O. 1982. Simulation of long-term transient density-dependent transport in groundwater. Advances in Water Resources 5, 73–88.

Garavito, A.M., H. Kooi, and C.E. Neuzil. 2006. Numerical modeling of a long-term in situ chemical osmosis experiment in the Pierre Shale, South Dakota. Advances in Water Resources 29, 481–492.

GOLDER. 2003. LLW Geotechnical Feasibility Study, Western Waste Management Facility, Bruce Site, Tiverton, Ontario. Golder Associates Ltd. report to Municipality of Kincardine and Ontario Power Generation, Technical Report 021-1570. Toronto, Canada.

Gonçalvès, J., S. Violette, and J. Wendling. 2004. Analytical and numerical solutions for alternative overpressuring processes: Application to the Callovo-Oxfordian sedimentary sequence in the Paris basin, France. Journal of Geophysical Research 109(B02110), 14.

Goode, D.J. 1996. Direct simulation of groundwater age. Water Resources Research 32(2), 289–296.

Guimerà, J., L. Duro, S. Jordana, and J. Bruno. 1999. Effects of Ice Melting and Redox Front Migration in Fractured Rocks of Low Permeability. Swedish Nuclear Fuel and Waste Management Co. (SKB), Technical Report TR-99-19. Stockholm, Sweden.

Gupta, N. 1993. Geologic and Fluid-density Controls on the Hydrodynamics of the Mt. Simon Sandstone and Overlying Geologic Units in Ohio and the Surrounding States. Ph.D. thesis, The Ohio State University, Columbus, Ohio.

Gutierrez, M.S. and R.W. Lewis. 2002. Coupling of fluid flow and deformation in underground formations. Journal of Engineering Mechanics 128(7), 779–787.

Guvanasen, V. 2007. FRAC3DVS-OPG Enhancements: Subgridding, Hydromechanical Deformation and Anisotropic Molecular Diffusion. Nuclear Waste Management Organization, Technical Report NWMO TR-2007-05. Toronto, Canada.

Hanor, J.S. 1979. Geochemistry of Hydrothermal Ore Deposits. John Wiley & Sons, New York, USA.

Hoaglund, J., G. Huffman, and N. Grannemann. 2002. Michigan Basin regional groundwater flow discharge to three Great Lakes. Ground Water 40(4), 390–406.

Hobbs, M.Y., S.K. Frape, O. Shouakar-Stash, and L.R. Kennell. 2011. Regional Hydrogeochemistry – Southern Ontario. Nuclear Waste Management Organization, Technical Report NWMO DGR-TR-2011-12 R000. Toronto, Canada.

Holditch, S.A., T. Patzek, J. Rutqvist, G. Moridis, and R. Plumb. 2008. Geomechanical Performance of Hydrate-bearing Sediments in Offshore Environments. Office of Fossil Energy, National Energy Technology Laboratory, United States Department of Energy, Final Scientific/Technical Report DOE Award No.: DE-FC26-05NT42664, CFDA Number: 81.089 (Fossil Energy Research and Development). Washington, DC, USA.

Hooke, R.L. 2005. Principles of Glacier Mechanics. Second edition. Cambridge University Press, Cambridge, UK.

Howell, P.D. and B.A. van der Pluijm. 1999. Structural sequences and styles of subsidence in the Michigan basin. Geological Society of America Bulletin 111(7), 974–991.

HSI GeoTrans. 2000. Theory and Implementation for SWIFT for Windows. The Sandia Waste-Isolation Flow and Transport Model for Fractured Media. Sterling, Virginia.

Huysmans, M. and A. Dassargues. 2005. Review of the use of Peclet numbers to determine the relative importance of advection and diffusion in low permeability environments. Hydrogeology Journal 13, 895–904.

INTERA. 1988. Inventory and Assessment of Hydrogeologic Conditions of Underground Openings in Sedimentary Rocks. INTERA Technologies Ltd. report to Ontario Hydro, H87-040.

INTERA. 2006. Geoscientific Site Characterization Plan, OPG's Deep Repository for Low and Intermediate Level Radioactive Waste. Intera Engineering Ltd. report to Ontario Power Generation, Technical Report OPG 00216-PLAN-00120-00002-R00. Toronto, Canada.

INTERA. 2011. Descriptive Geosphere Site Model. Intera Engineering Ltd. report for the Nuclear Waste Management Organization, NWMO DGR-TR-2011-24 R000. Toronto, Canada.

ITASCA. 1997. FLAC-3D Manual: Fast Lagrangian Analysis of Continua in 3-Dimensions – Version 2.0. Itasca Consulting Group, Inc., Minnesota, USA.

ITASCA. 2011. Long Term Geomechanical Stability Analysis. Itasca Consulting Group, Inc. report for the Nuclear Waste Management Organization, NWMO DGR-TR-2011-17 R000. Toronto, Canada.

ITASCA CANADA and AECOM. 2011. Three-Dimensional Geological Framework Model. Itasca Consulting Canada, Inc. and AECOM Canada Ltd. report for the Nuclear Waste Management Organization, NWMO DGR-TR-2011-42 R000. Toronto, Canada.

Jaeger, J.C., N.G.W. Cook, and R.W. Zimmerman. 2007. Fundamentals of Rock Mechanics. Fourth edition. Blackwell Publishing Ltd, Oxford, UK.

Johnston, P., P. Wu, and K. Lambeck. 1998. Dependence of horizontal stress magnitude on load dimension in glacial rebound models. Geophysical Journal International 132, 41–60.

Lampe, D.C. 2009. Hydrogeologic Framework of Bedrock Units and Initial Salinity Distribution for a Simulation of Groundwater Flow for the Lake Michigan Basin. United States Geological Survey, Technical Report 5060. Reston, Virginia.

Lemieux, J.M., E.A. Sudicky, W.R. Peltier, and L. Tarasov. 2008a. Dynamics of groundwater recharge and seepage over the Canadian landscape during the Wisconsinian glaciation. Journal of Geophysical Research 113, F01011.

Lemieux, J.M., E.A. Sudicky, W.R. Peltier, and L. Tarasov. 2008b. Simulating the impact of glaciations on continental groundwater flow systems: 1. Relevant processes and model formulation. Journal of Geophysical Research 113, F03017.

Lemieux, J.M., E.A. Sudicky, W.R. Peltier, and L. Tarasov. 2008c. Simulating the impact of glaciations on continental groundwater flow systems: 2. Model application to the Wisconsinian glaciation over the Canadian landscape. Journal of Geophysical Research 113, F03018.

Lusczynski, N.J. 1961. Head and flow of ground water of variable density. Journal of Geophysical Research 66(12), 4247–4256.

Marshall, S.J. 2005. Recent advances in understanding ice sheet dynamics. Earth and Planetary Science Letters 240, 191–204.

Marshall, S.J., L. Tarasov, G.K.C. Clarke, and W.R. Peltier. 2000. Glaciological reconstruction of the Laurentide ice sheet: Physical processes and modelling challenges. Canadian Journal of Earth Sciences 37(5), 769–793.

Mazurek, M. 2004. Long-term Used Nuclear Fuel Waste Management: Geoscientific Review of the Sedimentary Sequence in Southern Ontario. Institute of Geological Sciences, University of Bern, Technical Report TR 04-41. Bern, Switzerland.

Mazurek, M., F.J. Pearson, G. Volckaert, and H. Bock. 2003. Features, Events and Processes Evaluation Catalogue for Argillaceous Media. Nuclear Energy Agency (NEA), Organisation for Economic Co-operation and Development (OECD), Technical Report NEA4437. Paris, France.

McCauley, C.A., D.M. White, M.R. Lilly, and D.M. Nyman. 2002. A comparison of hydraulic conductivities, permeabilities and infiltration rates in frozen and unfrozen soils. Cold Regions Science and Technology 34(2), 117–125.

McIntosh, J.C. and L.M. Walter. 2006. Paleowaters in Silurian-Devonian carbonate aquifers: Geochemical evolution of groundwater in the Great Lakes region since the late Pleistocene. Geochimica et Cosmochimica Acta 70(10), 2454–2479.

Mehl, S. and M. Hill. 2002. Development and evaluation of a local grid refinement method for block-centered finite-difference groundwater models using shared nodes. Advances in Water Resources 25, 497–511.

Millington, R.J. and J.P. Quirk. 1961. Permeability of porous solids. Transactions of the Faraday Society 57, 1200–1207.

Moridis, G.J., M.B. Kowalsky, and K. Pruess. 2008. TOUGH+HYDRATE V1.0 User's Manual: A Code For The Simulation Of System Behavior In Hydrate-Bearing Geologic Media. Earth Sciences Division, Lawrence Berkeley National Laboratory, Berkeley, California. LBNL-149E.

Mualem, Y. 1976. A new model for predicting the hydraulic conductivity of unsaturated porous media. Water Resources Research 12(3), 513–522.

Neuzil, C. 1995. Abnormal pressures as hydrodynamic phenomena. American Journal of Science 295, 742–786.

Neuzil, C. 2000. Osmotic generation of 'anomalous' fluid pressures in geological environments. Nature 403, 182–184.

Neuzil, C.E. 2003. Hydromechanical coupling in geologic processes. Hydrogeology Journal 11(1), 41–83.

Nguyen, T.S. and A.P.S. Selvadurai. 1996. Modelling of thermal consolidation of sparsely fractured rock in the context of nuclear waste management. In Mechanics of Poroelastic Media (A.P.S. Selvadurai, ed.). Solid Mechanics and its Applications, Kluwer Academic Publishers, 159–180.

Normani, S.D. 2009. Paleoevolution of Pore Fluids in Glaciated Geologic Settings. Ph.D. thesis, University of Waterloo, Waterloo, Canada.

Normani, S.D., Y.J. Park, J.F. Sykes, and E.A. Sudicky. 2007. Sub-Regional Modelling Case Study 2005-2006 Status Report. Nuclear Waste Management Organization, Technical Report NWMO TR-2007-07. Toronto, Canada.

Novakowsi, K. and P. Lapcevic. 1988. Regional hydrogeology of the Silurian and Ordovician sedimentary rocks underlying Niagara Falls, Ontario Canada. Journal of Hydrogeology 104, 211–236.

NWMO. 2009. NWMO Technical Computing Software Procedure. Nuclear Waste Management Organization, Document NWMO-PROC-EN-0002. Toronto, Canada.

NWMO. 2011. Geosynthesis. Nuclear Waste Management Organization, Technical Report NWMO DGR-TR-2011-11 R000. Toronto, Canada.

Oldenburg, C.M., K. Pruess, and S.M. Benson. 2001. Process modeling of CO_2 injection into natural gas reservoirs for carbon sequestration and enhanced gas recovery. Energy and Fuels 15, 293–298.

Park, Y.J., E.A. Sudicky, and J.F. Sykes. 2009. Effects of Shield brine on the safe disposal of waste in deep geologic environments. Advances in Water Resources 32, 1352–1358.

Peltier, W.R. 2002. A Design Basis Glacier Scenario. Ontario Power Generation, Technical Report 06819-REP-01200-10069-R00. Toronto, Canada.

Peltier, W.R. 2003. Long-term Climate Change – Glaciation. Ontario Power Generation, Technical Report 06189-REP-01200-10113-R00. Toronto, Canada.

Peltier, W.R. 2011. Long-Term Climate Change. Nuclear Waste Management Organization, Technical Report NWMO DGR-TR-2011-14 R000. Toronto, Canada.

Person, M., B. Dugan, J.B. Swenson, L. Urbano, C. Stott, J. Taylor, and M. Willett. 2003. Pleistocene hydrogeology of the Atlantic continental shelf, New England. Geological Society of America Bulletin 115(11), 1324–1343.

Person, M., J. McIntosh, V. Bense, and V.H. Remenda. 2007. Pleistocene hydrology of North America: The role of ice sheets in reorganizing groundwater flow systems. Reviews of Geophysics 45, RG3007.

Post, V., H. Kooi, and C. Simmons. 2007. Using hydraulic head measurements in variable-density ground water flow analyses. Ground Water 45(6), 664–671.

Provost, A.M., C.I. Voss, and C.E. Neuzil. 1998. Site-94 – Glaciation and Regional Ground-Water Flow in the Fennoscandian Shield. Swedish Nuclear Power Inspectorate (SKI), SKI Report 96:11. Stockholm, Sweden.

Pruess, K., C. Oldenburg, and G. Moridis. 1999. TOUGH2 User's Guide, Version 2.0. Earth Sciences Division, Lawrence Berkeley National Laboratory, Berkeley, California. LBNL-43134.

Raven, K., K. Novakowski, R. Yager, and R. Heystee. 1992. Supernormal fluid pressures in sedimentary rocks of southern Ontario - western New York state. Canadian Geotechnical Journal 29, 80–93.

Rutqvist, J., L. Börgesson, M. Chijimatsu, A. Kobayashi, L. Jing, T.S. Nguyen, J. Noorishad, and C.F. Tsang. 2001. Thermohydromechanics of partially saturated geological media: governing equations and formulation of four finite element models. International Journal of Rock Mechanics and Mining Sciences 38, 105–127.

Rutqvist, J., Y.S. Yu, C.F. Tsang, and G. Bodvarsson. 2002. A modeling approach for analysis of coupled multiphase fluid flow, heat transfer, and deformation in fractured porous rock. International Journal of Rock Mechanics and Mining Sciences 39, 429–442.

Sanford, B.V. 1993. St. Lawrence platform. In Sedimentary Cover of the Craton in Canada (D.F. Stott and J.D. Aitken, eds.). Number 5 in Geology of Canada, Geological Survey of Canada, 709–798.

Sanford, B.V., F.J. Thompson, and G.H. McFall. 1985. Plate tectonics - a possible controlling mechanism in the development of hydrocarbon traps in southwestern Ontario. Bulletin of Canadian Petroleum Geology 33(1), 52–71.

Saripalli, K.P., R.J. Serne, P.D. Meyer, and B.P. McGrail. 2002. Prediction of diffusion coefficients in porous media using tortuosity factors based on interfacial areas. Ground Water 40(4), 346–352.

Selvadurai, A. and T. Nguyen. 1995. Computational modelling of isothermal consolidation of fractured porous media. Computers and Geotechnics 17, 39–73.

Singh, B.P. and B. Kumar. 2005. Isotopes in Hydrology, Hydrogeology, and Water Resources. Narosa Publishing House Pvt. Ltd., New Delhi, India.

Sterling, S. 2010. Bedrock Formations in DGR-1 and DGR-2. Intera Engineering Ltd., Technical Report TR-07-05. Ottawa, Canada. Revision 3.

Stonehouse, H.B. 1969. Studies of the Precambrian of the Michigan Basin, chapter The Precambrian Around and Under the Michigan Basin. Michigan Basin Geological Society, 15–27.

Sykes, E.A. 2007. Hydrogeologic Modelling to Assess Conditions Related to OPG's Proposed Deep Geologic Repository in Tiverton, Ontario. Master's thesis, University of Waterloo, Waterloo, Canada.

Tarasov, L. and W.R. Peltier. 1997. Terminating the 100 kyr ice age cycle. Journal of Geophysical Research 102(D18), 21665–21693.

Tarasov, L. and W.R. Peltier. 1999. Impact of thermomechanical ice sheet coupling on a model of the 100 kyr ice age cycle. Journal of Geophysical Research 104(D8), 9517–9545.

Tarasov, L. and W.R. Peltier. 2002. Greenland glacial history and local geodynamic consequences. Geophysical Journal International 150(1), 198–229.

Tarasov, L. and W.R. Peltier. 2004. A geophysically constrained large ensemble analysis of the deglacial history of the North American ice-sheet complex. Quaternary Science Reviews 34(3-4), 359–388.

Tarasov, L. and W.R. Peltier. 2005. Arctic freshwater forcing of the Younger Dryas cold reversal. Nature 435, 662–665.

Tarasov, L. and W.R. Peltier. 2006. A calibrated deglacial drainage chronology for the North American continent: evidence of an Arctic trigger for the Younger Dryas. Quaternary Science Reviews 25(7-8), 659–688.

Therrien, R., E.A. Sudicky, and R.G. McLaren. 2004. FRAC3DVS: An Efficient Simulator for Three-dimensional, Saturated-Unsaturated Groundwater Flow and Density-dependent, Chain-Decay Solute Transport in Porous, Discretely-Fractured Porous or Dual-porosity Formations. User's Guide. Groundwater Simulations Group, University of Waterloo, Waterloo, Ontario, Canada.

van der Kamp, G. and J.E. Gale. 1983. Theory of Earth tide and barometric effects in porous formations with compressible grains. Water Resources Research 19(2), 538–544.

van Genuchten, M. 1980. A closed-form equation for predicting hydraulic conductivity of unsaturated soils. Soil Sci. Soc. 44, 892–898.

van Weert, F.H.A., K. van Gijssel, A. Leijnse, and G.S. Boulton. 1997. The effects of Pleistocene glaciations on the geohydrological system of northwest Europe. Journal of Hydrology 195(1-4), 137–159.

Vinard, P., P. Blümling, J.P. McCord, and G. Aristorenas. 1993. Evaluation of hydraulic underpressures at Wellenberg, Switzerland. International Journal of Rock Mechanics and Mining Sciences & Geomechanics Abstracts 30(7), 1143–1150.

Vinard, P.H. 1998. Generation and Evolution of Hydraulic Underpressures in a Marl-shale Aquitard at Wellenberg, Central Switzerland. Ph.D. thesis, Université de Neuchâtel, Neuchâtel, Switzerland.

Walsh, R. 2010. Compilation and Consolidation of Field and Laboratory Data for Hydrogeological Properties. Intera Engineering Ltd., Technical Report TR-08-10. Ottawa, Canada. Revision 1A (January 27, 2010).

Ward, D.S., D.R. Buss, J.W. Mercer, and S.S. Hughes. 1987. Evaluation of a groundwater corrective action at the Chem-Dyne hazardous waste site using a telescopic mesh refinement modelling approach. Water Resources Research 23(4), 603–617.

Weast, R.C. (Ed.). 1983. CRC Handbook of Chemistry and Physics. 64th edition. CRC Press, Inc., Boca Raton, Florida, USA.

Weaver, T.R. 1994. Groundwater Flow and Solute Transport in Shallow Devonian Bedrock Formations and Overlying Pleistocene Units, Lambton County, Southwestern Ontario. Ph.D. thesis, University of Waterloo, Waterloo, Canada.

Westjohn, D.B. and T.L. Weaver. 1996. Hydrogeologic Framework of Mississippian Rocks in the Central Lower Peninsula of Michigan. United States Geological Survey, Water-resources Investigations Report 4246. Lansing, Michigan.

Zwally, H.J., W. Abdalati, T. Herring, K. Larson, J. Saba, and K. Steffan. 2002. Surface-melt induced acceleration of Greenland ice-sheet flow. Science 297, 218–222.

THIS PAGE HAS BEEN LEFT BLANK INTENTIONALLY

9. ABBREVIATIONS, ACRONYMS AND UNITS

3DGF	3D Geologic Framework
cm	centimetre
DEM	Digital Elevation Model
DGR	Deep Geologic Repository
DSI	Discrete Surface Interpolation
FEP	Features, Events and Processes
FEPCAT	Features, Events and Processes CATalogue
ft	feet
g/kg	gram per kilogram
g/L	gram per litre
GMWL	Global Meteoric Water Line
GPa	gigapascals
GSM	Glacial Systems Model
ka	kiloannum (a thousand years)
kg/L	kilogram per litre
kg/m^3	kilogram per cubic metre
km	kilometre
km/Ma	kilometre per megaannum
km^2	square kilometre
kPa	kilopascals
L&ILW	Low and Intermediate Level Waste
m	metre
m/a	metre per annum
m/ka	metre per kiloannum
m/m	metre per metre
m/s	metre per second
m/s^2	metre per second squared

m^2	metre squared
m^2/a	metre squared per annum
m^2/g	metre squared per gram
m^2/s	metre squared per second
m^{-1}	inverse metres
MA	Mean Age
Ma	megaannum (a million years)
mASL	metres Above Sea Level
mASL	metres Below Ground Surface
meq/L	milliequivalent per litre
mg/L	milligram per litre
MLE	Mean Life Expectancy
mm/a	millimetre per annum
mmol/kgw	millimol per kilogram weight
MNR	Ministry of Natural Resources
mol/kgw	mole per kilogram weight
MPa	megapascals
MPa^{-1}	inverse megapascals
NOAA	National Oceanic and Atmospheric Administration
NWMO	Nuclear Waste Management Organization
OGS	Ontario Geological Survey
OGSR	Oil, Gas and Salt Resources
OPG	Ontario Power Generation
Pa^{-1}	inverse pascals
PDF	Probability Density Function
RSA	Regional Study Area
SMOW	Standard Mean Ocean Water
SRTM	Shuttle Radar Topography Mission
TDS	Total Dissolved Solids

THM	Thermo-Hydro-Mechanical
TIN	Triangulated Irregular Network
TOC	Total Organic Carbon
UofT	University of Toronto
USGS	United States Geological Survey
VBA	Visual Basic for Applications

THIS PAGE HAS BEEN LEFT BLANK INTENTIONALLY

APPENDICES

THIS PAGE HAS BEEN LEFT BLANK INTENTIONALLY

APPENDIX A: ANALYSIS OF ABNORMAL PRESSURES

The following analyses are provided by Chris Neuzil of the United States Geological Survey, Reston, Virginia.

A.1 Osmosis

The pressures measured at the Deep Geologic Repository (DGR) site are notable with respect to the magnitude of both the under-pressures and the vertical pressure or head gradients. Such unusual results merit extra scrutiny, and it is reasonable to consider how errors might be introduced in measurements and what exactly is being measured. One of the assumptions used in analyzing the borehole responses for pressure estimates is that Darcy's law governs flow. Darcy's law accounts for hydraulic forces as drivers of flow. However, many fine grained sedimentary rocks, and especially those with clays, behave as semipermeable membranes (Neuzil and Provost 2009). In membranes chemical potentials can also drive flow, a phenomenon known as osmosis.

The under-pressured Ordovician section at the DGR site contains brine at about 250 to 300 g/L, while the boreholes were filled with brine of about 220 to 230 g/L from the Cambrian sandstone. The concentration difference between the borehole and formation fluids could osmotically drive flow from the borehole into the formation if it behaves as a membrane. This section considers whether osmotic flow could have affected pressure measurements. In particular, because osmosis would cause flow out of the borehole, it is of interest to explore whether the anomalously low measured pressures could be a result of osmosis.

A generalized constitutive law that includes chemically-driven flow can be written as (Bresler 1973)

$$q = -K\nabla h + \sigma K \nabla \pi \tag{A.1}$$

where q is the Darcy flux, K is hydraulic conductivity, π is a measure of chemical potential, and σ is the osmotic efficiency. σ is a measure of membrane function and a strong function of concentration (e.g. Bresler 1973).

In a closed system like the shut-in boreholes at the DGR site, osmosis would drive flow from the (relatively) low concentration borehole toward the high concentration formation until opposing hydraulic flow becomes large enough to offset it, resulting in an equilibrated system (q = 0) that would continue to evolve only as concentration contrasts are reduced by diffusion. The osmotically-generated pressure deficit in the borehole can be calculated by integrating Equation (A.1) for q = 0, which yields

$$\Delta p = \int_{C_{min}}^{C_{max}} \sigma(c) \frac{d\pi}{dc} dc \tag{A.2}$$

where C_{min} and C_{max} are the low and high concentrations. The osmotic properties of the Ordovician rocks at the DGR site are unknown, but diffusion experiments suggest that ion exclusion occurs in them, particularly the shale (INTERA 2011). Ion exclusion is the mechanism that causes membrane behavior in geologic media. Some degree of membrane behavior appears expectable in shale-like rocks; Neuzil and Provost (2009) suggest that osmotic specific surface area A_{so} is a way to characterize membrane function and commonly varies from about 5 to 150 m^2/g in shales and similar rocks. Assuming C_{min} and C_{max} values of 220 and 300 g/L, a

porosity of 0.05, and A_{so} values in the range reported, Equation (A.2) can be solved as described by Neuzil and Provost (2009) for p. Calculated values for p range from 14 MPa for A_{so} = 150 m^2/g to 10 kPa for A_{so} = 5 m^2/g. Because the largest under-pressure at the DGR site appears to be about 2.5 MPa, it is not possible to rule out osmosis as the cause of the low observed pressures on the basis of these scoping calculations alone.

Other considerations, however, suggest that osmosis has a minor influence, if any. First, although carbonates such as the Ordovician dolostone are generally thought to lack membrane properties (σ = 0), the under-pressure profile follows a fairly regular pattern that spans both the shale and dolostone. Stated differently, no under-pressures would be expected in the dolostone if they are artifacts of osmosis. This is tempered somewhat by noting that there appears to be a pressure discontinuity at or near the shale-dolostone contact in some cases (e.g. DGR-4, 15 Nov., 2009; INTERA 2011). In addition, the dolostone does contain some clay. Second, the gross shape of the under-pressure profile, with the largest under-pressures near the centre, suggests the influence of normally- to over-pressured boundaries in a flow system rather than pressures that are an artifact of processes near the borehole. Finally, osmotic effects should decline with time as diffusion raises concentrations in the boreholes to match the formation. Given the small porosities in the Ordovician rocks, it is unclear how long this would take, but any osmotic effects will diminish over time. Pressures, on the other hand, are continuing to decline in the under-pressured section.

In sum, it is unlikely that osmosis can account for the observed under-pressures. It is possible, however, that some part of the irregularities in pressure profiles can be explained in this manner.

A.2 Long-term Exhumation

The ability of long-term denudation – the gradual removal of overburden – to generate the anomalously low pressures at the DGR site is considered here. The mechanism can be summed up as follows. Decreasing overburden load allows the formations to rebound or expand elastically, increasing the pore space. Because rates of erosion and rebound are quite small, groundwater can generally flow in readily to accommodate the increased pore volume, and there are no effects on pressure. However, low-permeability formations such as the Ordovician section at the DGR may restrict inflow sufficiently that the pressure decreases. Whether this can explain the observed under-pressures depends on the rock properties and the long-term erosion rates at the DGR site. A first-order scoping calculation is presented below.

The scoping calculations simplify the problem in several respects. Long-term erosion is treated as a one-dimensional constant-rate process, thus ignoring spatial and temporal variations in erosion rate. Ice loading and unloading during glacial cycles are reversible, relatively short-term effects that are ignored. Layering heterogeneity in the Ordovician rocks is not considered except insofar as a range of rock properties representing the heterogeneity are considered for a homogeneous domain.

The problem can be approached using the groundwater flow equation written as (e.g. Ingebritsen et al. 2006, eq. 5.1)

$$\nabla \cdot K \nabla h = S_s \frac{\partial h}{\partial t} - \Gamma \qquad \text{(A.3)}$$

where K is hydraulic conductivity, S_s is specific storage, h is head, and Γ is a source-sink term with dimension inverse time. In this context, Γ is the rebound change in pore volume per volume per time. Simplifications implicit in Equation (A.3) include constant fluid density, K, and S_s.

Changes in overburden load from erosion can be incorporated in Equation (A.3) as changes in vertical stress. Ingebritsen et al. (2006) show that

$$\Gamma = S_s \zeta \frac{1}{\rho_f g} \frac{\partial \sigma_z}{\partial t} \tag{A.4}$$

can be used to represent overburden changes, where σ_z is vertical stress, ζ is one-dimensional loading efficiency, ρ_f is pore fluid density, and g is gravity. Analytical solutions of Equation (A.4) reveal that strong pressure anomalies, like the under-pressures at the DGR site, are generated when (Neuzil 1995, Ingebritsen et al. 2006)

$$|\Gamma| > \frac{K}{l} \tag{A.5}$$

where l is the half thickness of the pressure anomaly. Equation (A.5) must be cast in terms of erosion rate rather than rate of stress change. At any elevation z below land surface the vertical stress from overburden is

$$\sigma_z = [\rho_s g(1 - n) + \rho_f g n](l_s - z) \tag{A.6}$$

where l_s is land surface elevation, ρ_s is solid grain density, and n is porosity. Thus

$$\frac{\partial \sigma_z}{\partial t} = [\rho_s g(1 - n) + \rho_f g n] \frac{\partial l_s}{\partial t} \tag{A.7}$$

where $\partial l_s / \partial t$ is the erosion rate. As a result, Equation (A.4) can be expressed as

$$\Gamma = S_s' \zeta R_\rho \frac{\partial l_s}{\partial t} \tag{A.8}$$

where R_ρ is given by

$$R_\rho = \frac{\rho_s g(1 - n) + \rho_f g n}{\rho_f g} \tag{A.9}$$

The quantities in the numerator in Equation (A.9) pertain to the eroded section, so generic values are used. Here it is assumed that n is 0.1, ρ_ss is 2.6×10^3 kg/m^3, f is 1.2×10^3 kg/m^3, and g is 9.8 m/s^2. The condition necessary for generating strong under-pressures, Equation (A.5), can now be written

$$\frac{\partial l_s}{\partial t} > \frac{K}{S_s' \zeta R_\rho l}. \tag{A.10}$$

The right-hand side of Equation (A.10) is the approximate minimum long-term erosion rate, in m/s, that is needed. The under-pressured Ordovician section is approximately 300 m thick (l = 150 m). Using measured values of permeability, compressibility, and other properties of the Ordovician rocks, Equation (A.10) yields minimum erosion rates between about 5 and 10 m/ka. These are unusually large rates for long-term erosion, which is typically two or three orders of magnitude slower (e.g. Schaller et al. 2001). Unless (1) rapid, deep erosion denudation occurred by glaciation, (2) permeability is much smaller than test values, or (3) the rocks are significantly more compressible than test values, this suggests it is unlikely that under-pressures at the DGR site can be attributed to long-term erosion.

A.3 References

Bresler, E. (1973), Anion exclusion and coupling effects in nonsteady transport through unsaturated soils: I. Theory, Soil Sci. Soc. Am. Proc., 37(5), 663–669.

Ingebritsen, S. E., W. E. Sanford, and C. E. Neuzil, Groundwater in Geologic Processes, Cambridge Univ. Press, 535 p., 2006.

INTERA. 2011. Descriptive Geosphere Site Model. Intera Engineering Ltd. report for the Nuclear Waste Management Organization, NWMO DGR-TR-2011-24 R000. Toronto, Canada.

Neuzil, C. E., Abnormal pressures as hydrodynamic phenomena, Amer. Jour. of Sci. 295(6), 742–786, 1995.

Neuzil, C. E., and A. M. Provost (2009), Recent experimental data may point to a greater role for osmotic pressures in the subsurface, Water Resour. Res., 45, W03410, doi:10.1029/2007WR006450

Schaller, M., F. von Blanckenburg, N. Hovius, and P.W. Kubik, Large-scale erosion rates from in situ-produced cosmogenic nuclides in European river sediments, Earth and Planetary Sci. Lett. 188, 441–458, 2001.

APPENDIX B: IMPACT OF CONSTANT FLUID DENSITY

LIST OF FIGURES

Page

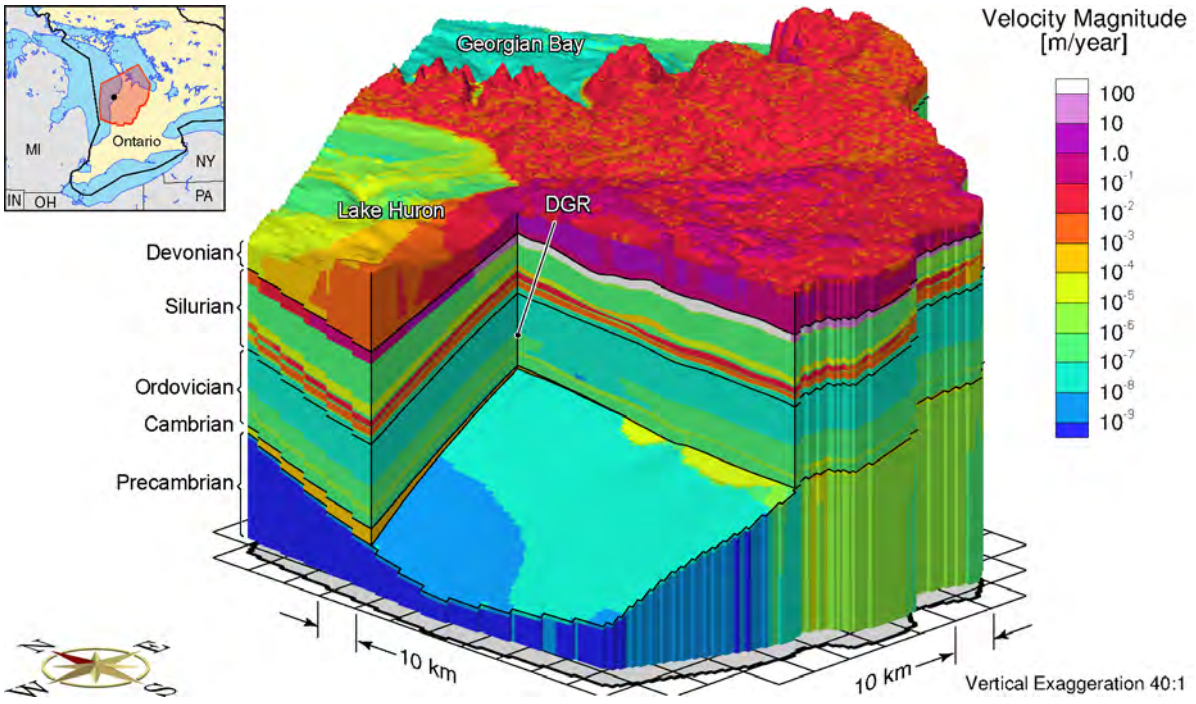

Figure B.1: Pore Water Velocity Magnitude for the Base Case Parameters and Constant Freshwater Fluid Density

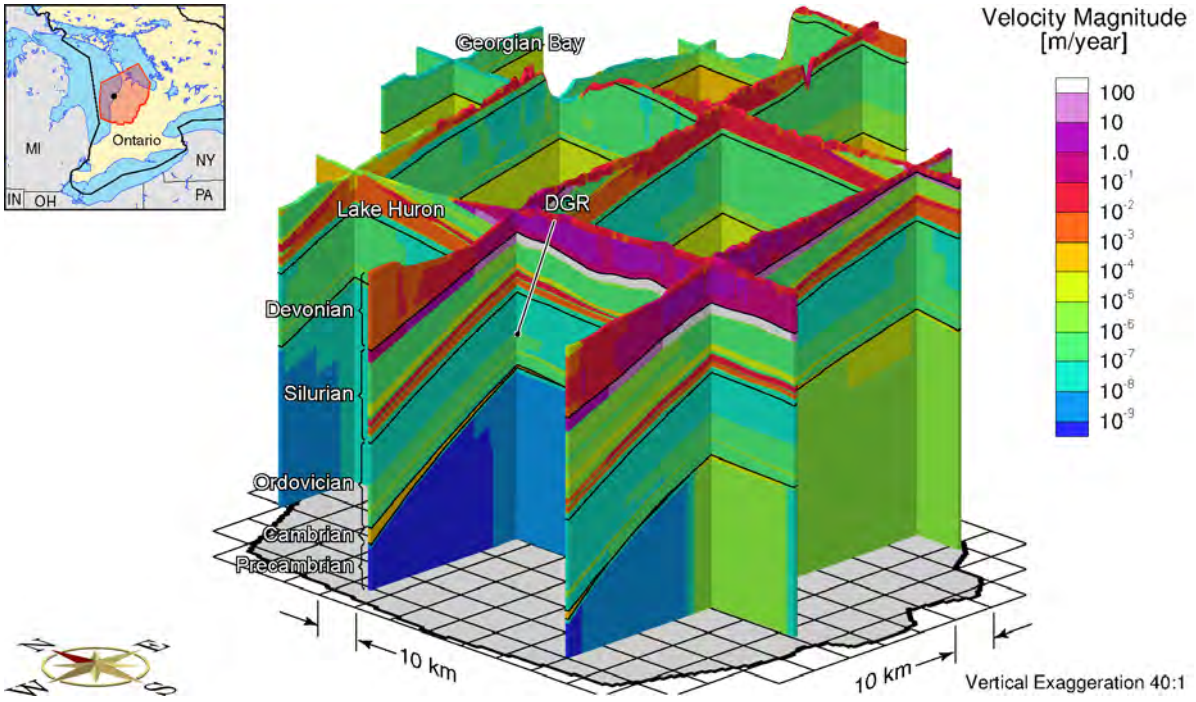

Figure B.2: Fence Diagram of the Pore Water Velocity Magnitude for the Base Case Parameters and Constant Freshwater Fluid Density

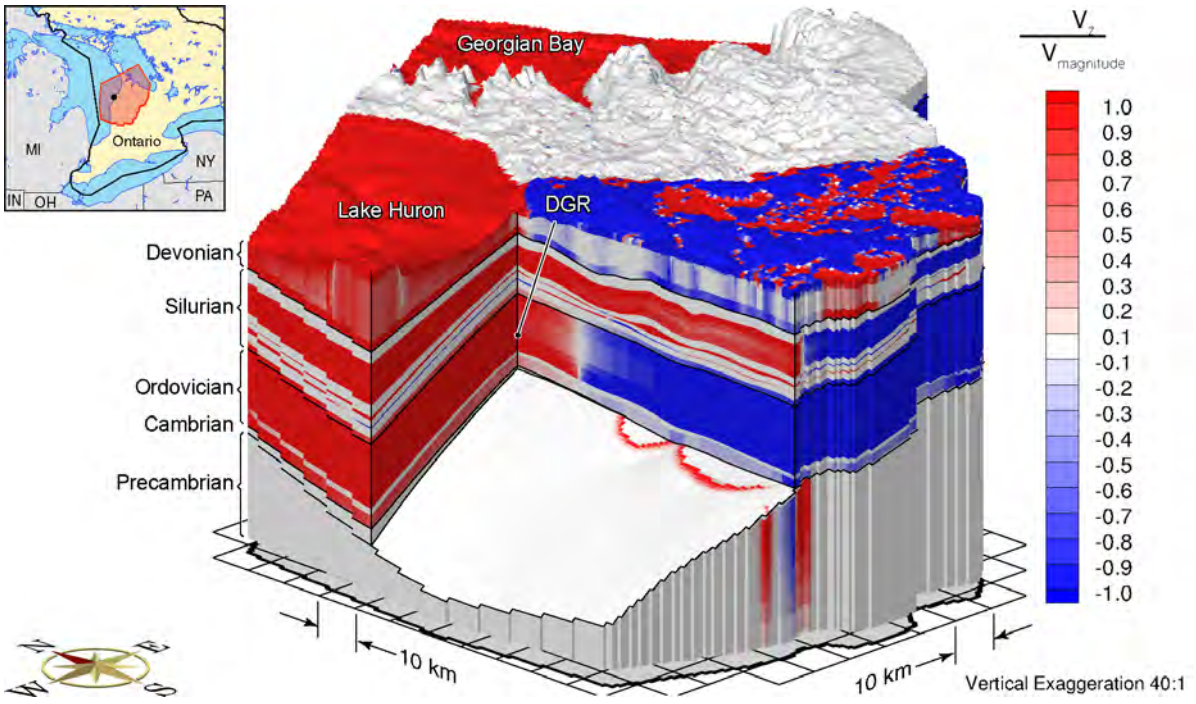

Figure B.3: Ratio of Vertical Velocity to the Velocity Magnitude for the Base Case Parameters and Constant Freshwater Fluid Density

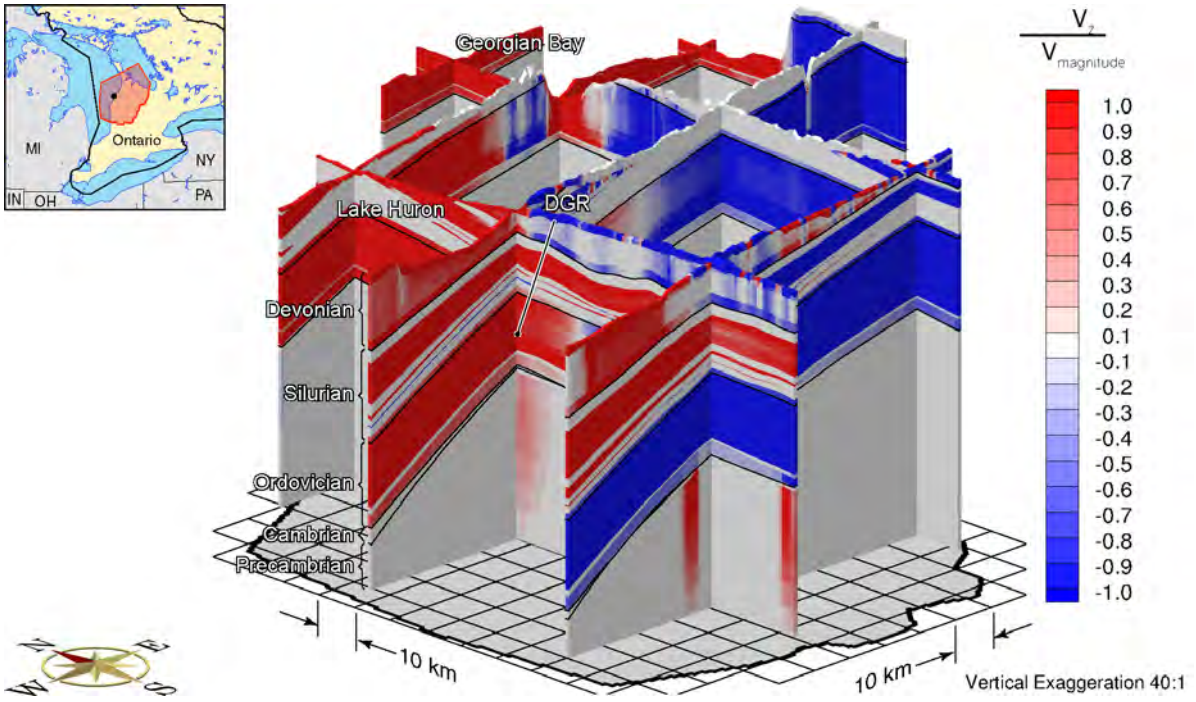

Figure B.4: Fence Diagram of the Ratio of Vertical Velocity to the Velocity Magnitude for the Base Case Parameters and Constant Freshwater Fluid Density

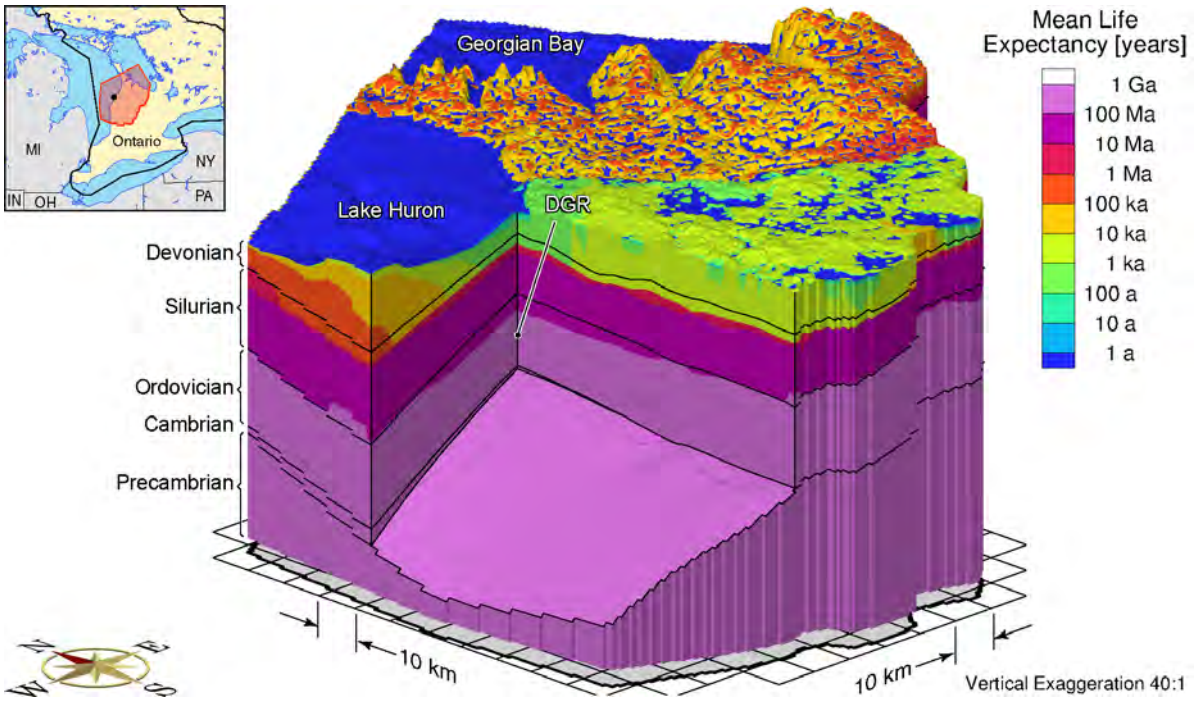

Figure B.5: Mean Life Expectancies for the Base Case Parameters and Constant Freshwater Fluid Density

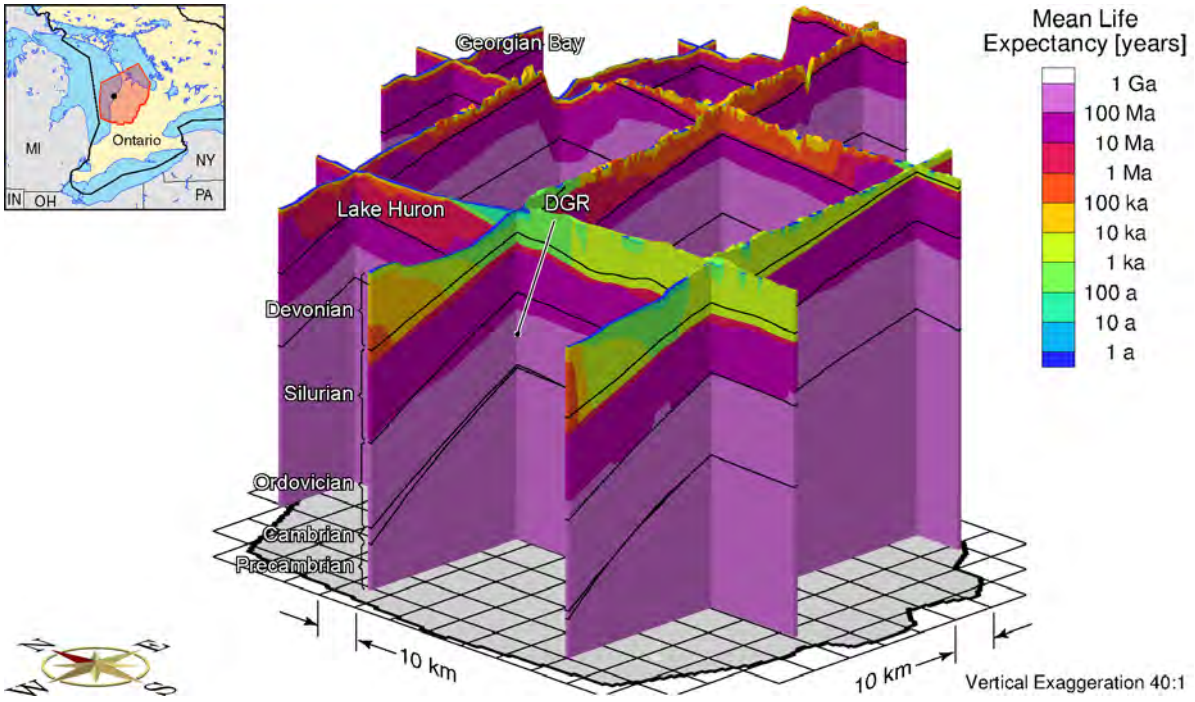

Figure B.6: Fence Diagram Showing the Mean Life Expectancies for the Base Case Parameters and Constant Freshwater Fluid Density

APPENDIX C: ANALYSIS OF SURFACE BOUNDARY CONDITION

LIST OF FIGURES

Page

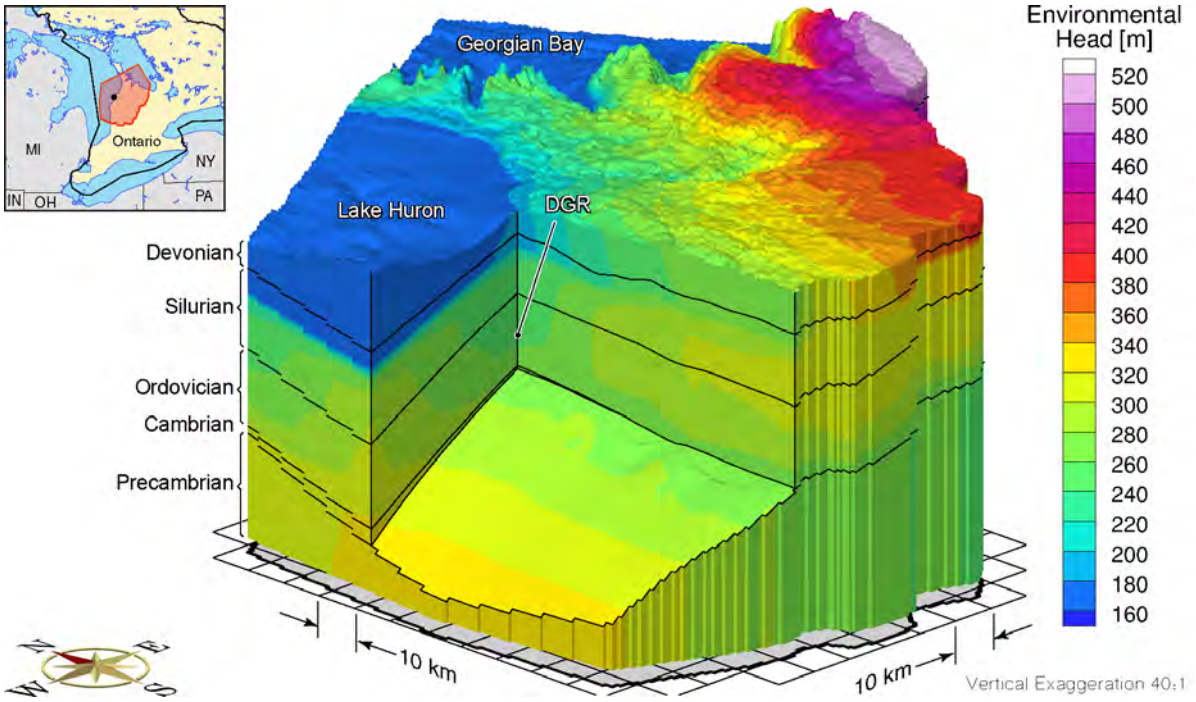

Figure C.1: Environmental Heads for the Base Case Parameters, 20 m Weathered Zone at the Surface and a Prescribed Net Recharge of 10 mm/a Above the Devonian and 0.01 mm/a Above the Silurian

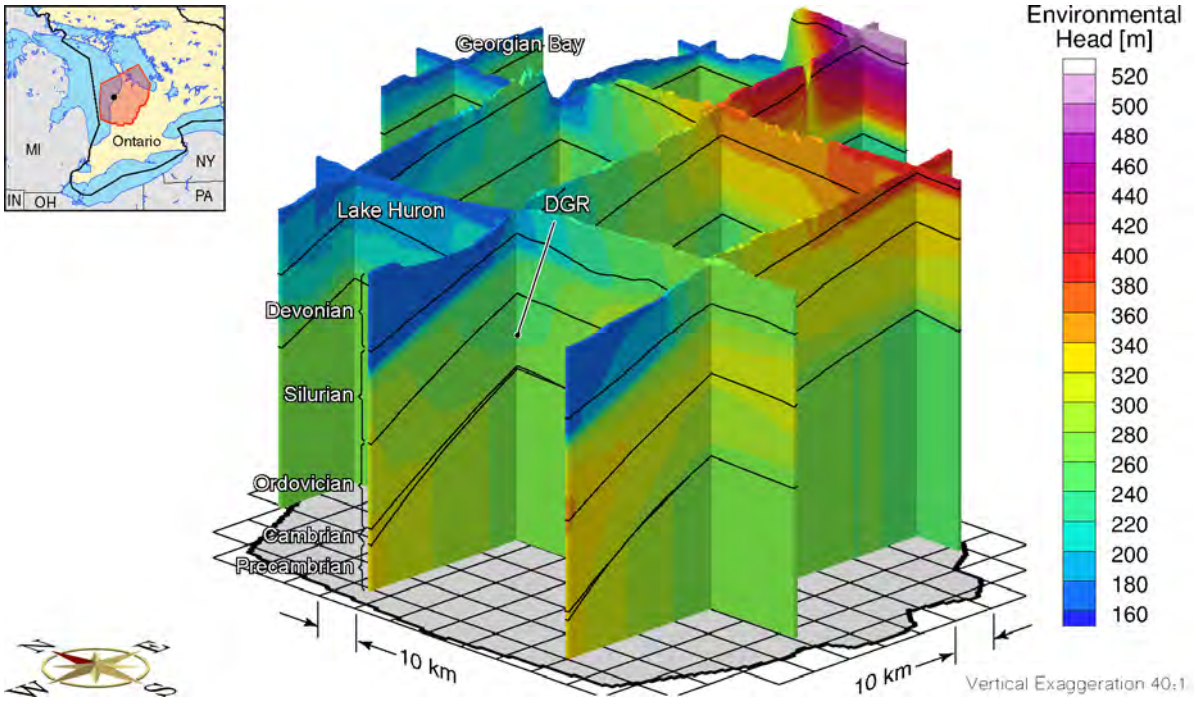

Figure C.2: Fence Diagram of Environmental Heads for the Base Case Parameters, 20 m Weathered Zone at the Surface and a Prescribed Net Recharge of 10 mm/a Above the Devonian and 0.01 mm/a Above the Silurian

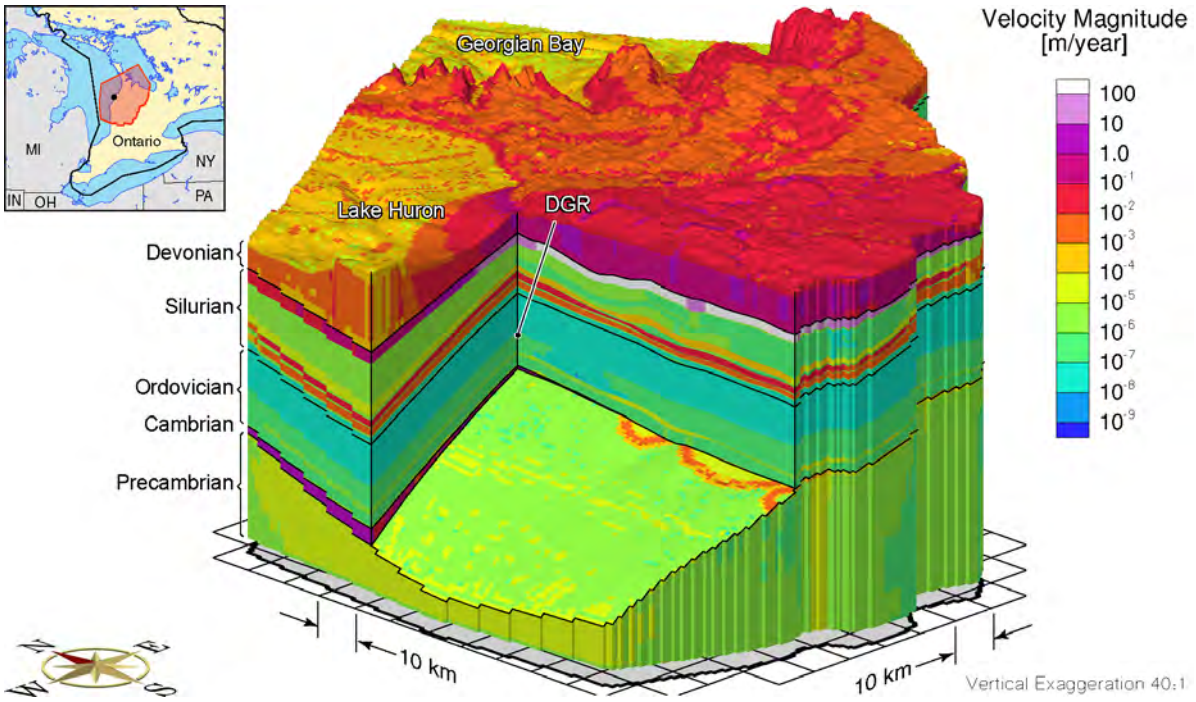

Figure C.3: Pore Water Velocity Magnitude for the Base Case Parameters, 20 m Weathered Zone at the Surface and a Prescribed Net Recharge of 10 mm/a Above the Devonian and 0.01 mm/a Above the Silurian

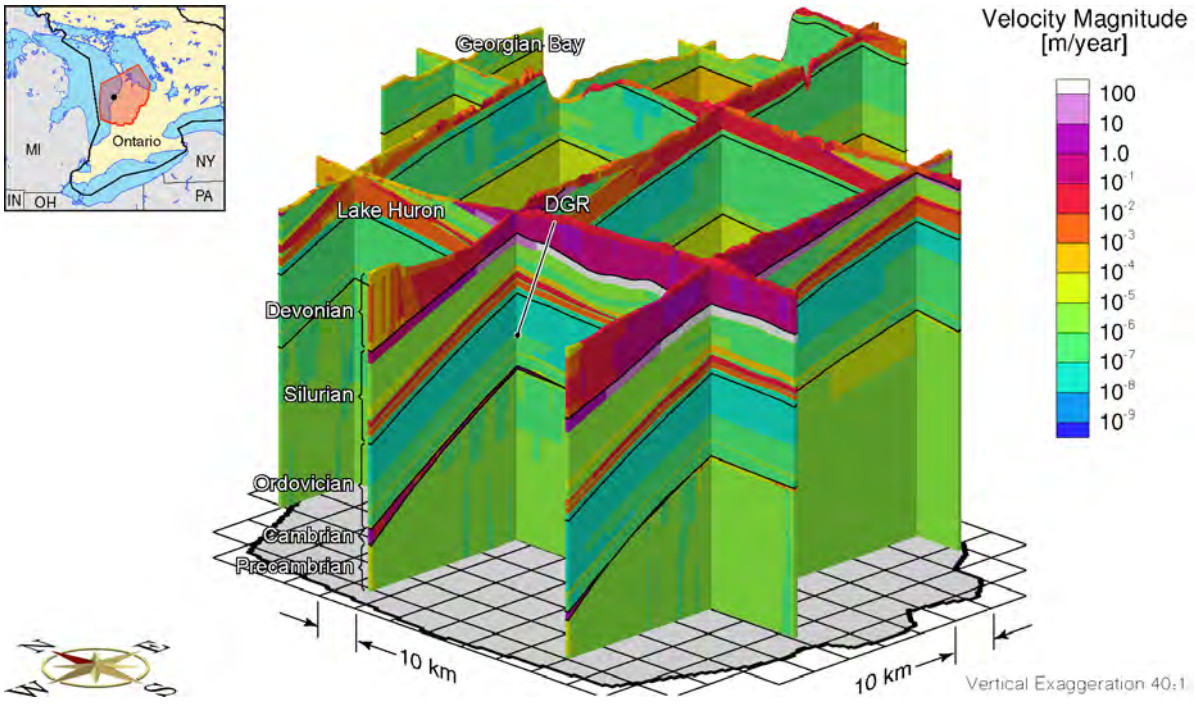

Figure C.4: Fence Diagram of Pore Water Velocity Magnitude for the Base Case Parameters, 20 m Weathered Zone at the Surface and a Prescribed Net Recharge of 10 mm/a Above the Devonian and 0.01 mm/a Above the Silurian

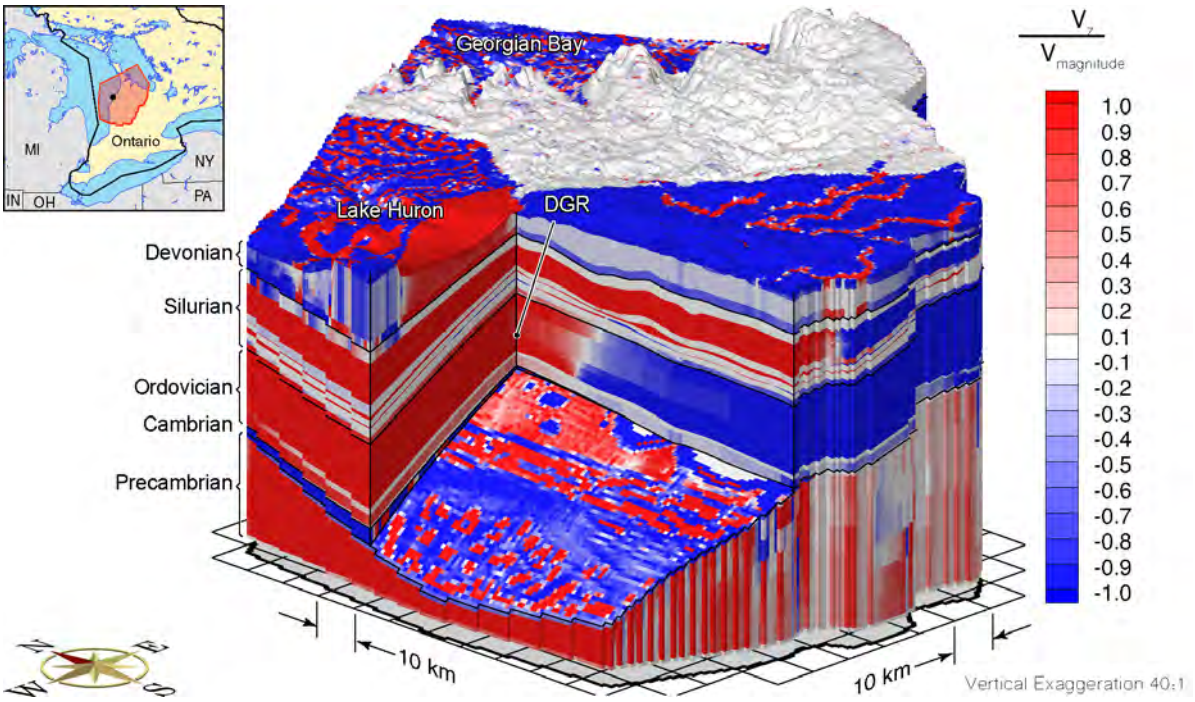

Figure C.5: Ratio of Vertical Velocity to the Velocity Magnitude for the Base Case Parameters, 20 m Weathered Zone at the Surface and a Prescribed Net Recharge of 10 mm/a Above the Devonian and 0.01 mm/a Above the Silurian

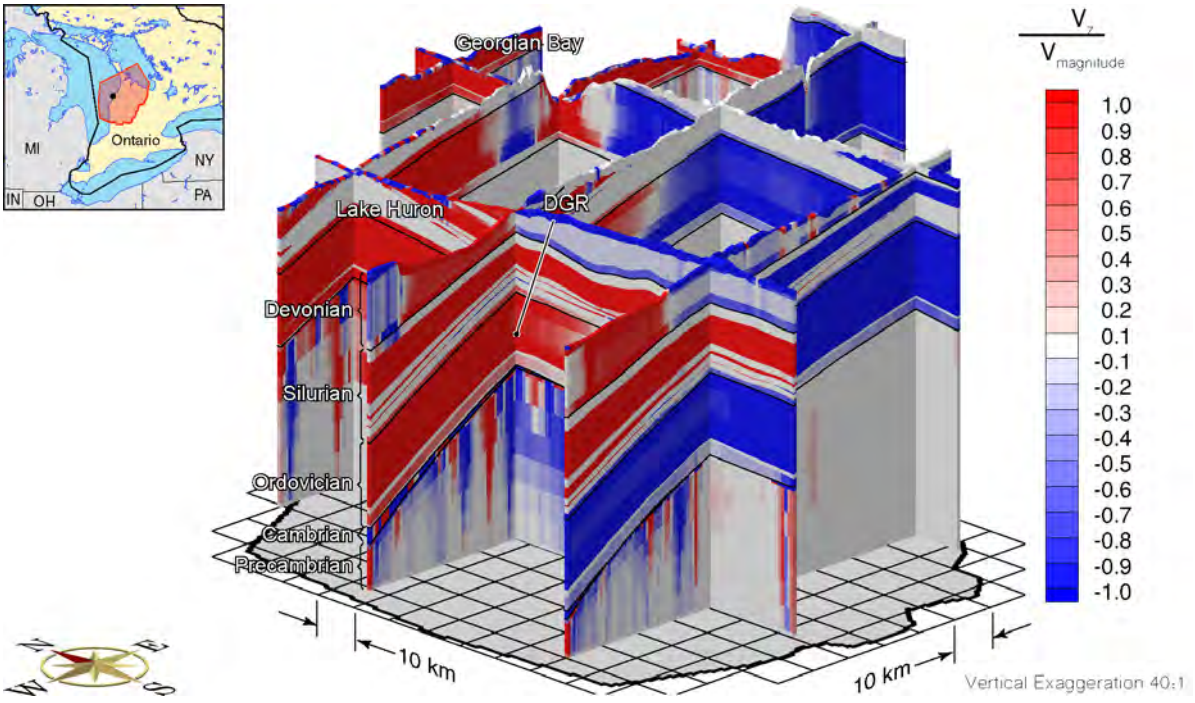

Figure C.6: Fence Diagram of the Ratio of Vertical Velocity to the Velocity Magnitude for the Base Case Parameters, 20 m Weathered Zone at the Surface and a Prescribed Net Recharge of 10 mm/a Above the Devonian and 0.01 mm/a Above the Silurian

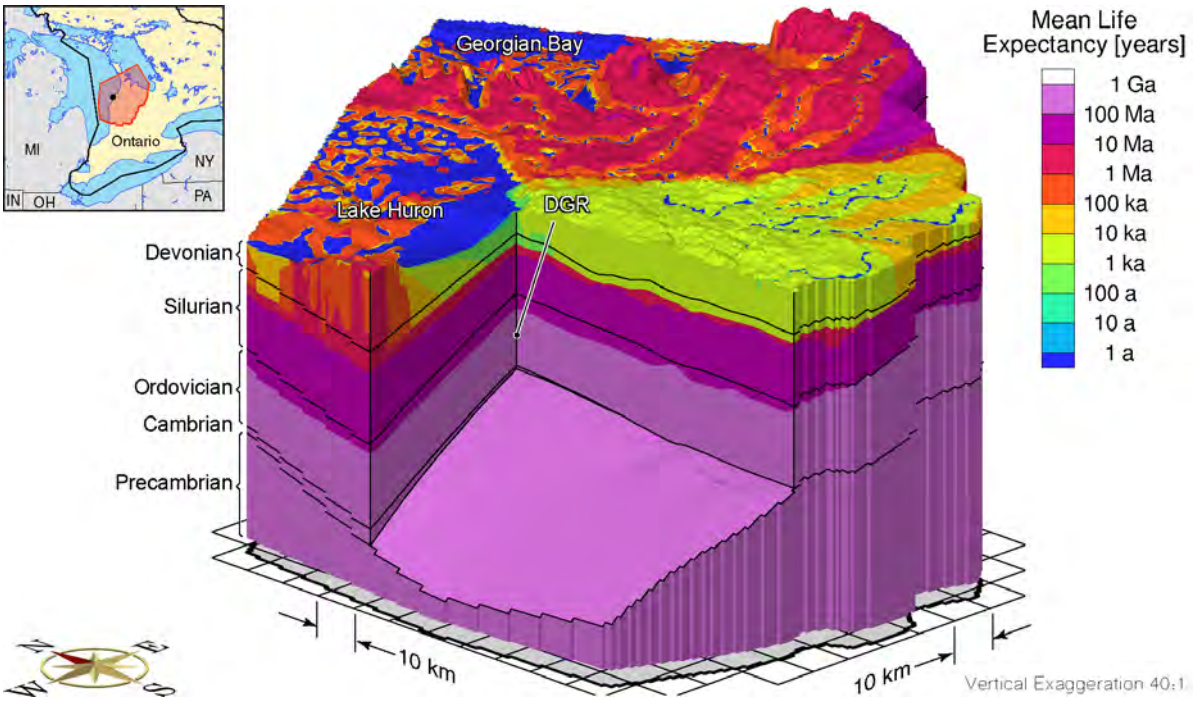

Figure C.7: Mean Life Expectancies for the Base Case Parameters, 20 m Weathered Zone at the Surface and a Prescribed Net Recharge of 10 mm/a Above the Devonian and 0.01 mm/a Above the Silurian

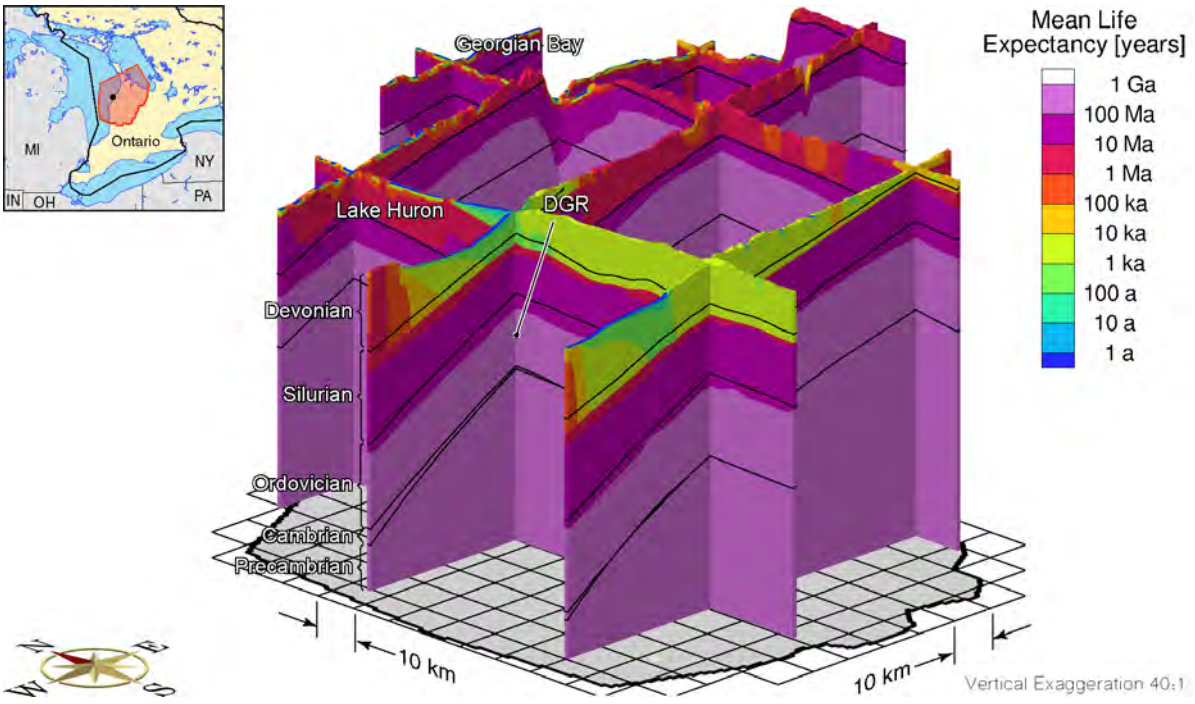

Figure C.8: Fence Diagram Showing the Mean Life Expectancies for the Base Case Parameters, 20 m Weathered Zone at the Surface and a Prescribed Net Recharge of 10 mm/a Above the Devonian and 0.01 mm/a Above the Silurian

THIS PAGE HAS BEEN LEFT BLANK INTENTIONALLY

APPENDIX D: CAMBRIAN HETEROGENEITY

LIST OF FIGURES

Page

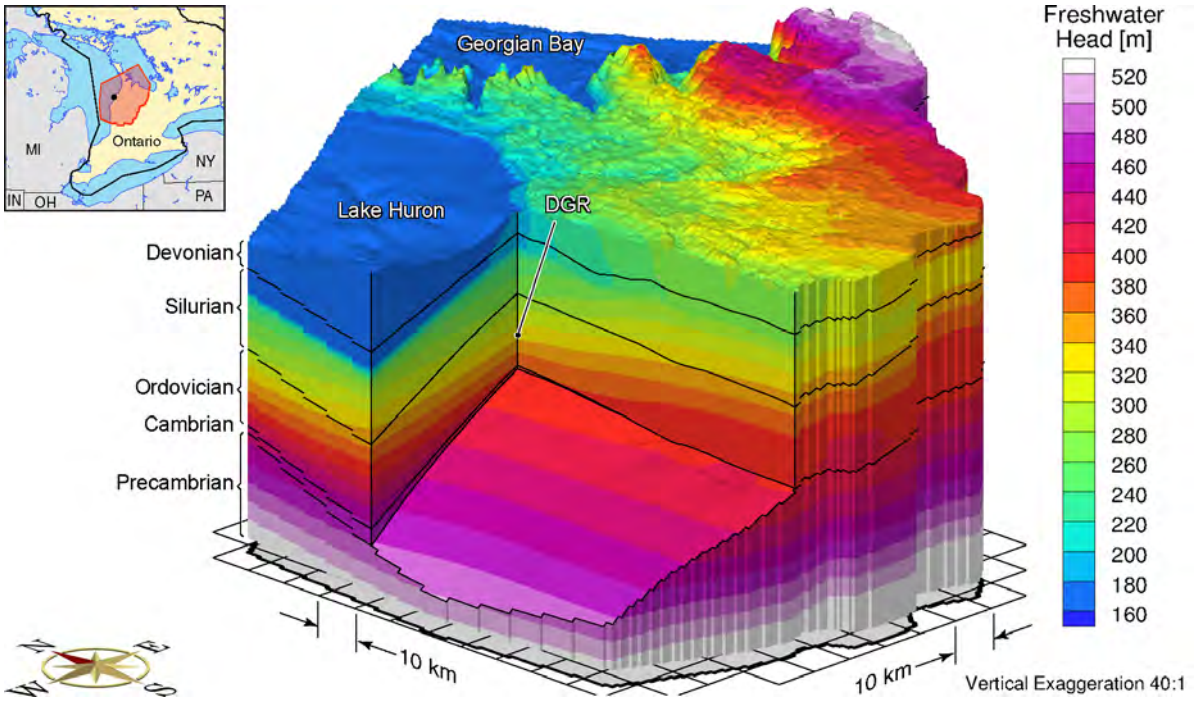

Figure D.1: Equivalent Freshwater Heads for the Base Case Parameters and the Cambrian Anisotropy K_1 Aligned East-West

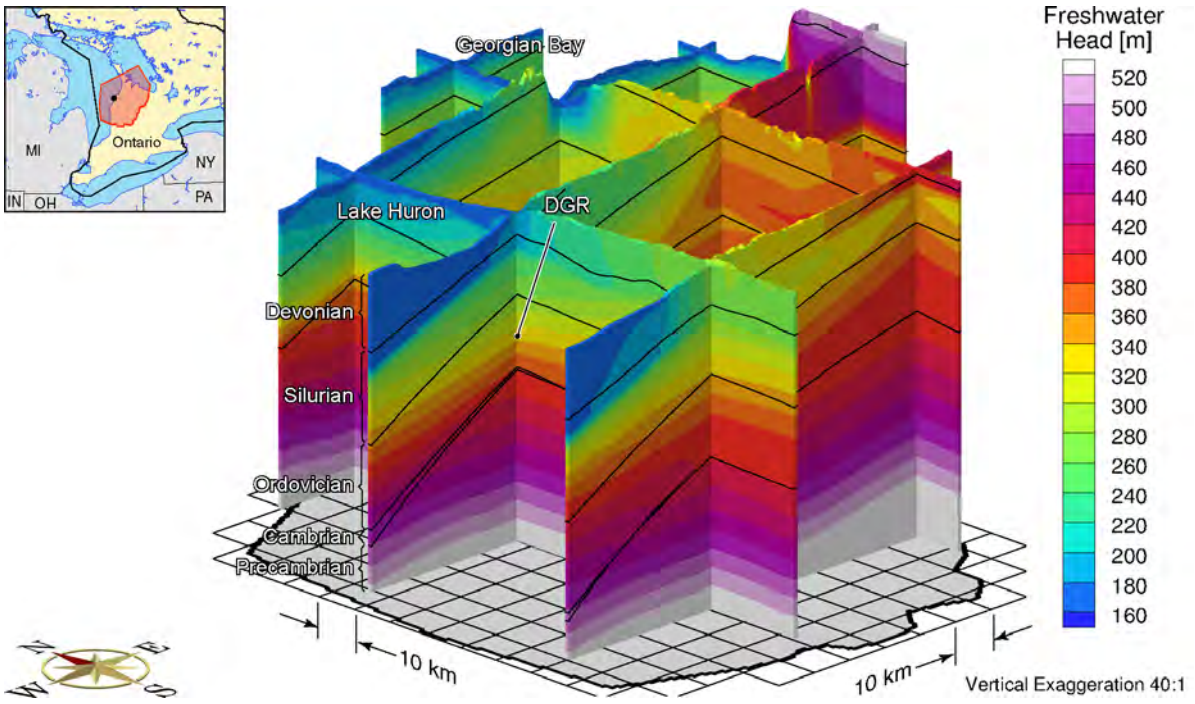

Figure D.2: Fence Diagram of Equivalent Freshwater Heads for the Base Case Parameters and the Cambrian Anisotropy K_1 Aligned East-West

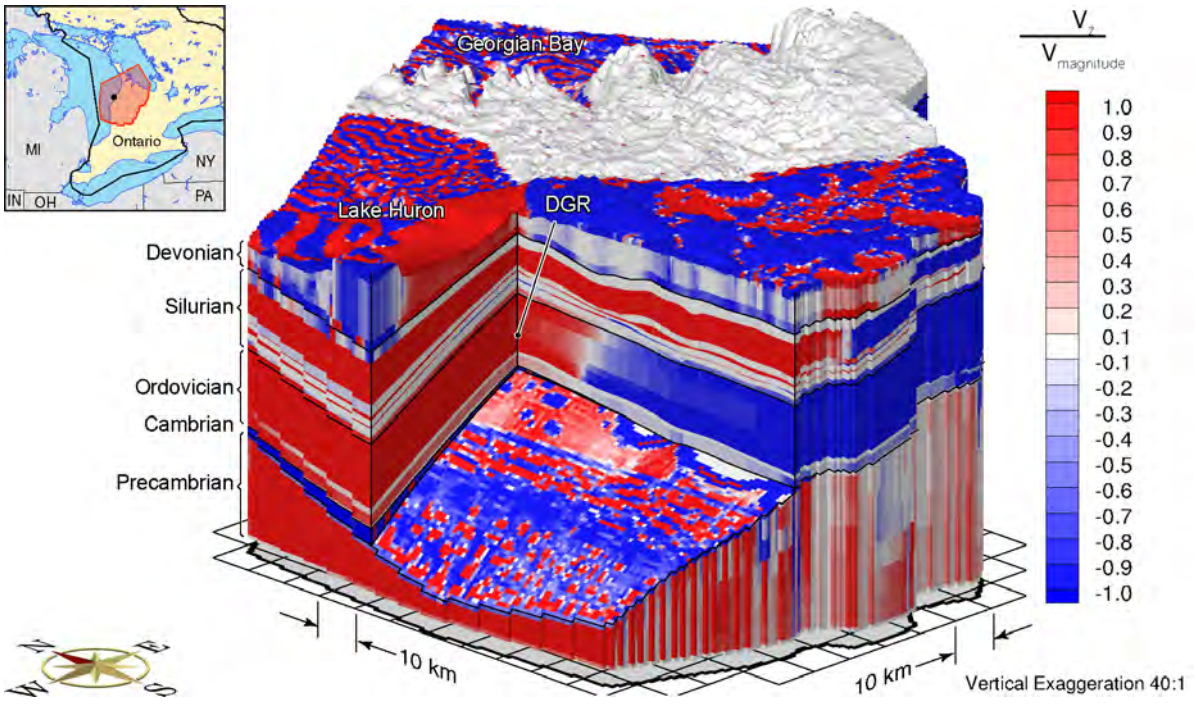

Figure D.3: Ratio of Vertical Velocity to the Velocity Magnitude for the Base Case Parameters and the Cambrian Anisotropy K_1 Aligned East-West

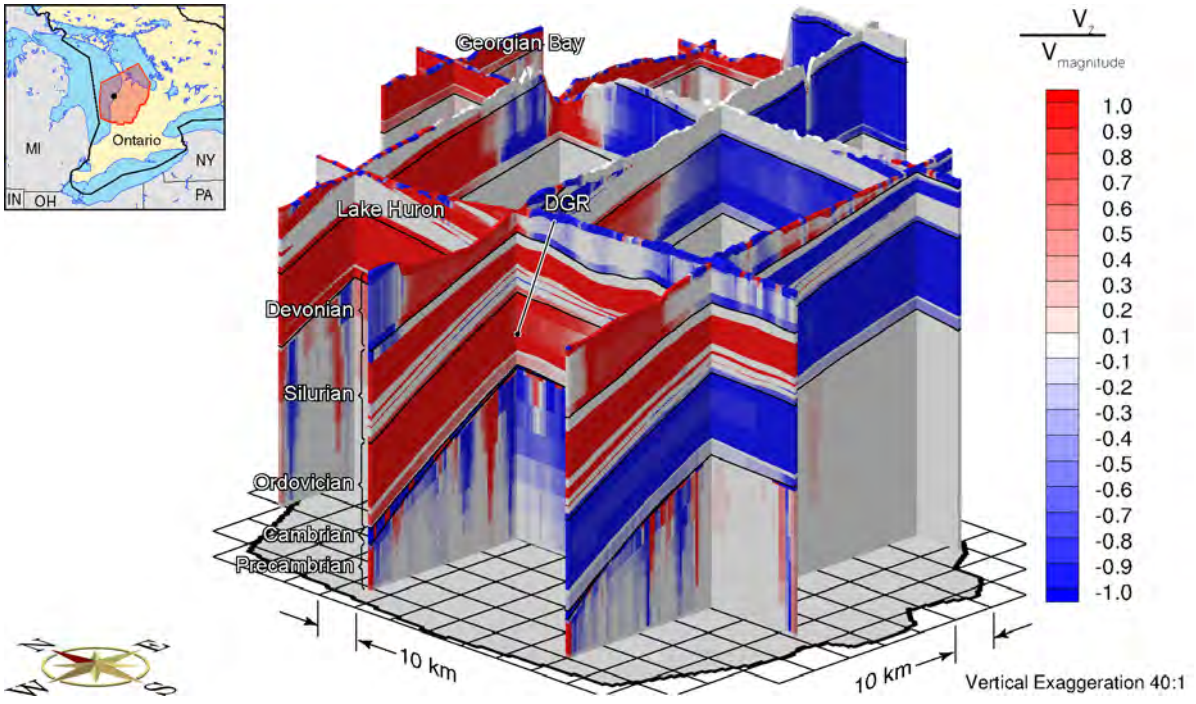

Figure D.4: Fence Diagram of the Ratio of Vertical Velocity to the Velocity Magnitude for the Base Case Parameters and the Cambrian Anisotropy K_1 Aligned East-West

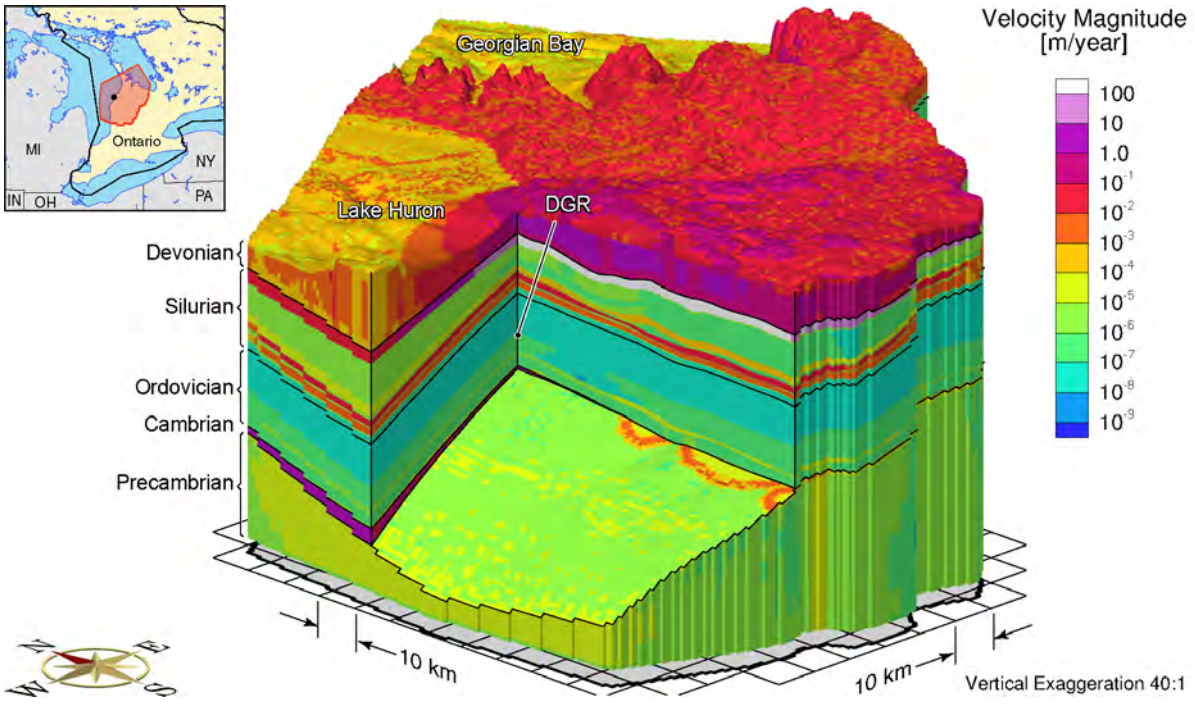

Figure D.5: Pore Water Velocity Magnitude for the Base Case Parameters and the Cambrian Anisotropy K_1 Aligned East-West

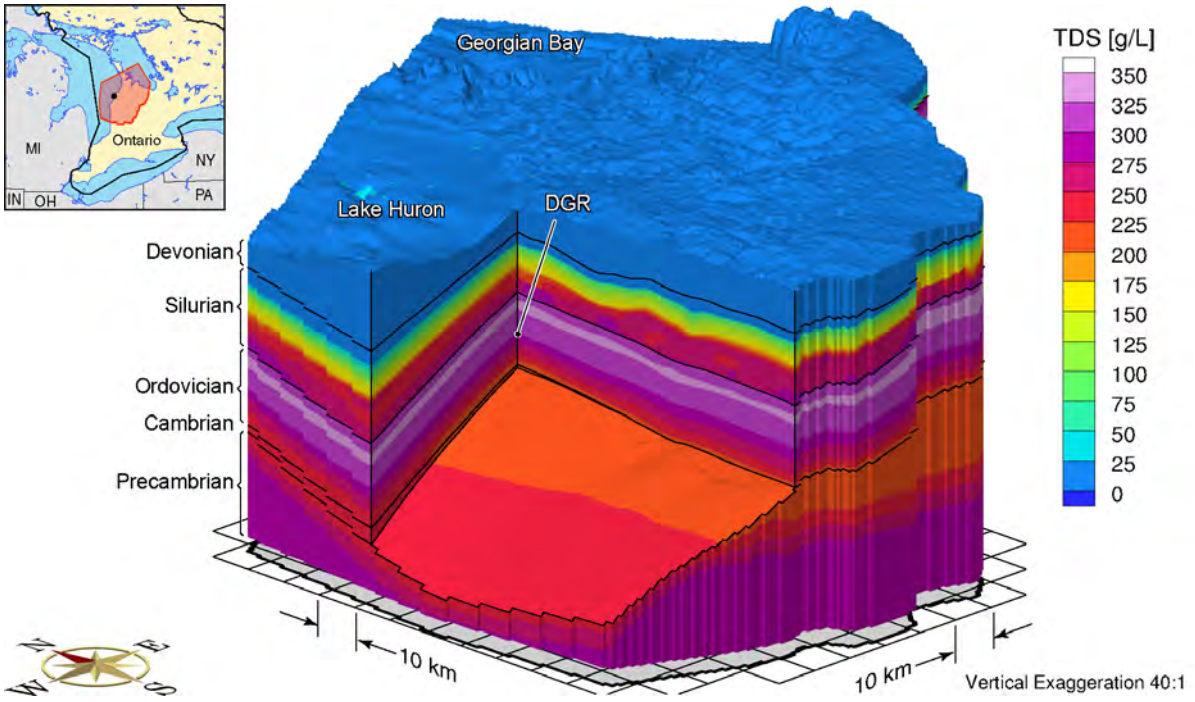

Figure D.6: Total Dissolved Solids Concentration for the Base Case Parameters and the Cambrian Anisotropy K_1 Aligned East-West

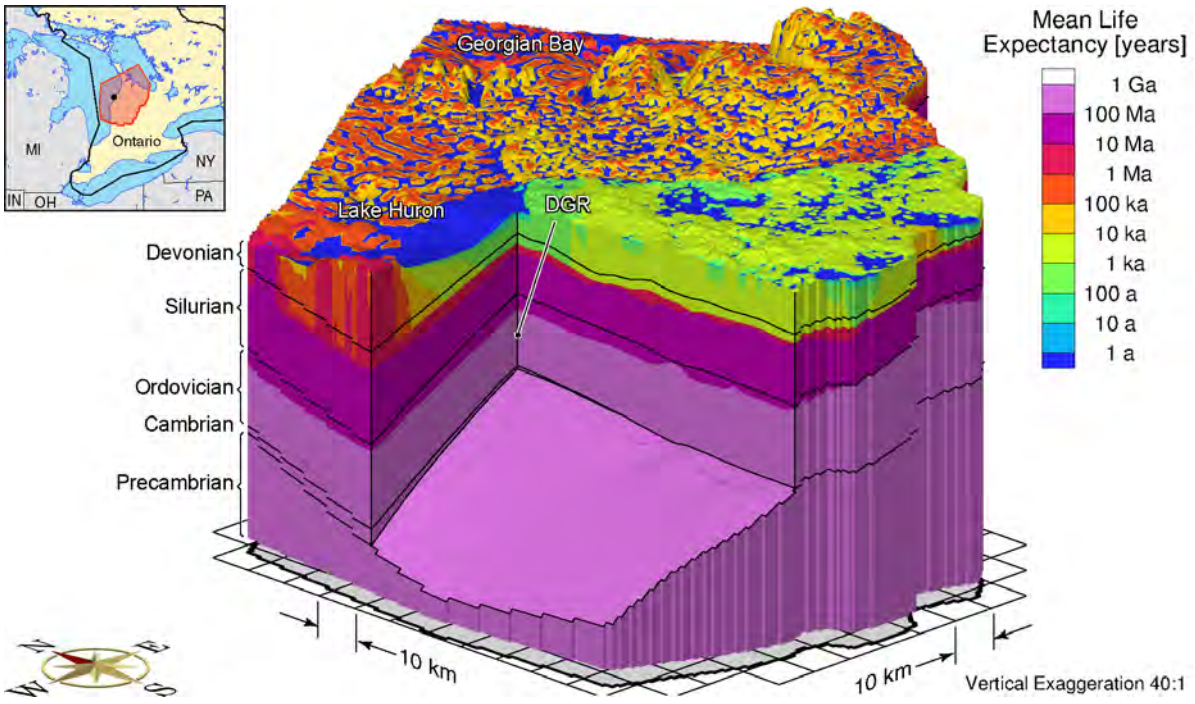

Figure D.7: Mean Life Expectancies for the Base Case Parameters and the Cambrian Anisotropy K_1 Aligned East-West

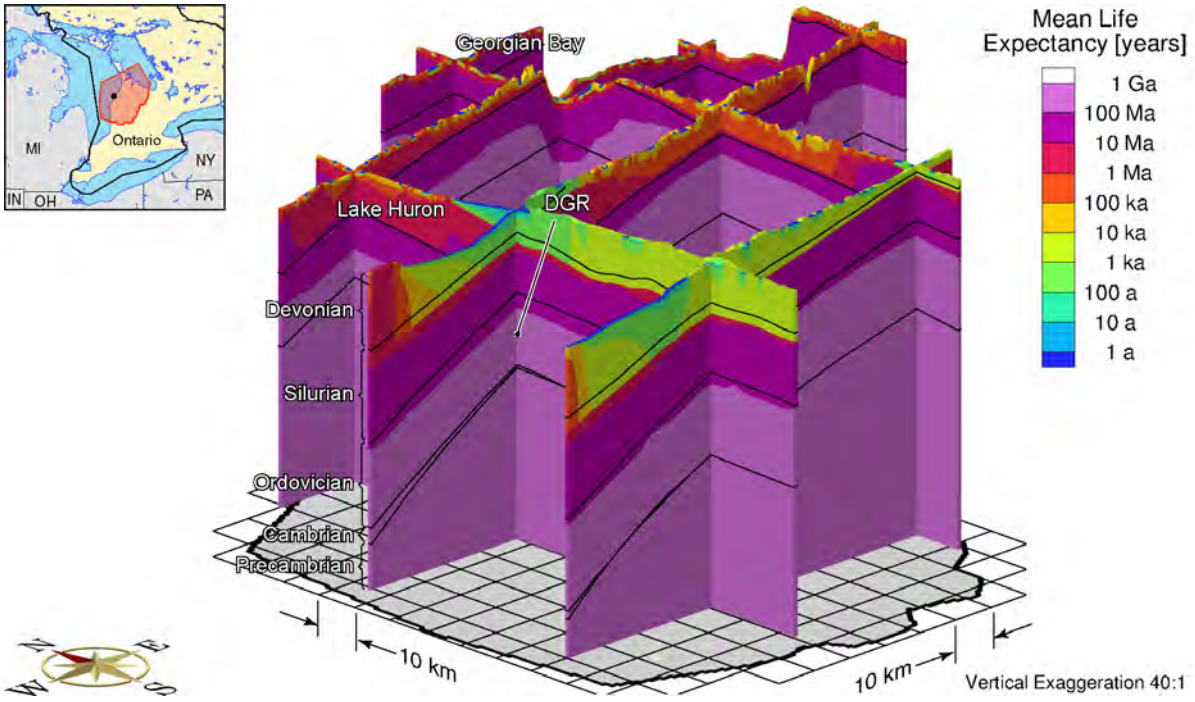

Figure D.8: Fence Diagram Showing the Mean Life Expectancies for the Base Case Parameters and the Cambrian Anisotropy K_1 Aligned East-West

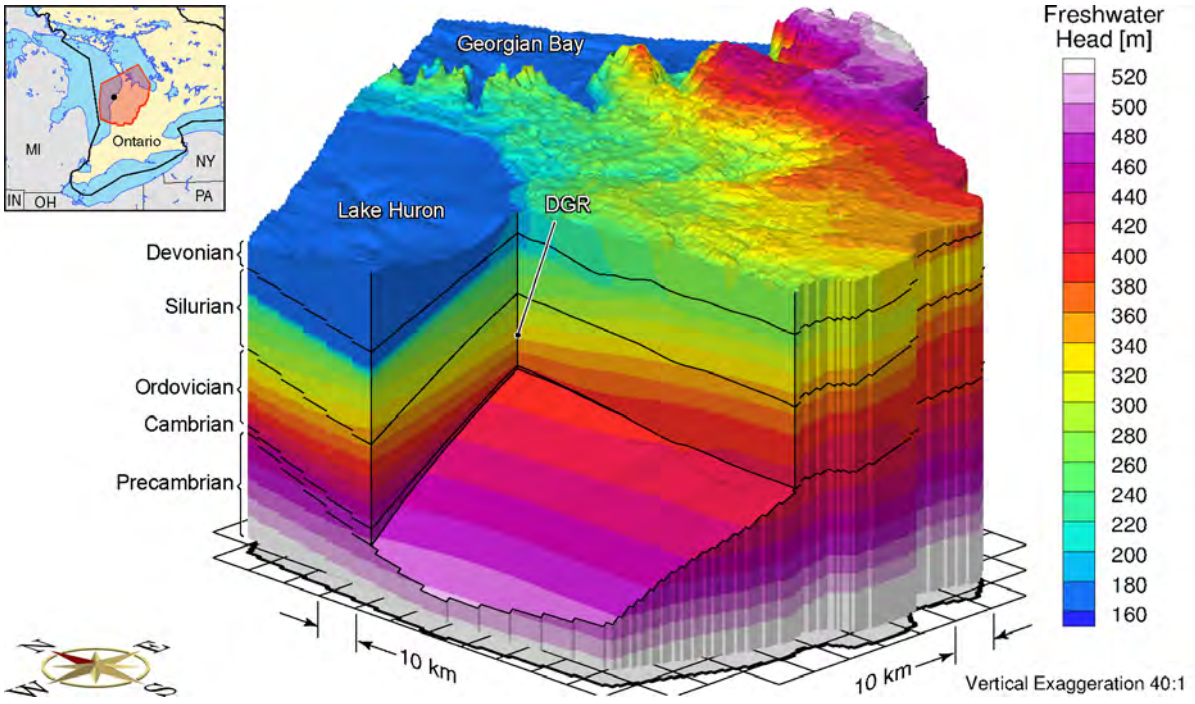

Figure D.9: Equivalent Freshwater Heads for the Base Case Parameters and the Cambrian Anisotropy K_1 Aligned North-South

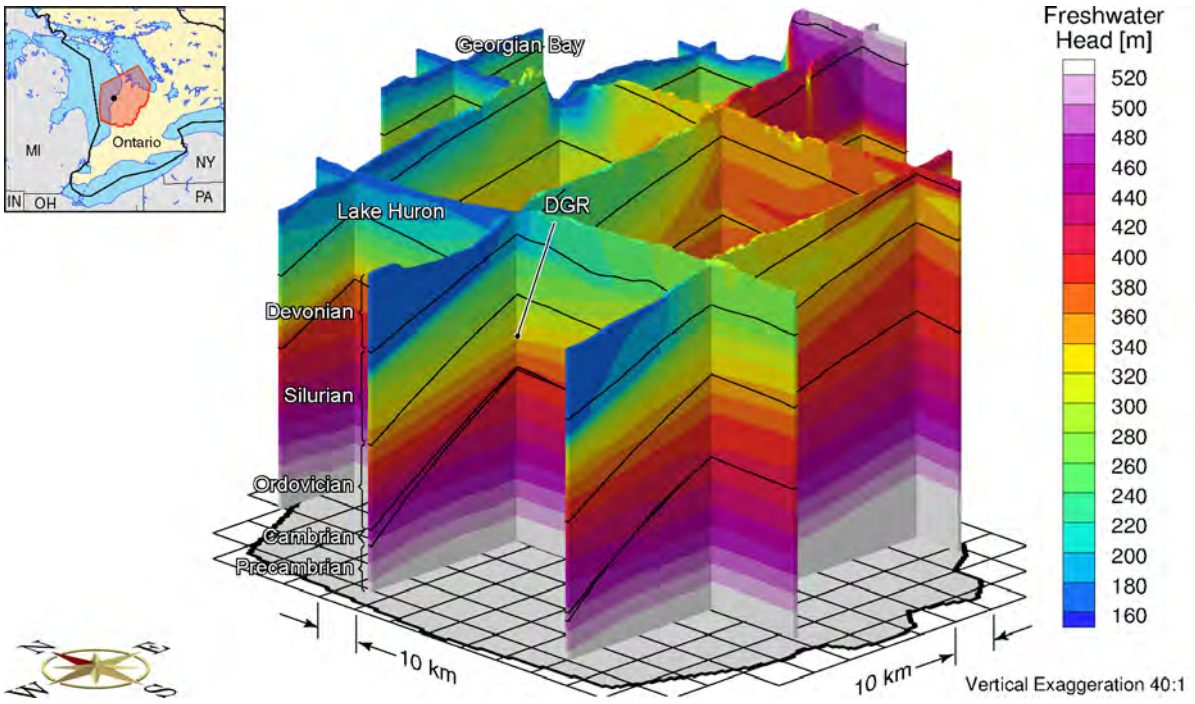

Figure D.10: Fence Diagram of Equivalent Freshwater Heads for the Base Case Parameters and the Cambrian Anisotropy K_1 Aligned North-South

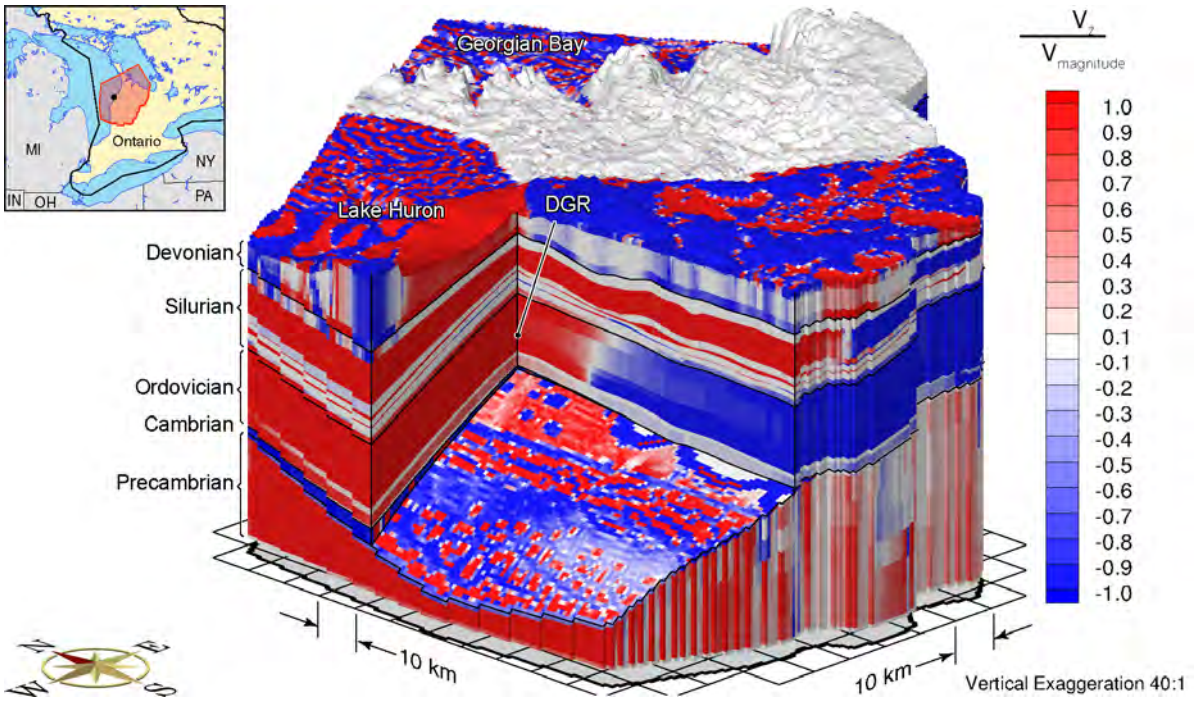

Figure D.11: Ratio of Vertical Velocity to the Velocity Magnitude for the Base Case Parameters and the Cambrian Anisotropy K_1 Aligned North-South

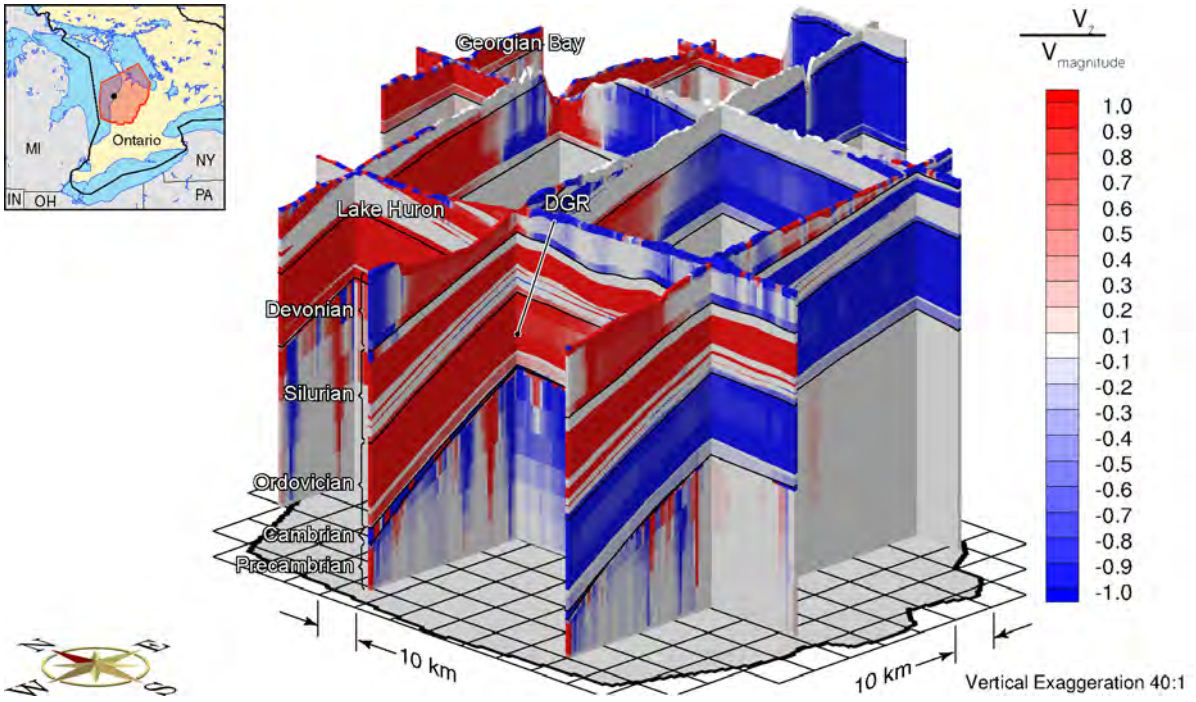

Figure D.12: Fence Diagram of the Ratio of Vertical Velocity to the Velocity Magnitude for the Base Case Parameters and the Cambrian Anisotropy K_1 Aligned North-South

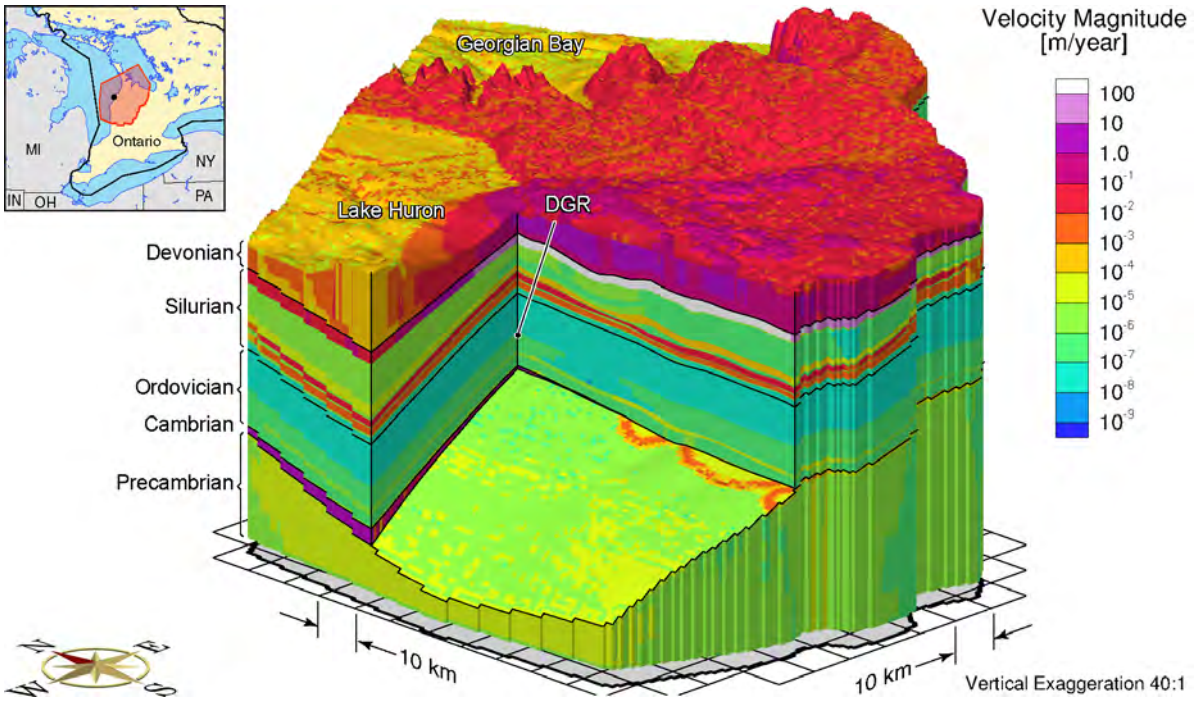

Figure D.13: Pore Water Velocity Magnitude for the Base Case Parameters and the Cambrian Anisotropy K_1 Aligned North-South

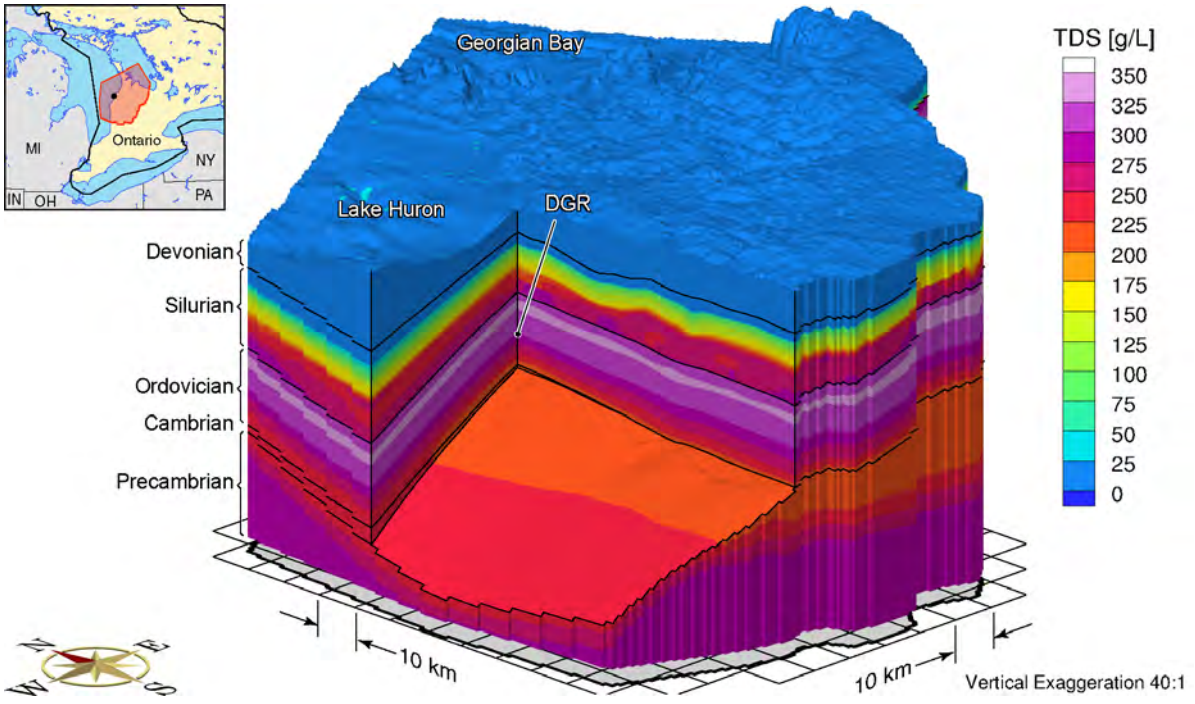

Figure D.14: Total Dissolved Solids Concentration for the Base Case Parameters and the Cambrian Anisotropy K_1 Aligned North-South

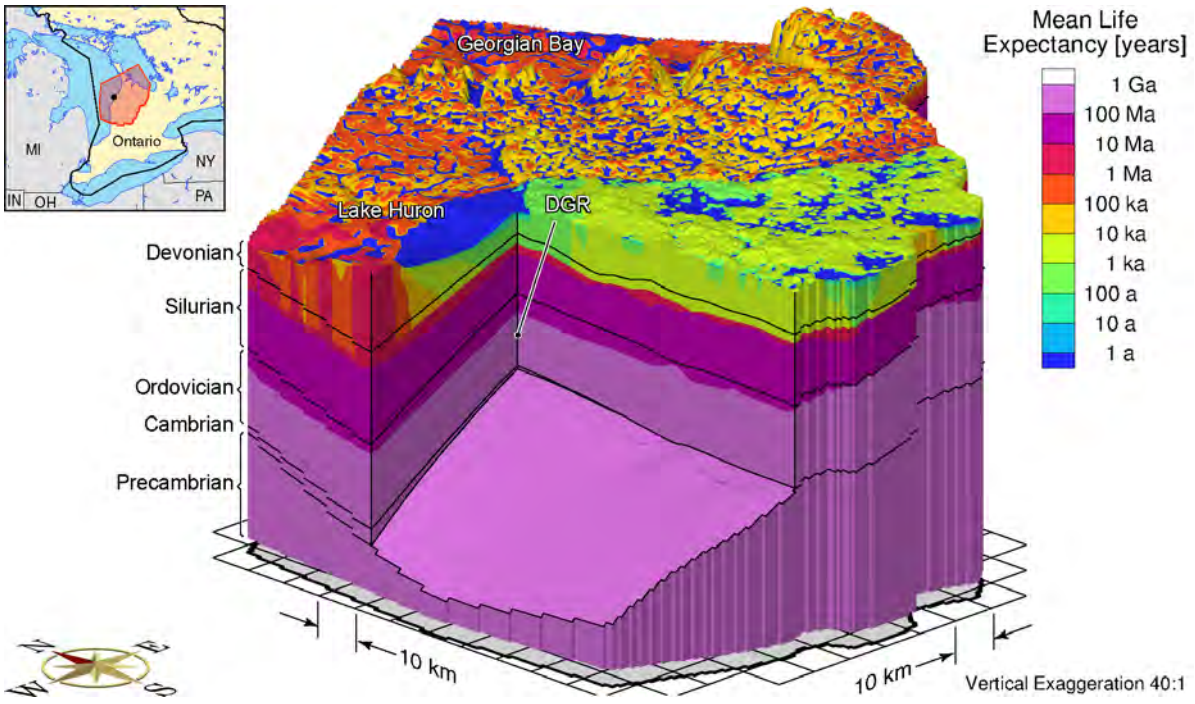

Figure D.15: Mean Life Expectancies for the Base Case Parameters and the Cambrian Anisotropy K_1 Aligned North-South

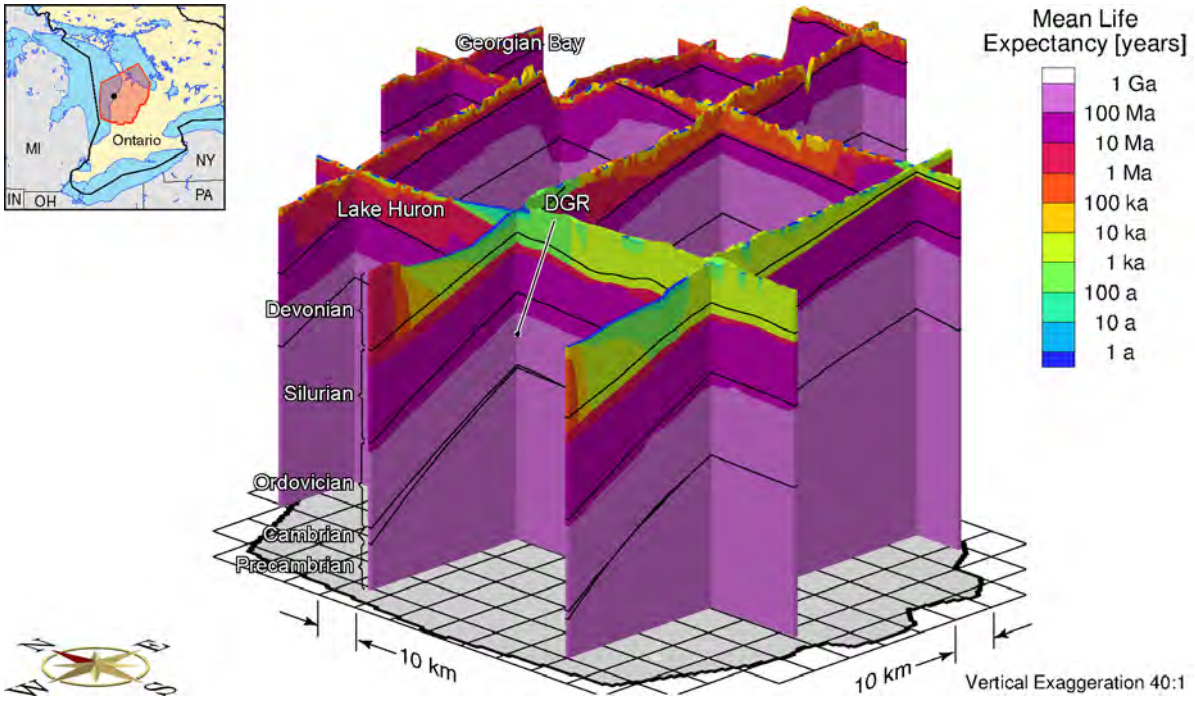

Figure D.16: Fence Diagram Showing the Mean Life Expectancies for the Base Case Parameters and the Cambrian Anisotropy K_1 Aligned North-South

THIS PAGE HAS BEEN LEFT BLANK INTENTIONALLY

APPENDIX E: ANALYSIS OF THE PRECAMBRIAN

LIST OF FIGURES

Page

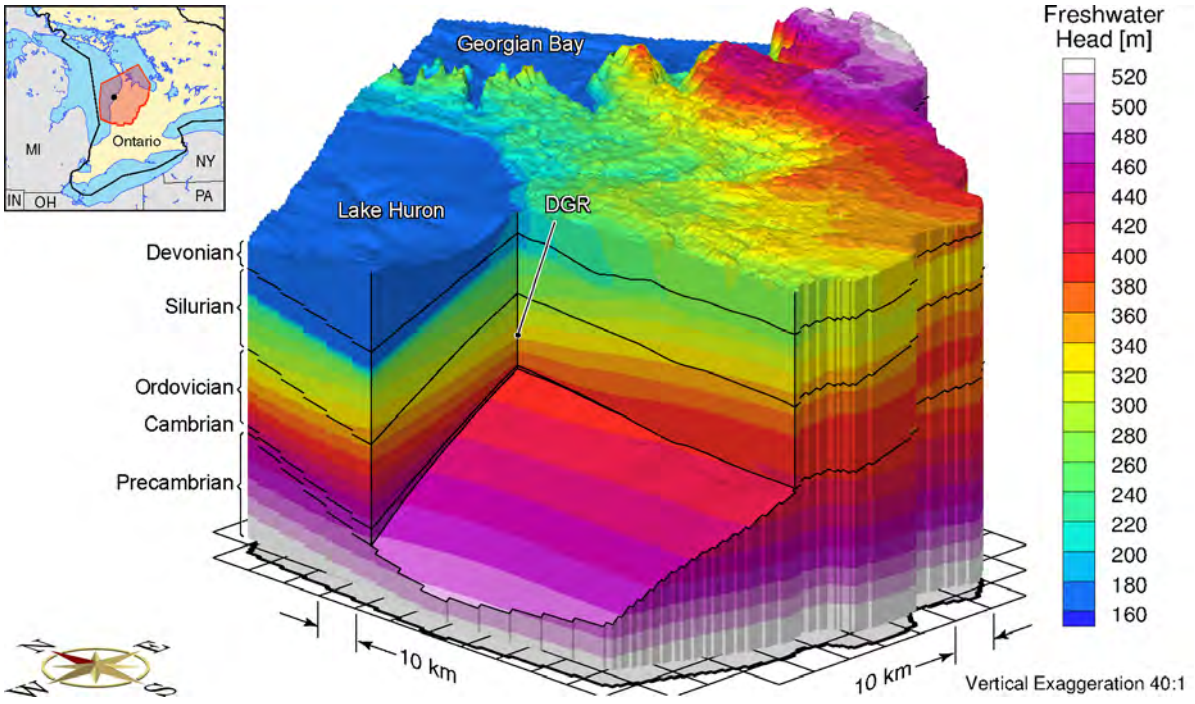

Figure E.1: Block Cut View of Freshwater Heads at an Equilibrium Time of 1 Ma for the High Conductivity Upper Precambrian Scenario

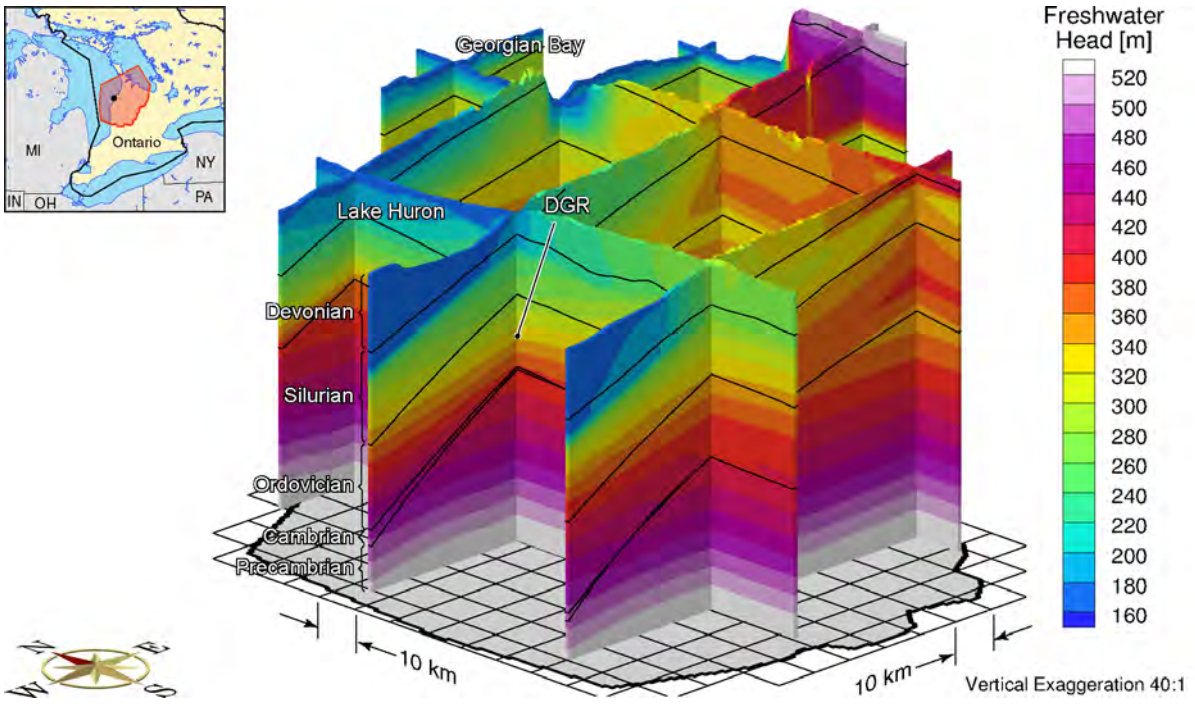

Figure E.2: Fence View of Freshwater Heads at an Equilibrium Time of 1 Ma for the High Conductivity Upper Precambrian Scenario

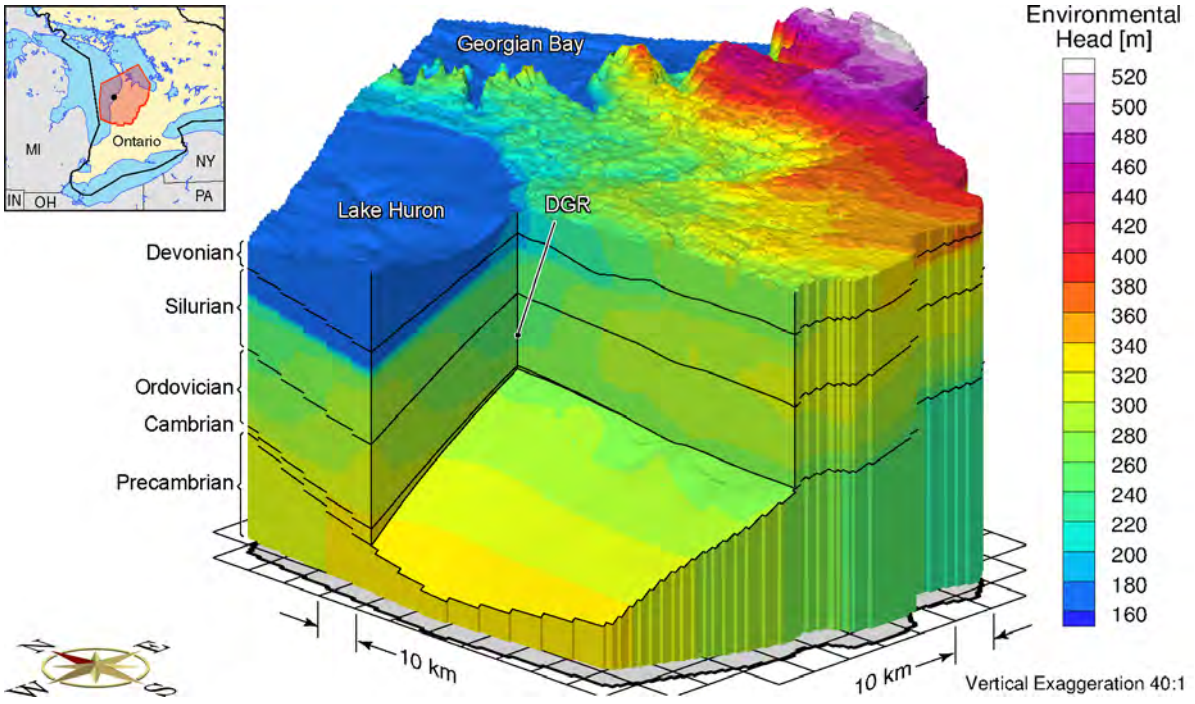

Figure E.3: Block Cut View of Environmental Heads at an Equilibrium Time of 1 Ma for the High Conductivity Upper Precambrian Scenario

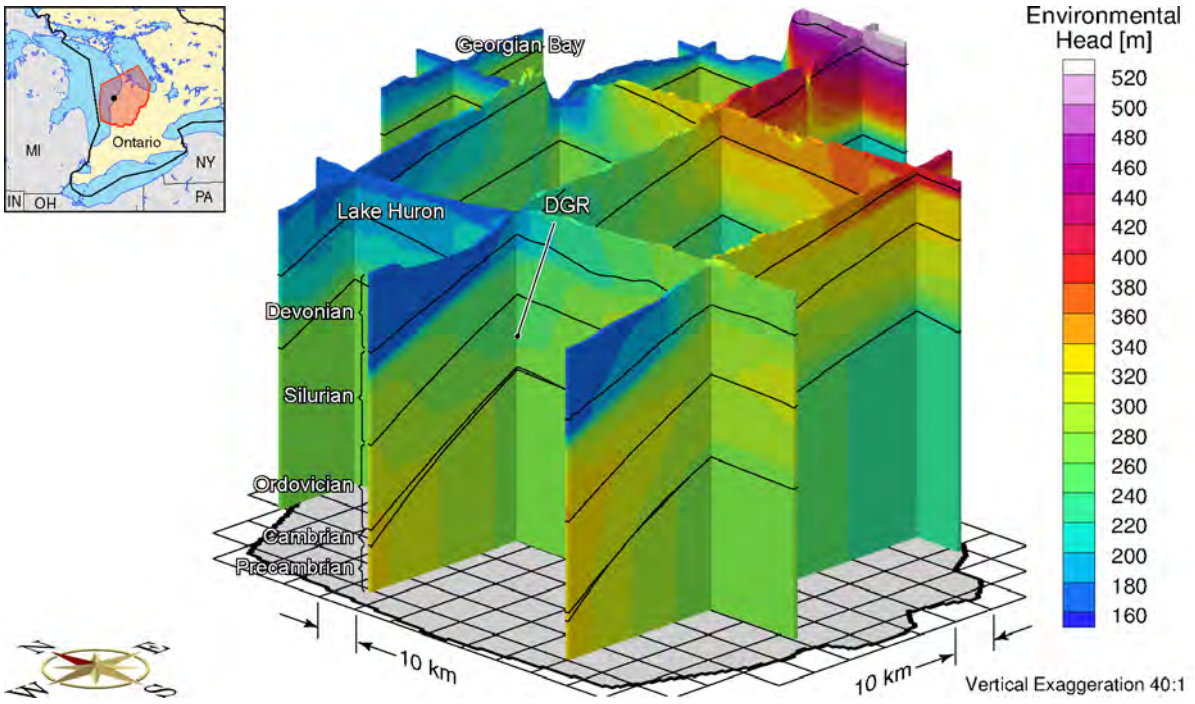

Figure E.4: Fence View of Environmental Heads at an Equilibrium Time of 1 Ma for the High Conductivity Upper Precambrian Scenario

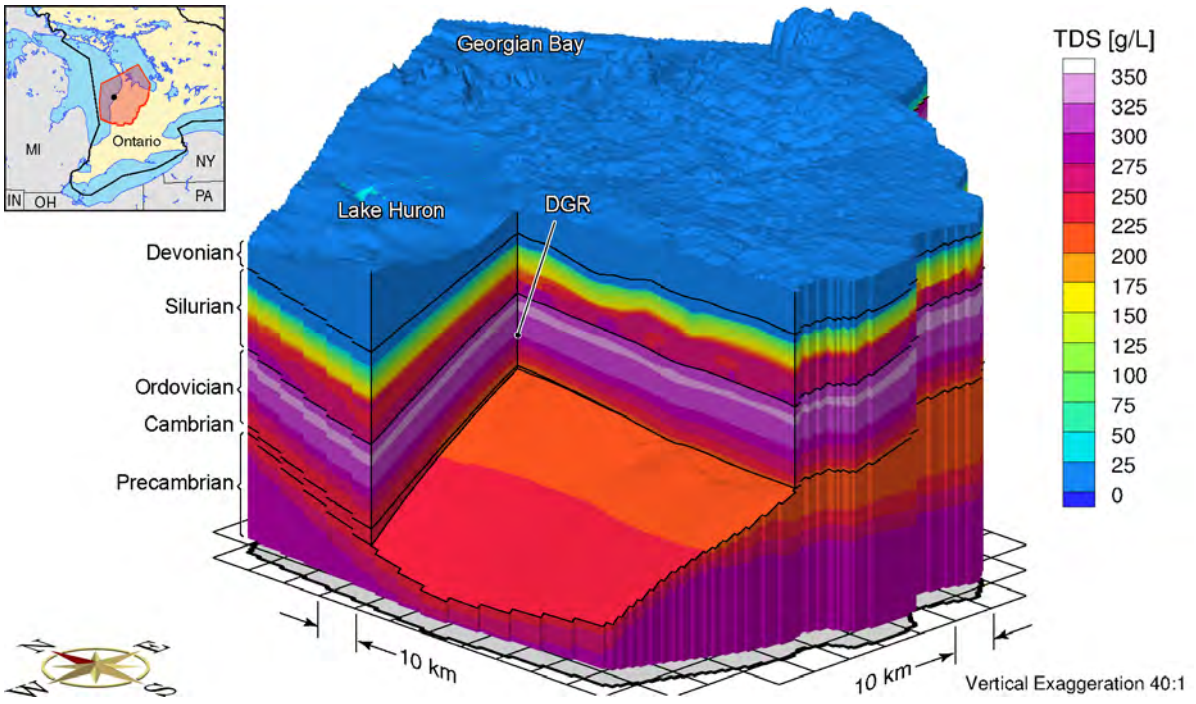

Figure E.5: Block Cut View of High Conductivity Upper Precambrian Total Dissolved Solids at an Equilibrium Time of 1 Ma for the High Conductivity Upper Precambrian Scenario

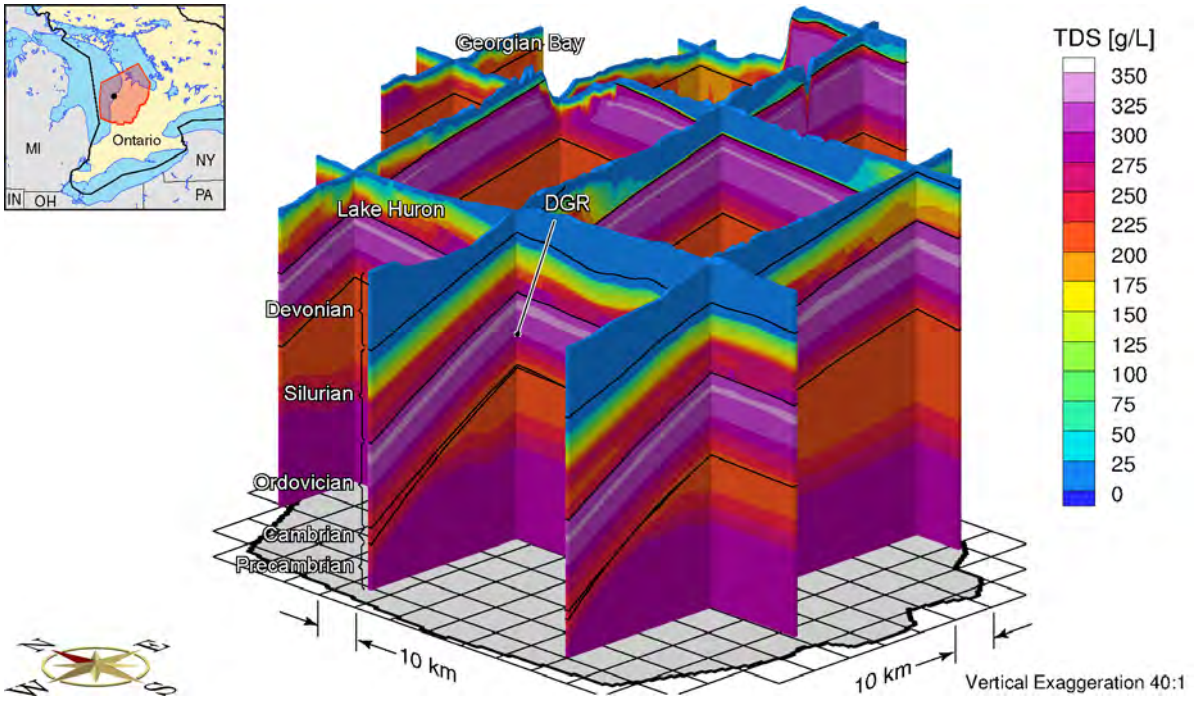

Figure E.6: Fence View of Total Dissolved Solids at an Equilibrium Time of 1 Ma for the High Conductivity Upper Precambrian Scenario

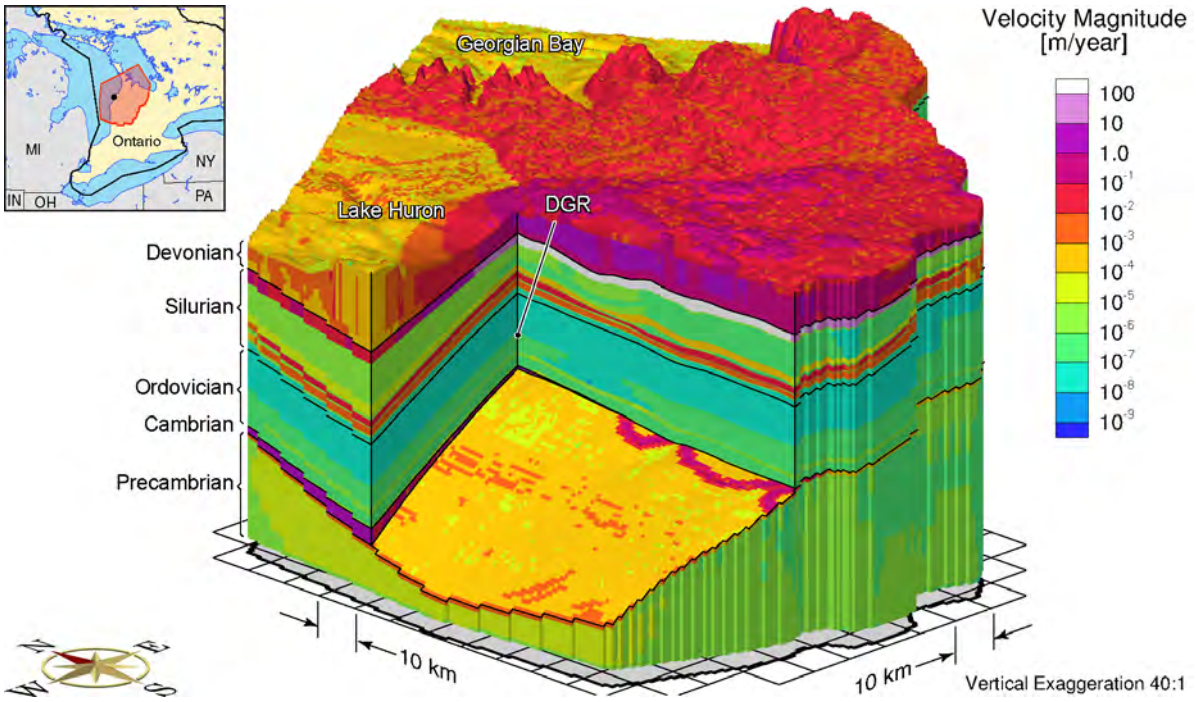

Figure E.7: Block Cut View of Pore Velocity Magnitude at an Equilibrium Time of 1 Ma for the High Conductivity Upper Precambrian Scenario

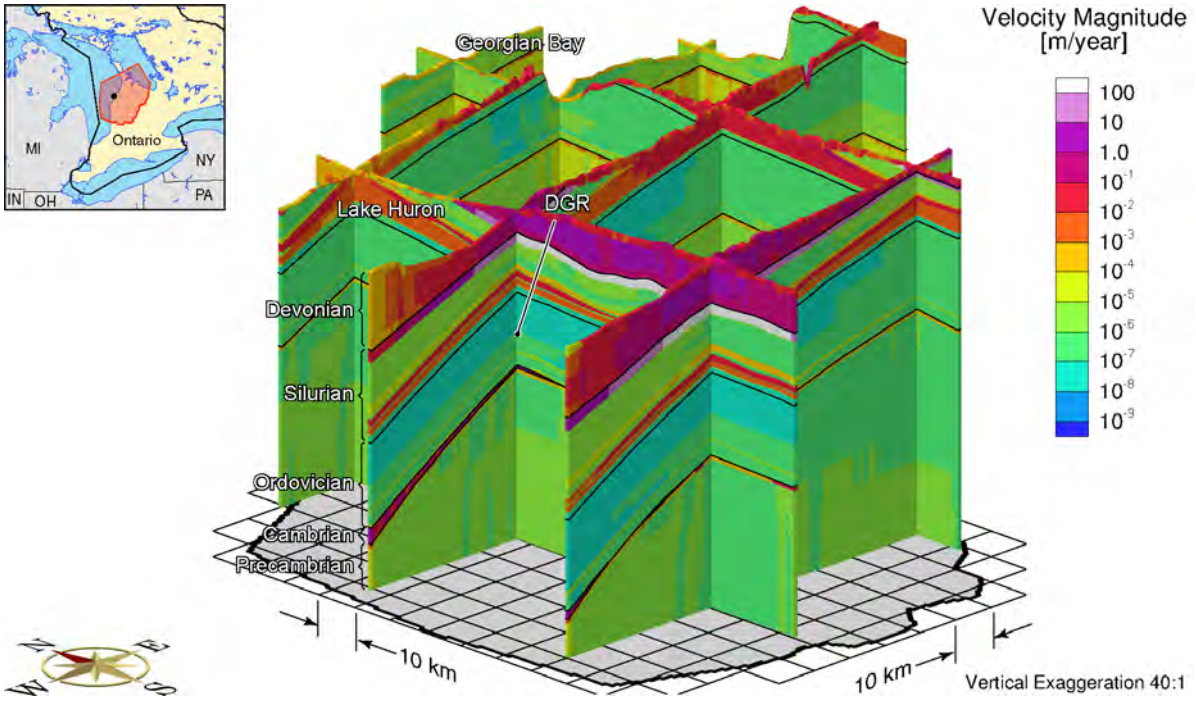

Figure E.8: Fence View of Pore Velocity Magnitude at an Equilibrium Time of 1 Ma for the High Conductivity Upper Precambrian Scenario

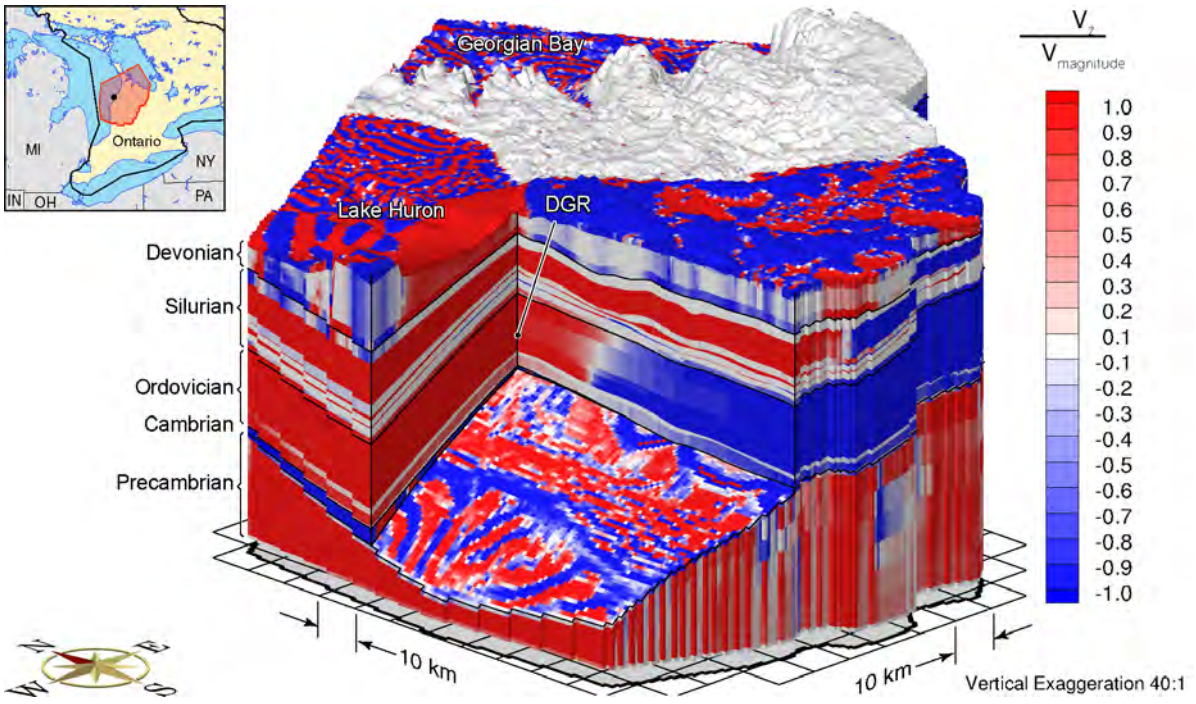

Figure E.9: Block Cut View of Ratio of Vertical Pore Velocity to Pore Velocity Magnitude at an Equilibrium Time of 1 Ma for the High Conductivity Upper Precambrian Scenario

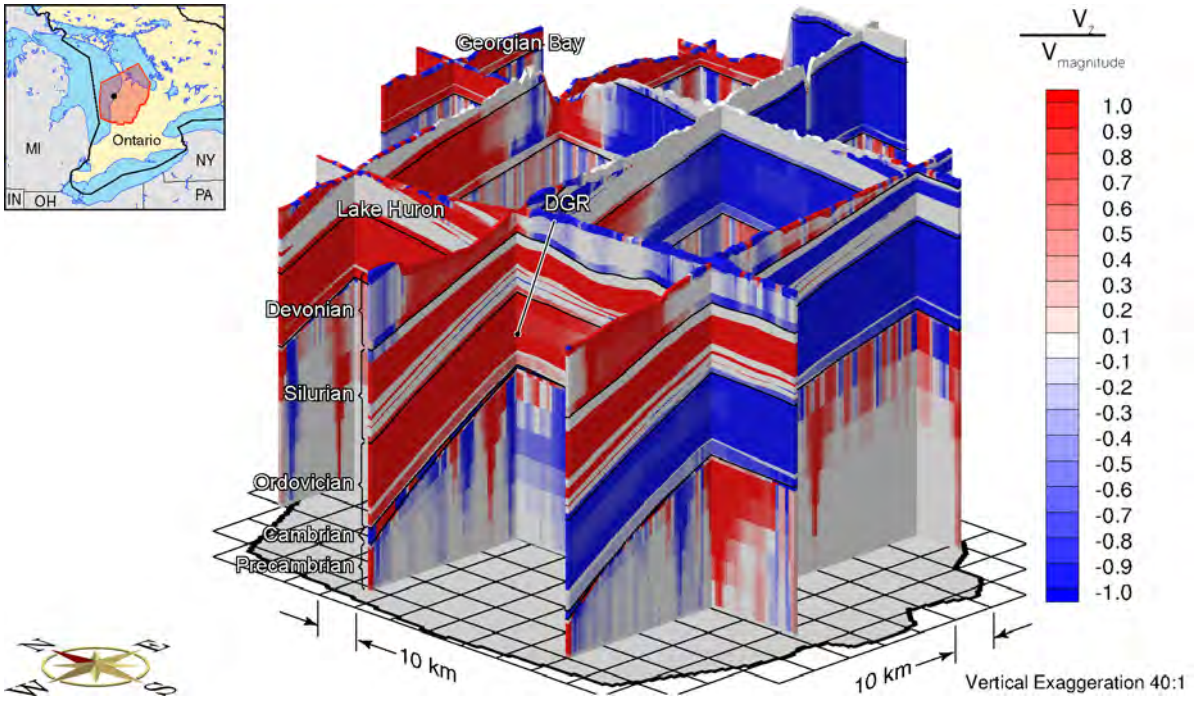

Figure E.10: Fence View of Ratio of Vertical Pore Velocity to Pore Velocity Magnitude at an Equilibrium Time of 1 Ma for the High Conductivity Upper Precambrian Scenario

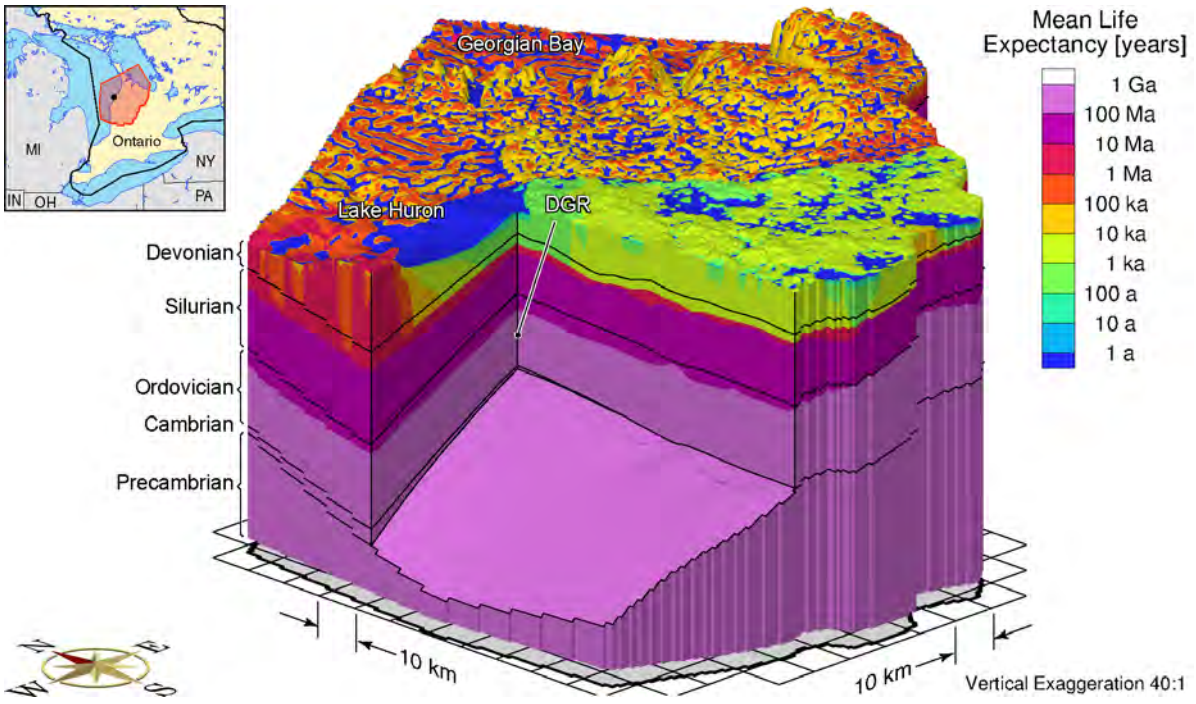

Figure E.11: Block Cut View of Mean Life Expectancy at an Equilibrium Time of 1 Ma for the High Conductivity Upper Precambrian Scenario

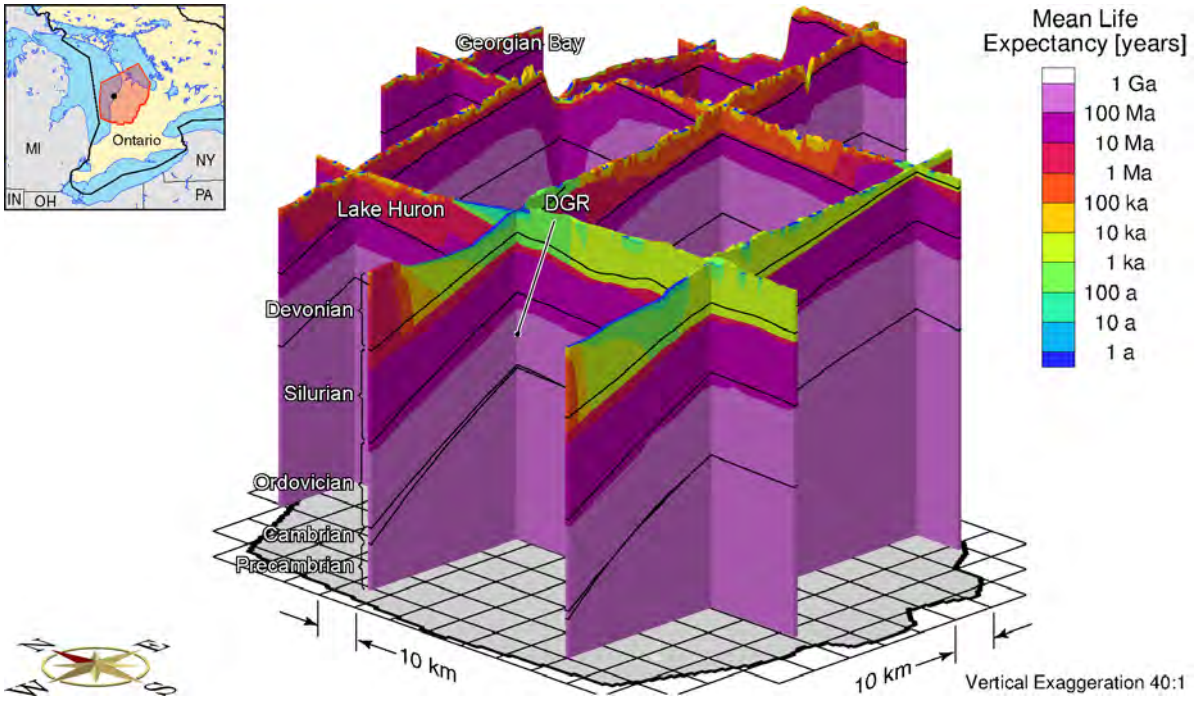

Figure E.12: Fence View of Mean Life Expectancy at an Equilibrium Time of 1 Ma for the High Conductivity Upper Precambrian Scenario

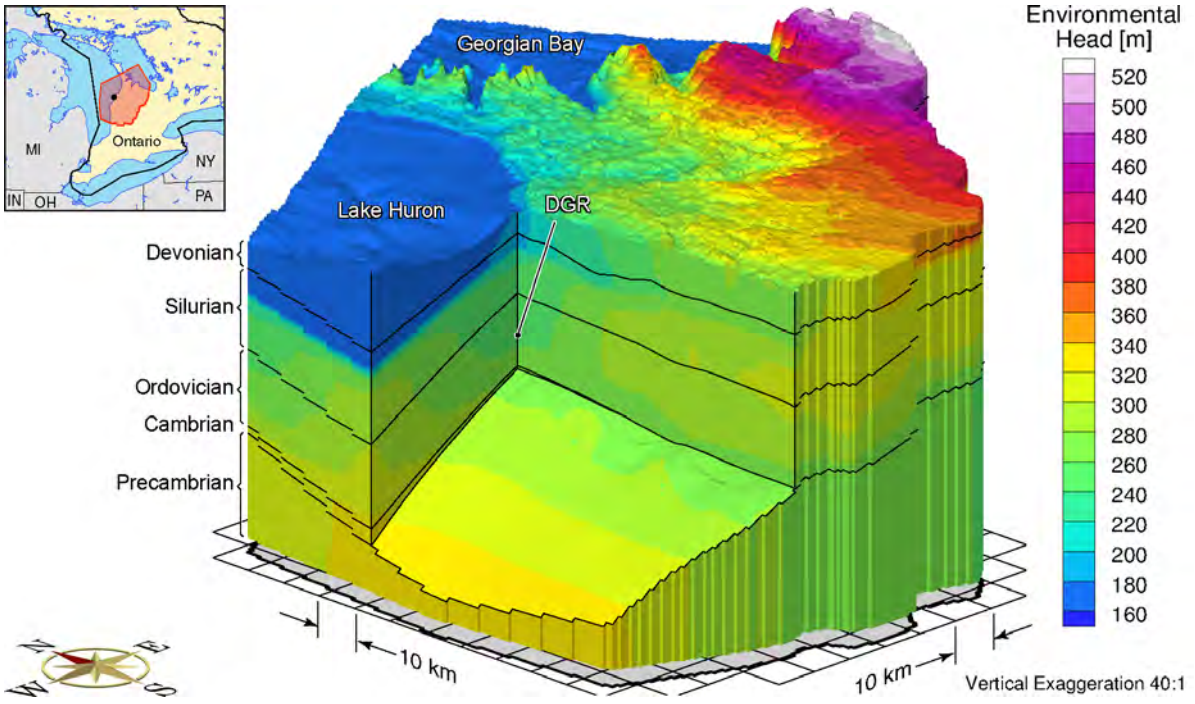

Figure E.13: Environmental Heads for the Base Case Parameters and a Uniform Hydraulic Conductivity for the Precambrian of 1×10^{-12} m/s

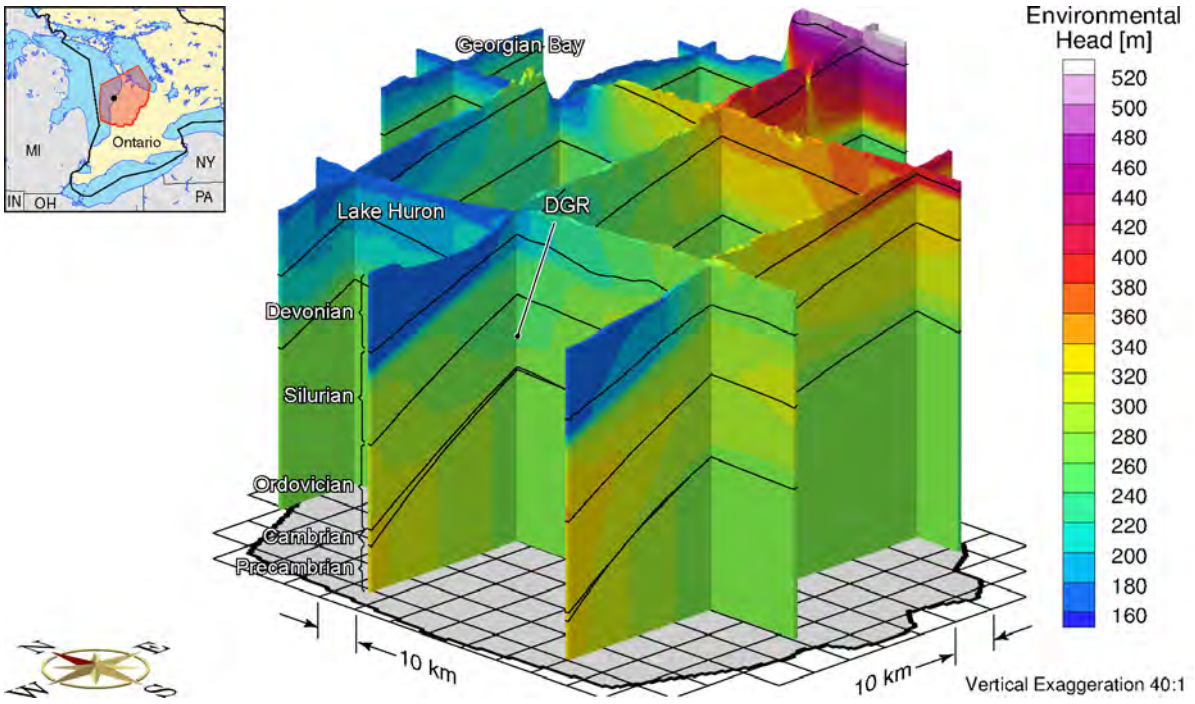

Figure E.14: Fence Diagram of Environmental Heads for the Base Case Parameters and a Uniform Hydraulic Conductivity for the Precambrian of 1×10^{-12} m/s

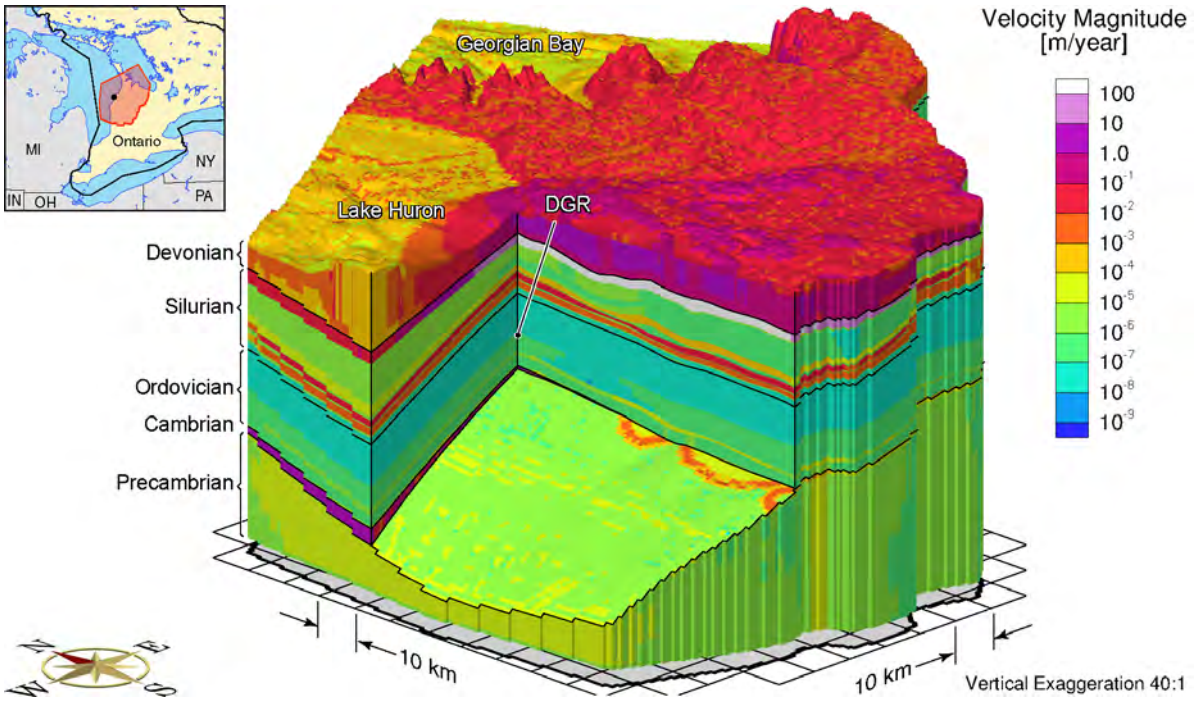

Figure E.15: Pore Water Velocity Magnitude for the Base Case Parameters and a Uniform Hydraulic Conductivity for the Precambrian of 1×10^{-12} m/s

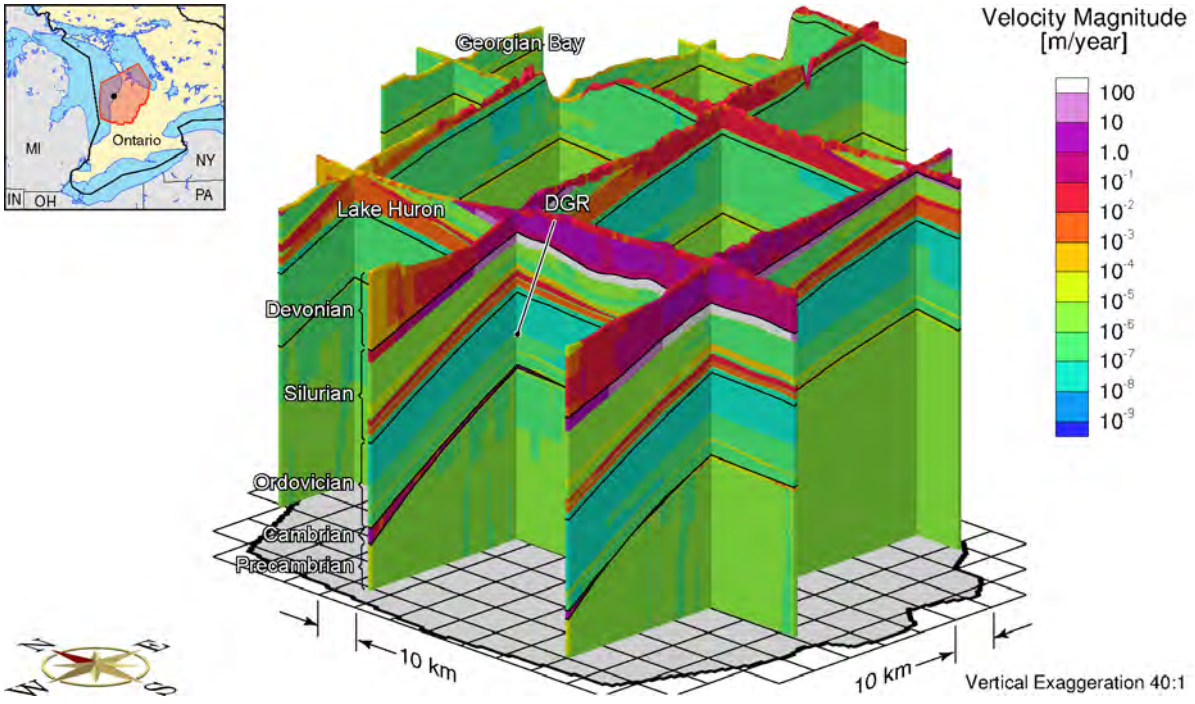

Figure E.16: Fence Diagram of Pore Water Velocity Magnitude for the Base Case Parameters and a Uniform Hydraulic Conductivity for the Precambrian of 1×10^{-12} m/s

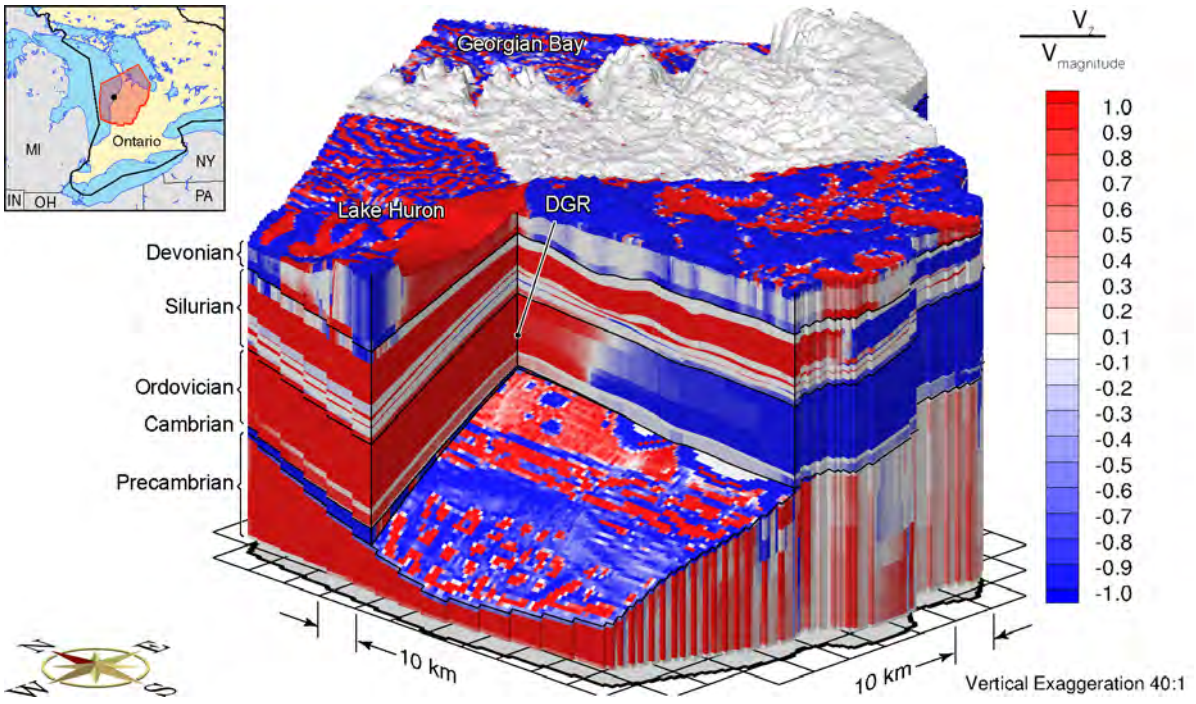

Figure E.17: Ratio of Vertical Velocity to the Velocity Magnitude for the Base Case Parameters and a Uniform Hydraulic Conductivity for the Precambrian of 1×10^{-12} m/s

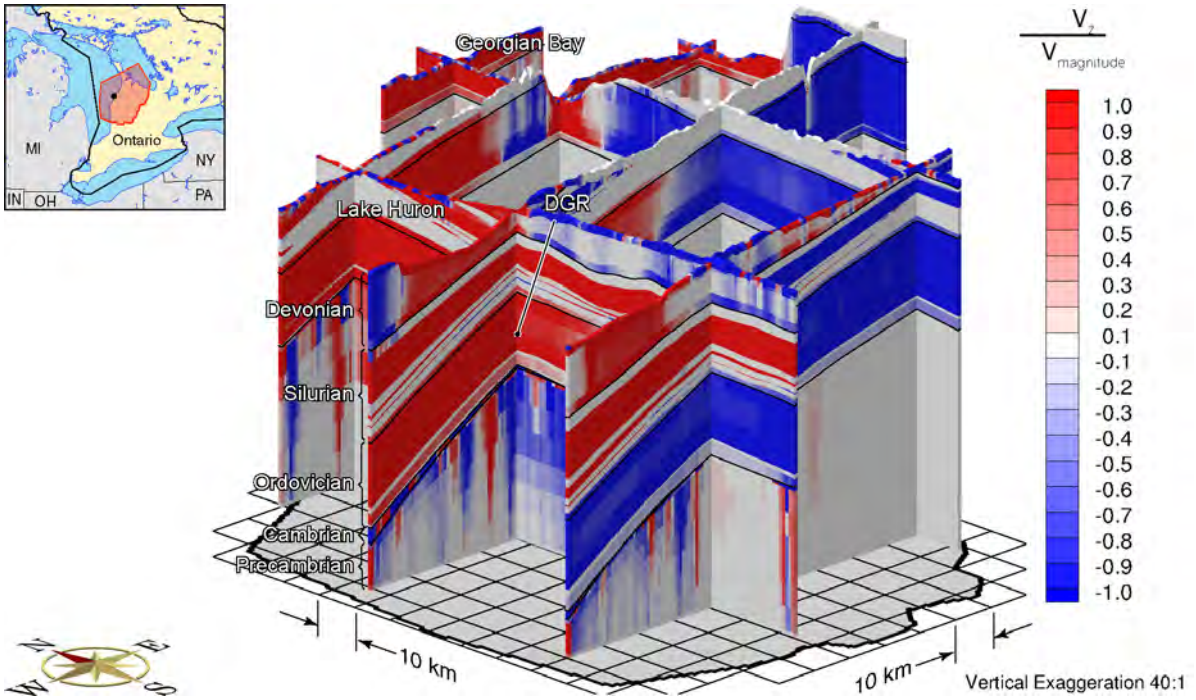

Figure E.18: Fence Diagram of the Ratio of Vertical Velocity to the Velocity Magnitude for the Base Case Parameters and a Uniform Hydraulic Conductivity for the Precambrian of 1×10^{-12} m/s

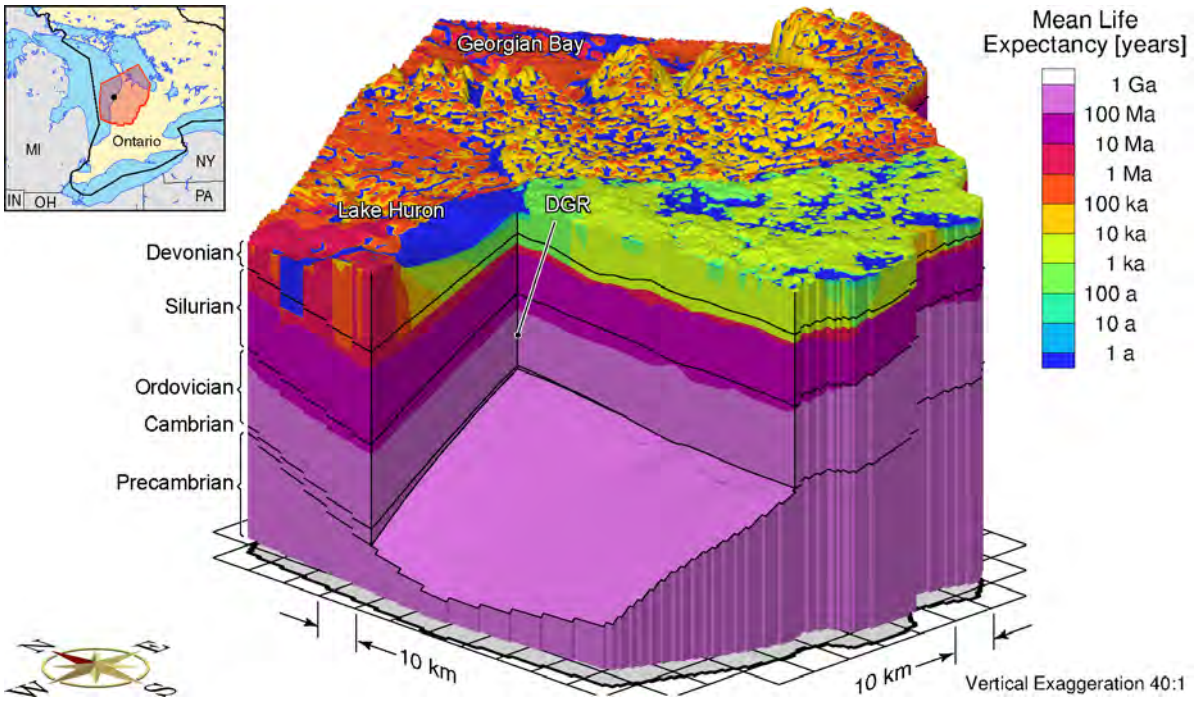

Figure E.19: Mean Life Expectancies for the Base Case Parameters and a Uniform Hydraulic Conductivity for the Precambrian of 1×10^{-12} m/s

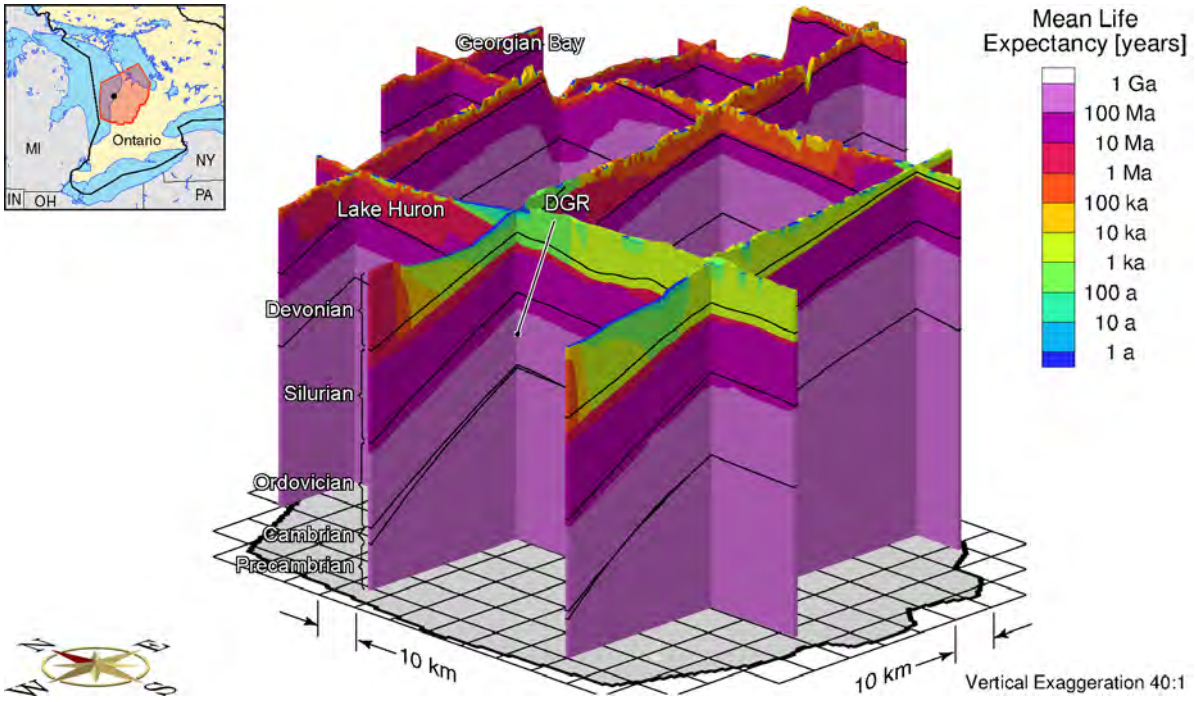

Figure E.20: Fence Diagram Showing the Mean Life Expectancies for the Base Case Parameters and a Uniform Hydraulic Conductivity for the Precambrian of 1×10^{-12} m/s

THIS PAGE HAS BEEN LEFT BLANK INTENTIONALLY

APPENDIX F: PALEOHYDROGEOLOGIC SIMULATIONS

LIST OF FIGURES

Page

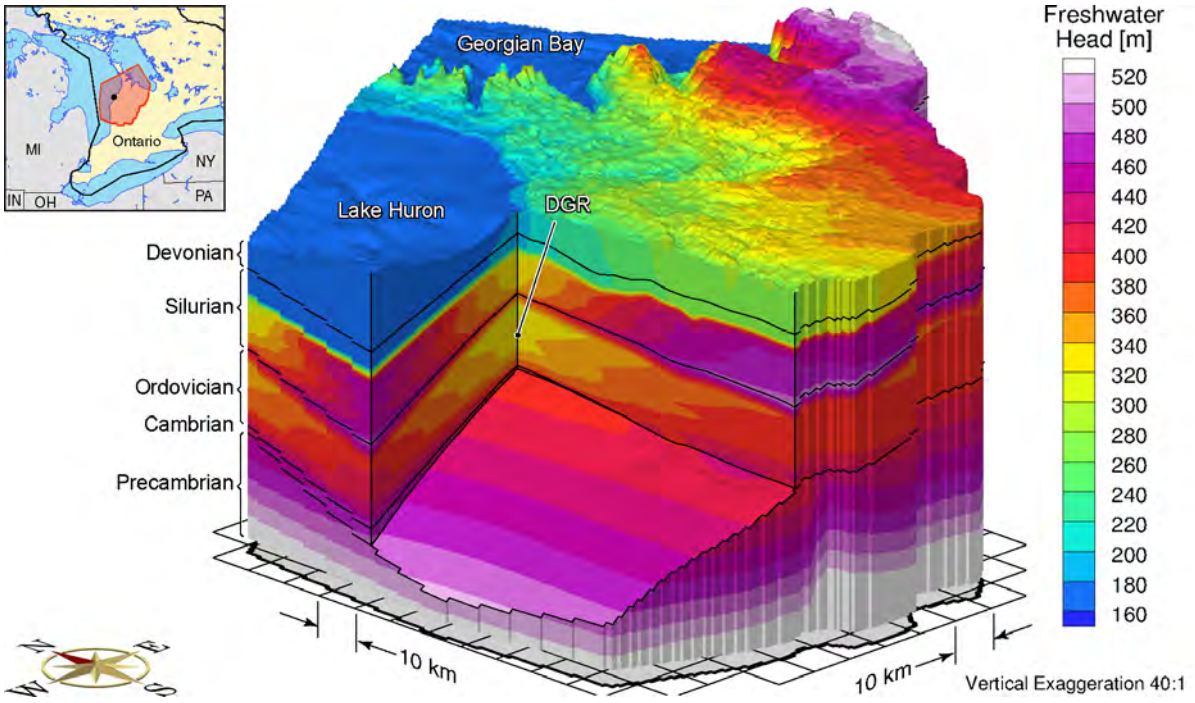

Figure F.1: Block Cut View of Freshwater Heads at Present for the Base Case Parameters

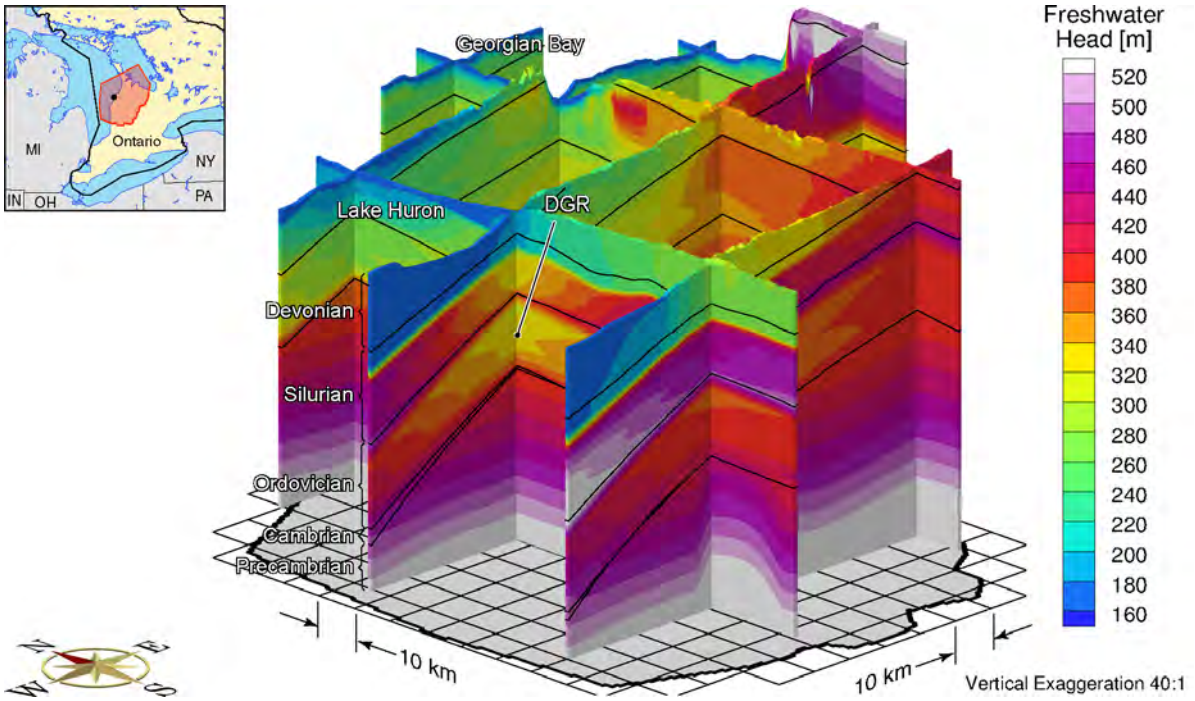

Figure F.2: Fence View of Freshwater Heads at Present for the Base Case Parameters

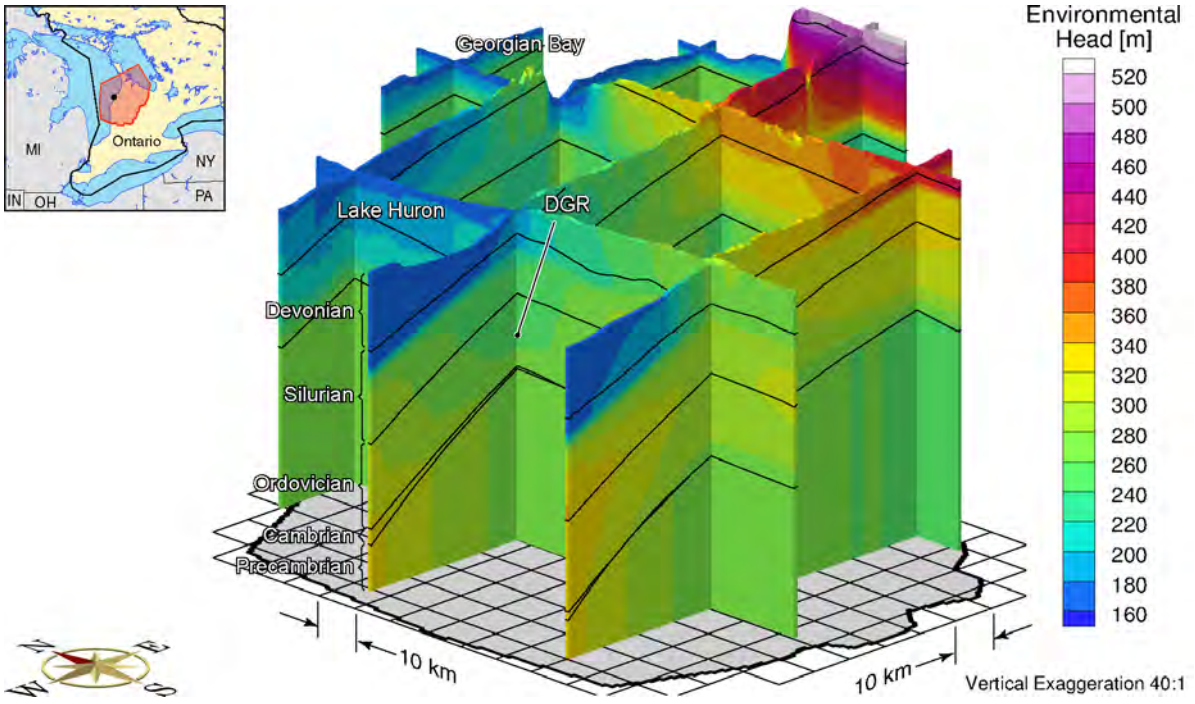

Figure F.3: Fence View of Environmental Heads at 90ka before Present for the Base Case Parameters

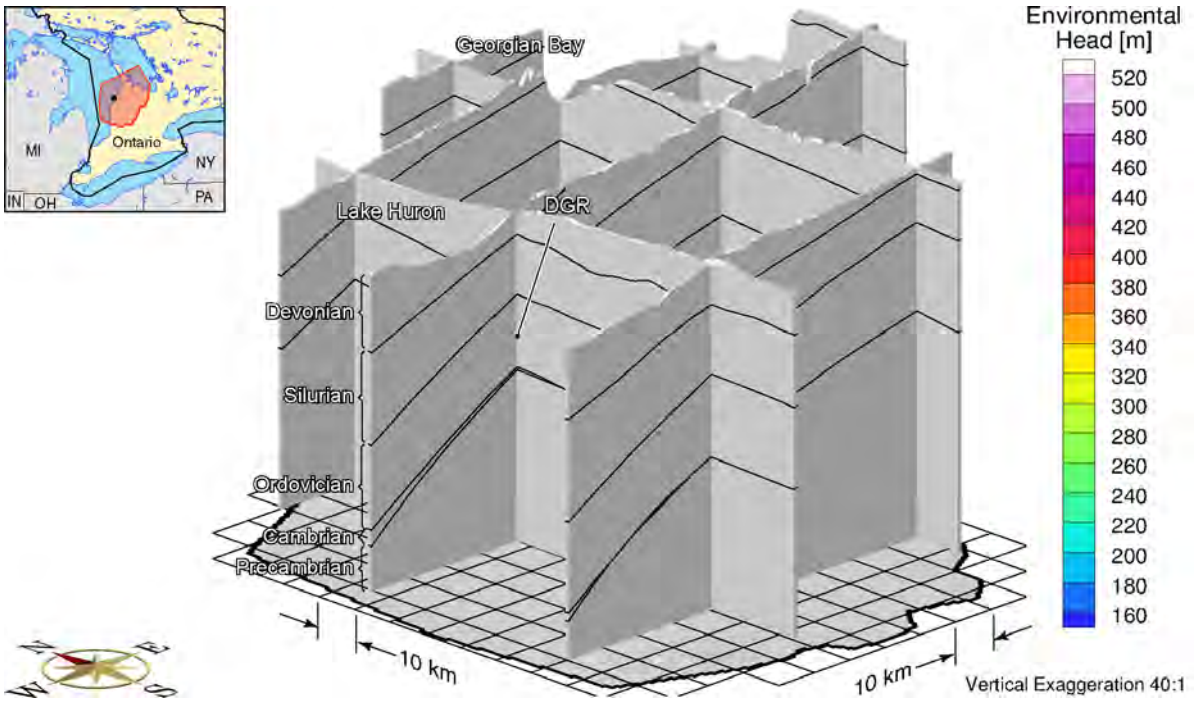

Figure F.4: Fence View of Environmental Heads at 60ka before Present for the Base Case Parameters

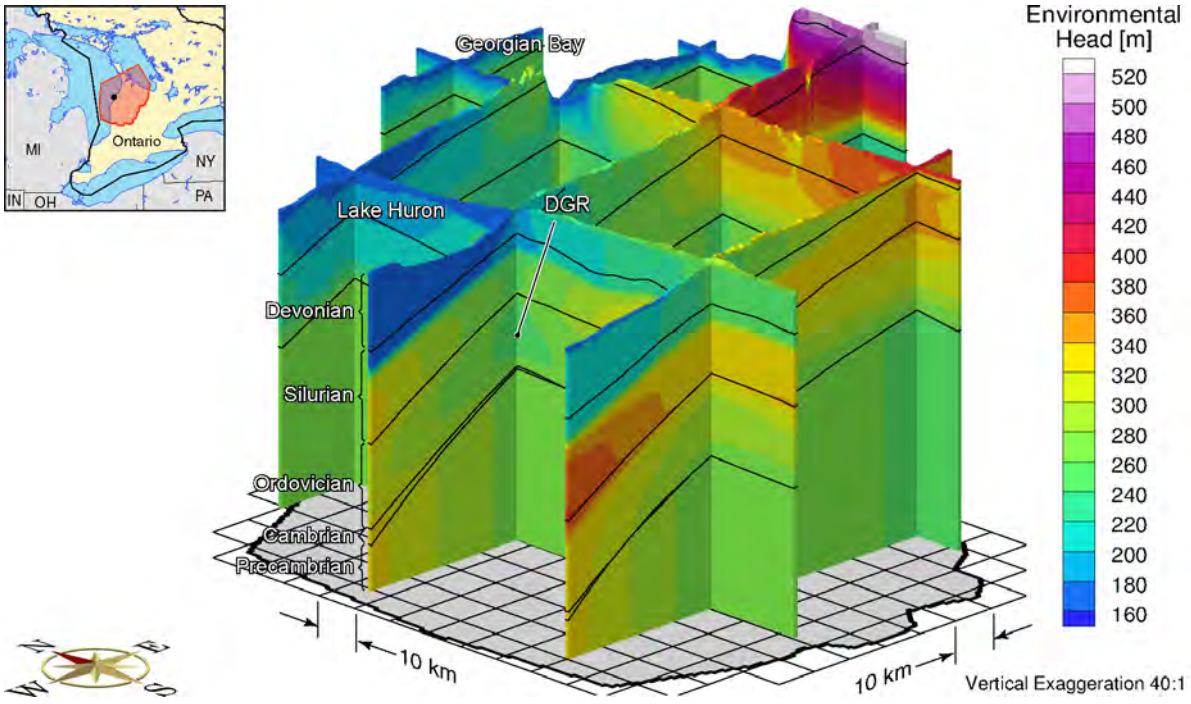

Figure F.5: Fence View of Environmental Heads at 30ka before Present for the Base Case Parameters

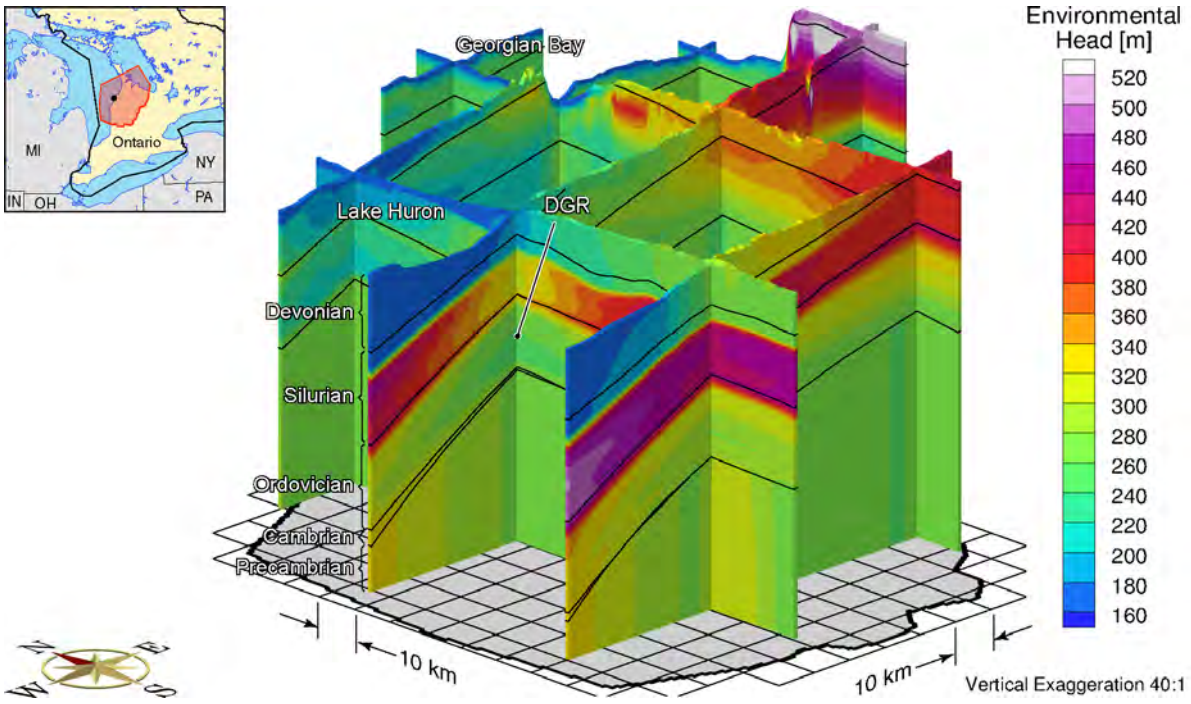

Figure F.6: Fence View of Environmental Heads at the Present for the Base Case Parameters

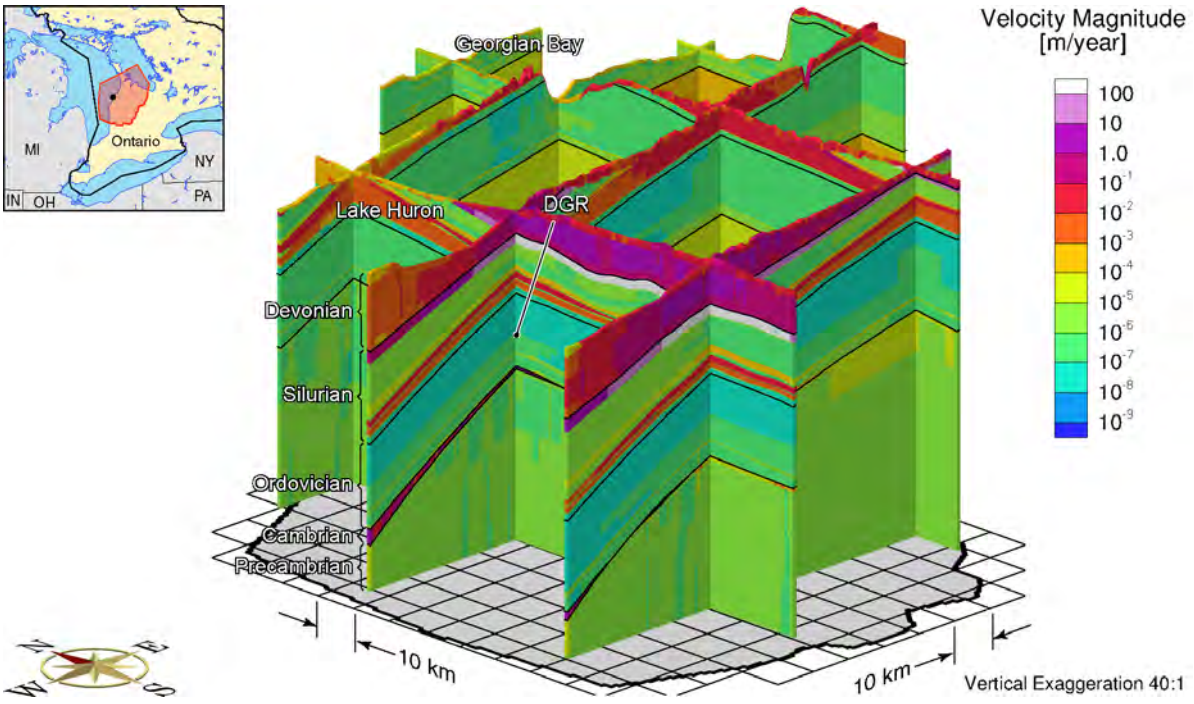

Figure F.7: Fence View of Pore Velocity Magnitude at 90ka before Present for the Base Case Parameters

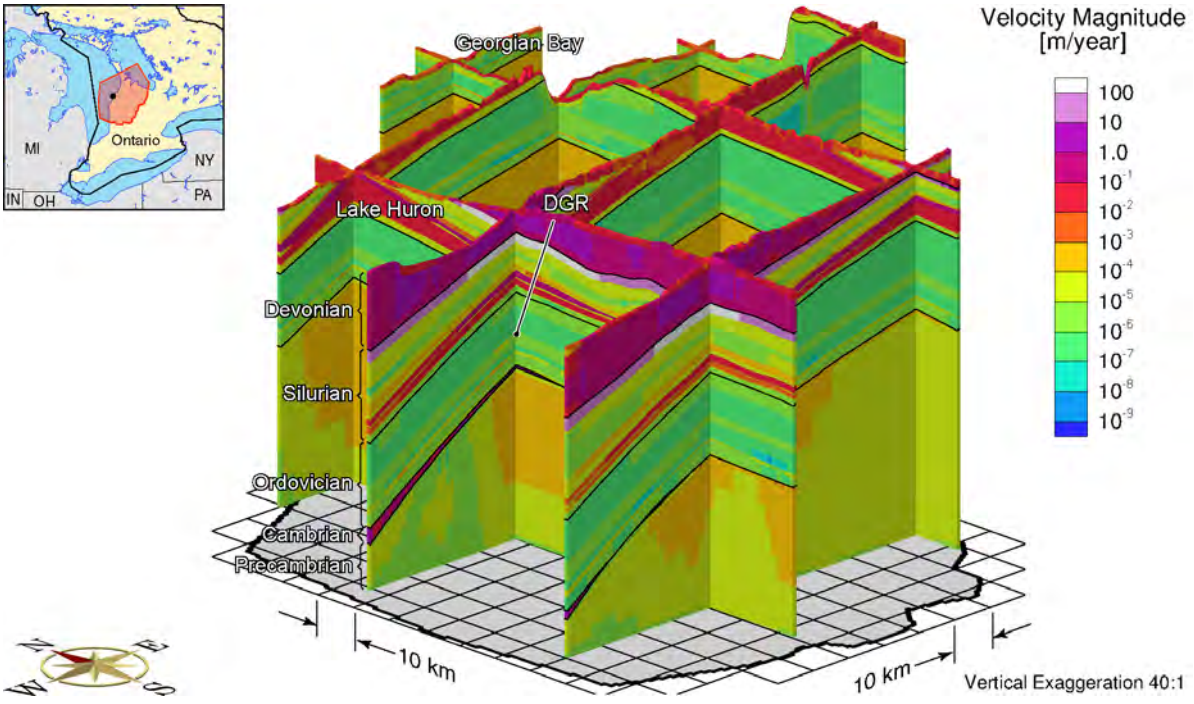

Figure F.8: Fence View of Pore Velocity Magnitude at 60ka before Present for the Base Case Parameters

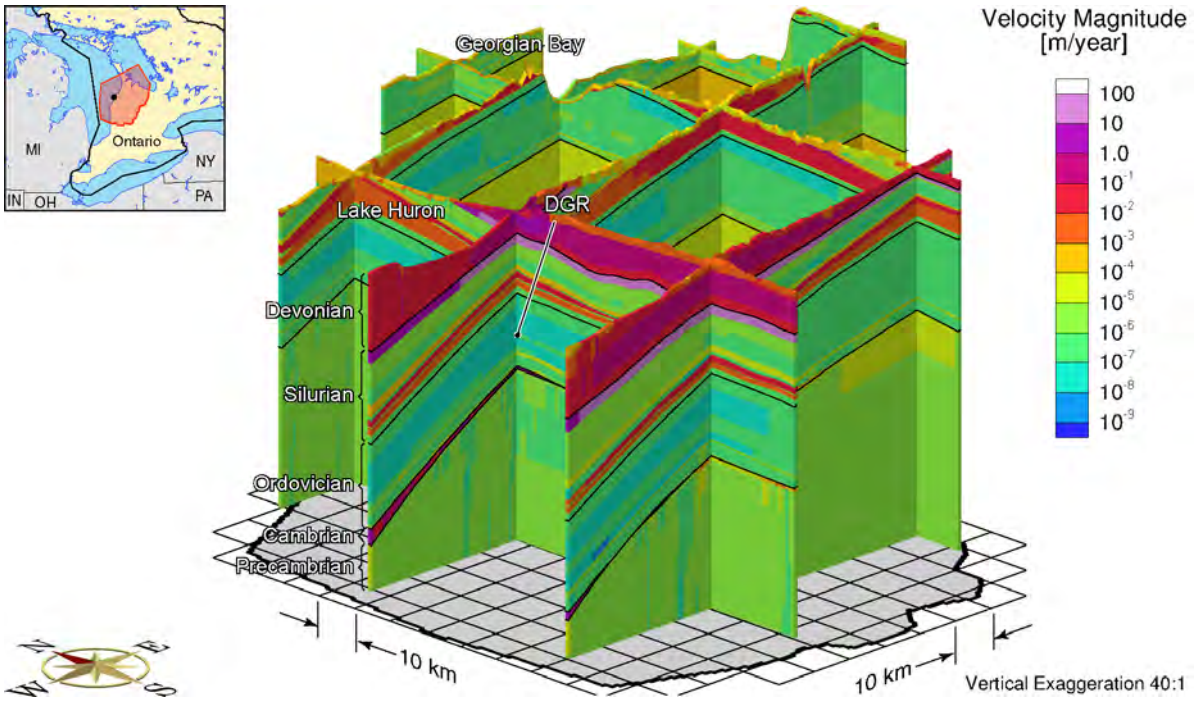

Figure F.9: Fence View of Pore Velocity Magnitude at 30ka before Present for the Base Case Parameters

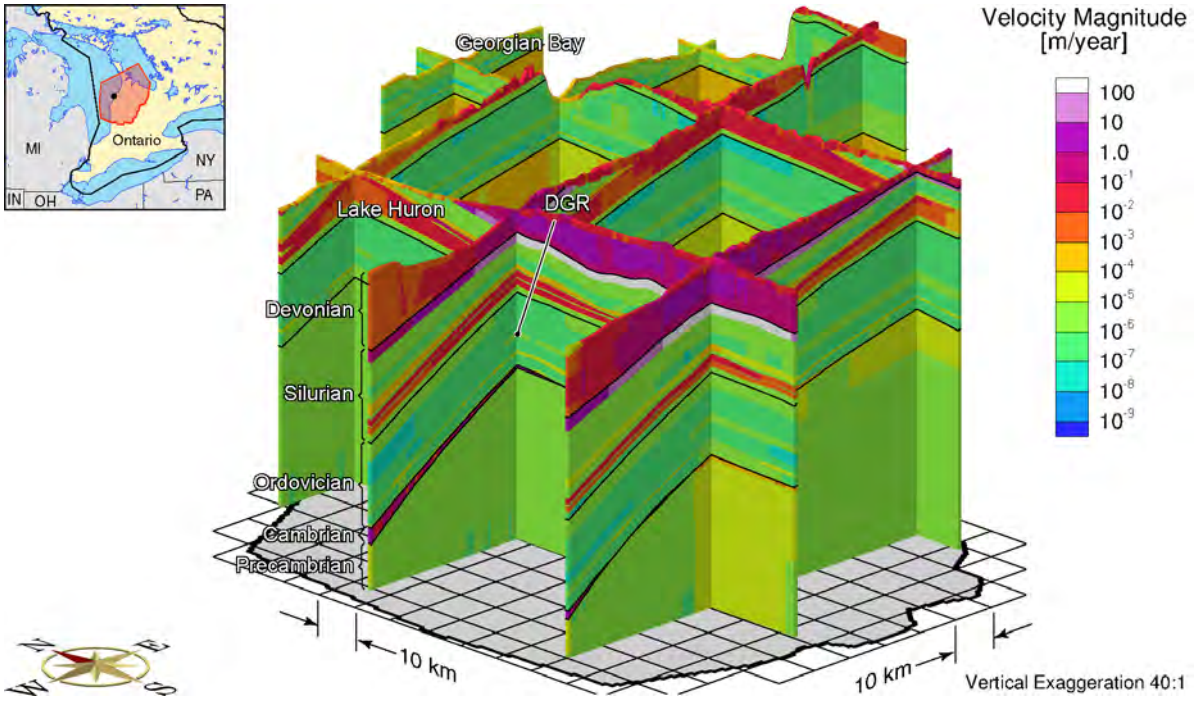

Figure F.10: Fence View of Pore Velocity Magnitude at Present for the Base Case Parameters

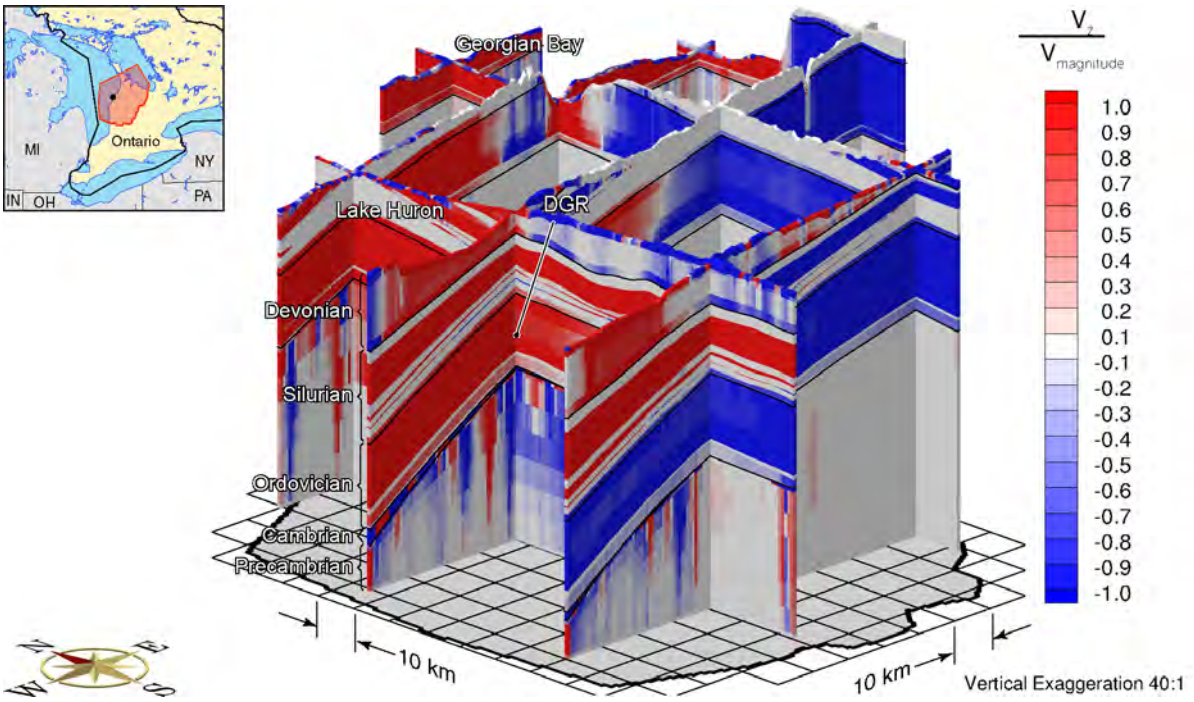

Figure F.11: Fence View Showing the Ratio of the Vertical Pore Water Velocity to the Velocity Magnitude at 90ka before Present for the Base Case Parameters

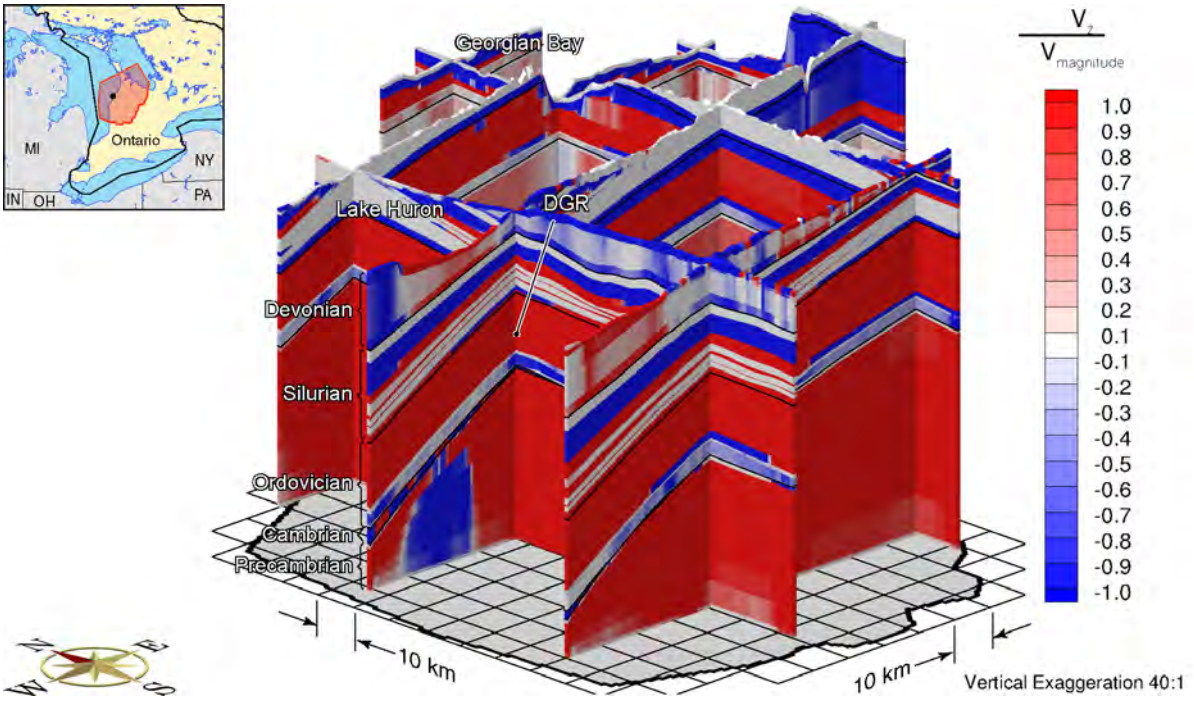

Figure F.12: Fence View Showing the Ratio of the Vertical Pore Water Velocity to the Velocity Magnitude at 60ka before Present for the Base Case Parameters

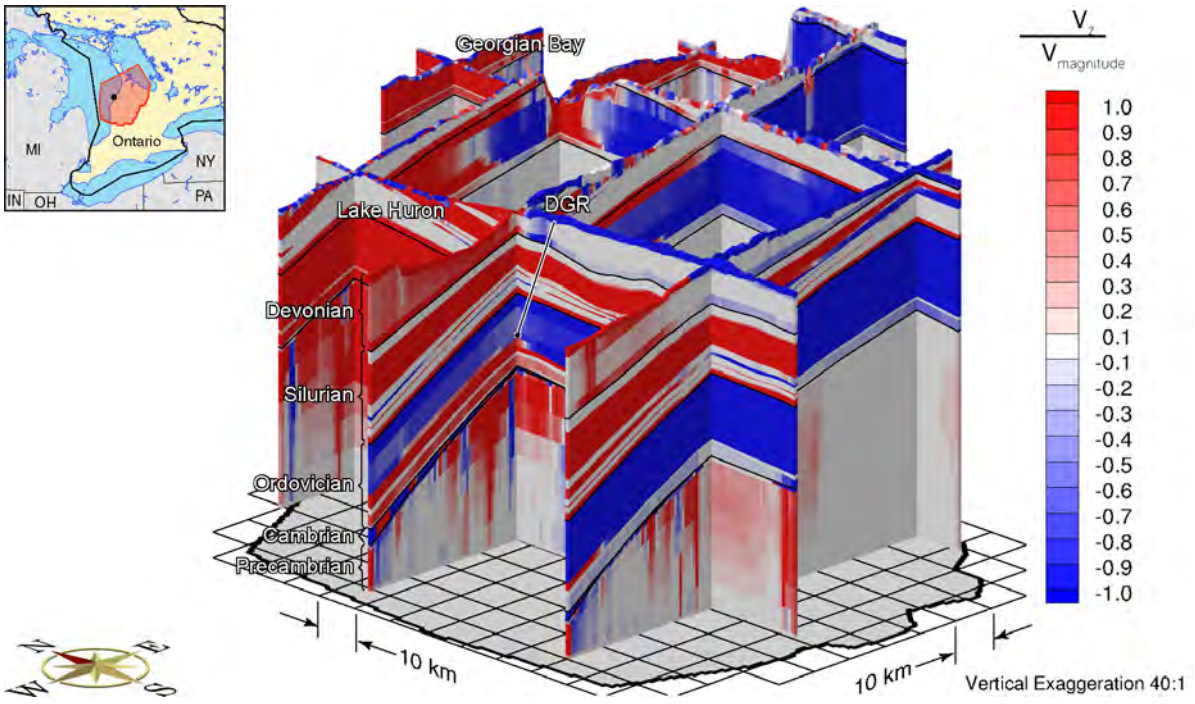

Figure F.13: Fence View Showing the Ratio of the Vertical Pore Water Velocity to the Velocity Magnitude at 30ka before Present for the Base Case Parameters

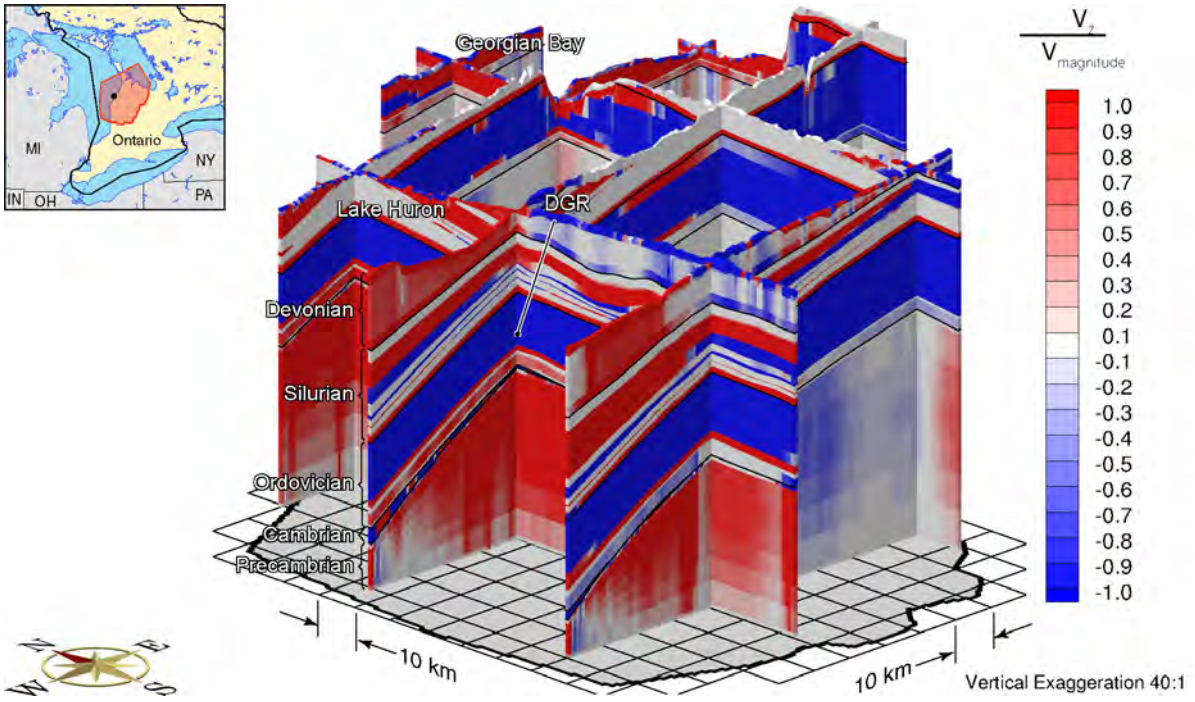

Figure F.14: Fence View Showing the Ratio of the Vertical Pore Water Velocity to the Velocity Magnitude at Present for the Base Case Parameters

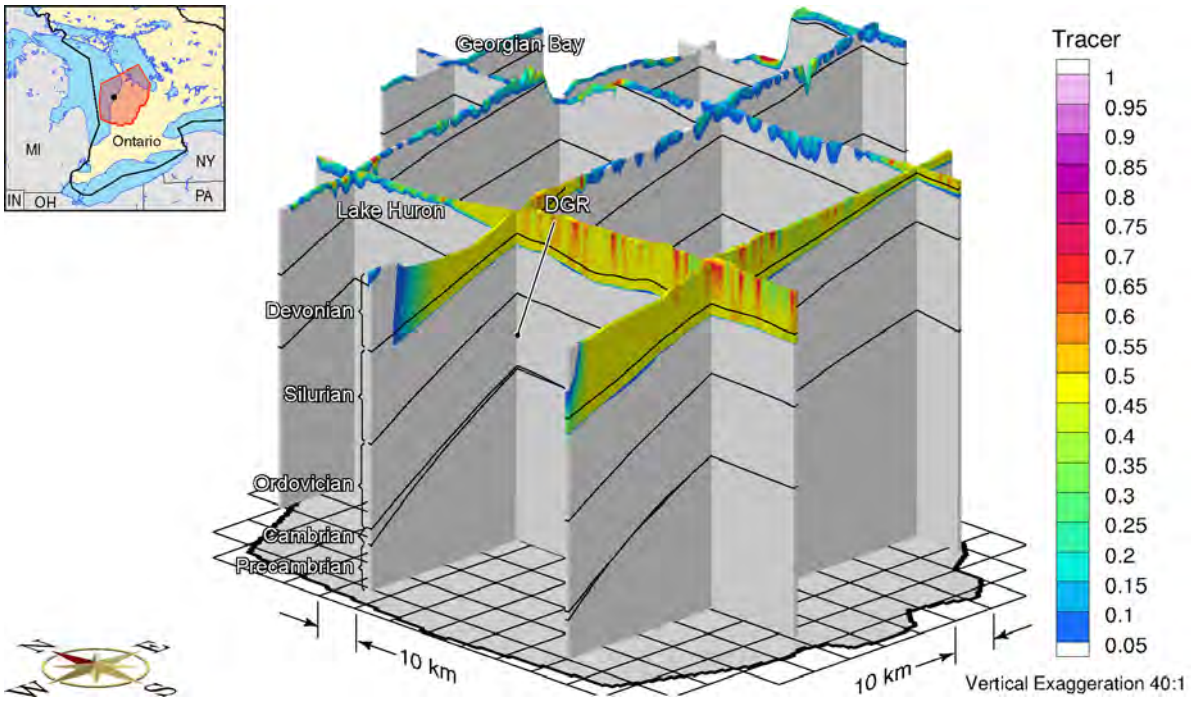

Figure F.15: Fence View Showing the Depth of Penetration of a Tracer at 90ka before Present for the Base Case Parameters

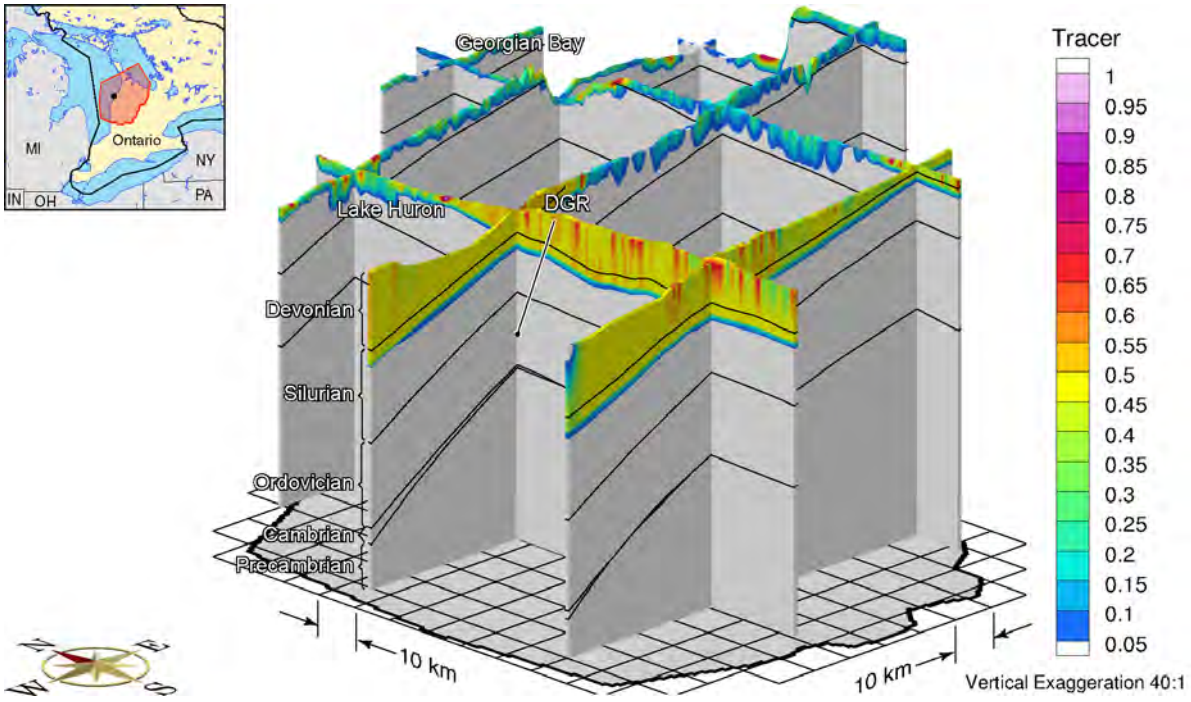

Figure F.16: Fence View Showing the Depth of Penetration of a Tracer at 60ka before Present for the Base Case Parameters

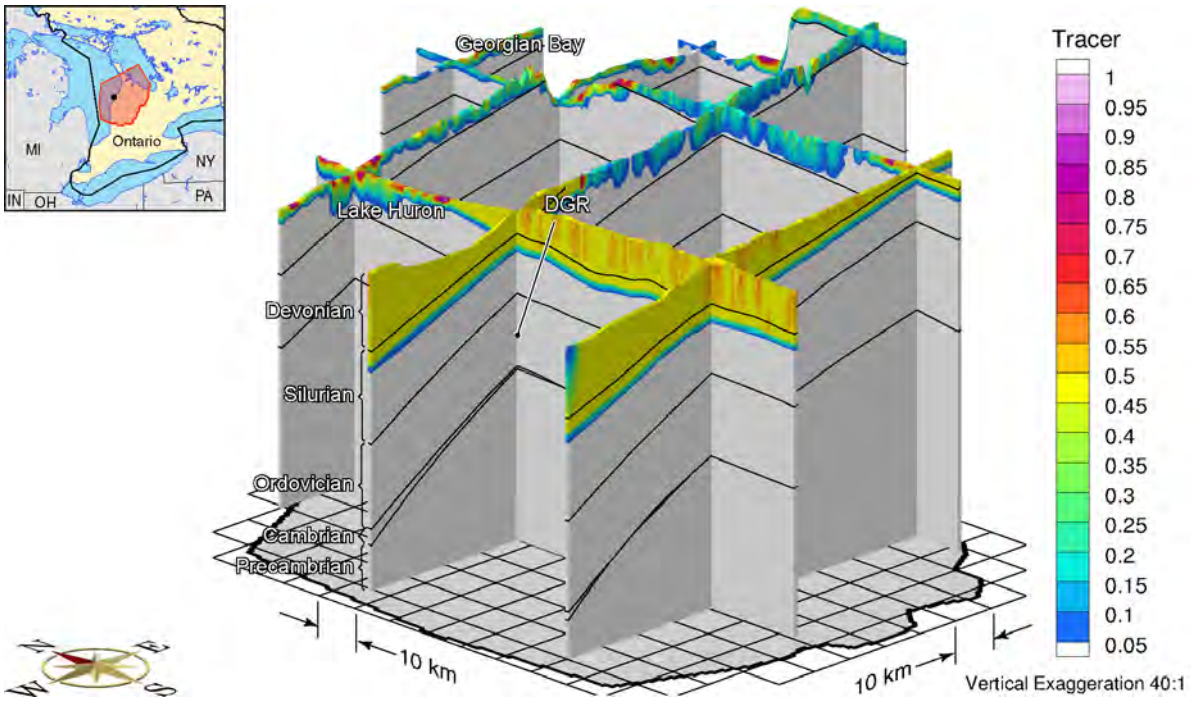

Figure F.17: Fence View Showing the Depth of Penetration of a Tracer at 30ka before Present for the Base Case Parameters

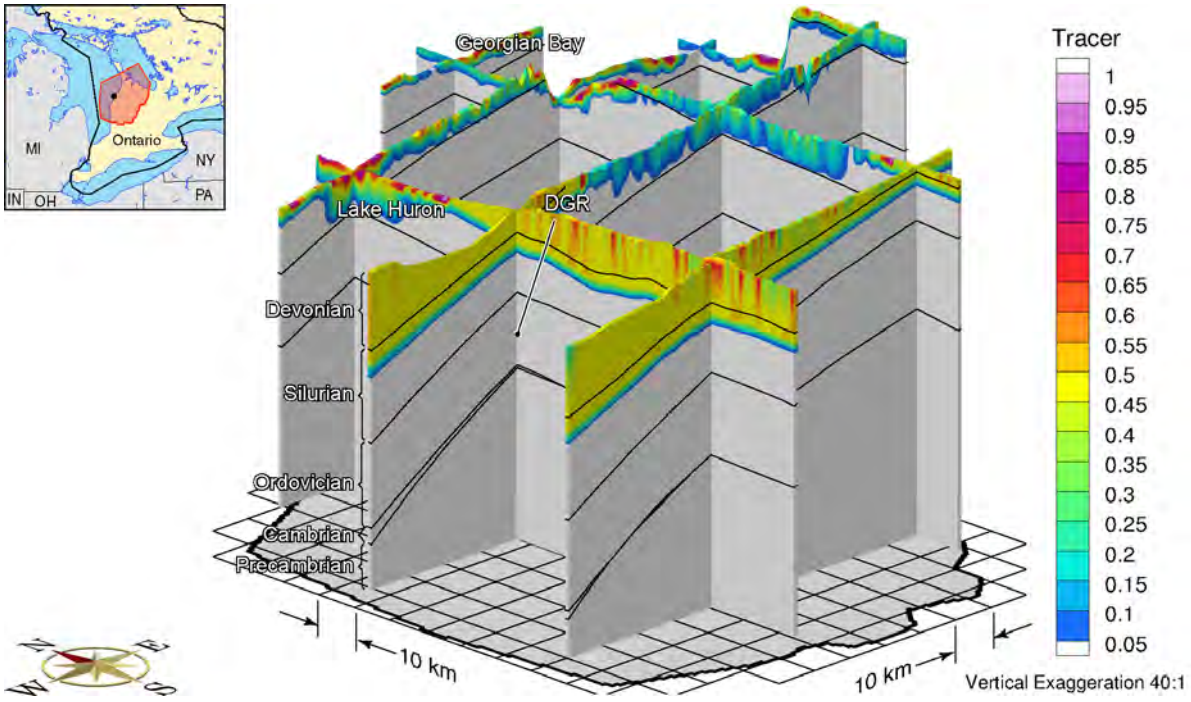

Figure F.18: Fence View Showing the Depth of Penetration of a Tracer at Present for the Base Case Parameters

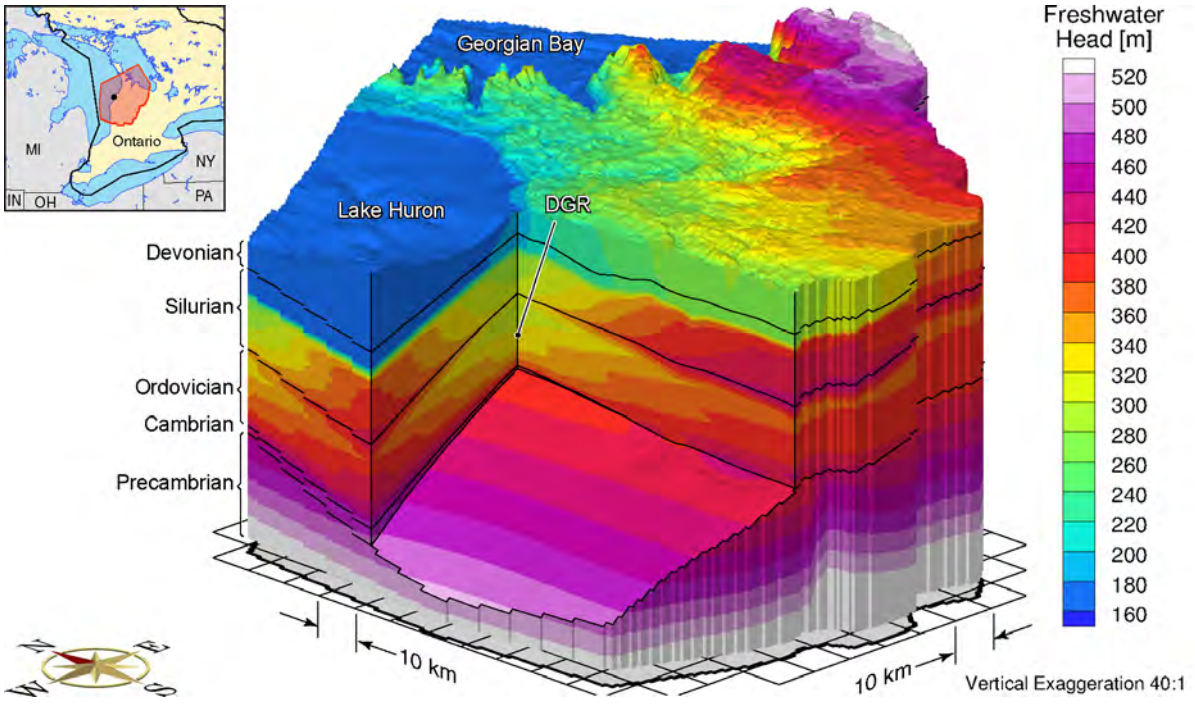

Figure F.19: Block Cut View of Freshwater Heads at Present with the Surface Boundary Condition Based on 80% of Ice Thickness

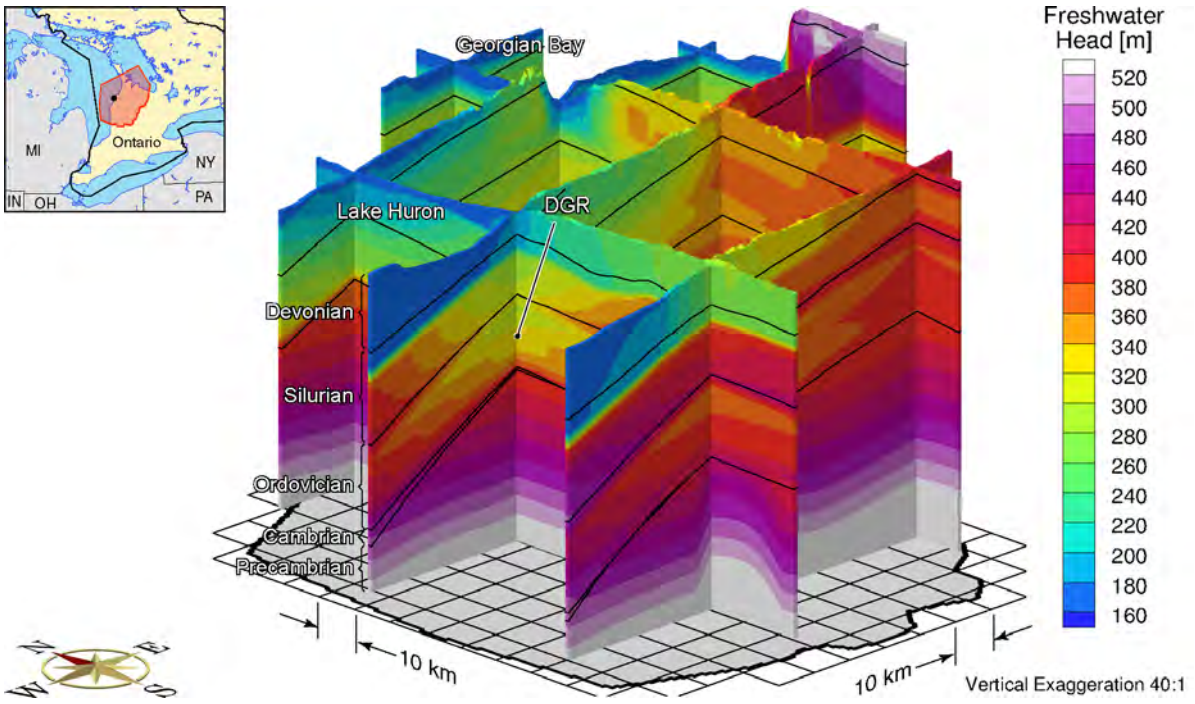

Figure F.20: Fence View of Freshwater Heads at Present with the Surface Boundary Condition Based on 80% of Ice Thickness

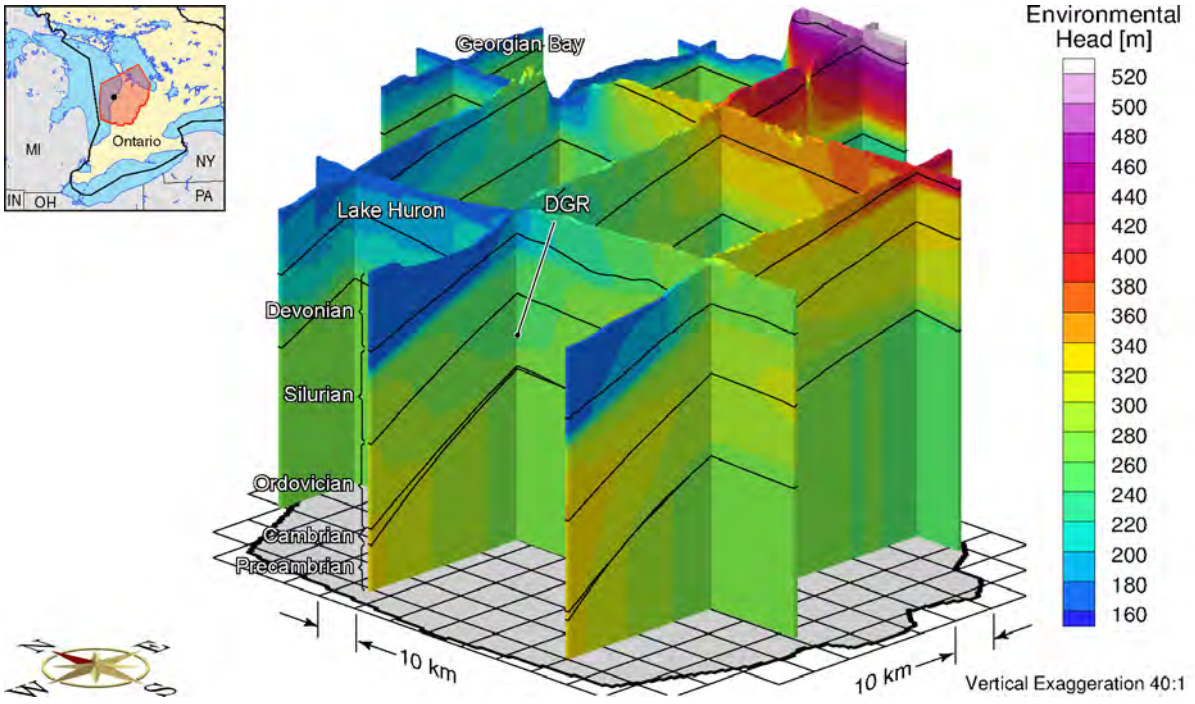

Figure F.21: Fence View of Environmental Heads at 90ka before Present with the Surface Boundary Condition Based on 80% of Ice Thickness

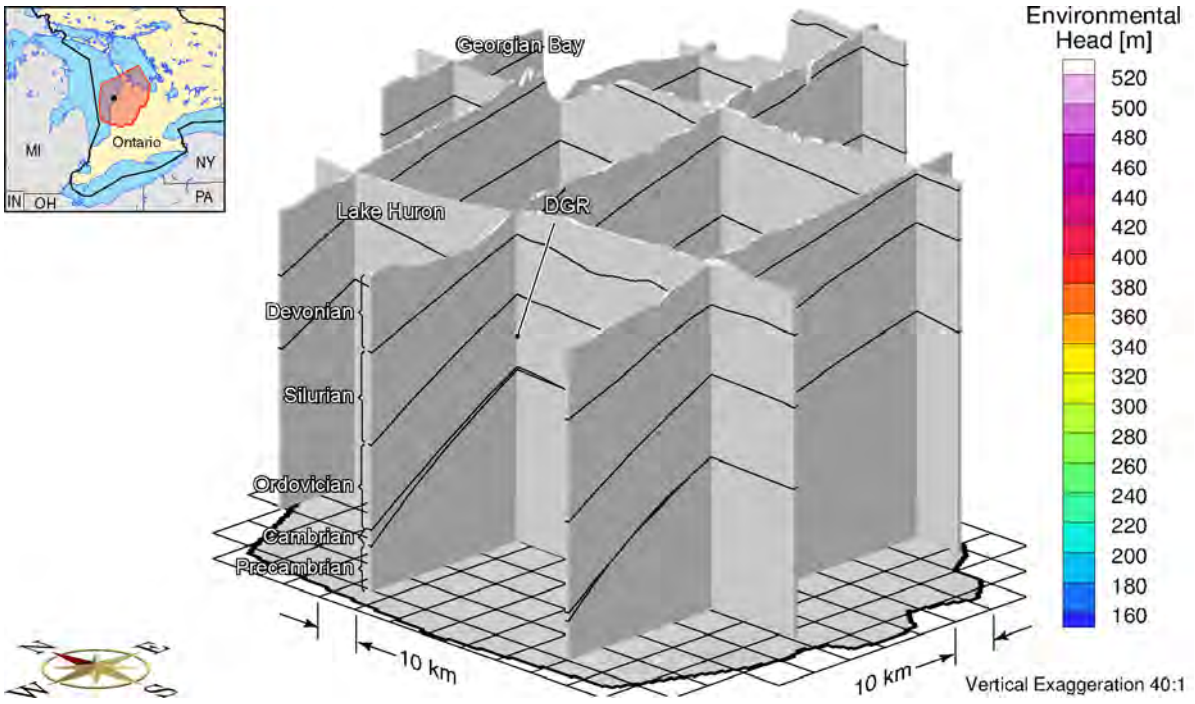

Figure F.22: Fence View of Environmental Heads at 60ka before Present with the Surface Boundary Condition Based on 80% of Ice Thickness

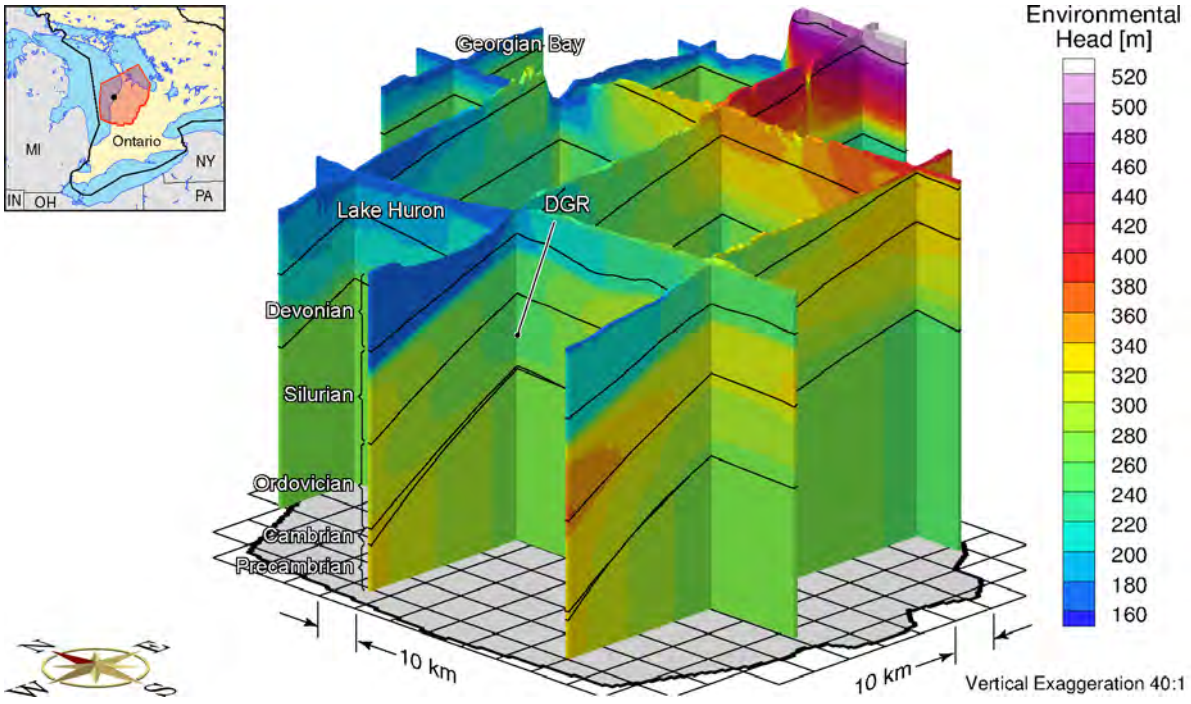

Figure F.23: Fence View of Environmental Heads at 30ka before Present with the Surface Boundary Condition Based on 80% of Ice Thickness

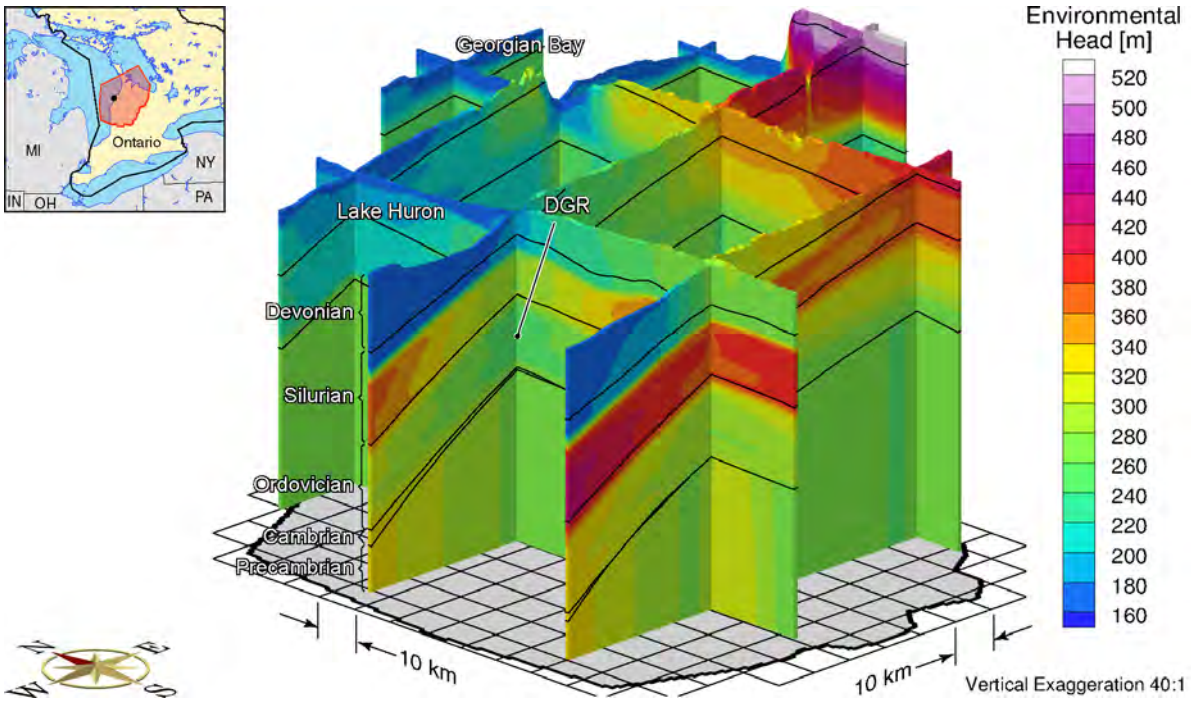

Figure F.24: Fence View of Environmental Heads at the Present with the Surface Boundary Condition Based on 80% of Ice Thickness

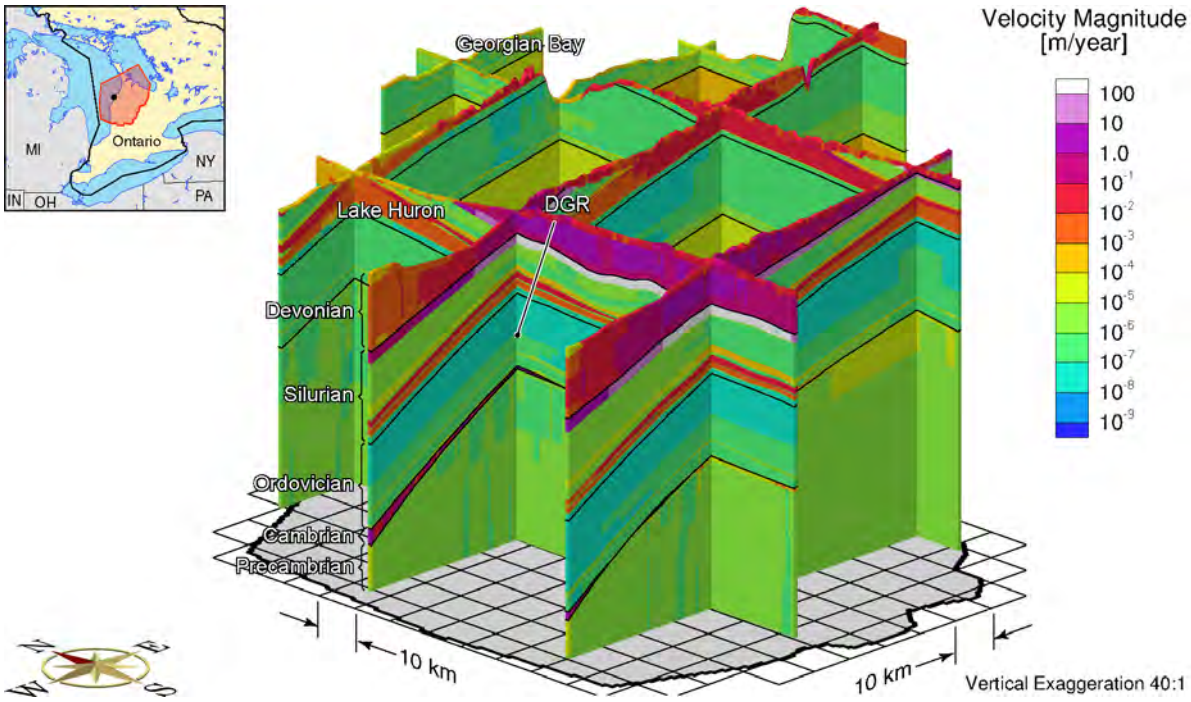

Figure F.25: Fence View of Pore Velocity Magnitude at 90ka before Present with the Surface Boundary Condition Based on 80% of Ice Thickness

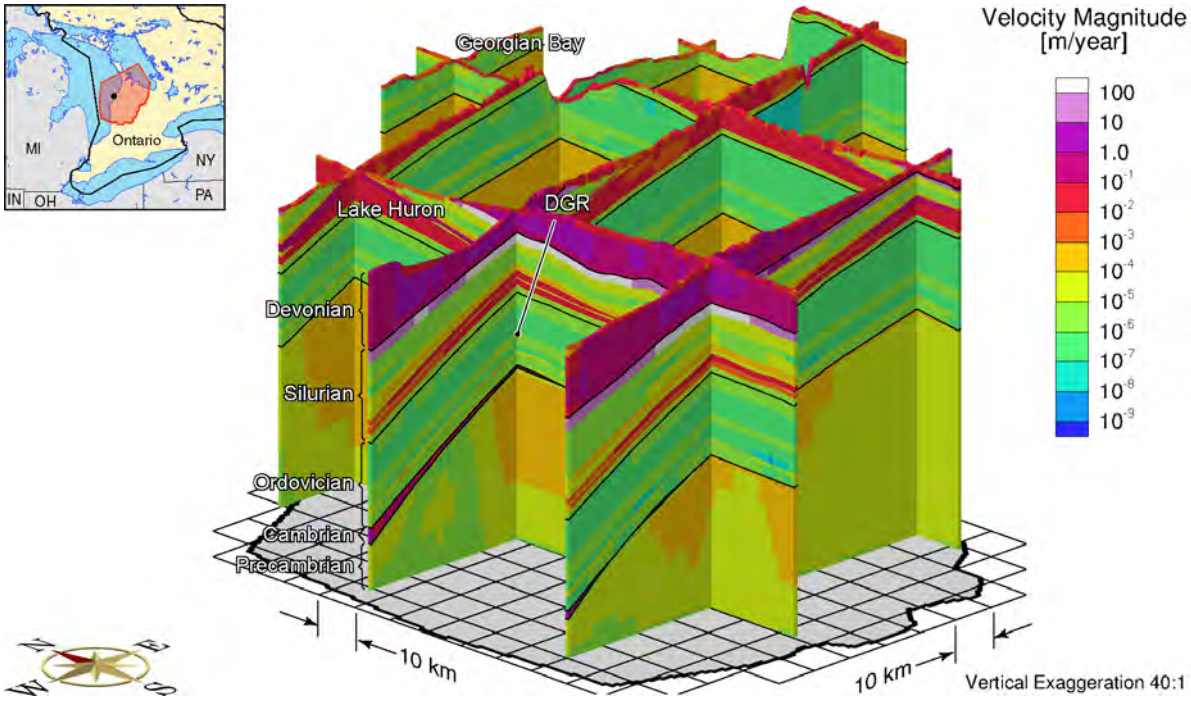

Figure F.26: Fence View of Pore Velocity Magnitude at 60ka before Present with the Surface Boundary Condition Based on 80% of Ice Thickness

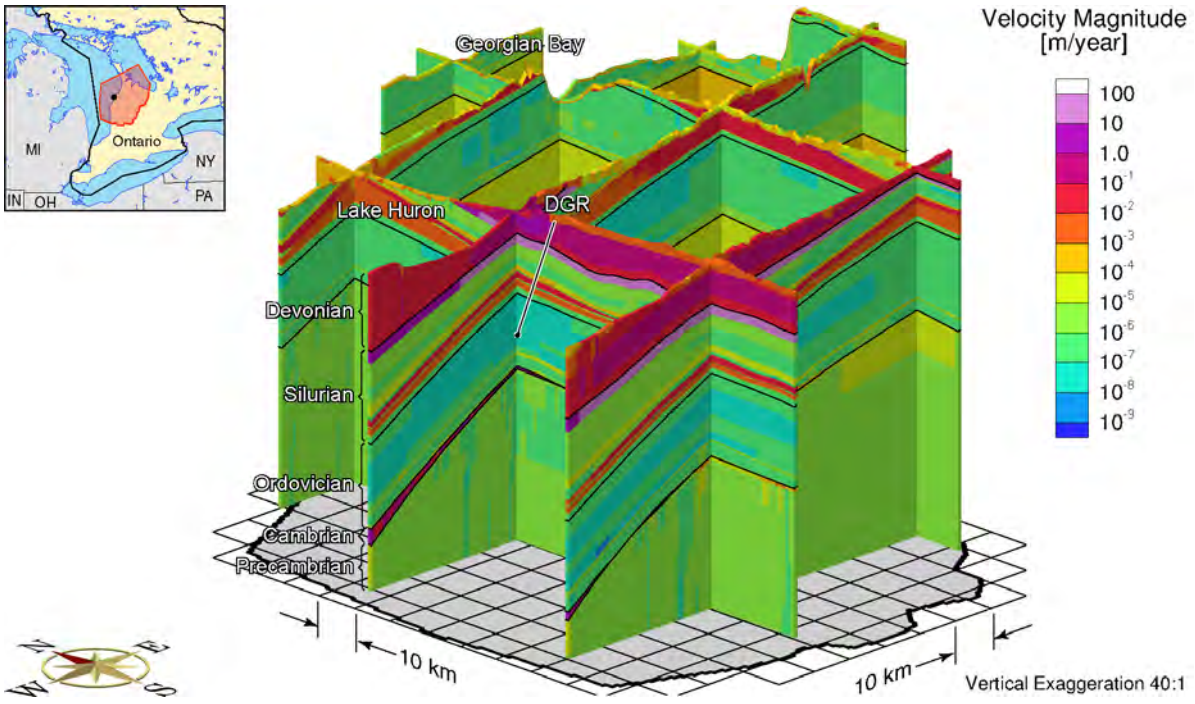

Figure F.27: Fence View of Pore Velocity Magnitude at 30ka before Present with the Surface Boundary Condition Based on 80% of Ice Thickness

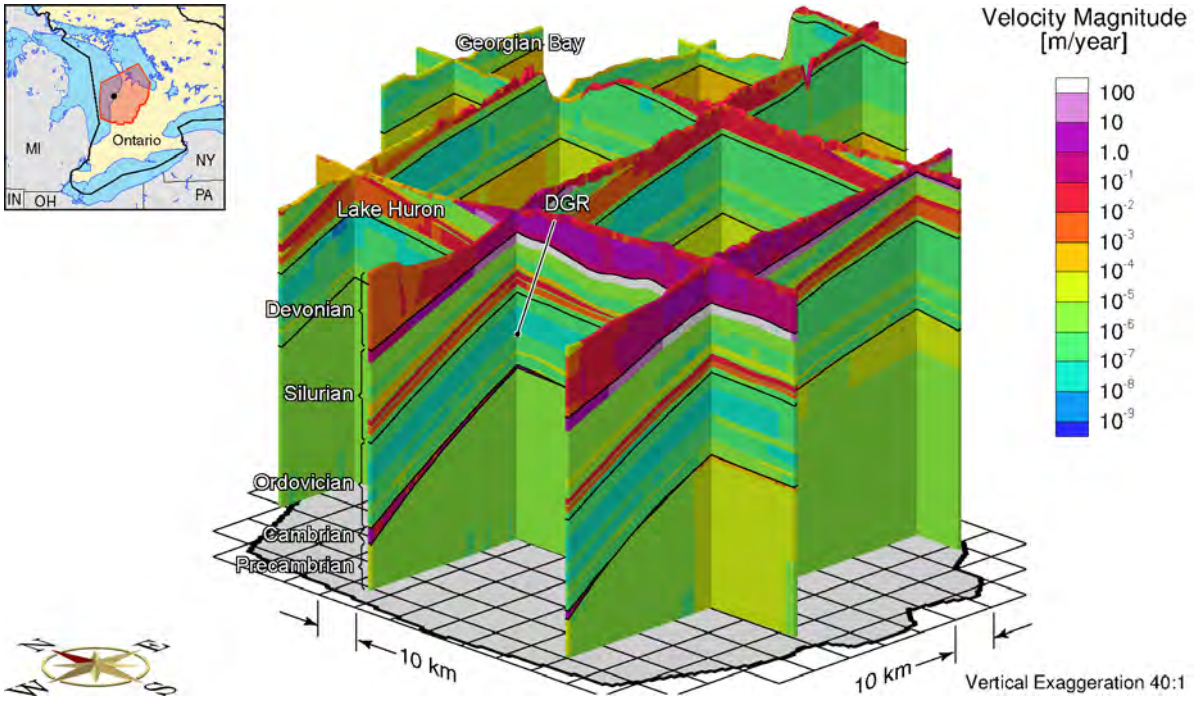

Figure F.28: Fence View of Pore Velocity Magnitude at Present with the Surface Boundary Condition Based on 80% of Ice Thickness

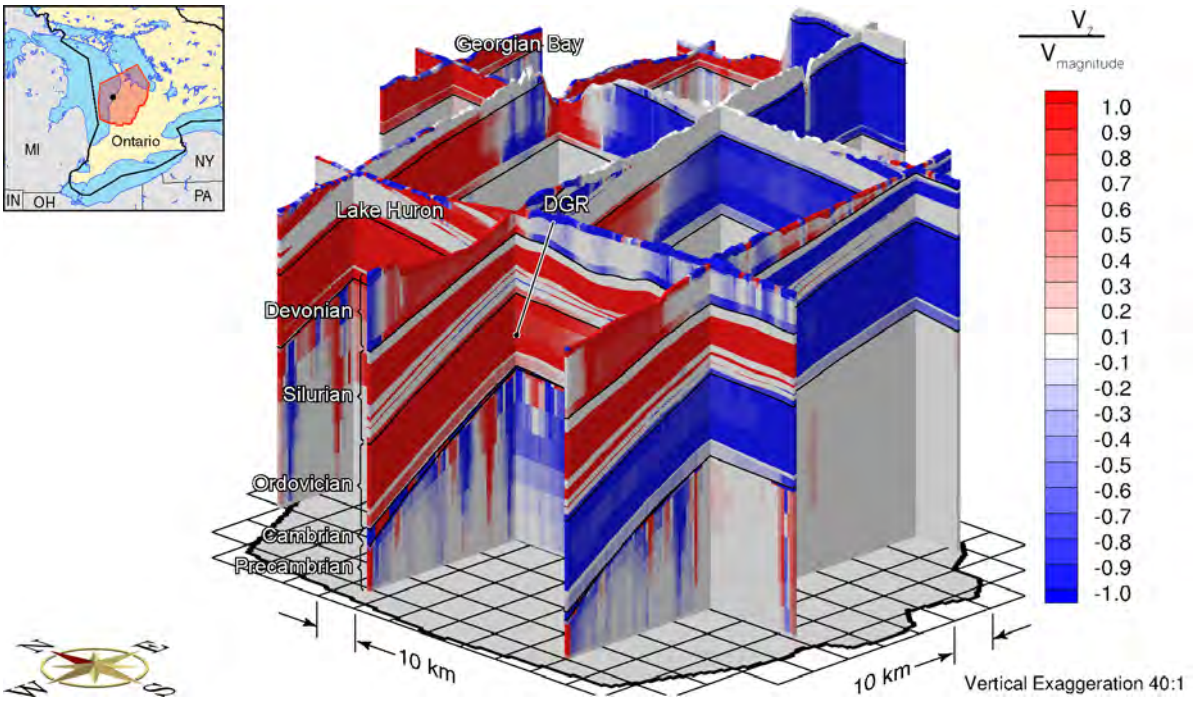

Figure F.29: Fence View Showing the Ratio of the Vertical Pore Water Velocity to the Velocity Magnitude at 90ka before Present with the Surface Boundary Condition Based on 80% of Ice Thickness

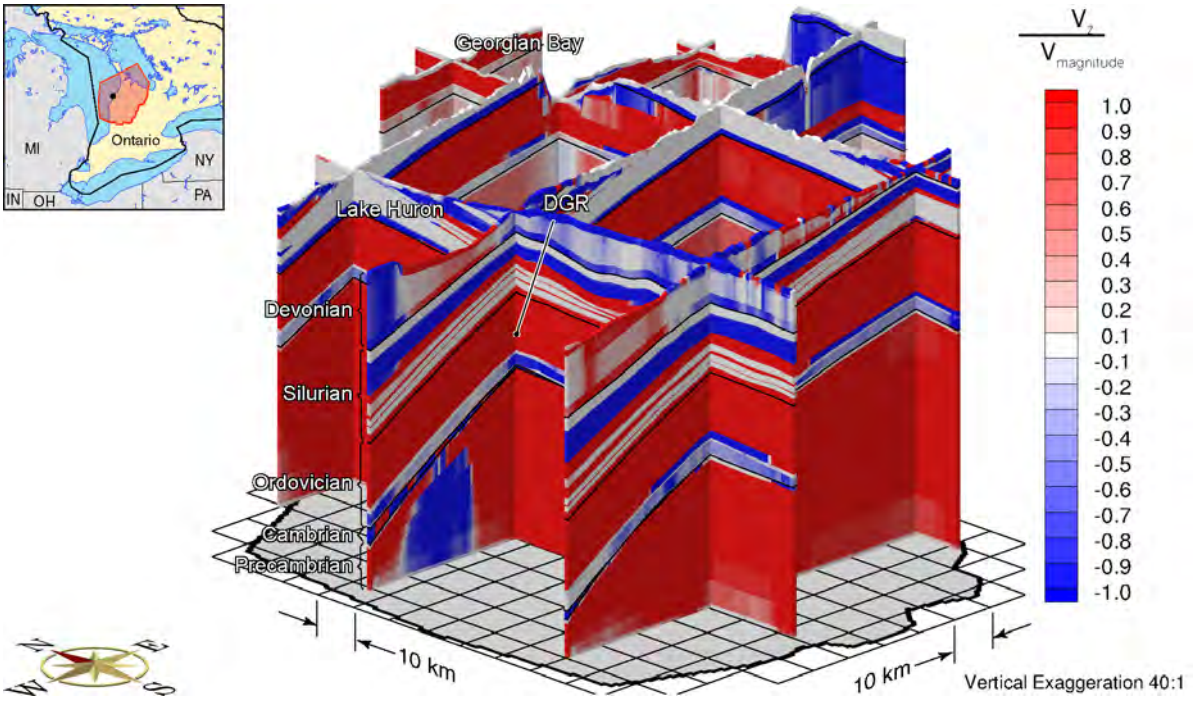

Figure F.30: Fence View Showing the Ratio of the Vertical Pore Water Velocity to the Velocity Magnitude at 60ka before Present with the Surface Boundary Condition Based on 80% of Ice Thickness

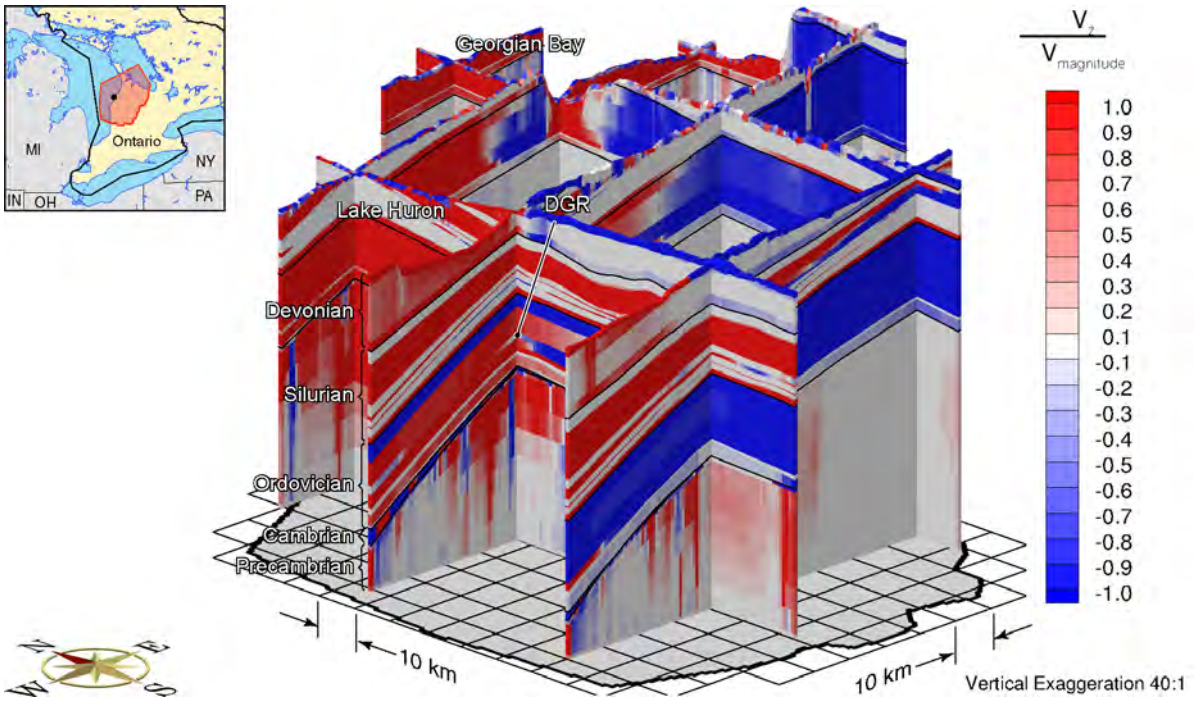

Figure F.31: Fence View Showing the Ratio of the Vertical Pore Water Velocity to the Velocity Magnitude at 30ka before Present with the Surface Boundary Condition Based on 80% of Ice Thickness

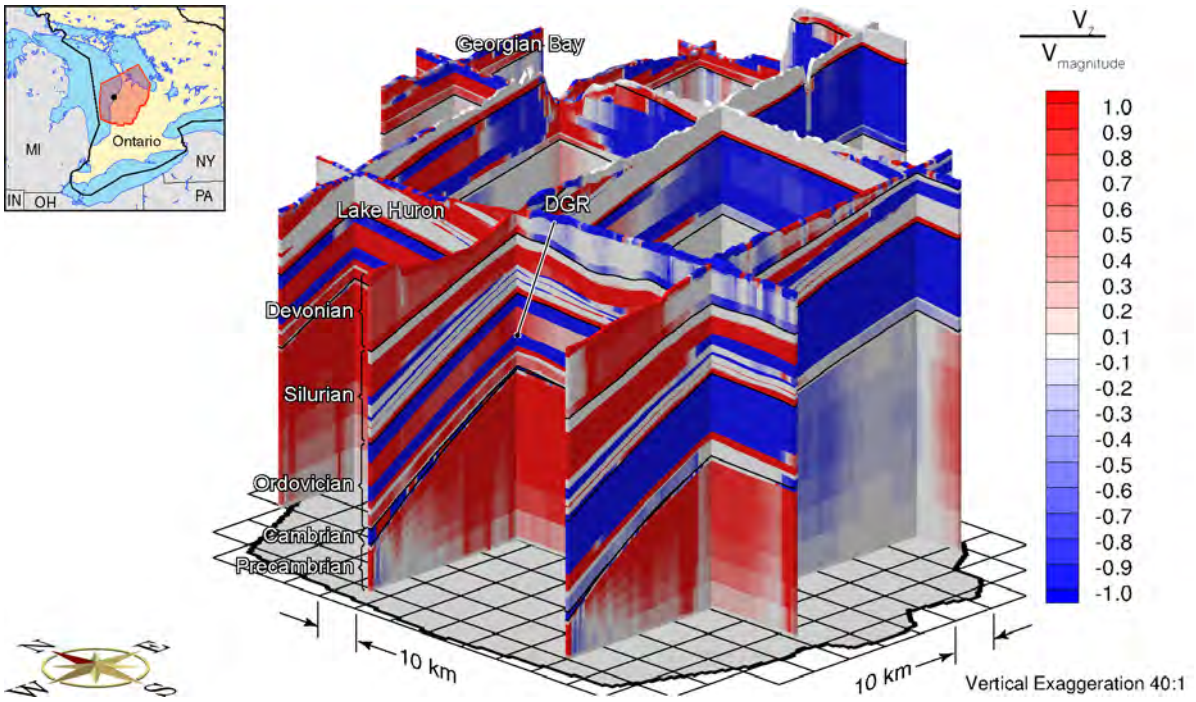

Figure F.32: Fence View of Ratio of Vertical Pore Velocity to Pore Velocity Magnitude at Present with the Surface Boundary Condition Based on 80% of Ice Thickness

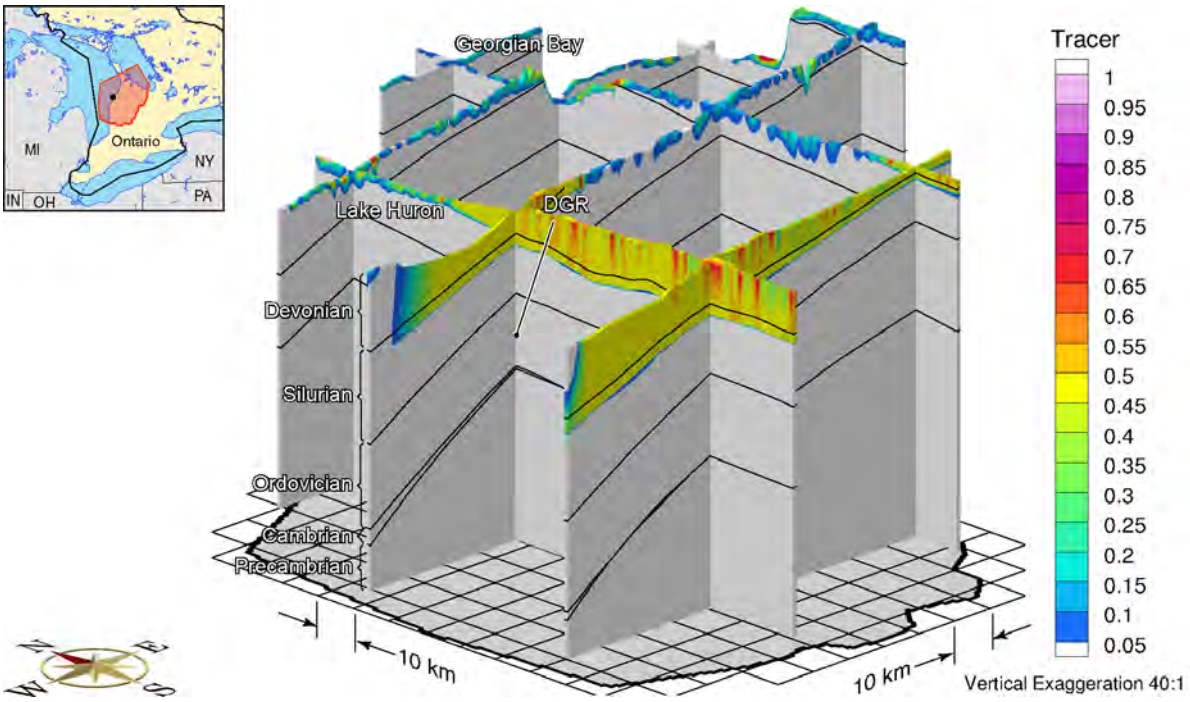

Figure F.33: Fence View Showing the Depth of Penetration of a Tracer at 90ka before Present with the Surface Boundary Condition Based on 80% of Ice Thickness

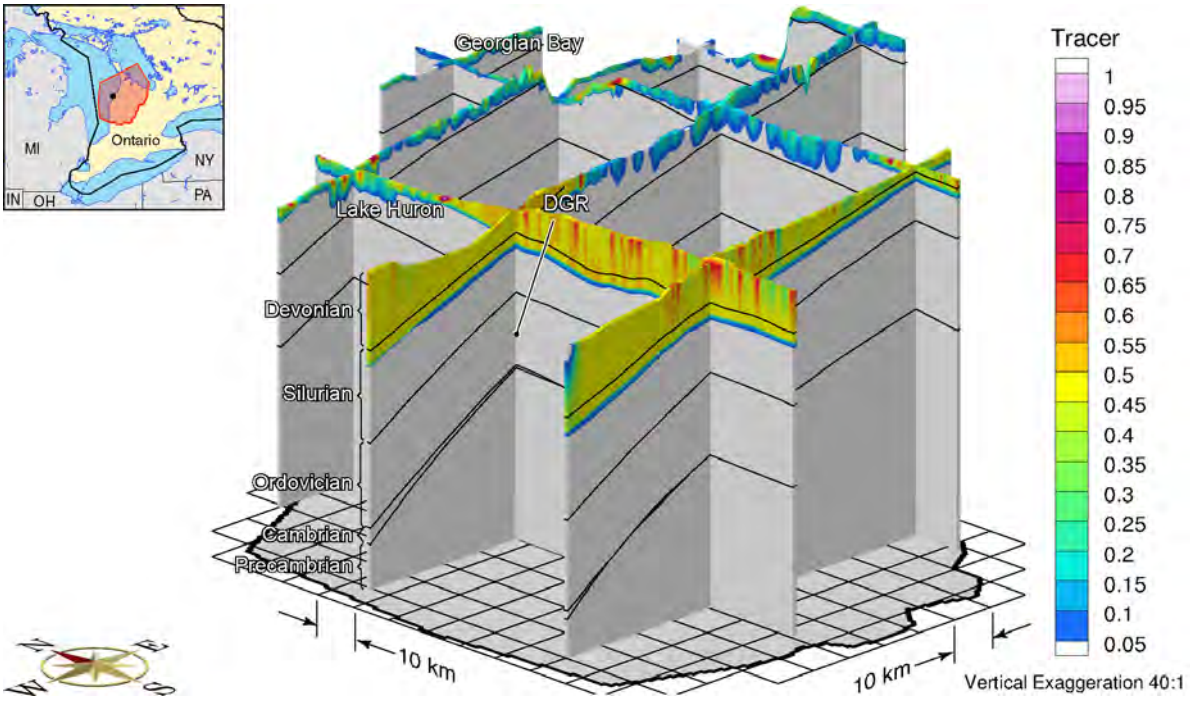

Figure F.34: Fence View Showing the Depth of Penetration of a Tracer at 60ka before Present with the Surface Boundary Condition Based on 80% of Ice Thickness

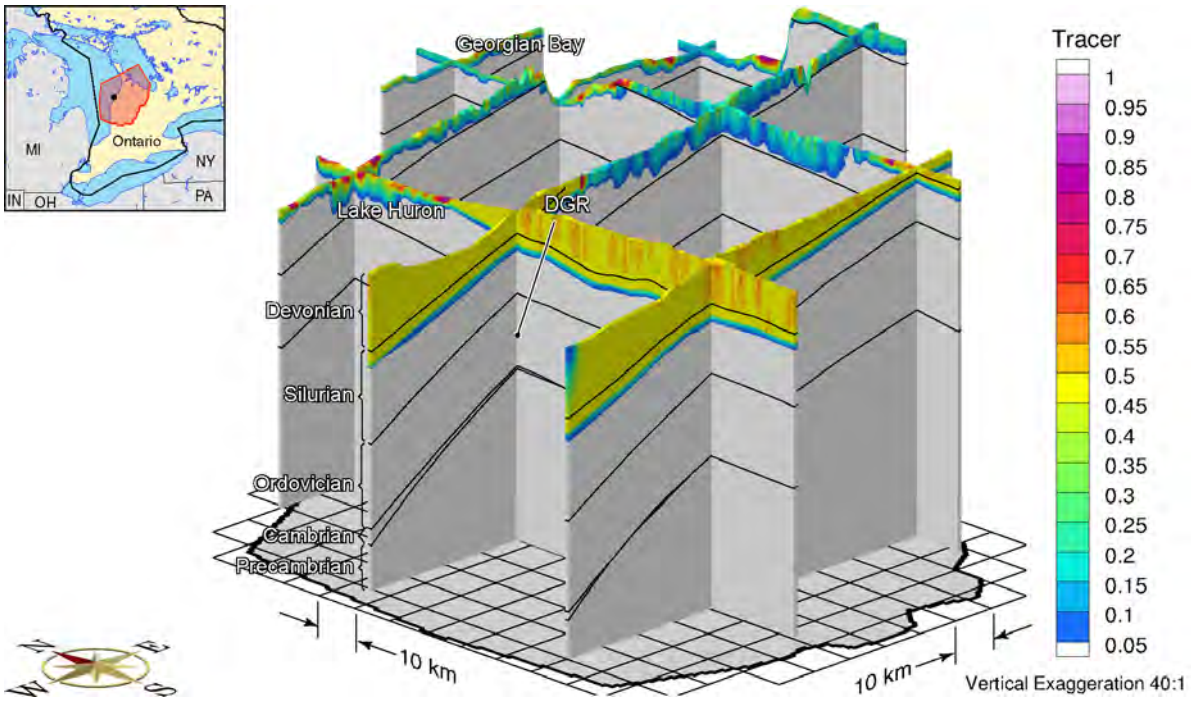

Figure F.35: Fence View Showing the Depth of Penetration of a Tracer at 30ka before Present with the Surface Boundary Condition Based on 80% of Ice Thickness

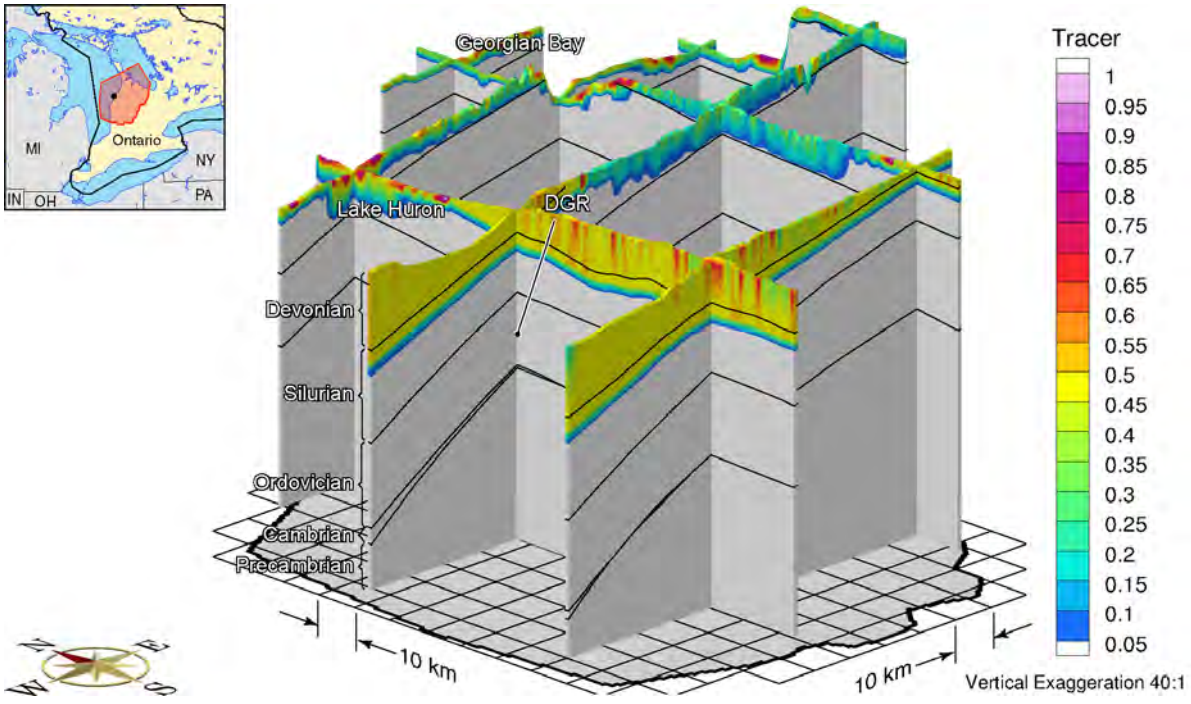

Figure F.36: Fence View Showing the Depth of Penetration of a Tracer at Present with the Surface Boundary Condition Based on 80% of Ice Thickness

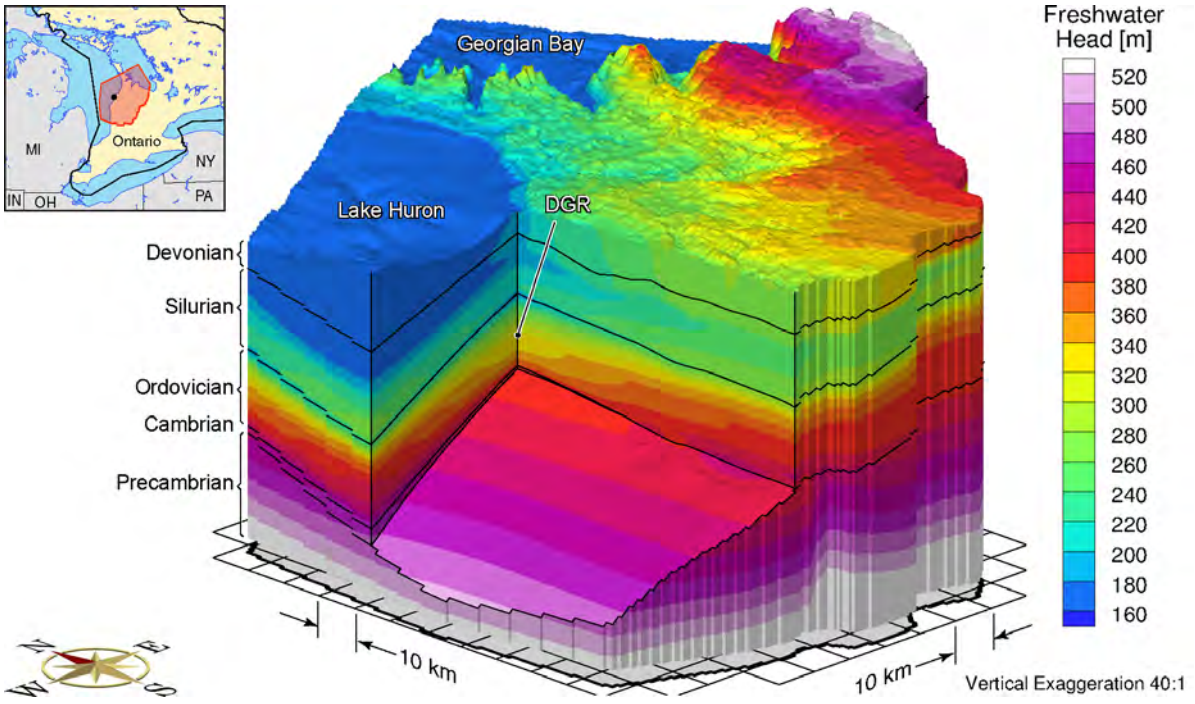

Figure F.37: Block Cut View of Freshwater Heads at Present with the Surface Boundary Condition Based on 30% of Ice Thickness

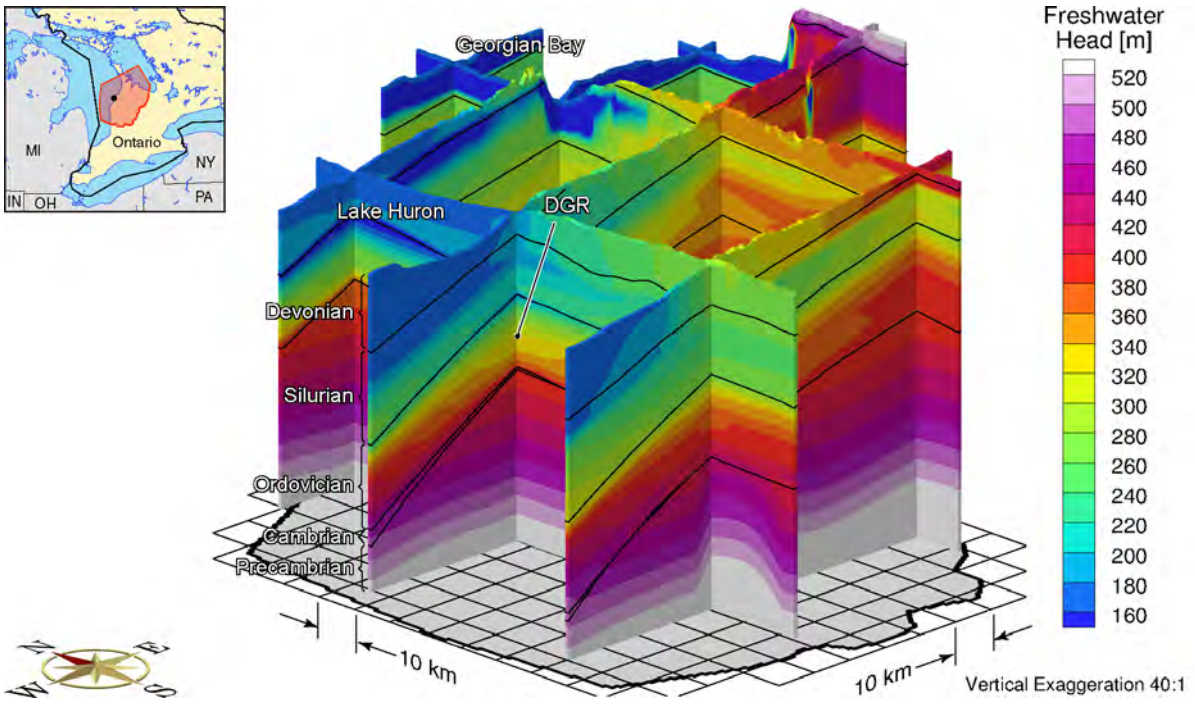

Figure F.38: Fence View of Freshwater Heads at Present with the Surface Boundary Condition Based on 30% of Ice Thickness

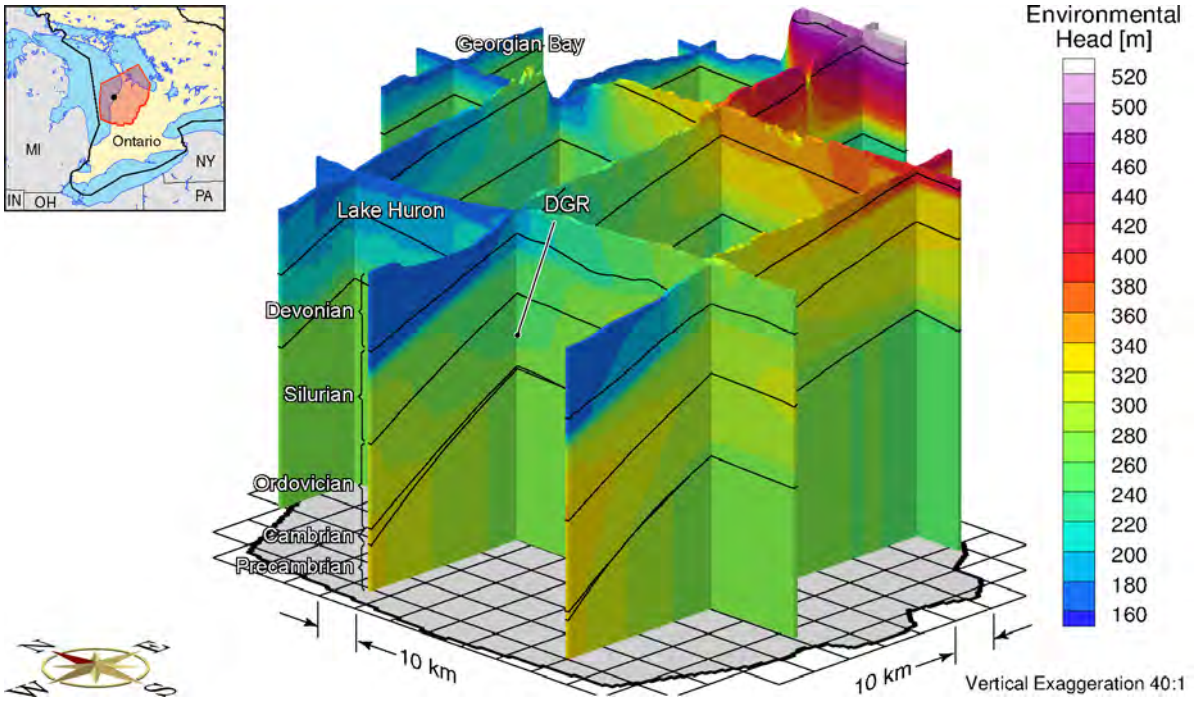

Figure F.39: Fence View of Environmental Heads at 90ka before Present with the Surface Boundary Condition Based on 30% of Ice Thickness

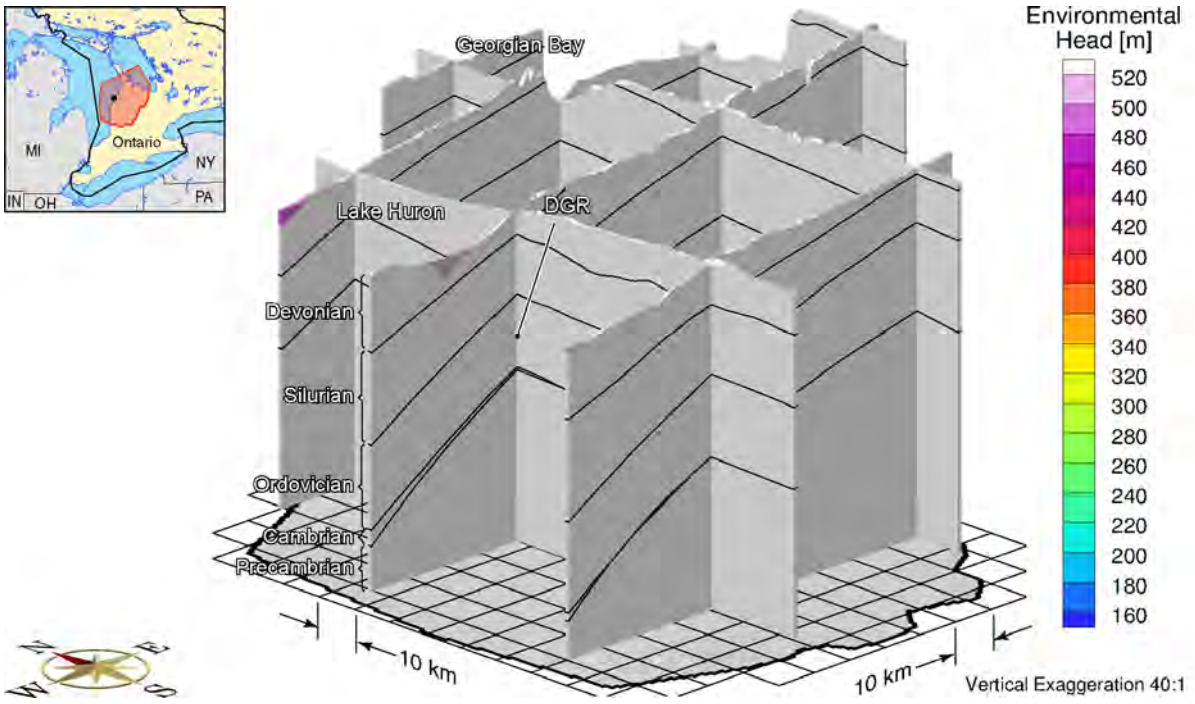

Figure F.40: Fence View of Environmental Heads at 60ka before Present with the Surface Boundary Condition Based on 30% of Ice Thickness

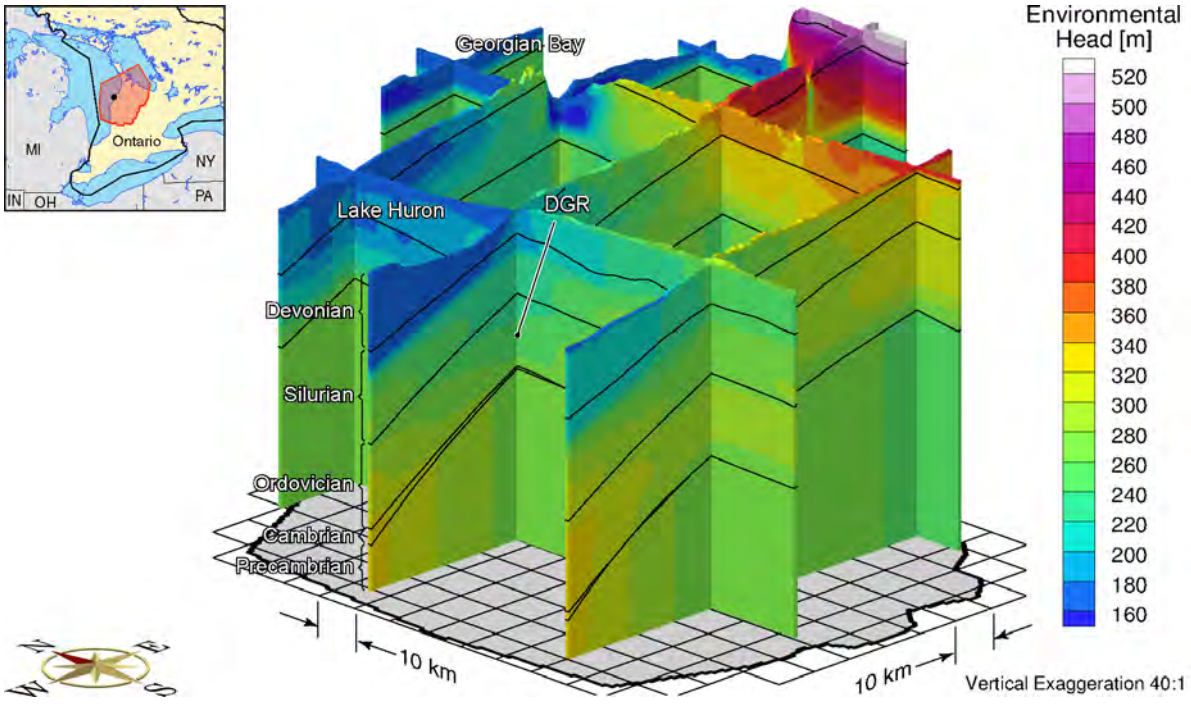

Figure F.41: Fence View of Environmental Heads at 30ka before Present with the Surface Boundary Condition Based on 30% of Ice Thickness

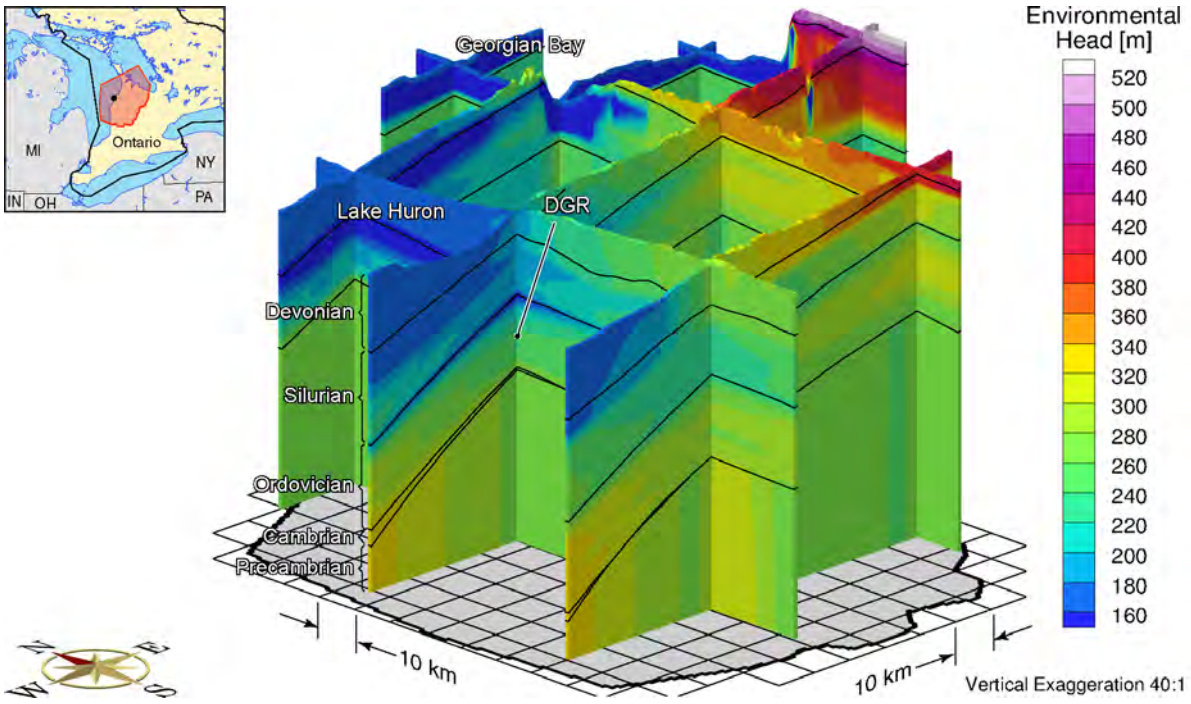

Figure F.42: Fence View of Environmental Heads at the Present with the Surface Boundary Condition Based on 30% of Ice Thickness

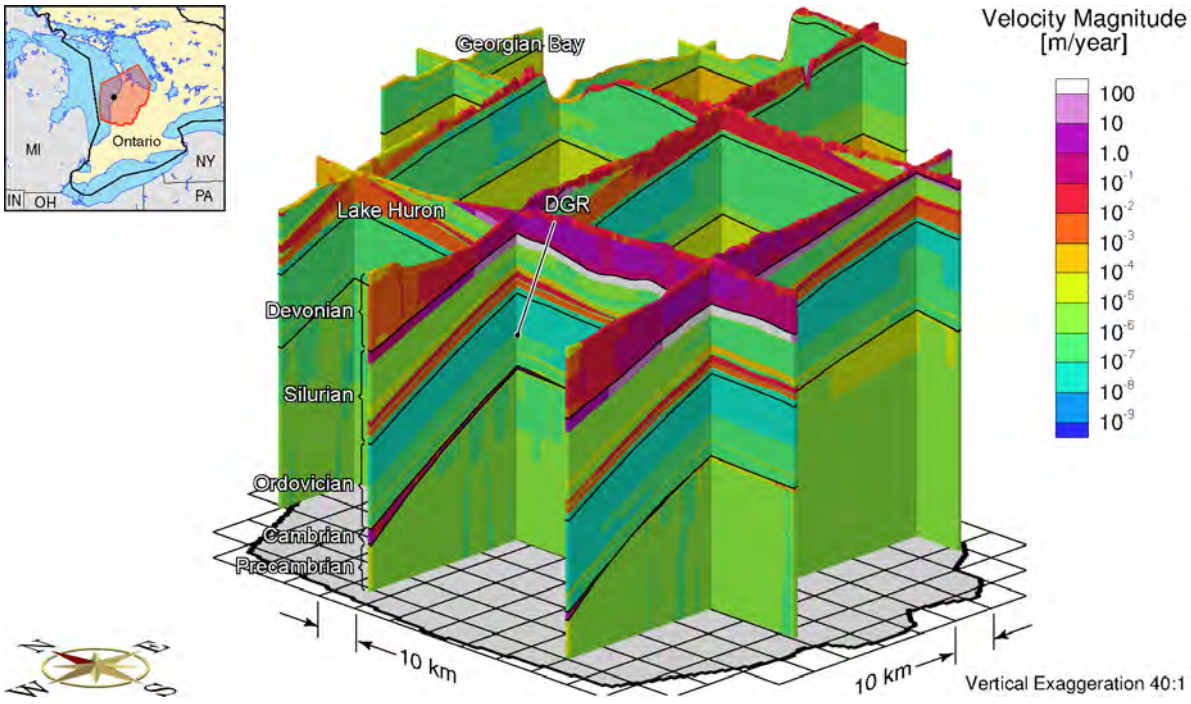

Figure F.43: Fence View of Pore Velocity Magnitude at 90ka before Present with the Surface Boundary Condition Based on 30% of Ice Thickness

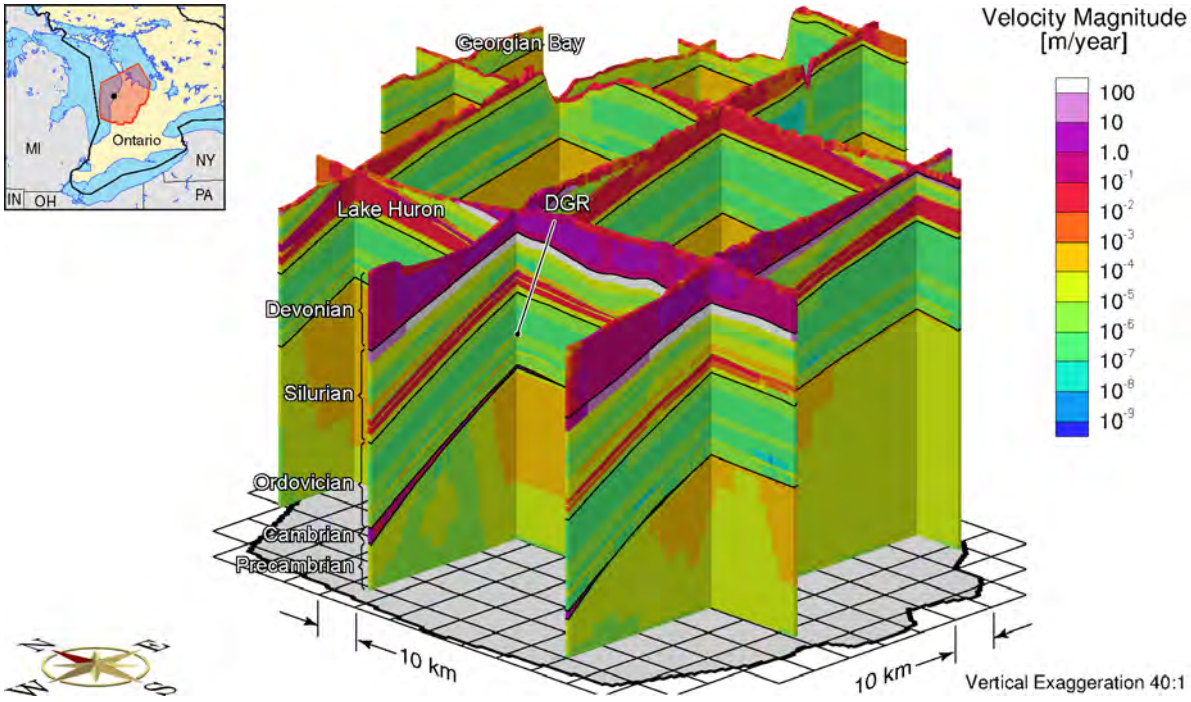

Figure F.44: Fence View of Pore Velocity Magnitude at 60ka before Present with the Surface Boundary Condition Based on 30% of Ice Thickness

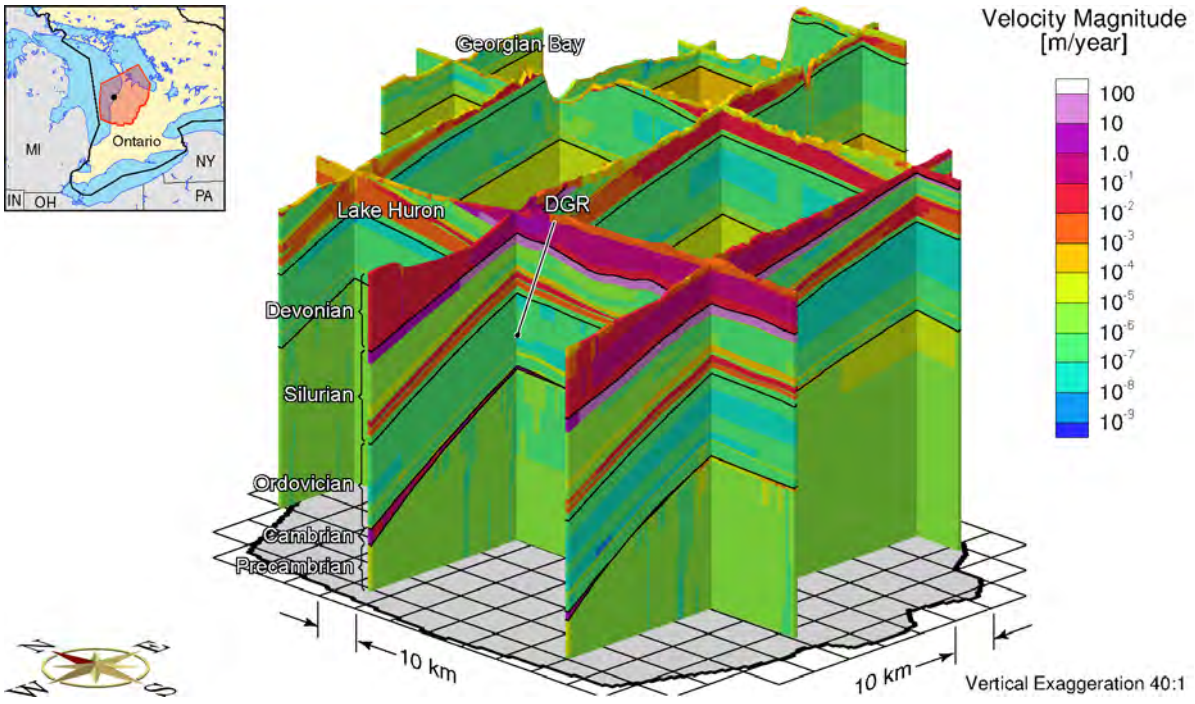

Figure F.45: Fence View of Pore Velocity Magnitude at 30ka before Present with the Surface Boundary Condition Based on 30% of Ice Thickness

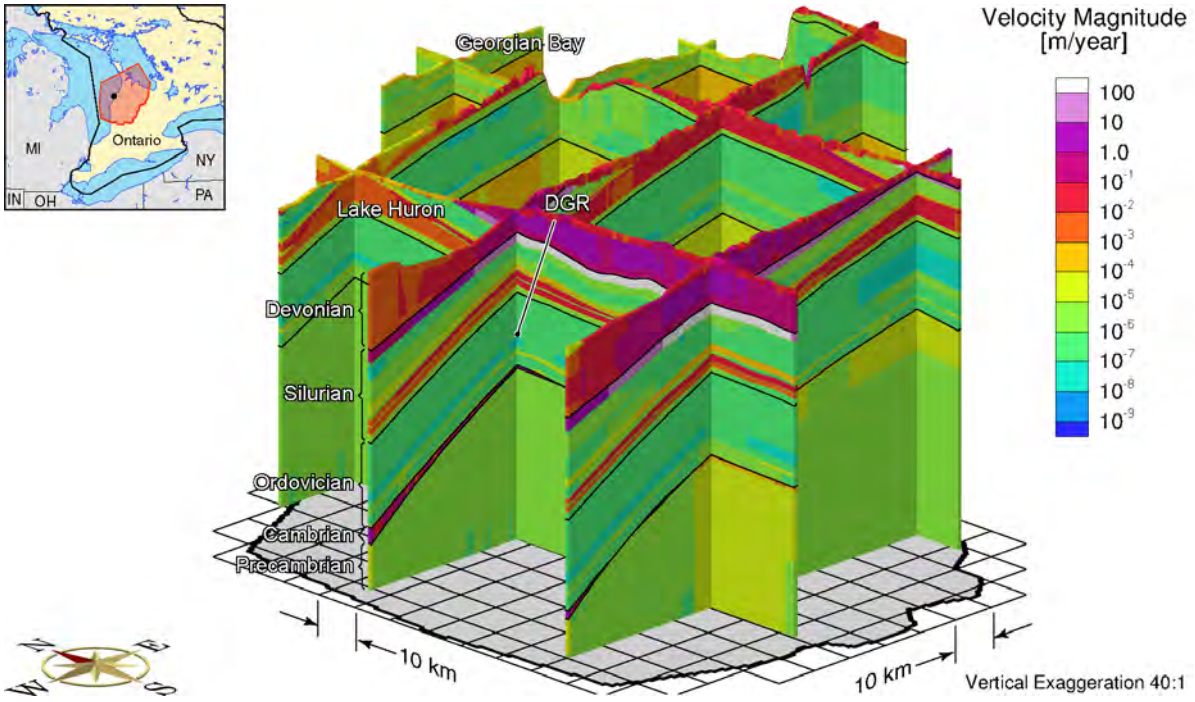

Figure F.46: Fence View of Pore Velocity Magnitude at Present with the Surface Boundary Condition Based on 30% of Ice Thickness

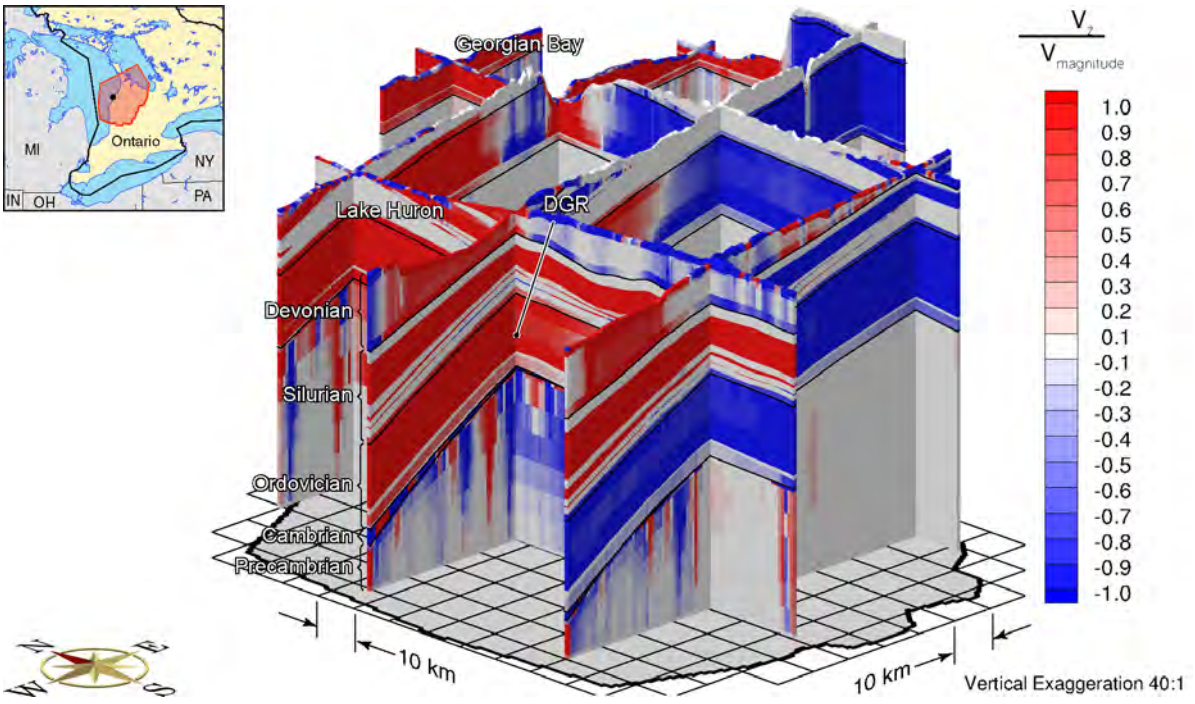

Figure F.47: Fence View Showing the Ratio of the Vertical Pore Water Velocity to the Velocity Magnitude at 90ka before Present with the Surface Boundary Condition Based on 30% of Ice Thickness

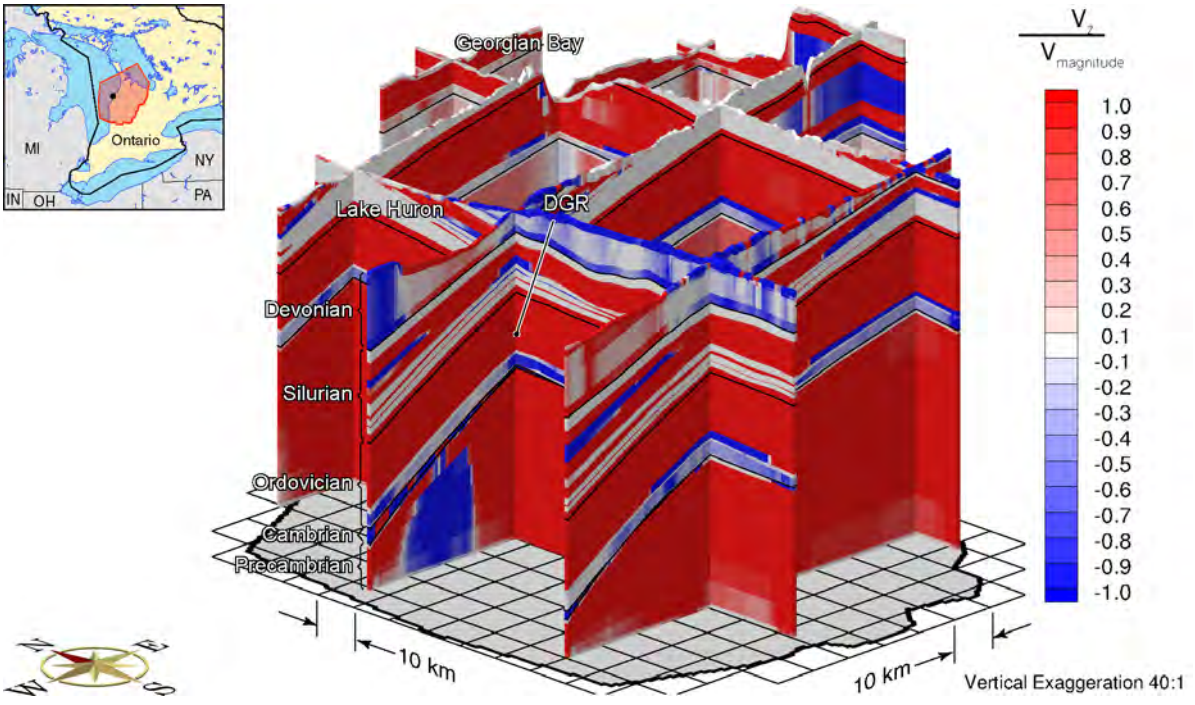

Figure F.48: Fence View Showing the Ratio of the Vertical Pore Water Velocity to the Velocity Magnitude at 60ka before Present with the Surface Boundary Condition Based on 30% of Ice Thickness

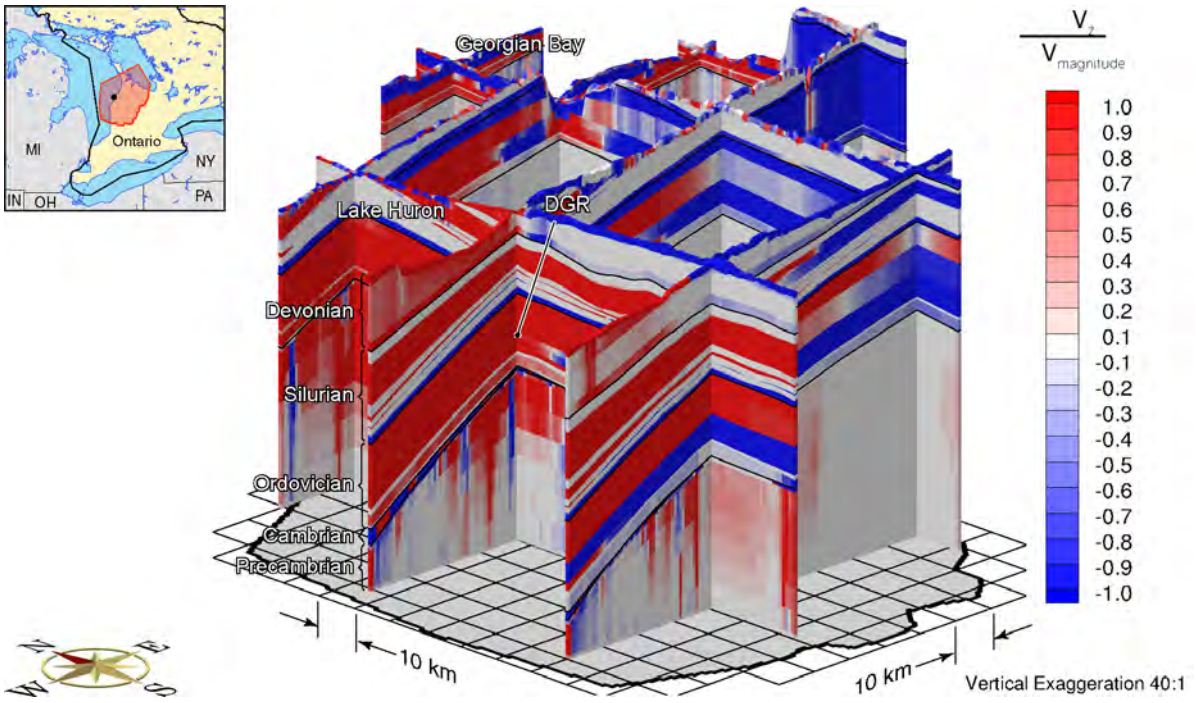

Figure F.49: Fence View Showing the Ratio of the Vertical Pore Water Velocity to the Velocity Magnitude at 30ka before Present with the Surface Boundary Condition Based on 30% of Ice Thickness

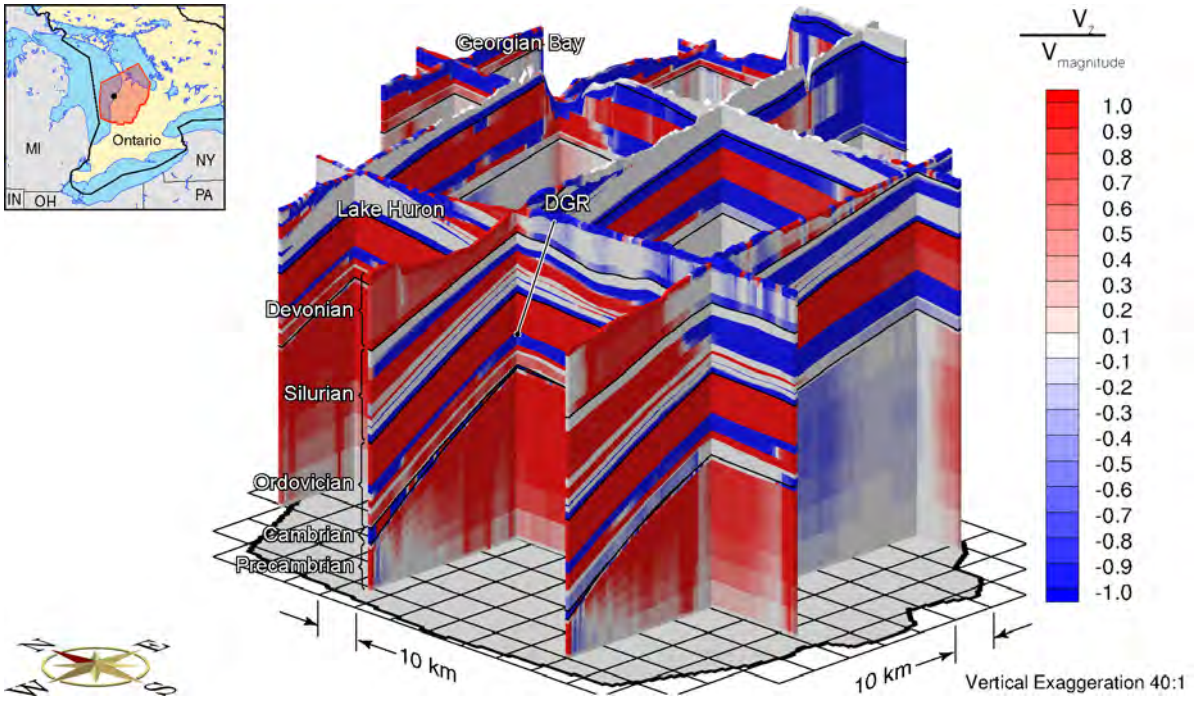

Figure F.50: Fence View of Ratio of Vertical Pore Velocity to Pore Velocity Magnitude at Present with the Surface Boundary Condition Based on 30% of Ice Thickness

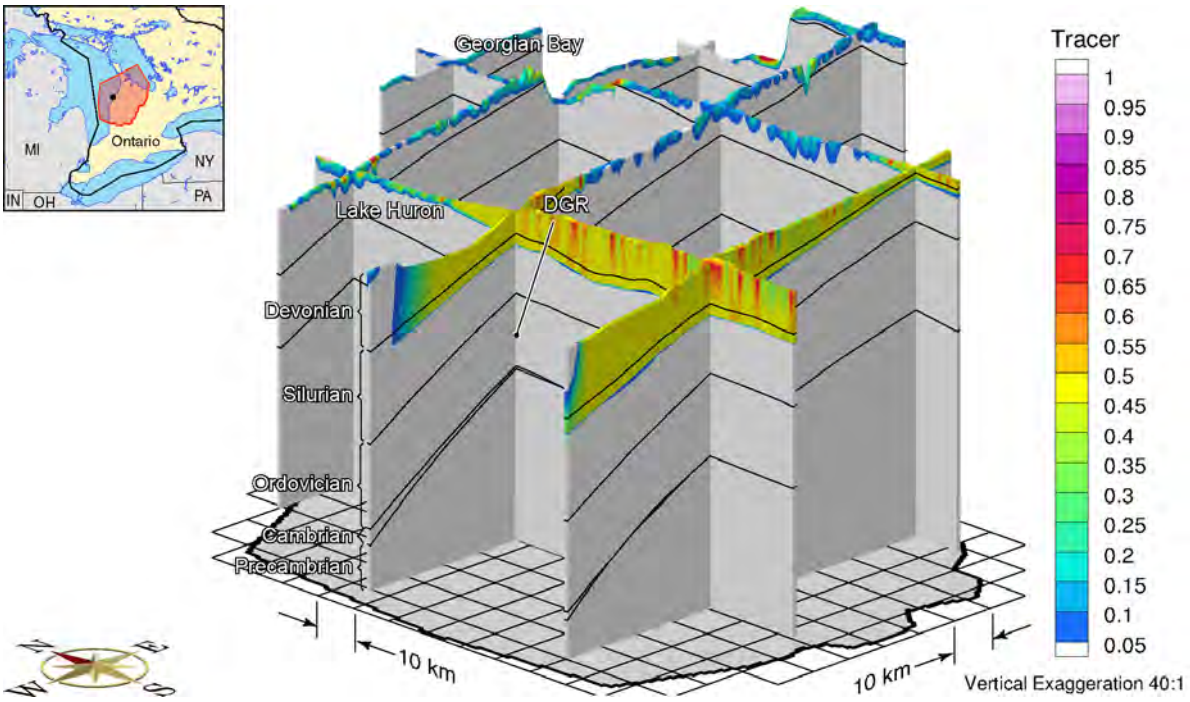

Figure F.51: Fence View Showing the Depth of Penetration of a Tracer at 90ka before Present with the Surface Boundary Condition Based on 30% of Ice Thickness

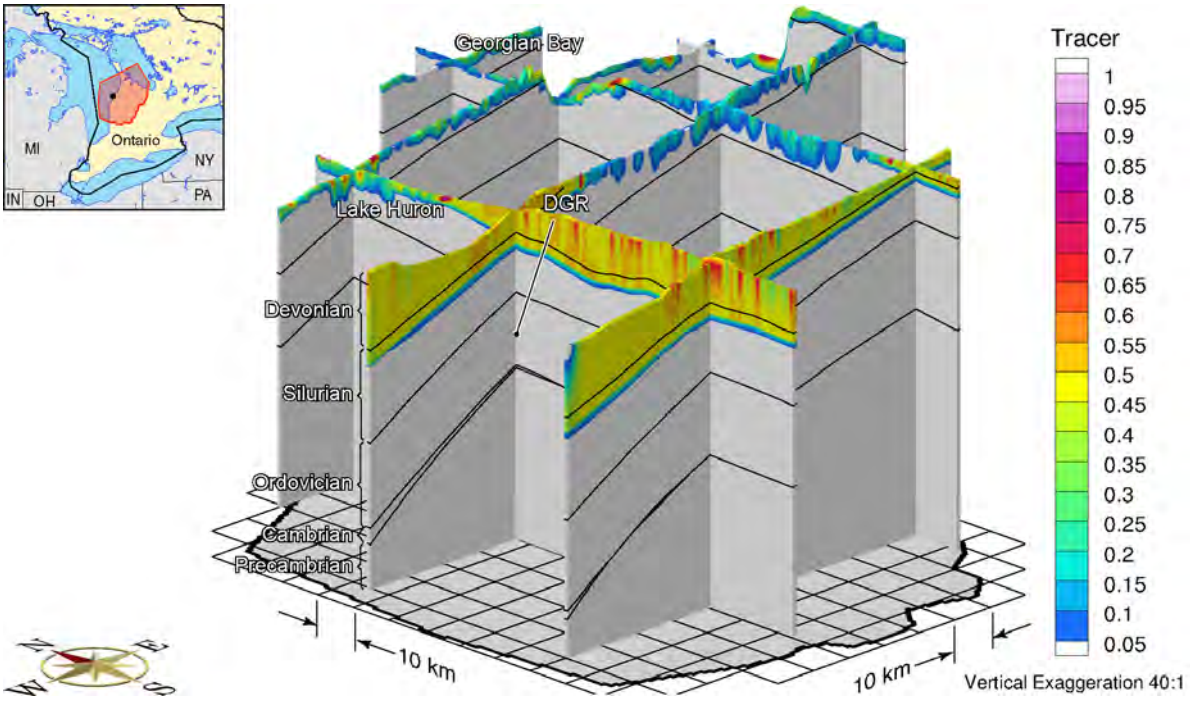

Figure F.52: Fence View Showing the Depth of Penetration of a Tracer at 60ka before Present with the Surface Boundary Condition Based on 30% of Ice Thickness

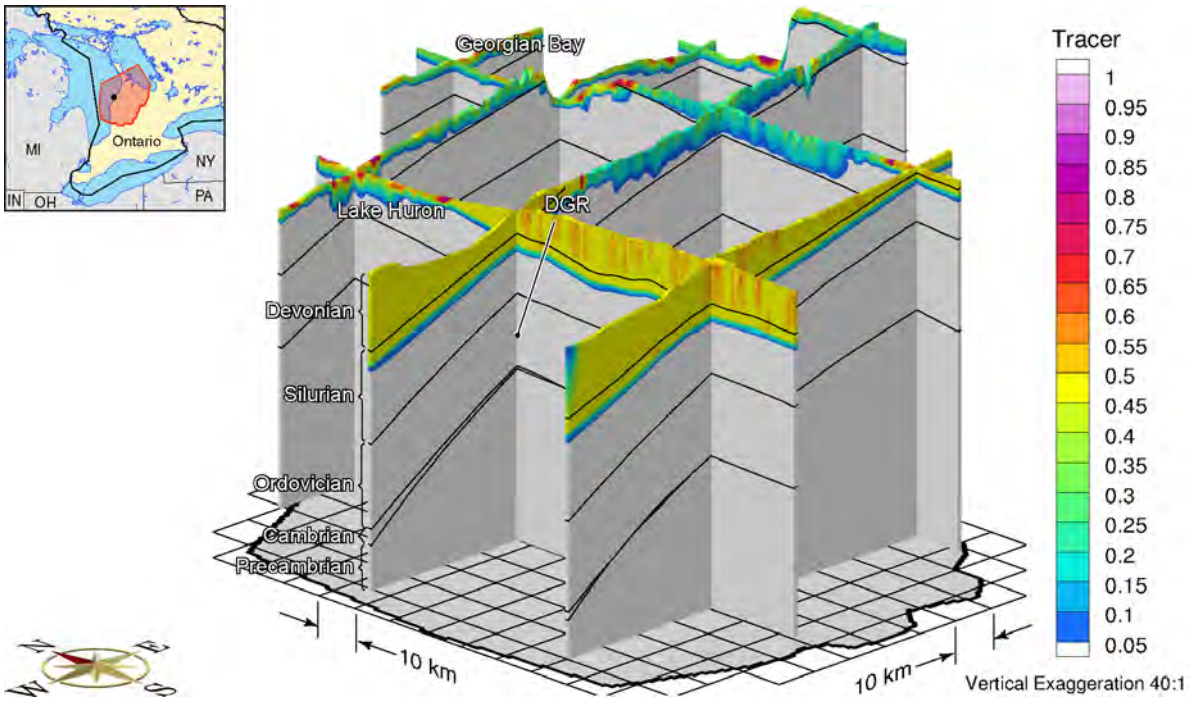

Figure F.53: Fence View Showing the Depth of Penetration of a Tracer at 30ka before Present with the Surface Boundary Condition Based on 30% of Ice Thickness

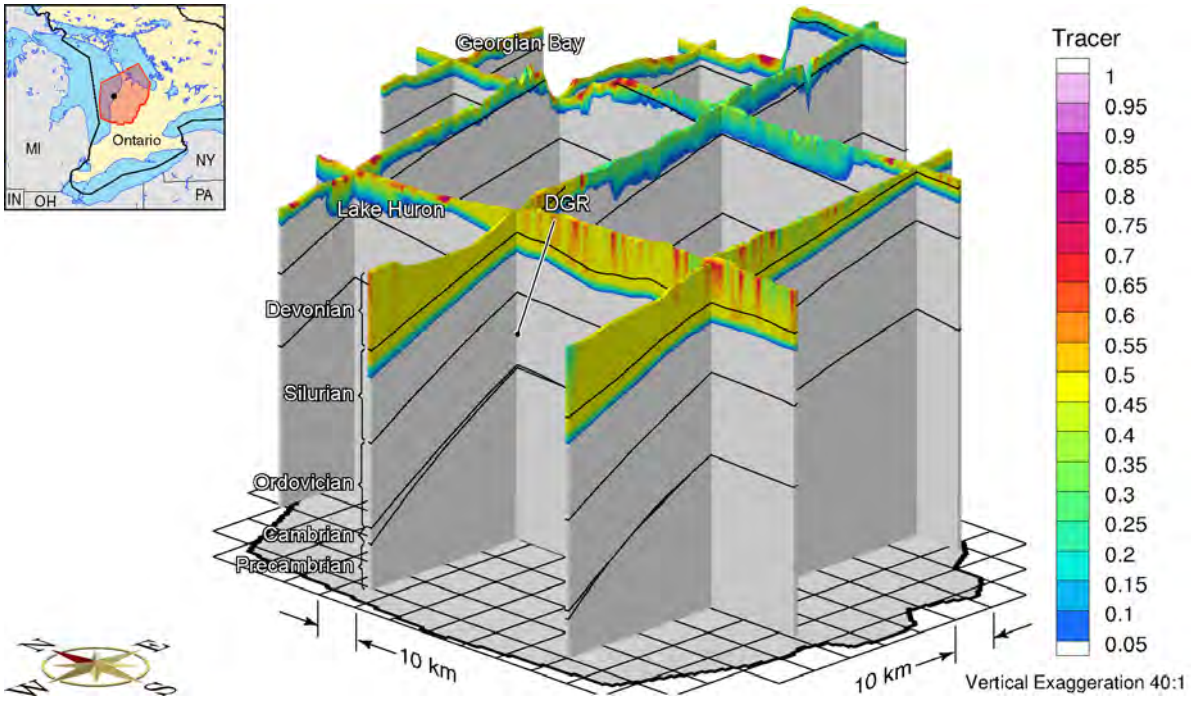

Figure F.54: Fence View Showing the Depth of Penetration of a Tracer at Present with the Surface Boundary Condition Based on 30% of Ice Thickness

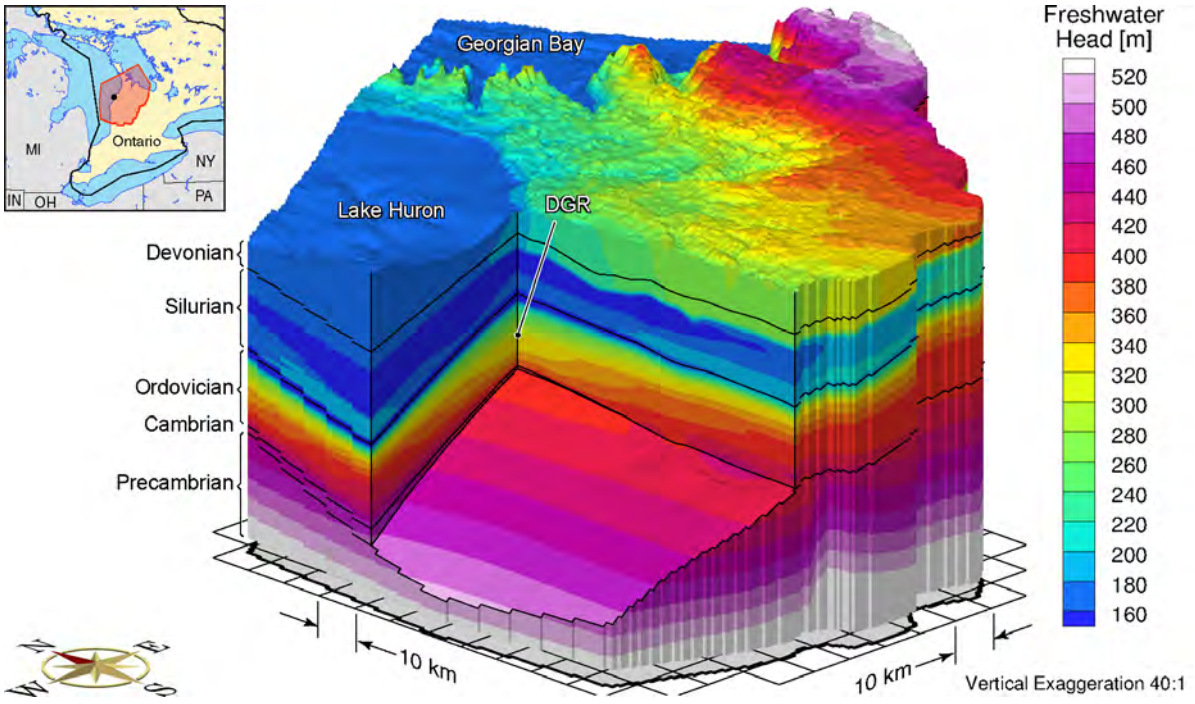

Figure F.55: Block Cut View of Freshwater Heads at Present with a Free Draining Surface Boundary Condition

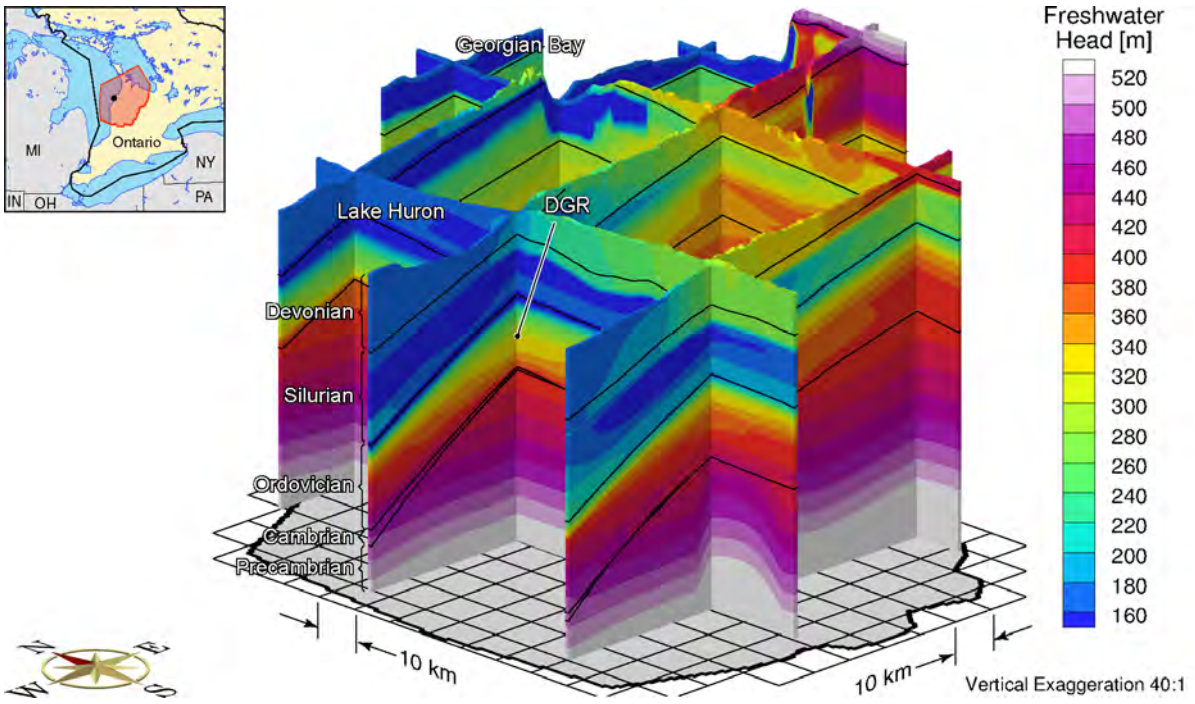

Figure F.56: Fence View of Freshwater Heads at Present with a Free Draining Surface Boundary Condition

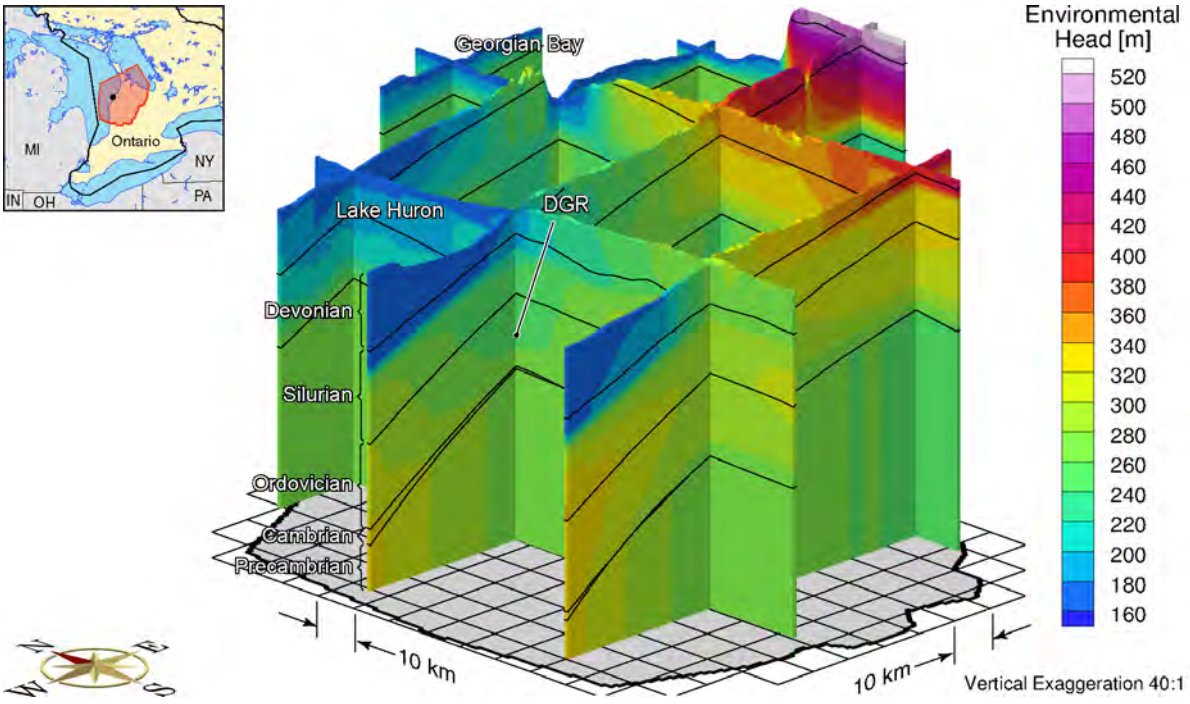

Figure F.57: Fence View of Environmental Heads at 90ka before Present with a Free Draining Surface Boundary Condition

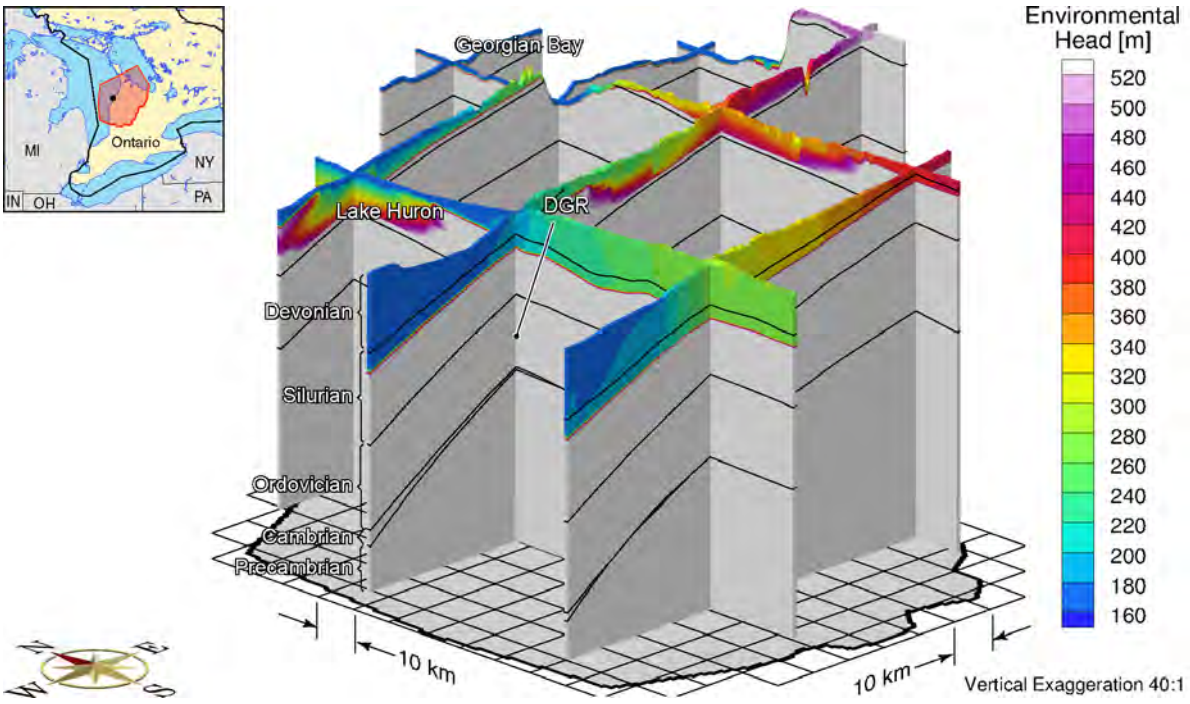

Figure F.58: Fence View of Environmental Heads at 60ka before Present with a Free Draining Surface Boundary Condition

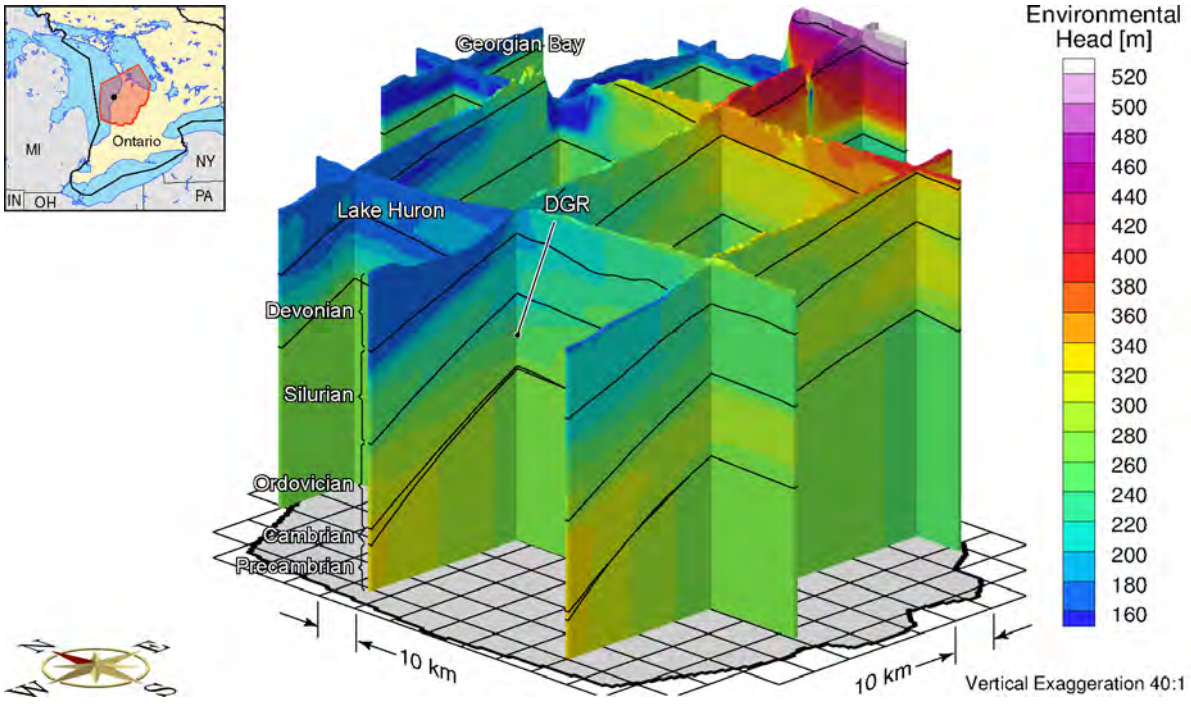

Figure F.59: Fence View of Environmental Heads at 30ka before Present with a Free Draining Surface Boundary Condition

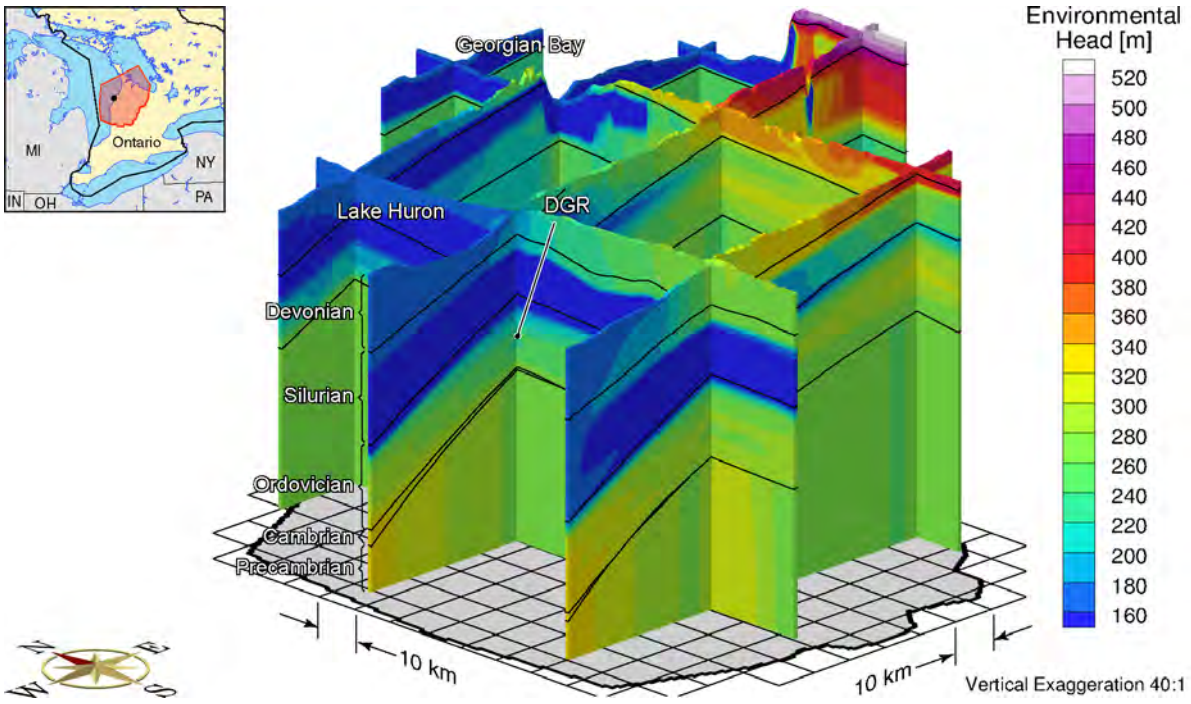

Figure F.60: Fence View of Environmental Heads at the Present with a Free Draining Surface Boundary Condition

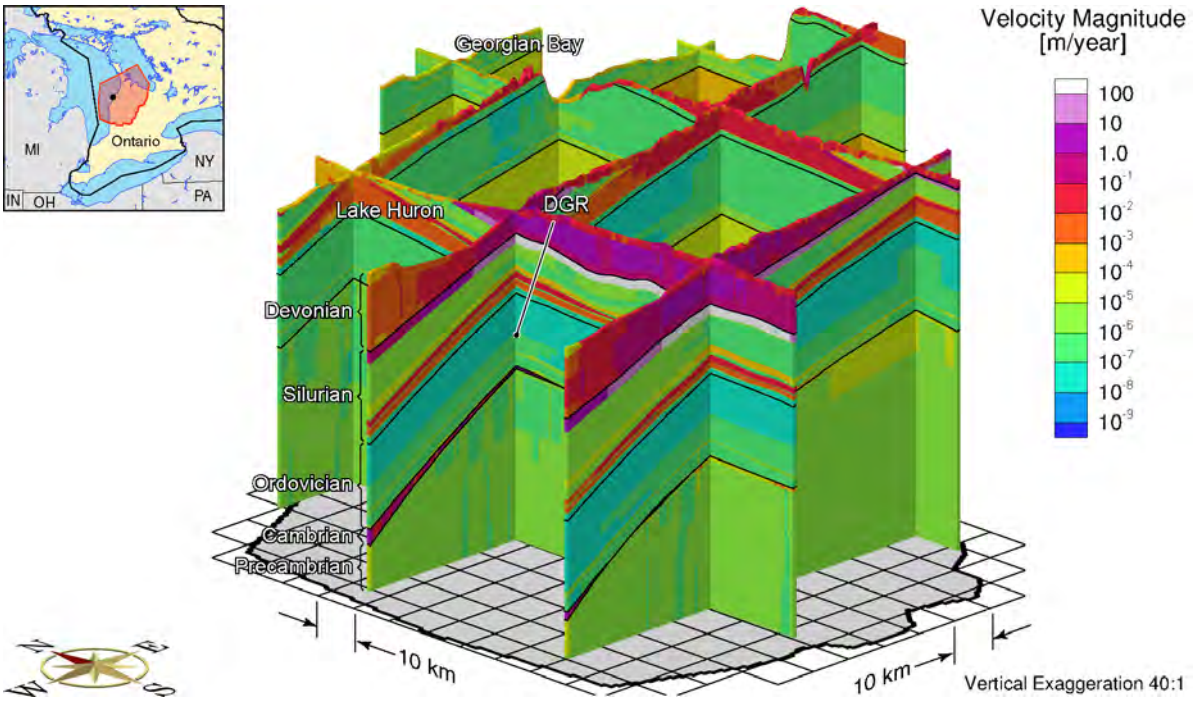

Figure F.61: Fence View of Pore Velocity Magnitude at 90ka before Present with a Free Draining Surface Boundary Condition

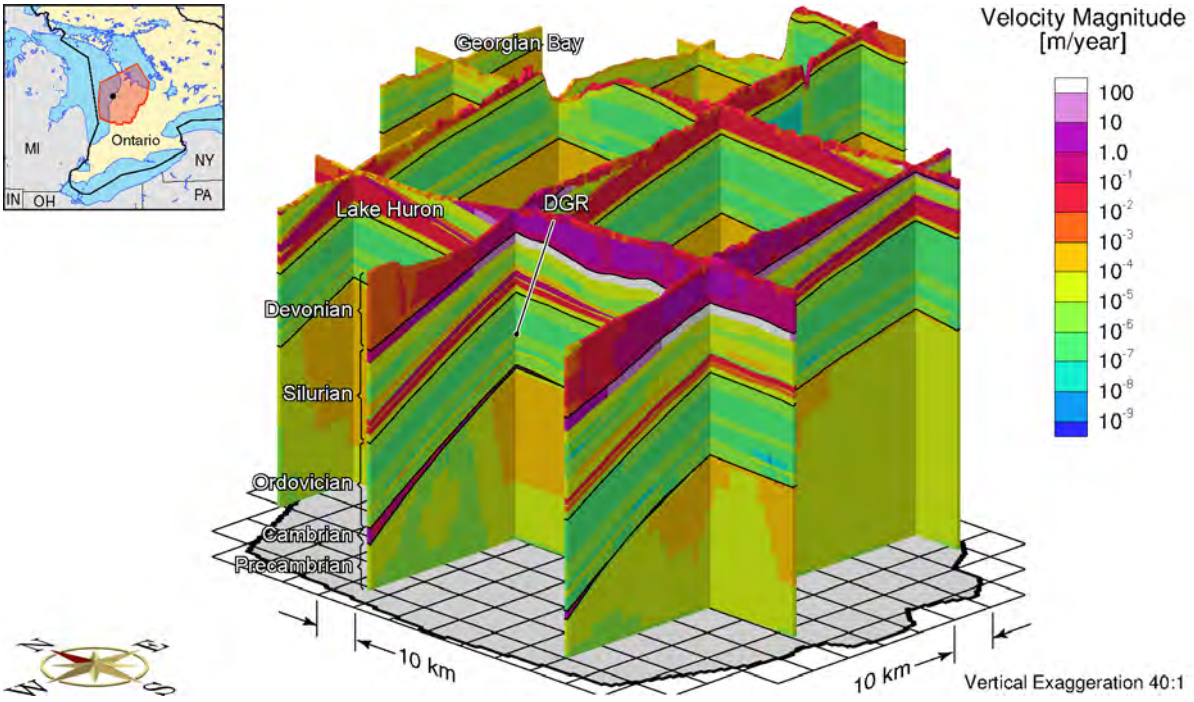

Figure F.62: Fence View of Pore Velocity Magnitude at 60ka before Present with a Free Draining Surface Boundary Condition

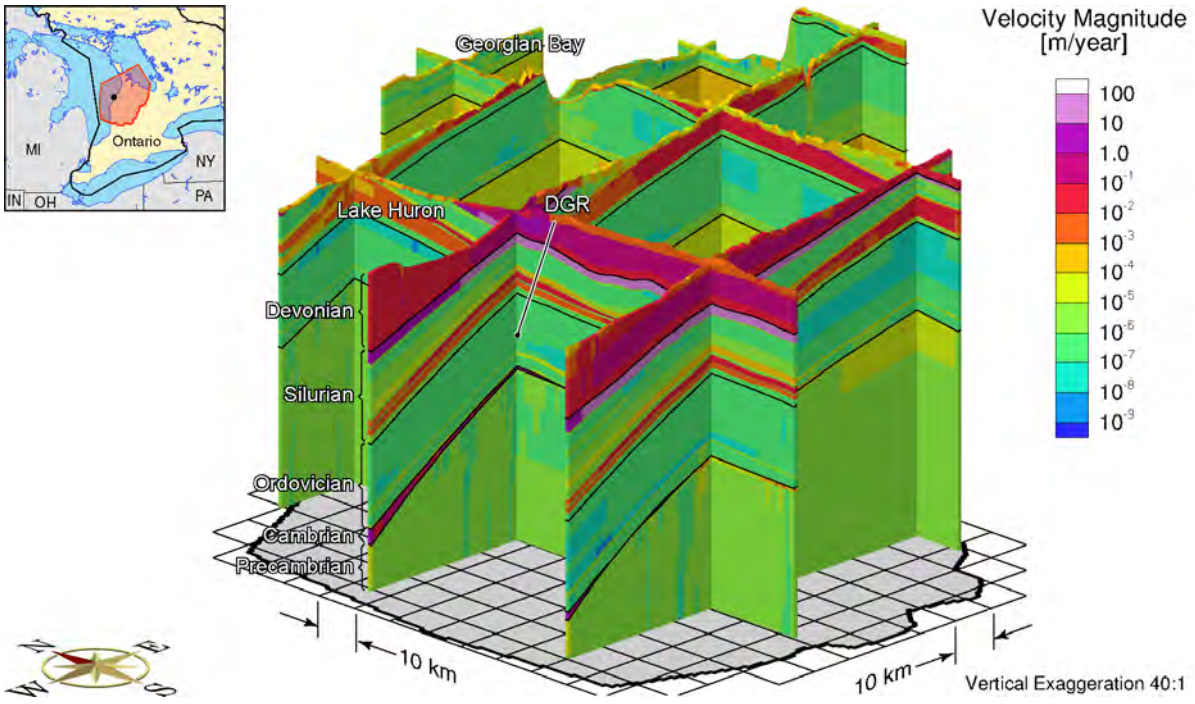

Figure F.63: Fence View of Pore Velocity Magnitude at 30ka before Present with a Free Draining Surface Boundary Condition

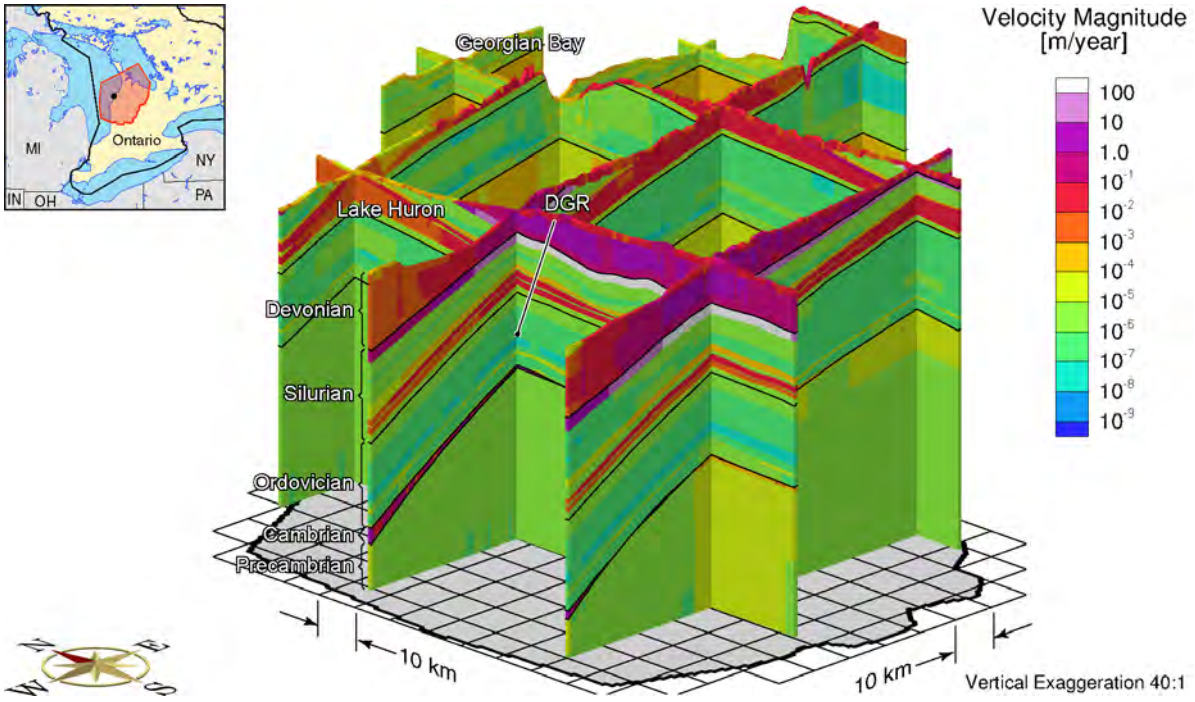

Figure F.64: Fence View of Pore Velocity Magnitude at Present with a Free Draining Surface Boundary Condition

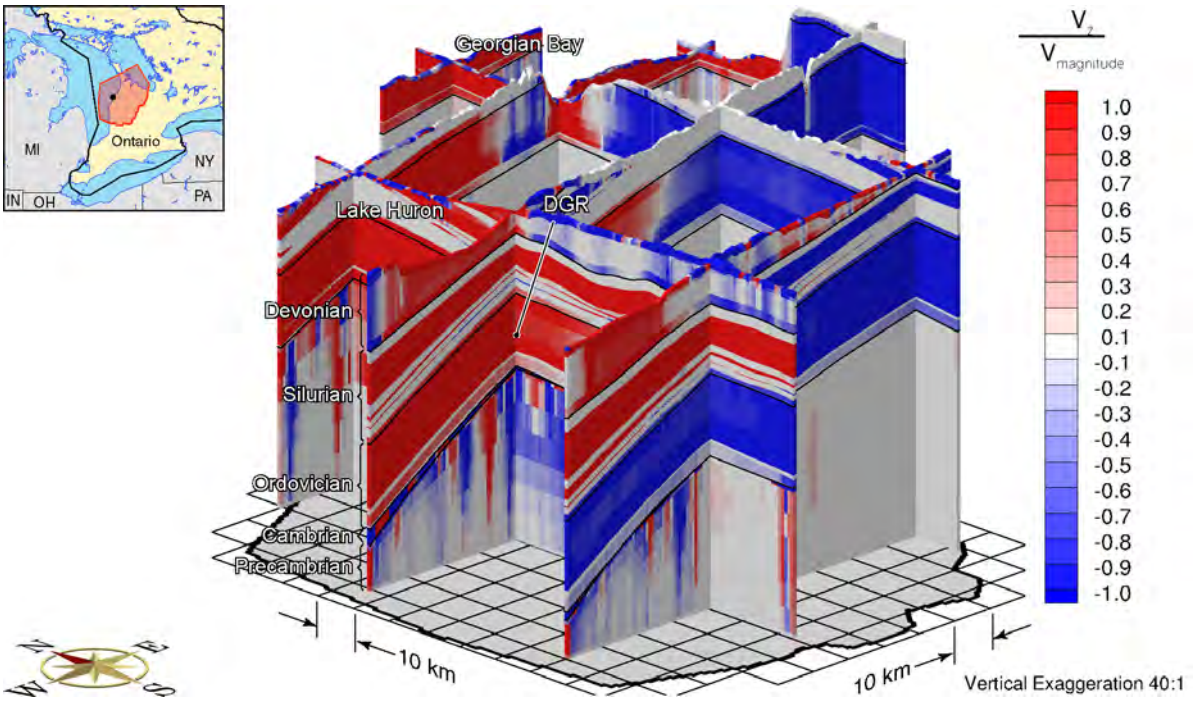

Figure F.65: Fence View Showing the Ratio of the Vertical Pore Water Velocity to the Velocity Magnitude at 90ka before Present with a Free Draining Surface Boundary Condition

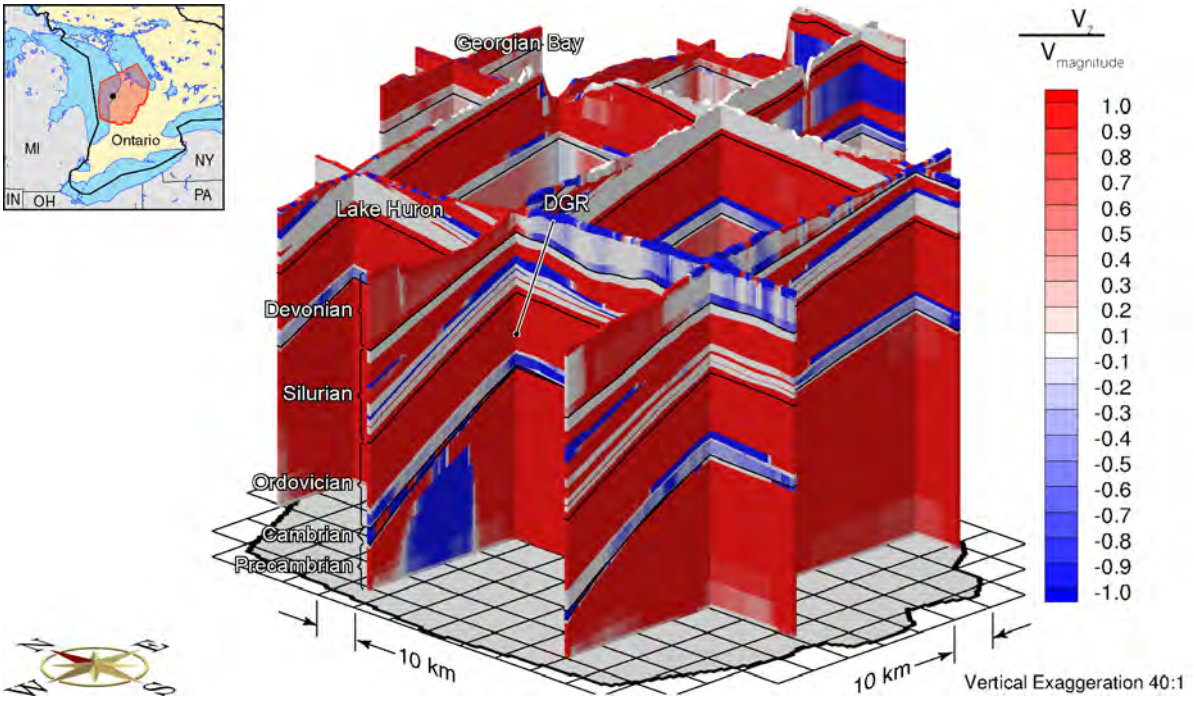

Figure F.66: Fence View Showing the Ratio of the Vertical Pore Water Velocity to the Velocity Magnitude at 60ka before Present with a Free Draining Surface Boundary Condition

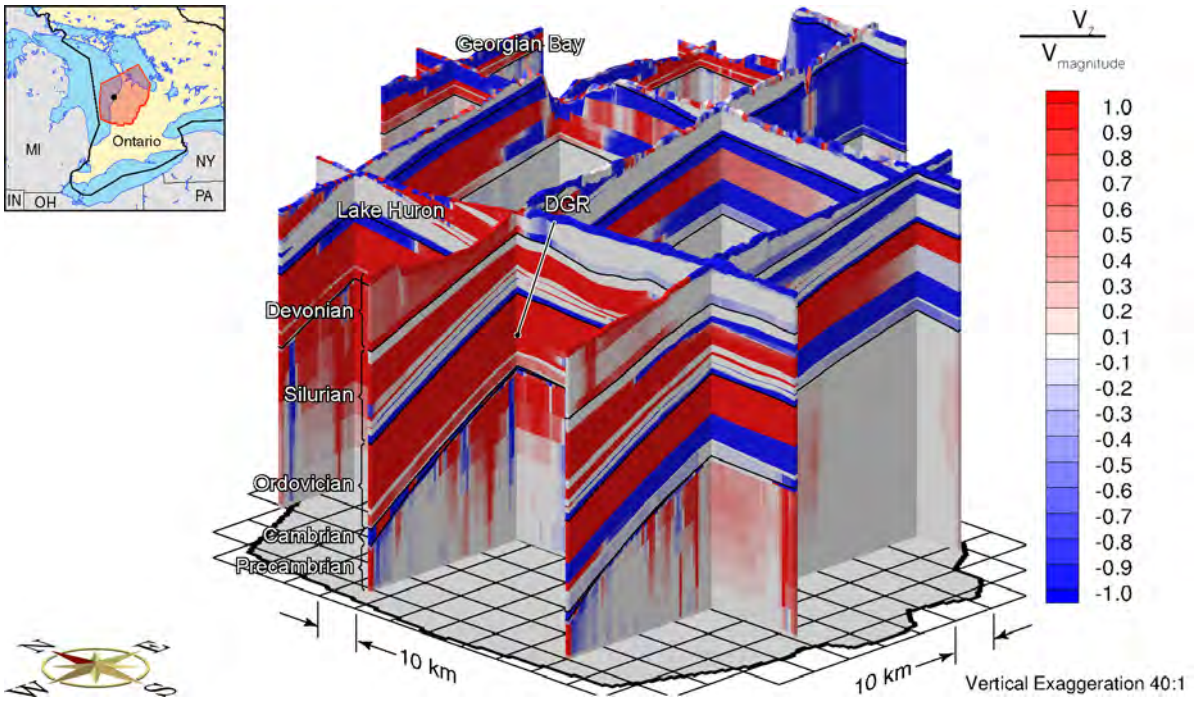

Figure F.67: Fence View Showing the Ratio of the Vertical Pore Water Velocity to the Velocity Magnitude at 30ka before Present with a Free Draining Surface Boundary Condition

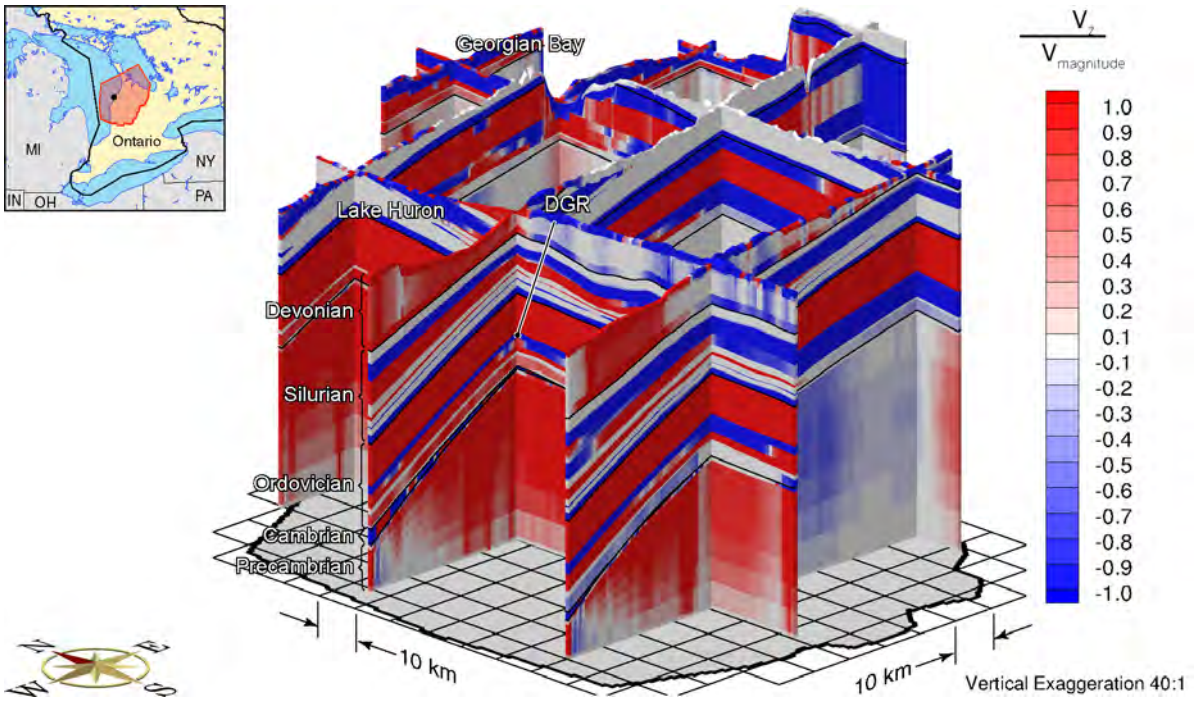

Figure F.68: Fence View of Ratio of Vertical Pore Velocity to Pore Velocity Magnitude at Present with a Free Draining Surface Boundary Condition

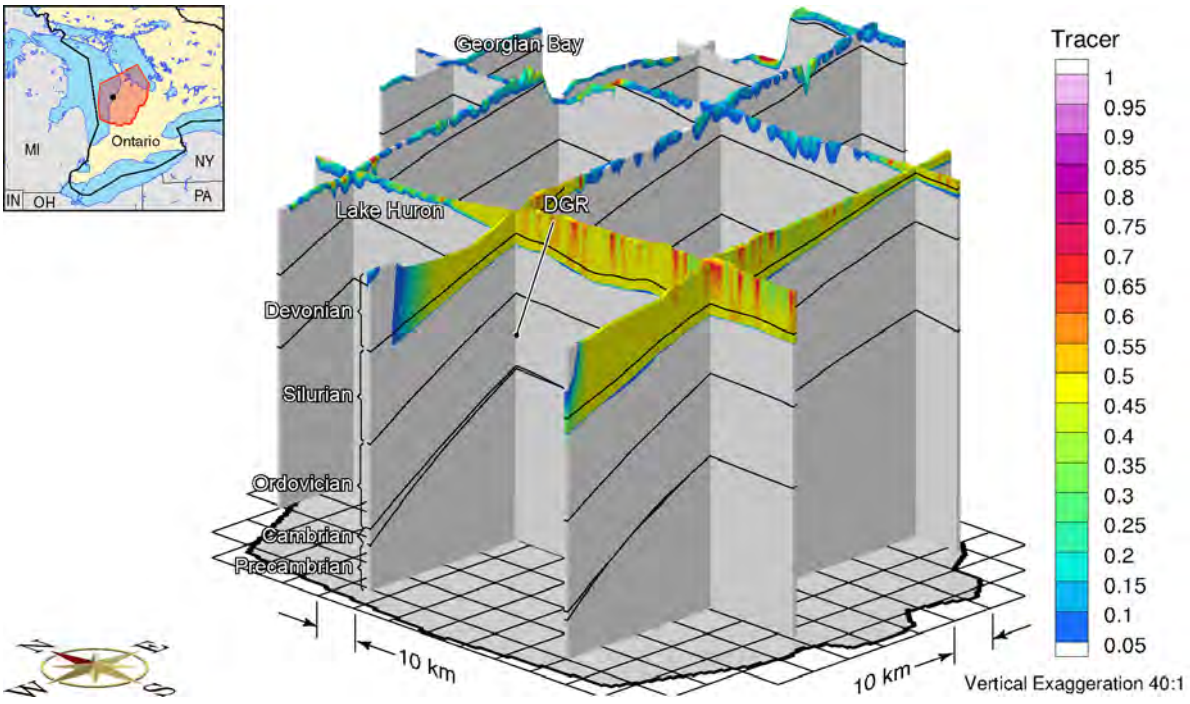

Figure F.69: Fence View Showing the Depth of Penetration of a Tracer at 90ka before Present with a Free Draining Surface Boundary Condition

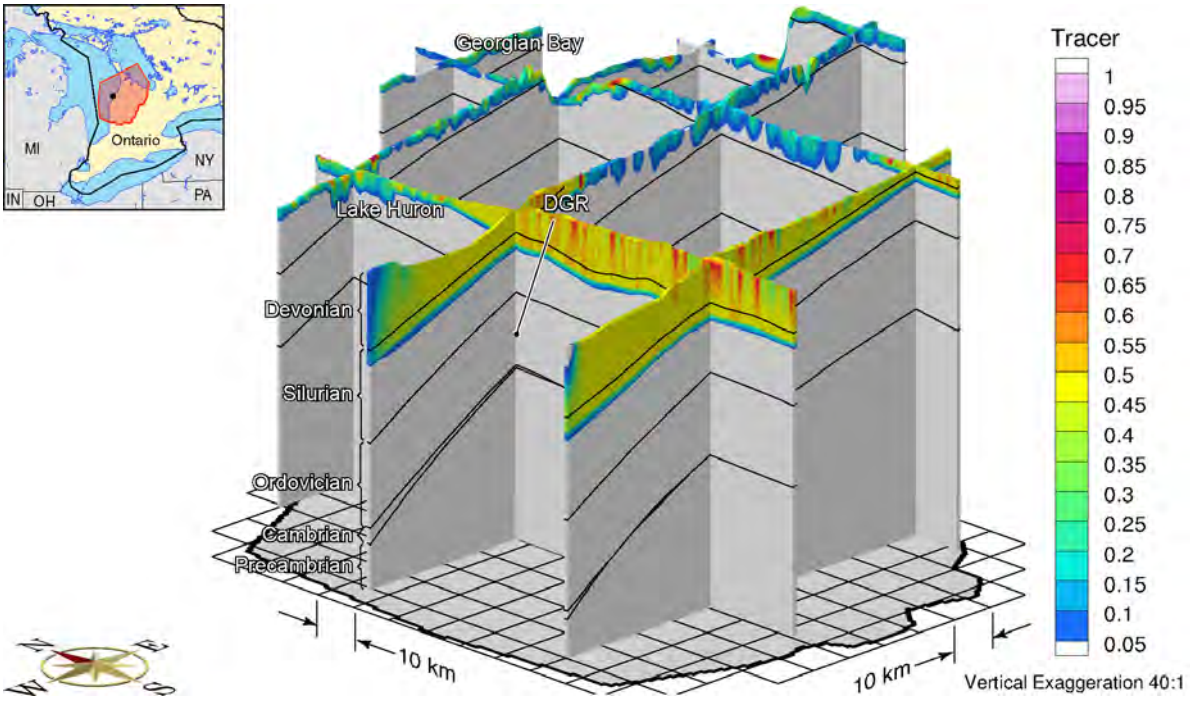

Figure F.70: Fence View Showing the Depth of Penetration of a Tracer at 60ka before Present with a Free Draining Surface Boundary Condition

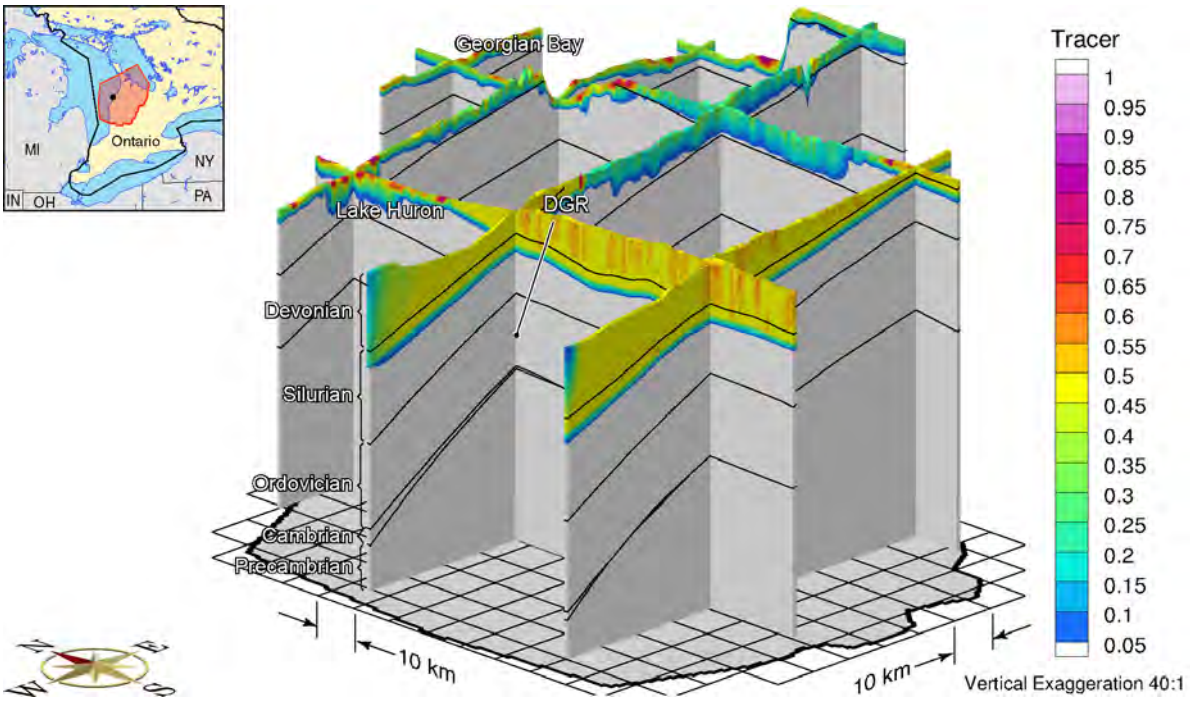

Figure F.71: Fence View Showing the Depth of Penetration of a Tracer at 30ka before Present with a Free Draining Surface Boundary Condition

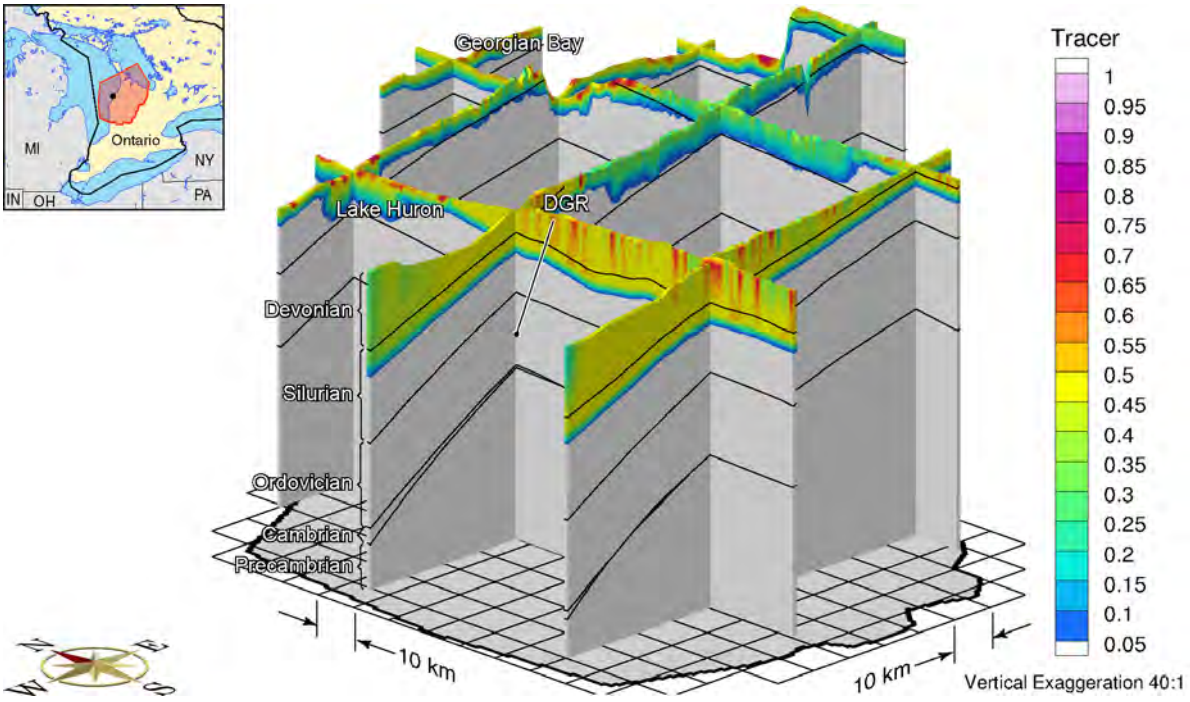

Figure F.72: Fence View Showing the Depth of Penetration of a Tracer at Present with a Free Draining Surface Boundary Condition

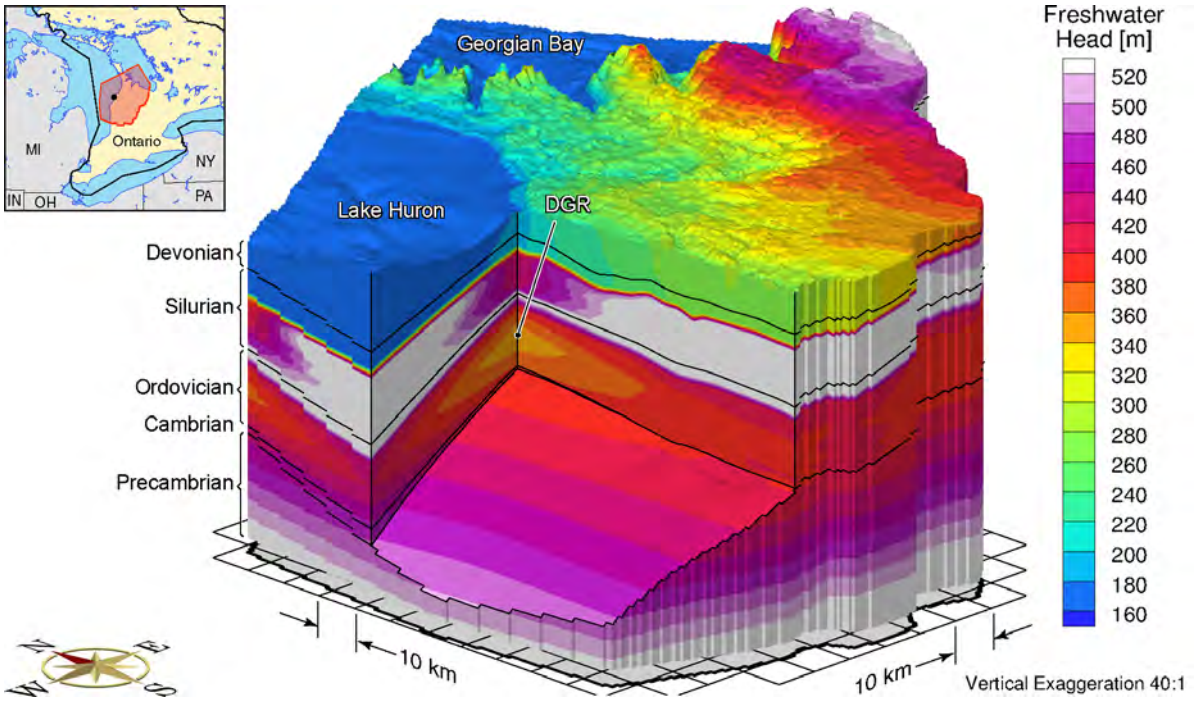

Figure F.73: Block Cut View of Freshwater Heads at Present with a One-dimensional Loading Efficiency of Zero

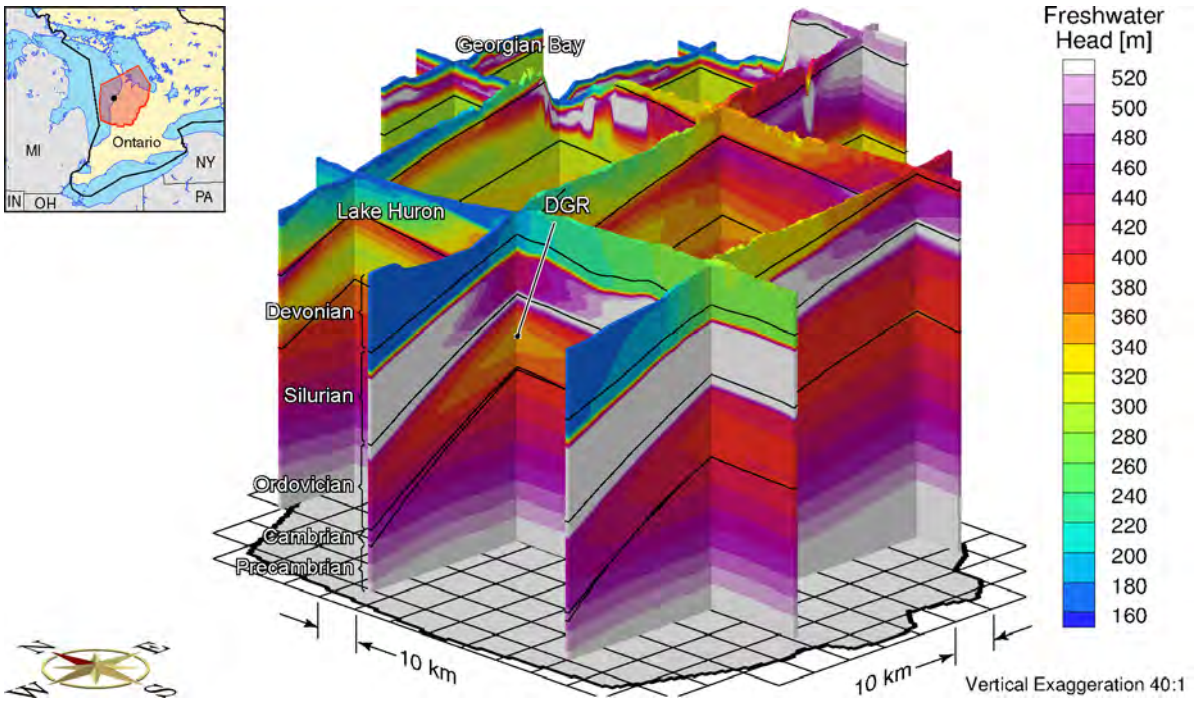

Figure F.74: Fence View of Freshwater Heads at Present with a One-dimensional Loading Efficiency of Zero

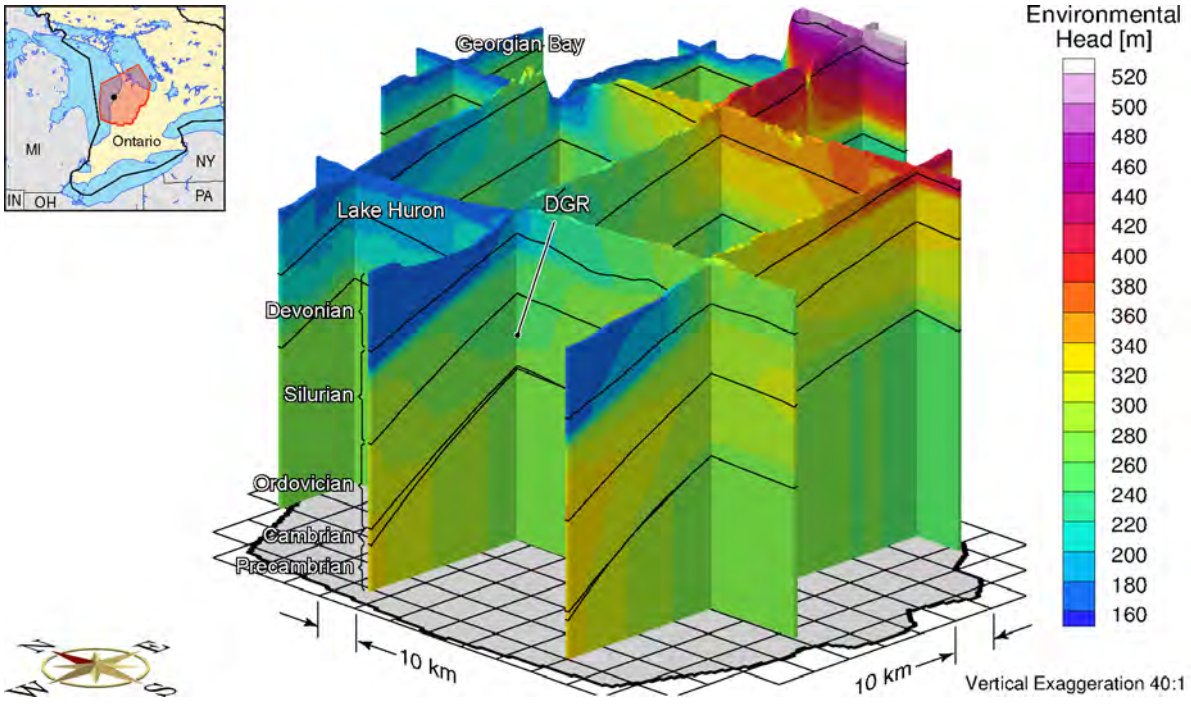

Figure F.75: Fence View of Environmental Heads at 90ka before Present with a One-dimensional Loading Efficiency of Zero

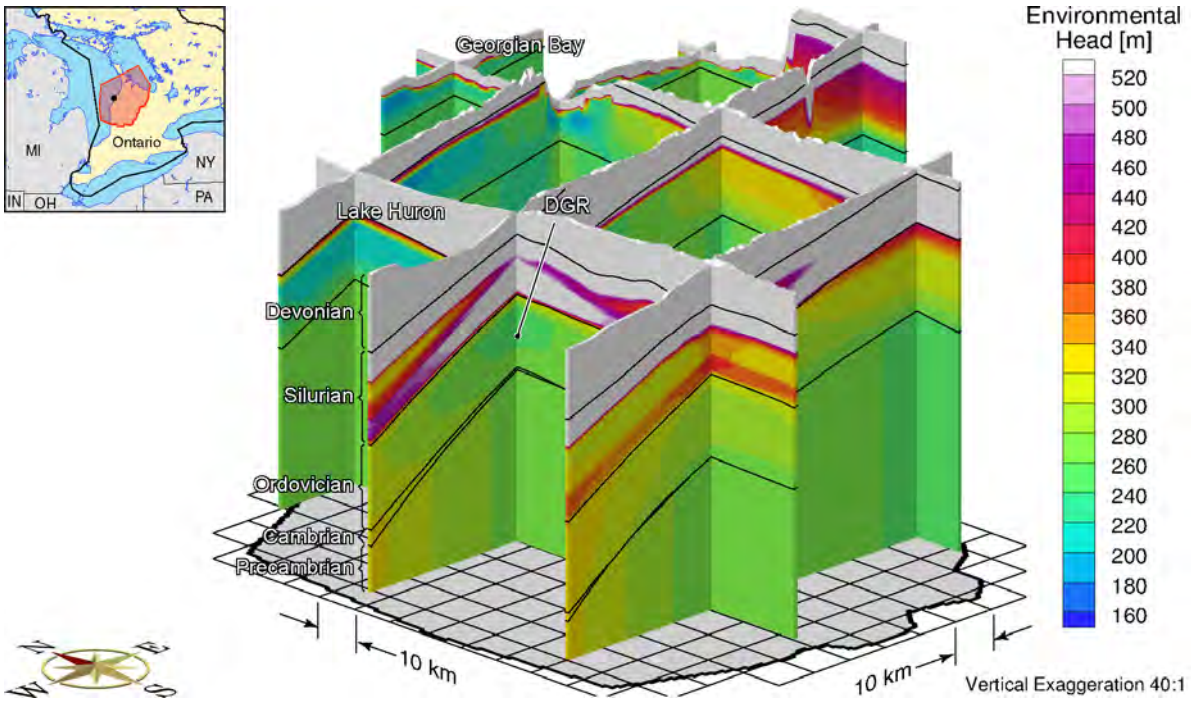

Figure F.76: Fence View of Environmental Heads at 60ka before Present with a One-dimensional Loading Efficiency of Zero

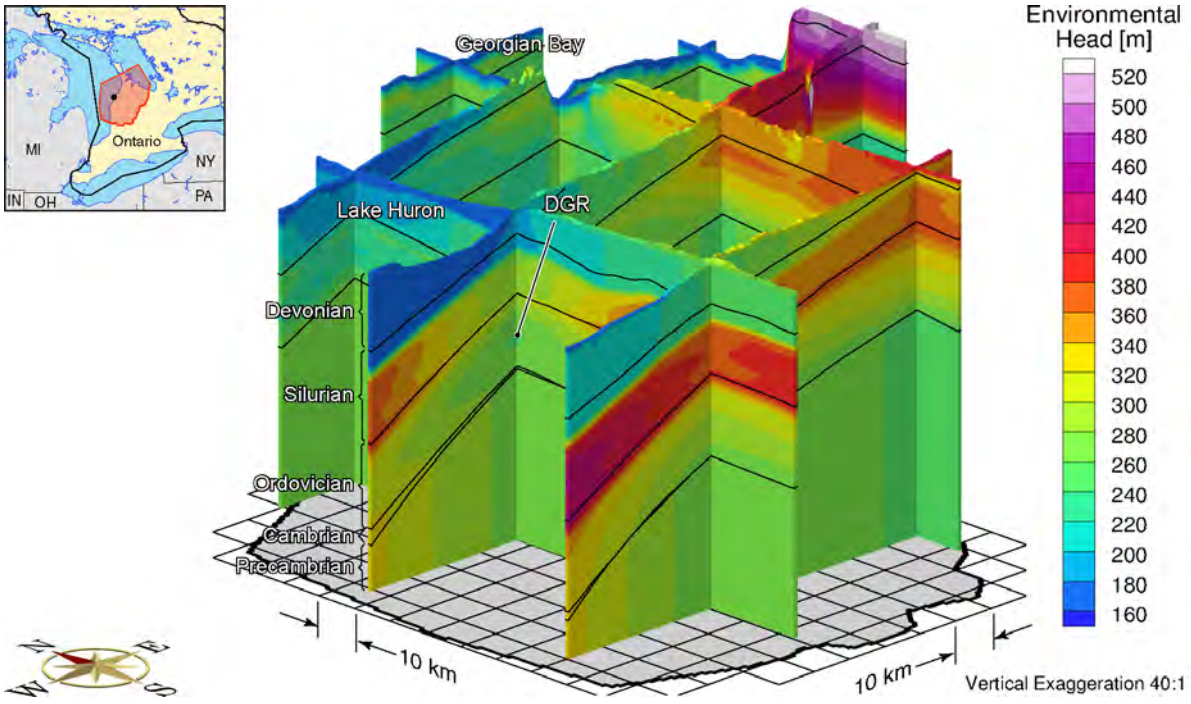

Figure F.77: Fence View of Environmental Heads at 30ka before Present with a One-dimensional Loading Efficiency of Zero

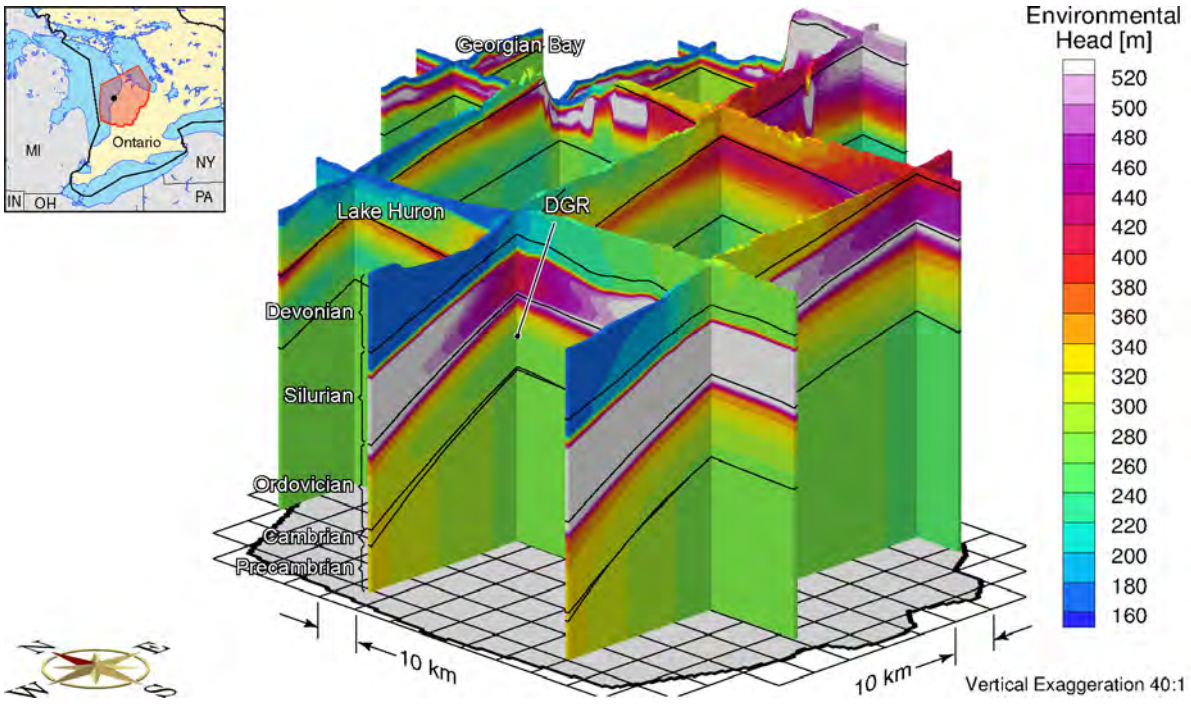

Figure F.78: Fence View of Environmental Heads at the Present with a One-dimensional Loading Efficiency of Zero

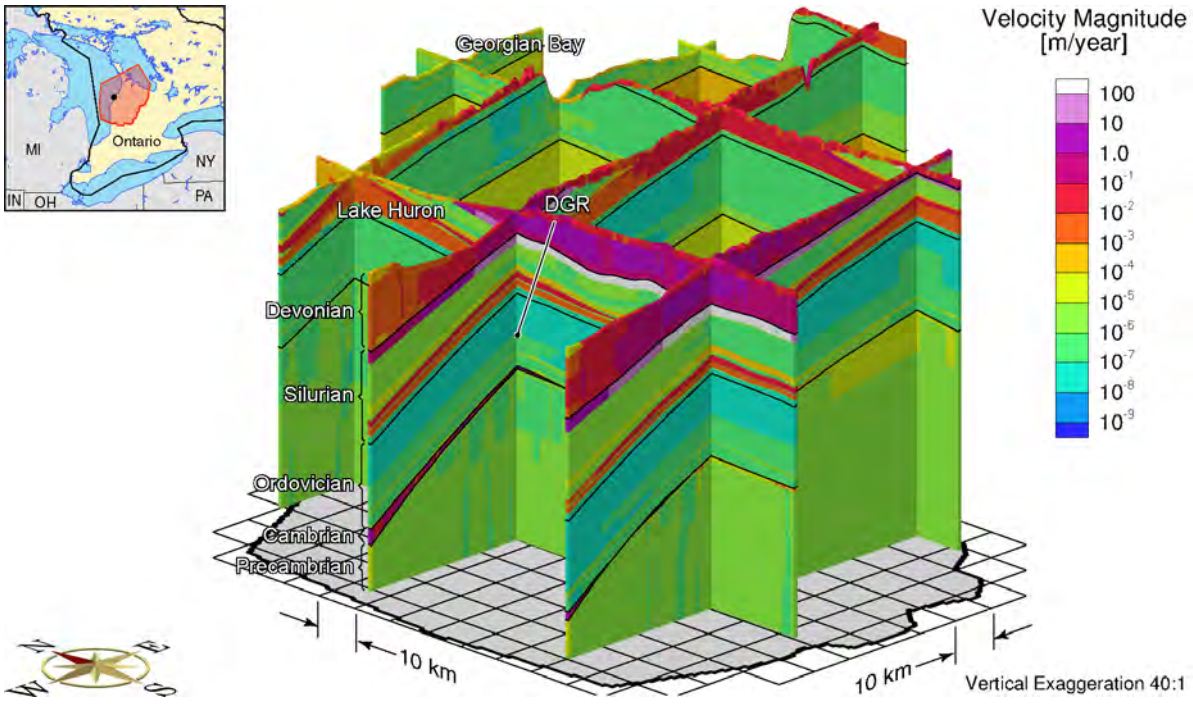

Figure F.79: Fence View of Pore Velocity Magnitude at 90ka before Present with a One-dimensional Loading Efficiency of Zero

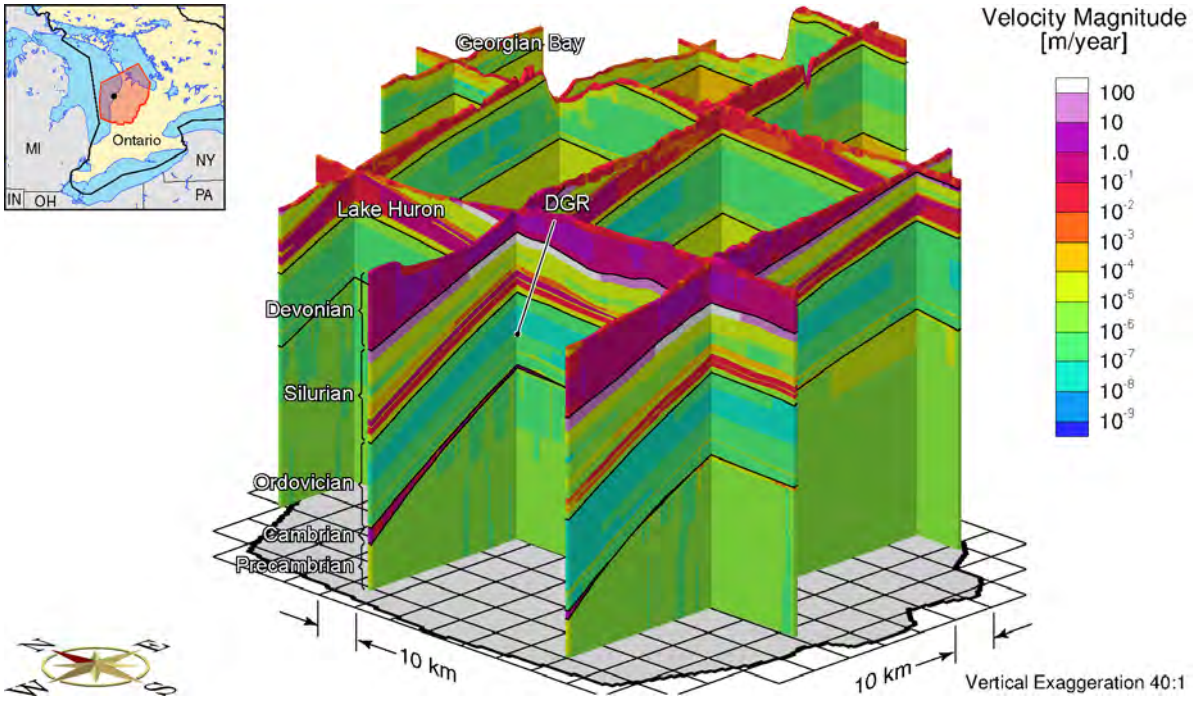

Figure F.80: Fence View of Pore Velocity Magnitude at 60ka before Present with a One-dimensional Loading Efficiency of Zero

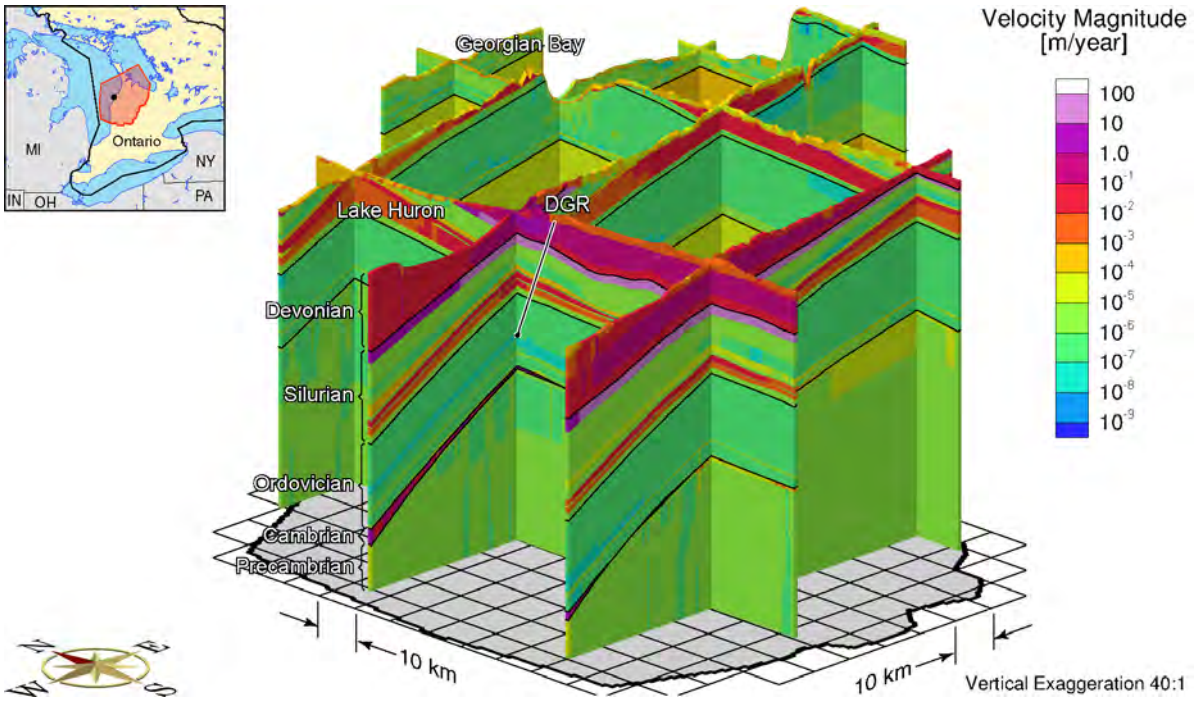

Figure F.81: Fence View of Pore Velocity Magnitude at 30ka before Present with a One-dimensional Loading Efficiency of Zero

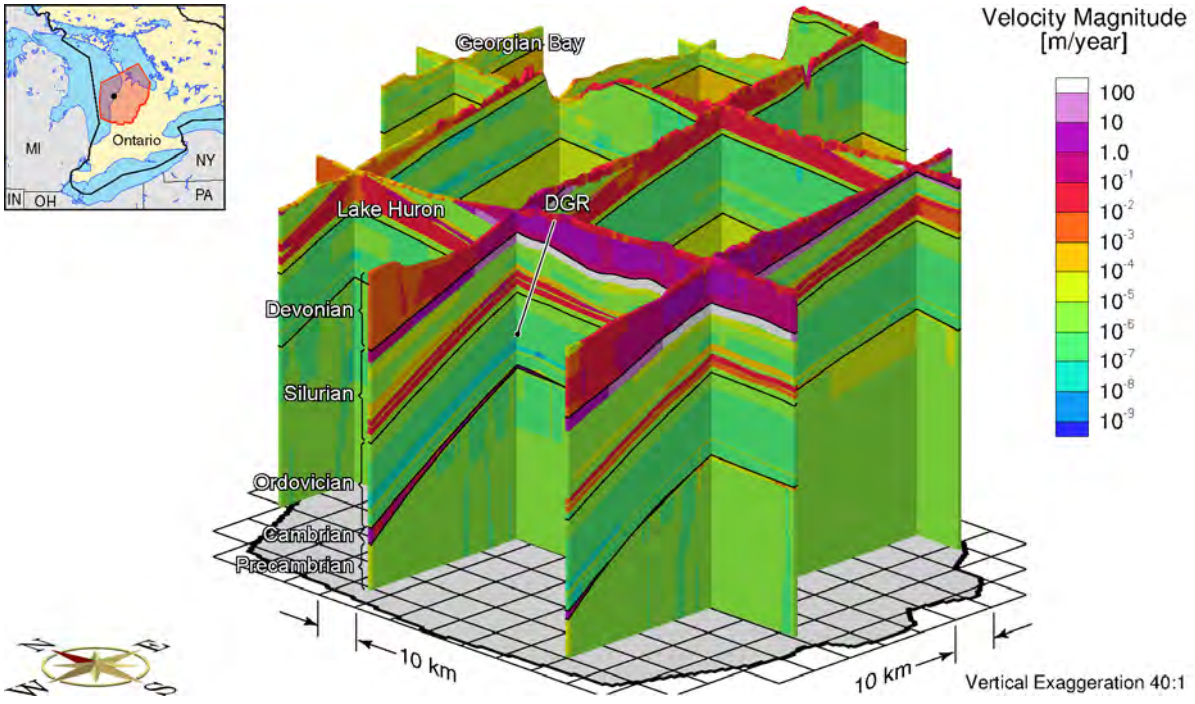

Figure F.82: Fence View of Pore Velocity Magnitude at Present with a One-dimensional Loading Efficiency of Zero

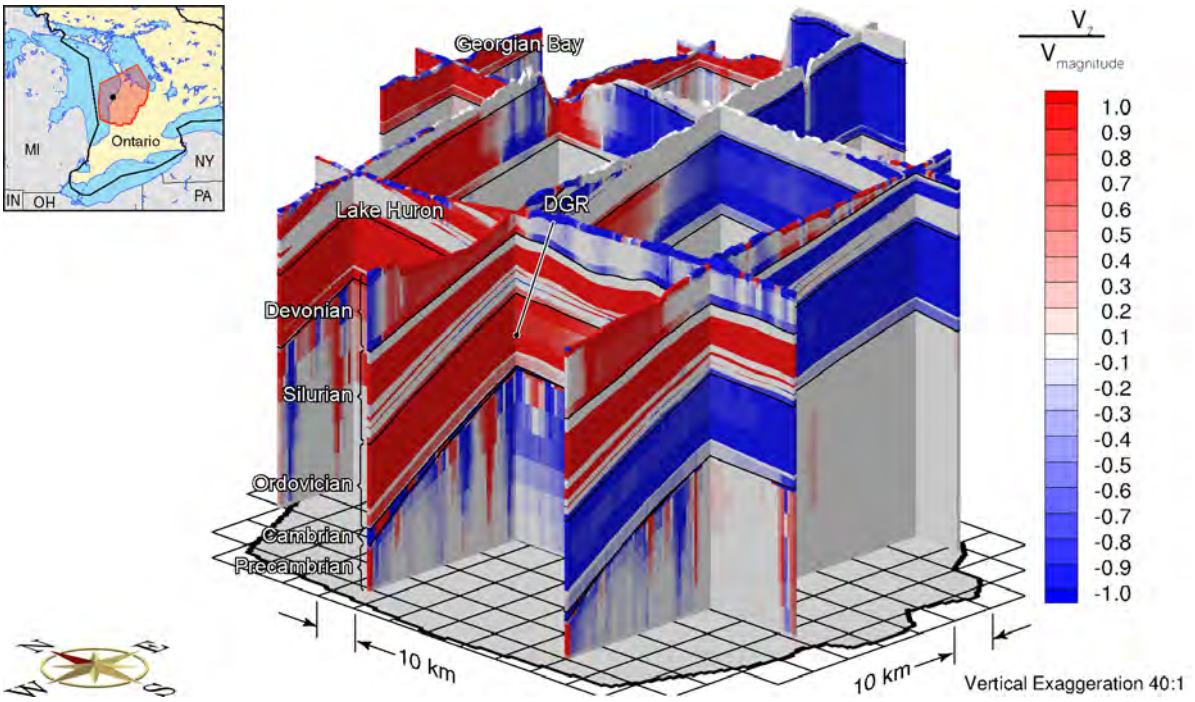

Figure F.83: Fence View Showing the Ratio of the Vertical Pore Water Velocity to the Velocity Magnitude at 90ka before Present with a One-dimensional Loading Efficiency of Zero

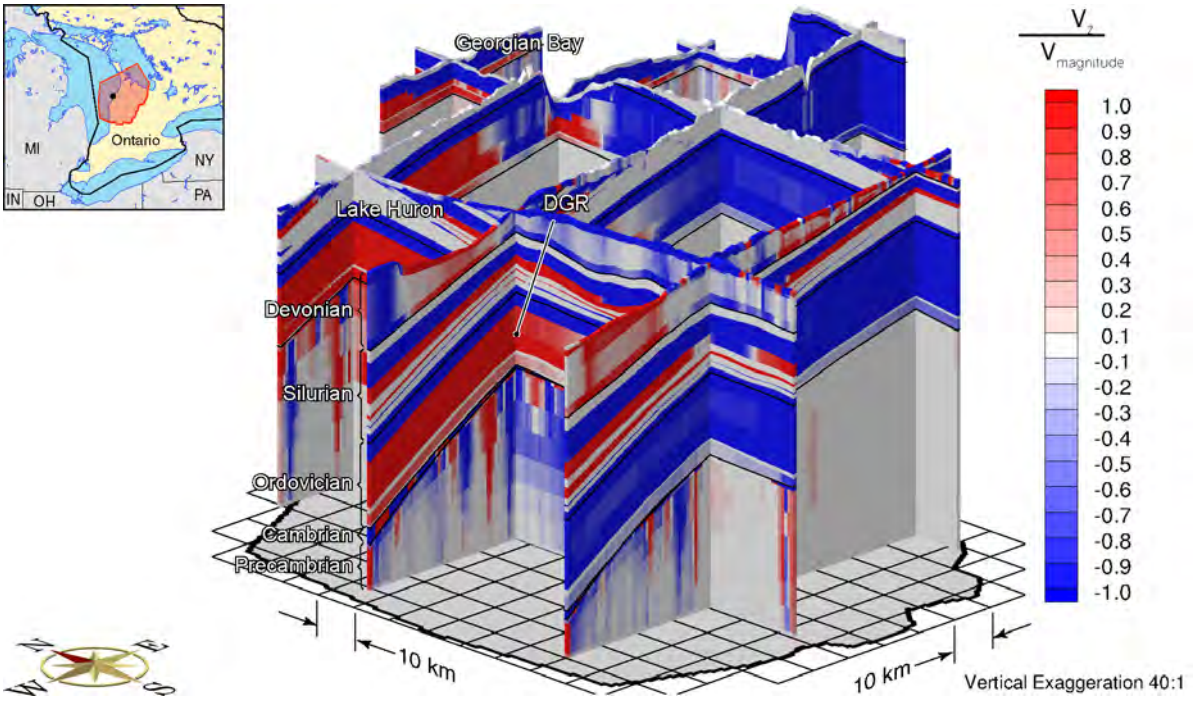

Figure F.84: Fence View Showing the Ratio of the Vertical Pore Water Velocity to the Velocity Magnitude at 60ka before Present with a One-dimensional Loading Efficiency of Zero

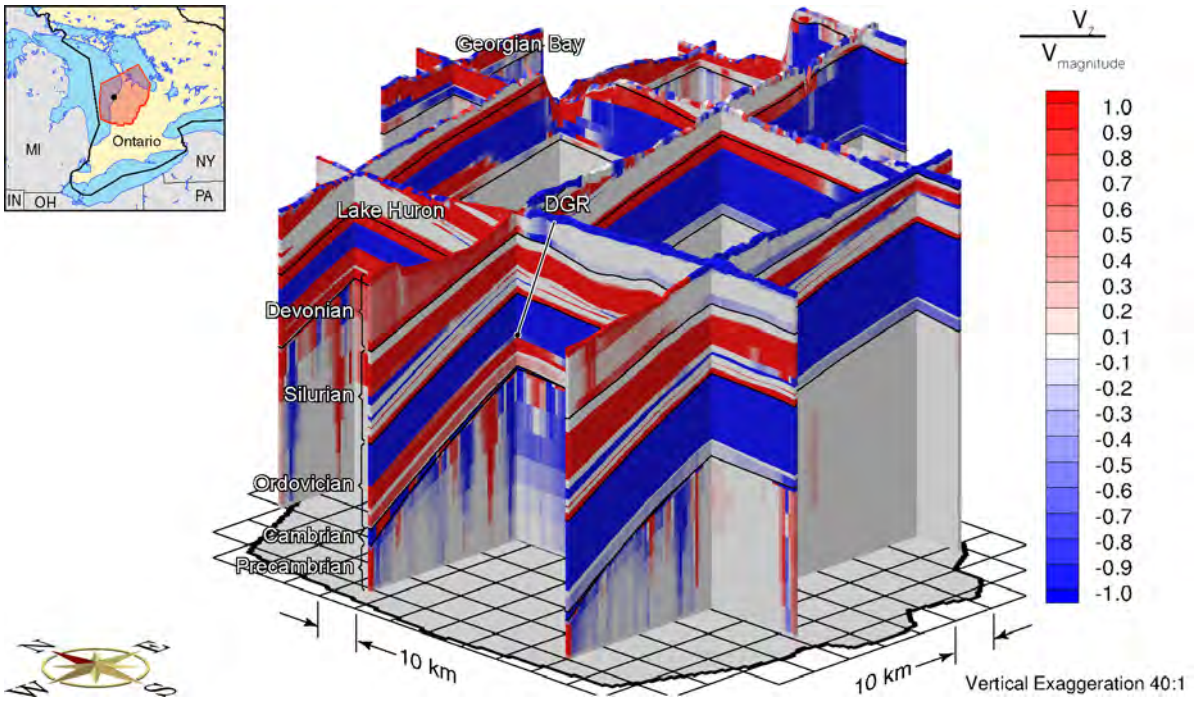

Figure F.85: Fence View Showing the Ratio of the Vertical Pore Water Velocity to the Velocity Magnitude at 30ka before Present with a One-dimensional Loading Efficiency of Zero

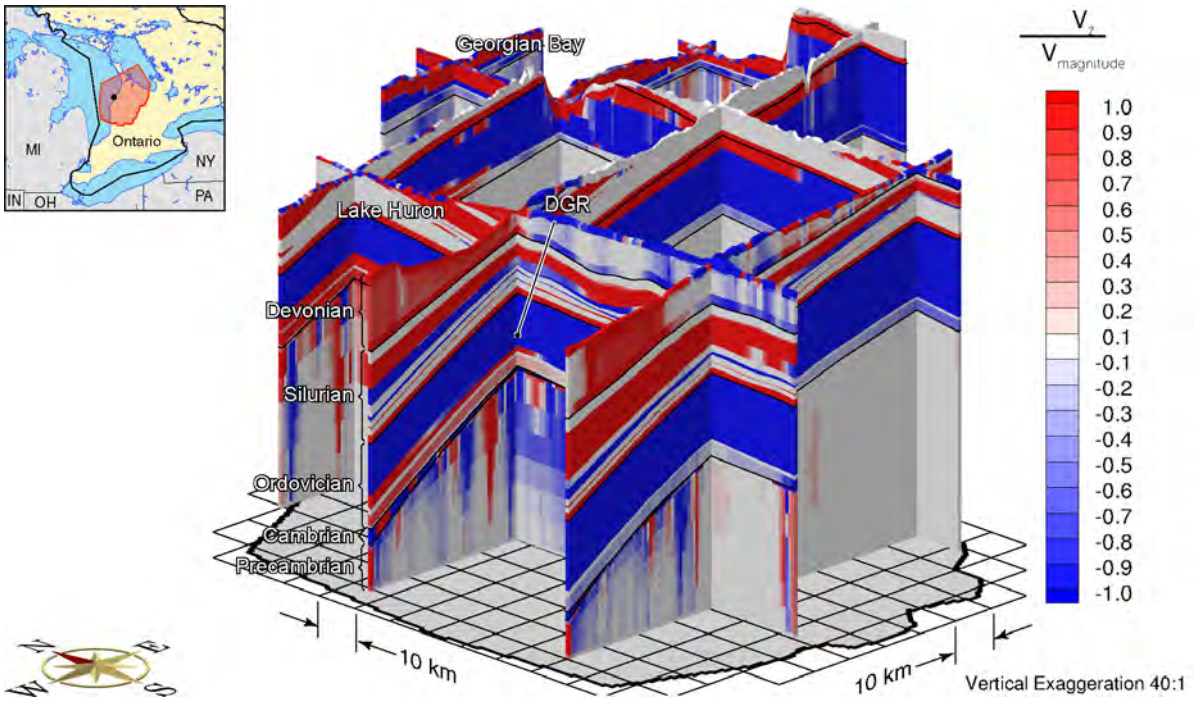

Figure F.86: Fence View of Ratio of Vertical Pore Velocity to Pore Velocity Magnitude at Present with a One-dimensional Loading Efficiency of Zero

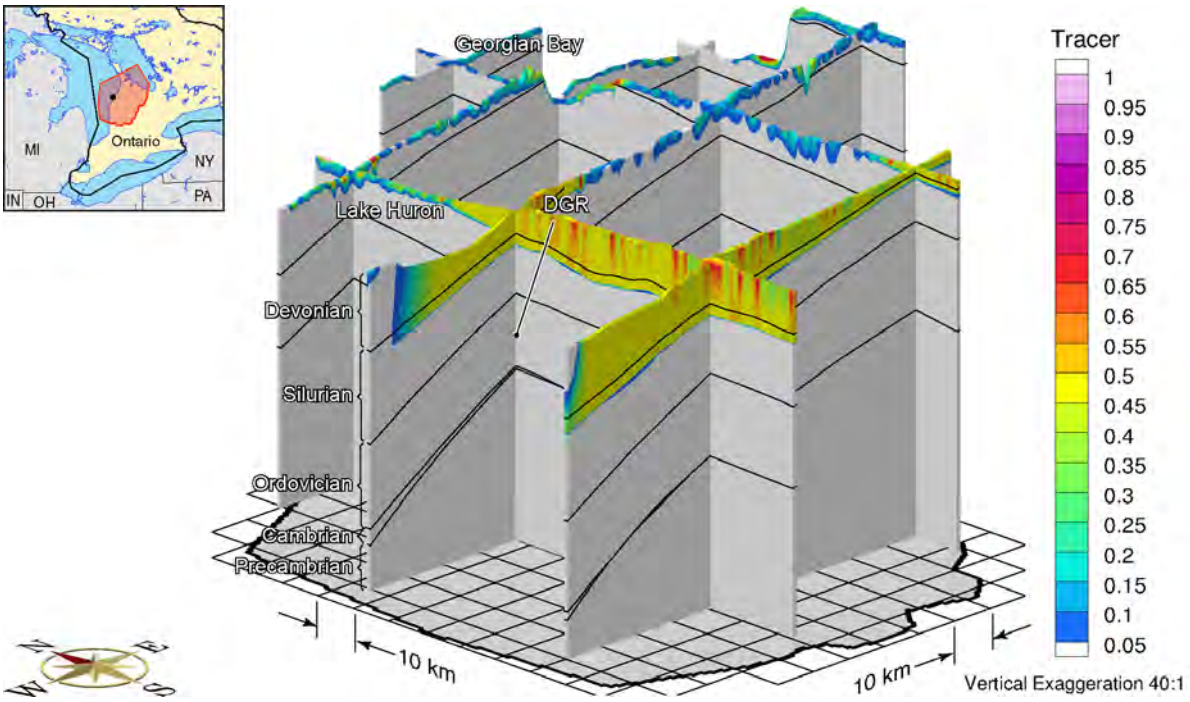

Figure F.87: Fence View Showing the Depth of Penetration of a Tracer at 90ka before Present with a One-dimensional Loading Efficiency of Zero

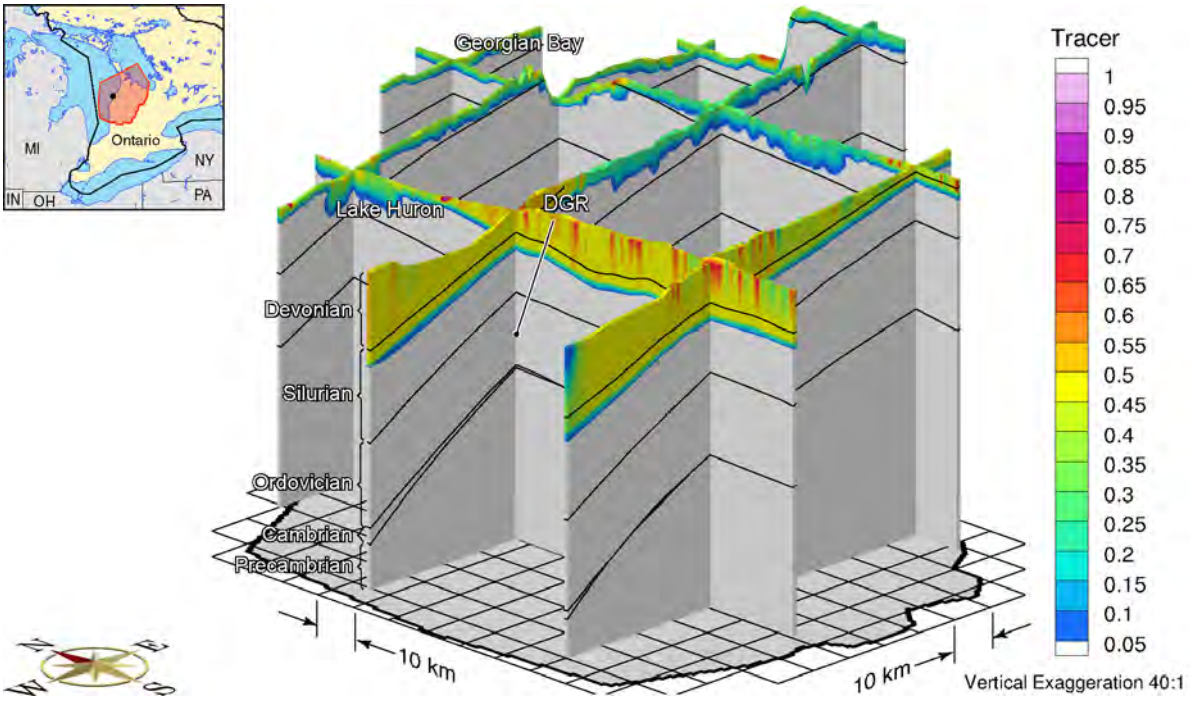

Figure F.88: Fence View Showing the Depth of Penetration of a Tracer at 60ka before Present with a One-dimensional Loading Efficiency of Zero

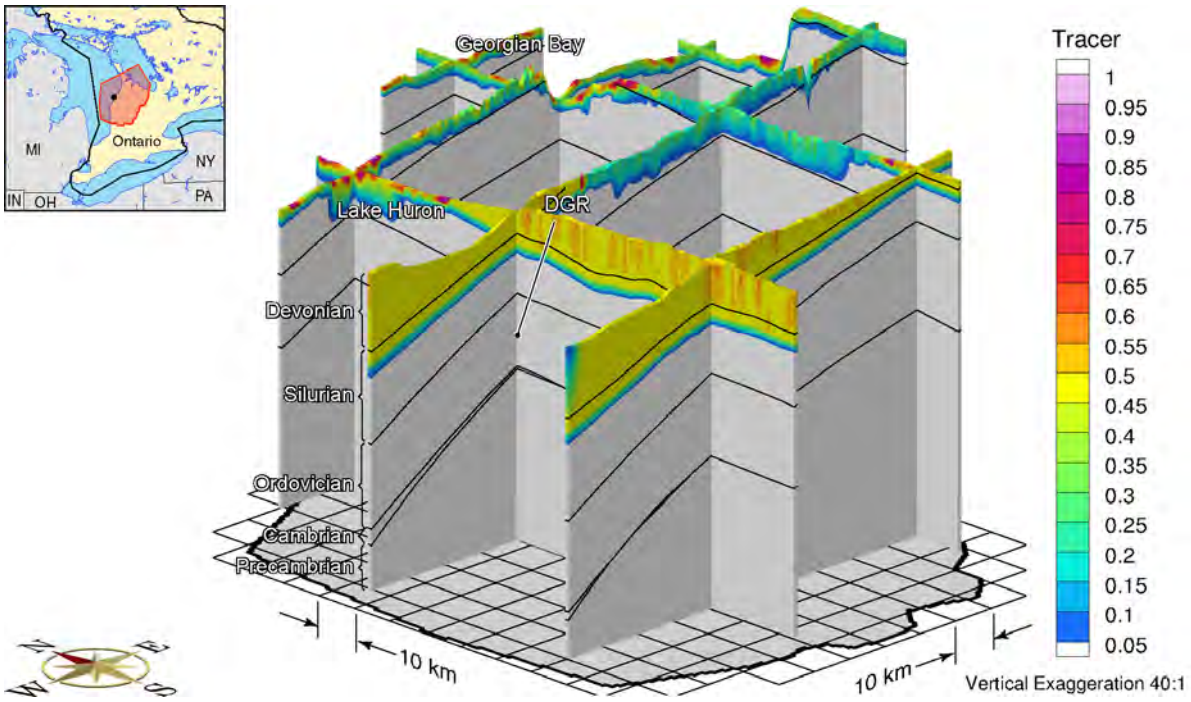

Figure F.89: Fence View Showing the Depth of Penetration of a Tracer at 30ka before Present with a One-dimensional Loading Efficiency of Zero

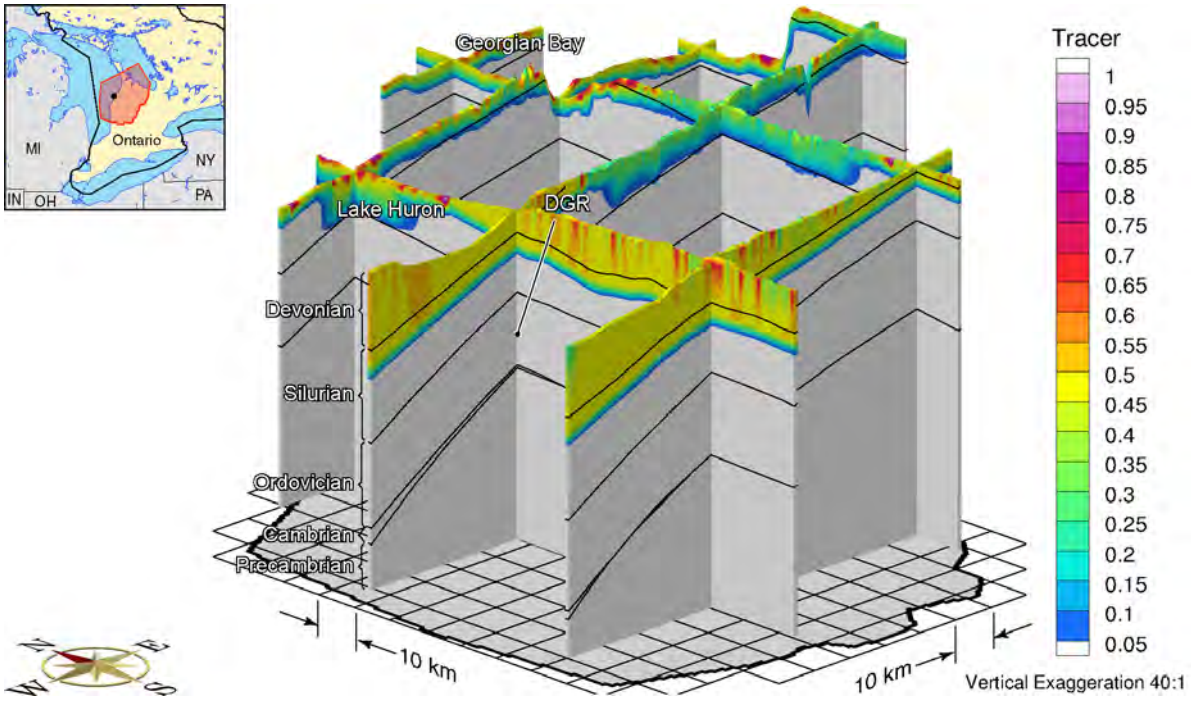

Figure F.90: Fence View Showing the Depth of Penetration of a Tracer at Present with a One-dimensional Loading Efficiency of Zero

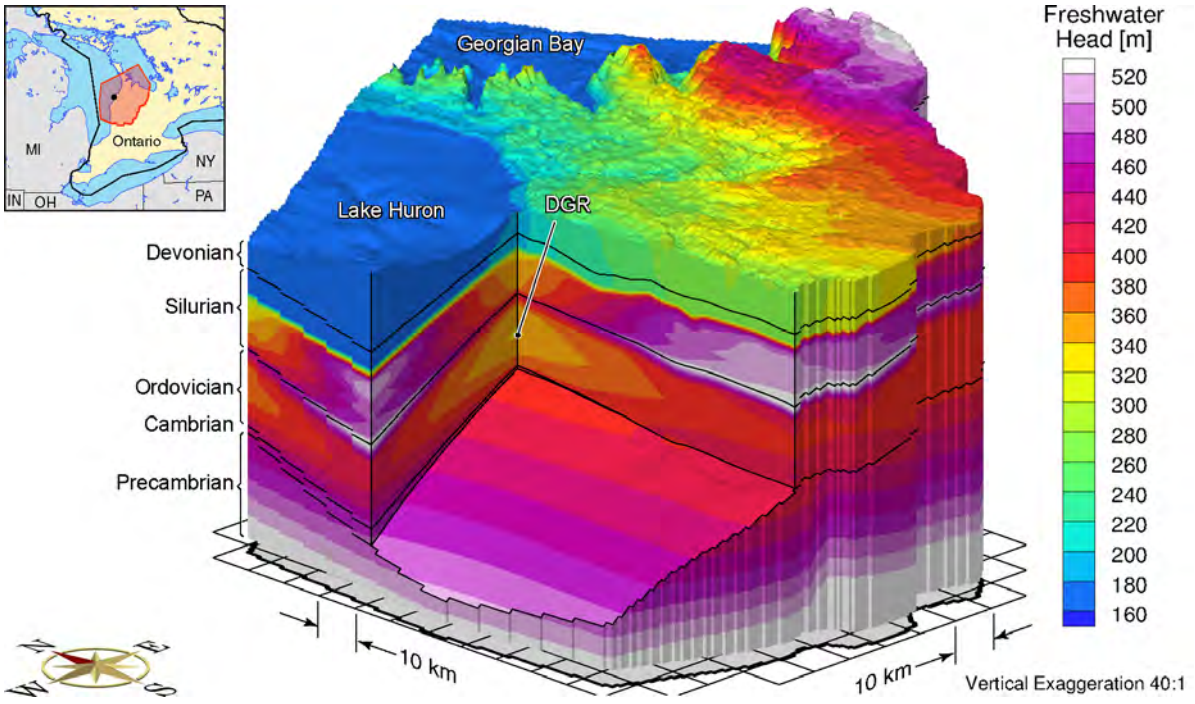

Figure F.91: Block Cut View of Freshwater Heads at Present with the Base-case Parameters and a Biot Coefficient of 0.5

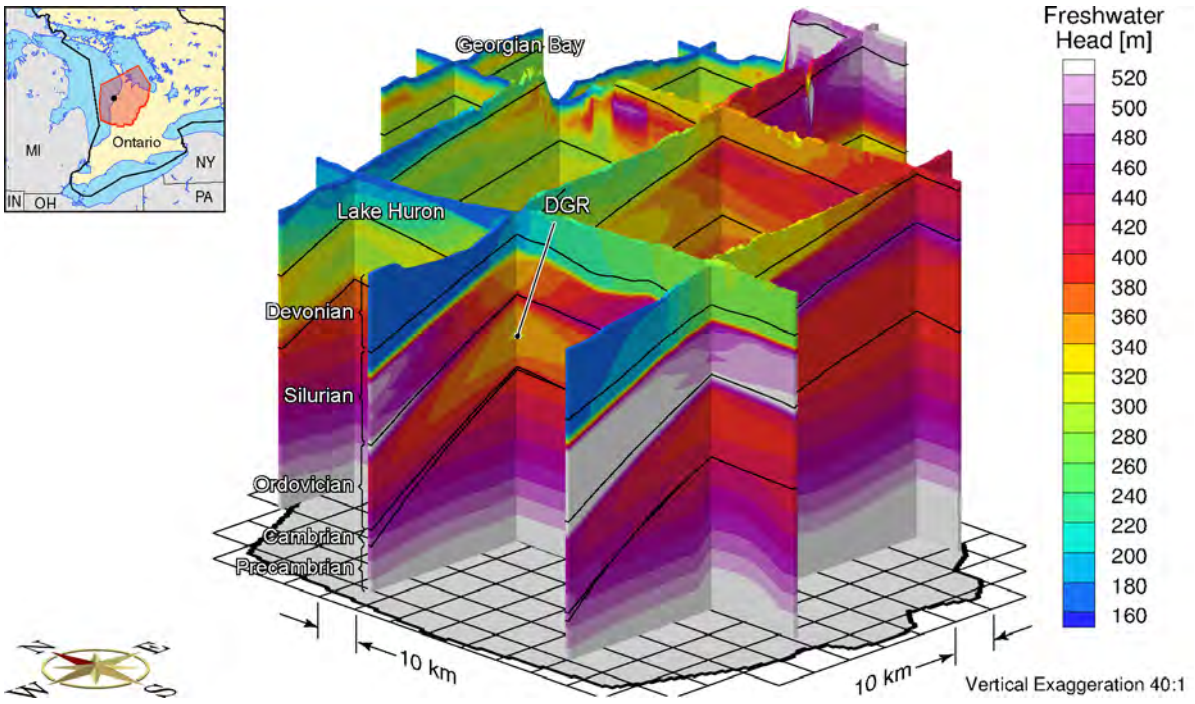

Figure F.92: Fence View of Freshwater Heads at Present with the Base-case Parameters and a Biot Coefficient of 0.5

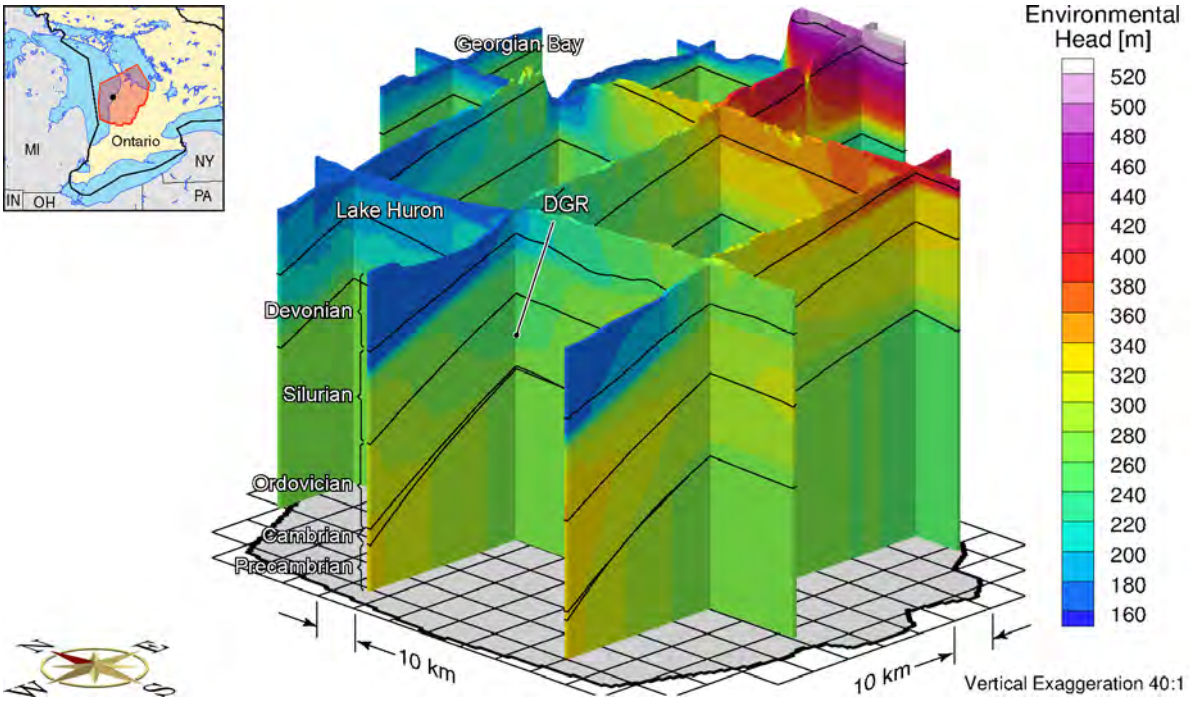

Figure F.93: Fence View of Environmental Heads at 90ka before Present with the Base-case Parameters and a Biot Coefficient of 0.5

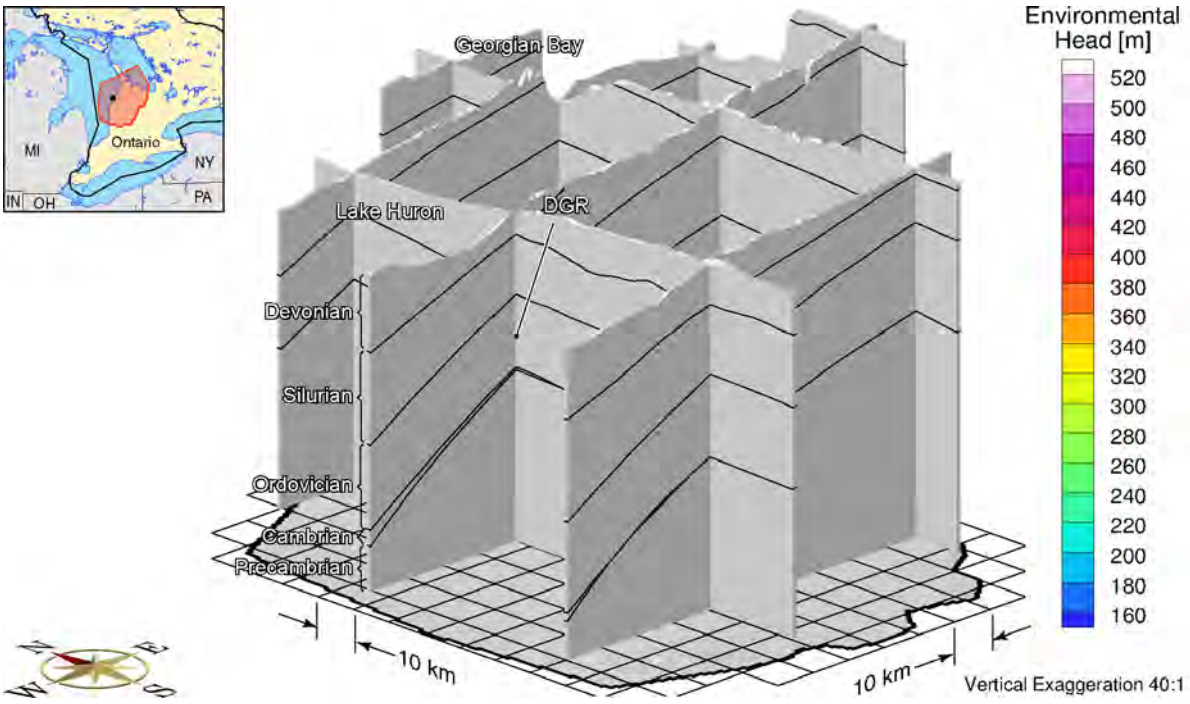

Figure F.94: Fence View of Environmental Heads at 60ka before Present with the Base-case Parameters and a Biot Coefficient of 0.5

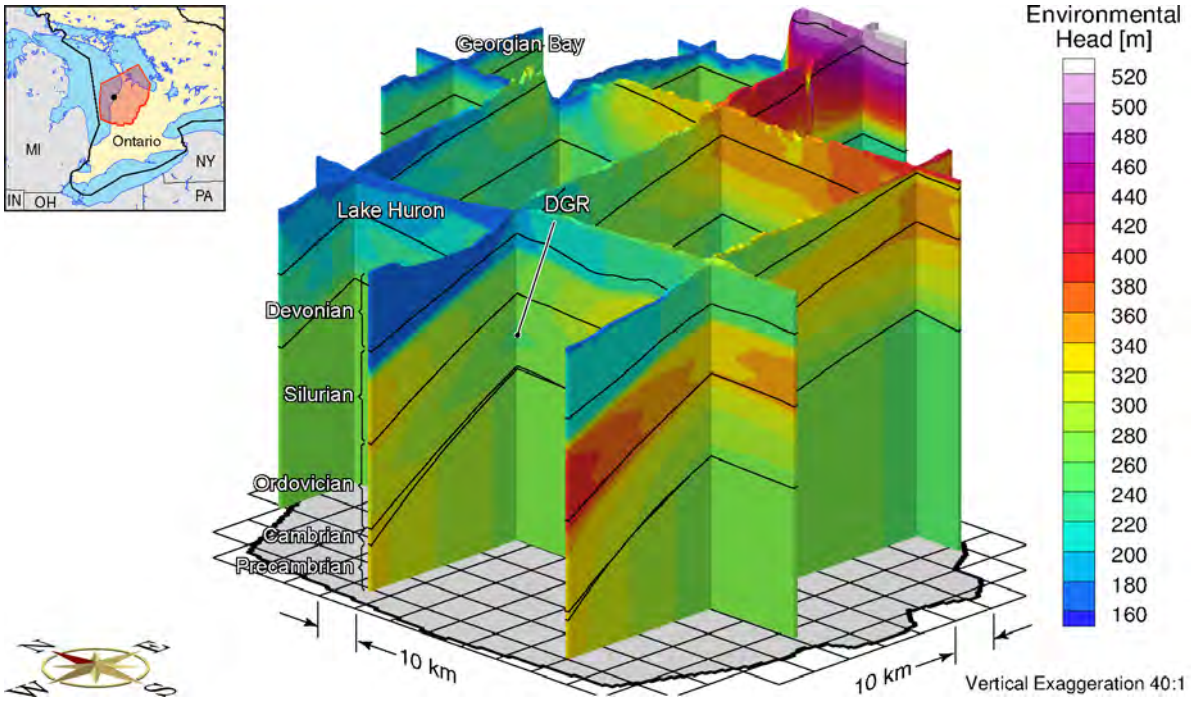

Figure F.95: Fence View of Environmental Heads at 30ka before Present with the Base-case Parameters and a Biot Coefficient of 0.5

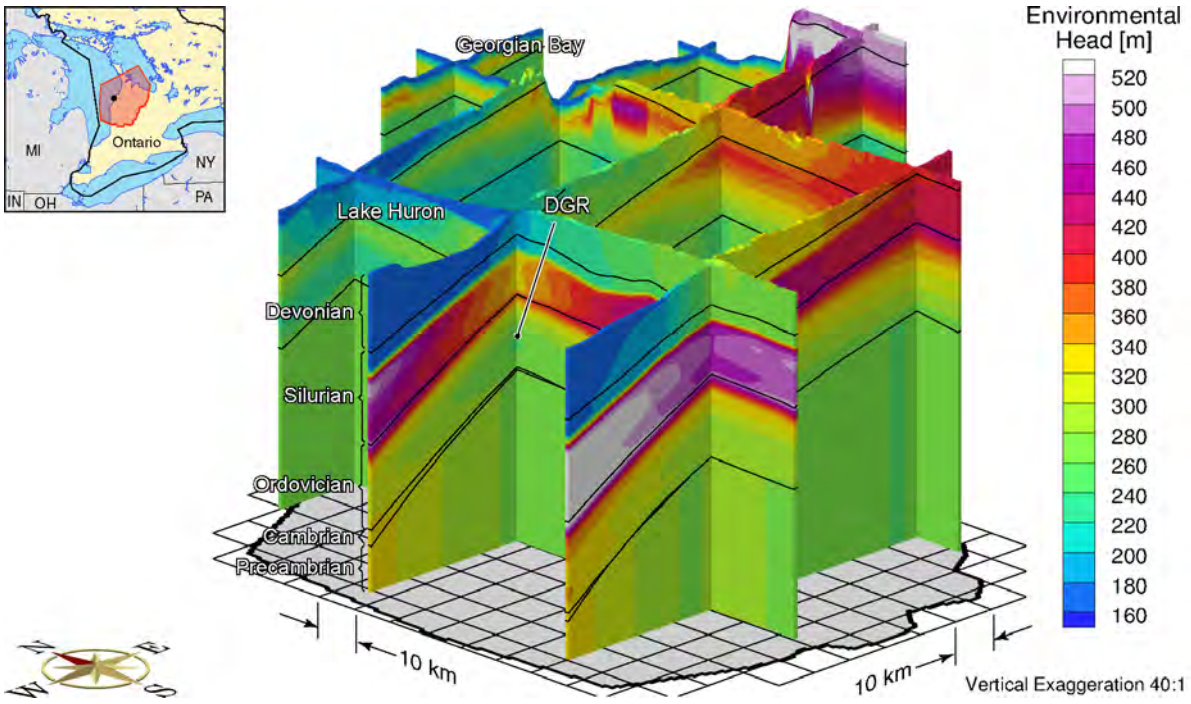

Figure F.96: Fence View of Environmental Heads at the Present with the Base-case Parameters and a Biot Coefficient of 0.5

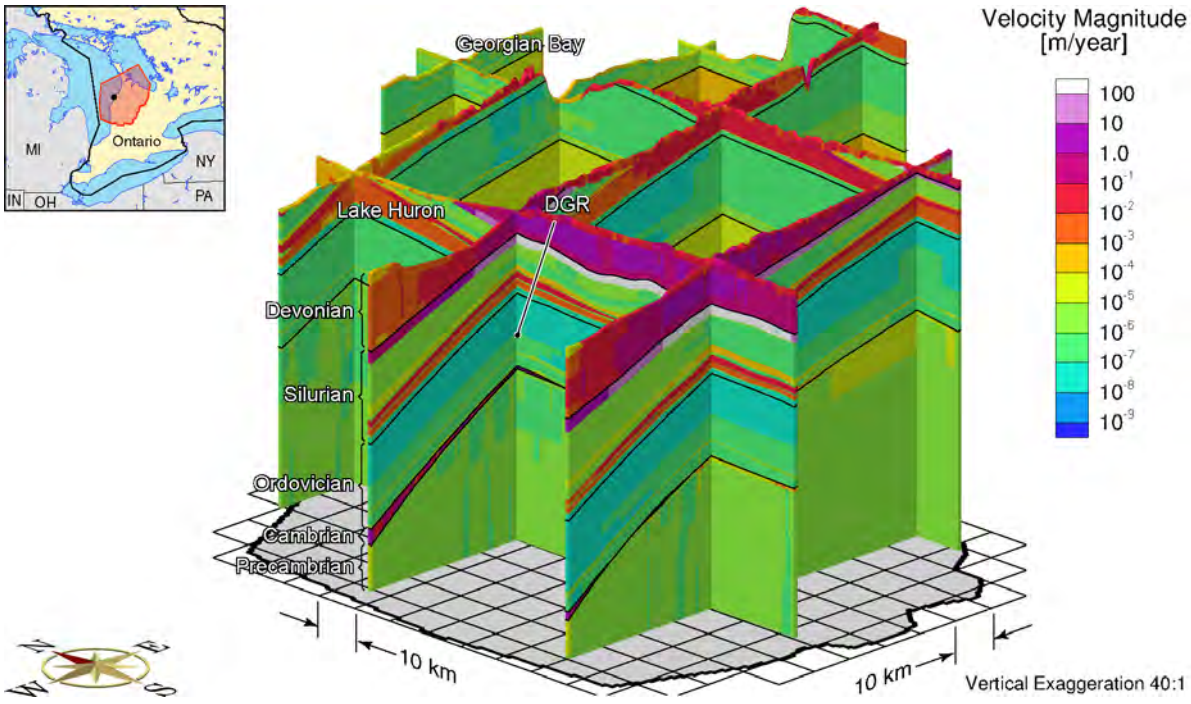

Figure F.97: Fence View of Pore Velocity Magnitude at 90ka before Present with the Base-case Parameters and a Biot Coefficient of 0.5

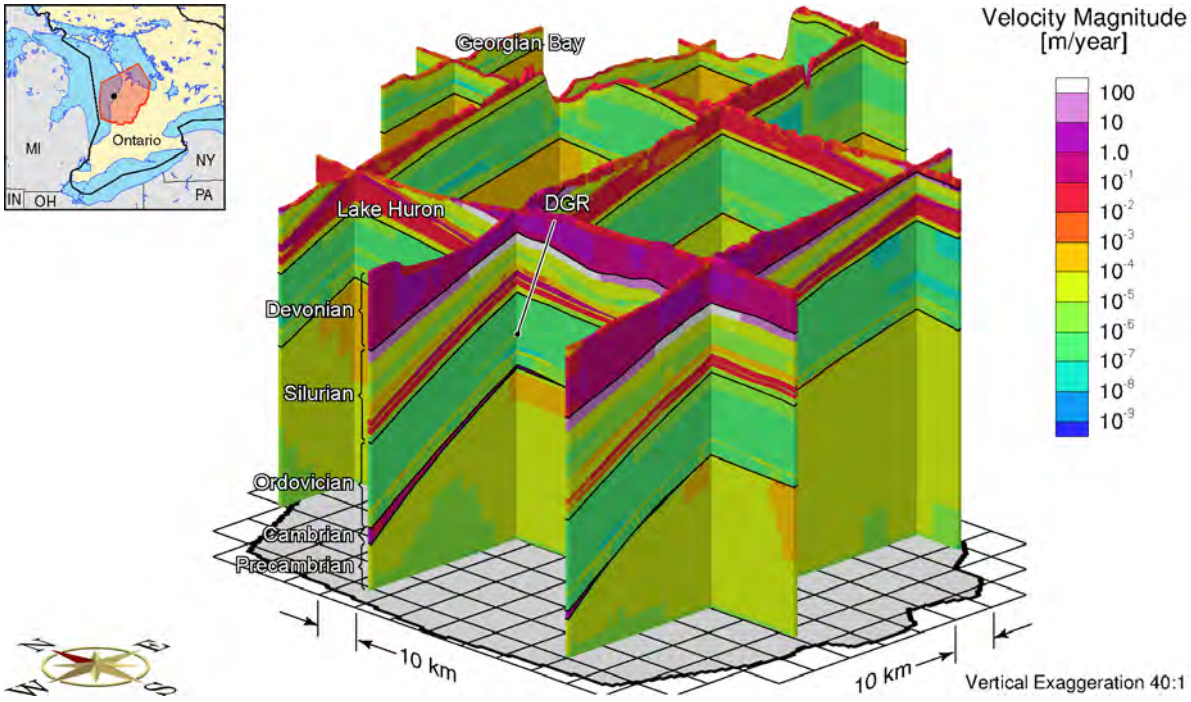

Figure F.98: Fence View of Pore Velocity Magnitude at 60ka before Present with the Base-case Parameters and a Biot Coefficient of 0.5

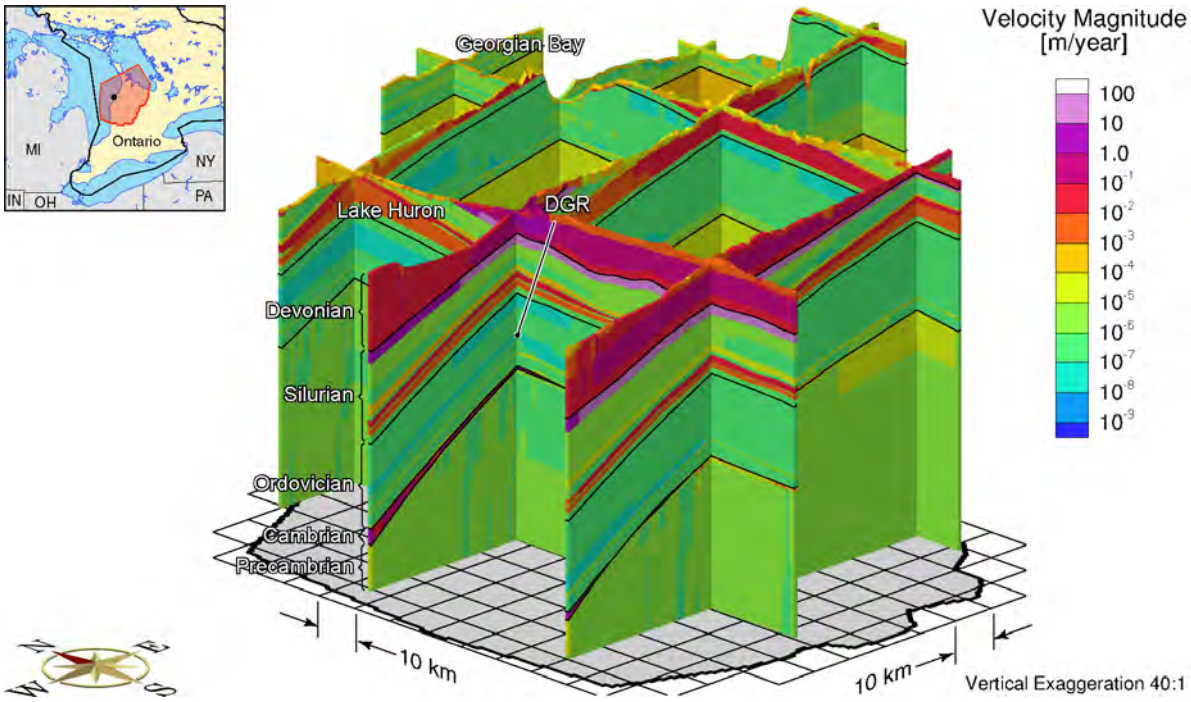

Figure F.99: Fence View of Pore Velocity Magnitude at 30ka before Present with the Base-case Parameters and a Biot Coefficient of 0.5

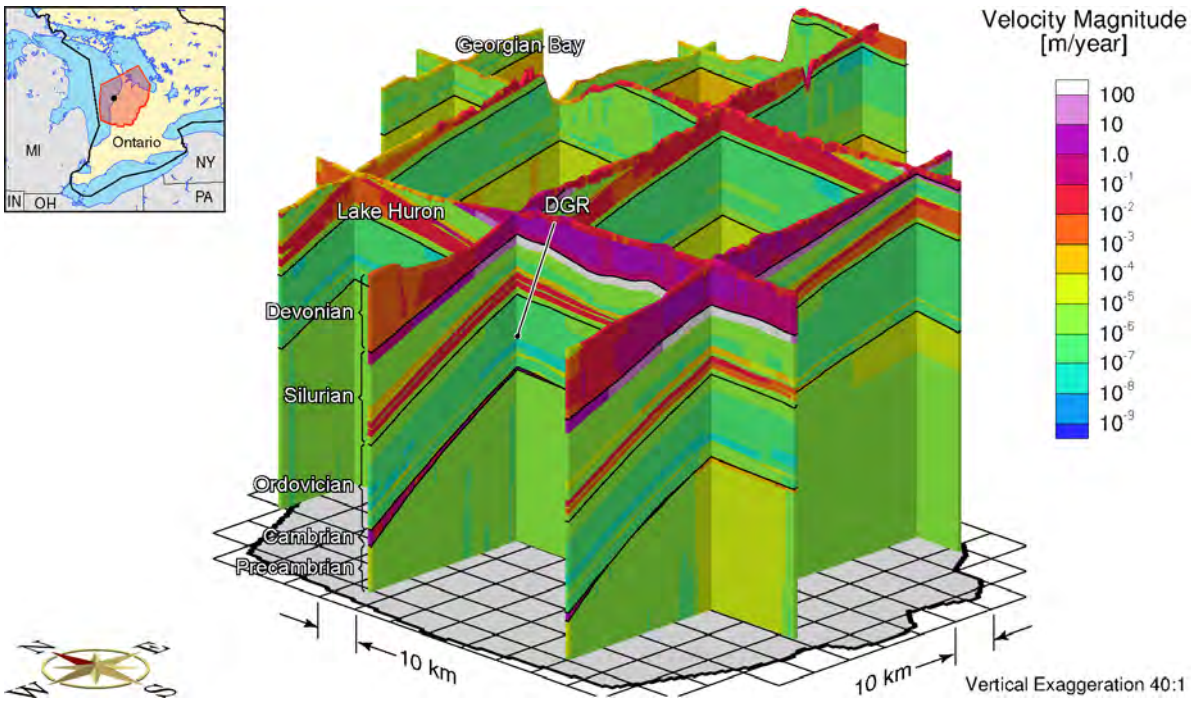

Figure F.100: Fence View of Pore Velocity Magnitude at Present with the Base-case Parameters and a Biot Coefficient of 0.5

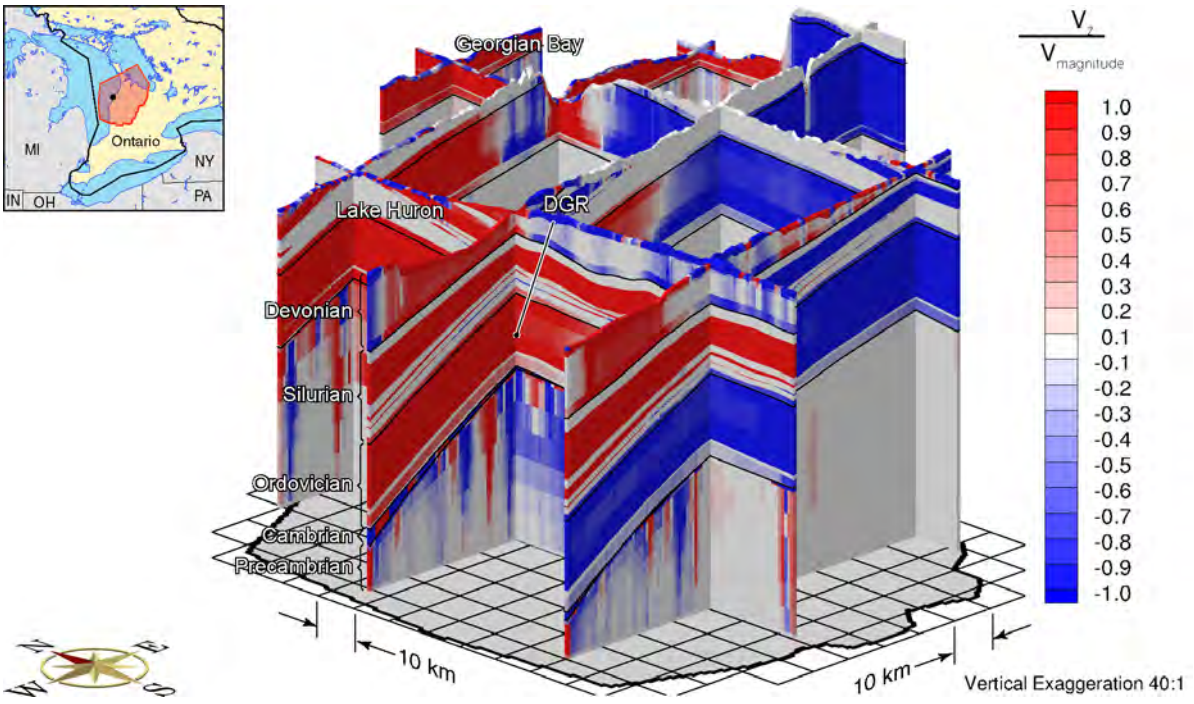

Figure F.101: Fence View Showing the Ratio of the Vertical Pore Water Velocity to the Velocity Magnitude at 90ka before Present with the Base-case Parameters and a Biot Coefficient of 0.5

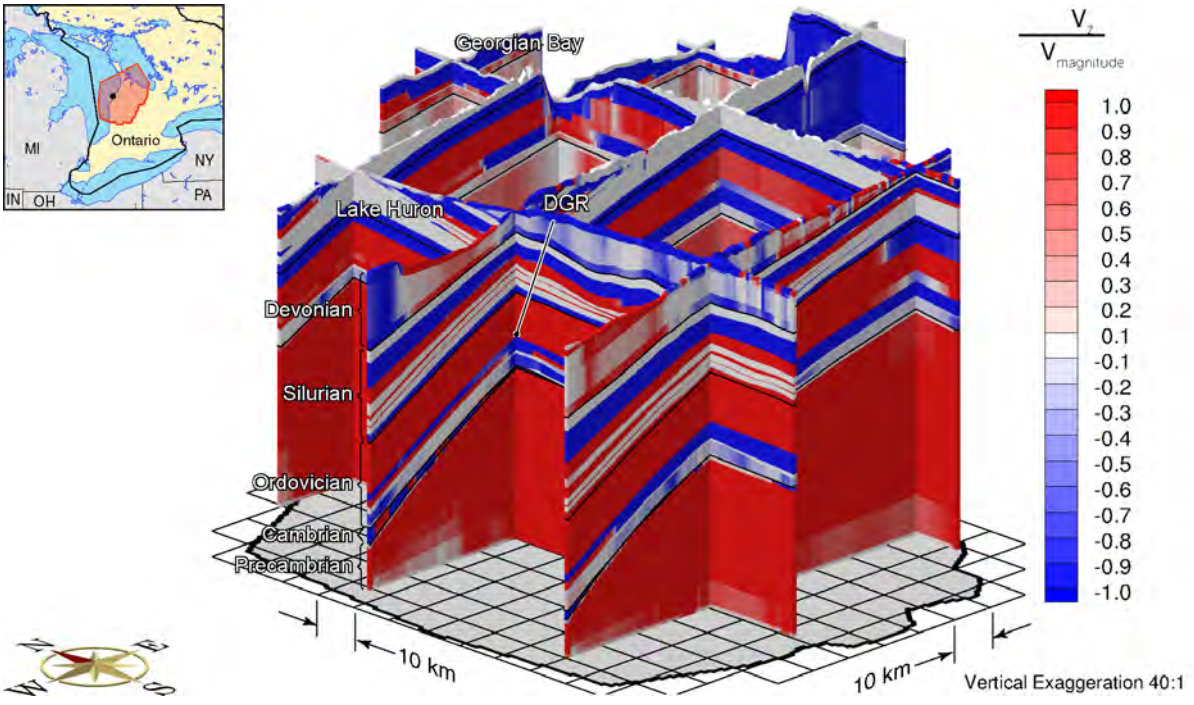

Figure F.102: Fence View Showing the Ratio of the Vertical Pore Water Velocity to the Velocity Magnitude at 60ka before Present with the Base-case Parameters and a Biot Coefficient of 0.5

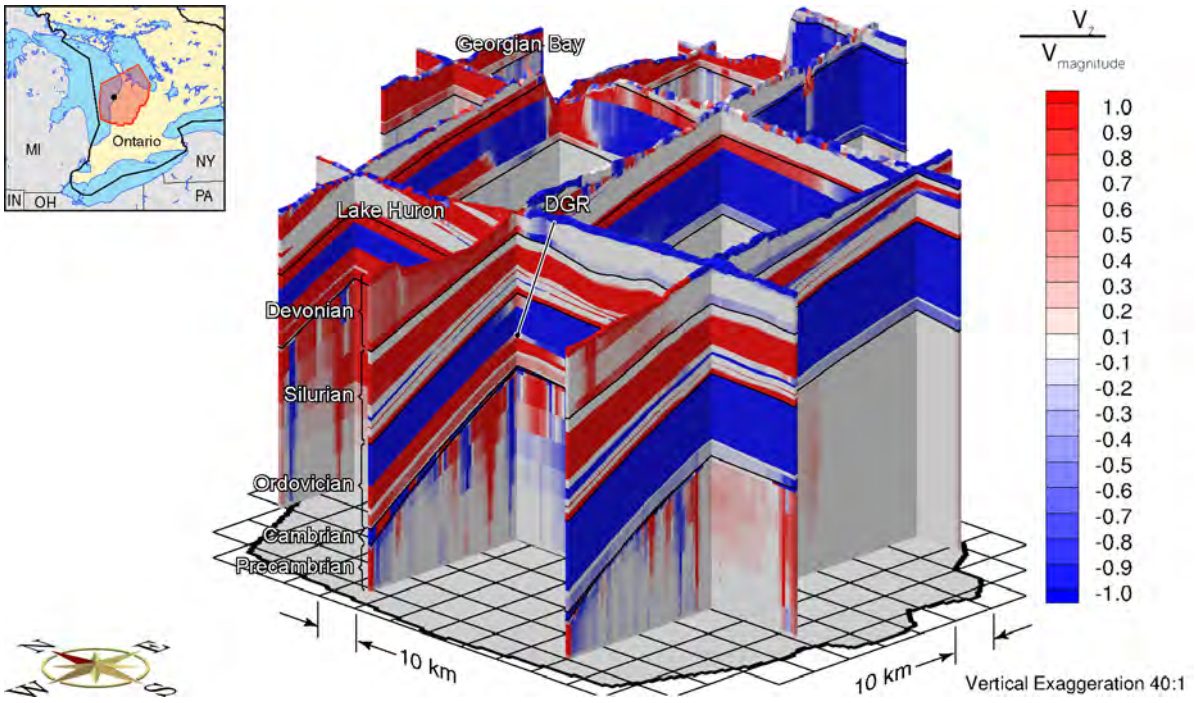

Figure F.103: Fence View Showing the Ratio of the Vertical Pore Water Velocity to the Velocity Magnitude at 30ka before Present with the Base-case Parameters and a Biot Coefficient of 0.5

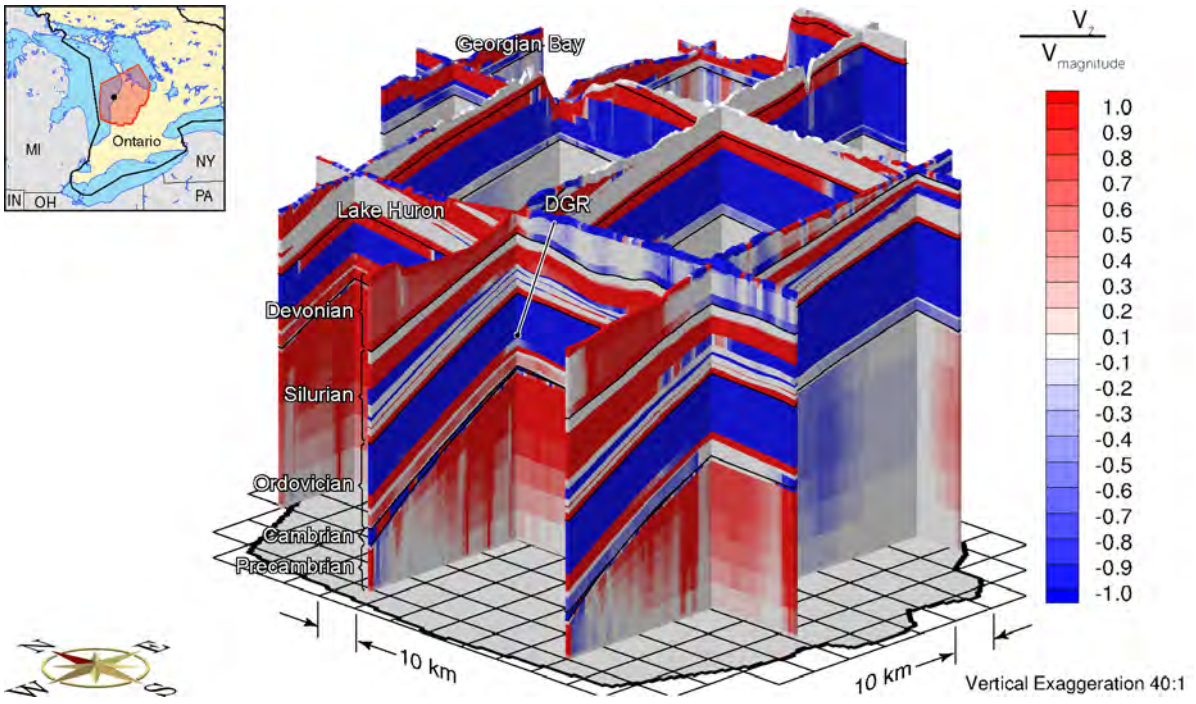

Figure F.104: Fence View of Ratio of Vertical Pore Velocity to Pore Velocity Magnitude at Present with the Base-case Parameters and a Biot Coefficient of 0.5

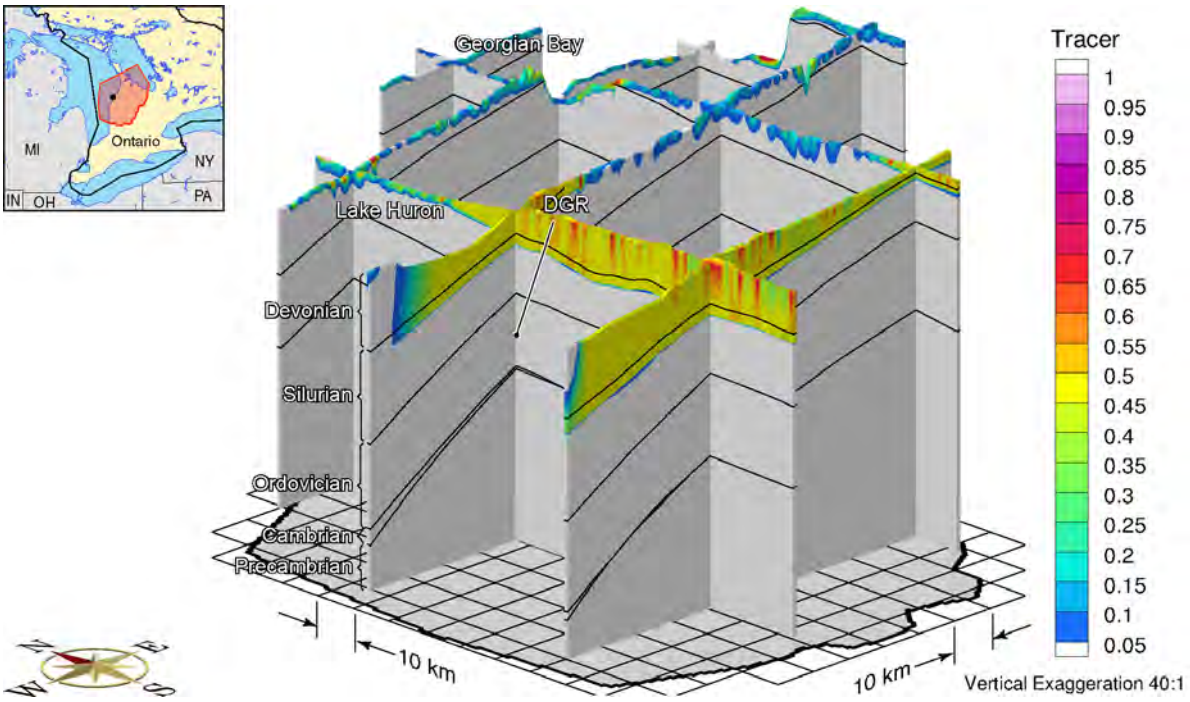

Figure F.105: Fence View Showing the Depth of Penetration of a Tracer at 90ka before Present with the Base-case Parameters and a Biot Coefficient of 0.5

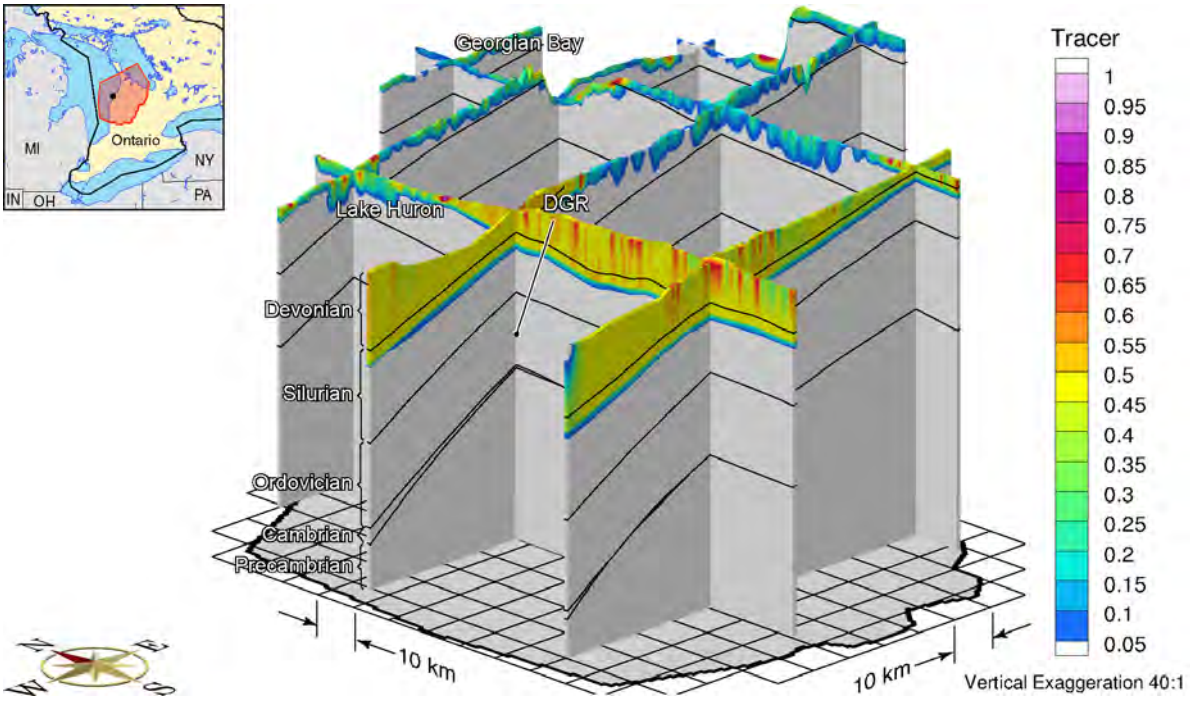

Figure F.106: Fence View Showing the Depth of Penetration of a Tracer at 60ka before Present with the Base-case Parameters and a Biot Coefficient of 0.5

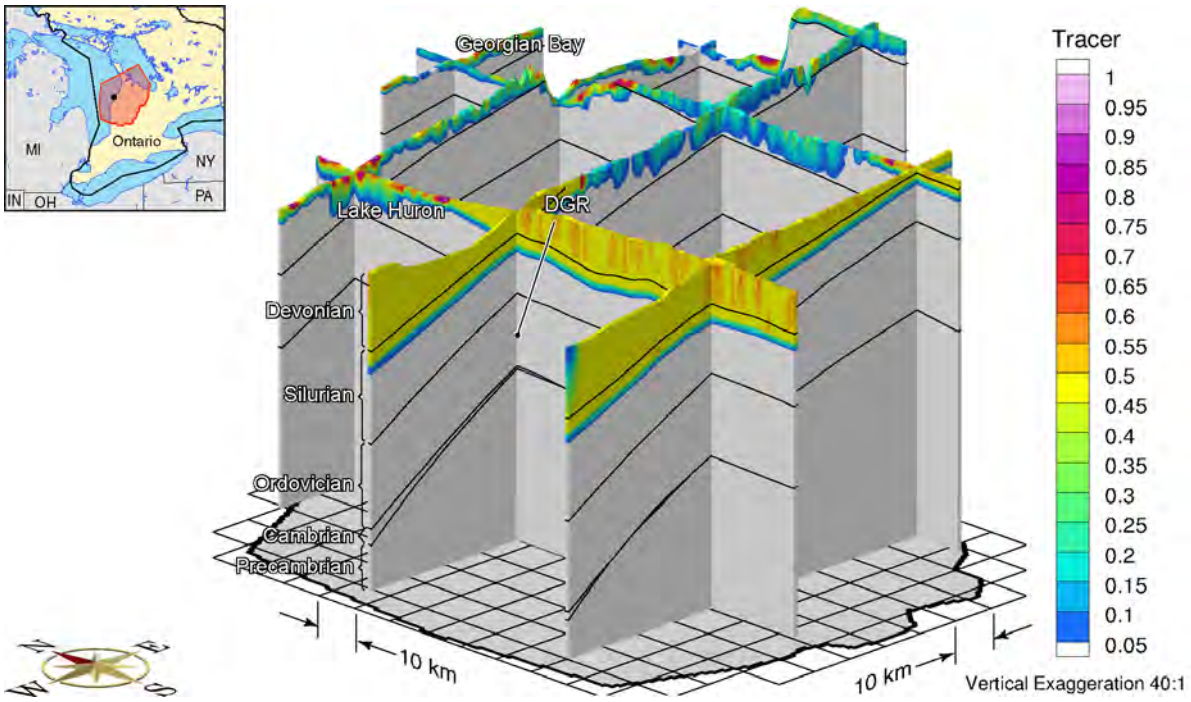

Figure F.107: Fence View Showing the Depth of Penetration of a Tracer at 30ka before Present with the Base-case Parameters and a Biot Coefficient of 0.5

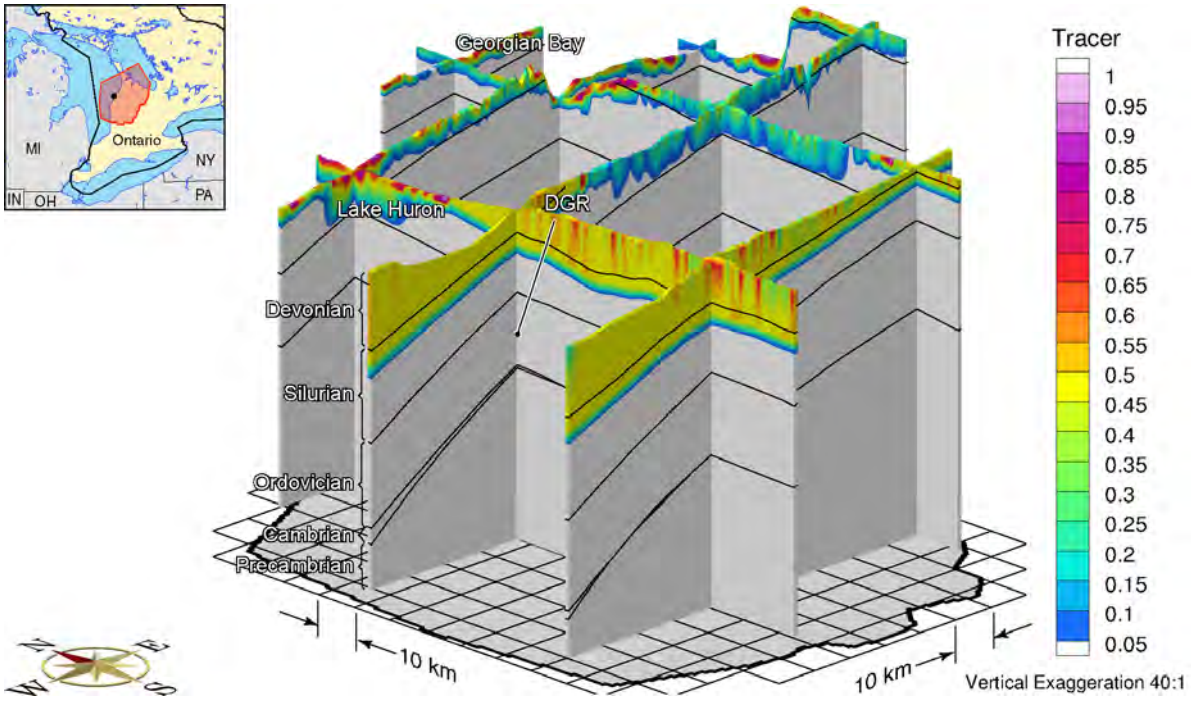

Figure F.108: Fence View Showing the Depth of Penetration of a Tracer at Present with the Base-case Parameters and a Biot Coefficient of 0.5

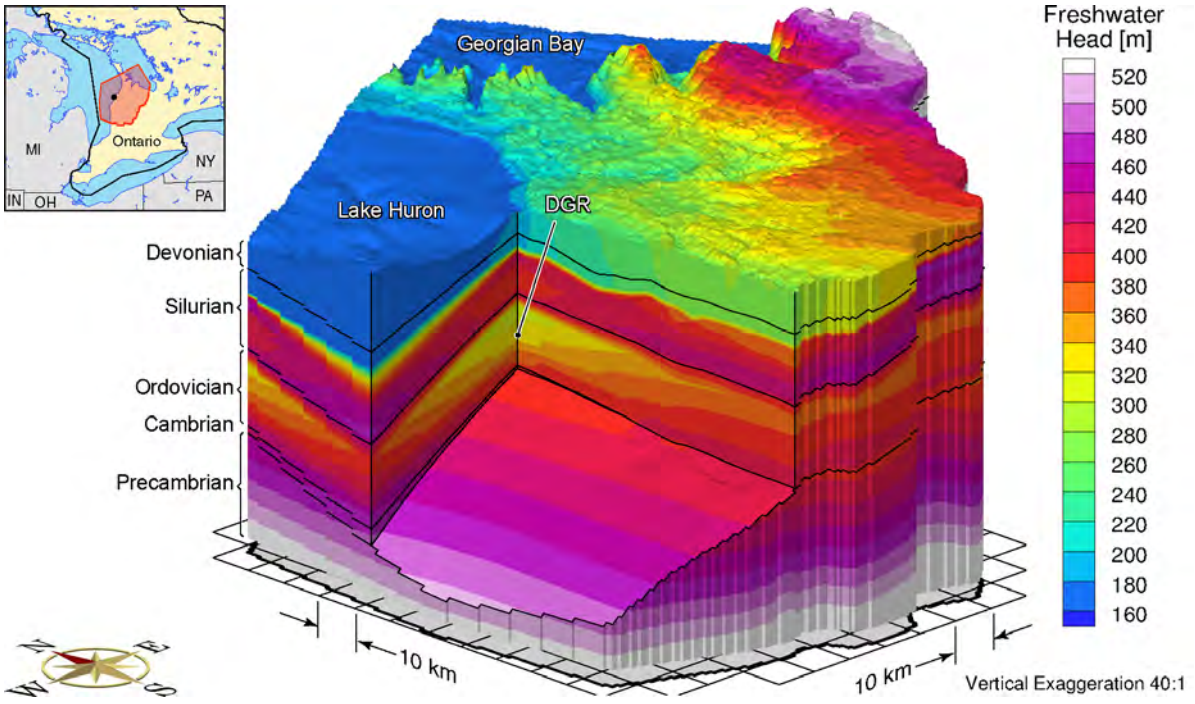

Figure F.109: Block Cut View of Freshwater Heads at Present with the One-dimensional Loading Efficiency and Storage Coefficients Reflecting the Presence of a Gas Phase

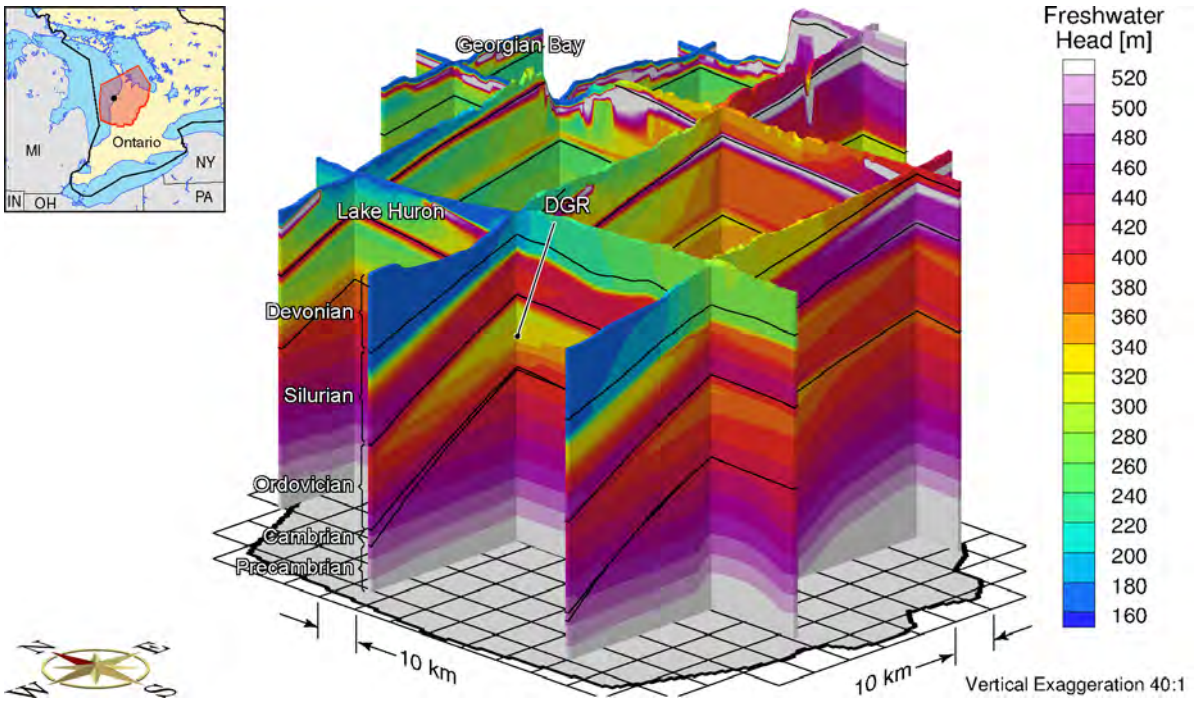

Figure F.110: Fence View of Freshwater Heads at Present with the One-dimensional Loading Efficiency and Storage Coefficients Reflecting the Presence of a Gas Phase

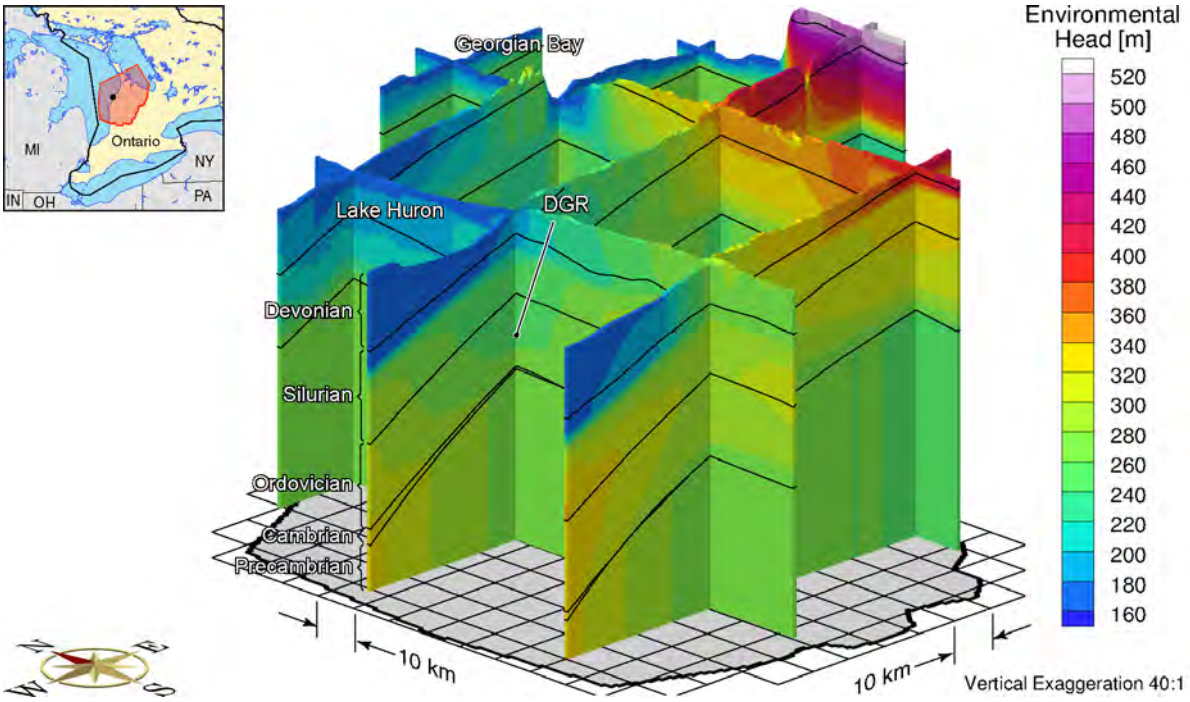

Figure F.111: Fence View of Environmental Heads at 90ka before Present with the One-dimensional Loading Efficiency and Storage Coefficients Reflecting the Presence of a Gas Phase

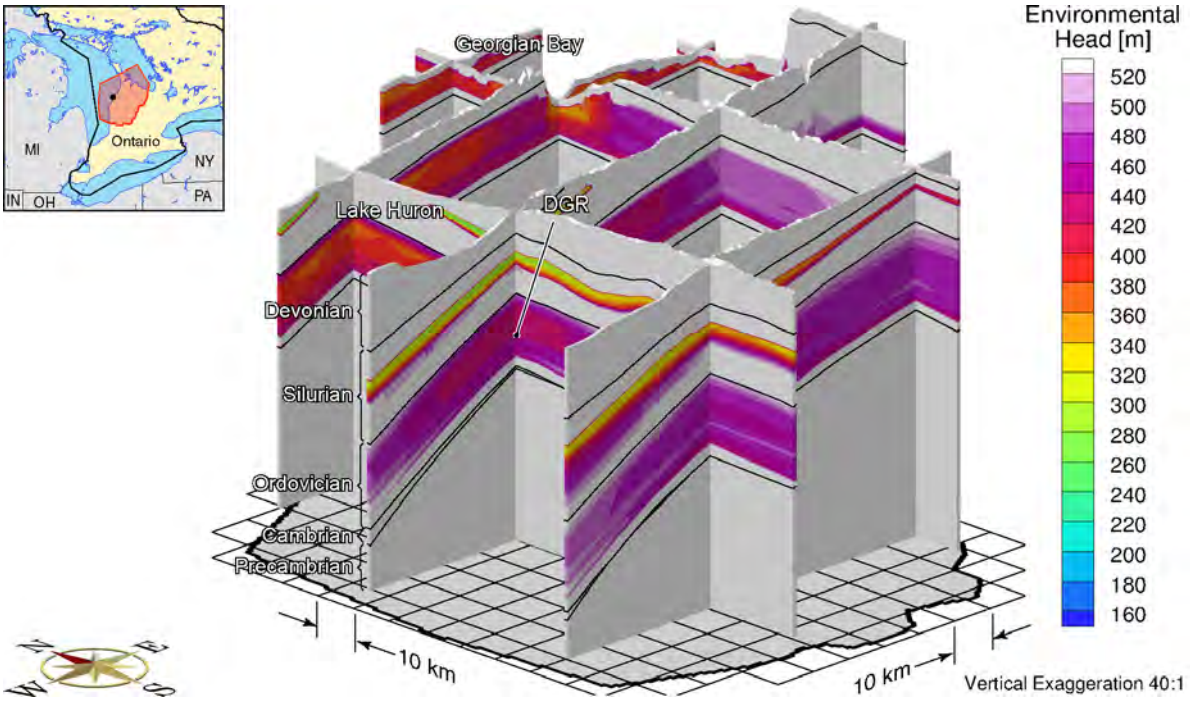

Figure F.112: Fence View of Environmental Heads at 60ka before Present with the One-dimensional Loading Efficiency and Storage Coefficients Reflecting the Presence of a Gas Phase

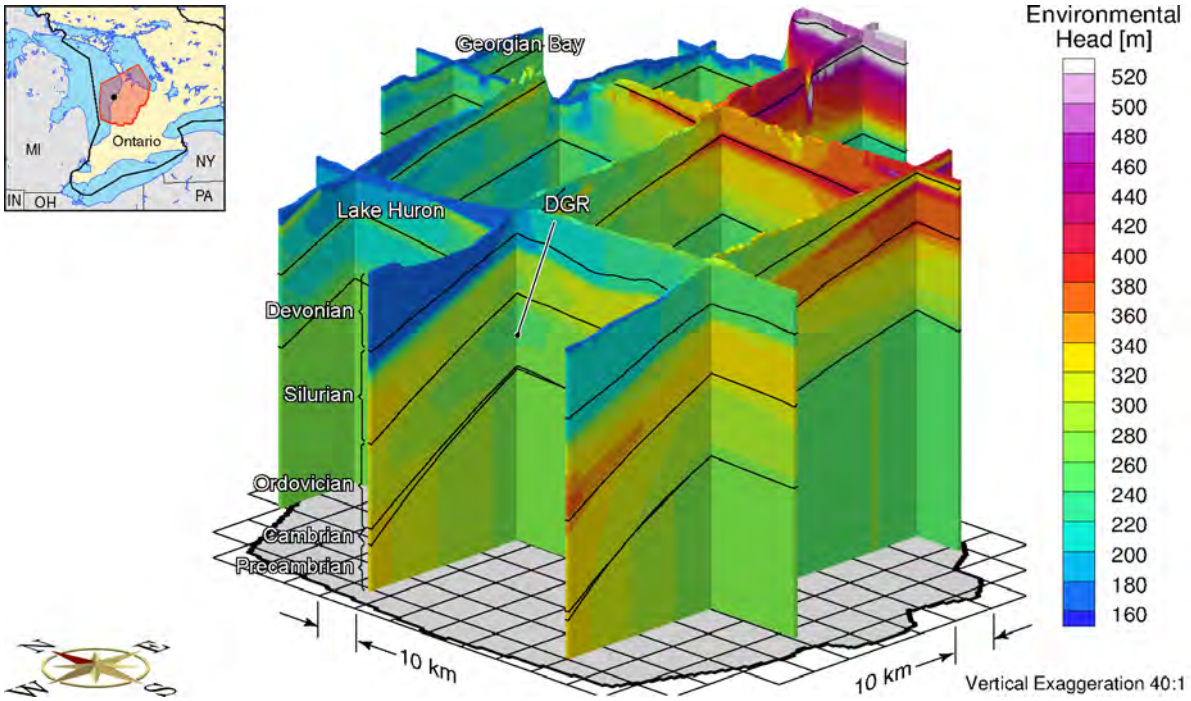

Figure F.113: Fence View of Environmental Heads at 30ka before Present with the One-dimensional Loading Efficiency and Storage Coefficients Reflecting the Presence of a Gas Phase

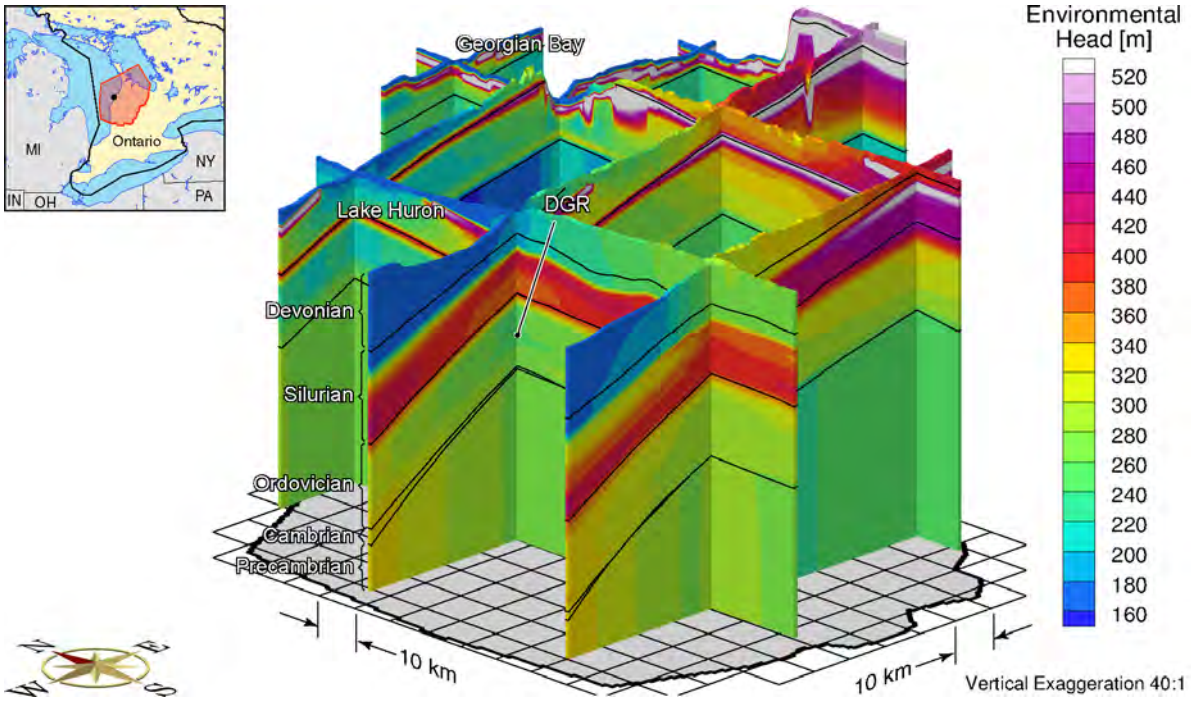

Figure F.114: Fence View of Environmental Heads at the Present with the One-dimensional Loading Efficiency and Storage Coefficients Reflecting the Presence of a Gas Phase

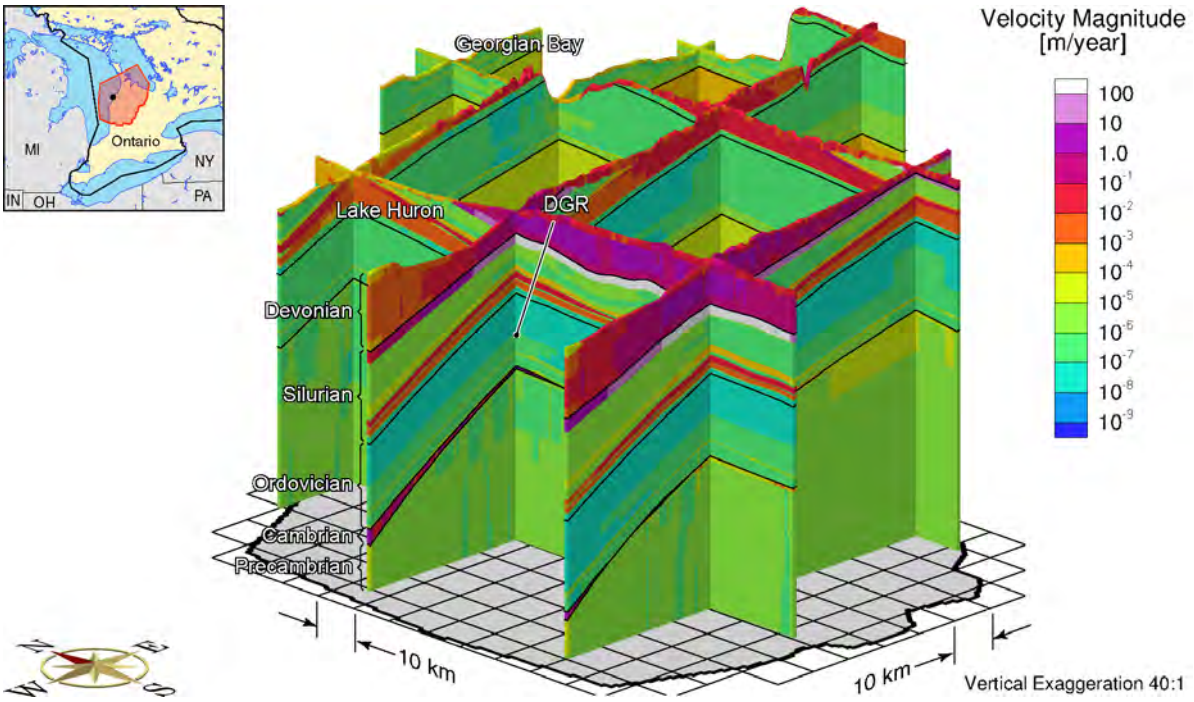

Figure F.115: Fence View of Pore Velocity Magnitude at 90ka before Present with the One-dimensional Loading Efficiency and Storage Coefficients Reflecting the Presence of a Gas Phase

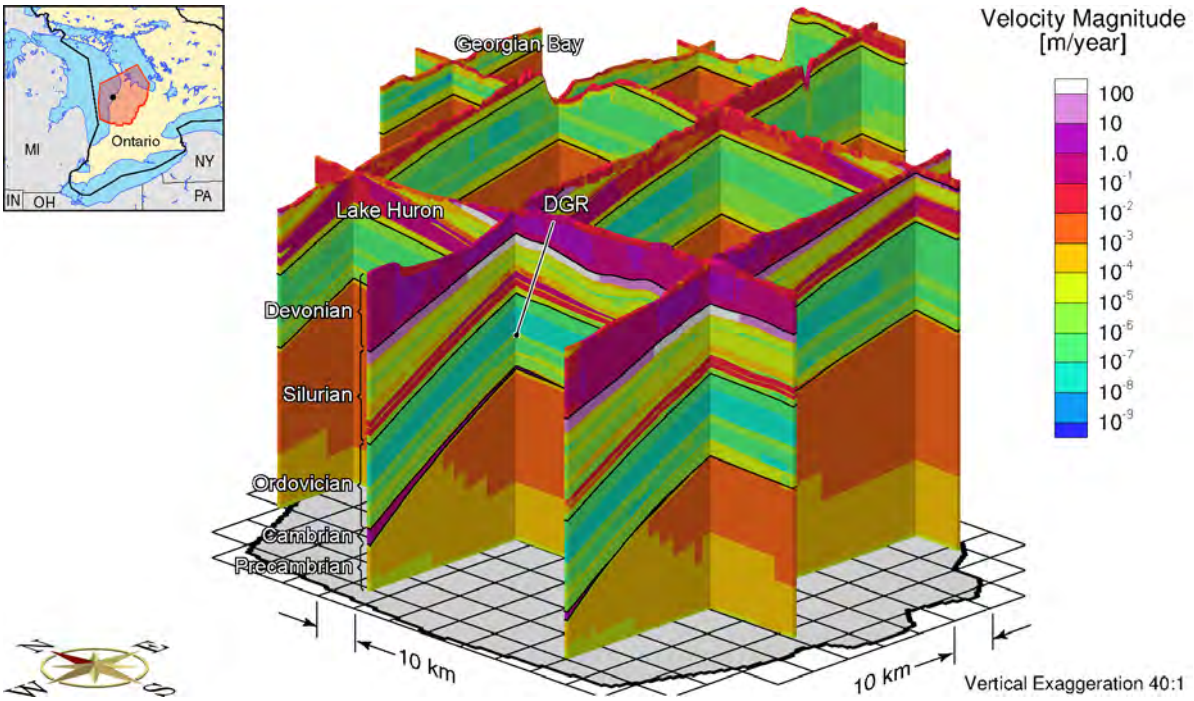

Figure F.116: Fence View of Pore Velocity Magnitude at 60ka before Present with the One-dimensional Loading Efficiency and Storage Coefficients Reflecting the Presence of a Gas Phase

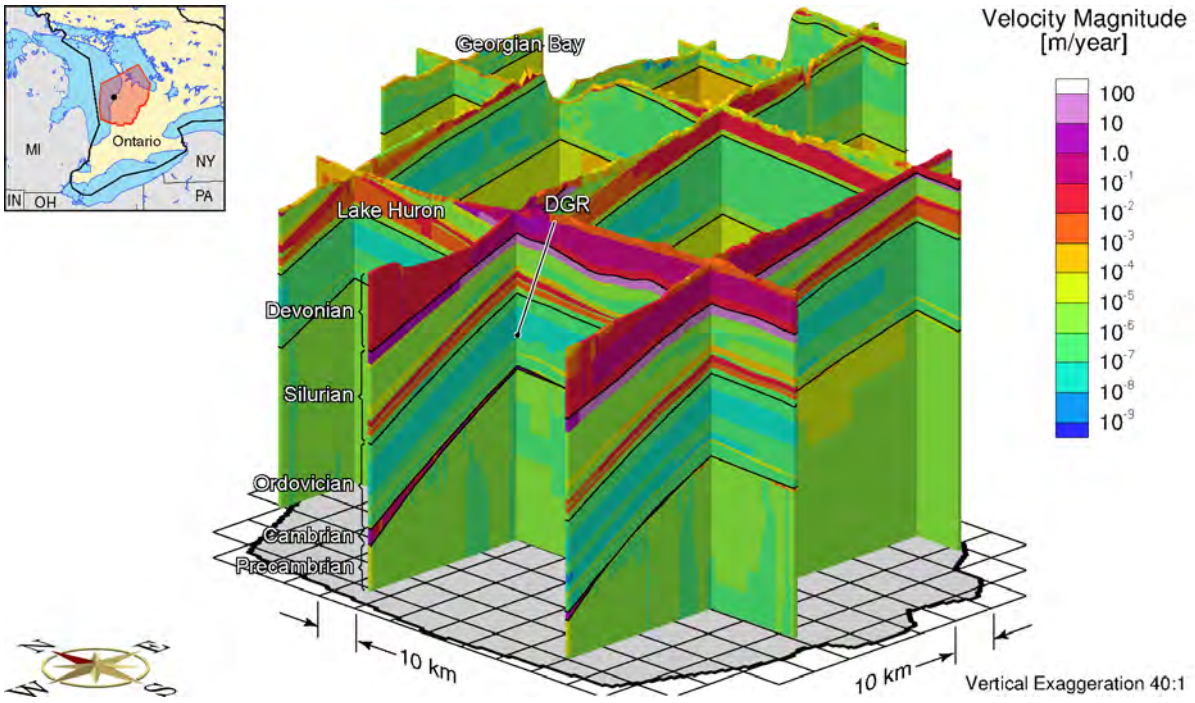

Figure F.117: Fence View of Pore Velocity Magnitude at 30ka before Present with the One-dimensional Loading Efficiency and Storage Coefficients Reflecting the Presence of a Gas Phase

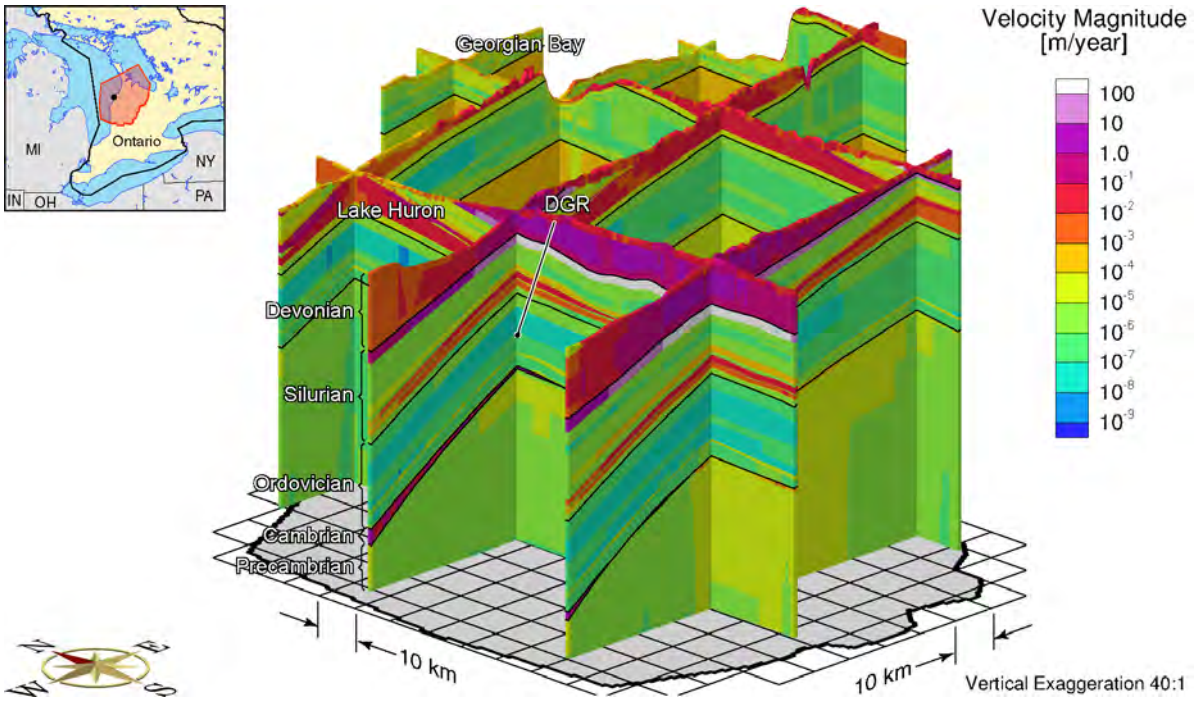

Figure F.118: Fence View of Pore Velocity Magnitude at Present with the One-dimensional Loading Efficiency and Storage Coefficients Reflecting the Presence of a Gas Phase

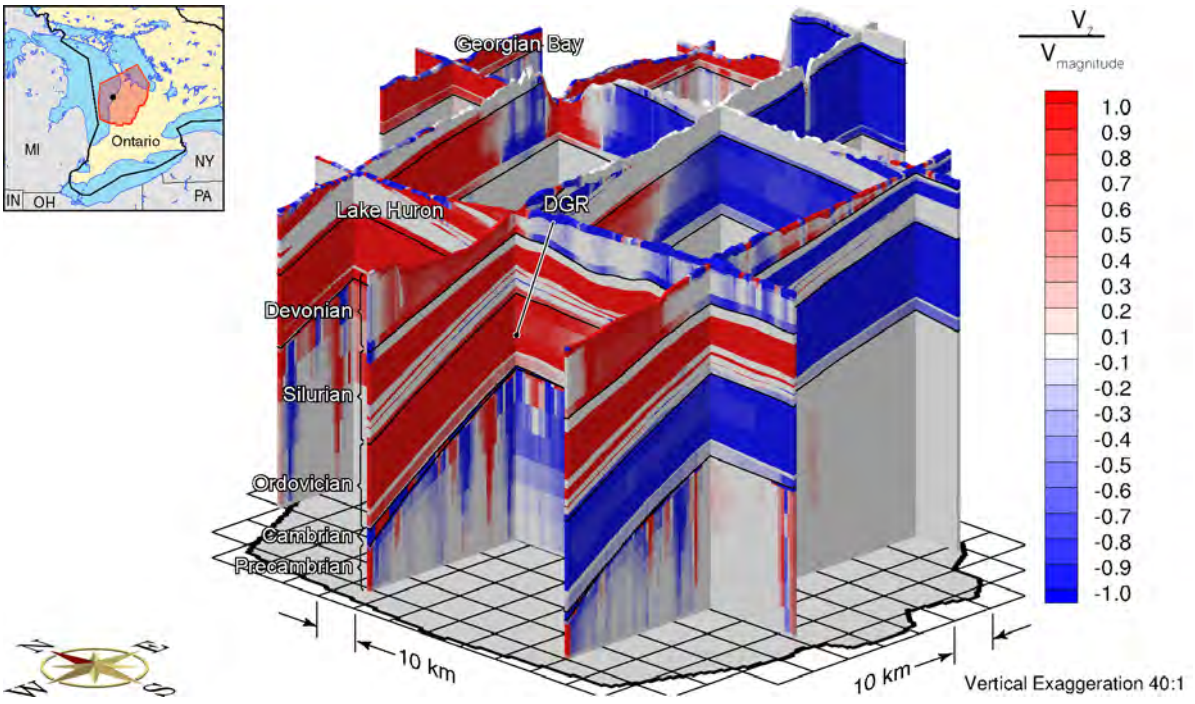

Figure F.119: Fence View Showing the Ratio of the Vertical Pore Water Velocity to the Velocity Magnitude at 90ka before Present with the One-dimensional Loading Efficiency and Storage Coefficients Reflecting the Presence of a Gas Phase

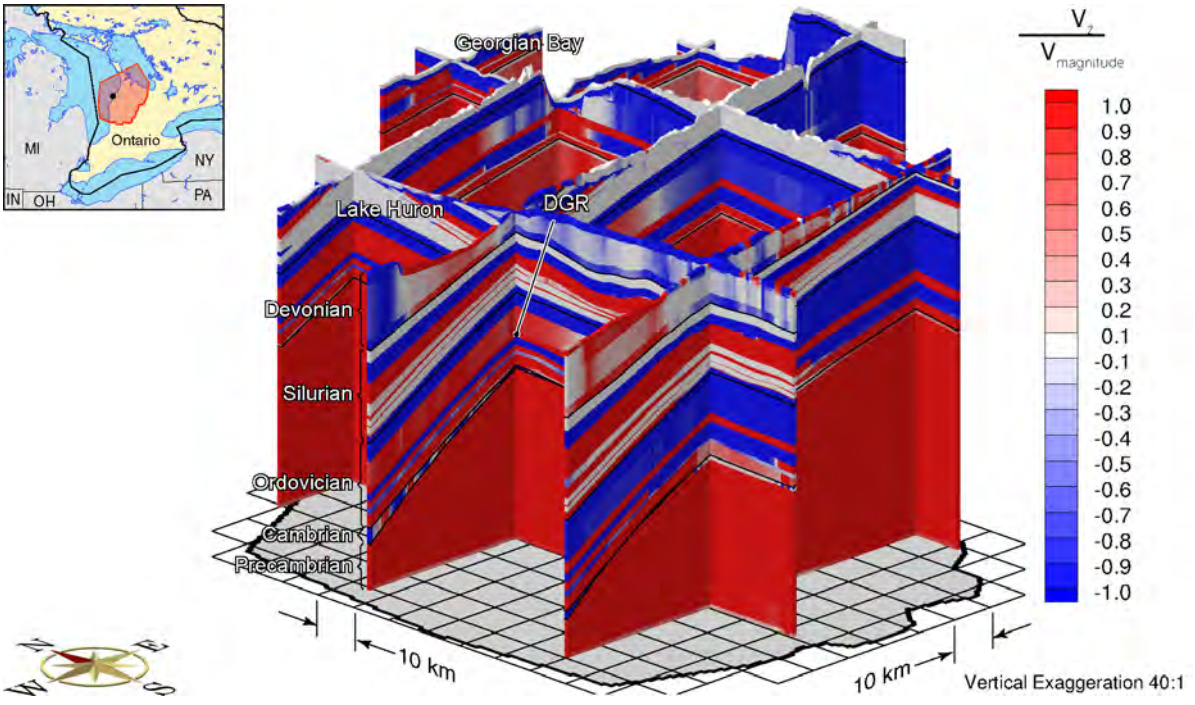

Figure F.120: Fence View Showing the Ratio of the Vertical Pore Water Velocity to the Velocity Magnitude at 60ka before Present with the One-dimensional Loading Efficiency and Storage Coefficients Reflecting the Presence of a Gas Phase

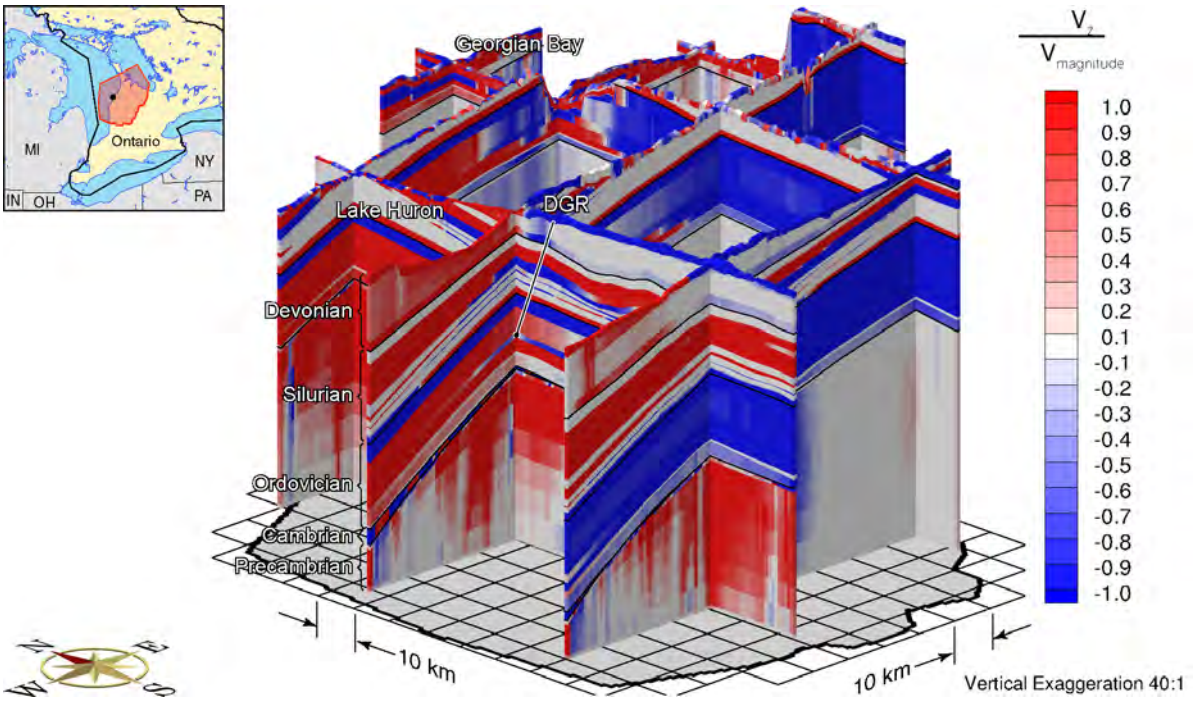

Figure F.121: Fence View Showing the Ratio of the Vertical Pore Water Velocity to the Velocity Magnitude at 30ka before Present with the One-dimensional Loading Efficiency and Storage Coefficients Reflecting the Presence of a Gas Phase

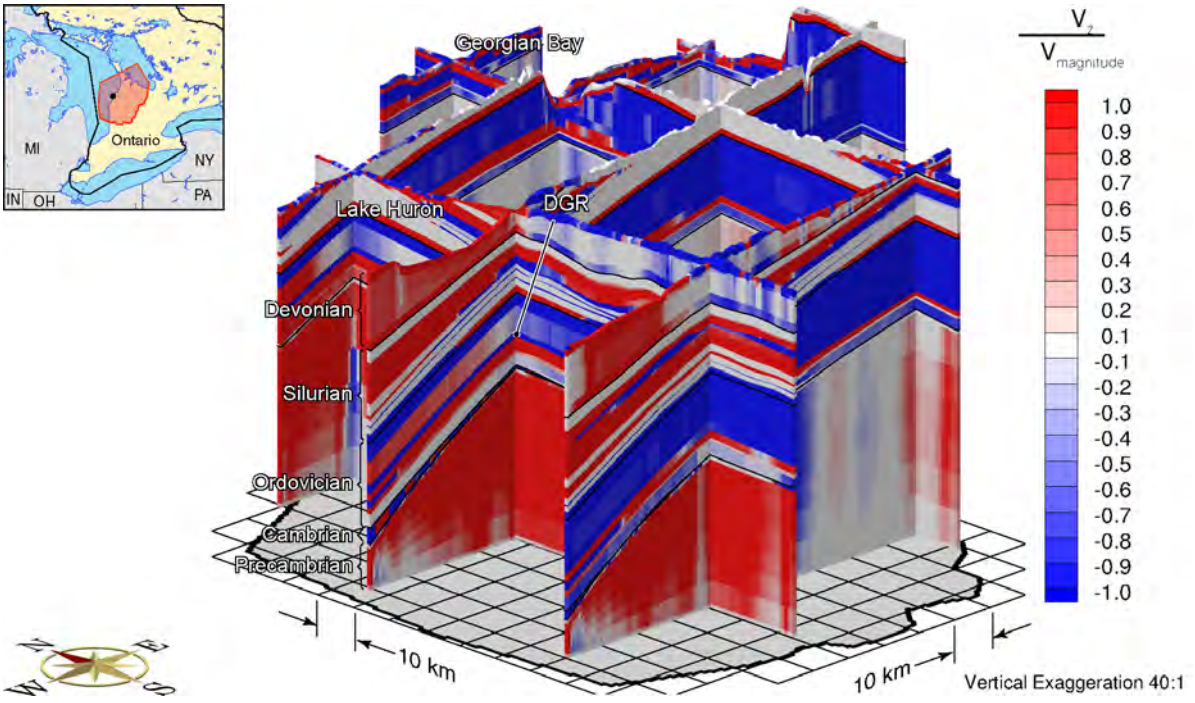

Figure F.122: Fence View of Ratio of Vertical Pore Velocity to Pore Velocity Magnitude at Present with the One-dimensional Loading Efficiency and Storage Coefficients Reflecting the Presence of a Gas Phase

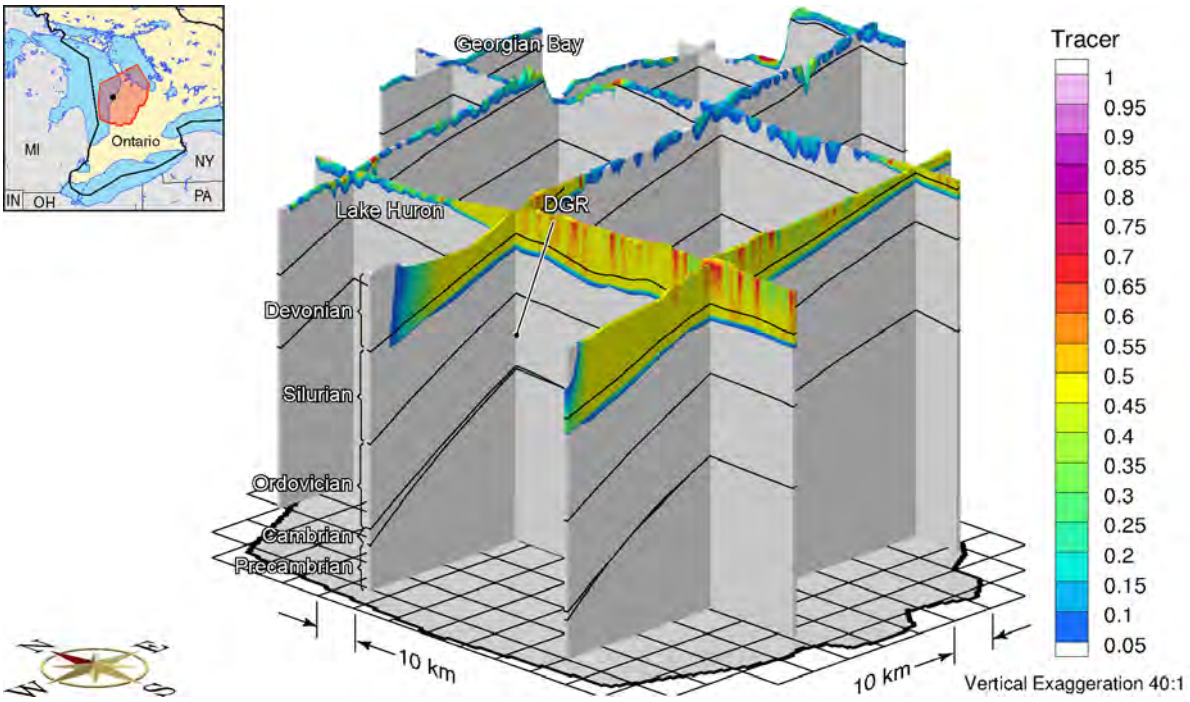

Figure F.123: Fence View Showing the Depth of Penetration of a Tracer at 90ka before Present with the One-dimensional Loading Efficiency and Storage Coefficients Reflecting the Presence of a Gas Phase

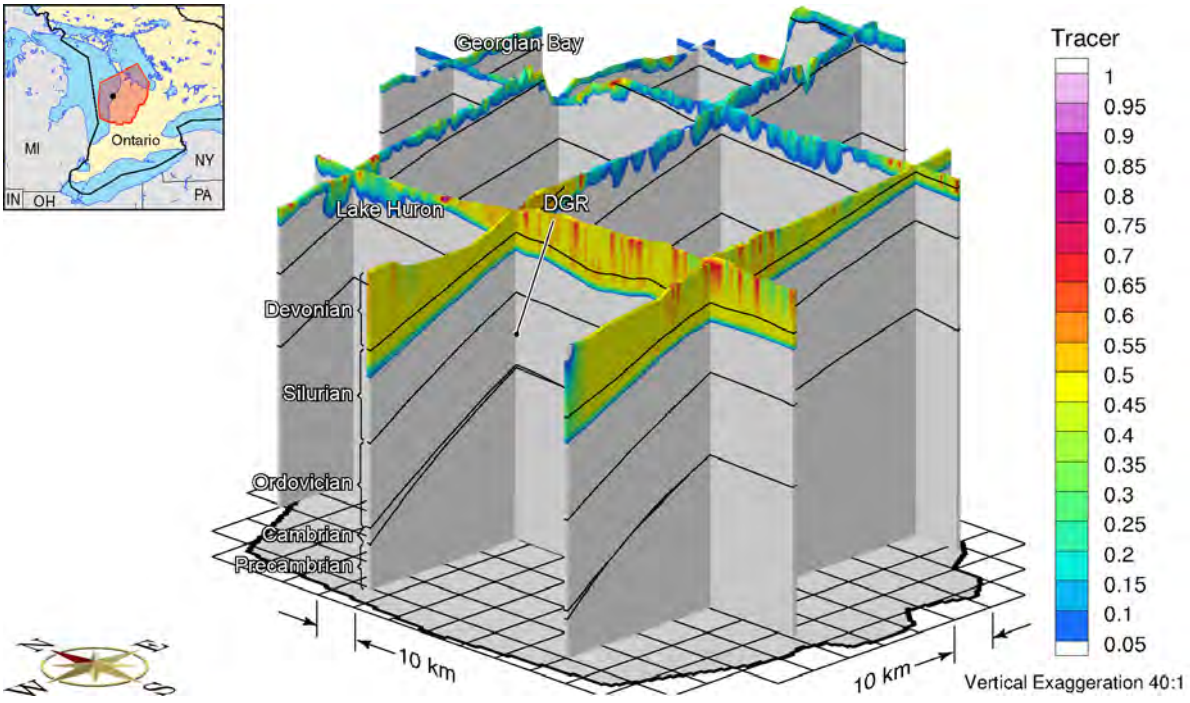

Figure F.124: Fence View Showing the Depth of Penetration of a Tracer at 60ka before Present with the One-dimensional Loading Efficiency and Storage Coefficients Reflecting the Presence of a Gas Phase

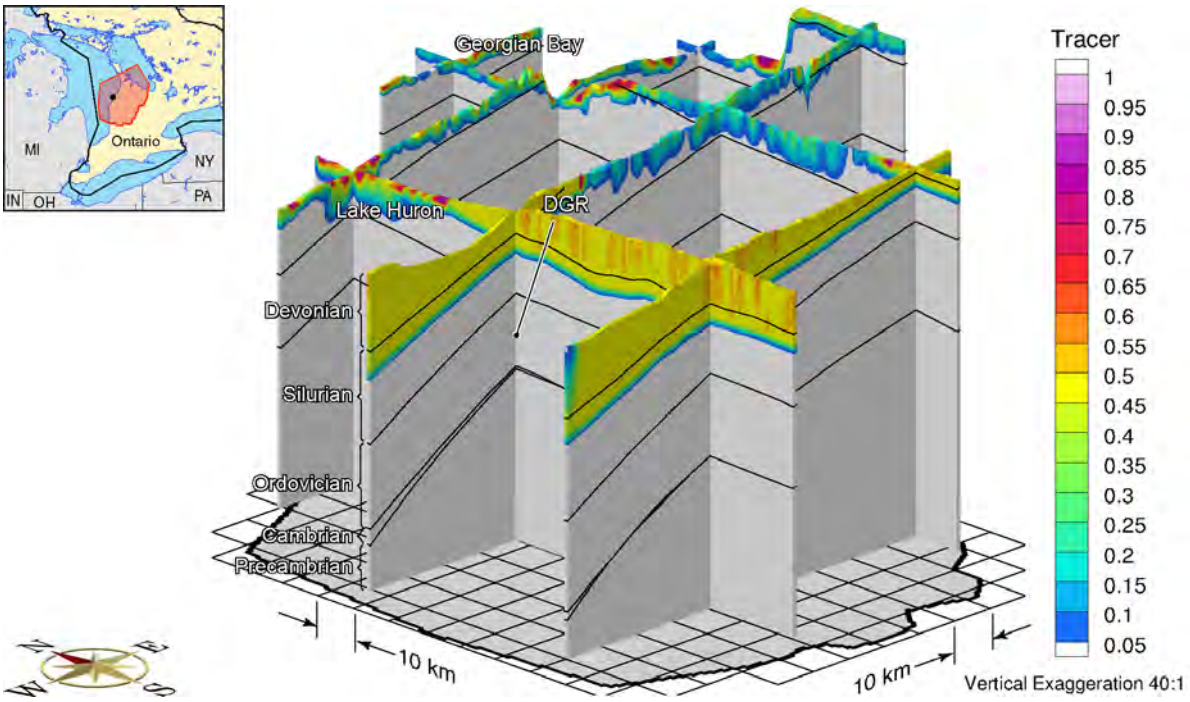

Figure F.125: Fence View Showing the Depth of Penetration of a Tracer at 30ka before Present with the One-dimensional Loading Efficiency and Storage Coefficients Reflecting the Presence of a Gas Phase

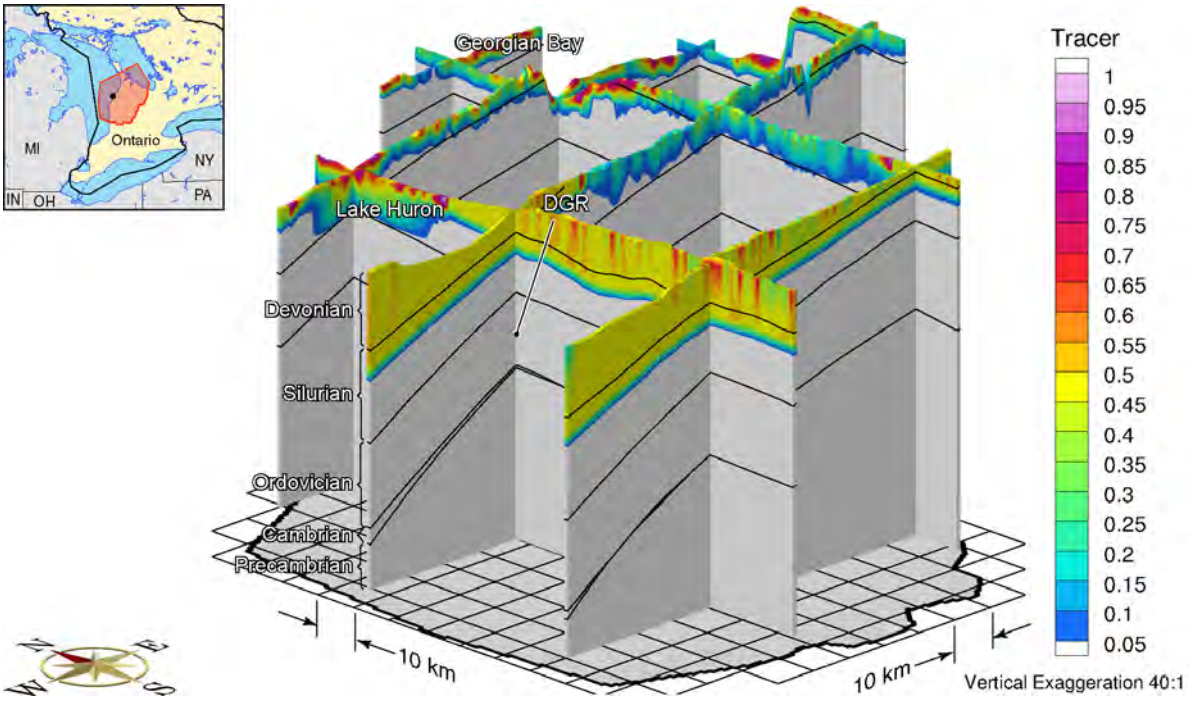

Figure F.126: Fence View Showing the Depth of Penetration of a Tracer at Present with the One-dimensional Loading Efficiency and Storage Coefficients Reflecting the Presence of a Gas Phase

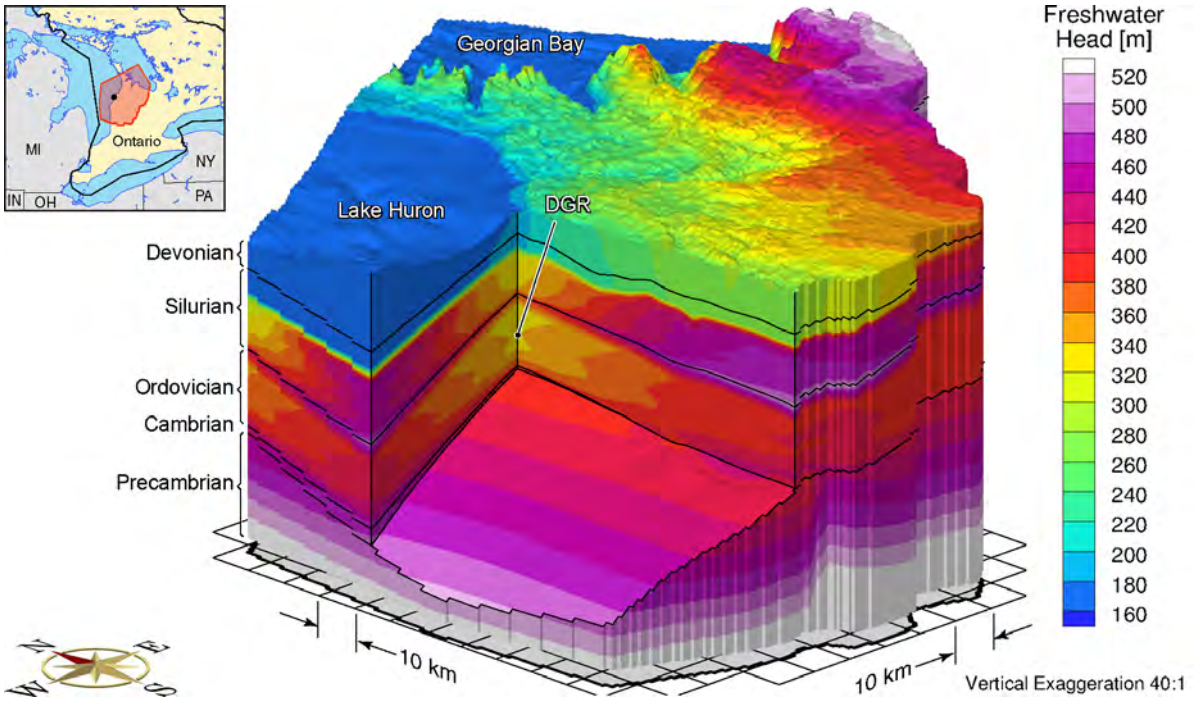

Figure F.127: Block Cut View of Freshwater Heads at Present After Two Paleohydrogeologic Cycles of 120 ka

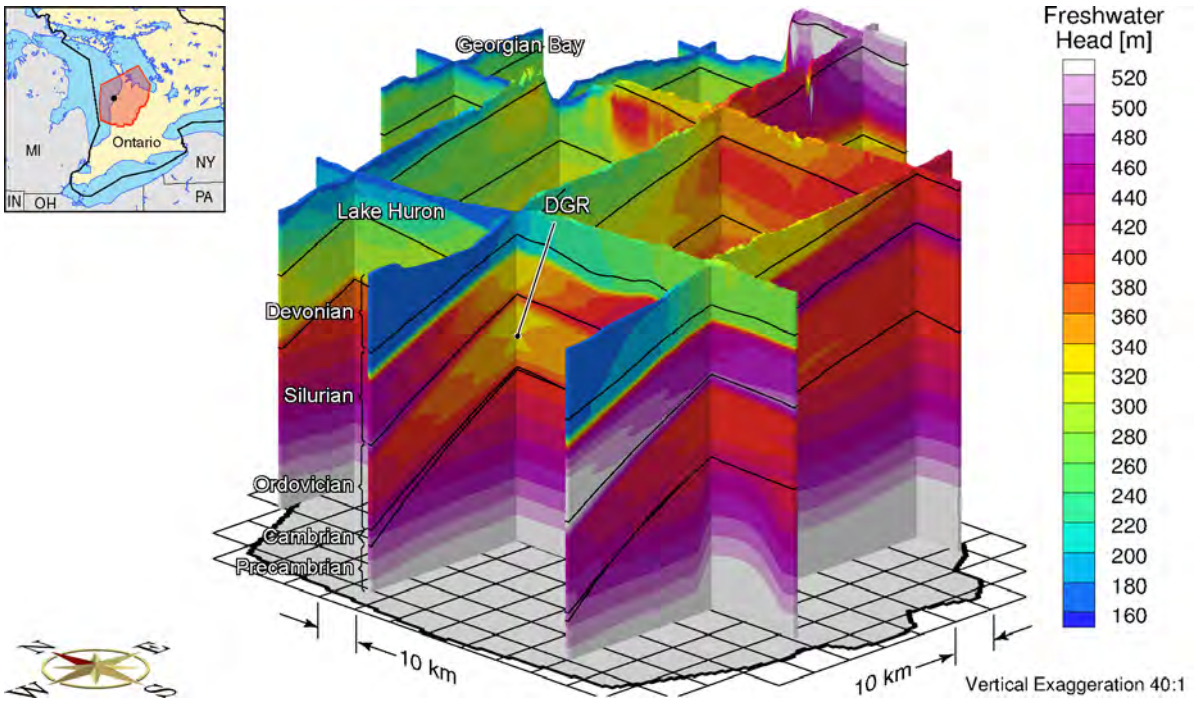

Figure F.128: Fence View of Freshwater Heads at Present After Two Paleohydrogeologic Cycles of 120 ka

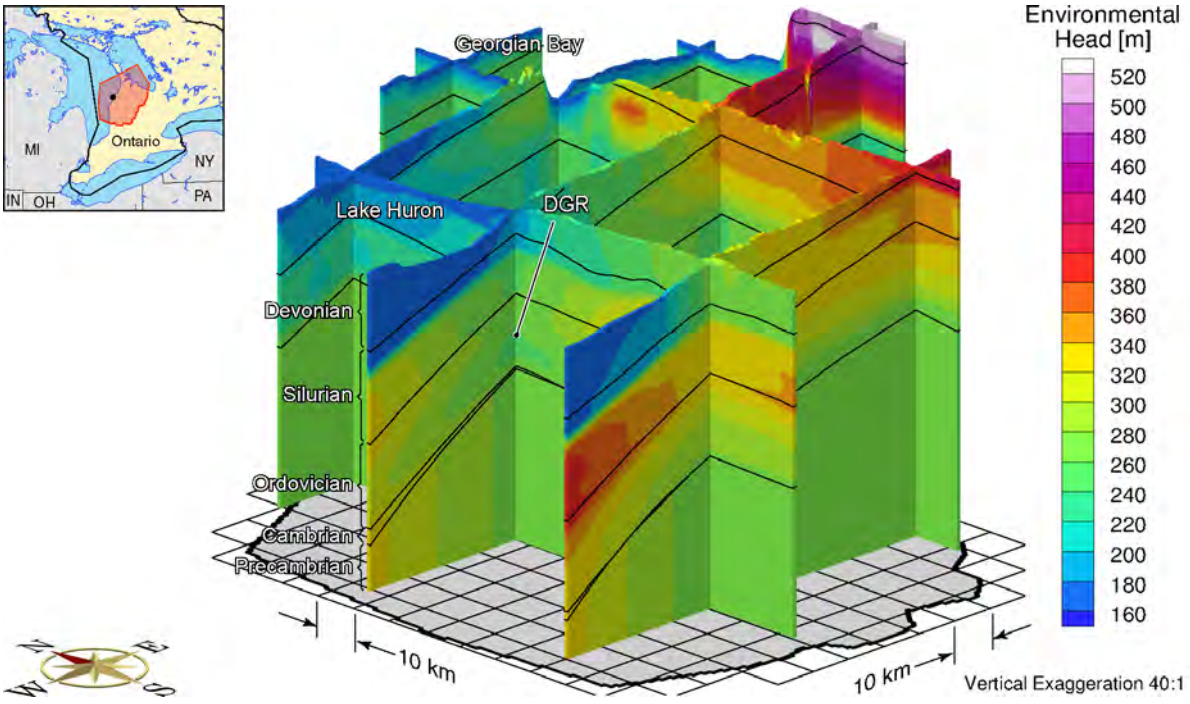

Figure F.129: Fence View of Environmental Heads at 90ka before Present for Two Paleohydrogeologic Cycles of 120 ka

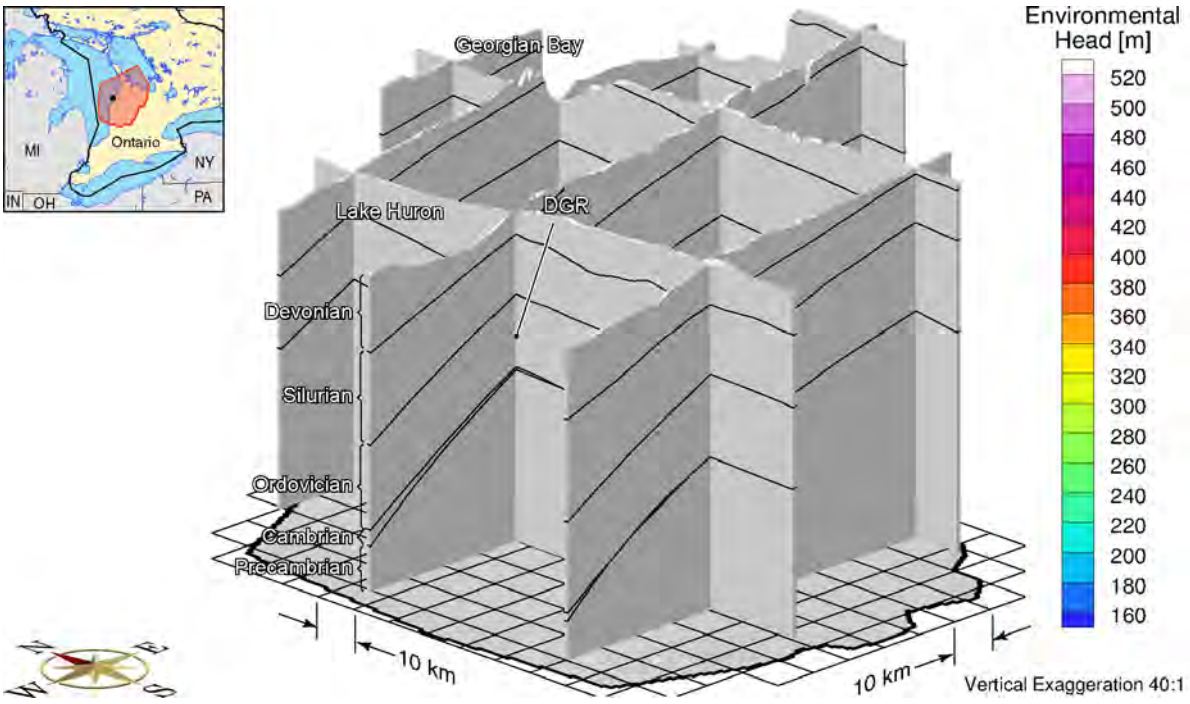

Figure F.130: Fence View of Environmental Heads at 60ka before Present for Two Paleohydrogeologic Cycles of 120 ka

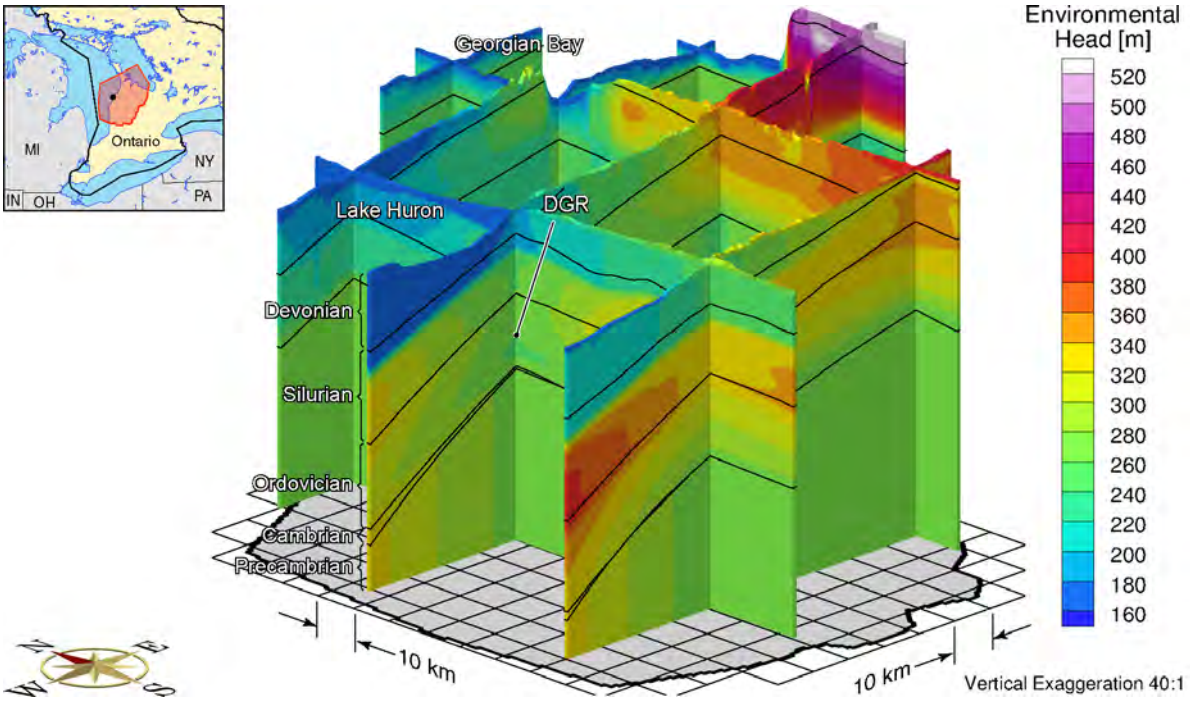

Figure F.131: Fence View of Environmental Heads at 30ka before Present for Two Paleohydrogeologic Cycles of 120 ka

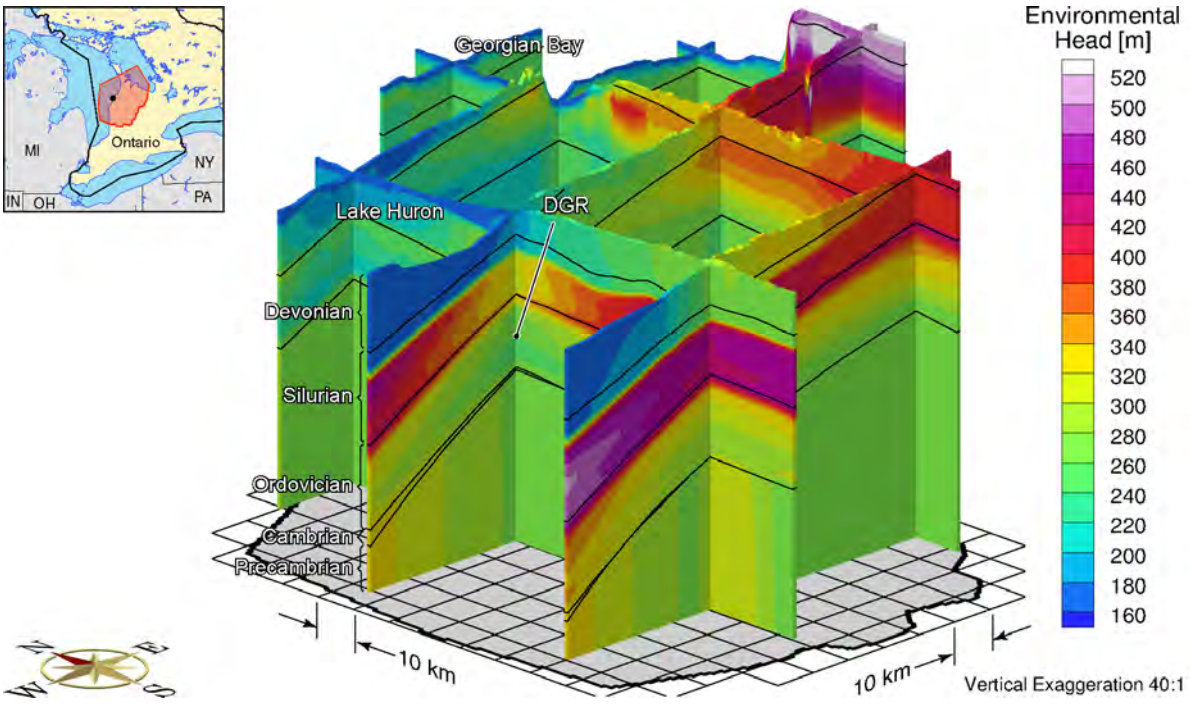

Figure F.132: Fence View of Environmental Heads at the Present for Two Paleohydrogeologic Cycles of 120 ka

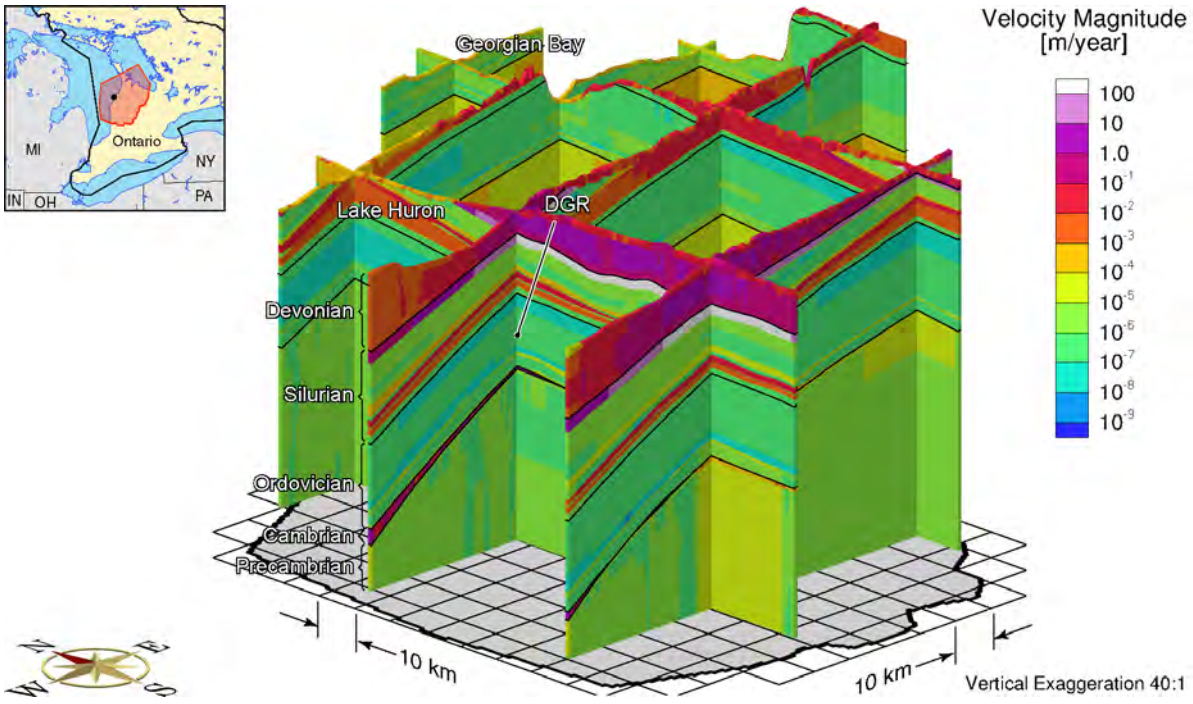

Figure F.133: Fence View of Pore Velocity Magnitude at 90ka before Present for Two Paleohydrogeologic Cycles of 120 ka

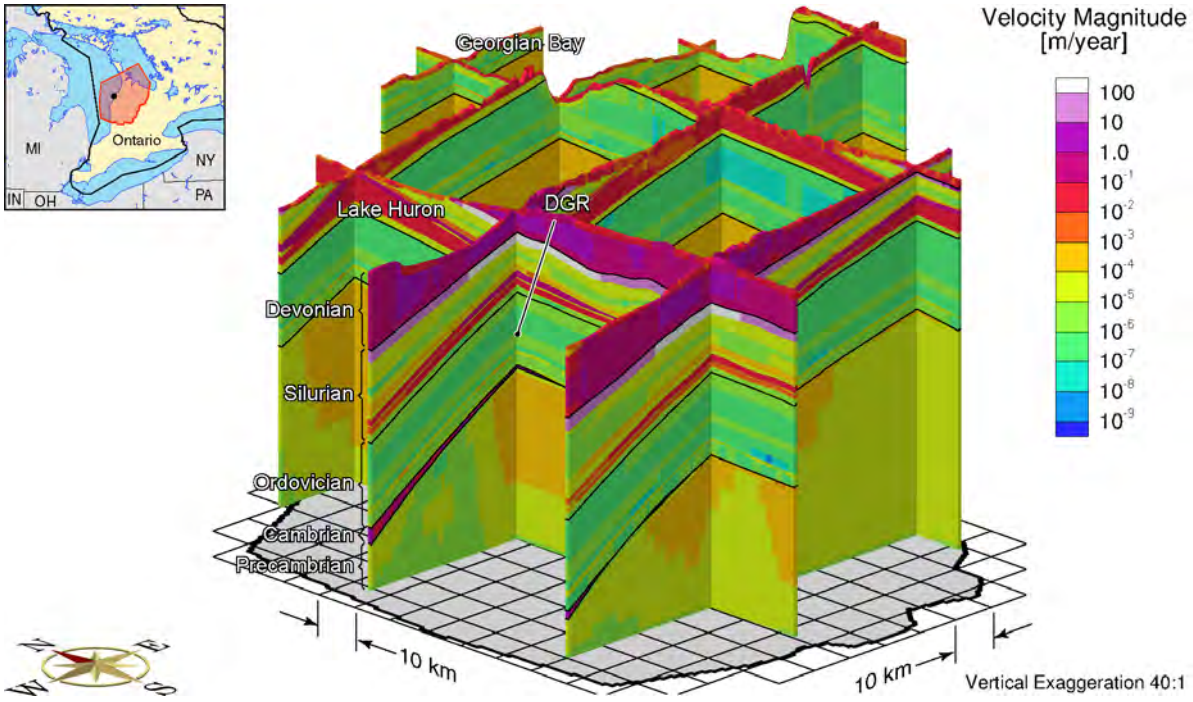

Figure F.134: Fence View of Pore Velocity Magnitude at 60ka before Present for Two Paleohydrogeologic Cycles of 120 ka

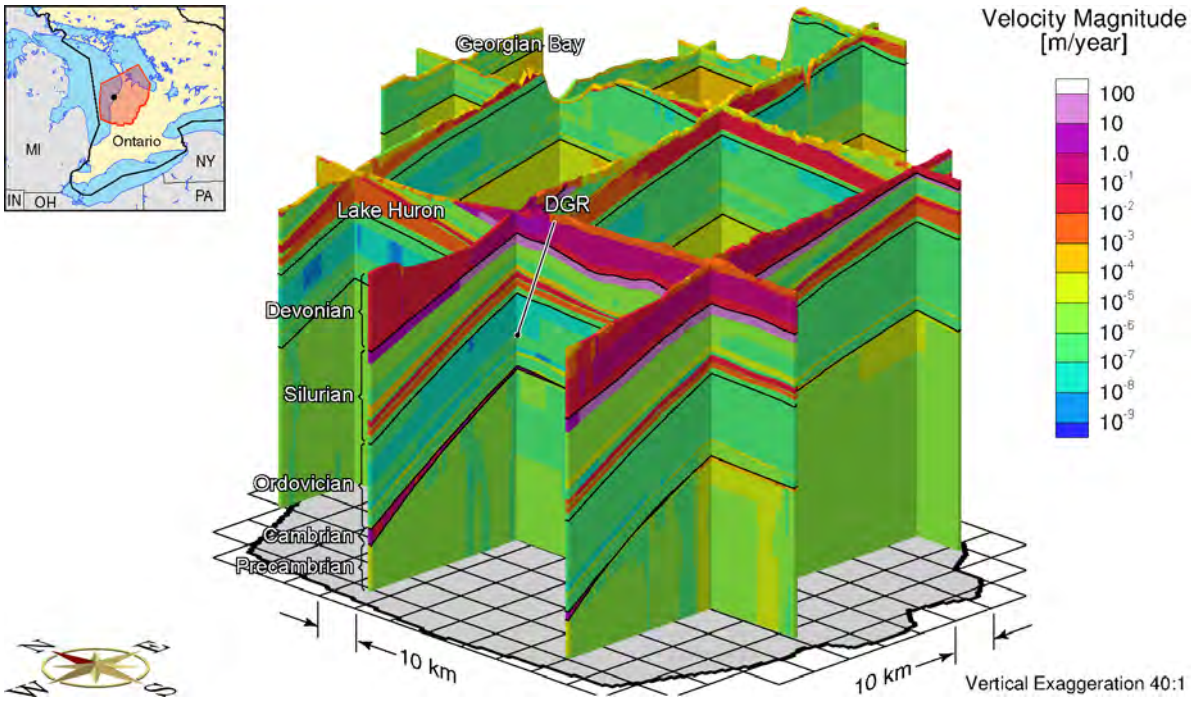

Figure F.135: Fence View of Pore Velocity Magnitude at 30ka before Present for Two Paleohydrogeologic Cycles of 120 ka

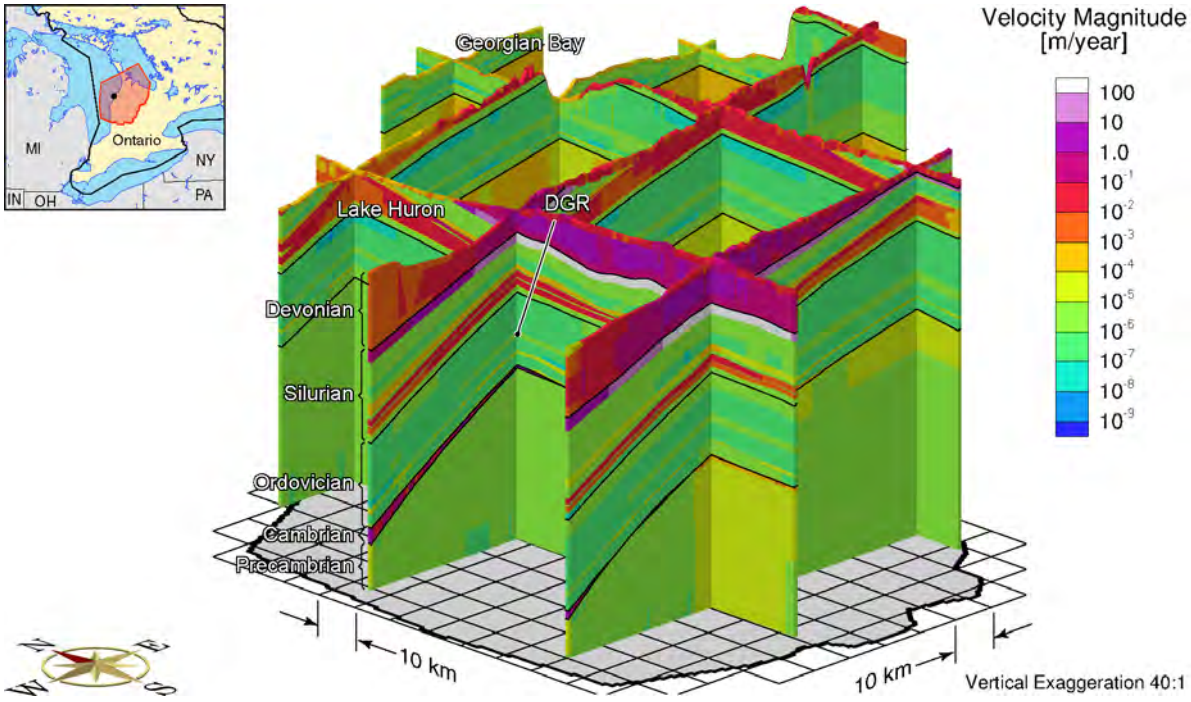

Figure F.136: Fence View of Pore Velocity Magnitude at Present for Two Paleohydrogeologic Cycles of 120 ka

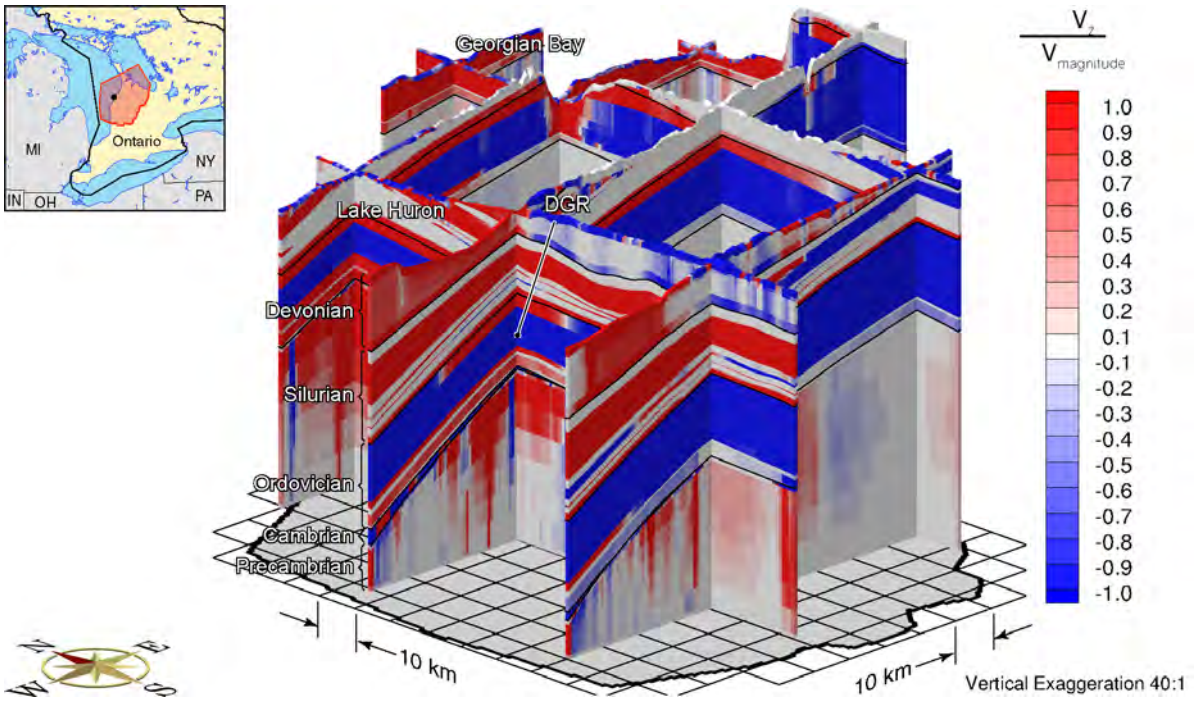

Figure F.137: Fence View Showing the Ratio of the Vertical Pore Water Velocity to the Velocity Magnitude at 90ka before Present for Two Paleohydrogeologic Cycles of 120 ka

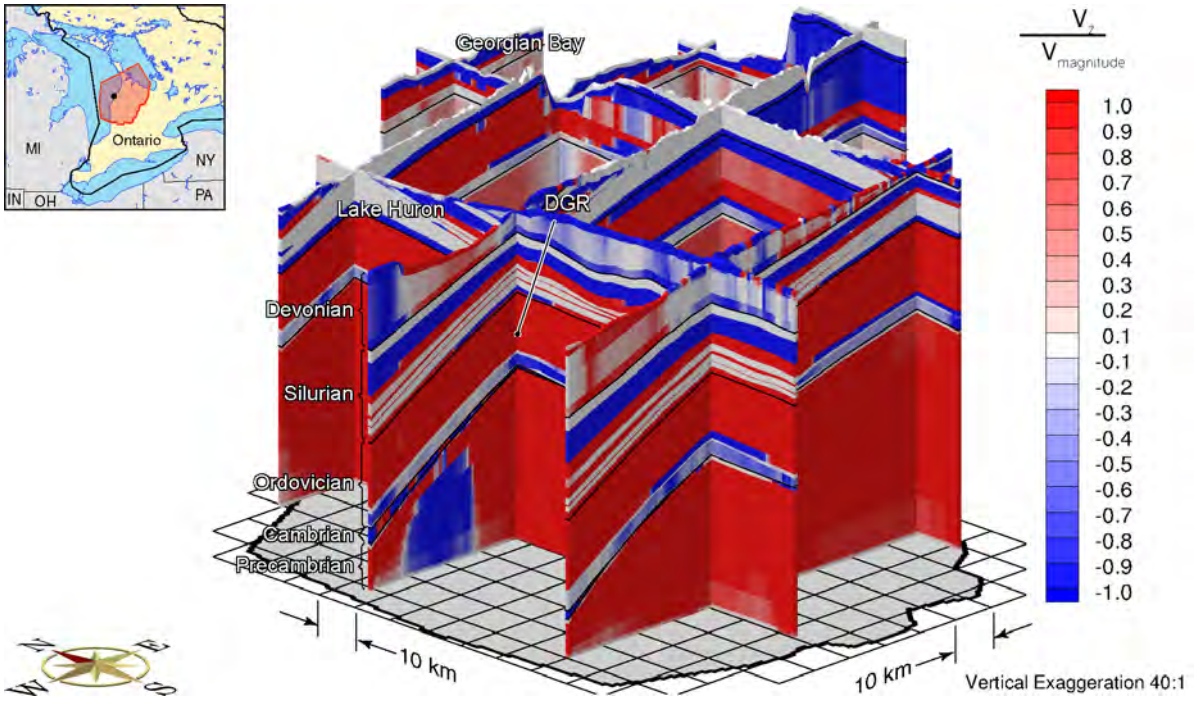

Figure F.138: Fence View Showing the Ratio of the Vertical Pore Water Velocity to the Velocity Magnitude at 60ka before Present for Two Paleohydrogeologic Cycles of 120 ka

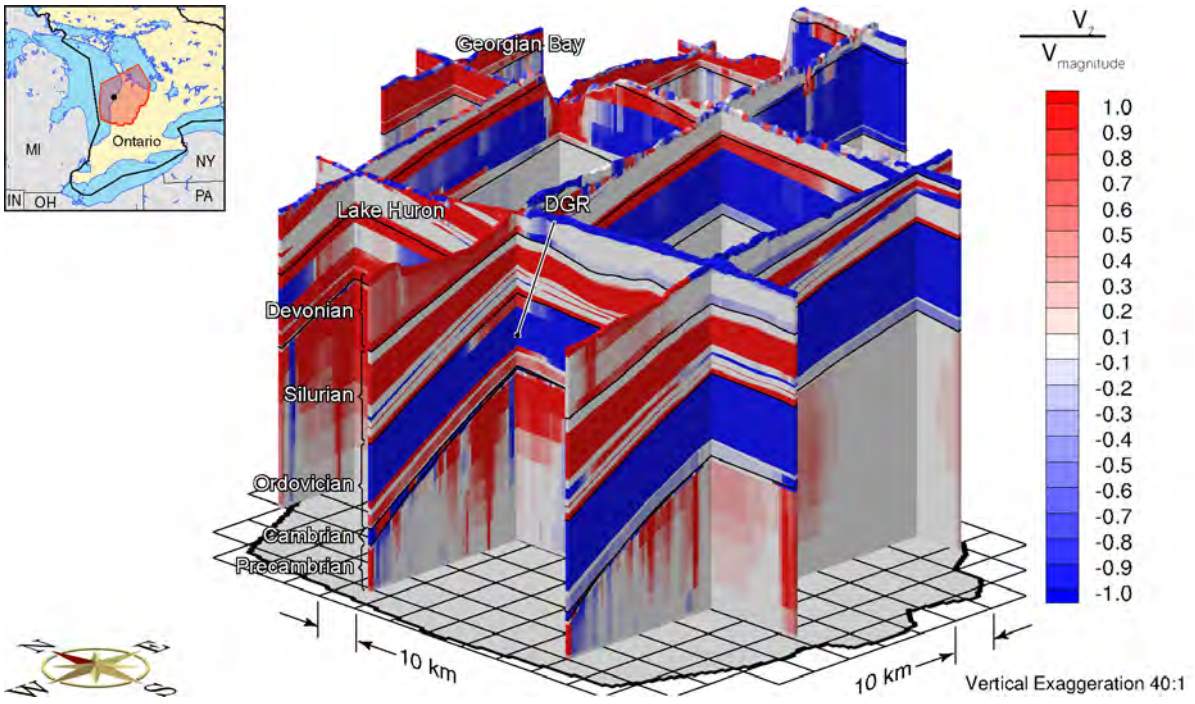

Figure F.139: Fence View Showing the Ratio of the Vertical Pore Water Velocity to the Velocity Magnitude at 30ka before Present for Two Paleohydrogeologic Cycles of 120 ka

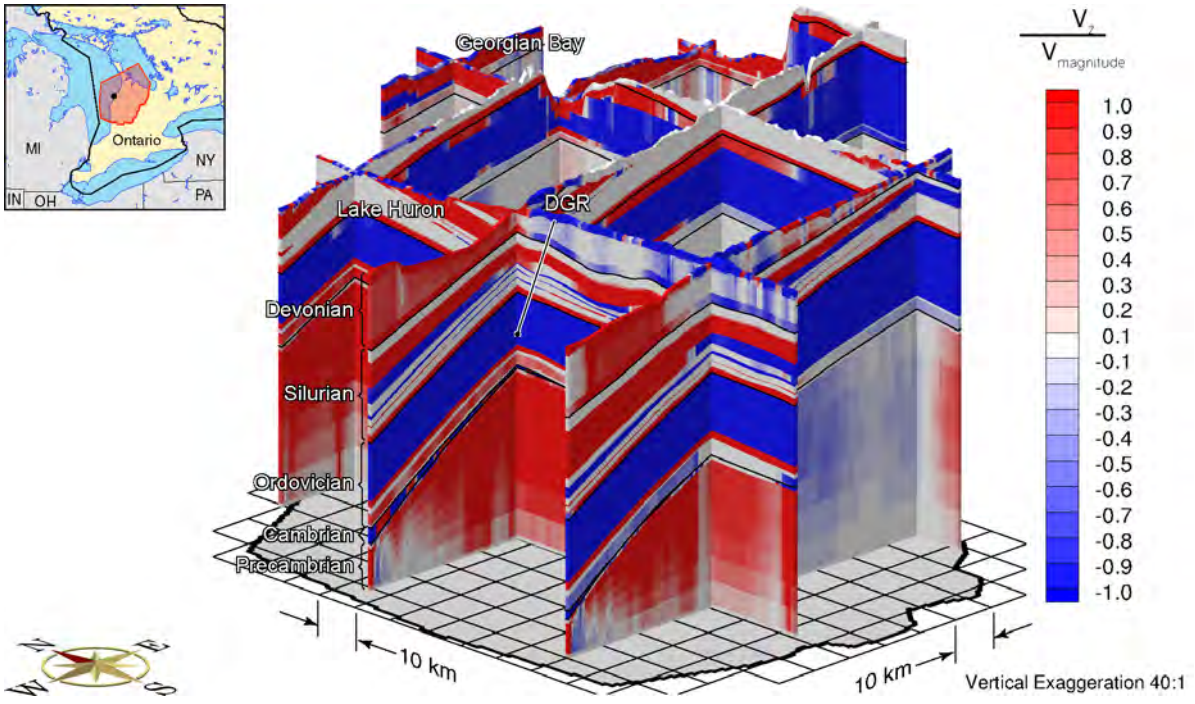

Figure F.140: Fence View of Ratio of Vertical Pore Velocity to Pore Velocity Magnitude at Present for Two Paleohydrogeologic Cycles of 120 ka

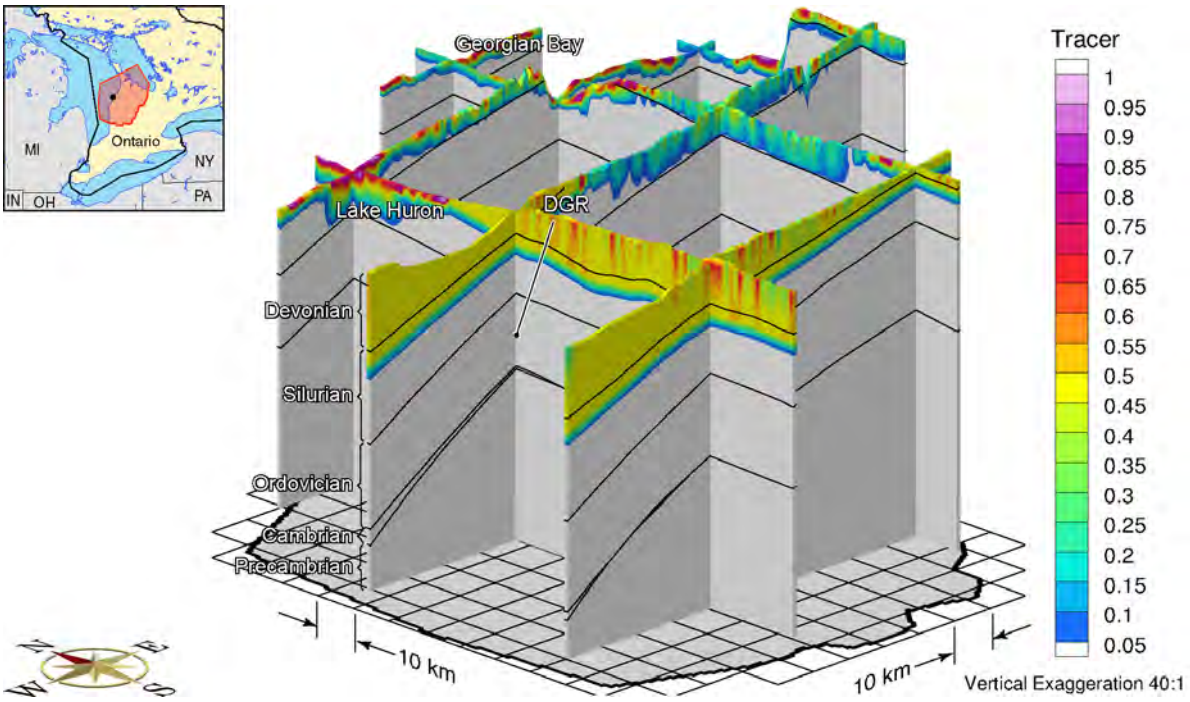

Figure F.141: Fence View Showing the Depth of Penetration of a Tracer at 90ka before Present for Two Paleohydrogeologic Cycles of 120 ka

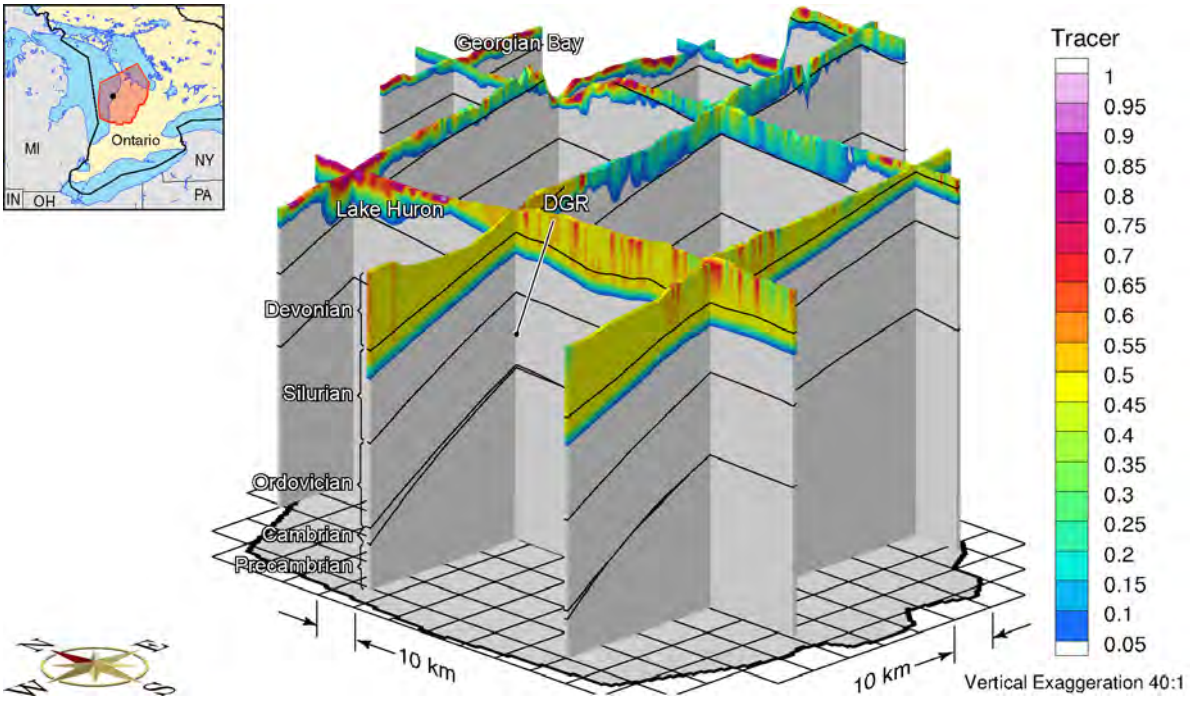

Figure F.142: Fence View Showing the Depth of Penetration of a Tracer at 60ka before Present for Two Paleohydrogeologic Cycles of 120 ka

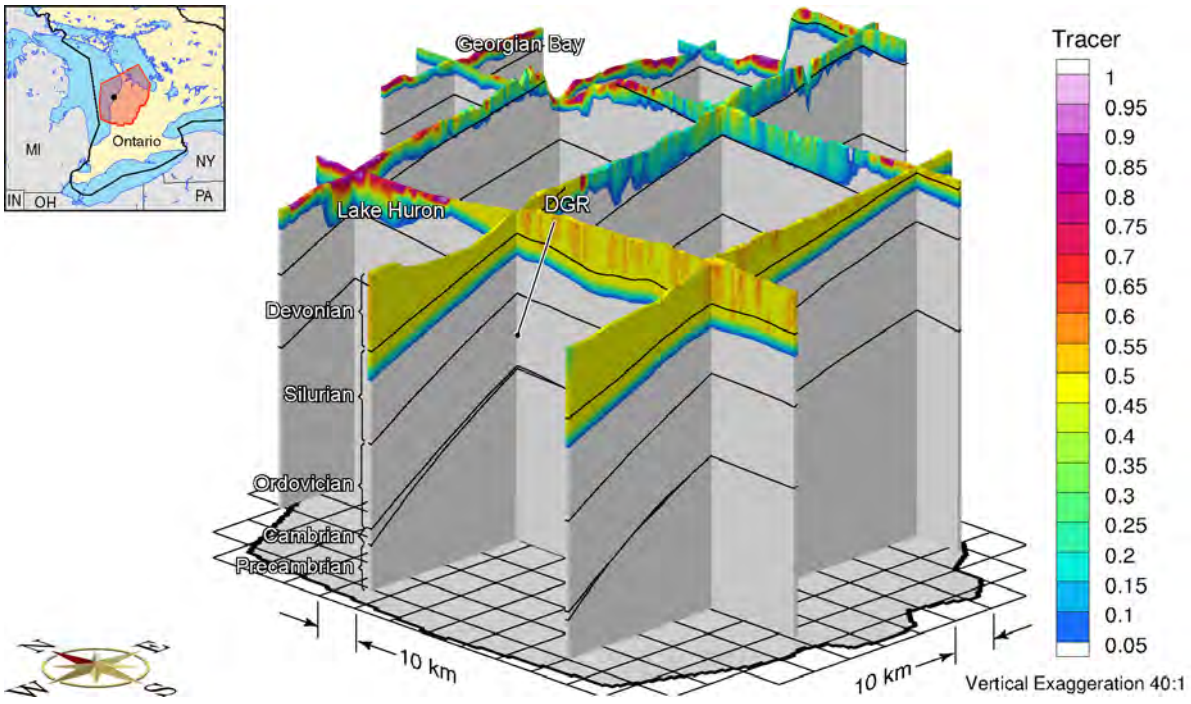

Figure F.143: Fence View Showing the Depth of Penetration of a Tracer at 30ka before Present for Two Paleohydrogeologic Cycles of 120 ka

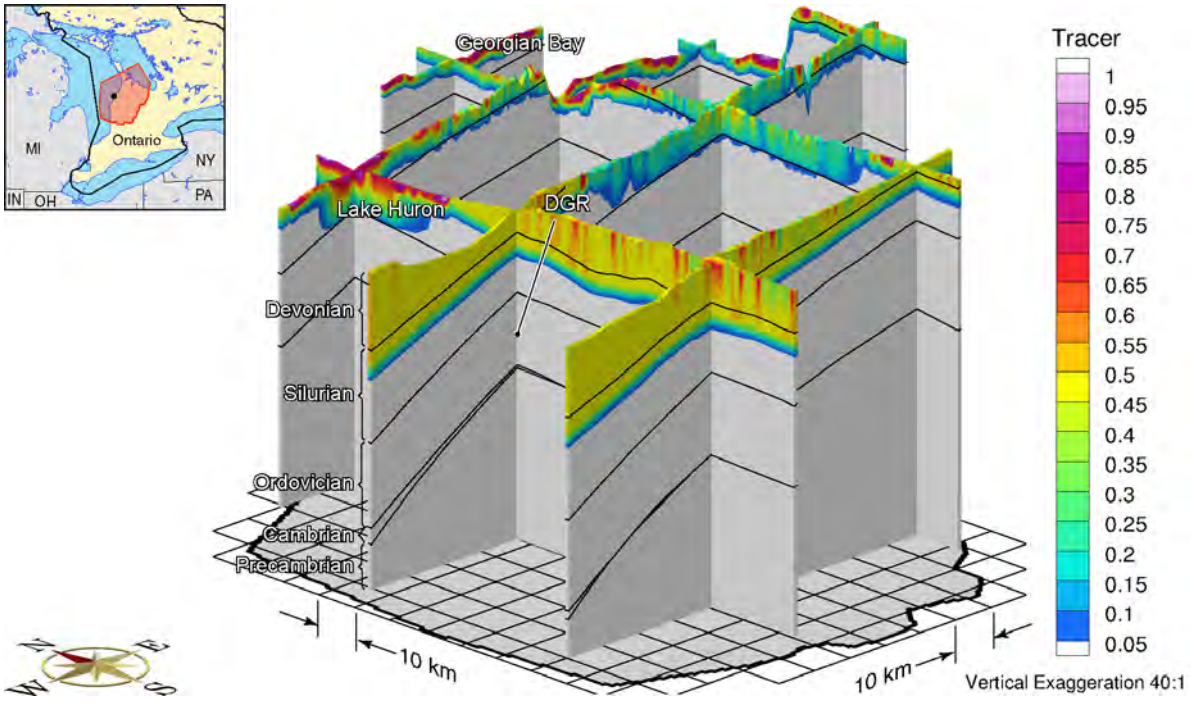

Figure F.144: Fence View Showing the Depth of Penetration of a Tracer at Present for Two Paleohydrogeologic Cycles of 120 ka

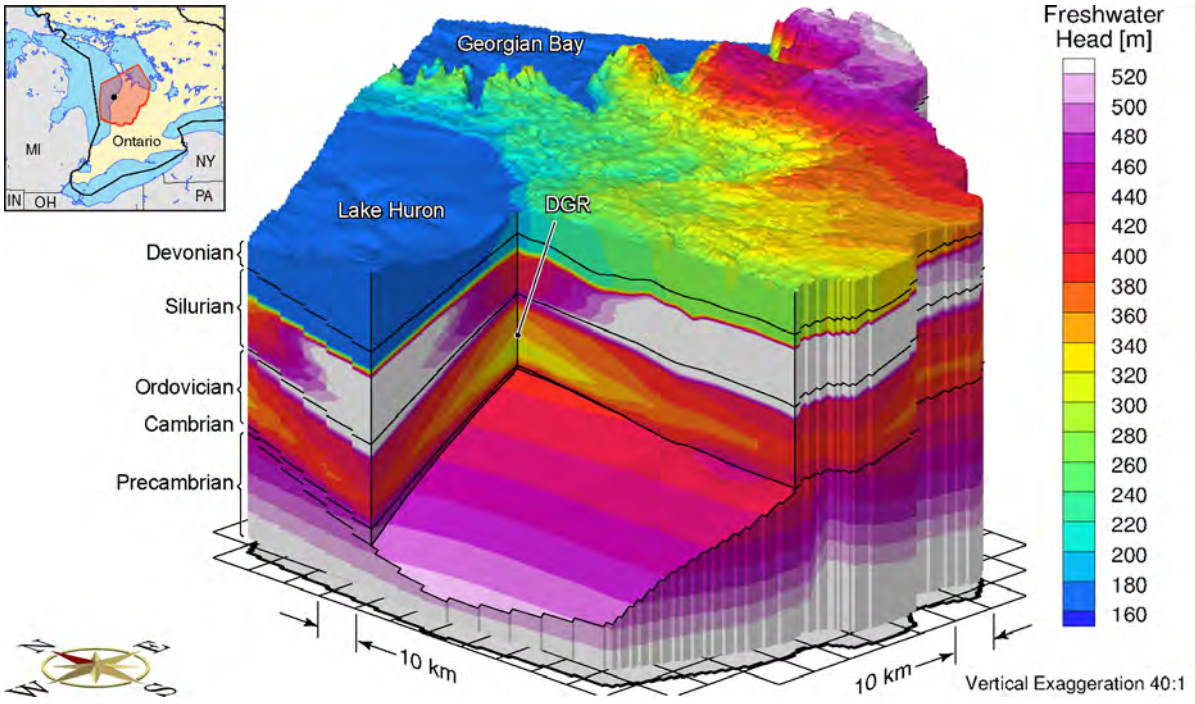

Figure F.145: Block Cut View of Freshwater Heads at Present for the Alternate Paleoclimate Model nn9921 and the Base-case Parameters

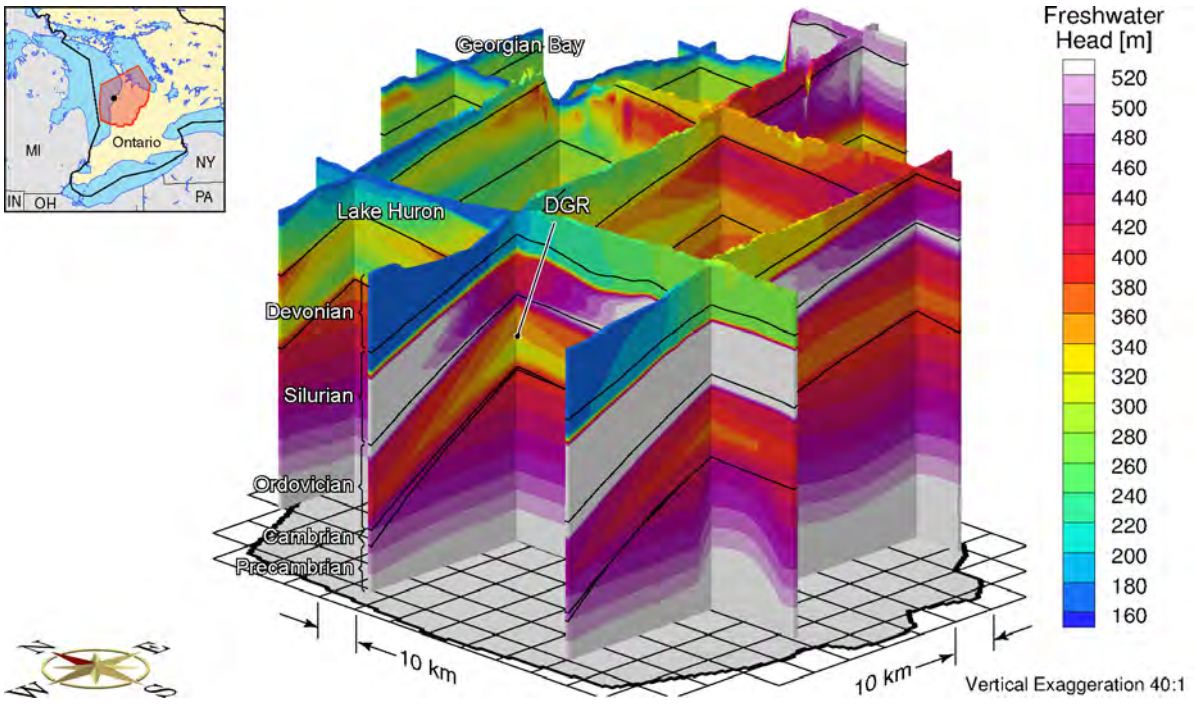

Figure F.146: Fence View of Freshwater Heads at Present for the Alternate Paleoclimate Model nn9921 and the Base-case Parameters

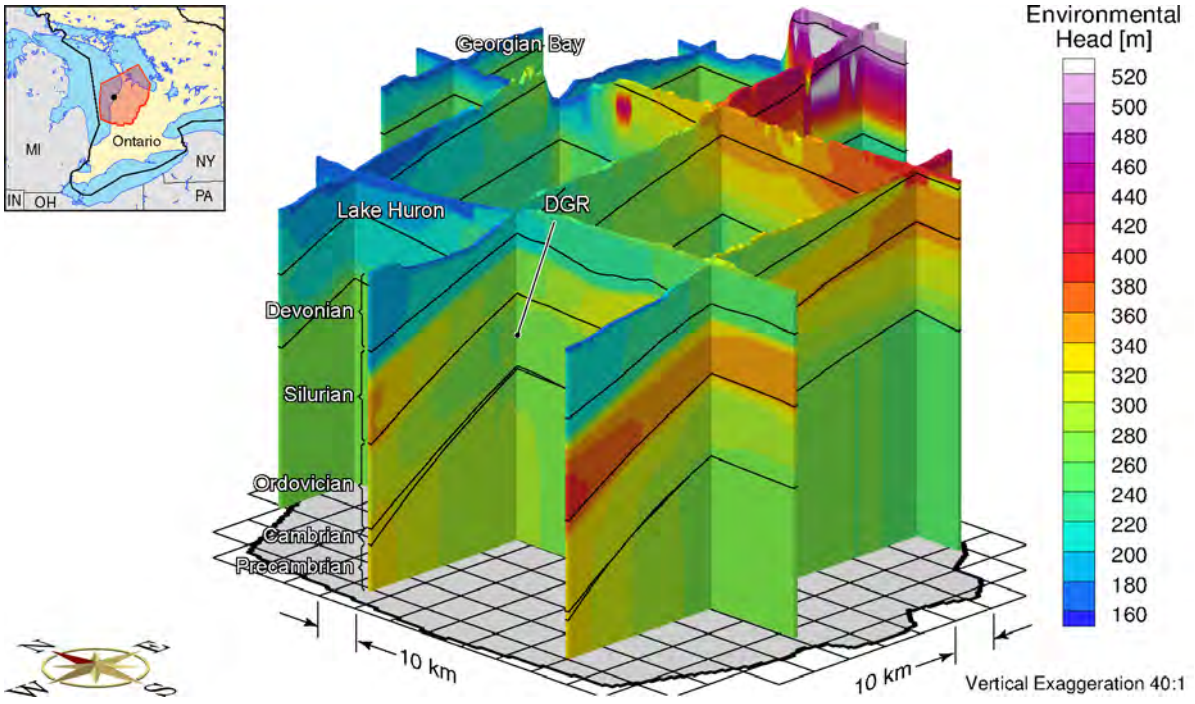

Figure F.147: Fence View of Environmental Heads at 90ka before Present for the Alternate Paleoclimate Model nn9921 and the Base-case Parameters

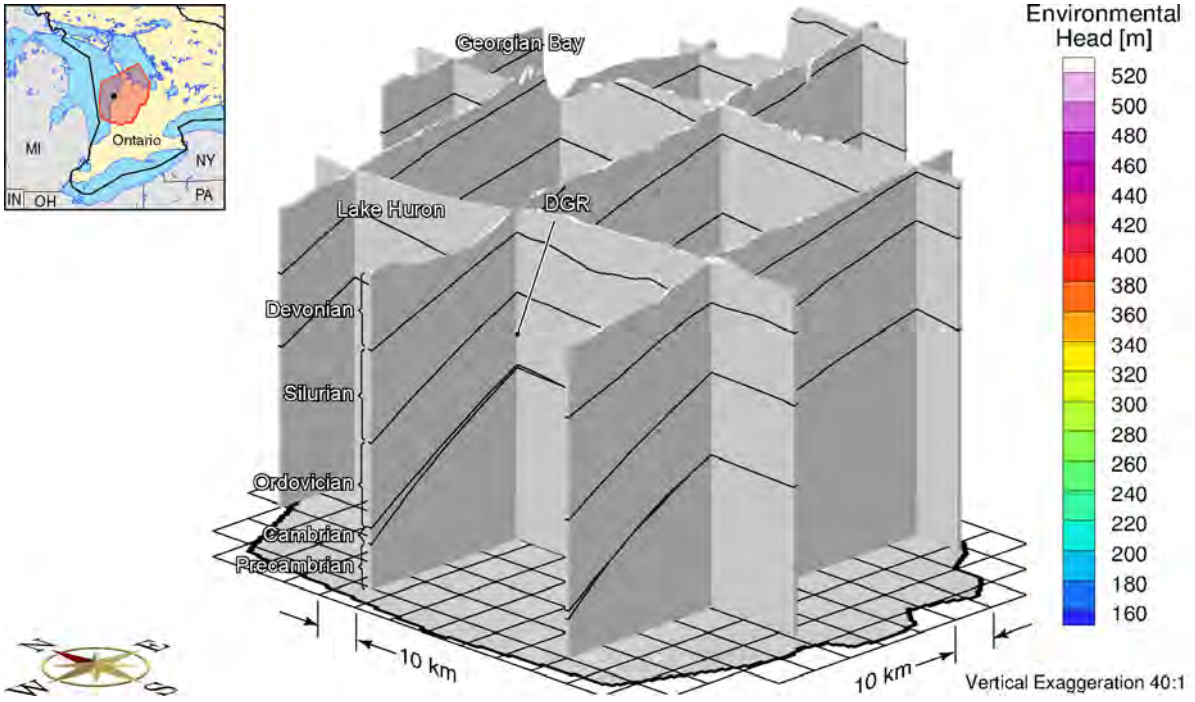

Figure F.148: Fence View of Environmental Heads at 60ka before Present for the Alternate Paleoclimate Model nn9921 and the Base-case Parameters

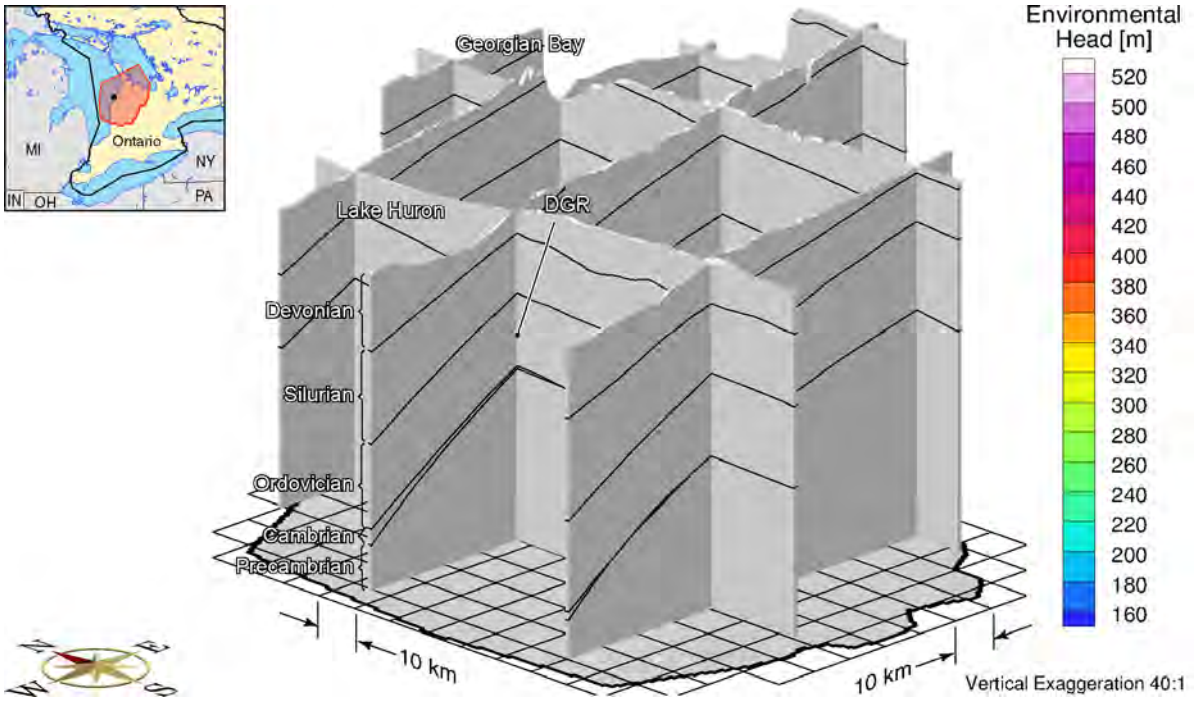

Figure F.149: Fence View of Environmental Heads at 30ka before Present for the Alternate Paleoclimate Model nn9921 and the Base-case Parameters

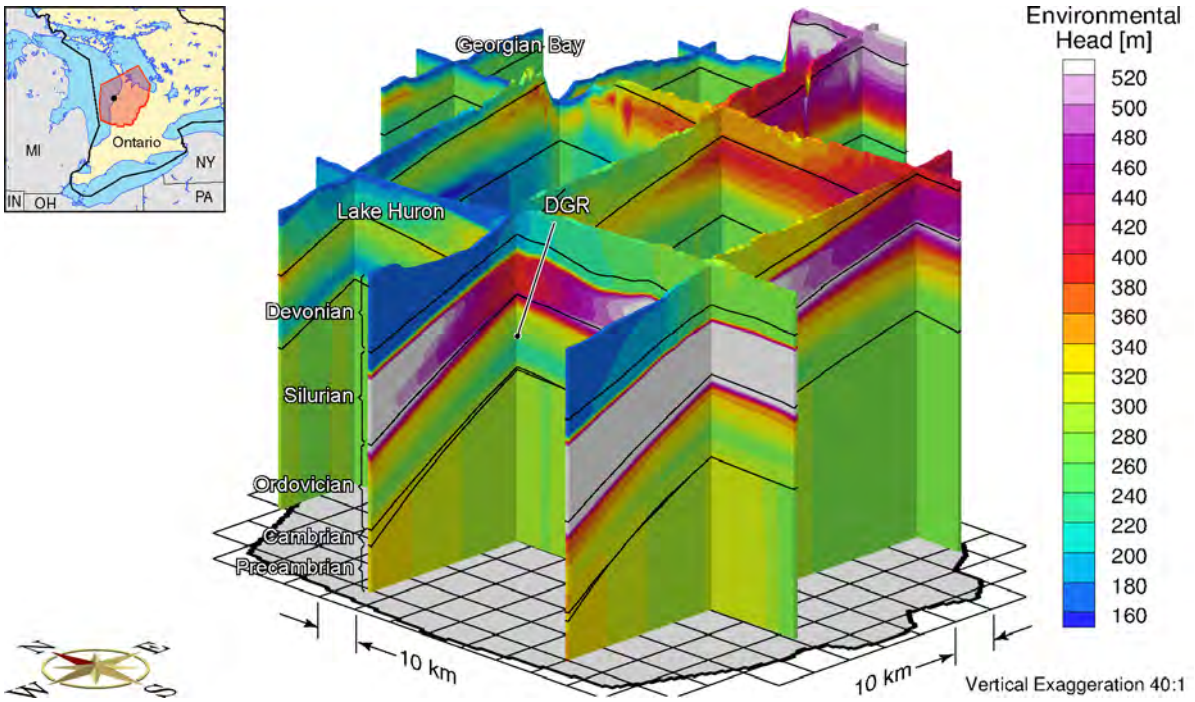

Figure F.150: Fence View of Environmental Heads at the Present for the Alternate Paleoclimate Model nn9921 and the Base-case Parameters

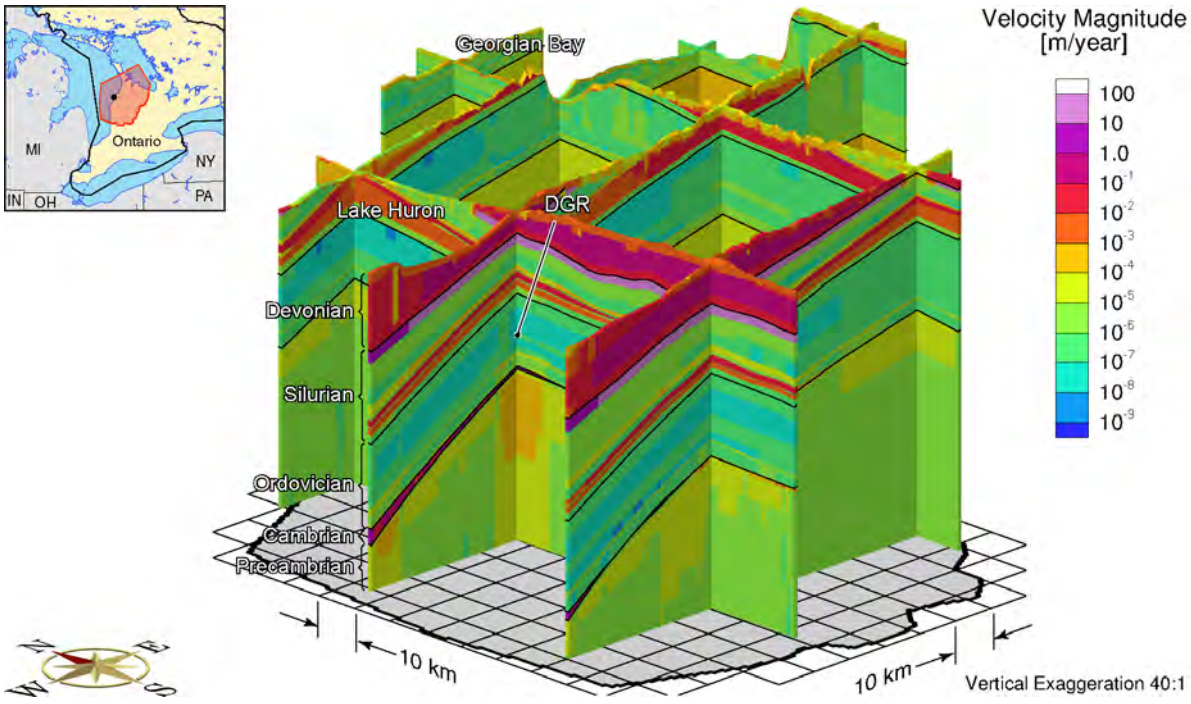

Figure F.151: Fence View of Pore Velocity Magnitude at 90ka before Present for the Alternate Paleoclimate Model nn9921 and the Base-case Parameters

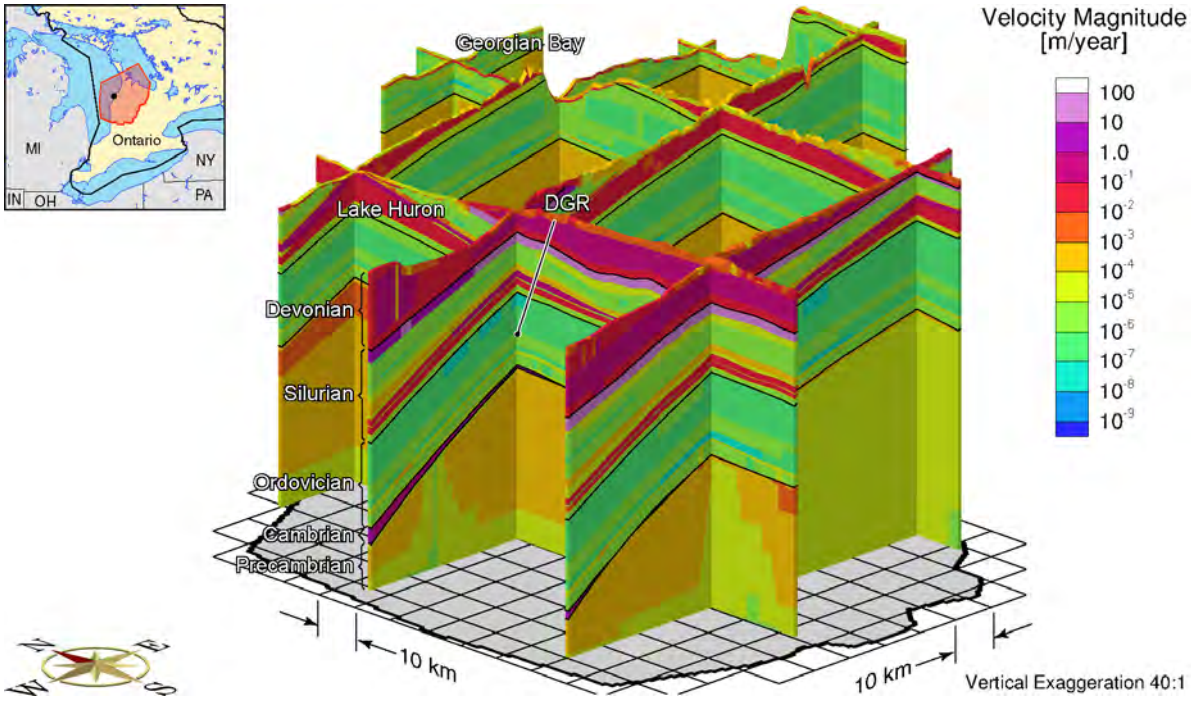

Figure F.152: Fence View of Pore Velocity Magnitude at 60ka before Present for the Alternate Paleoclimate Model nn9921 and the Base-case Parameters

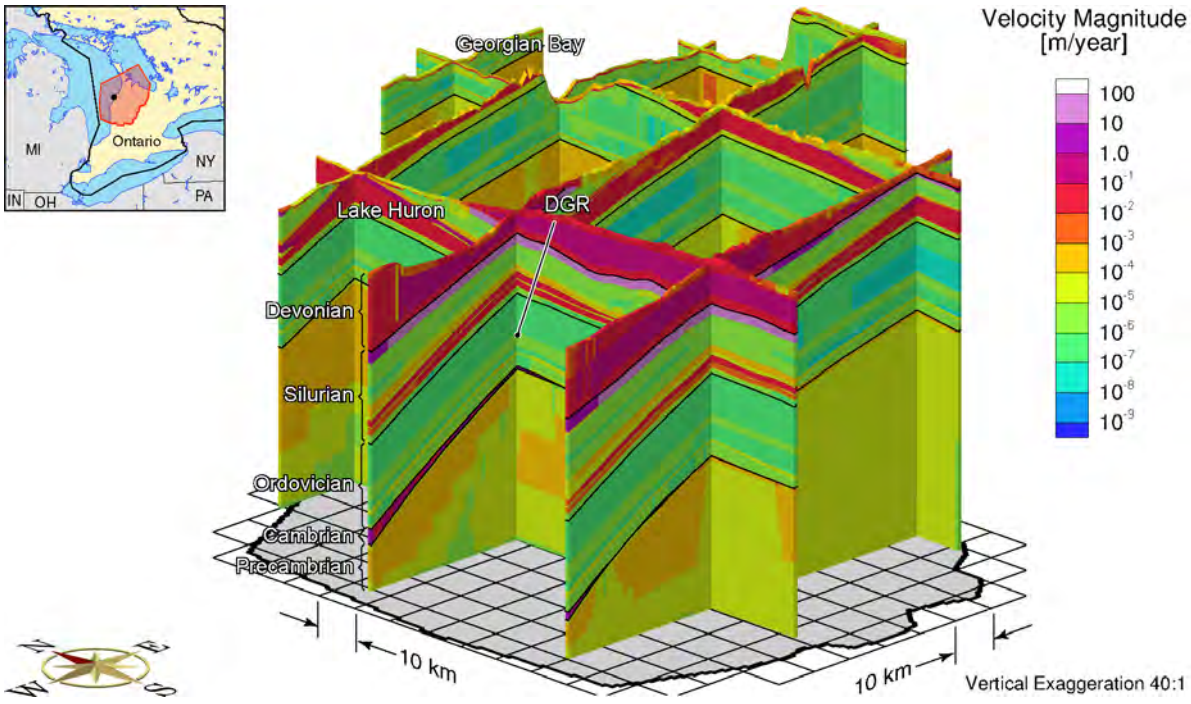

Figure F.153: Fence View of Pore Velocity Magnitude at 30ka before Present for the Alternate Paleoclimate Model nn9921 and the Base-case Parameters

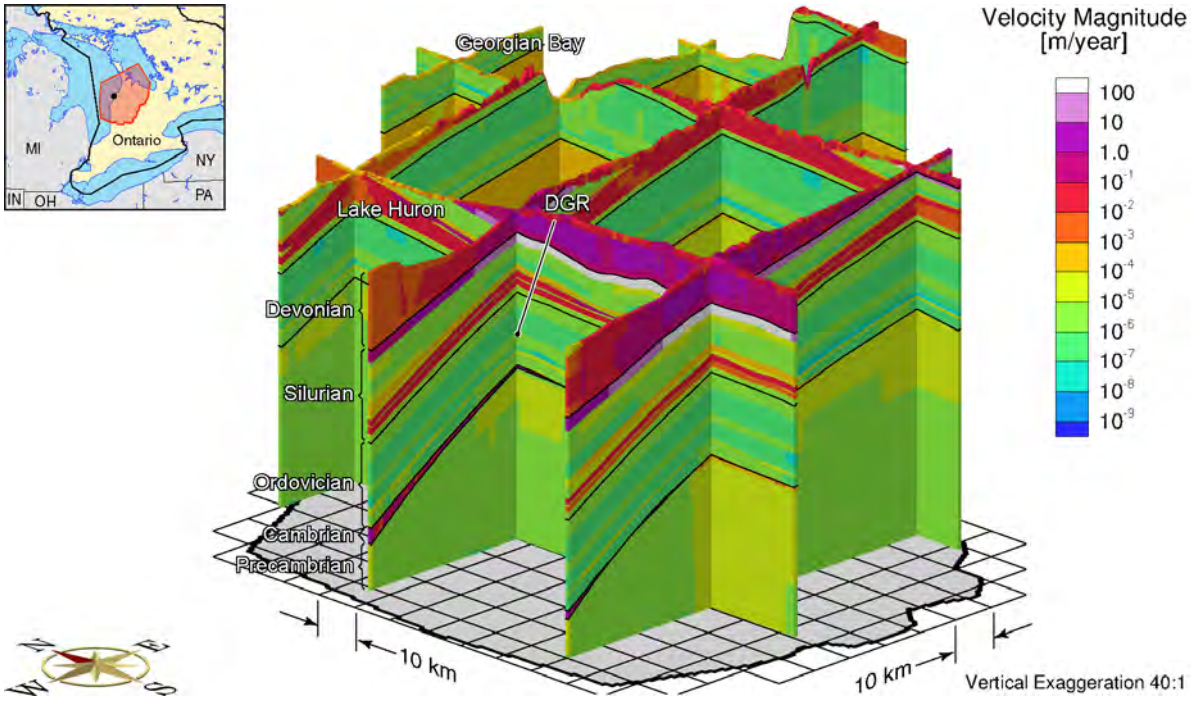

Figure F.154: Fence View of Pore Velocity Magnitude at Present for the Alternate Paleoclimate Model nn9921 and the Base-case Parameters

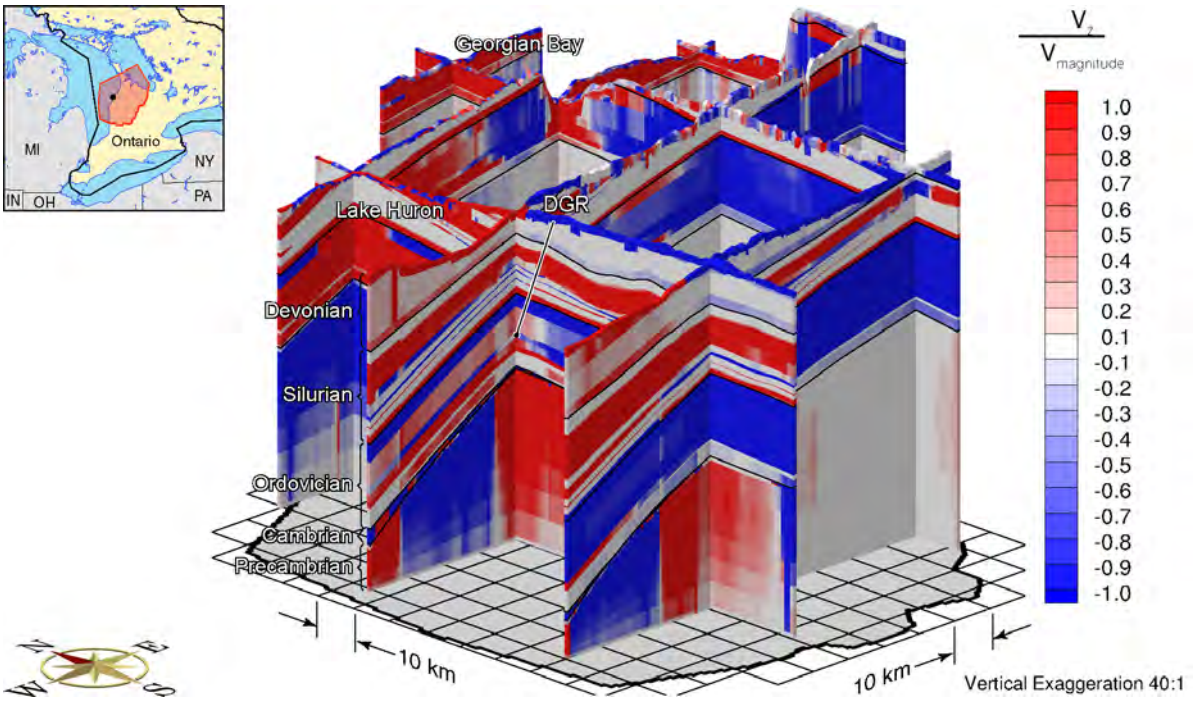

Figure F.155: Fence View Showing the Ratio of the Vertical Pore Water Velocity to the Velocity Magnitude at 90ka before Present for the Alternate Paleoclimate Model nn9921 and the Base-case Parameters

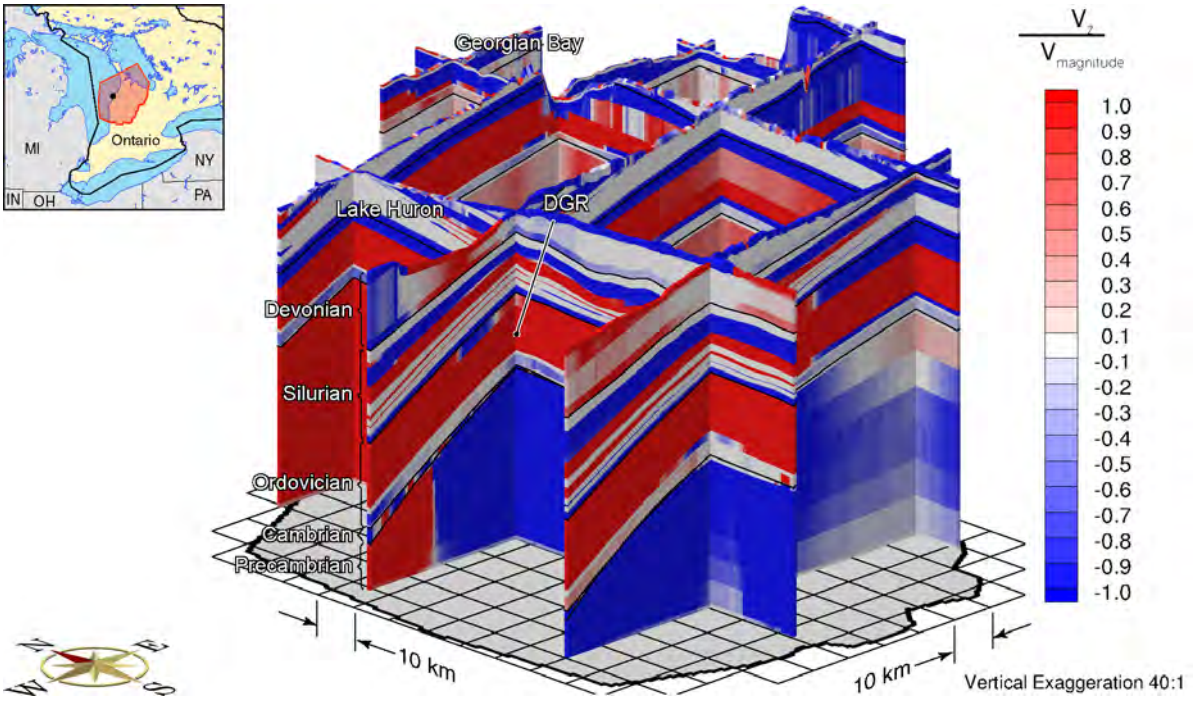

Figure F.156: Fence View Showing the Ratio of the Vertical Pore Water Velocity to the Velocity Magnitude at 60ka before Present for the Alternate Paleoclimate Model nn9921 and the Base-case Parameters

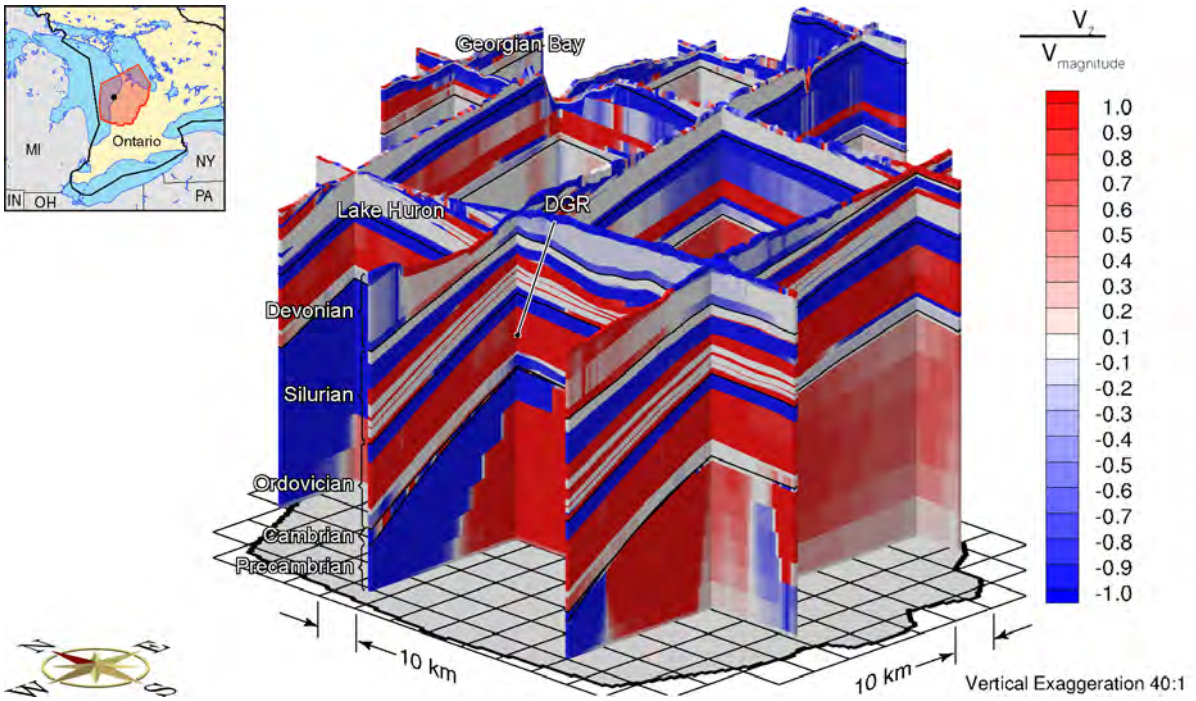

Figure F.157: Fence View Showing the Ratio of the Vertical Pore Water Velocity to the Velocity Magnitude at 30ka before Present for the Alternate Paleoclimate Model nn9921 and the Base-case Parameters

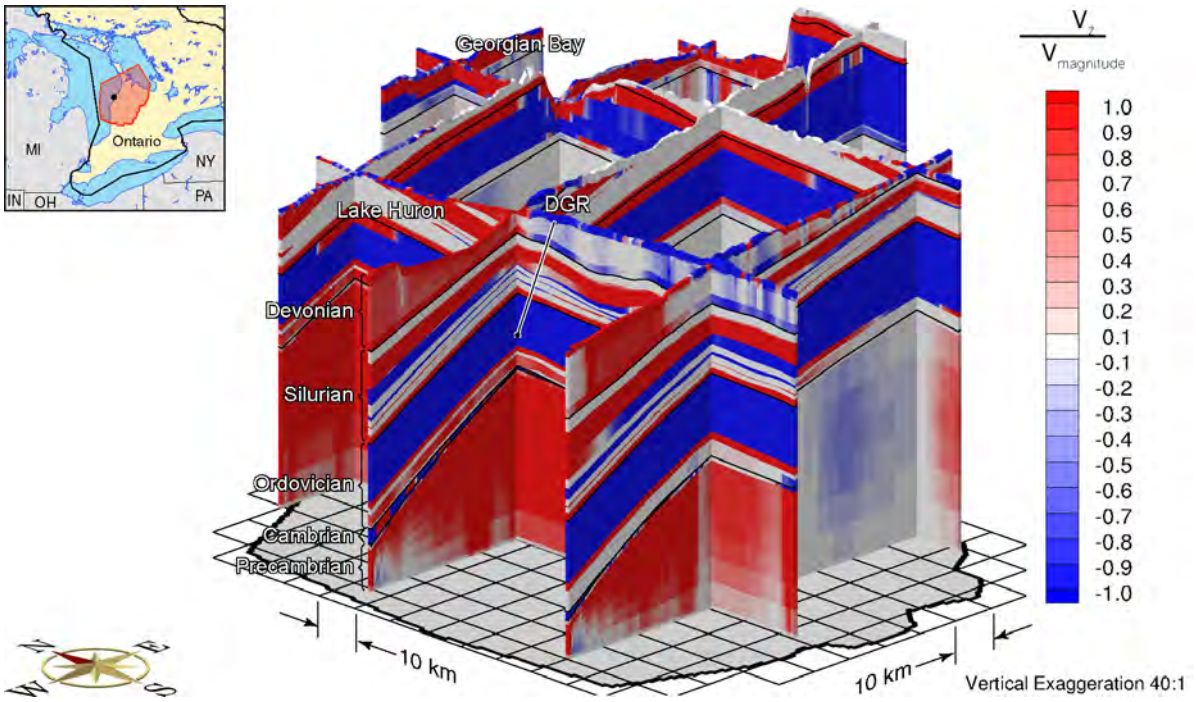

Figure F.158: Fence View of Ratio of Vertical Pore Velocity to Pore Velocity Magnitude at Present for the Alternate Paleoclimate Model nn9921 and the Base-case Parameters

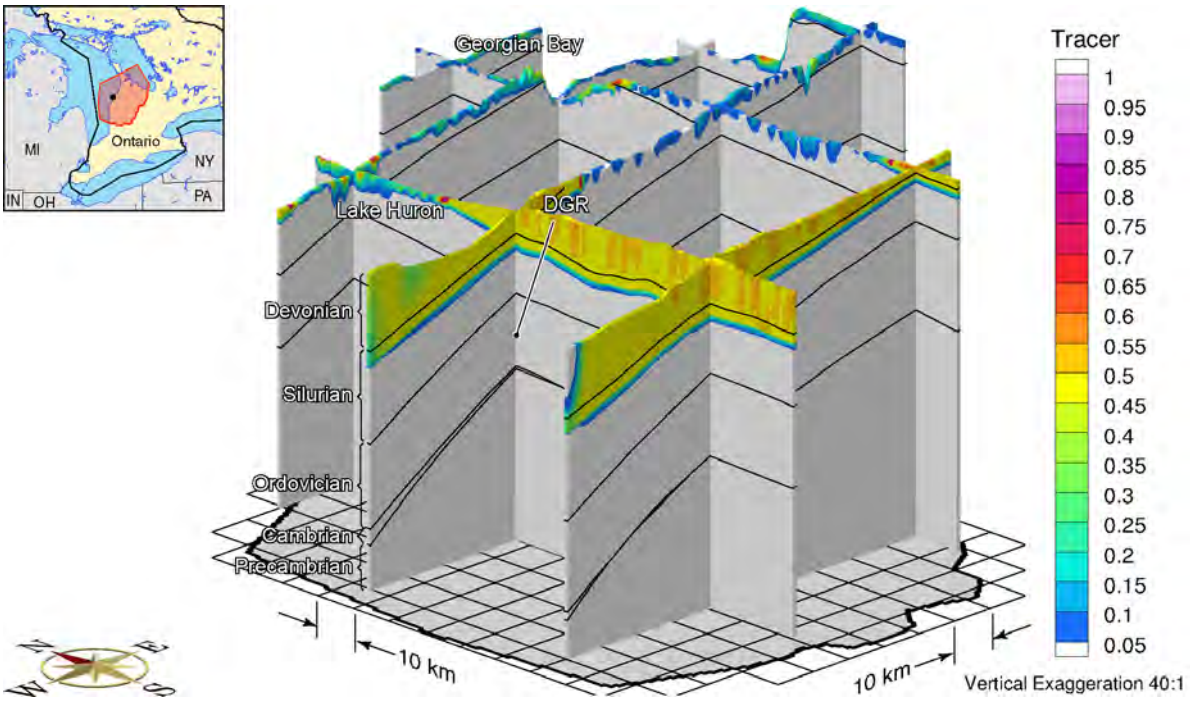

Figure F.159: Fence View Showing the Depth of Penetration of a Tracer at 90ka before Present for the Alternate Paleoclimate Model nn9921 and the Base-case Parameters

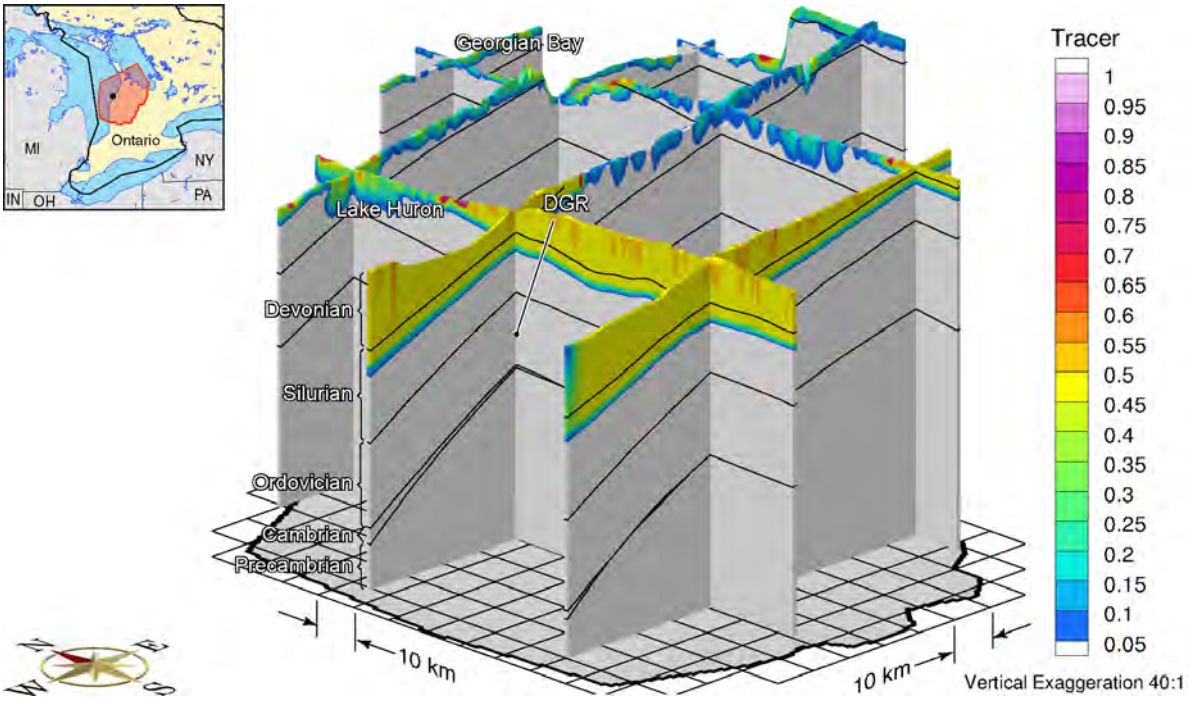

Figure F.160: Fence View Showing the Depth of Penetration of a Tracer at 60ka before Present for the Alternate Paleoclimate Model nn9921 and the Base-case Parameters

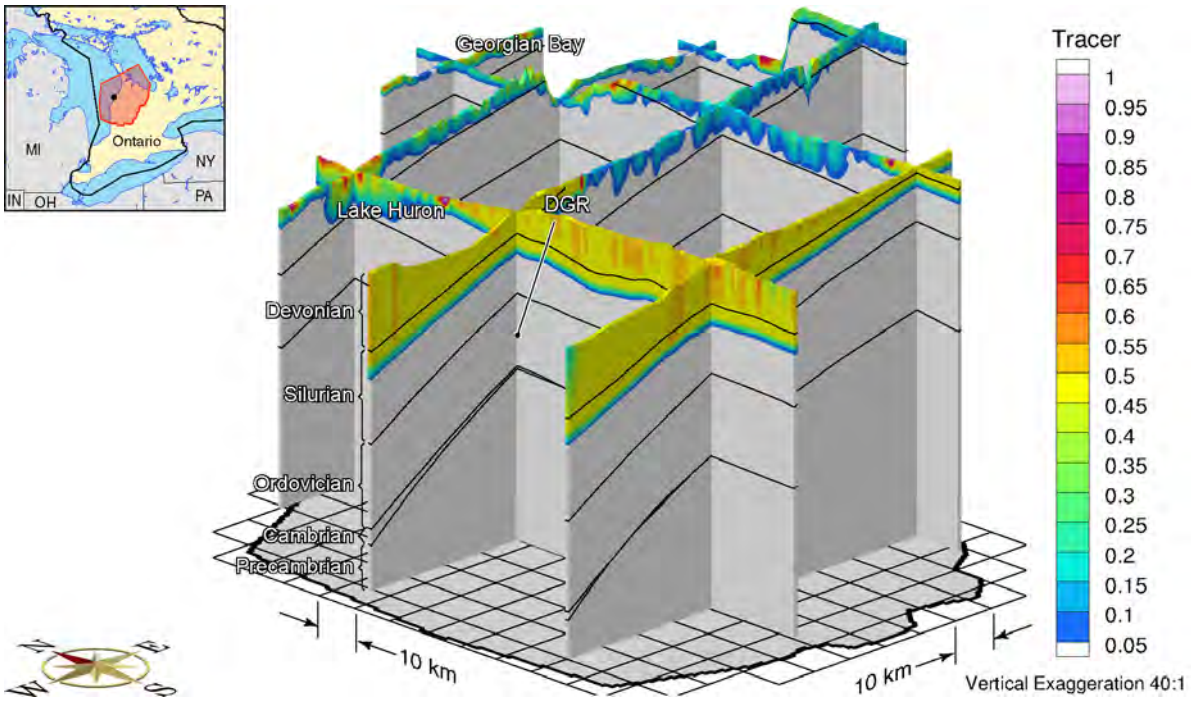

Figure F.161: Fence View Showing the Depth of Penetration of a Tracer at 30ka before Present for the Alternate Paleoclimate Model nn9921 and the Base-case Parameters

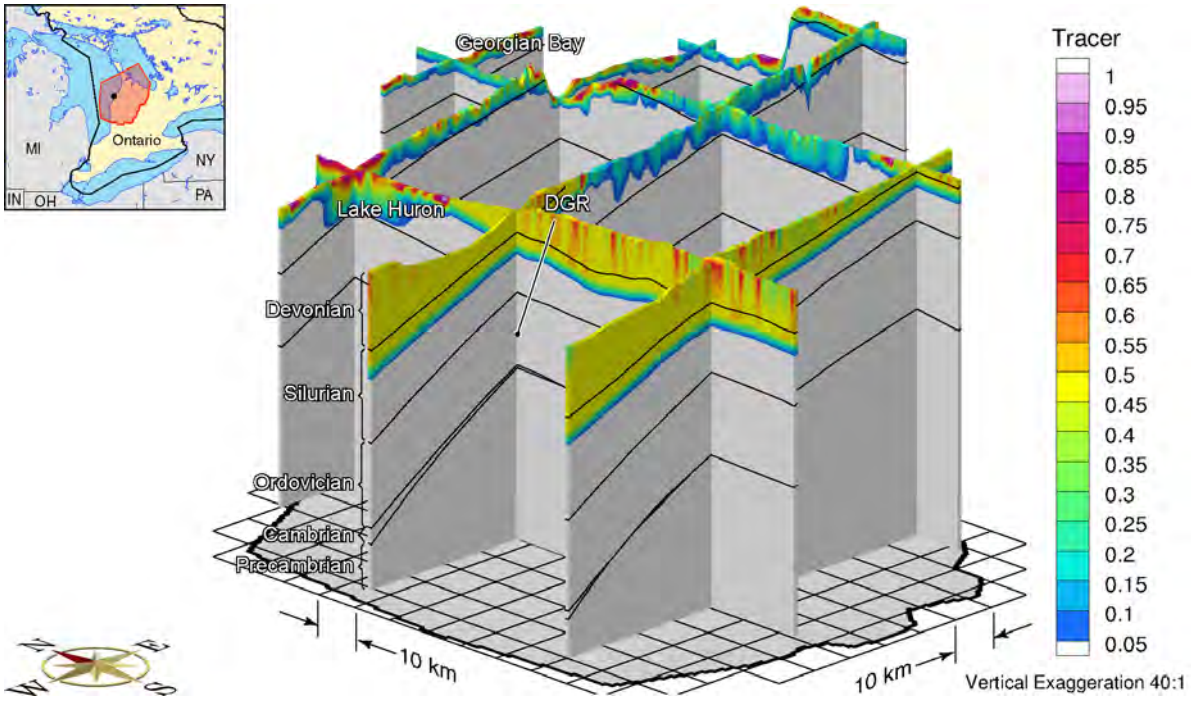

Figure F.162: Fence View Showing the Depth of Penetration of a Tracer at Present for the Alternate Paleoclimate Model nn9921 and the Base-case Parameters

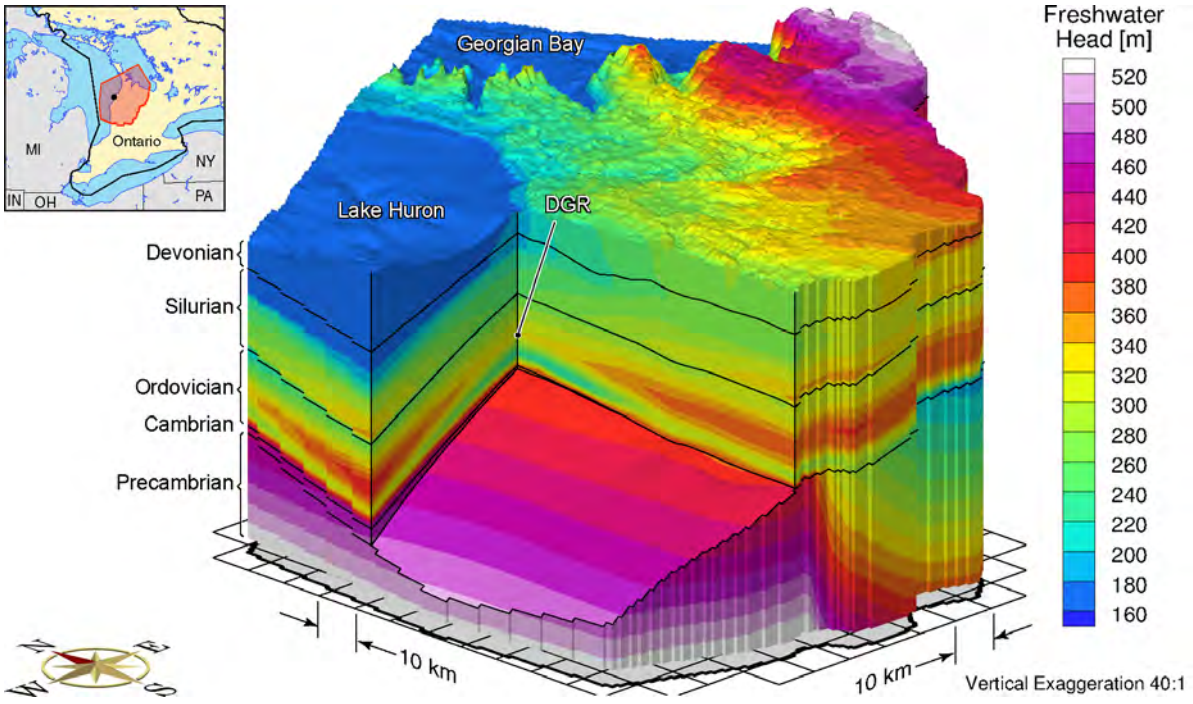

Figure F.163: Block Cut View of Freshwater Heads at Present for the Open Boundary Paleohydrogeologic Model and the Base-case Parameters

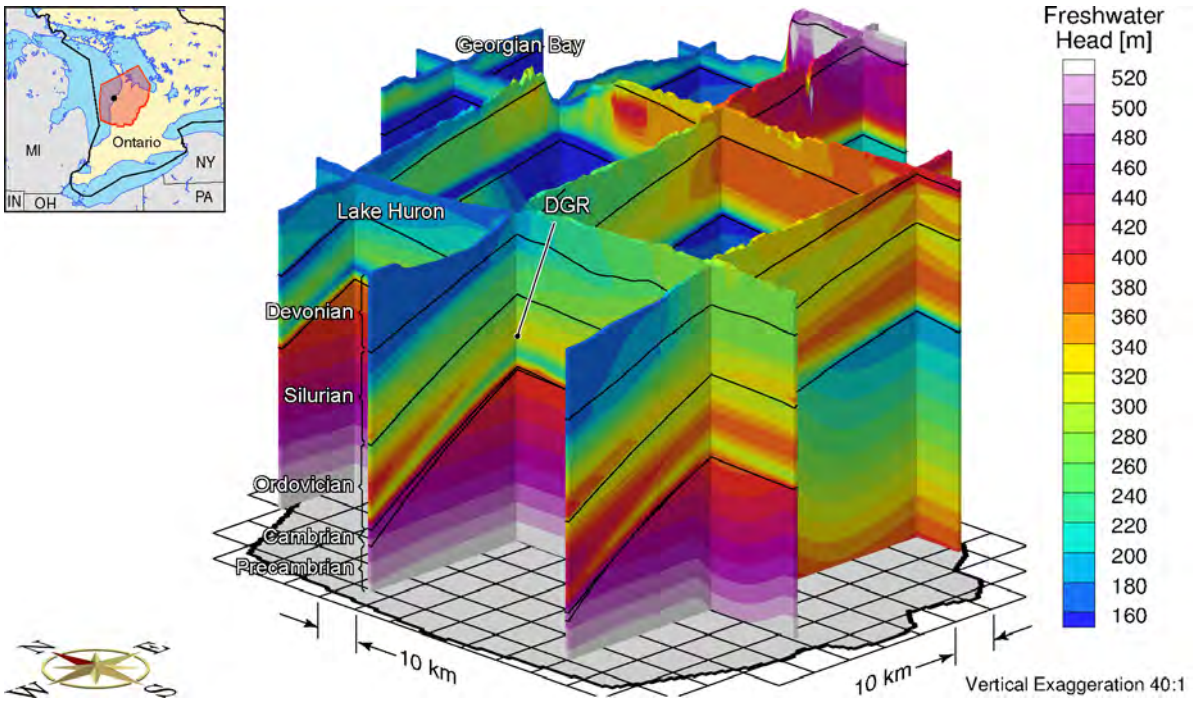

Figure F.164: Fence View of Freshwater Heads at Present for the Open Boundary Paleohydrogeologic Model and the Base-case Parameters

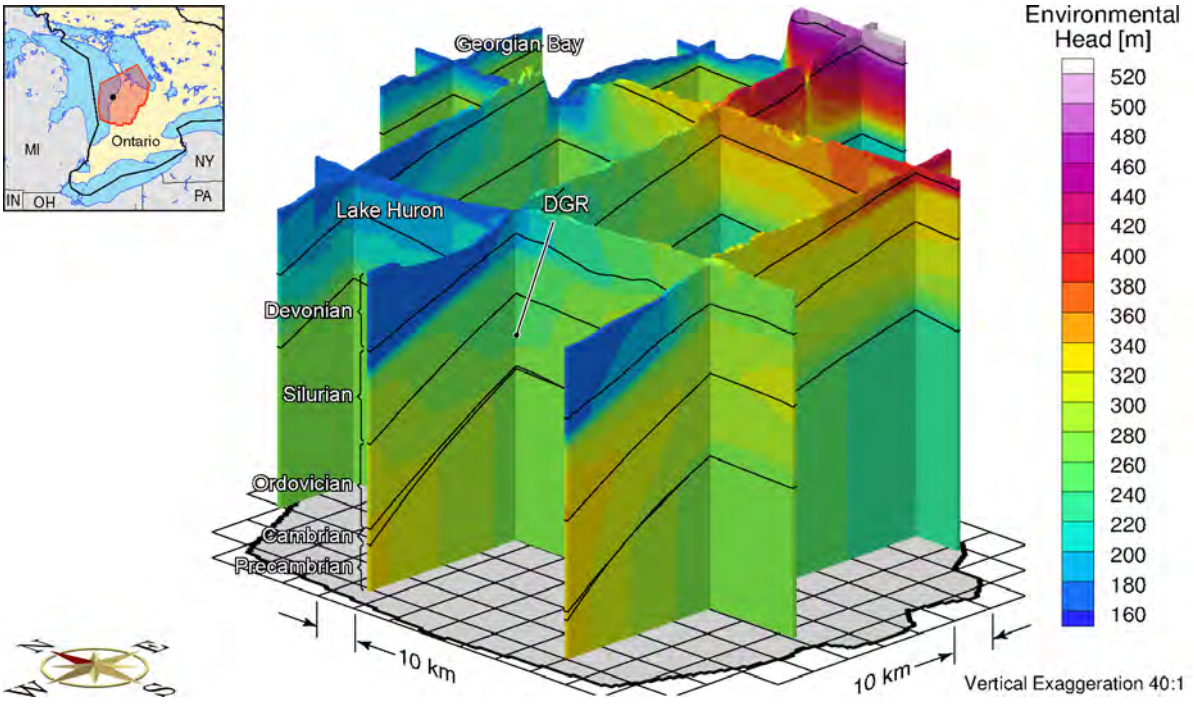

Figure F.165: Fence View of Environmental Heads at 90ka before Present for the Open Boundary Paleohydrogeologic Model and the Base-case Parameters

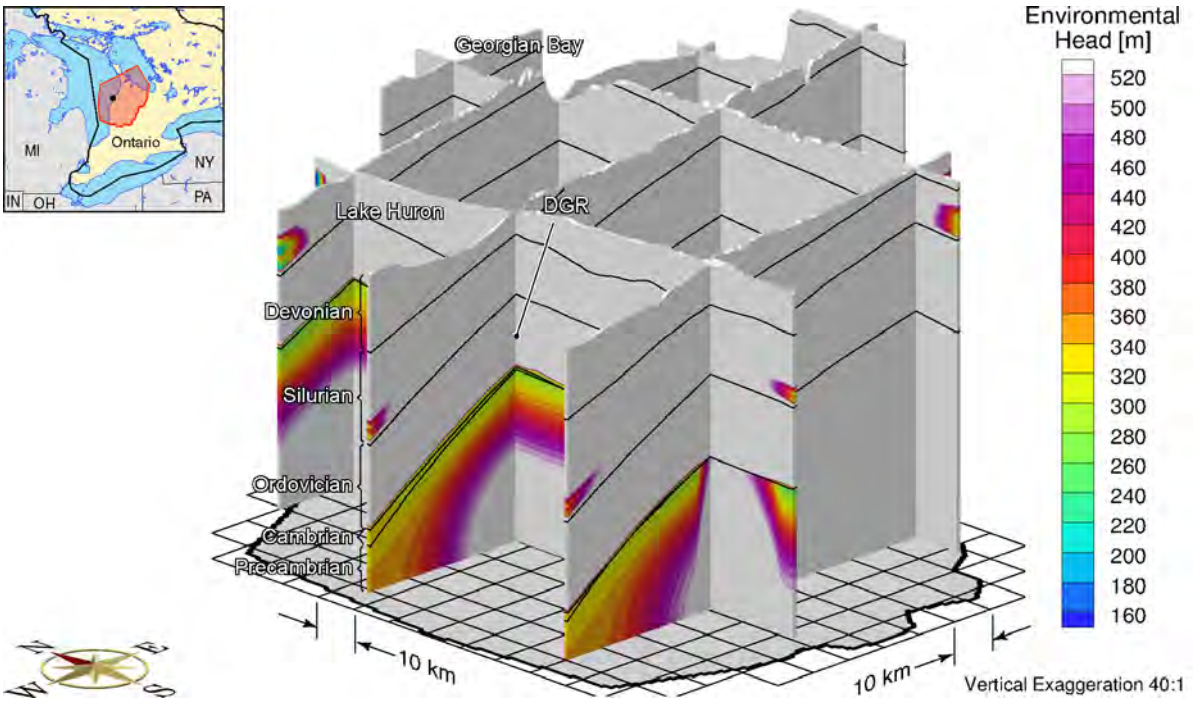

Figure F.166: Fence View of Environmental Heads at 60ka before Present for the Open Boundary Paleohydrogeologic Model and the Base-case Parameters

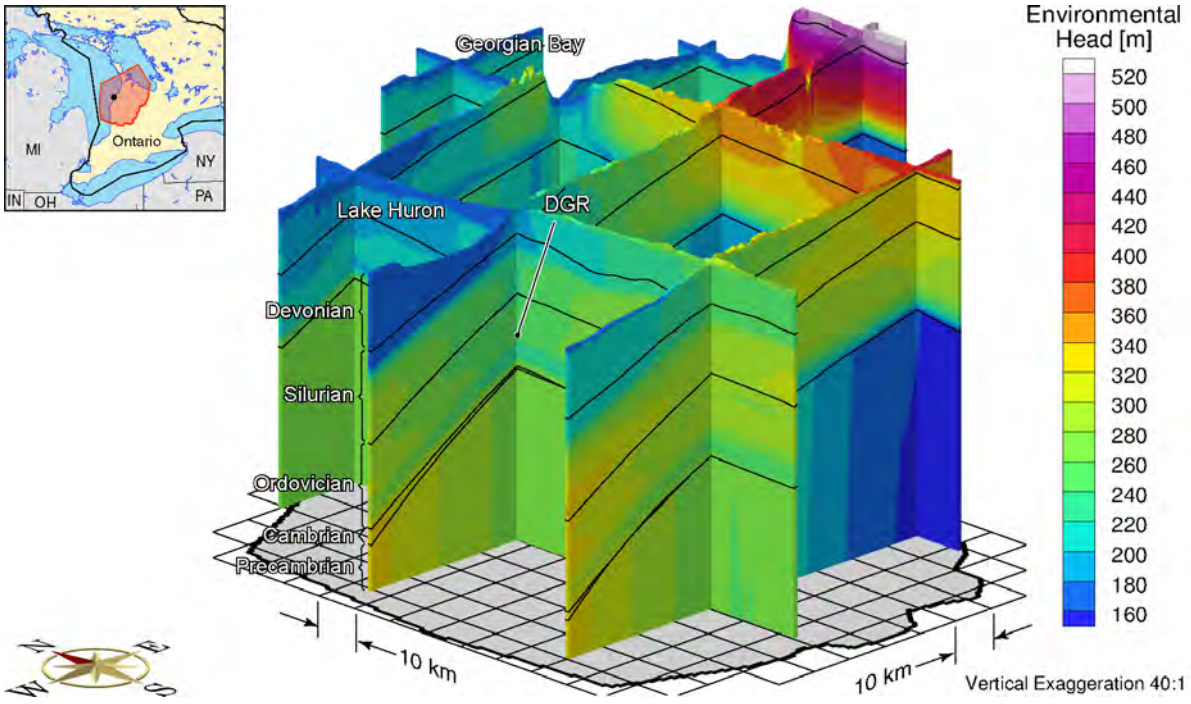

Figure F.167: Fence View of Environmental Heads at 30ka before Present for the Open Boundary Paleohydrogeologic Model and the Base-case Parameters

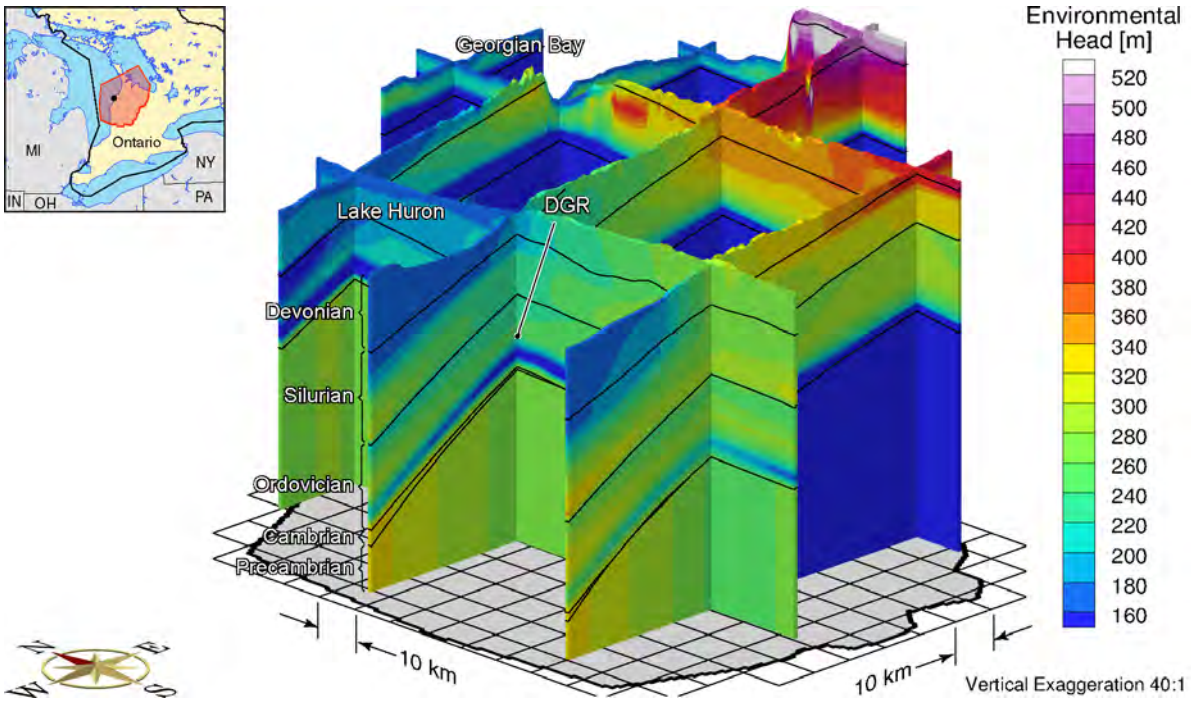

Figure F.168: Fence View of Environmental Heads at the Present for the Open Boundary Paleohydrogeologic Model and the Base-case Parameters

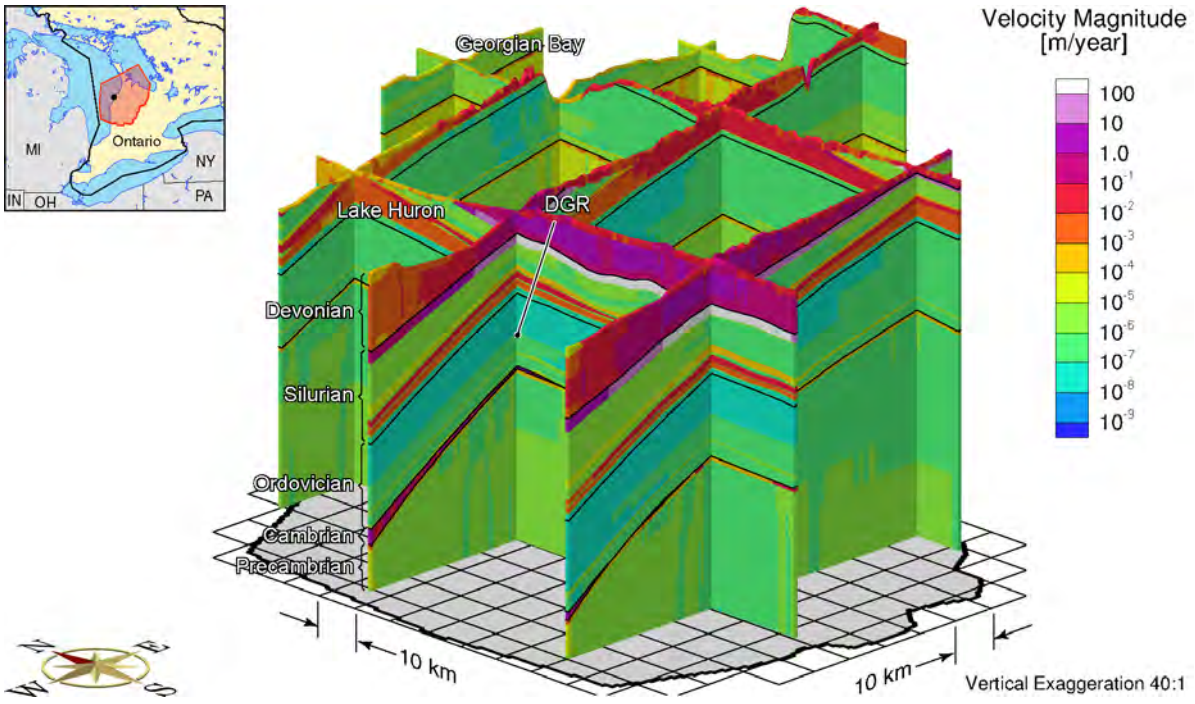

Figure F.169: Fence View of Pore Velocity Magnitude at 90ka before Present for the Open Boundary Paleohydrogeologic Model and the Base-case Parameters

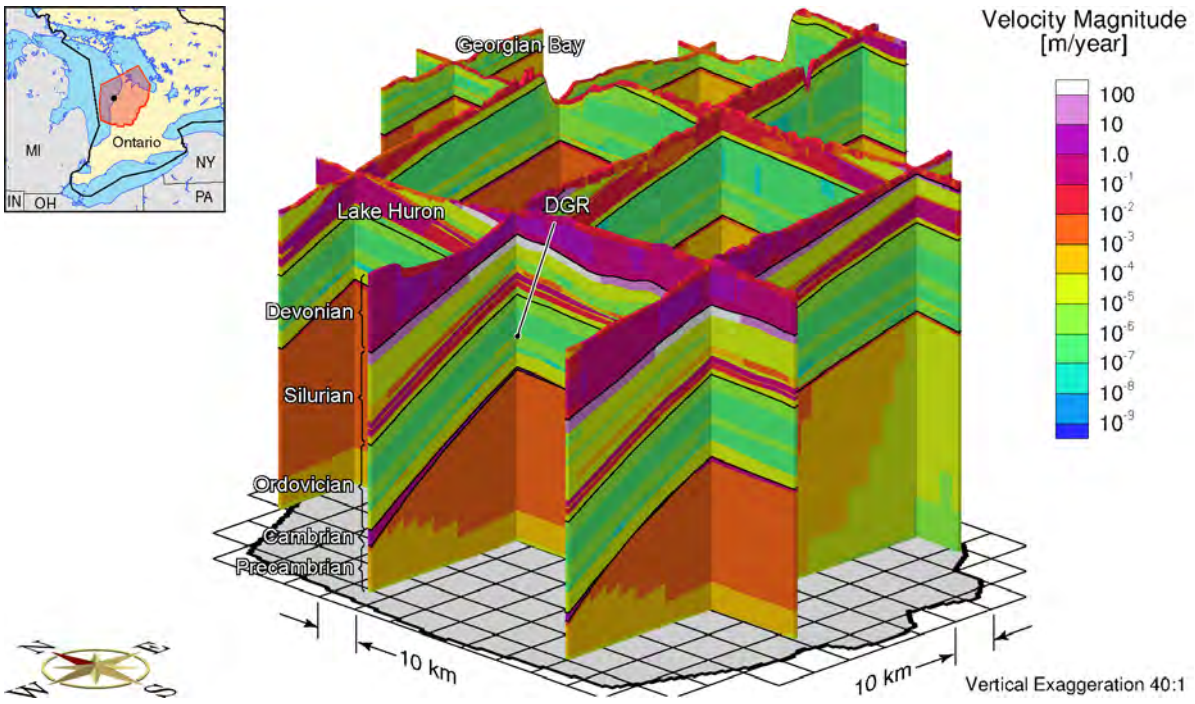

Figure F.170: Fence View of Pore Velocity Magnitude at 60ka before Present for the Open Boundary Paleohydrogeologic Model and the Base-case Parameters

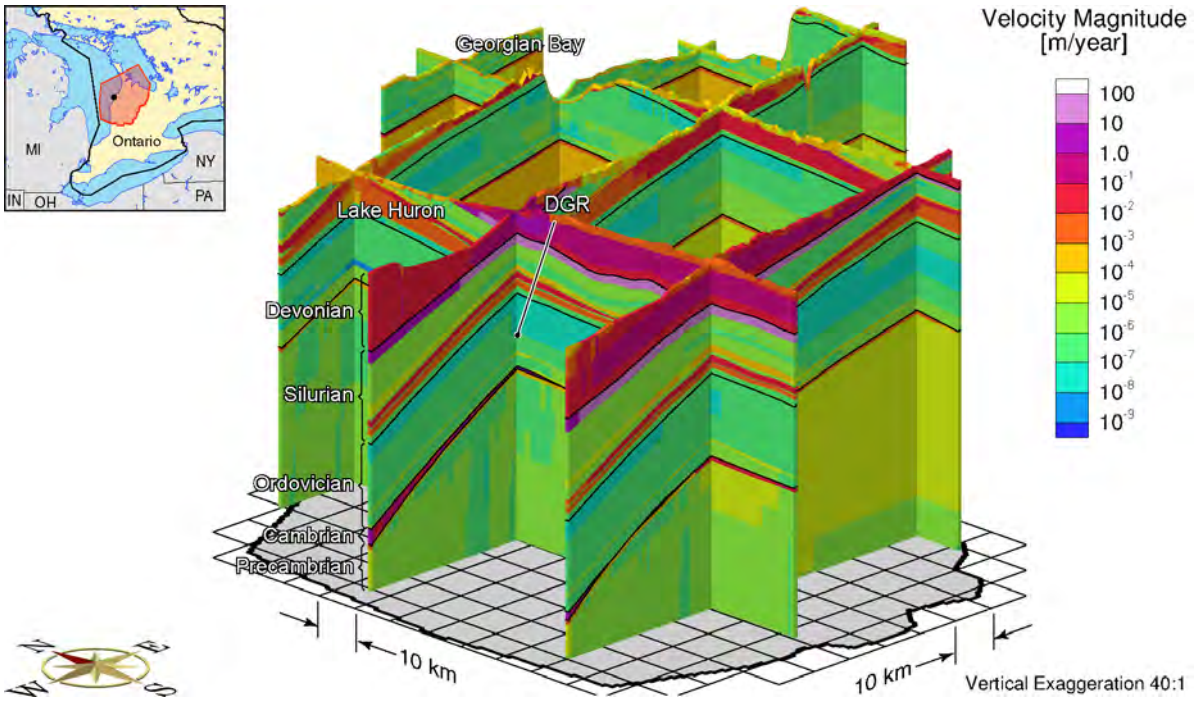

Figure F.171: Fence View of Pore Velocity Magnitude at 30ka before Present for the Open Boundary Paleohydrogeologic Model and the Base-case Parameters

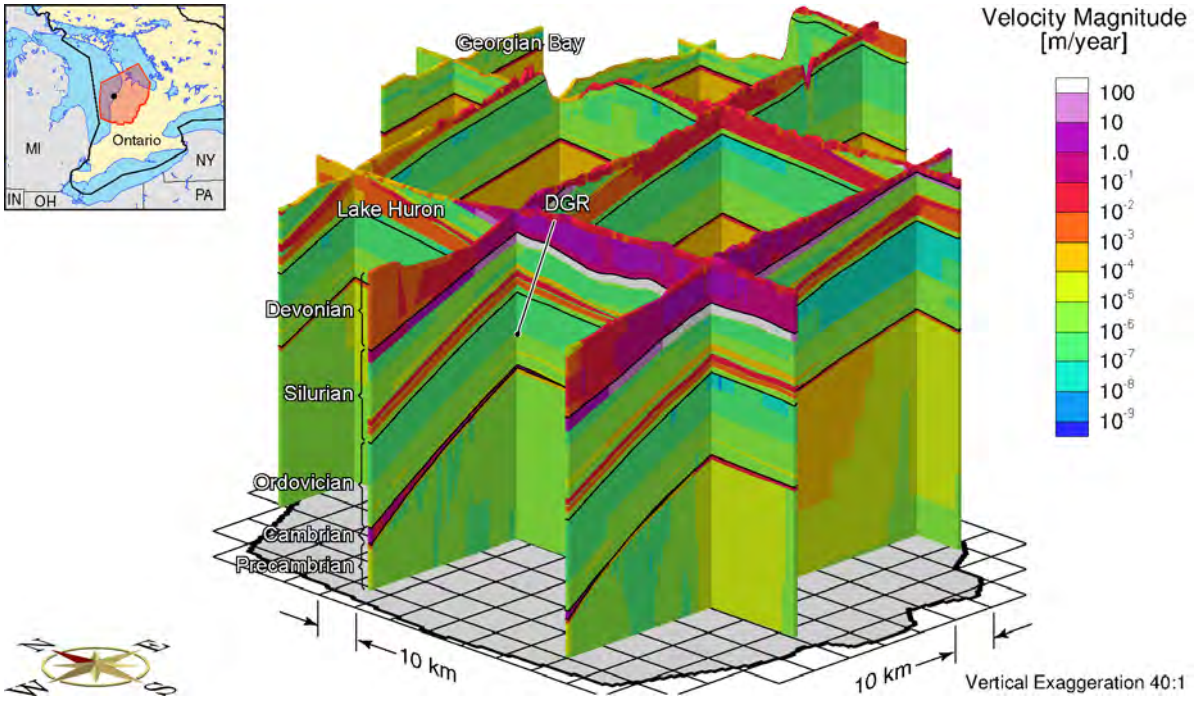

Figure F.172: Fence View of Pore Velocity Magnitude at Present for the Open Boundary Paleohydrogeologic Model and the Base-case Parameters

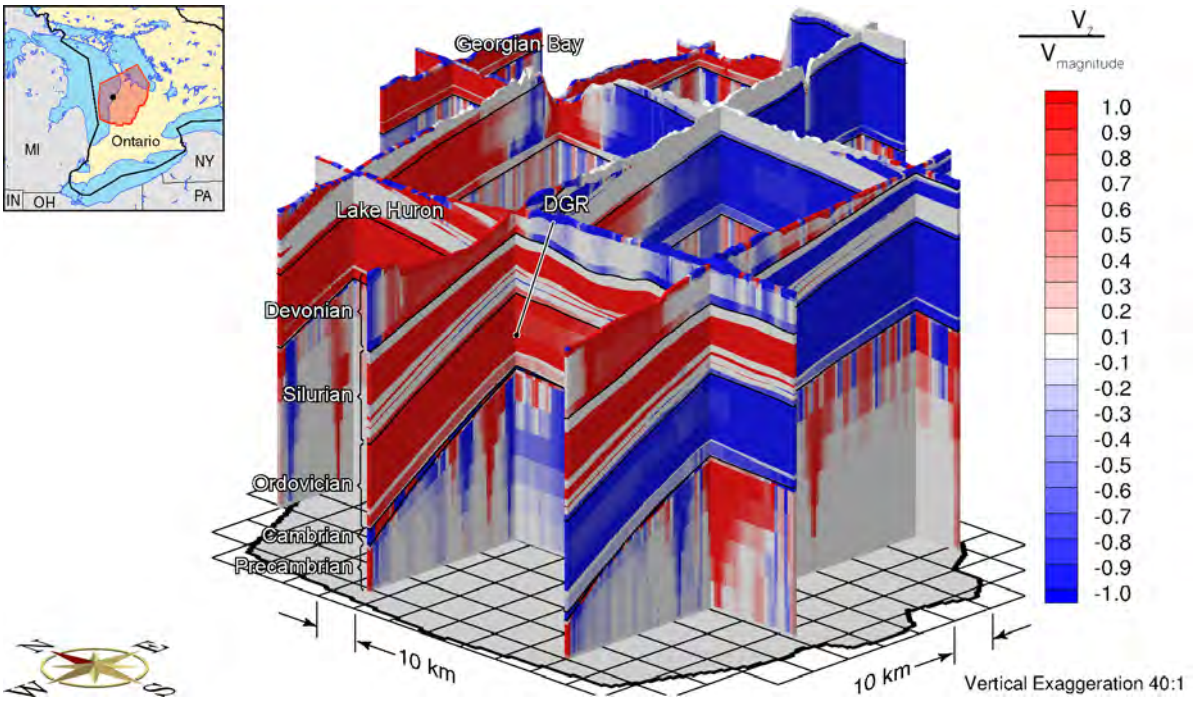

Figure F.173: Fence View Showing the Ratio of the Vertical Pore Water Velocity to the Velocity Magnitude at 90ka before Present for the Open Boundary Paleohydrogeologic Model and the Base-case Parameters

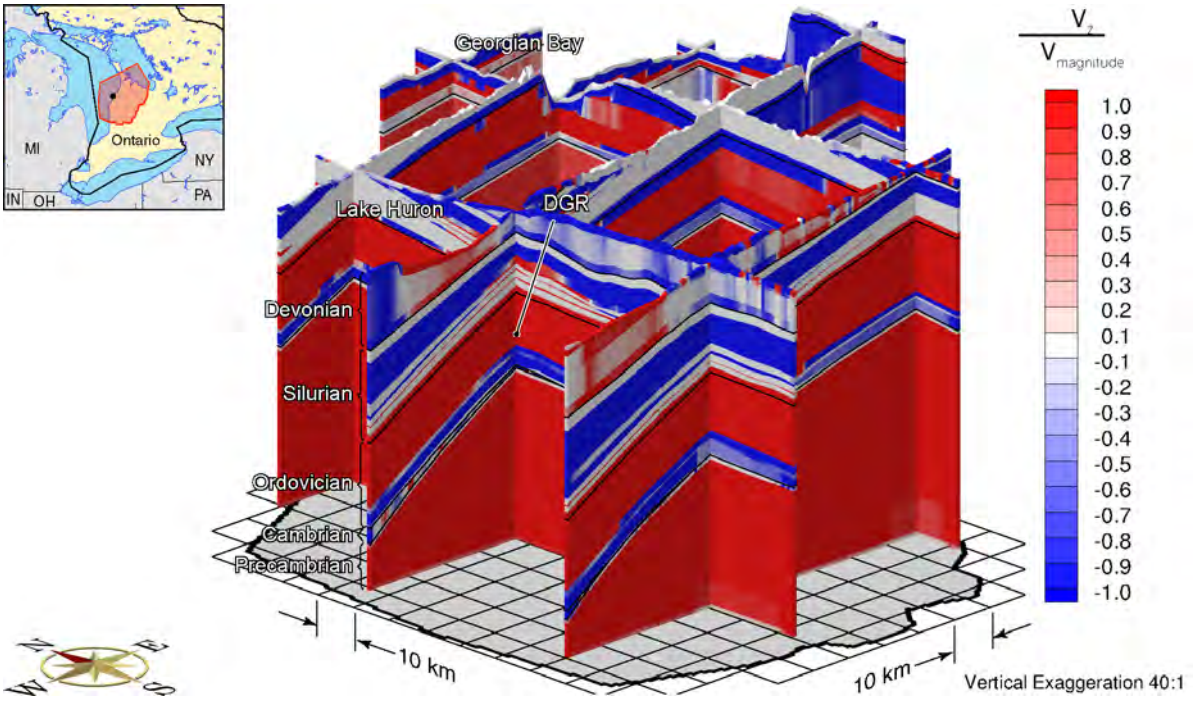

Figure F.174: Fence View Showing the Ratio of the Vertical Pore Water Velocity to the Velocity Magnitude at 60ka before Present for the Open Boundary Paleohydrogeologic Model and the Base-case Parameters

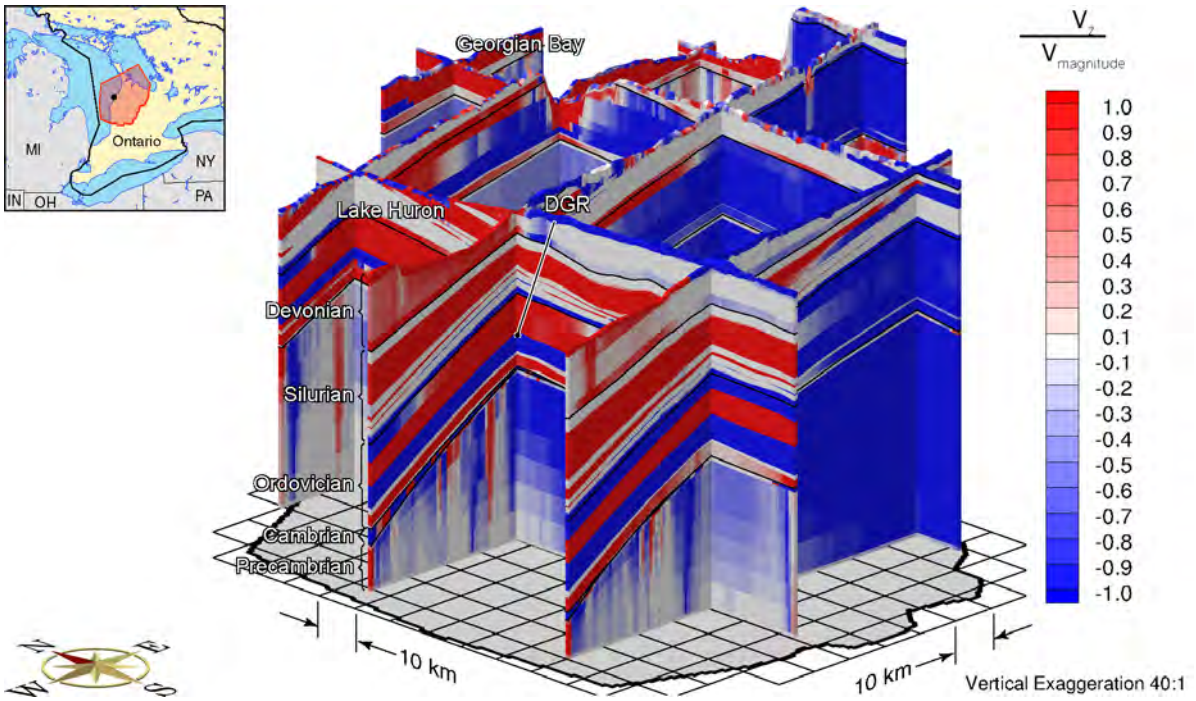

Figure F.175: Fence View Showing the Ratio of the Vertical Pore Water Velocity to the Velocity Magnitude at 30ka before Present for the Open Boundary Paleohydrogeologic Model and the Base-case Parameters

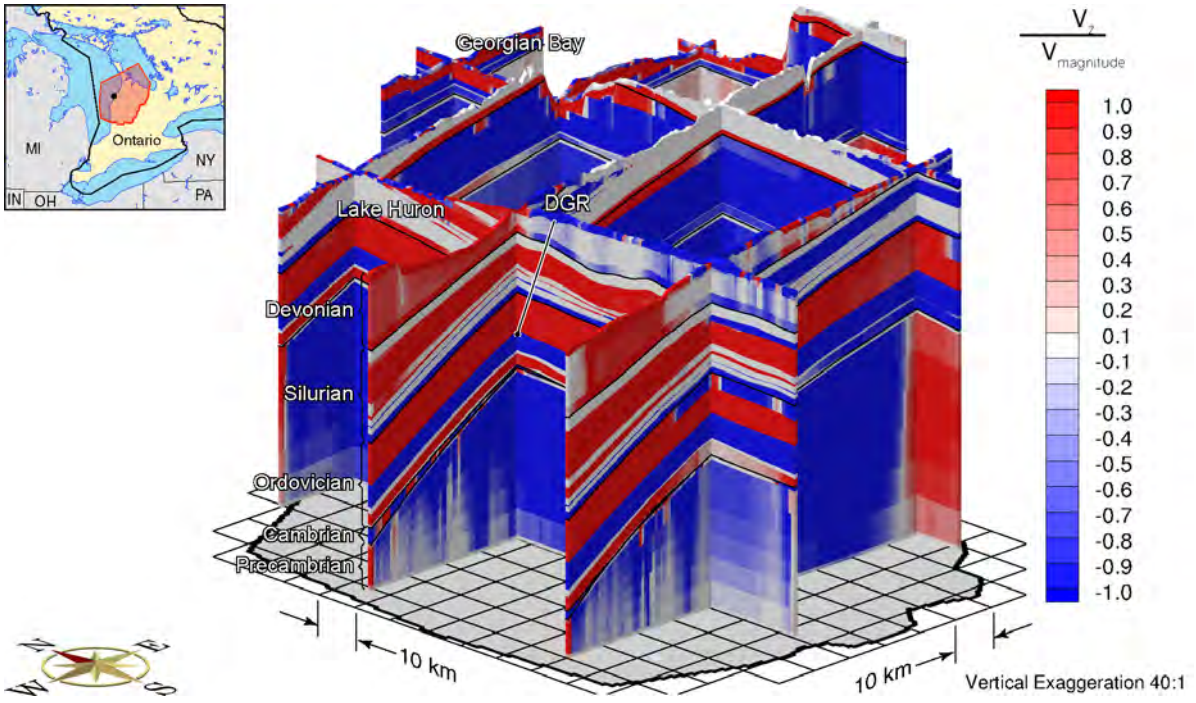

Figure F.176: Fence View of Ratio of Vertical Pore Velocity to Pore Velocity Magnitude at Present for the Open Boundary Paleohydrogeologic Model and the Base-case Parameters

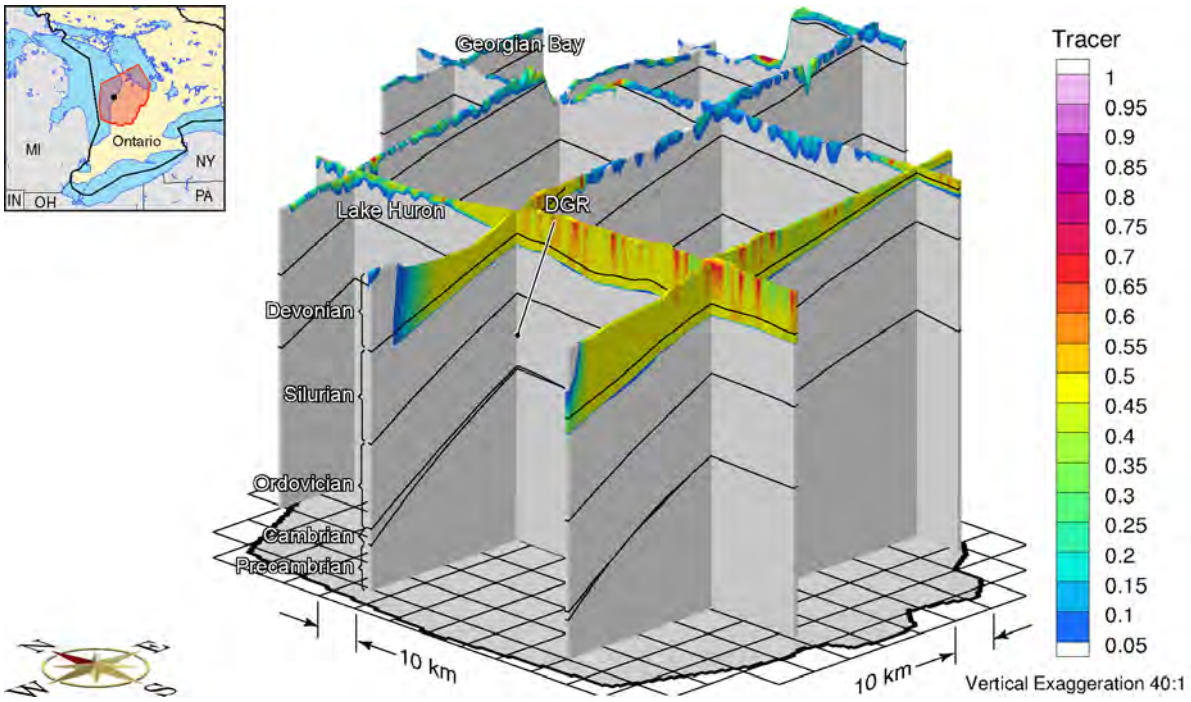

Figure F.177: Fence View Showing the Depth of Penetration of a Tracer at 90ka before Present for the Open Boundary Paleohydrogeologic Model and the Base-case Parameters

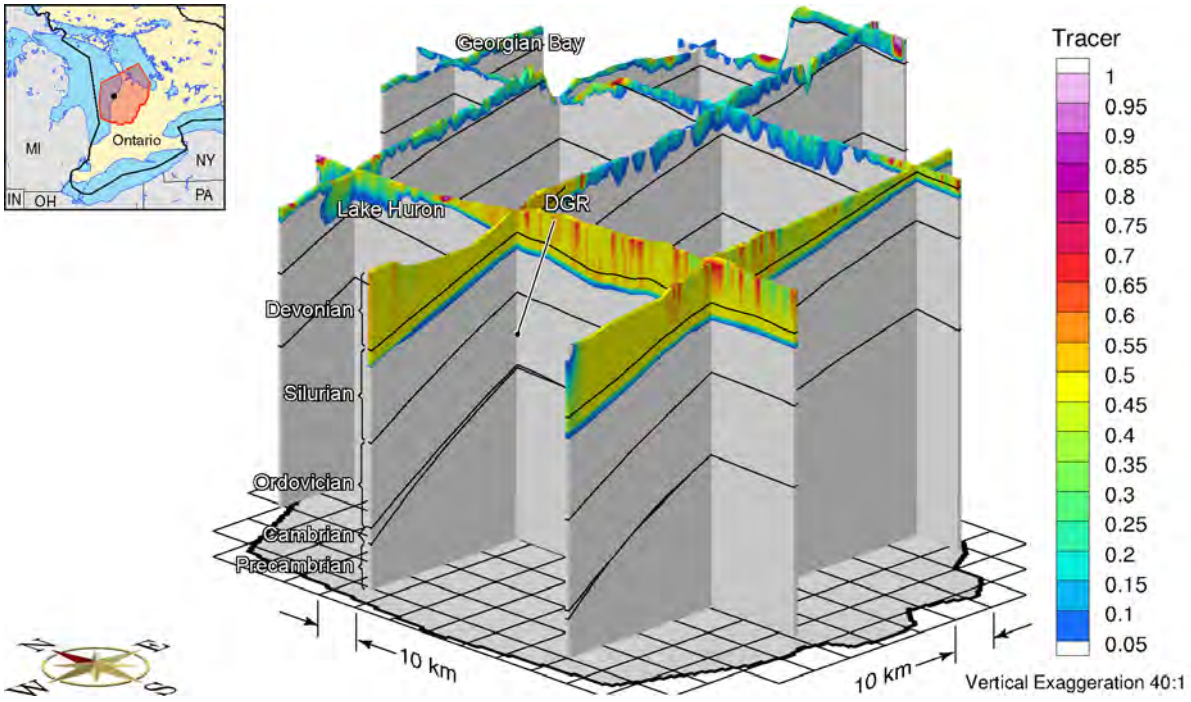

Figure F.178: Fence View Showing the Depth of Penetration of a Tracer at 60ka before Present for the Open Boundary Paleohydrogeologic Model and the Base-case Parameters

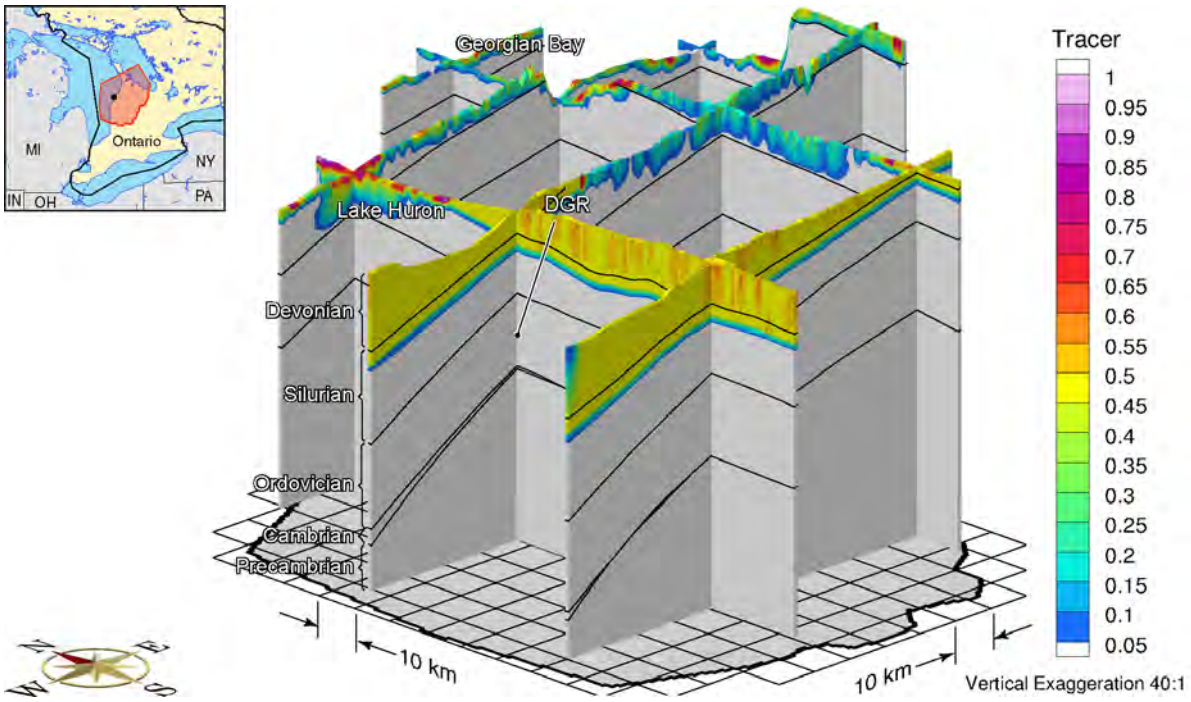

Figure F.179: Fence View Showing the Depth of Penetration of a Tracer at 30ka before Present for the Open Boundary Paleohydrogeologic Model and the Base-case Parameters

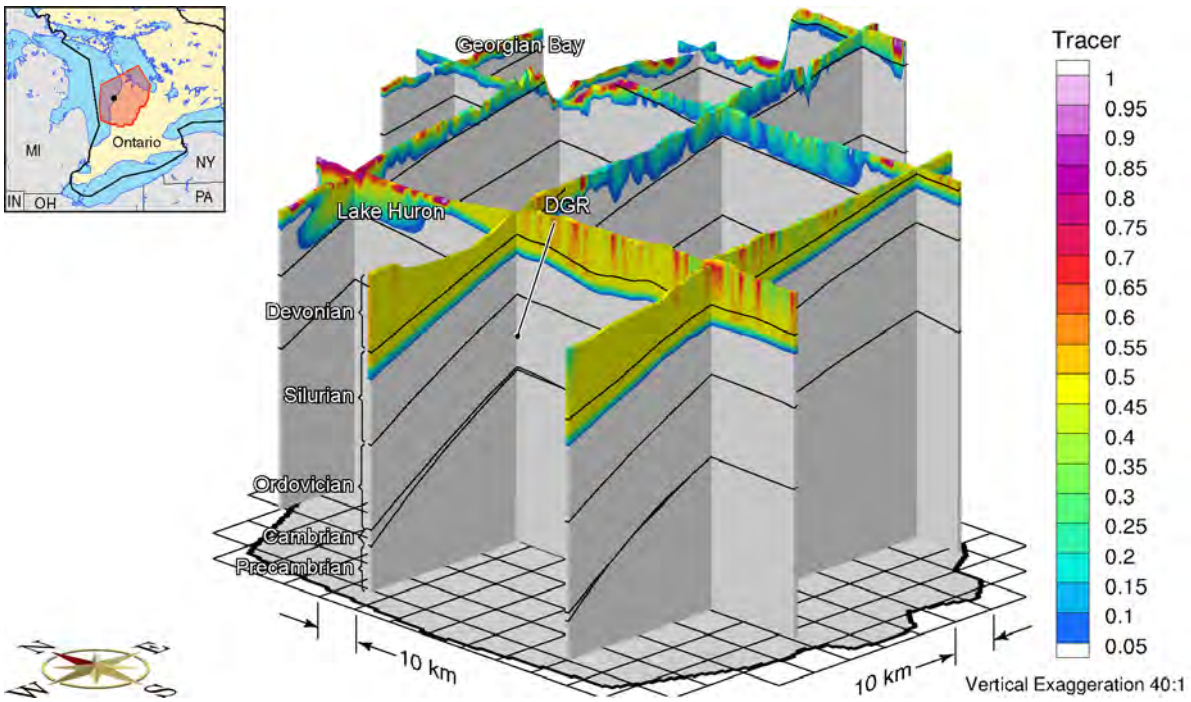

Figure F.180: Fence View Showing the Depth of Penetration of a Tracer at Present for the Open Boundary Paleohydrogeologic Model and the Base-case Parameters

THIS PAGE HAS BEEN LEFT BLANK INTENTIONALLY

APPENDIX G: ANALYSIS OF MICHIGAN BASIN CROSS-SECTION

LIST OF FIGURES

Page

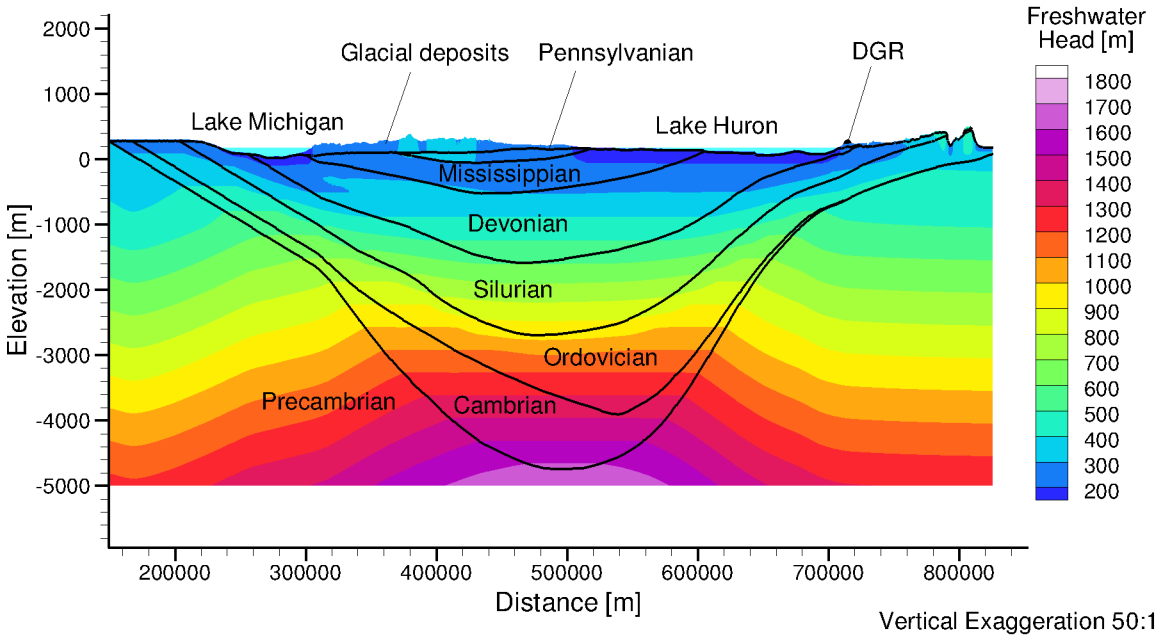

Figure G.1: Hypothetical Higher Permeability Zone in the Precambrian: Freshwater Heads for Defined TDS Distribution

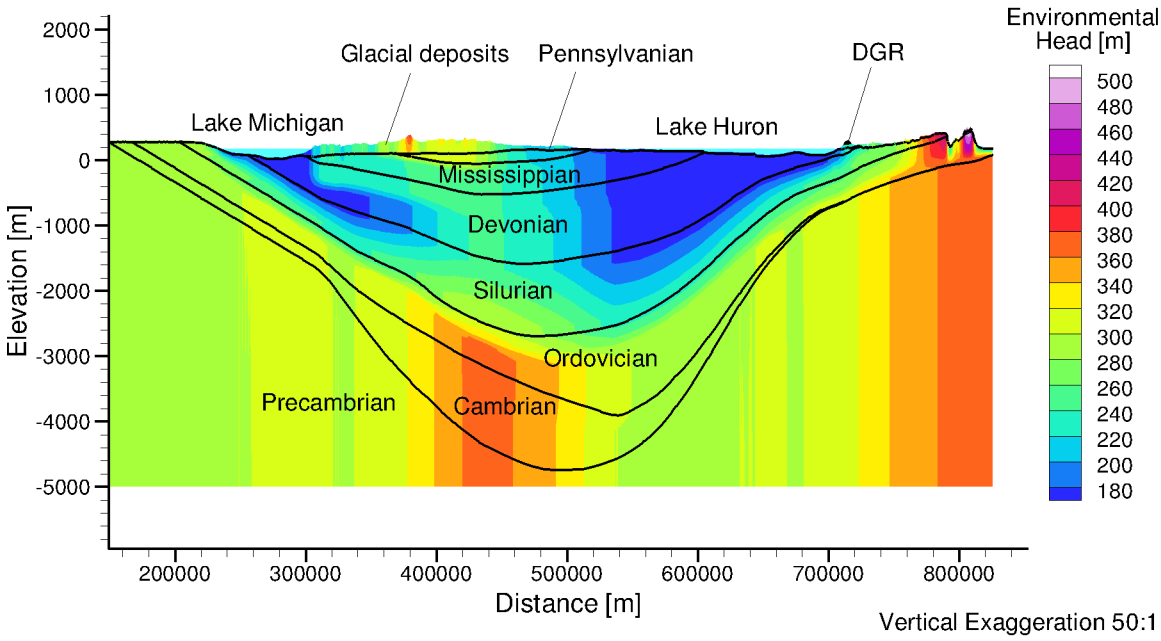

Figure G.2: Hypothetical Higher Permeability Zone in the Precambrian: Environmental Heads for Defined TDS Distribution

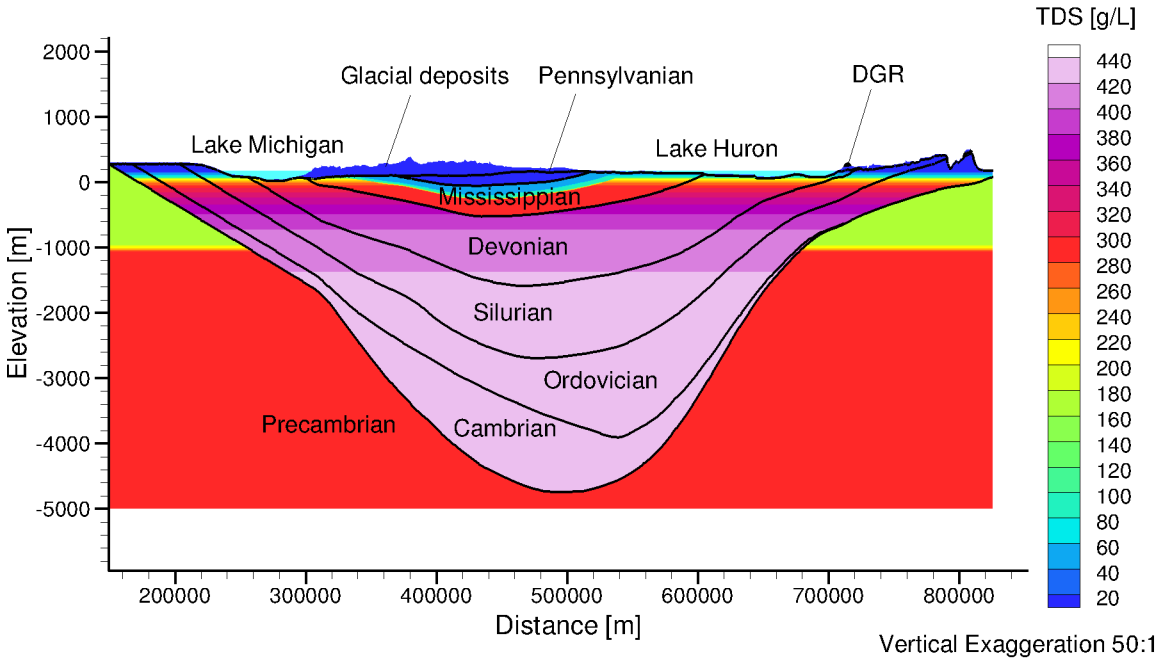

Figure G.3: Initial Total Dissolved Solids Distribution for Intera TDS Versus Fluid Density Relationship

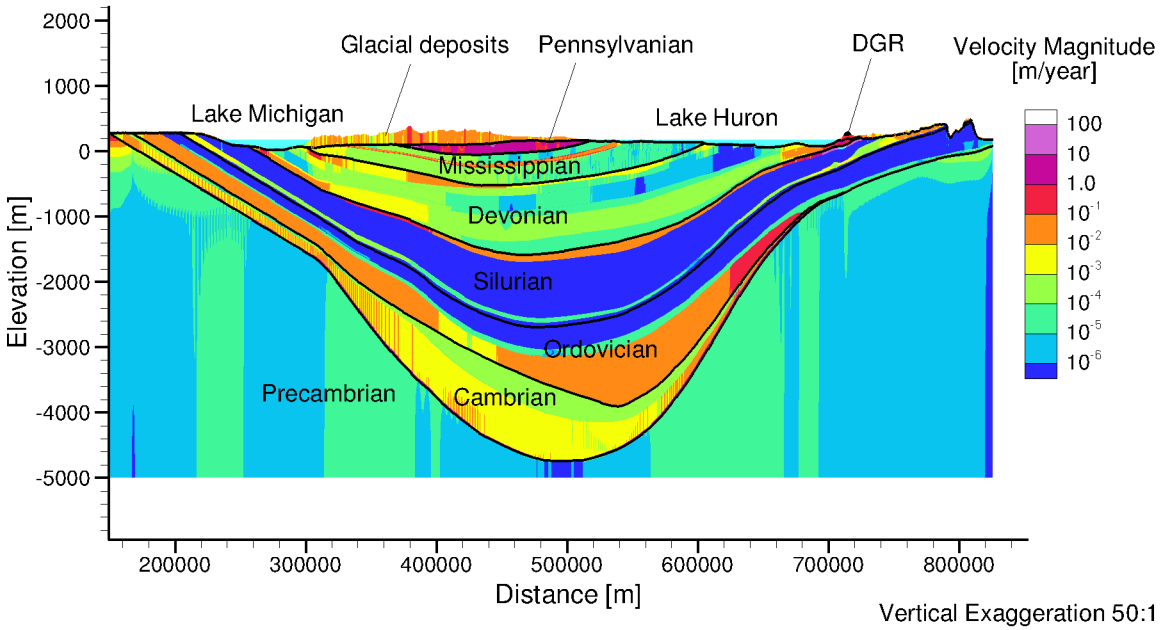

Figure G.4: Pore Water Velocity Magnitude for the Intera TDS Versus Fluid Density Relationship

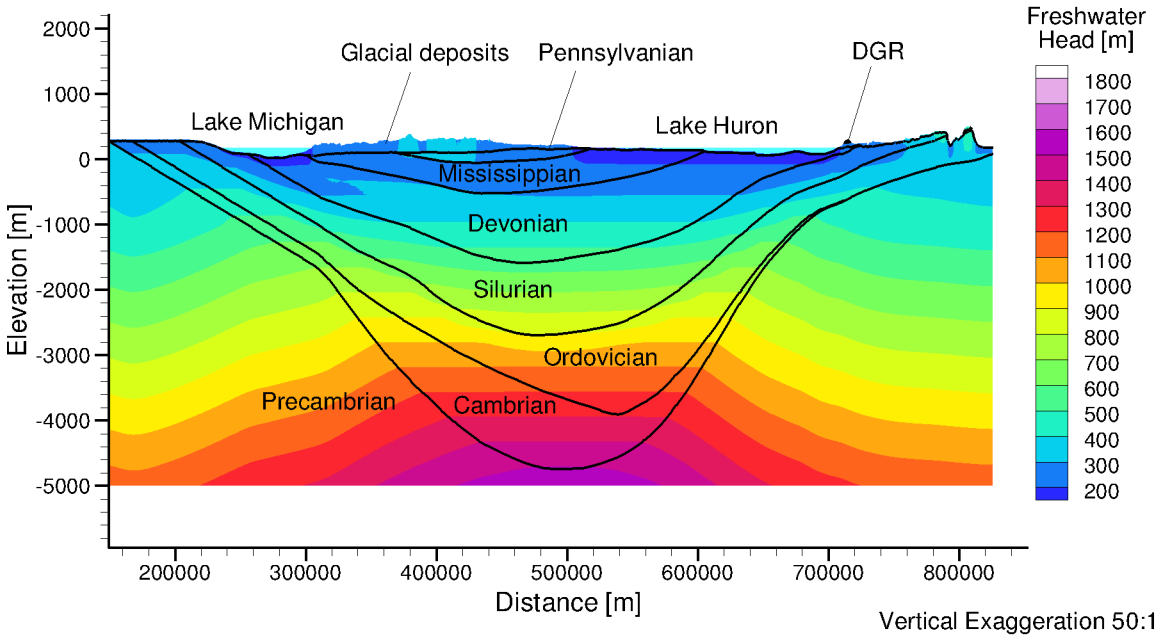

Figure G.5: Freshwater Heads for the Intera TDS Versus Fluid Density Relationship

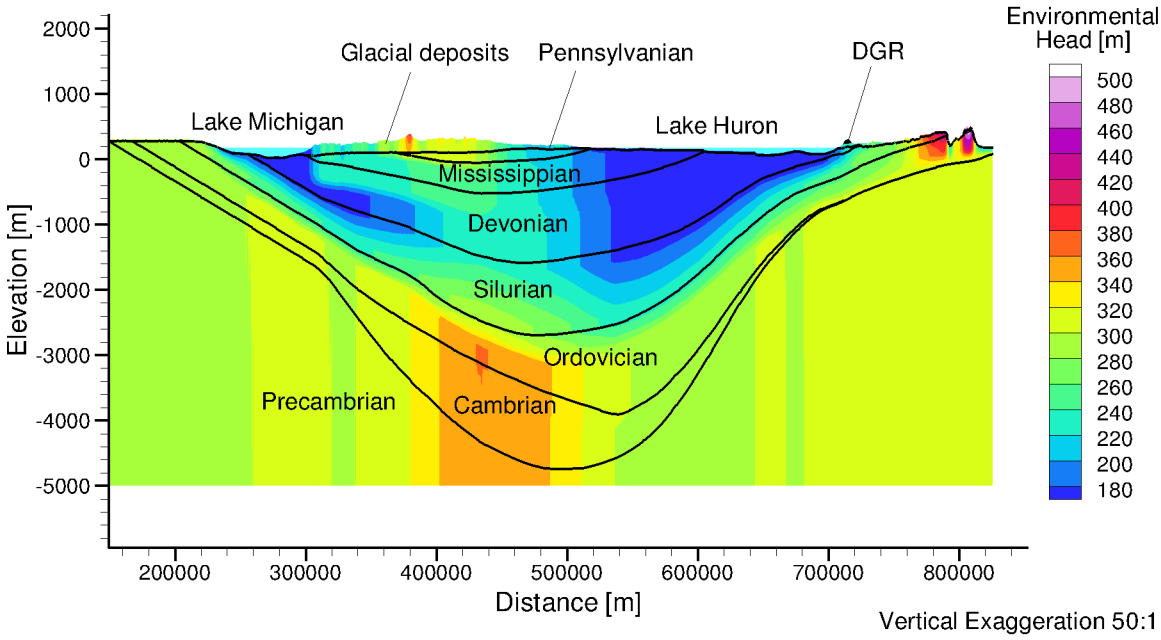

Figure G.6: Environmental Heads for the Intera TDS Versus Fluid Density Relationship

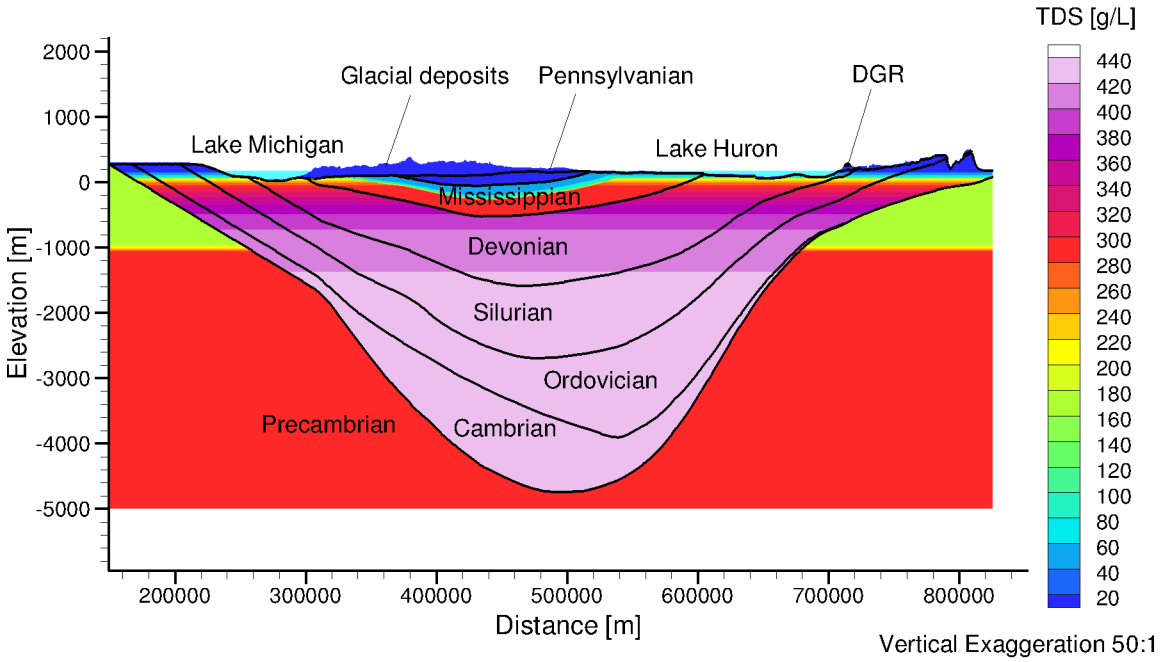

Figure G.7: Initial Total Dissolved Solids Distribution for the USGS TDS Versus Fluid Density Relationship

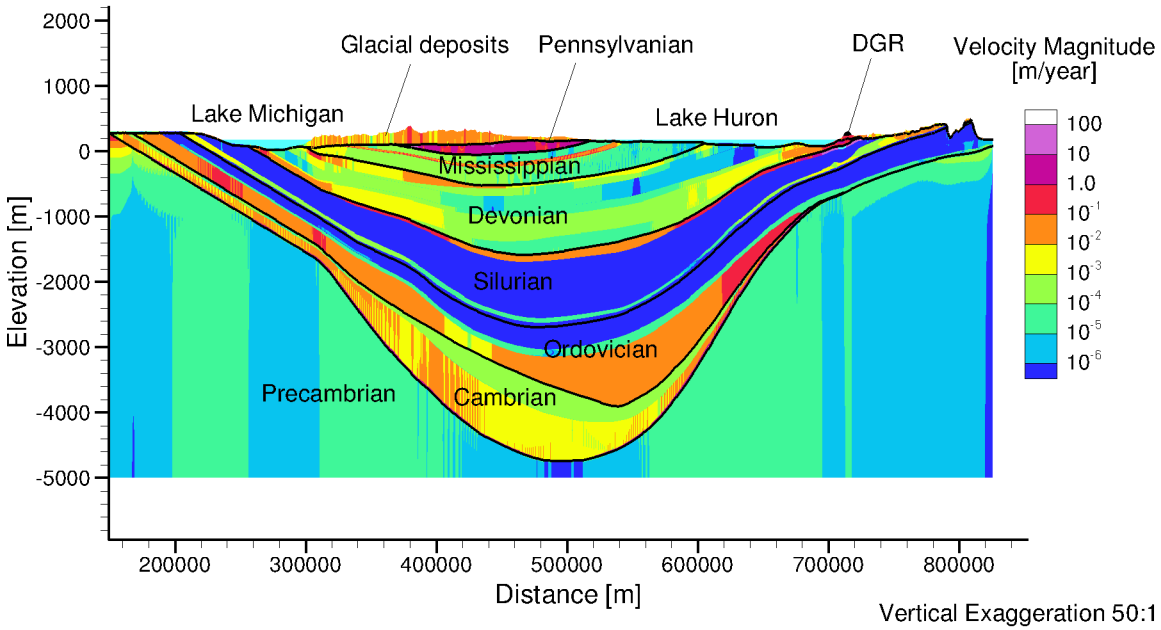

Figure G.8: Pore Water Velocity Magnitude for the USGS TDS Versus Fluid Density Relationship

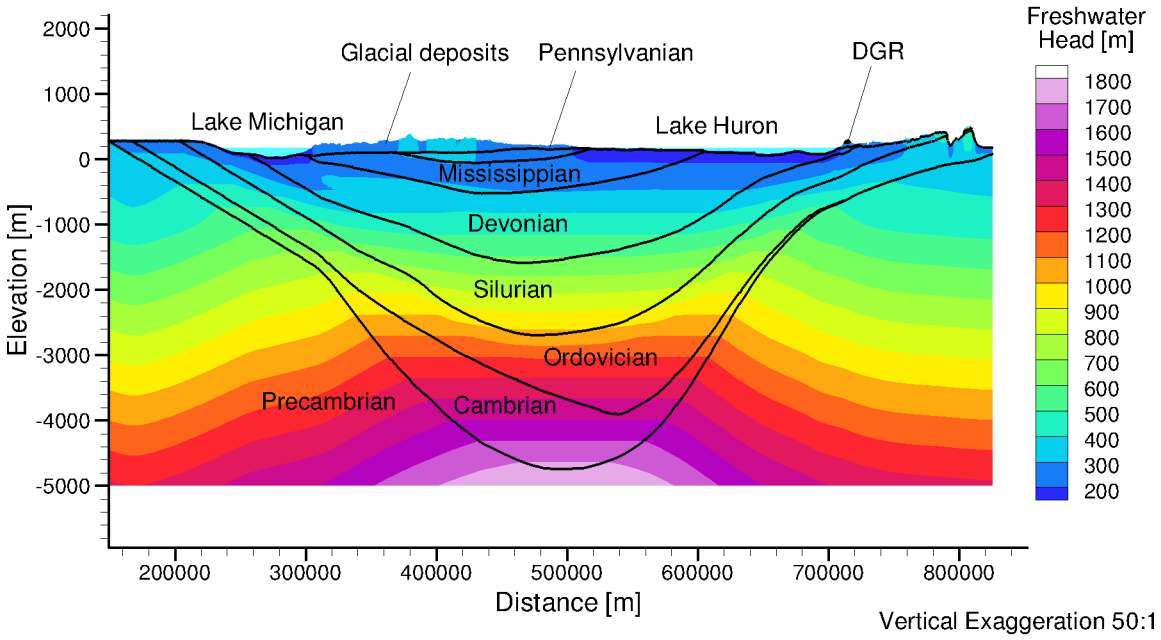

Figure G.9: Freshwater Heads for the USGS TDS Versus Fluid Density Relationship

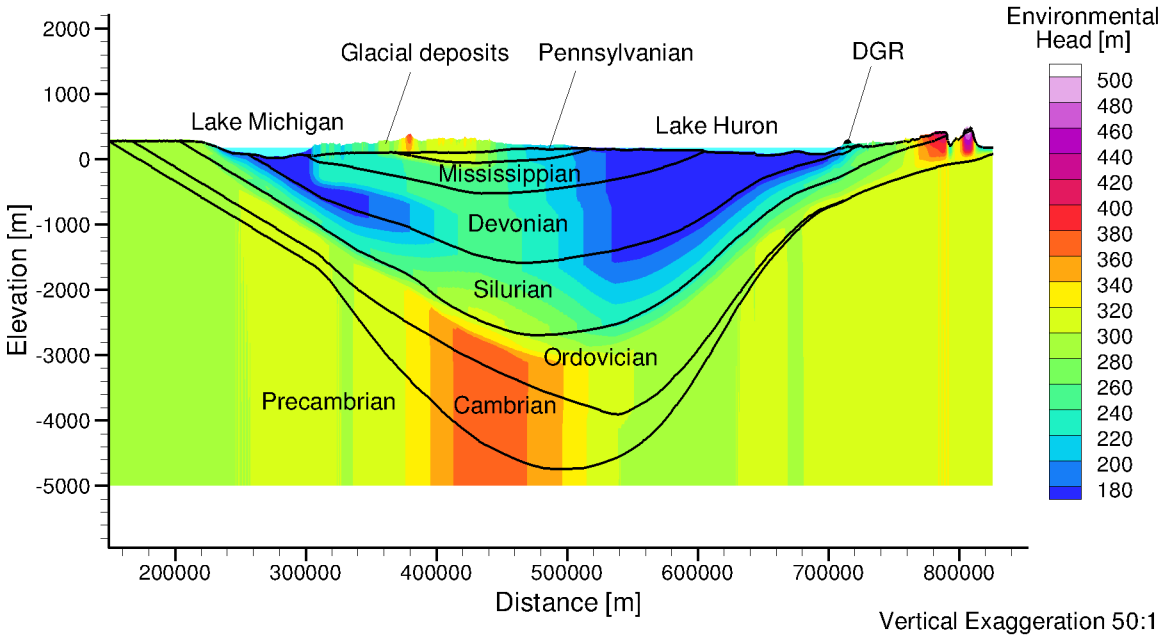

Figure G.10: Environmental Heads for the USGS TDS Versus Fluid Density Relationship